„Derivation of forest inventory parameters from high-resolution satellite imagery for the Thunkel area, Northern Mongolia. A comparative study on various satellite sensors and data analysis techniques.”

Dissertation

zur Erlangung des mathematisch-naturwissenschaftlichen Doktorgrades
"Doctor rerum naturalium"
der Georg-August-Universität Göttingen

im Promotionsprogramm Geowissenschaften / Geographie
der Georg-August University School of Science (GAUSS)

vorgelegt von / submitted by

Holger Vogt

aus Mainz

Göttingen 2021

Betreuungsausschuss / advisory board members:

1. Prof. Dr. Martin Kappas, Abteilung Kartographie, GIS und Fernerkundung, Geographisches Institut, Fakultät für Geowissenschaften und Geographie, Universität Göttingen
2. Dr. Dominik Seidel, Waldbau und Waldökologie der gemäßigten Zonen, Fakultät für Forstwissenschaften und Waldökologie, Universität Göttingen
3. Prof. Dr. Daniela Sauer, Geographisches Institut, Abteilung Physische Geographie, Fakultät für Geowissenschaften und Geographie, Universität Göttingen
4. Dr. Daniel Wyss, Abteilung Kartographie, GIS und Fernerkundung, Geographisches Institut, Fakultät für Geowissenschaften und Geographie, Universität Göttingen
5. Prof. Dr. Heiko Faust, Geographisches Institut, Abteilung Humangeographie, Fakultät für Geowissenschaften und Geographie, Universität Göttingen
6. Prof. Dr. Christian Ammer, Waldbau und Waldökologie der gemäßigten Zonen, Fakultät für Forstwissenschaften und Waldökologie, Universität Göttingen
7. Prof. Dr. Ralph Mitlöhner, Waldbau und Waldökologie der Tropen, Fakultät für Forstwissenschaften und Waldökologie, Universität Göttingen

Mitglieder der Prüfungskommission / members of the examination commission

Referent: Prof. Dr. Martin Kappas, Abteilung Kartographie, GIS und Fernerkundung, Geographisches Institut, Fakultät für Geowissenschaften und Geographie, Universität Göttingen
Korreferent: Dr. Dominik Seidel, Waldbau und Waldökologie der gemäßigten Zonen, Fakultät für Forstwissenschaften und Waldökologie, Universität Göttingen

weitere Mitglieder der Prüfungskommission:

1. Prof. Dr. Daniela Sauer, Geographisches Institut, Abteilung Physische Geographie, Fakultät für Geowissenschaften und Geographie, Universität Göttingen
2. Dr. Daniel Wyss, Abteilung Kartographie, GIS und Fernerkundung, Geographisches Institut, Fakultät für Geowissenschaften und Geographie, Universität Göttingen
3. Prof. Dr. Heiko Faust, Geographisches Institut, Abteilung Humangeographie, Fakultät für Geowissenschaften und Geographie, Universität Göttingen
4. Prof. Dr. Christian Ammer, Waldbau und Waldökologie der gemäßigten Zonen, Fakultät für Forstwissenschaften und Waldökologie, Universität Göttingen
5. Prof. Dr. Ralph Mitlöhner, Waldbau und Waldökologie der Tropen, Fakultät für Forstwissenschaften und Waldökologie, Universität Göttingen

Tag der mündlichen Prüfung / date of thesis defense: 10.05.2021

Table of Contents

I. Summary

With the demise of the Soviet Union and the transition to a market economy starting in the 1990s, Mongolia has been experiencing dramatic changes resulting in social and economic disparities and an increasing strain on its natural resources. The situation is exacerbated by a changing climate, the erosion of forestry related administrative structures, and a lack of law enforcement activities. Mongolia's forests have been afflicted with a dramatic increase in degradation due to human and natural impacts such as overexploitation and wildfire occurrences. In addition, forest management practices are far from being sustainable. In order to provide useful information on how to viably and effectively utilise the forest resources in the future, the gathering and analysis of forest related data is pivotal. Although a National Forest Inventory was conducted in 2016, very little reliable and scientifically substantiated information exists related to a regional or even local level. This lack of detailed information warranted a study performed in the Thunkel taiga area in 2017 in cooperation with the GIZ. In this context, we hypothesise that (i) tree species and composition can be identified utilising the aerial imagery, (ii) tree height can be extracted from the resulting canopy height model with accuracies commensurate with field survey measurements, and (iii) high-resolution satellite imagery is suitable for the extraction of tree species, the number of trees, and the upscaling of timber volume and basal area based on the spectral properties.

The outcomes of this study illustrate quite clearly the potential of employing UAV imagery for tree height extraction (R^2 of 0.9) as well as for species and crown diameter determination. However, in a few instances, the visual interpretation of the aerial photographs were determined to be superior to the computer-aided automatic extraction of forest attributes. In addition, imagery from various satellite sensors (e.g. Sentinel-2, RapidEye, WorldView-2) proved to be excellently suited for the delineation of burned areas and the assessment of tree vigour. Furthermore, recently developed sophisticated classifying approaches such as Support Vector Machines and Random Forest appear to be tailored for tree species discrimination (Overall Accuracy of 89%). Object-based classification approaches convey the impression to be highly suitable for very high-resolution imagery, however, at medium scale, pixel-based classifiers outperformed the former. It is also suggested that high radiometric resolution bears the potential to easily compensate for the lack of spatial detectability in the imagery. Quite surprising was the occurrence of dark taiga species in the riparian areas being beyond their natural habitat range. The presented results matrix and the interpretation key have been devised as a decision tool and/or a vademecum for practitioners. In consideration of future projects and to facilitate the improvement of the forest inventory database, the establishment of permanent sampling plots in the Mongolian taigas is strongly advised.

1. Introduction

1.1. Digest and background

Mongolia's taiga forests are part of the northern most forest formations on our planet also referred to as the "borealis". This label was coined to pay tribute to the god of the cold north wind "Boreas" rooted in the Greek mythology. Being used interchangeably the "taiga" (originating from the Yakutian word for forest) represents globally the second largest biomes covering an area of between 12 and 20 Mio sqkm (depending on the definition), and as such embodies one third of the total forest area (Bonan and Shugart, 1989, Venzke, 2008). The borealis is a broad, circumpolar mix of cool coniferous and deciduous tree species with a north-south stretch of about 2800 km running from 73° North to about 45 ° North. Despite the harsh conditions such as low temperatures, long winters, and nutrient-poor soils, a wide array of flora and fauna have adapted surprisingly well to their hostile environment. Dry continental climate and low sun angle determine the prevailing conditions and because of the high albedo in winter time only the transport of advective air masses can compensate for the negative net radiation balance (Ackerman and Knox, 2012, Kappas, 2009, van Cleve and Yarie, 1986, Venzke, 2008). Main drivers of boreal ecology are climate, solar radiation, soil moisture, topography, permafrost, nutrient availability and sequestration, as well as wildfires and insect outbreaks, with all factors resulting in a mosaic pattern of forest types and stand productivity (Adams *et al.*, 2010, Adams, 2013, Bonan and Shugart, 1989, Ediriweera *et al.*, 2016). Many studies have been conducted in the past, particularly by Russian scientists (Hilbig, 1990), however, our knowledge about the interaction of the ecological determinants, let alone in combination with anthropogenic factors, remains patchy.

Mongolia's taiga forest occupies the southern fringes of the boreal biome creating a green blanket of about 12.9 million ha (Dulamsuren *et al.*, 2005a, Dulamsuren *et al.*, 2016, FAO, 2014b, Soja *et al.*, 2007). The most prevalent tree species are Siberian larch (*Larix sibirica*, LEDEB.), Siberian pine (*Pinus sibirica*, DU TOUR), Scots pine (*Pinus sylvestris*, L.), Siberian spruce (*Picea obovata*, LEDEB.), Siberian fir (*Abies sibirica*, LEDEB.), interspersed with Siberian silver birch (*Betula platyphylla*, Sukaczev), poplar (*Populus spec*., L.) and willow (*Salix spec*., L.), whereas the Saxaul (*Holoxylon ammodendron*, BUNGE) only occupies the arid climatic zone, i.e., the southern part of the country. Taiga forests are specified by a so-called "dark taiga", which comprises shade tolerant species such as Siberian pine and Siberian spruce, whereas the term "light taiga" includes species that demand for a patchy canopy structure such as Siberian larch and Siberian birch (Byambasuren, 2011, Dulamsuren, 2004, Dulamsuren *et al.*, 2016, Dulamsuren and Hauck,

2008, Mühlenberg *et al.,* 2006, Mühlenberg, 2012). Microclimatic variability and edaphic diversity are closely intertwined with slope, aspect and altitude, thus shaping the forest landscape (Begum *et al.*, 2010, Treter, 1996, Zueghart, 2017). South-facing slopes and valleys are represented by steppe, meadow and riverine vegetation, when in fact light and dark taiga are the prevailing features of the north-facing slopes (Cleve *et al.*, 1986, Dulamsuren *et al.*, 2005a, Dulamsuren and Hauck, 2008, Méndez-Toribio *et al.*, 2016). Topography not only affects vegetation distribution and composition, but there are strong indications, that it is also a cause for repercussions on the local and regional climate. Although a lot of recent research activities focus on the complex nature of these interactions, most of the underlying mechanisms are still poorly understood.

Forests are pivotal for the provision of ecosystem services such as pure water, timber for construction and fuel, purification of the air, and for supplying non-timber forest products such as berries, pine kernels and mushrooms. Mongolian forests are also home to many endangered species, and in addition, embody a distinct spiritual value. With an ecosystem as sensitive as the taiga forests, these biomes are extremely susceptible for disturbances caused by climate change and socio-economic pressure (Byambasuren, 2011, Byambasuren, 2018, Dulamsuren and Hauck, 2008, Miehe *et al.*, 2007). The demands in Mongolia for conserving the precious nature, the human needs to sustain a living of a certain standard and the uplifting of a faltering economy seem irreconcilable. A sustainable, climate change mitigating forest management strategy appears to be mandatory to tackle these challenges adequately (Baasan, 2010, Erdenebat, 2014, Gustafson *et al.*, 2010, Gustafson *et al.*, 2011). These days the Mongolian forestry sector is still afflicted with improper silviculture practices, illegal logging activities, and a severe lack of law enforcement partly due to corruption. Forest cover has decreased for about 1.2 million ha over the past 20 years due to inappropriate land use practices and overgrazing expediting to land degradation and desertification (Tsogtbaatar, 2004a, Tsogtbaatar, 2013, Wyss, 2007). The current situation is exacerbated by clear indications of climate change leading to longitudinal, altitudinal and compositional shift in the taiga biome, but has also triggered an increasing number of forest fires and other disturbances like pest outbreaks (Allen *et al.*, 2010, Batima *et al.,* 2005, James, 2011, Kasischke *et al.*, 1995, Kirilenko and Sedjo, 2007, Pachauri *et al.*, 2015, Seidl *et al.*, 2017, Soja *et al.*, 2007, Tautenhahn *et al.*, 2016, Tchebakova and Parfenova, 2012, Tsogtbaatar, 2013). A silver lining on the horizon is expressed by passing specific bills and regulations by the Mongolian government to meet the demands for mitigation and conservation strategies, in particular in the light of Mongolia taking part in the REDD+ (Reducing Emissions from Deforestation and Forest Degradation) programme of the United Nations (Byambasuren, 2018, The Secretariat of the State Great Hural, 2016, UN-REDD, 2018). The implementation of these objectives not only requires

technical support and well trained and competent personnel, but in addition the provision of relevant information on the forest resources under a changing climate in the country. Subsequently, many research projects have been initiated to untangle the role of climate for forest productivity and the response among sites and species. Mitigation strategies in accordance with good management practice can only be devised and implemented if the feedback mechanisms of light and dark taiga to global changes are understood (James, 2011, Streck and Scholz, 2006, Thurner *et al.*, 2014).

In the wake of those activities remote sensing technology and Geographic Information Systems (GIS) have proven to be invaluable tools for the compilation and analysis of environmentally relevant data to gain critical insight in the complexity of interacting systems and make predictions based on sound information (Ciesla, 2000, Hansen *et al.*, 2013, Hildebrandt, 1996: 360–361, Lausch *et al.*, 2016, Tomppo *et al.,* 2014). Substantial advances in sensor and platform technology as well as cost efficiency make this a paramount choice in conjunction with monitoring activities, forest inventories and the assessment of land cover change and health status. With the advent of sub meter ground resolution multispectral satellite imagery, laser technologies such as LiDAR, and the availability of low-cost UAVs new opportunities are created to replace or complement expensive and laborious ground-based measurements (Bohlin *et al.*, 2012, Franklin, 1986, Hyyppä *et al.*, 2008, Järnstedt *et al.*, 2012, Laliberte and Rango, 2011, Næsset, 2002b, Næsset *et al.*, 2016, Rango *et al.*, 2009, Steinmann *et al.*, 2013, Tuominen *et al.*, 2015, Tuominen and Pekkarinen, 2005, Wallace *et al.*, 2016). In a great many instances, remote sensing technology offers the only feasible approach to gain a synoptic view on environmental processes and the pertaining ramifications (Cracknell and Hayes, 2007: 1, Jones and Vaughan, 2010, Lillesand *et al.*, 2015: 2–3, van Laar and Akça, 2007). In addition, new methodological approaches and image analysis techniques originating from computer vision and robotics have been introduced to extract better information from the sensed objects and phenomena (Canty, 2014, Dong and Chen, 2018, Kentsch *et al.*, 2020, Ma *et al.*, 2019, Nezami *et al.*, 2020).

1.2. Goals and hypotheses

At present, appropriate management strategies, law enforcement, the participation of the relevant stakeholders and local communities in particular, along with scientific advance are compelling to be able to deal with a complex number of environmental and socio-economic challenges (Gradel, 2007, Schmidt-Corsitto, 2016, Wyss, 2007, Yamamura, 2013). In this respect, international development aid has gained momentum in Mongolia. One example for providing expertise and funds for tackling the pressing issues is the German Federal Enterprise for International Cooperation (GIZ). The presented study related to the forestry

sector was conducted in collaboration with the GIZ and as such is unique in the sense that development aid and applied scientific research are linked for the benefit of the Mongolian people and their environment. Although a great deal of forest research was carried out before, sound information on the state of the Mongolian forest had been lacking. For this reason, a national forest inventory (NFI) was conducted in 2014 for fulfilling the information needs on a national and regional level (Altrell and Erdenejav, 2016). Nonetheless, a more detailed and refined approach is required to gain more insights into forest structure and as such calls for scrutiny on a local or even stand level. So far, no studies have been carried out on a local and stand level employing remote sensing technology – the analysis of UAV imagery also seems to be novel in this context. As a consequence, a joint research initiative between the GIZ[1] and the University of Göttingen was launched and a research site in proximity of the hamlet Thunkel in the Khentii Mountain area north of Ulaanbaatar chosen to investigate the feasibility of gathering relevant data on taiga forest structure. Field work was carried out in the 61-ha forest compartment 435, which has been serving as a GIZ school forest for many years and been subject to former inventory cruises. Salient features of this site are variations in altitude, tree species composition of the dark and light taiga, as well as in silvicultural treatment. Unfortunately, part of the school forest was subject to a devastating wildfire during field operations.

Exploration comprised a variety of parameters taken into consideration:

- Forest inventory parameters such as diameter breast height (dbh), tree height, tree species, basal area, number of trees per plot, tree quality, tree vitality, slope and aspect were taken during field survey.
- Furthermore, an UAV was employed to gather high resolution aerial imagery for generation of a 3D canopy model and visual interpretation of tree species distribution and composition.
- High resolution multispectral satellite imagery was procured to accomplish spectral separability of the light and dark taiga and to correlate inventory parameters with spectral signature.
- Various vegetation indices and image classification methods will be tested for suitability of spectral discrimination of tree species and the potential transferability on other forest areas.

[1] German Federal Enterprise for International Cooperation

Subsequently, the following hypotheses will be investigated:

- Tree species and composition (regularity and mingling) can be identified on the aerial imagery.
- Tree height can be extracted from the resulting canopy height model as generated from the aerial imagery with accuracies commensurate with field survey measurements.
- High resolution satellite imagery is suitable for the extraction of tree species, number of trees, and carry enough spectral information to correlate satisfactorily with inventory parameters such as timber volume and basal area.

Finally, in accordance with the overall objective of this study, it will be reviewed to what extend the findings can be implemented and integrated into sustainable forest management practices by providing a decision supporting tool to help determine the best sensor – platform – classification method/algorithm combination for a specific assignment. In addition, it is expected that the outcomes of this project largely contribute to the assessment quality of forest ecosystem services, as well as forest fire risk management.

The author is aware of the fact, that the audience of this dissertation is mainly recruited from various disciplines with diverse scientific credentials and skills. To cater for these readers, some of the chapters provide a broader background of specific topics as opposed to the customs related to writing a scientific paper. In addition, exhaustive chapters are endowed with a wrap-up section at the end for the reader's comfort and ease.

2. Mongolia and its forest resources

2.1. A country profile

The subsequent chapters are aimed at providing information at a glance related to the geographic location of Mongolia, the prevailing climatic conditions, its socio-economic situation, and to conclude with the flora of Mongolia and the boreal tree species in particular.

2.1.1. Geographic location and topography

Sandwiched between the big neighbours Russia in the North and China in the South, Mongolia covers an area of 1.565 million km^2, thus being more than four times the size of Germany. The latitudinal stretch is about 1200 km (41^o North to 52^o North), the longitudinal extent being around 2400 km (88^o East to 120^o East).

Figure 2.1: Physical map of Mongolia (source: ezilon Maps, 2009).

The physical map above reflects quite impressively the elevated character of the country dominated by vastly stretching plateaus ranging from 1500 to 2000 meters (above sea level (a.s.l.)). The main plateaus are flanked by mountain ranges with impressive peaks of more than 4000 meters found in the Mongolian Altai range. The lowest point in the country is represented by a salt lake in the Udz basin in the East with 552 meters (a.s.l.) (Hilbig, 1995). About 85% of the country's area is elevated above 1000 meters (a.s.l.). Due to its specific topography, Mongolia is located on a major watershed running East-West, with rivers running North to the Arctic or Pacific Ocean, and South to the Central Asian Depression .

2.1.2. Climate in Mongolia

The high altitude and the continental position of Mongolia determine the climate featuring extreme contrasts – temperatures can drop as low as -50°C in winter, while summers are warm with temperatures exceeding 40°C (Dagvardoj *et al.,* 2014). The annual mean temperature has been calculated to be 0.6°C, with a mean of more than 9°C for Germany in comparison (Deutscher Wetter Dienst, 2021). The aridity increases from North to South with precipitation rates ranging from 600 mm per year at the Khuvsgul and Khentii mountains to a low of 25 mm per year or less in the Gobi desert (Gunin *et al.*, 1999). The annual distribution of the precipitation shows strong peaks in summer (about 70% of total precipitation), and winter (about 5-10% of total), however, snow cover does not seem very common. Most of the precipitation falls in showers and thunderstorms, and droughts become an increasingly common phenomenon with a changing climate (Dulamsuren and Hauck, 2008, Khansaritoreh *et al.*, 2017). Autumn tends to start with a drastic decrease in precipitation and dwindling temperatures, contributing to the overall harsh climatic conditions. A very special weather phenomenon in Mongolia deserves a special mention, since these extreme conditions have wiped out great proportions of the livestock in recent years. The so-called *white dzud* refers to an extreme plunge of winter temperatures associated with heavy snowfall. In contrast, the *black dzud* lacks the high precipitation, but temperatures can go down to -58 degrees Celsius (Haeseler and Schmitt, 2017). Although being well adapted to harsh conditions, the nomads' most valuable assets (i.e., goat, sheep, camels, cattle, horses) are not able to withstand these extreme plights and die of a lack of forage and hypothermia (in the winter of 2015/2016 and 2016/2017 more than 1.1 million animals perished).

2.1.3. Socio-economic and political factors

Mongolia features a total population of an estimated 2.8 million (figures vary with source, since there is no official resident registration in Mongolia), with half of the population residing in the Mongolian capital Ulaanbataar these days. Traditionally, being a people cherishing the nomadic lifestyle, with the decline of the Soviet Union in the 1990s and the cease of the markets and investors, a fair amount of the Mongolians had been seeking to make a living in the capital, thus causing an enormous rural exodus. The picture below (Figure) depicts a view to the North with clear indications of an increasing urban sprawl.

Figure 2.2: Photograph showing urban sprawl in the North of Ulaanbataar (source: Vogt, 2017).

In the following years, the collapse of the industry sector in particular has led on to a sharp increase of the unemployment rate, and as such, evoked poverty, lack of shelter, and also the disintegration of the public health and educational sector. This development has caused a reversal of the exodus trend, with people getting more and more dedicated to the traditional lifestyle of animal husbandry. However, in the recent years, with the transition to and a transformation into a democracy, and with an influx of substantial foreign aid, Mongolia has managed to triple the DGP per capita since 1991 (World Bank, 2021). The country with its vast livestock and mineral resources has also managed to get the rate of illiteracy down to under 2%. In summary, the development prospects look promising in the long term, however, with a changing climate and the ramifications of the Covid-19 pandemic, new challenges arise.

Mongolia is divided into 21 provinces, the so-called *aimags*, with subsequent subdivision into districts, also known as *soums*. This extremely sparsely populated country contains very little arable land, forcing it to import most of its food resources from countries such as China or Russia. An important backbone ensuring the Mongolian market activities is the train line running from North to South, connecting settlements and mining areas to the neighbouring nations Russia and China. In the recent years, rich mineral deposits of cooper, coal, tungsten and gold have caused a boom in the mining sector, however, the country still struggles to overcome a significant trade deficit. According to the World Bank, around 30% of the population are estimated to be still below the poverty line (World Bank, 2021).

2.1.4. Vegetation zones

This subchapter mainly focuses on the driving factors for the extent of the boreal forests in Mongolia. Nevertheless, it is worth mentioning, that an impressive body of research has been conducted and published by Russian and other experts dealing with the high diversity of flora and fauna in this fascinating country (e.g. Gunin *et al.*, 1999, Dulamsuren *et al.*, 2005a, Dulamsuren, 2004, Hilbig, 1995, Mühlenberg, 2012, Department of Biology, School of Arts and Sciences, National University of Mongolia, 2017, Mühlenberg *et al.*, 2004, Endicott, 2012, Schwanghart, 2008, Yamamura, 2013). An impressive repository on the flora of Mongolia is maintained by the University of Greifswald featuring a plant database with thousands of entries (University of Greifswald, 2010).

Being located in the Palaearctic zone, the vegetation zones in Mongolia are determined by (i) climate characteristics, (ii) by altitude, and (iii) by the composition of the tree species.

(i) The zoning of the vegetation apparently corresponds quite well with the gradient of precipitation rates from North to South. Thus, the Northern part of the country adjoining the Russian territory is dominated by dense coniferous forests, also referred to as *taiga*. The Siberian Larch (*Larix sibirica*) is by far the most common tree species, with Siberian Pine (*Pinus sibirica*), Scots Pine (*Pinus sylvestris*), and Siberian Spruce (*Picea obovata*) ranking next. The more light demanding White Birch (*Betula platyphylla*), representing the broad-leafed deciduous tree species with the highest proportion, often occurs either intermingled with Siberian Larch, or in pure stands ensuing forest disturbances like wildfires, or after copious felling activities. Moving further South, with precipitation rates between 300 and 400 mm, the *forest steppe* zone dominates the landscapes as a mix of grassland and forest. To avoid the high evapotranspiration as a consequence of the intense solar radiation, the forest tree species are compelled to populate the Northern slopes (Treter, 1996). In the zone with precipitation below 300 mm per year only grasses and other well-adapted non-tree species are able to survive to present the well-known *steppe*. The vast grass plains are dominated by the bunch grass *Stipa capillata*, L., forming mottled carpets associated with a selection of wormwood (*Artemisia*). Soil types have then changed from the forest influenced parachernozems to castanozems being typical for the steppe zone (Hilbig, 1995). When approaching the desert zone of the Gobi, precipitation drops to less than 100 mm per annum. Grid and stone deserts dominate the scenery, with a few desert-adapted

Saxaul (*Haloxylon ammodendron*) trees interspersed. The following map provides a good overview on the overall distribution of the various vegetation zones in Mongolia.

(ii) and (iii) The Mongolian taiga grows under extreme conditions to represent almost 2% of the world's taiga forest cover. Altitude and slope exposition are other major drivers for zonality of the taiga forests. In recent years a number of researchers investigating the

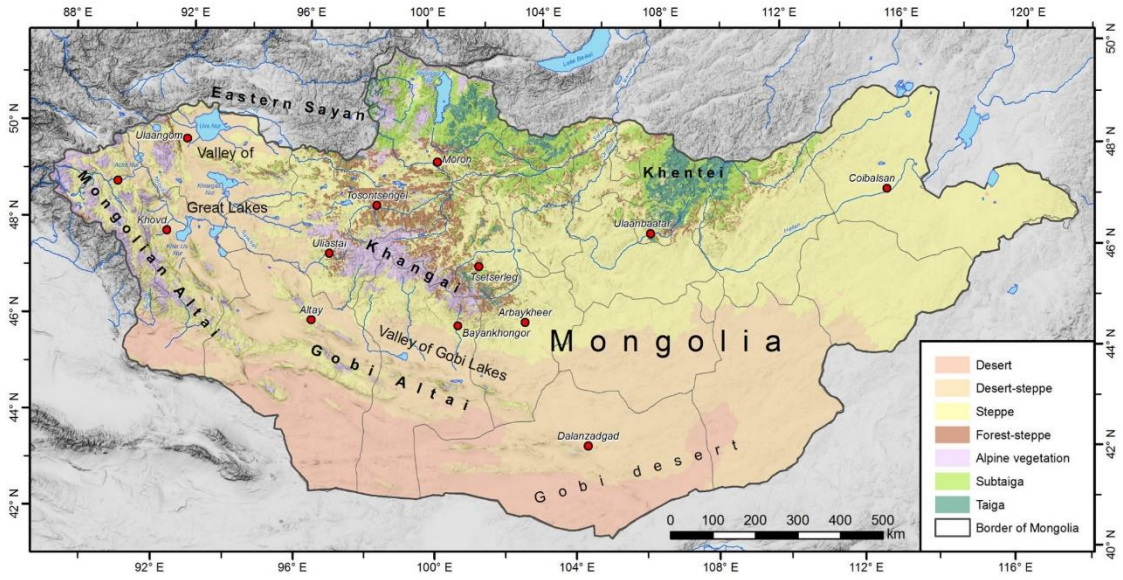

Figure 2.3: Vegetation zones in Mongolia (source: Klinge, et.al. 2018).

Mongolian landscapes and ecotones have come up with suggestions on how to zonally structure the occurrence of forests (Dulamsuren, 2004, Gunin *et al.*, 1999, Hilbig, 1990, 1995, Hilbig, 2006, Mühlenberg *et al.*, 2004, Sabloff, 2011, Yamamura, 2013: 65–70). The graph (Figure 2.4) extracted from the work by Dulamsuren (2004), slightly modified by Wecking (2017: 30), illustrates quite simply, what ecological niches are occupied by the various biomes. In the altitude zones between 900 and around 1300 meters (a.s.l.) taiga forests dominate the northern slopes, whereas in the altitudes from 1200 to 1600 m (a.s.l.) the variation in exposition does not seem to be of importance. The term *dark taiga* refers to shade tolerant tree species, like Siberian Spruce and Siberian Pine. In contrast, the *light taiga* constitutes tree species being light-demanding, like White Birch, and Siberian Larch. Light taiga species only occur, where shade-tolerant species perish for climatic or edaphic reasons. With an increase in altitude climatic conditions become more and more adverse, putting coniferous trees in a more advantageous position because of their higher productivity (Grabherr, 1997: 320–323, Mühlenberg *et al.*, 2012a).

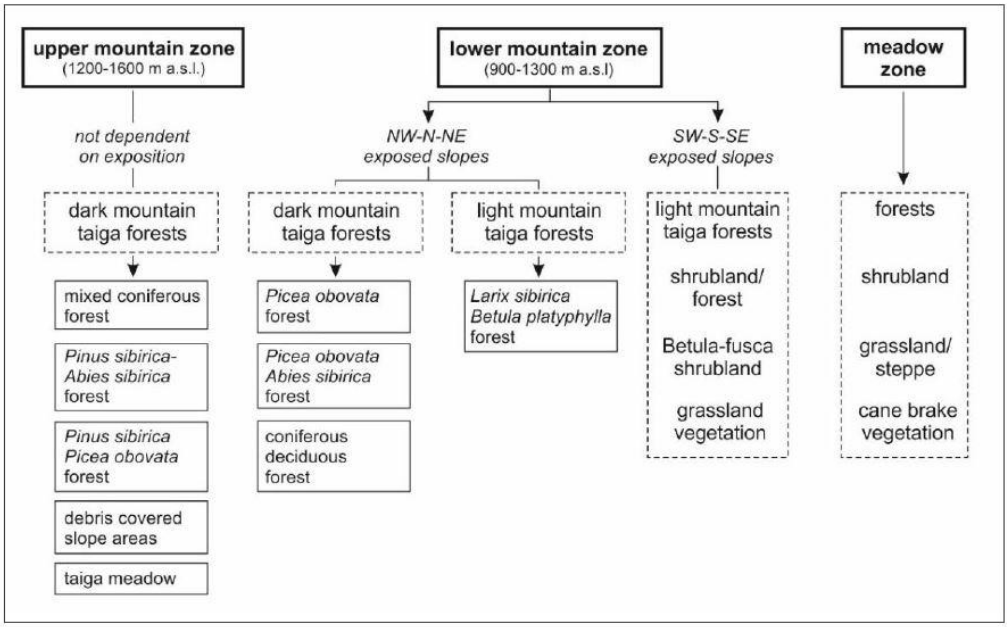

Figure 2.4: Classification scheme of boreal forest communities in Mongolia (Wecking, 2017:30).

All driving factors mentioned above would be incomplete, if there were not additional ones controlling the presence or absence of specific flora species. Natural disturbances like wildfire or insect pest attacks – not to mention climate change - have a great impact on the shape of the landscapes, but they also affect energy flows and biochemical cycles. As a result forest stand structure, species composition, and forest growth are influenced (Baldocchi *et al.*, 2000, Byambasuren, 2011, Danilin and Tsogt, 2014, Dulamsuren *et al.*, 2010a, Goldammer and Furyaev, 2010, Gradel *et al.*, 2017b, Malhi *et al.*, 2002, Schulze *et al.*, 2005, Schulze *et al.*, 2012, Stocks *et al.*, 2001).

2.1.5. Tree species of the Mongolian forests

In total around 140 different woody plants, shrubs, and tree species have been found and recorded in Mongolian forests so far (Altrell and Erdenejav, 2016: 10–11). However, the coniferous boreal forests and forest steppe in the North and the Saxaul forests of the southern desert and desert steppe comprise only a few prominent species. The main tree species are introduced in the following for the dark, as well as for the light taiga. The photographs below are all retrieved from the website of Manfred Vester and thus are indicated as such (Vesper, 2005).

Figure 2.5: Common tree species in Mongolia – from left to right - top: Siberian larch; White birch; Siberian pine. Bottom: Siberian spruce; Scots pine; Siberian fir. Source: Vesper, 2005.

As mentioned above it is distinguished between the *light taiga* with light-demanding tree species, whereas the *dark taiga* features more shade-tolerant species. The main light taiga species comprise the Siberian larch, the White birch, with Scots pine. Dark taiga species are Siberian pine, Siberian spruce, and Siberian fir. Other tree species like various poplar and willow species almost exclusively populate the riverine areas.

The Siberian larch (*Larix sibirica*, L.) dominates the scenery of the light taiga. The tree height is up to 40 meters, and this species sheds the needles in autumn (i.e., deciduous). It can withstand extreme climatic conditions, but prefers well aerated soils. The timber is used for construction and for pulp in the paper industry (Farjon, 2017).

The Siberian birch (*Betula platyphylla*, Sukaczev) grows up to 20meters heigh and is very conspicuous because of its white bark and the lush green foliage (Farjon, 2017). It can tolerate high temperatures, but is also well adapted to winter conditions. The larch can occur in pure stands or in mix with the Siberian larch. Interestingly, the birch is not being utilised in Mongolia at all, although the high content of essential oils would make it an excellent

firewood (Schmidt-Corsitto, 2017). In other countries birch is valued as wood for flooring, pulp and paper, furniture, and as firewood.

The Scots pine (*Pinus sylvestris*, L.) in its Mongolian variety has its natural range in eastern Siberia, around the Baikal lake, and in the light taiga belt of Northern Mongolia. Tree heights are up to 40 meters, and habitat preferences are low profile, except for light. Scots pine is commonly associated with other coniferous species, but also mingles with broad-leafed species. Utilisation is focused on timber and paper production, as well as on mining props for the mining industry (Farjon, 2017).

The Siberian pine (*Pinus sibirica*, Du Tour) represents one of the most common species of the dark taiga. It can reach heights of up to 40 meters with diameters (DBH) of easily 50 centimetres. It has a high demand of water, but can cope with a low nutrient content of the soil. Individuals grow slowly, but can attain an age of more than 850 years. The wood is used for construction and furniture, and trees are tapped for resin, and the kernels sold on markets (Farjon, 2017).

Siberian spruce (*Picea obovata*, Ledeb.) can also grow quite tall (up to 40 metres), with diameters often exceeding 50 centimetres. The Siberian spruce has a high demand for water and prefers humid and shady sites. It also constitutes dark taiga riverine forests (Dulamsuren *et al.*, 2005a). The needles of this species are much darker than those of the Siberian pine, and Scots pine. Picea obovata has shown to be sensitive to rapid temperature changes, as well as to late spring and summer frosts (Farjon, 2017).

The Siberian fir (*Abies sibirica*, Ledeb.) is also one of the key dark taiga species. It prefers sites with a good availability of water and nutrients, and fancies well drained soils free of permafrost (Farjon, 2017). According to investigations by Dulamsuren *et al.* (2005a) Abies sibirica features a limited range with occurrences only in the Khuvsgul and Khentii region, as well as on mountain ridges. Due to its high market value the Siberian fir has become red-listed as a very rare species (Dulamsuren *et al.*, 2005b).

Figure 2.6: Saxaul tree (Vesper, 2005).

The Saxaul tree (*Haloxylon ammodendron*) occupies arid habitats like sandy deserts, and grows only 1 to 4 metres high. The leaves are reduced to scale-like organs and as such are almost inconspicuous. The Saxaul plant can tolerate high salt contents in the soils, and can even form dense 'forests'. The wood is very hard and thus extremely difficult to work with, and is mainly used as firewood and for dune stabilisation (Vesper, 2005).

2.2. The ‘borealis’

With an extent of more than 920 million hectares the boreal forest ecosystem represents almost 29% of the entire global forest area (Kuusela, 1992). The following graphical representations convey a very good impression on the vastness of this zonobiome.

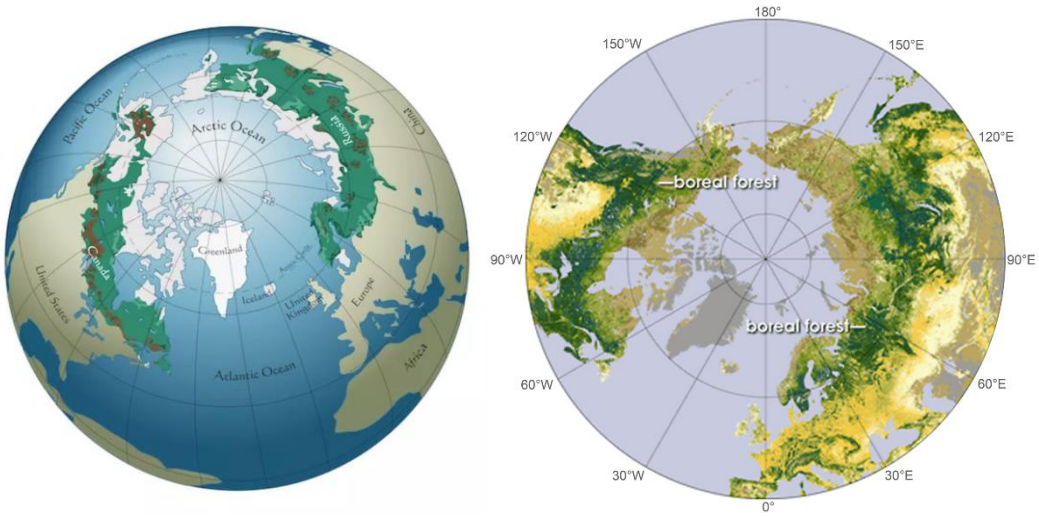

Figure 2.7: Extent of the boreal forest zonobiome. Sources: www.shutterstock/Atomic.Roderick; Kayes and Mallik, 2020.

The borealis rings the northern hemisphere between 45º and 73º latitude to include China, Russia, Mongolia, Canada, parts of Japan, and Scandinavia. The vast forests are interspersed by myriads of lakes and wetland systems. The flora mainly consists of cold-tolerant and fire-adapted conifer trees (spruces, larches, pines, firs), deciduous broad-leafed trees (birches, poplars, maples), tall shrubs, and a great variety of grasses, ferns, mosses, and lichen (Kayes and Mallik, 2020). The boreal zone is engulfed by the treeless tundra in the North, and by the nemoral zone or the forest steppe in the South (Venzke, 2008: 3–4). The natural habitat of the boreal forests is determined by temperature and precipitation, with an amplitude of -3 degrees Celsius for the coldest month and 10 degrees Celsius for the warmest month (i.e., climatic zone D). Permafrost soils are salient features of the boreal zone with either discontinued or permanent character. The growing period presents itself extremely short with three months exceeding an average temperature of 10 degrees Celsius (Bonan and Shugart, 1989). However, in the last few years, temperature maxima of -32 degrees Celsius to more than 35 degrees Celsius have been observed, which are attributed to a changing climate (Stephanowitz, 2020).

In addition to other numerous factors, the occurrence of boreal forests largely relates to the existence of permanently frozen soils (permafrost). The low decomposition processes of organic material are inextricably linked with the overall low temperatures, thus making nutrient supply for the flora fairly arduous. On the other hand, the thawing water in the soils

during the warmer periods guarantees a well-dosed constant flow of water at the disposal of the vegetation. Continuous and discontinuous permafrost scenarios largely regulate the patchy, mosaic-like appearance of the tundra and forest landscape. Wildfires, insect pests, and logging activities result in the removal of tree cover, thus largely affecting the thermo-regulation of the soils. According to numerous investigations, only the occurrence of a dense forest vegetation causes an insulation effect on the ground below, and as such has the potential to provoke the formation of new permafrost areas. However, the trend for an increased degradation of the boreal forests has detrimental effects on the permafrost layers. The thawing of those sheets induces water stress in higher plants in the long run to spark off an expansion of the less water demanding tundra (grass, moss, lichen, shrubs) flora – negative feedback loops have been affirmed already (Dulamsuren *et al.*, 2010b, Etzelmüller *et al.*, 2006, Eugster *et al.*, 2000, Juřička *et al.*, 2020, Kopp *et al.*, 2014, Sharkhuu *et al.*, 2007, Sugimoto *et al.*, 2002, van Cleve and Yarie, 1986). With a changing climate the degradation of the boreal forests at a galloping speed will present further disastrous scenarios with increasing rates of wildfires (especially smouldering ground fires) and soaring levels of carbon and methane emissions due to biomass decomposition caused by tapering permafrost (Harden *et al.*, 2000, IPCC, 2020, McRae *et al.*, 2009, Mukhortova *et al.*, 2015, Ōsawa, 2010: 459–463, Shvidenko and Schepaschenko, 2013, Watson, 2009). For further information on the impact of wildfires on the Mongolian boreal forests, please refer to chapter 5.2.

2.3. The Mongolian forest resources

The Mongolian taiga forests, as being part of the boreal zonobiome, are home to a diverse flora and fauna scenery. However, this wilderness is at peril and at stake for numerous reasons. The subsequent account will attempt to shed light on the various causes by presenting the most up-to-date facts for perusal.

2.3.1. Forest extent and structure

NB: Many of the following graphs and tables reflect the outcomes of the National Forest Inventory (NFI) conducted in the years 2014-2016. Although the figures currently represent the most reliable and profound data base, care has to be taken when interpreting the depicted state of the forests in Mongolia for the following reasons: according to the NFI report, the control measurements showed that only 80% of the measurements carried out by the inventory team were within the tolerated deviation, with tree species identification, fire damage, and slope direction showing an error rate of less than 10%, but for determination of DBH, and height a deviation of between 30-60% were observed (Altrell and Erdenejav, 2016: 116)! Despite the presented shortcomings of the NFI, it remains the most up to date inventory resource for the time being – in particular considering the flaws

(i.e. either not retrievable, not updated, or in Mongolian) of the official Forest-Atlas website entertained by the Mongolian Ministry of Nature, Environment and Tourism (Ministry of Environment and Tourism, Mongolia, 2020).

Since all data of the NFI report are based on the Mongolian specific definition of forest, the FAO related variation is as follows:

- Minimum tree canopy coverage of 10%.
- Minimum height of the species of 2 metres.
- Minimum extent of forest area of 1.35 hectares.

The following map depicting the extent and distribution of the boreal forests (i.e., without the *Saxaul* forests in the semi-desert in the South) in Mongolia was created in the course of the nationwide assessment of the forests in Mongolia (NFI). The derived forest mask for the year 2015 is based on the classification of Landsat 8 imagery with acquisition dates between June and end of August (vegetation growing period). More than 50 image tiles were classified by applying Random Forest as a machine learning method, with Google Earth data and Bing maps used for reference point interpretation and validation.

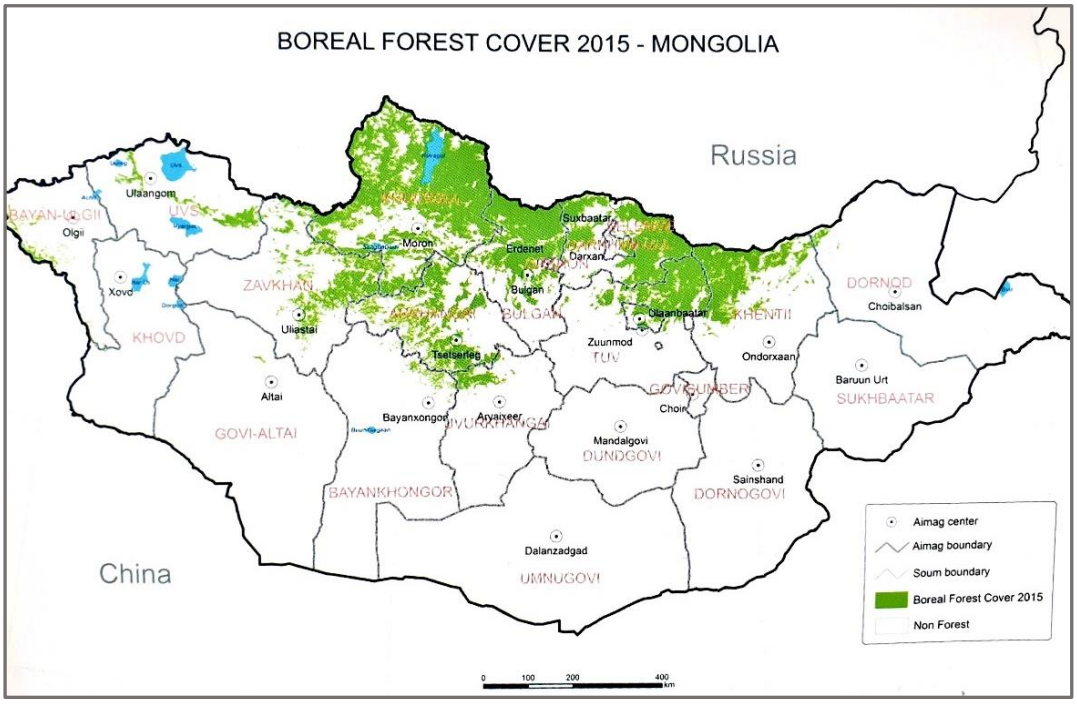

Figure 2.8: Geographic distribution of boreal forest in Mongolia (NFI report: Altrell, Erdenejav, 2016:40).

The resulting country map indicates the focal coverage of boreal forests being in the north-centre of the country (i.e., provinces (so-called Aimags) of Bulgan, Khuvsgul, Arkhangai, Selenge, and arts of Khentii) , with patchy stretches of forest in the western part. The NFI reports about 6% of the entire state territory to be populated with boreal forest, which

translates into about 9.49 million hectares. Overall map accuracies were calculated to be almost 90% (Altrell and Erdenejav, 2016). The table below (Table 2-1) conveys a good impression on the coverage of boreal forests with respect to the related political provinces.

Please note, that the subsequent graphs and tables use the forest inventory regions not being congruent with the specific aimags. For the five forest inventory regions (i.e. Altai, Khangai, Khuvsgul, Khentii, and Boreal Buffer Zone) the ranking is (proportion of forest area): (i) Khuvsgul 47.7%, (ii) Khentii 26.4%, (iii) Khangai 18.7%, (iv) the Boral Buffer Zone 5.5%, and (v) Altai 1.9% (Altrell and Erdenejav, 2016: 38).

Table 2-1: Boreal forest area (ha) by Aimag (Province) (NFI report: Altrell, Erdenejav, 2016:39).

Boreal Forest Area by Aimag (Province), *ha* , %							
Aimag		Forest area**		Aimag		Forest area**	
		(ha)	Proportion			(ha)	Proportion
1	Arkhangai	792 340	8.7%	10	Khuvsgul	3 041 668	33.4%
2	Bayan-Ulgii	39 145	0.4%	11	Orkhon	13 578	0.1%
3	Bayankhongor	33 508	0.4%	12	Ovorkhangai	118 900	1.3%
4	Bulgan	1 448 018	15.9%	13	Selenge	1 353 368	14.9%
5	Darhan-Uul	57 496	0.6%	14	Tuv	764 752	8.4%
6	Dornod	28 725	0.3%	15	Ulaanbaatar	75 869	0.8%
7	Gobi-Altai	2 347	0.03%	16	Uvs	129 321	1.4%
8	Khentii	704 777	7.7%	17	Zavkhan	490 960	5.4%
9	Khovd	1 153	0.01%		**Mongolia**	**9 095 925***	**100%**

* Total Mongolia Boreal Stocked Forest Area is derived from systematic dot-grid sampling of Google Earth data from 2014
** The distribution of boreal forest in the different aimags (provinces) is estimated through forest cover mapping using Landsat 8 data from 2015

Since the satellite data were not subjected to a species classification undertaking, all subsequent information provided is based on the field data acquired during the NFI mission.

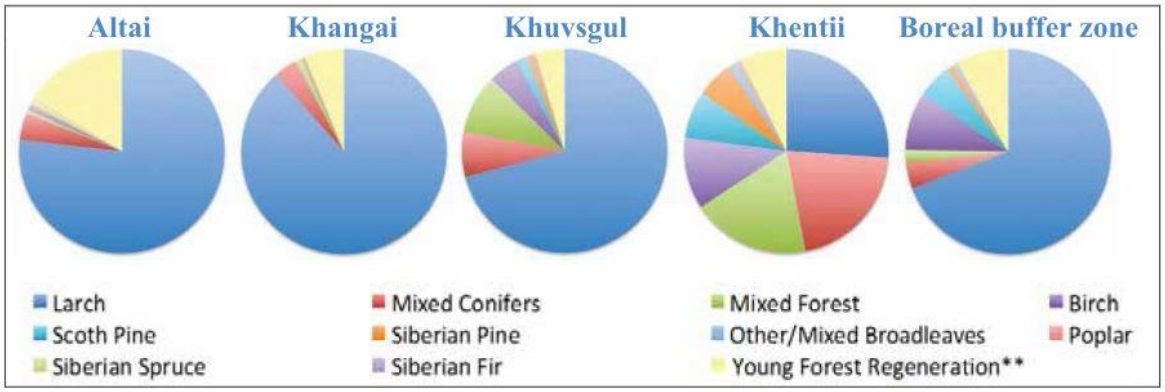

Figure 2.9: Regional forest types distribution according to tree species composition (NFI report: Altrell, Erdenejav, 2016:61).

According to above figure (Figure 2.3) the inventory area featuring the highest diversity in forest species is Khentii, where the test area of the presented study is located. It is also striking, that the Siberian Larch (*Larix sibirica*) dominates the entire scenery. The following

table (Table 2-2) provides a more detailed account on the various tree species within the boreal part of the country. Interestingly, the Siberian Larch hardly dominates the forests in the Khentii area, but rather appears intermingled with other species such as the White Birch (*Betula platyphylla*) and other conifers like Scots Pine (*Pinus sylvestris*) and Siberian Pine (*Pinus sibirica*) (Altrell and Erdenejav, 2016: 59–61).

Table 2-2: Forest area proportion per tree species (NFI report: Altrell, Erdenejav, 2016:61).

Proportion of forest area by forest type (level 3) and Forest Inventory Region, %						
Forest type	Forest Inventory Region					Mongolia
	Altai	Khangai	Khuvsgul	Khentii	Boreal buffer zone	
Siberian Larch	76.8	88.5	70.9	26.1	69.2	62.4
Scotch Pine	-	-	1.6	7.5	5.5	3.1
Siberian Pine	-	0.2	1.0	5.9	1.0	2.1
Siberian Spruce	0.8	0.1	0.2	0.1	-	0.1
Siberian Fir	0.1	-	-	0.1	-	0.02
Mixed Conifers	4.3	3.6	7.2	20.9	4.1	9.9
White Birch	0.7	0.2	4.9	11.4	9.1	5.9
Poplars	0.4	-	0.1	0.6	0.2	0.2
Mixed Broadleaves	-	0.0	0.2	1.4	0.6	0.5
Mixed Forest**	0.6	1.0	9.4	18.7	2.0	9.7
Forest Regeneration***	16.4	6.2	4.5	7.3	8.3	6.0

* Forest types based on Tree Species-specific Basal Area Proportions
** Mixed Broadleaved and Coniferous tree species
*** Undefined Forest Type with no trees with Dbh ≥ 6 cm

Another interesting finding of the NFI was, that the bulk of the boreal forests present themselves as at least two-layered stand structures (see Table 2-3). Single storey structures are commonly a result of disturbances in the forest caused for example by wildfires, cutting activities, or insect pest attacks, prompting succession tree species like the Siberian Birch to fill the forming gaps. We already learned in a previous chapter that the dark taiga forests are of a far more complex nature and as such appear as at least three-layered structures.

Table 2-3: Distribution of forest area by stand structure (NFI report: Altrell, Erdenejav, 2016:65).

Proportion of Forest Area by Stand Structure and Forest Inventory Region, %				
Regions	Stand Structure			
	One-layer	Two-layer	Three-layer	Multi-layer
Mongolia	**28**	**53**	**17**	**2**
Altai	42	55	2	1
Khangai	40	40	14	6
Khuvsgul	28	52	20	1
Khentii	18	60	19	3
Boreal buffer zone	43	51	5	1

The subsequent table (Table 2-4) provides a good insight into the age distribution of the boreal forest, indicating, that there is an apparent lack of young forest areas. This means grave implications for the conduction of a sustainable forest management in the sense, that there will be hardly any harvesting potential over the long term (Altrell and Erdenejav, 2016: 69).

Table 2-4: Proportion of forest area by age class and forest inventory region (NFI report: Altrell, Erdenejav, 2016:69).

Proportion of Forest Area by Age Class and Forest Inventory Region, %						
Region	Age Class, years					
	<20	20-50	50-100	100-200	200-300	>300
Mongolia	**0.5**	**4.6**	**38.9**	**48.5**	**6.1**	**0.5**
Altai	0.3	7.9	23.2	43.5	21.3	3.9
Khangai	0.1	1.7	40.4	51.9	4.5	0.5
Khuvsgul	0.3	4.1	38.3	49.0	7.6	0.6
Khentii	0.9	6.5	41.8	45.5	2.6	0.1
Boreal buffer zone	1.5	8.9	30.9	47.5	9.7	1.1

Another feature to take note of is the proportion of boreal forest populating different parts of the forested landscape. In an earlier note, scientists like Dulamsuren and Hauck (2008), Hilbig (2006), and Klinge *et al.* (2018) already stressed that the southern slopes of the mountainous areas are almost void of trees, or at least of forest patches. These findings are strongly supported by the NFI assessments presented in the following table (Table 2-5) (Altrell and Erdenejav, 2016: 97).

Table 2-5: Proportion of forest area by slope aspect (NFI report: Altrell, Erdenejav, 2016:97).

Proportion of Forest Area by Slope Aspect and Forest Inventory Region, %									
Forest Region	Aspect (Direction)								
	N	NE	E	SE	S	SW	W	NW	NN*
Mongolia	28.4%	19.7%	8.2%	5.8%	3.1%	5.9%	8.5%	19.6%	0.8%
Altai	38.7%	25.0%	8.0%	1.6%	2.0%	0.8%	1.7%	21.8%	0.5%
Khangai	40.7%	16.8%	8.2%	1.9%	1.8%	0.7%	9.5%	18.6%	1.7%
Khuvsgul	27.7%	19.3%	7.4%	7.4%	3.8%	7.2%	8.0%	18.9%	0.3%
Khentii	18.4%	21.3%	9.5%	7.0%	3.3%	8.3%	9.7%	21.6%	1.1%
Boreal buffer zone	36.1%	22.8%	8.6%	1.6%	1.4%	2.9%	6.8%	19.1%	0.6%

Another forest structural feature most foresters pay a lot of interest into, is the growing performance of certain tree species related to the site conditions. The NFI reports an overall amplitude for growing stock ranging from about 60 m^3/ha to around 132 m^3/ha throughout all species (Table 2-6) (Altrell and Erdenejav, 2016: 44–45). Once again, the overwhelming presence of the Siberian Larch largely contributes to the growing stock volume of the boreal forests with 80.7% of the total (Table 2-7).

Table 2-6: Growing stock volume by tree DBH class (NFI report: Altrell, Erdenejav, 2016:44).

Growing Stock Volume, by Tree Dbh class and Forest Inventory Region, m^3/ha								
Regions	Boreal Average Forest				Boreal Production Forest			
	Tree Dbh class			Total	Tree Dbh class			Total
	>30 cm	15-30 cm	6-15 cm	≥6 cm	>30 cm	15-30 cm	6-15 cm	≥6 cm
Mongolia	**59.1**	**41.9**	**12.9**	**113.9**	**62.6**	**40.1**	**12.6**	**115.3**
Altai	36.7	26.0	11.4	74.1	29.2	20.4	8.2	57.8
Khangai	62.8	50.7	16.3	129.8	62.8	49.7	15.5	127.9
Khuvsgul	64.8	42.7	13.8	121.3	75.8	42.1	14.0	131.9
Khentii	50.2	36.0	9.2	95.5	43.9	28.7	7.5	80.2
Boreal buffer zone	48.8	39.4	10.9	99.2	48.2	36.9	11.8	96.9

Table 2-7: Average growing stock volume by tree species (NFI report: Altrell, Erdenejav, 2016:45).

Growing Stock Volume by Tree Species and Forest Inventory Region, m^3/ha							
Tree Species	**Forest Inventory Region**					**Mongolia**	
	Altai	**Khangai**	**Khuvsgul**	**Khentii**	**Boreal buffer zone**	*(m^3/ha)*	*(%)*
All tree species	**74.1**	**129.8**	**121.3**	**95.5**	**99.2**	**113.9**	**100**
Larix sibirica	70.5	125.7	105.1	47.5	83.4	91.9	80.7
Pinus sibirica	0.1	3.5	5.1	16.1	5.1	7.6	6.7
Betula platyphylla	0.1	0.5	7.2	13.4	4.0	7.3	6.4
Pinus sylvestris	0.004	0.01	2.5	15.3	5.9	5.6	4.9
Picea obovata	2.8	0.1	1.1	1.1	0.5	0.9	0.8
Populus tremula	0.0004	0.02	0.1	1.2	0.2	0.4	0.3
Abies sibirica	0.2	-	0.05	0.8	0.1	0.2	0.2
Populus suaveolens	0.4	0.01	0.03	0	0	0.02	0.02
Populus laurifolia	-	0.003	0.03	0.01	0	0.02	0.01
Ulmus pumila	-	0.003	0.01	0.003	0	0.01	0.01
Populus diversifolia	-	0.001	-	0.002	0	0.001	0.001

The former Mongolian Botanical Institute published a handbook for forest mensuration in 2012 (unfortunately not available), in which actual and optimal forest volume were compared. According to this source, the forest volume could be more than doubled, if the forest stands were kept healthy and well-stocked (Altrell and Erdenejav, 2016: 49). This goal might sound rather optimistic, given the current situation of the forest management structures, however, clearly indicate, that the Mongolian forests are a far cry from being in a perfect condition.

It also comes to no surprise, that Larix Sibirica ranks first, when looking at the growing stock density per tree species (Table 2-8). Nevertheless, it has to be borne in mind, that the presented figures below reflect the calculated average of all age classes.

Table 2-8: Growing stock stand density by tree species (NFI report: Altrell, Erdenejav, 2016:48).

Growing Stock Stand Density by Tree Species and Forest Inventory Region *stems/ha*							
Tree species	**Forest Inventory Regions**					**Mongolia**	
	Altai	**Khangai**	**Khuvsgul**	**Khentii**	**Boreal buffer zone**	*(stems/ha)*	*(%)*
All tree species	**469**	**685**	**586**	**444**	**500**	**560**	**100**
Larix sibirica	441	645	445	151	381	401	71.6
Betula platyphylla	3	12	87	151	67	87	15.6
Pinus sibirica	1	25	30	74	29	40	7.2
Pinus sylvestris	0.02	0.1	7.2	46	17	17	3.0
Picea obovata	22	1.7	13	7.7	2.7	9	1.6
Populus tremula	0.1	0.3	2.5	9.8	2.3	4	0.7
Abies sibirica	2	-	0.4	4.9	0.6	2	0.3
Populus laurifolia	-	0.1	0.3	0.1	-	0.2	0.03
Ulmus pumila	-	0.2	0.1	0.04	-	0.1	0.01
Populus suaveolens	1	0.05	0.05	-	-	0.1	0.01
Populus diversifolia	-	0.01	-	0.03	-	0.01	0.002

As trees grow older, the fiercer the competition for light and nutrients gets. As a consequence, the stronger individuals survive, leading to a lower tree number per hectare as compared to much younger forest stands. For the Khentii region the NFI reports stem numbers per hectare for DBH >30 cm 45 trees, for the DBH class 15-30 cm 144 trees, and for DBH 6-15 cm 255 trees, totalling 444 stems per hectare (Altrell and Erdenejav, 2016: 47). The authors of the presented figures emphasize, that stem densities in mature forests are a fraction of the numbers of stands in an early stage of development.

Another key variable of forest appraisal is represented by the basal area (BA) of a tree class and per specie. BA is calculated as the cross-sectional area at breast height (i.e., 1.3 m). The table below (Table 2-9) indicates fairly low average values between 11.8 and 18.9 m^2 per hectare. However, this finding is very much in line with assessments carried out by Canadian scientists, who calculated similar figures (i.e. 13.59 m^2/ha) for boreal forests across Canada (Matasci *et al.*, 2018).

Table 2-9: Growing stock basal area (BA) by tree DBH class (NFI report: Altrell, Erdenejav, 2016:51).

Growing Stock Basal Area by Tree Dbh class and Forest Inventory Region, m^2/ha				
Region	Tree DBH class			Total
	>30 cm	15-30 cm	6-15 cm	
Mongolia	**6.9**	**6.3**	**2.8**	**15.9**
Altai	4.9	4.3	2.6	**11.8**
Khangai	7.7	7.7	3.4	**18.9**
Khuvsgul	7.4	6.3	3.0	**16.6**
Khentii	5.7	5.4	2.2	**13.2**
Boreal buffer zone	5.9	6.0	2.4	**14.4**

The NFI also mentions Siberian Larch as the dominating tree species for BA with an average of 12.5 m^2/ha, with White Birch following suit with 1.4 m^2/ha for the whole of Mongolia. Values calculated for Khentii are 6.2 m^2/ha for Siberian Larch, 2.5 m^2/ha for White Birch, 2.2 m^2/ha for Siberian Pine, and 1.9 m^2/ha for Scots Pine, thus reflecting a much more diverse forest structure (Altrell and Erdenejav, 2016: 51–52).

Forest ground vegetation constitutes a vital part of the boreal ecosystem, however, it can be a crucial interference factor for the computer-based classification of multispectral aerial or satellite imagery. Dark shrubs not being concealed can create darker spectral signatures in bright forest areas (e.g., larch, birch), whereas lush bright green grass or herb layers have the potential to 'fool' the interpreter or classifier and mock a healthy forest instead of identifying forest patches being completely defoliated or dead. Below figure (Figure 2.4) illustrates these potential caveats for the inventory region of Khentii. Apparently, herbs, grasses, as well as mosses, and shrubs play an important role in forest floor flora

community. Having said this, forest floor vegetation is far from forming uniform rugs, but is rather controlled by even small changes in topography and micro-climate.

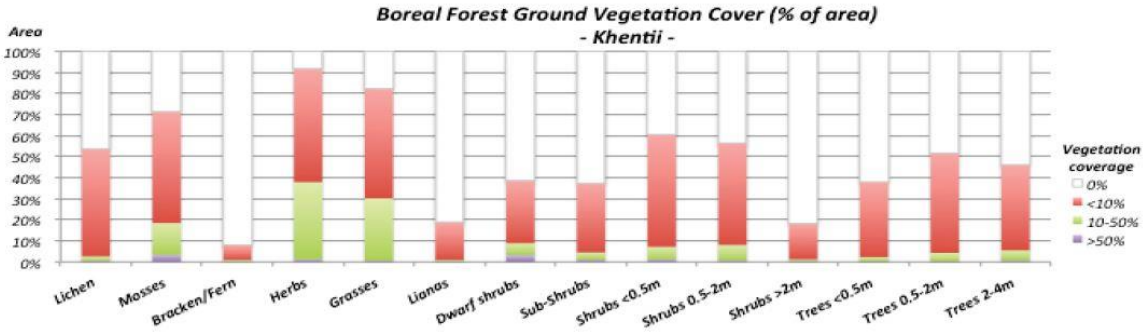

Figure 2.10: Forest ground vegetation cover (% of area) for the Khentii region (NFI report: Altrell, Erdenejav, 2016:66).

2.3.2. Forest policies

For centuries, the boreal forests of Mongolia have been a refuge for a rich wildlife, but also for people roaming the vast taigas for hunting, gathering firewood, and collecting non-timber forest products such as berries, mushrooms, lichen, pine kernels, and antlers. However, it was only in the 1970s, Mongolia's government realised, that forest fires, illegal cutting of timber for construction and firewood, and numerous devastating insect attacks were increasingly threatening the biodiversity and merits for the water regime. With the transition from a centrally-planned economy to a market-oriented system in the 1990s, the Mongolian government was faced with the need for forestry-related legislative acts and forest policies to meet the demands of a growing population, but also to govern and control the utilisation of the forest resources in a sustainable manner (Tsogtbaatar, 2004b). The table below (Table 2-10) reflects the most relevant forest laws and policy acts for responding to the depletion of the forests. The Forest Law of Mongolia from 1995 (revised in 2012) clearly states the purpose of the law as to 'regulate the protection of forests, the proper utilization and regeneration of forests'. The law also constitutes: '…forest resources are **state property** under the sole authority of the Mongolian people' (Mongolian Ministry of Justice, 2012). However, tenure rights can be granted to communities and private companies by administrative bodies on the aimag, or soum level (Tsogtbaatar, 2004b). According to the Natural Environment Conservation Law the Ministry of Nature and Environment bears the duty to work out and implement state policy on the conservation and proper utilisation of the forest resources, whereas the Ministry of Trade and Industry '…responds in wood and forest policy and in the execution of this policy' (Munkhzorig, 2009). The author also states, that the implementation of the various programmes is very slow due to lack of resources and deficits in improving the legal environment for relevant state agencies, NGOs, and enterprises. Apparently, progress has been made in the abolishment of illegal wood

supplies from the forest, and in the reduction of damages caused by fire and harmful insects. In addition, reforestation work has been intensified, and initiatives for the investment in wood processing plants initiated. Nevertheless, a few major problems still exist, namely the execution of forest policy and financial support of the timber industry due to economic predicaments (Munkhzorig, 2009, Wyss, 2007: 14–15).

Table 2-10: Regulatory framework for forestry and forest management in Mongolia (sources: FAO, 2020, World Bank, 2004, Mongolian Ministry of Tourism, Nature and Environment, 2020, Tsogtbaatar, 2004).

Mongolian Forestry and Forest Management Policy Framework
• First forest laws (1940-1954) • Law on Forest (revised in 1995) • National Forestry Program (2001) • Green Belt Eco-Strip National Program (2005) • State Policy on Forest (2015) • Green Development Policy of Mongolia (2015) • Action Program of the Government of Mongolia 2016-2020 (2016) • Mongolia Sustainability Development Vision 2016-2030 (2016)

An important stipulation to be found in the Law on Forest concern the protection of the boreal forests in Mongolia. Three categories have been defined, namely *special*, *protection*, and *utilisation* zones (more details on utilisation of forests are provided in chapter 2.3.3.). Protected areas comprise for example forests around villages and towns, saxaul forests, and forests populating slopes exceeding 30 degrees. Specific actions are to be taken or prohibited in those areas, including fire management, the protection from disease and harmful insects, and from negative impacts of human activity. Forests within special zones consist of sub-alpine forests, virgin zones and specific areas in Conservation Parks. All forests not being designated as special or protection forests are available for economic use (Tsogtbaatar, 2004b).

2.3.3. Forest utilisation and management

With the revision of the Forest Law in 2012, only two administrative zones for the management of the forest resources have remained: the *protected zone* and the *utilisation forest zone*. In the utilisation forest zone, the boreal forests are managed by forest user groups (FUGs) as community-based management groups, as well as by private enterprises. Activities comprise logging, reforestation, and forest cleaning. The table below indicates, that more than 30% of the forested land are still kept under strict protection rules, with 21% of the forests being designated for production. All utilisation licences are authorised and

issued by the Mongolian Ministry of Environment and Tourism (MET). FUGs can lease the forest land from the State for up to 60 years, however, they are not allowed to cut standing trees, and as such, the motivation to engage in forest management activities has been extremely low (Altrell and Erdenejav, 2016: 13–14).

Table 2-11: Designation of boreal forest area in 2015 (NFI report: Altrell, Erdenejav, 2016:41).

Designation of Boreal Forest Area			
Designation		**Forest area (ha)**	**Percentage (%)**
Protected	State Protected Area (SPA)	2 799 567	31
Production	915 forest user groups	1 528 343	17
	76 forest concession	369 263	4
"Undesignated"	Not yet officially assigned	4 135 375	48
Total		**9 095 925**	**100**

A number of authors have mentioned the depletion of the forest resources in the recent decades, associated with the decline of forest areas due to wildfire and insect attacks, as well with illegal logging activities and the lack of law enforcement (FAO, 2007, Munkhzorig, 2009, Teusan, 2018, Tsogtbaatar, 2004b, World Bank, 2021). Findings of the NFI in 2016 reveal, that the average timber volume for Siberian larch, White birch, and Scots pine is about 61 m^3 per hectare. The average stem volume of the logged trees per hectare was estimated to be 14 m^3 for the whole of the boreal inventory areas, thus providing a rough indication on the over-utilisation of the forests (Altrell and Erdenejav, 2016: 53–57). Unfortunately, no precise figures on the amount of cut timber per annum exist. In order to get a much better idea on the real magnitude on the depletion of the forest resources, the annual increment of the tree volume would be very useful to learn. At least it seems common practice in many countries to only cut the incremental volume in order to achieve a sustainable system. Only a few studies by Gradel (2017) and Gradel *et al.* (2017a) provide some clues on the growth development of Siberian larch and White birch. Figures on local forest taxation carried out by private companies are either not available or are based on ocular estimation, thus making any inferences based on sound scientific methods pure speculation (Altrell and Erdenejav, 2016: 107–108).

According to recent reports of the World Bank and the FAO the Mongolian forestry sector seemingly struggles to get back on its feet after the collapse of the Russian regime in 1990 (Corsi *et al.,* 2002, Crisp *et al.,* 2004, Erdenechuluun, 2006, FAO, 2010, 2013, 2014a, 2020b, Ykhanbai, 2010). Indications that that Mongolia is rapidly approaching a crisis are striking.

The major conclusions of the various consecutive reports are:

- The levels of forest harvesting are not sustainable, with the period from 1970 to 1994 coined as a period of 'forest liquidation'.
- Estimates range from 36 to 80% for illegal harvesting activities.
- Fuelwood contributes between 65 and 80% of total wood harvest.

Further quotes seem to underpin the desolate situation: 'There is no sense in which forests of Mongolia can be said to have ever been subject to science-based sustainable forest management (SFM)…', and '…, though Mongolia has a credible body of forest legislation, regulations, policies and programs, the planning, management and control systems to achieve these on the ground do not presently exist' (Crisp *et al.,* 2004). This is a truly a damning indictment for the execution of the forest policy legislation. To make things worse, the previously well working system of local responsibilities with communities being in charge and with a forest service being in place, was abolished in the 1990s. In addition, at the ministerial level (i.e., MNE) a lot of restructuring and reorganisation took place in 2004 resulting in a new administerial system with no sole responsibilities for the forestry sector. As a consequence, the formerly strong and unified stewardship for the forests gets increasingly watered down. However, with the recovery of the Mongolian economy in association with an increase in foreign aid (e.g., FAO, IWF, World Bank, GIZ, UN-REDD), the prospects for creating a sustainable forest management in connection with capacity building efforts should be not that bleak.

2.3.4. Threats and challenges

As mentioned above, structural deficits have already afflicted the adequate management of the taiga forests in Mongolia. Other factors such as increasing wildfire incidents and attacks of harmful insects hold the potential to exacerbate the situation. As an example, the following figure illustrates the magnitude of insect inflicted damage on taiga forests.

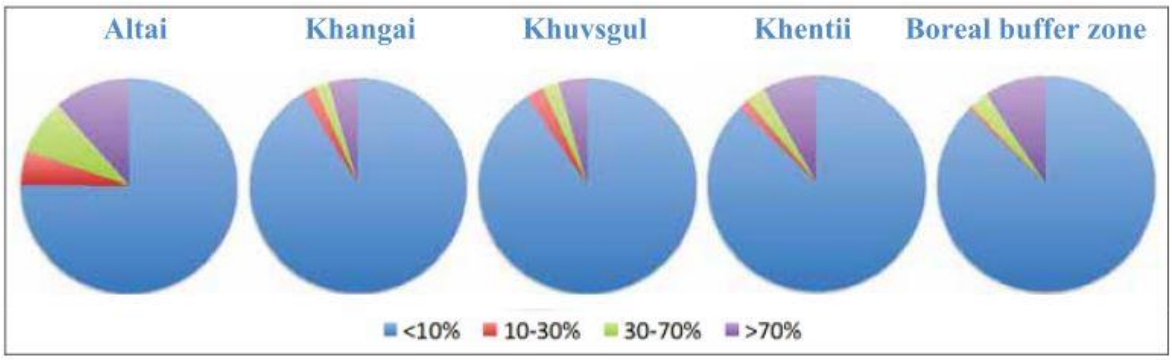

Figure 2.11: Proportion of damaged forest area, by insect damage severity (proportion of damaged basal area) – source: NFI report ((Altrell and Erdenejav, 2016: 88)

Above graph reflects quite strikingly, that insect pests cannot be considered a miniscule problem. Notably, in the light of a changing climate and the associated repercussions on tree health, insect populations will have to monitored closely. According to the 2016 NFI report about 70% of the boreal forest were found to be in a healthy condition showing no or little damage caused by snow/ice, fire, insects, grazing activities, or by lightning (Altrell and Erdenejav, 2016: 80–84). However, the situation with respect to the rate of damage caused by wildfire gives cause for concern. In recent years about 35% of the entire Khentii area were affected by fire (for more details on wildfires in Mongolia please refer to chapter .2.) (Altrell and Erdenejav, 2016: 85–86). However, with reports from other scientists and own observations this figure seems quite optimistic, given the fact, that fire occurrences are increasing with intervals getting shorter (Batima *et al.,* 2005, Byambasuren, 2011, Chu *et al.*, 2016, Flannigan *et al.*, 2009, Goldammer and Furyaev, 2010). For example, Gradel (2017: 155–157) reports that the forest ecosystems in the Altansumber and Bugant research are evidently severely disturbed by fire. Grazing of the livestock in the forest regions also seems to be causing tree damage (Yamamura, 2013: 65,83,145). The NFI report describes varying degrees of impact on the forest, with the Altai region leading the statistics by showing a rate of 20% with high impact (Altrell, 2017: 92).

Reports by big international institutions indicate a severe loss of forest area in Mongolia during the last few decades (Crisp *et al.,* 2004, FAO, 2014a, 2020b, World Bank, 2021). The causes of those losses are manifold (e.g., logging, wildfires). In his research Teusan (2018) calculated an overall decline of 15% for the forest cover, with a reduction of the Scots pine area of 30% for the Selenge province for the period from 1990 to 2015. By analysing big sets of satellite data, he found forest fires to represent the major cause for the immense reduction in forest area. The Mongolian government has conceived the situation some time ago and as such has undergone great efforts to counteract this trend. Fire-fighting strategies were developed and re-, and afforestation programmes enacted and implemented. Annually around 400,00 to 600,00 US$ are being invested for such programmes, the bulk of the sum being endorsed by foreign aid organisations (World Bank, 2021, Wyss, 2007: 27). Due to

the harsh climatic conditions, the increasing damage caused by livestock, and the lack of manpower (for watering the plants) only 5% of the afforested areas can be considered to be secured (Crisp *et al.,* 2004).

Local experts identify the main threats and challenges for the national forest resources as: (i) a soaring demand for fuel and industrial wood, (ii) the increasing numbers of livestock with forests being used as foraging areas, and (ii) the massive impacts of wildfires (Erdenechuluun, 2006, Gradel *et al.*, 2019, Schmidt-Corsitto, 2016, Schmidt-Corsitto, 2017, Tsogtbaatar, 2013). With a dwindling economy, a weak law enforcement, the lack of expertise, and the presence of corruption, illegal logging will have to be curbed and the transition from a need-oriented to a sustainable forestry initiated. First steps in this direction have already been taken (Gradel *et al.*, 2019, Schmidt-Corsitto, 2017).

2.3.5. Remote sensing in Mongolia

There is a growing awareness in Mongolian institutions that remote sensing in association with GIS bears the potential to help facilitate the assessment and monitoring of the natural resources (Mongolian Ministry of Environment and Tourism, 2016, Wyss, 2007). Near real estimates of forest loss, the degree of forest degradation, as well as the determination of carbon stocks, and the occurrence of wildfires are perfect candidates for remotely sensed imagery. Since most of the areas in Mongolia are near to inaccessible, a view from above remains unmatched and can also reduce costs for acquiring field data (Ciesla, 2000: 3, Xulu *et al.*, 2019). Initially, only B&W aerial imagery were utilised for delineating forest areas in Mongolia. In 1989 the first images acquired from spaceborne platforms were employed to update the forest inventory maps and process meteorological. Since then, a growing number of national organisations such as The Ministry for Nature and Environment, the National Remote Sensing Center, The Ministry of Agriculture and Enterprises, as well as the State Agencies for Forest and Water Management have been favouring satellite imagery from various sensors. Furthermore, the Academy of Sciences, and The State Agency of Geology operate their own remote sensing centres (Khuldumur and Erdenetuya, 2010). Highlights for the establishment of a remote sensing infrastructure in Mongolia certainly were the foundation of the Information and Computer Center (ICC) in 1987 to receive NOAA satellite imagery (later also MODIS , Himawari, and Suomi NPP images), and the integration of the Remote Sensing Center into the National Agency for Meteorology, Hydrology and Environment. The retrievable product line from their website (www.icc.mn) comprises satellite maps generated related to fire incidents, vegetation (NDVI), drought, land surface temperature, snow cover, and also dust storms and aerosols. Currently, a great deal of remote sensing research and teaching is performed at the National University of Mongolia (NUM), GIS laboratory, chaired by Prof. Tsolmon Renchin. Extensive

use of satellite imagery is also reported for the Fire Management Resource Center - Central Asia Region at the NUM, with Oyunsanaa Byambasuren being head – as a trained forester, he also holds the office as General Director of the Department of Forest Policy and Coordination at the MET.

Rest of page intentionally left blank

3. Forest inventory

According to Scott and Gove (2002: 814) ‘Forest inventory is an accounting of trees and their related characteristics of interest over a well-defined land area’. The pursuant chapter is dedicated to the basic concepts and related disciplines with respect to the sampling design, as well as to the gathering and analysis of tree or forest associated traits. Current techniques are portrayed and future trends outlined. The distinguished reader will find impressively detailed work in publications such as by Kangas and Maltamo (2009), Köhl *et al.* (2010), Loetsch and Haller (1964), van Laar and Akça (2007), Vries (1986), and Zöhrer (1980) for extensive reading.

3.1. Introduction and concepts

3.1.1. General concepts

‘Forest inventories usually generate a specific set of data mainly descriptive statistics including precision statements on qualitative (e.g. species) and quantitative (e.g. tree diameter) attributes’ (Kleinn, 2014). In simple terms, forest inventories provide information on the extent, quantity and condition of the forests (Kangas, 2010). Being truly interdisciplinary, forest inventory involves disciplines such as digital data processing (IT), biometry, remote sensing / GIS, forest growth and yield, with providing useful information for decision makers in the fields of silviculture, (forest) economics, (forest) politics, environmental protection and nature conservation, forest road construction, and timber harvesting (Zöhrer, 1980: 13–15).

The increasing number of the population in concurrence with a flourishing mining and salt production industry caused a severe shortage of the forest resources in many parts of Europe in the 14th and 15th century. The construction of large fleets for military (e.g., Armada) and commercial purposes also largely contributed to the devastation of vast forest areas. These circumstances prompted the first forest inspections and taxations (e.g. Nürnberger Reichswald) to result in the concept of sustainable forestry coined and devised by Hans Carl von Carlowitz 300 years ago (Hasel, 1985: 41,104,221-230). In the early days the forest taxations were based on visual estimation, since it was swift and fairly cheap. The advancements in mathematics and statistics, however, induced a true paradigm shift in forest inventory and resulted for instance in the first inventories on a national scale were introduced and conducted in Scandinavia in the 1920s (Kangas and Maltamo, 2009: 5–6). In recent years new technologies based on the development of new air-, and spaceborne sensors (very high resolution multi-, and hyperspectral imagery, laser scanning) and the

mindboggling progress in data processing caused a revolution in the forest inventory sector (Kangas and Maltamo, 2009: 8, Kleinn, 2014).

Inventory goals can be manifold, largely depending on the available resources for the conduction and the size of the forest areas to be inventoried (i.e., scale). In countries with intensively managed forestry activities very detailed information on the stocked area, timber volume, increment, biomass, nature conservation and site conditions are crucial. In contrast, in countries with vast forest areas (e.g., in the tropics) the required information is very much focused on merchantable timber volumes and species. Whereas taxations are usually restricted on smaller areas (compartments, stands) with a high intensity on data gathering, large scale inventories (regions, countries) commonly are restricted on the mining of data related to the extent of the forests, the available species, trends in forest extent and biomass, and the growing stock (e.g. FAO Forest Resources Assessment) (FAO, 2020a, Kangas and Maltamo, 2009: 279–281, Loetsch and Haller, 1964: 4–6, Zöhrer, 1980: 15–16). However, when high spatial variation of forests need to be considered, even inventories on a national scale have to be very detailed (e.g. NFIs in Germany, Finland, Sweden) (Kangas and Maltamo, 2009: 195, 295-300). Forest inventories not only serve as a basis for planning forest related specific activities, but also proved to be very powerful tools for controlling and monitoring to detect trends of any kind (Zöhrer, 1980: 16).

A complete census would undoubtedly yield the best inventory results, however, proves to be virtually impossible to achieve due to the large extent of the forest areas. For this reason, the acquisition of the required information is commonly based on sampling strategies involving only a proportion of the population. Two main schools have evolved in recent years, namely the *design-based* and *model-based* sampling approaches. Forest inventories primarily rely on design-based concepts, but with the progress in computer science and mathematics model-based concepts are becoming increasingly popular (see chapter 3.1.5.). For the design-based inference the randomness in the sampling process is entirely hinged on the random selection of the sampling units. In model-based inference the randomness is an intrinsic part of the model to describe the population (Kangas and Maltamo, 2009: 3–4). For a few decades there has been very controversial debates on whether sampling has to be systematic or randomised. In cases of heterogenous populations randomised sampling strategies have outperformed systematic ones, however, an increased precision can be obtained from the latter (Kangas and Maltamo, 2009: 6, Scott and Gove, 2002: 815–816).

3.1.2. Sampling designs

In the last decades sampling designs have been devised in abundance. They comprise methods like cluster sampling, double sampling, simple random sampling, stratified sampling, systematic sampling, two-stage sampling, and angle count sampling, just to name a few. Sampling plots can also be of a permanent (for monitoring) or temporary nature. The most common designs are portrayed in the following.

Areal-based methods

Areal-based sample plots are commonly simply-shaped units (square, circle), which can be easily located on the ground. Individual trees are sampled in varying numbers to allow inference of estimates based on a per-unit-area basis (e.g., volume per hectare) to sufficiently characterise a forest area and to make work more efficient. Between-plot variation can be reduced by increasing the plot size (entailing greater within-plot variation). For further concentration of effort in the field it has become common practice to use *clusters* of plots. The so-called *strip* and *line-plot* cruising methods have been standard procedures in Scandinavian countries for many years. Strip sampling encompasses the sampling of all trees in a strip of land with the width being fixed. Line-plot approaches are based on a line scheme running through a forest on which fixed-area plots are visited at regular intervals, having the advantage of providing the same accuracy as strip-based methods, but with a smaller area to be surveyed (Kangas and Maltamo, 2009: 6, Scott and Gove, 2002: 817–818). Some ground-breaking work was done by a scientist by the name of D.J. Finney, who found out that a *stratification* prior to conducting work in the field showed numerous merits (Finney, 1950). His observations were confirmed by other authors, who describe the method to work particularly well for large-scale environmental patterns, where the area is broken up into relatively homogenous subareas to be sampled (Green, 1979: 35–38, Kangas and Maltamo, 2009: 24, Prodan, 2014: 280).

An areal-based method known as plotless timber cruising can be ranked as one of the most influential developments in forest sampling. It was introduced by Bitterlich in the late 1940s and is also known as *angle count sampling* describing a method, by which the sampled area is associated with each tree and is thus variable in size (Zöhrer, 1980: 30–35). The technique was devised to get a simple and quick estimate of the basal area represented by trees in a specific area. The person in the field counts those trees whose diameter appears bigger than a specific critical angle α. With a 360 degrees sweep of a sample point the estimate of the aggregate basal area per hectare is carried out (Prodan,

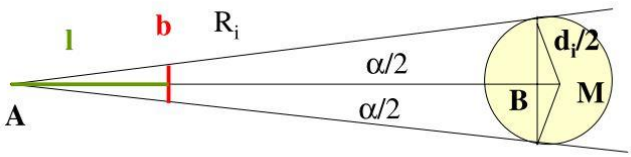

Figure 3.1: Concept of the angle count sampling (Nagel, 2001).

2014: 94–97, Scott and Gove, 2002: 818, Zöhrer, 1980: 30–35). The letters in the graph denote: **A** position of surveyor, **B** tree diameter to be counted as tree being member of sample, **α** for angle, **l** for distance between human eye and tally plate, **b** for width of tally plate.

Grosenbaugh extended the method portrayed above by applying probability proportional to size sampling (*PPS*) to get an estimate of any tree attribute (e.g., biomass, volume, tree number). Another variation of the point-to-tree distance technique was introduced as the so-called *6th-tree sampling*. It considers a fixed number of tress (here: six) nearest to the sample point to be measured. This method was developed by Prodan in 1969 to be used for the estimation of stand density, and basal area. Many exhaustive studies on the tree distance approach showed that with a sufficient amount of trees included in the sampling process very good estimates on tree number, basal area, and tree volume can be achieved.

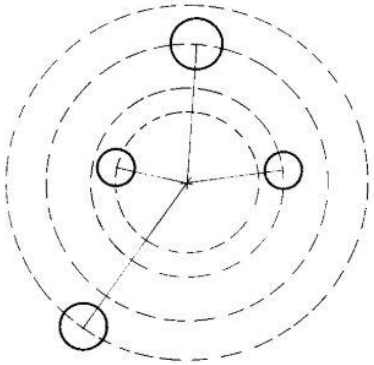

Figure 3.2: Point-tree distance method (Pelz, 1983).

The 6th-tree method is very easy to apply in the field, with only the distances of the 6 nearest trees and their DBH to be measured. Although the 6th-tree sampling yields satisfactory results in a very efficient manner, bias has been reported for forest stand not following a Poisson distribution (Pelz, 1983). In addition, the coefficient of variation has been fund to be substantial resulting in a very limited applicability in practice (Suzuki, 2012). Zöhrer (1980: 45–46) also reports on bias due to clumping effects of tree groups.

Tree-based methods

These methods are based on the traits on the individual tree instead of describing characteristics a sub-population. This can turn out to be very useful, when information such as individual tree volume is required for timber sales. Grosenbaugh for example developed the so-called *3P sampling* (probability proportional to prediction sampling) with the sample size being random and the sampling concentrated on the tree of most interest (Scott and Gove, 2002: 818–819). Detailed measurements on the specific tree are a main characteristic of this method. Very good and unbiased estimates for tree volumes have been reported by Scott and Gove (2002) and van Deusen (1987).

The selection of an appropriate sampling method seems to be far from being trivial. Optimal data acquisition can be approached and judged differently. Traditionally, the sampling

design yielding a minimum of variance for e.g., volume within in certain budget bracket is given preference. Authors like Burkhart et al. (1978) suggest that the largest variance (or the variance of the most relevant variable) shall be favoured to determine the sample size. In contrast, authors like Scott and Köhl (1993) prefer the accuracy relative to the desired level of accuracy (Kangas and Maltamo, 2009: 35–36). In addition to the choice of the sampling approach the size of the sampling plots also needs to be taken into account. The larger the plots, the higher the costs for data gathering are. For example, clusters of smaller sub-plots have proven to be expedient in large-area surveys. The optimal plot size is driven by the surveying costs and the variation observed. Studies have shown that apparently the spatial patterns of forests greatly affect the optimal plot size. For a clustered population it is suggested to choose a larger plot size. The following graph demonstrates the effect of spatial patter and plot size on the coefficient of variation.

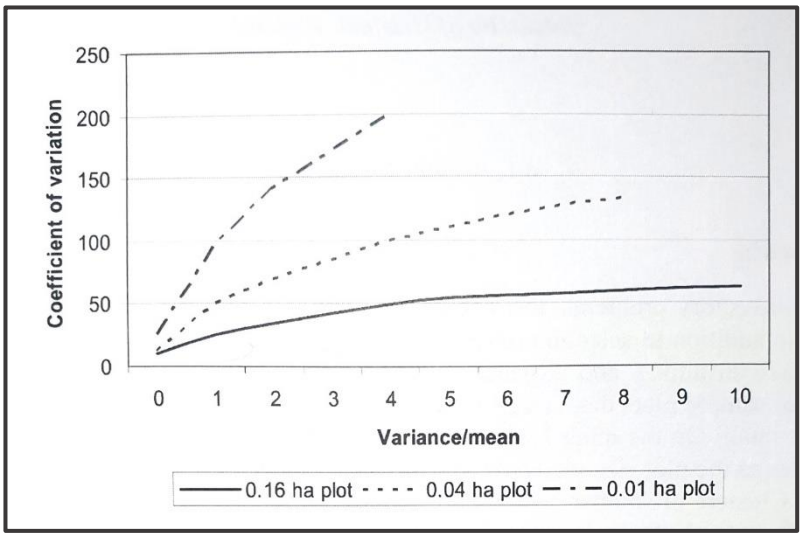

Figure 3.3: Coefficient of variation and the related variance for various plot sizes (Kangas and Maltamo, 2009:54).

3.1.3. Forest mensuration

In this subchapter the most relevant measurement devices and methods are portrayed. The characteristics of the pertaining inventory parameters are described in the subsequent chapter (3.1.4.).

Diameter Breast Height (DBH)

As one of the most relevant variable DBH is measured by means of a calliper or measuring tape in a distance of 1.30 meters above ground. DBH is used to determine basal area and tree volume. Since no tree follows the form of a perfect cylinder, specific measuring rules apply as depicted below. In addition, tree cross-sections deviate from a circle and thus a

single measurement taken with a calliper would cause huge errors. Using a measuring tape minimises these errors.

The diameter distribution provides good insight into the structure of a forest stand. DBH and tree height are closely correlated. Tree diameters at certain tree heights can be measured by using special optical callipers to determine the taper of the tree.

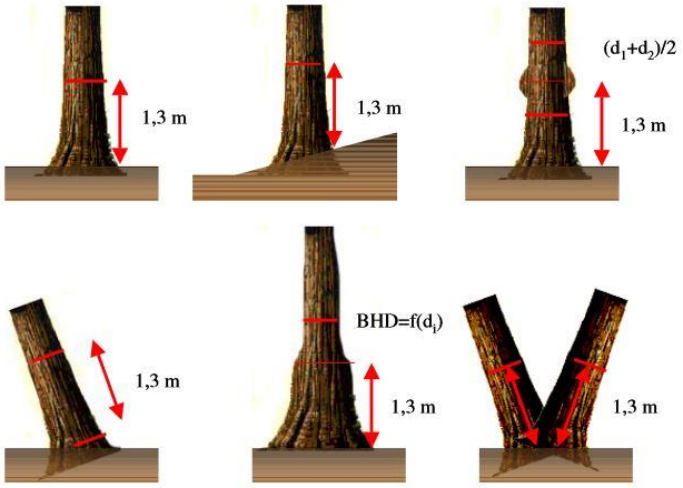

Figure 3.4: Measuring instructions for DBH (Nagel, 2001:3).

Tree height

Another pivotal variable is tree height. Measurements are either based on the geometric or trigonometric principle, with the latter being the most common and precise one. The graph below depicts the trigonometric principle, with the height (h) calculated as: $h = e * \tan \alpha$.

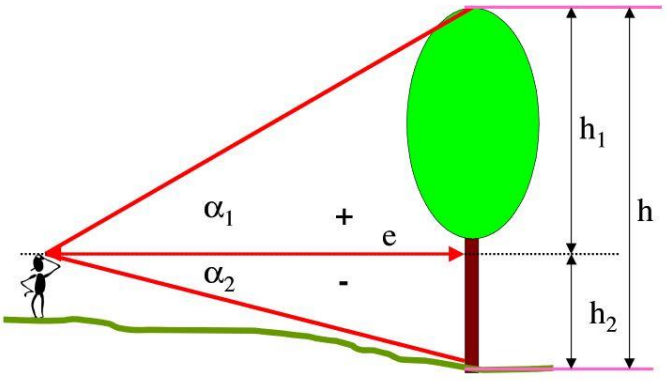

Figure 3.5: Measurement of tree height based on the trigonometric principle (Nagel, 2001:4).

The distance to the tree can be measured using a tape, or the height measuring device features a distance gauge integrated (e.g., transponder). Both heights h_1 and h_2 have to be added to account for the size of the surveyor's body. In a sloping terrain tree height

measurement will have to be corrected – some devices such as the Vertex do that automatically.

Figure 3.6: Examples of tree height measuring devices (Nagel 2001:4).

Stem volume

Determining water displacement is the only direct method to directly measure stem volume. Some useful theoretical approaches are described in the next sub-chapter (3.1.4.).

Tree age and increment

The age of a tree constitutes a good indicator for the growing condition and the competition situation in the observed forest stand. Ocular estimations performed by an experienced surveyor in consideration of tree height and DBH can yield good estimates for the tree age. However, a tree ring analysis with the annual rings counted still represents the gold standard in forest inventory. In the field bore cores are taken by means of a borer (see below). By analysis the core sample the annual increment can also be determined.

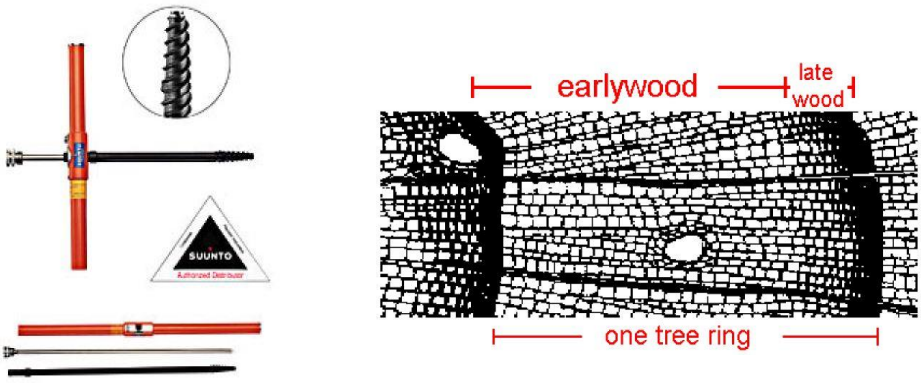

Figure 3.7: Tree increment borer and tree ring analysis (Nagel, 2001:22-24).

Increment is traditionally calculated by observing the tree diameter at the beginning and end of a given time period. These days, special devices are attached to trees for getting direct readings of the increment (see graph below). The ring analyses do not only provide information on the increment of a tree, but also help to detect stress periods (e.g., drought) and damage caused by lightning and fire.

Figure 3.8: Increment tape (Nagel, 2001:22).

Crown attributes

Attributes of a tree crown can give a good representation of the growing conditions on site, as well as an excellent indication of a required silvicultural action (e.g., felling neighbouring trees for providing more space for the crown). Various crown attributes can be determined (e.g., crown length, height), with the crown diameter measured being the most common attribute. It is measured in the field with a so-called crown mirror, enabling the surveyor to precisely determine the brim of the crown. Usually, the distances between the brim outlines in N-S and E-W direction are measured by using a measuring tape to represent the horizontal extent of the crown.

Figure 3.9: Crown mirror (Nagel, 2001:19).

Area determination

The area populated by a certain number of trees is an important indicator for the growing conditions and competition situation. For this purpose, the area itself needs to be properly delineated. Traditionally, the specific areas can be retrieved from existing inventory maps, be measured in the field (GPS, laser devices), or extracted from high resolution imagery taken from above (i.e., airborne or spacebourne platforms). However, the correct retrieval from imagery largely hinges on the clear definition of the boundary between forest and non-forest. The graph below provides a good example for the surveyor and image interpreter are faced with.

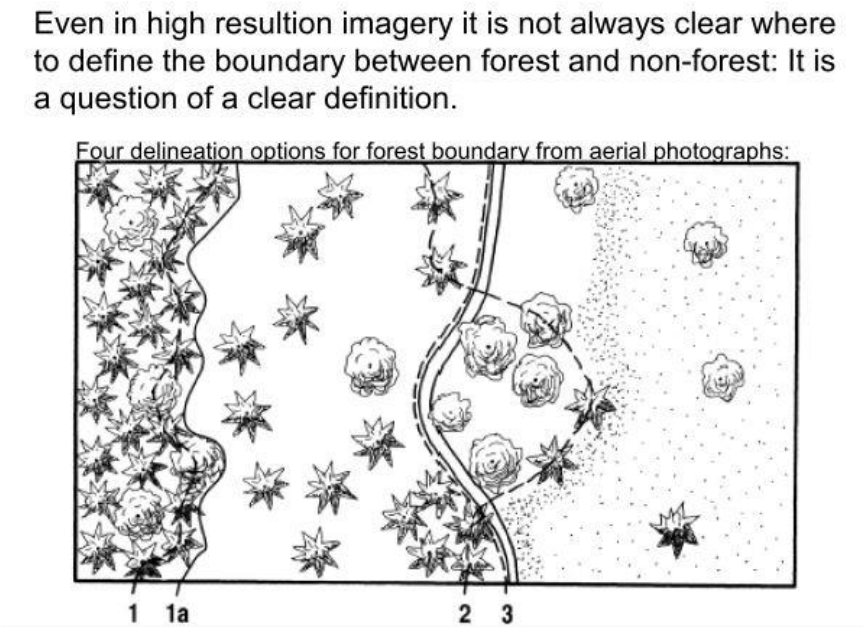

Figure 3.10: Forest definition and delineation problem in high-resolution imagery (Kleinn, 2017).

Once the delineation has been properly set, the number of trees can be counted in the field or on the imagery accordingly to yield an indication of the tree density per area unit.

Basal area (BA)

The basal area of a single tree can be determined by measuring the pertaining DBH of a tree and using the formula $BA = \pi * (DBH/2)^2$ for calculation. This method, however, turns out to be very laborious for calculating the basal area of a given stand. The angle count approach seems to present an efficient way of going the easy, but precise route. The method has been described previously (chapter 3.1.2.) – some of the devices used in the field are presented below.

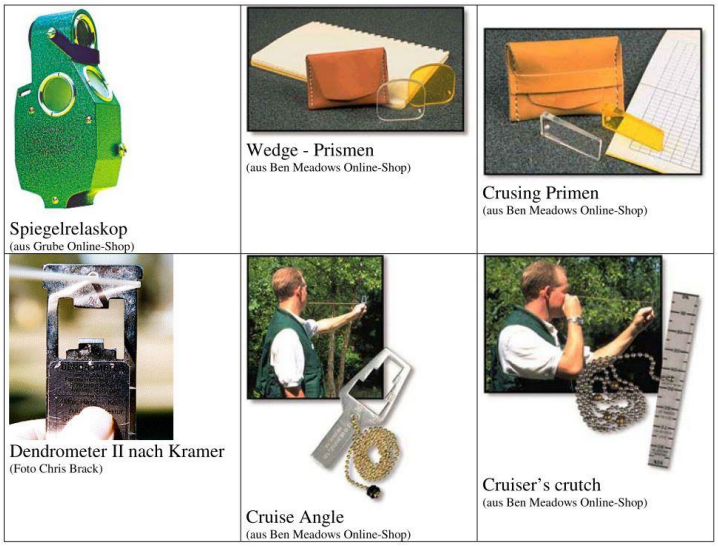

Figure 3.11: Popular angle count devices (Nagel, 2001:46).

The most popular devices in Europe are the *mirror relascope* (top left on the graph) and the *Kramer dendrometer* (below the mirror relascope). Cruise angles and prisms are much more common in the USA and other English-speaking countries.

3.1.4. Relevant inventory parameters

In forest management inventories it is quite common to observe 20-35 variables, however, in 'fine-grained' inventories the number of variables can easily exceed 200 (Kleinn, 2014). The core set of forest and tree attributes comprises:

- Forest area
- **Diameter Breast Height (DBH)**
- **Tree height**
- Tree/stand age
- Tree volume
- Basal area (BA)
- Biomass
- Tree density
- Crown attributes
- Diameter increment
- Stem shape
- Tree quality
- Diversity factors (e.g., Shannon index)
- Tree sociological position

A few of these variables are detailed in the following. For more information please refer to literature published for instance by Edwards (1998), Nagel (2001), Prodan (2014), van Laar and Akça (2007), and West (2009).

Tree height

Tree height has proven to be a relevant predictor for tree growth and as such serves as a reference for site productivity (site index). In this context it is noteworthy, that tree density affects soil nutrient dynamics, above ground biomass, and crown characteristics, and in turn determines height growth, wood quality, and silvicultural treatment for optimal results (Benomar *et al.*, 2013). Inferences on height increment can also provide a sound base for growth models and volume prediction. Canopy height models (CHM) seem to be particularly suited for the determination of height and other valuable vegetation parameters (Dandois and Ellis, 2010) – for details on CHMs please refer to chapter 4.6. Tree tops and their associated locations can be either directly derived from 3D point clouds (LiDAR) or CHMs (Reitberger *et al.*, 2009, Tompalski *et al.*, 2014b). For the extraction of height and tree locations, local maxima calculations, inverse watershed algorithms, or direct measurements from CHMs have demonstrated to be viable options (Edson and Wing, 2011, Panagiotidis *et al.*, 2017, Tiede *et al.*) . The measurement of tree height in the field is traditionally carried out using devices based on the measured distances and angles (trigonometric principle). The measurement itself seems very straightforward, but error sources are abundant. These

error sources are related to flaws in distance and angle determination, the lack of visibility of the tree tops, and the wrong calibration of the devices.

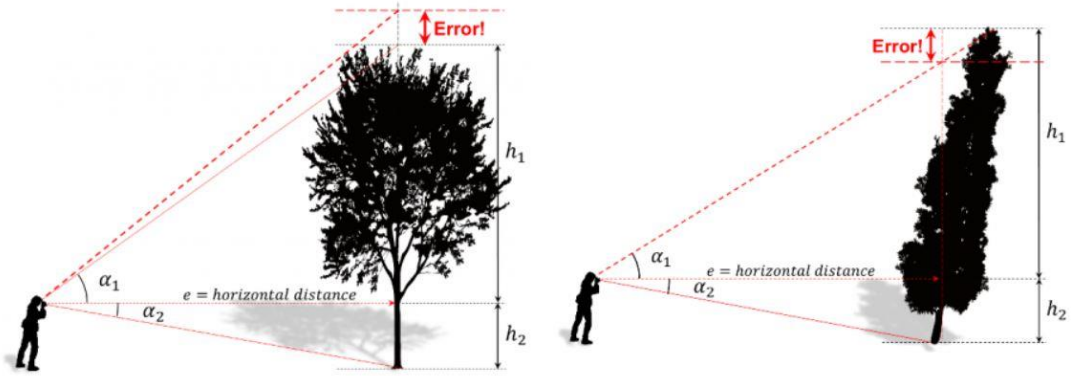

Figure 3.12: Potential errors in tree height measurement (Kleinn, 2014).

With respect to measurements of tree height and DBH in the field a study conducted by Kitahara *et al.* (2010) revealed that inexperienced surveyors produce great errors in measurements with the choice of the measuring device being less important. They also strongly suggest that teams need to be trained with sufficient feedback. According to their investigation tree height errors were greatest with broad-leaved trees (see Figure 3.4.). These findings are supported by statements of other authors, who worked out that the standard error in stand derived data from compartment-based forest taxations (i.e. ground truth data) are in the range of 26 – 36% (Kangas and Maltamo, 2009: 352–353). Another revelation was made by authors finding that the employment of the most modern mensuration equipment (e.g. laser based callipers and height-measuring devices, electronic dendrometers) did not necessarily improve the efficiency and cost saving capacity as initially anticipated (Kangas and Maltamo, 2009: 353).

Diameter Breast Height (DBH)

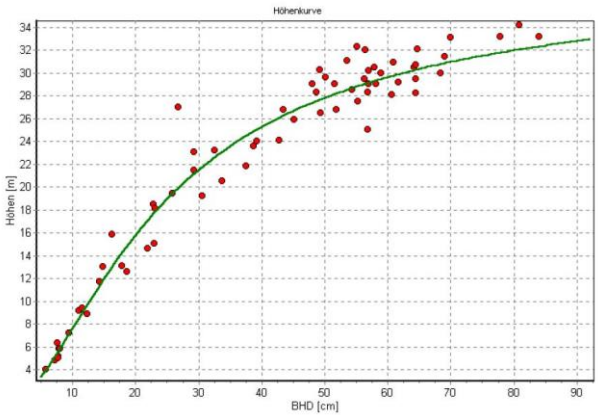

This predictor is another key variable in forest inventory in addition to tree height. It can be measured fairly easily in the field and serves as an entry into calculation of basal area and thus to timber volume. The graph below shows the DBH (BHD) to height (Höhe) relationship.

Figure 3.13: DBH to tree height relationship (Nagel, 2001:35).

Timber volume

Three main indirect methods of calculating timber volume have been established in forest inventory, namely (i) volume calculation by section, (ii) calculation using taper curves (they model the stem shape), and (iii) modelling volume through regression allometric formulas). Volume calculation by section is cumbersome, but yields good estimates of the tree volume. In practice the DBH and lengths of the particular section need to be measured.

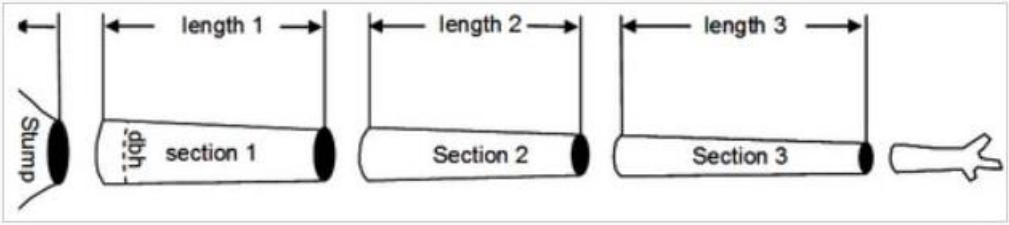

Figure 3.14: Subdivision of a stem into possible sections (Kleinn, 2014).

In the most simple form, the volume of the different sections can be calculated as:

$$V = ghf = \frac{\pi}{4} d^2 hf$$

G denotes the cross-section area at a specific position of a section (e.g., 1.3m, which equals DBH), *f* an additional optional specific form factor that can be integrated to account for a tree shape. The most common approaches for tree volume determination by section calculation are by Huber (corresponding to a cylinder), Smalian and Newton.

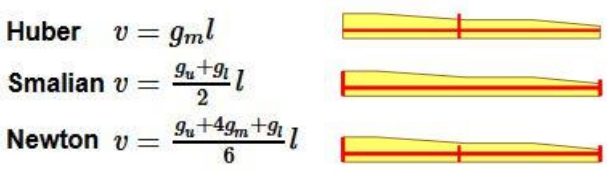

Figure 3.15: Tree volume determination approaches (Nagel, 2001:10).

g_m denotes the cross-section diameter taken at the middle of the section, g_l and g_u denoting measurements at the lower and upper end. Newton's approach gives the best results for trees with a conical stem shape, Huber and Smalian are best for shapes resembling a cylinder.

As mentioned before, statistical methods can be used to retrieve useful estimates for timber volume. The figure below shows sampled tree measurements with a fitted curve reflecting a close DBH – tree volume relationship.

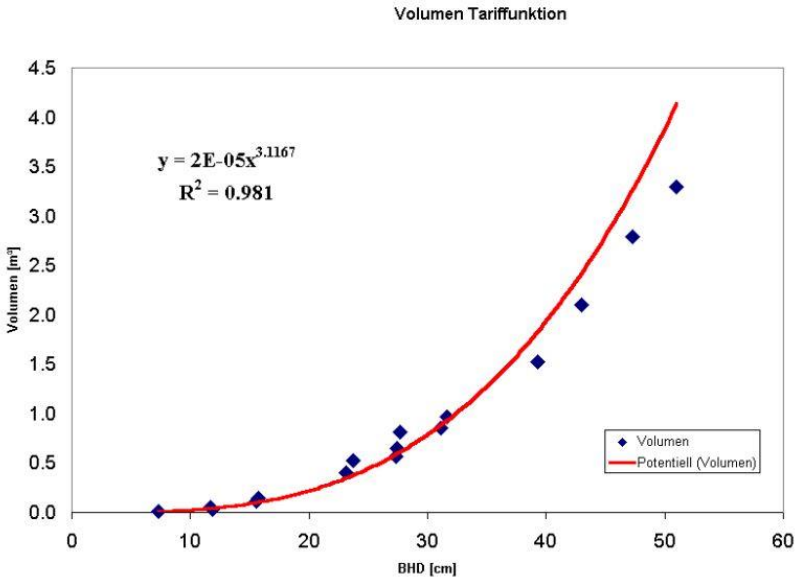

Figure 3.16: Typical DBH – tree volume relationship (Nagel, 2001:11).

Tree volume tables and the underlying relationships have to be constructed for each tree species and site condition if possible, to account for specific growing conditions and tree related traits. The table below introduces a few examples for the so-called volume tariffs – with formulas provided and their suitability for specific scales and site conditions.

Table 3-1: Examples of the most common volume tariffs (Kleinn, 2014).

$v = f(dbh)$	$v = b_0 + b_1 dbh^2$	**Also called volume tarifs.**
	$v = b_0 + b_1 dbh + b_2 dbh^2$	Mainly for local studies where homogeneity of site conditions is expected, including relatively strong relationships between *dbh* and *height* and between *dbh* and *form factor*.
$v = f(dbh, \mathrm{h})$	$v = b_1 dbh^2 h$ $v = v = b_0 + b_1 dbh^2 h$	Mainly for regional forest inventories.
$v = f(dbh, h, d_u)$	$v = b_0 + b_1 * d_u dbh * h$	For larger area forest inventories where heterogeneous site conditions are expected. Therefore, *height* is included into the model to cope for variability of height curves; and an upper diameter d_u to cope for variability of form factor.

Although good progress has been made in many countries in the modelling of tree volume, a lot of research needs to be carried out to account for species- and site-specific conditions. As for Mongolia, only a few generic allometric formulas for the main tree species exist. According to Tompalski *et al.* (2014a) generic allometric formulas bear a great risk of generating huge errors in volume calculation.

Biomass

The above ground biomass (AGB) is an important indicator for the growing conditions of a tree species on a specific site, and also allows for the calculation of the carbon content for

forest areas. Since biomass is closely related to stem volume the principles of volume functions do also hold for ABG determination. According to the Kyoto protocol forest play a crucial role in serving as carbon sinks. A number of carbon reduction programmes have been developed and implemented in the last few decades (e.g., UN-REDD+). An increasing number of studies is related to the estimation of carbon storage in forests (Byambasuren, 2018, Dore *et al.*, 2010, Gower *et al.*, 2001, Kasischke *et al.*, 1995, Petrokofsky *et al.*, 2012, UN-REDD, 2018, Watson, 2009). Although a great amount of the carbon found in forests can be attributed to the biomass below ground (i.e., roots, soil), the ABG estimation has attracted the most research in the last decades. The most commonly applied function is based on the following design:

$cf = ef * x * dw * x * cc$	
cf	Conversion factor from stem volume to total biomass C-content
ef	Expansion factor from stem volume to total tree biomass
dw	Conversion factor to dry matter
cc	C-content

Figure 3.17: Basic equation for the calculation of carbon in biomass (Kleinn, 2014).

In addition to the presented method the application of allometric equations has become quite popular. Petrokofsky *et al.* (2012) provide an excellent overview of the most widely applied methods of determining the various carbon stocks and sources in terrestrial ecosystems. A detailed description of those would most certainly be beyond the scope of this work.

Relationship LAI – NDVI

Another good example of close relationships between certain tree or forest attributes constitutes the LAI – NDVI correlation (Wulder *et al.*, 1998).

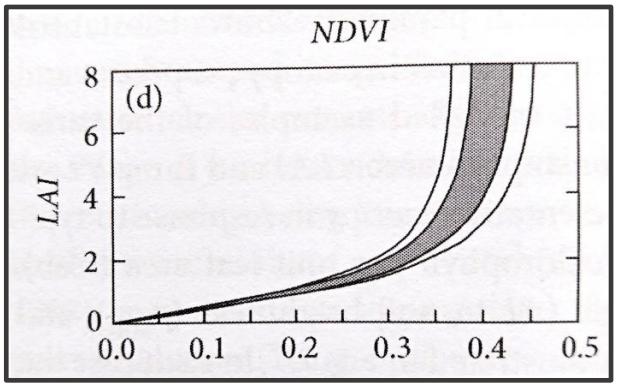

Figure 3.18: Relationship between LAI and NDVI – the grey areas show the sensitivity to variation in chlorophyll per unit leaf area (Jones and Vaughan, 2010).

Both indices – LAI and NDVI – are good indicators for the vigour of a specific forest area. LAI and NDVI can be measured in the field, but also estimated from remotely sensed data. For more information on spectral indices please see chapter 4.3.3.

Structure attributes

The ecological structure of a plant community is largely determined by its vertical and horizontal distribution in space. This holds also true for forest communities. Forest structure is characterised by the position of the trees, the DBH distribution, the diversity of its species, and the vertical tree structure. The specific forest structure presents itself as being important for making inferences on the biodiversity of a forest ecosystem, as well as on tree growth (Nagel, 2001: 47). One good example for the description of a forest structure is represented by the so-called *Shannon-Index*. In essence, it reflects the degree of diversity within a forest by considering the tree species – thus, the higher the index value, the higher the species diversity. The index is calculated as follows:

$$H' = \sum_{i=1}^{R} pi * \ln pi$$

where p_i is the proportion of individuals belonging to the *i*th species in the dataset.

Other popular structural indices are the ones devised by Clark and Evans, Simpson, and von Gadow.

Data analysis

The analysis of the gathered inventory data per tree and per stand commonly involves statistical methods such as Analysis of Variance (ANOVA), regression and modelling approaches, testing strategies for parametric or non-parametric characteristics (e.g. Wilcoxon ranking test, z-test), and correlation analyses (Leonhart, 2017, Zar, 2010). The most commonly calculated statistical parameters comprise: mean, median, standard deviation, standard error, and variance. For detailed work on forest related data analysis and statistics the reader is kindly referred to publications by Le and Eberly (2016), Prodan (2014), and van Laar (1991). More details will also be provided in chapter 7.3. dealing with the methods applied within the scope of this thesis.

A brief note on inventory parameter extraction employing remote sensing technologies

In an extensive review Surový and Kuželka (2019) looked into the acquisition of forest attributes using remote sensing techniques to find that: 'The most easily accessible forest variable described in many works is stand or tree height, followed by other inventory variables like basal area, tree number, diameters, and volume, which are crucial in decision making process, especially for thinning and harvest planning, and timber transport optimization'. They continue to state, that '…information about zonation and species composition are often described as more difficult to assess…' (Surový and Kuželka, 2019). The authors also found investigations on forest health to be rising in numbers in context with climate change. The extraction of the most relevant forest inventory parameters will be dealt with in detail in chapter 4.6. of this thesis.

3.1.5. Forest attributes in a modelling and simulation context - examples

(i) The growth of plants is affected by genetic and environmental factors (temperature, moisture, incident light). In addition, competition (inter-, and intra-specific) pressure highly determines the growth rate and development of the vegetation (Bögre *et al.*, 2008, Grassi and Giannini, 2005). Lintunen (2013) found out, that crown architecture of the species (*Betula pendula* and *Pinus sylvestris* in this case) responded to increased competition intensity primarily by reducing branch number and size. Further, she states: 'Lower overall growth but added height growth was found in mixed stands of birch and pine, when a tree was surrounded by interspecific neighbours compared to trees surrounded by intraspecific neighbours'. Since growth processes are dependent on plant structure, functional-structural plant models (e.g. GroIMP) have been developed to simulate the unfolding of the structures with respect to plant physiology and environmental aspects (Fabrika *et al.*, 2019, Kniemeyer *et al.*, 2007). In addition, empirical models have been devised for the prediction of biometrical variables (e.g., increments of tree DBH and tree height), to be subsequently transformed to tree morphology development by applying functional-structural models.

Growth modelling and simulation has been taken a step further by the North-West German Forest Research Institute (NW-FVA) in cooperation with the Institute of Ecoinformatics, Biometrics and Forest Growth of the University of Göttingen, to devise a tool (ForestSimulator) for forest practitioners, but also for researchers. 'Forest growth simulators are essential tools in the implementation of the current silviculture programs in the areas of silvicultural scenario analysis, training and forest inventory. They can theoretically map any existing situation, the future development of which is forecast and analyzed in detail. The

core of the forest growth simulator BWINPro is a statistical growth model, which is based on the long-term time series of the NW-FVA experimental data' (NW-FVA, 2020). ForestSimulator is based on the TreeGrOSS (Tree Growth Open Source Software) project, with Java (Oracle) used as the programming language. The following graph (Figure 3.19) shows a simulation example including the 3D visualisation of the resulting activity of selective logging.

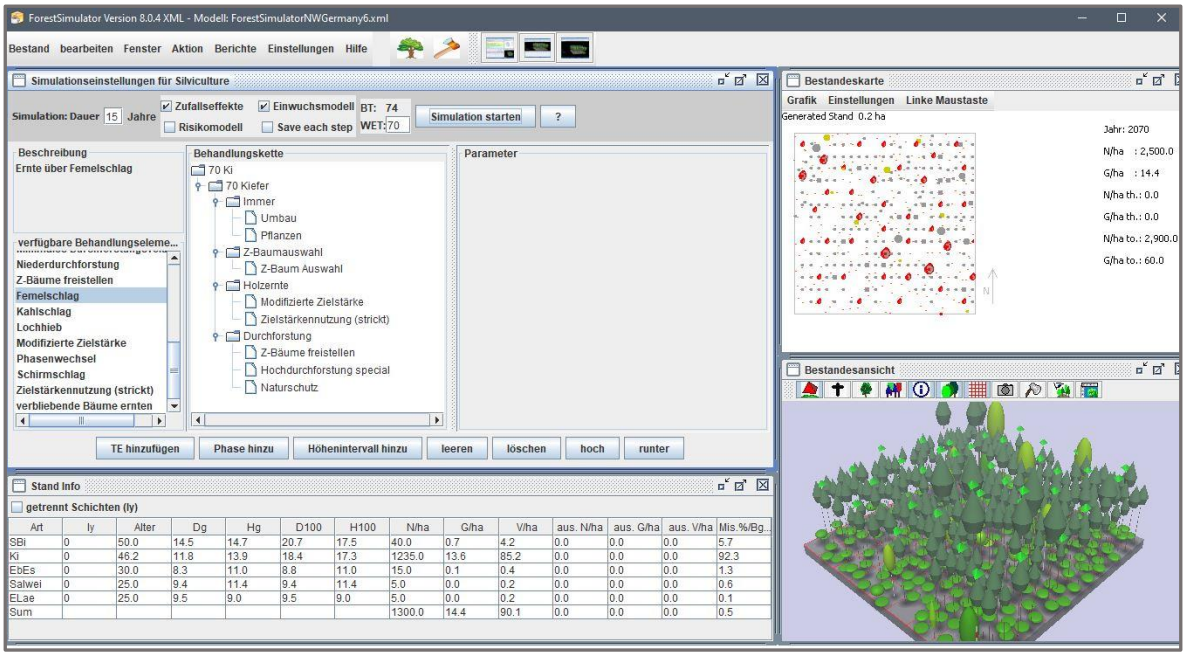

Figure 3.19: Example of forest growing simulation – here: ForestSimulator developed by NW-FVA,Göttingen (NW-FVA, 2020). Various treatments of the forest stand with changing species can be simulated and values (e.g., basal area, timber volume) calculated.

Yet, it needs to be stressed, that the portrayed simulator has been tuned for site conditions and tree species which prevail in the Northern part of Germany. To the best of the author's knowledge, no such simulation interface exists for forest set-ups in Mongolia.

(ii) The spatial structure of forests is strongly related to a variety of ecosystem functions and services (Bartsch *et al.*, 2020: 12,34,496, Pommerening, 2002). Carbon storage, habitat provisioning, timber production , climate regulation, and water purification are salient examples for such services. The structural complexity of a tree / a forest comprises 'all dimensional, architectural, and distributional patterns of a tree's organ at a given point in time' (Seidel *et al.*, 2019). For the last few decades surrogates of the 3D structure have been widely applied, such as diameter distribution of trees, or specific indices based on tree heights and tree positions, structural complexity, or the Clark and Evans index of aggregation (Seidel *et al.*, 2020). With the advent of technologies, like terrestrial or airborne LiDAR, or high-resolution UAV imagery, the derivation of structural parameters from 3D point clouds offers great potential for gaining new insights and for increasing efficiency in

data sampling. Since ground data gathering proves to be very tedious, airborne LiDAR applications seem to be cut out for large-scale investigations in particular. A novel approach was introduced by Seidel *et al.* (2020) by using fractal analysis (i.e. box dimension), that can be applied to any point cloud originating from arbitrary sources and platforms (see Figure 3.20 below). The box dimension can be determined for any kind of object, and it integrates the distribution and density of plants in space. The authors proved conclusively, that ALS-derived box dimension offers the capability to identify differences ($0.34 < R > 0.51$) in forest type, management scheme, development phase, and stand age.

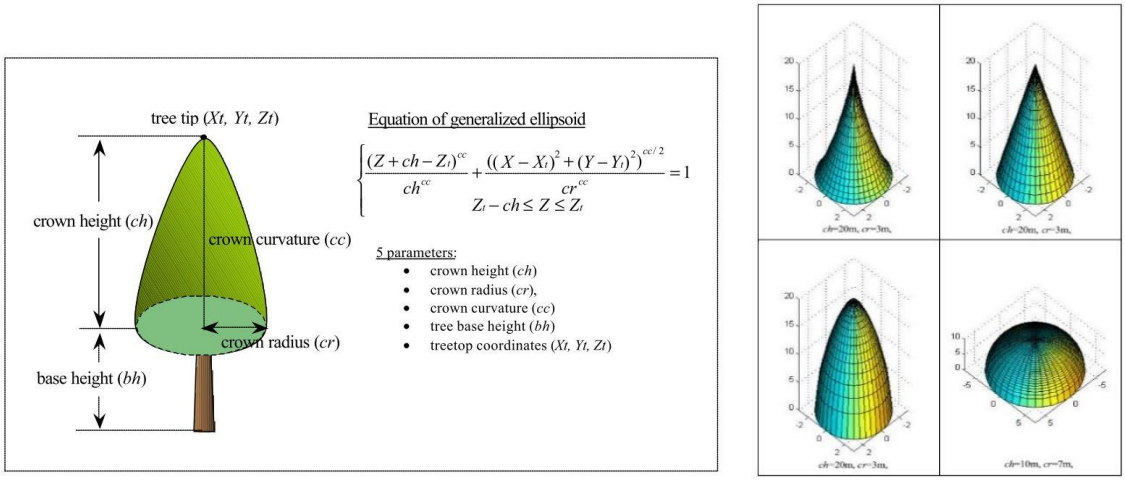

Figure 3.20: Models of a tree crown represented by various resulting shapes (Seidel et al., 2020).

3.2. Forest inventories in Mongolia

3.2.1. A brief history

The first attempts for a nationwide forest inventory were undertaken with support from the Soviet experts in the 1950s. This first real assessment of the forest resources was based on aerial photo interpretation in combination with ocular estimations of stand parameters in the field. This first inventory was updated in 1974 resulting in an improved extension map with corresponding statistics on forest attributes. With the decline of the former Soviet Union and the transition to a market economy in 1990, forest appraisals were only conducted at provincial levels until 2014. The period from 1989-2005 showed the first utilisation of satellite images for mapping forest extent, with the introduction of the first Geographic Information System (GIS) in 2002 for the development of forest maps. However, ocular estimations for gathering data in the field (i.e. tree species, stand volume, tree height, etc.) still prevailed until the implementation of the current NFI (Altrell and Erdenejav, 2016: 14–15).

The current National Forest Inventory (NFI) can be considered a joint effort between several Mongolian institutions (e.g. Department of Forest Policy and Coordination (DFPC), Ministry of Environment and Tourism (MET), Forest Research and Development Centre (FRDC), National University of Mongolia (NUM), Mongolian University of Science and Technology (MUST)), experts from international organisations such as the Food and Agriculture Organisation of the United Nations (FAO), the United Nations Environmental Programme (UNEP), the United Nations Development Programme (UNDP), the United Nations Programme for Reducing Emissions from Deforestation and Degradation of forests in developing countries (UN-REDD), as well as experts from various consulting firms. Financial support was granted by the MET and the German Federal Ministry for Economic Cooperation and Development (BMZ) in association with the German Federal Enterprise for International Cooperation (GIZ), the latter helping to design and implement the NFI. Apparently the requirements of the Un-REDD+ framework, Mongolia is a beneficiary of, prompted the Mongolian government to embark of a nationwide forest inventory, which forms a critical basis for the calculation of biomass related carbon sequestration (Altrell and Erdenejav, 2016: 1–3).

3.2.2. Structure and design of the current National Forest Inventory (NFI)

The overall objective of a forest inventory at national level is the gathering and provision of forest related attributes for forest and climate change related policy decisions as well as for reporting to national and international institutions. As such, the multipurpose NFI was conducted during the vegetation period in 2014 to cover all boreal forest stocked areas in Mongolia. Apart from the myriads of experts consulted, 22 field crews and five quality control

teams were involved in the implementation of the NFI. Field vehicles and modern equipment (e.g., Vertex for tree height measurement) had to be procured, and teams trained. Prior to sending the people into the field, a forest cover map was created exploiting more than 50 Landsat 8 multispectral images. This detailed representation served as the basis for the field inventory, with a systematic dot grid generated for the identification of potential sampling points. Statistical calculation resulted in a total of 1100 sampling units for the national grid (9x9 km), with additional 2406 sampling units for three intensified grid regions (4x4 km). To cover the variety of vegetation density changes within small distances, clusters of 3 sampling units were created, with the field assessments done in circles of different radius. Plot radius variants are 2 metres, 6 metres, 12 metres, and 20 metres, for different DBH brackets and forest structure variables to be gathered (Altrell and Erdenejav, 2016). The above detailed lay-out of the sampling design is portrayed in the following graph (Figure 3.21).

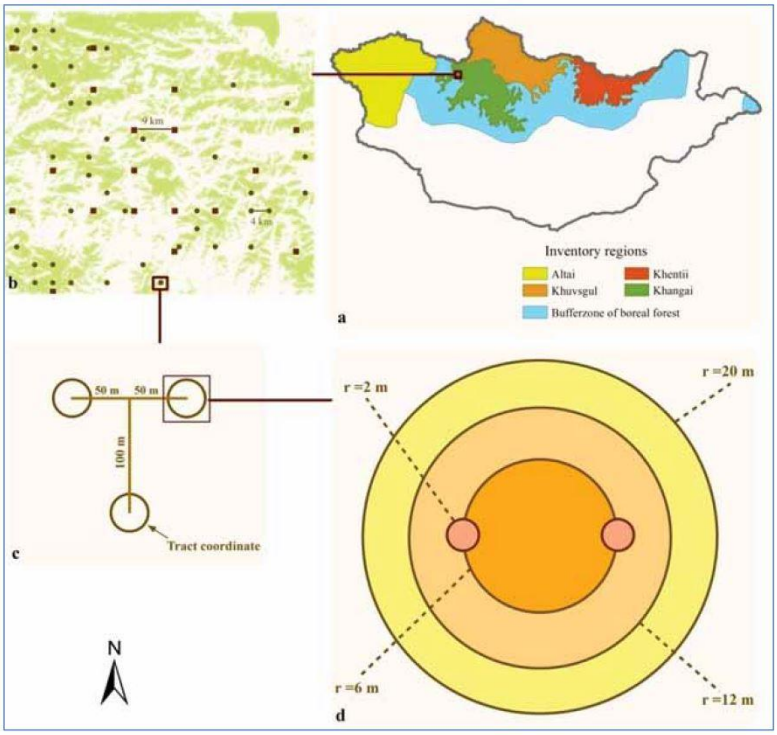

Figure 3.21: Layout of NFI sampling units, with (a) NFI inventory regions over the Mongolian boreal forest, (b) spacing of sampling units in the stocked area, (c) sampling unit – cluster of sample plots, (d) sample plot design – nested circular plots. Source: NFI report: Altrell, Erdenejav, 2016:24.

The following forest structure and ancillary data had to be compiled in the field:

Forest type	Tree health	Soil texture
Tree species	Tree quality	Litter type
DBH	Dead wood	Forest fire marks
Tree height	Ground vegetation	Erosion
Tree age	Slope / aspect	Grazing marks

Once all field data were collected, they were processed in MS ACCESS databases, with additional timber volume, biomass, and carbon stocks modelling performed.

The presented NFI report also entails recommendations for future activities. Among many, the authors suggest to have a proportion of 10% of the NFI samples revisited and appraised each year to ensure forest monitoring on a continuous basis. Furthermore, the forest definition needs to be reconsidered and adopted to FAO standard to warrant comparability with succeeding inventories and other international inventory datasets. There also seems to be a compelling demand for building and maintaining national capacities related to sampling design, field data collection, data analysis, and remote sensing. It is also sensed to be of importance, to make it clear to decision-makers and stakeholders, that common forest management inventories and the multipurpose NFI do not share the same objectives, and thus, should not be integrated (Altrell and Erdenejav, 2016: 122–123).

Rest of page intentionally left blank

4. Remote sensing in forestry

For many decades forest inventory had been concerned with the determination of timber volume (per tree and stand) and tree species, as well as the calculation of growth and yield, until, more recently, demands have extended to also look into the assessment of forest ecosystem services (Hyyppä *et al.*, 2008). Wit recent technological advances in sensors, platforms and algorithms, a paradigm shift from employing ground mensuration, visual interpretation and analysis of coarse satellite data, to the analysis of three-dimensional high resolution (spatially and radiometrically) forest and tree related data sets has taken place (White *et al.*, 2016). The subsequent chapter is designed to provide only a very concise account on technologies employed in forestry applications these days. Detailed information on the extraction of forest inventory parameters from various sources is furnished in chapters 4.7. and 6.8. Remote sensing principles are exhaustively presented in works such as by Albertz (2013), Cracknell and Hayes (2007), Jones and Vaughan (2010), Liu and Mason (2016), and Sabins (2020), and are not the subject of this chapter and will only be dealt with if this is necessary for providing a better understanding of the particular topic covered.

4.1. Imaging platforms and sensors

For the last two decades a clear trend towards multisensory systems, and an increased spatial, temporal, and radiometric resolution can be observed (Belward and Skøien, 2015). With the latest UAV technology for example, ground sampling distances of less than one decimetre have become possible. In the course of these improvements new challenges have arisen with respect to analysing these complex datasets. As a remedy, new algorithms associated with object-oriented image analysis and machine learning (e.g. Random Forest and Convolutional Neural Networks) have been devised and successfully applied in recent years (Lee *et al.*, 2020).

The following graph (Figure 4.1) conveys an excellent insight in the technologies and the advancements involved in spatial data acquisition.

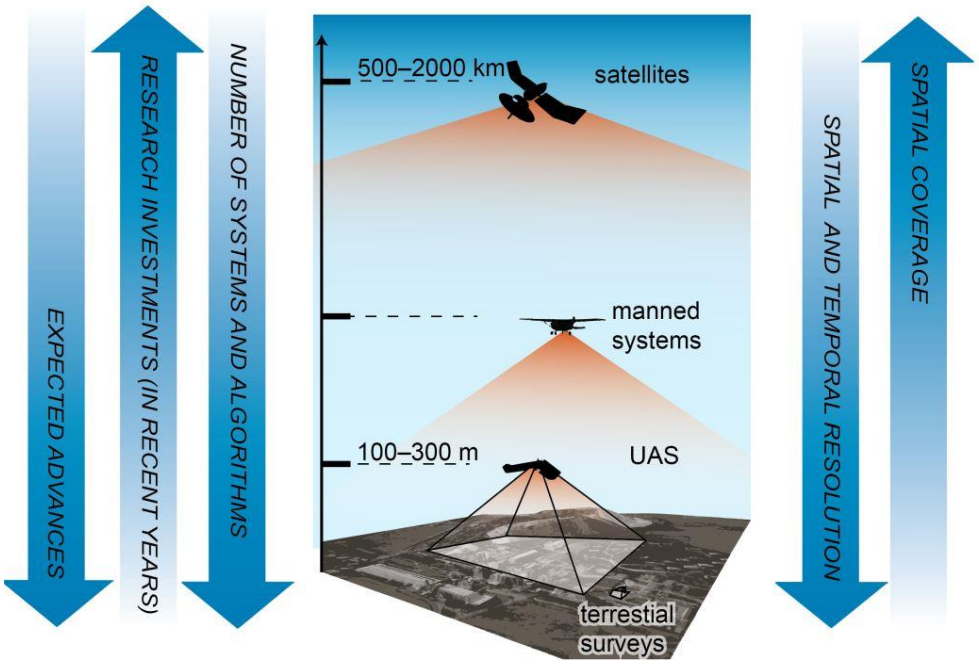

Figure 4.1: Comparison of the most important aspects of spatial data acquisition (source: Jeziorska, 2019).

Regarding forestry applications, common tree and forest stand parameters include: location, DBH, basal area (BA), height, species identification, tree density, and crown size and closure. Other parameters such as timber volume, health status, biomass, and carbon sequestration rates can be derived from the former. 'This renders the field survey techniques for forest inventories expensive, time consuming, and unsuited for large areas' (Gomes and Maillard, 2016). More than ever forest information must be accurate, up to date, and detailed. With new platforms launched and sensors refined, modern technologies are at the user's disposal to make forest inventories, at whatever scale, more efficient and less straining.

The following list (Table 4-1) provides an overview of typical sensor platform configurations with the most relevant characteristics (Toth and Jóźków, 2015):

Table 4-1: Typical sensor and platform configurations (source: Toth and Jóźków, 2015).

Applicability and operation aspects	Data acquisition platforms			
	Satellite (spaceborne)	Airborne	UAS	Mobile/static (ground)
Maneuverability	No/limited	Moderate	High	Limited
Observation space	Worldwide	Regional	Local	Local
Sensor diversity	MS/HSI/SAR	MS/HSI/LiDAR/SAR	MS (LiDAR/HSI)	MS/LiDAR (HSI)
Environment	Outdoors	Outdoors	Outdoors/indoors	Outdoors/indoors
Scale (inverse sensor range)	Small	Small/medium	Medium/large	Medium/large
Ground coverage	Large (10 km)	Medium (1 km)	Small (100 m)	Small (50 m)
FOV	Narrow	Wide	Wide/super wide	Wide/super wide
Repeat rate	Day	Hours	Minutes	Minutes
Spatial resolution (GSD)	0.30–300 m	5–25 cm	1–5 cm	1–5 cm
Spatial accuracy	1–3 m	5–10 cm	1–25 cm	3–50 cm
Deployability	Difficult	Complex	Easy	Moderate
Observability	Vertical/oblique	Vertical/oblique	Vertical/oblique/360°	Oblique/360°
Operational risk	Moderate	High	Low	Moderate
Cost	$$$$$	$$$	$	$$

MS: Multispectral, HSI: Hyperspectral Image, LiDAR: Light Detection And Ranging, SAR: Synthetic Aperture Radar.

Although more traditional remote sensing approaches still deserve a lot of credit, recent developments in laser technology (airborne and terrestrial), robotics (Unmanned Aerial Vehicles), and spacebourne sensors (Very High spatial Resolution Satellite optical and hyperspectral imagery) are set about to supersede or at least complement modern forest inventory. Some of these fresh advances are outlined in the following.

Spacebourne platforms

The study of individual trees with remote sensing was limited to the interpretation of aerial photographs for many decades. Although orbital optical remote sensing began in the 1970s, it was only towards the end of the 1990s, that high resolution satellite imagery with a spatial resolution of less than 1 m became operational and accessible to the user community (Hildebrandt, 1996: 1–2). With the advent of VHR imagery, all of a sudden branches and irregularities within the tree crowns became visible, resulting in high intra-class variance. This has sparked off a lot of interest in the computer vision and forestry community to deal with issues, like low spectral contrast, and tree proximity, and to devise algorithms for the automatic detection of trees. Local maxima filtering, template matching, and watershed analysis are just a few representatives of those high-level complex algorithms developed.

Unfortunately, the increase in spatial resolution has not been automatically accompanied by higher spectral resolution. The following table (4-1) gives account on recent very high-resolution (VHR) satellite platforms.

Table 4-2: VHR satellite platforms with their resolutions and spectral bands (Gomes and Maillard, 2016).

Satellite	Launch Year	Px resolution* (m)	Mx resolution* (m)	Multispectral bands
Ikonos II	1999	0.82	3.2	Blue, Green, Red, Near IR (4)
QuickBird	2001	0.65	2.62	Blue, Green, Red, Near IR (4)
WorldView-1	2007	0.46	-	-
Geoeye-1	2008	0.46	1.84	Blue, Green, Red, Near IR (4)
WorldView-2	2009	0.46	1.85	Coastal, Blue, Green, Yellow, Red, Red Edge, Near IR, Near IR2 (8)
Pleiades 1A	2011	0.5	2.0	Blue, Green, Red, Near IR (4)
Pleiades 1B	2012	0.5	2.0	Blue, Green, Red, Near IR (4)
Kompsat-3	2012	0.7	2.8	Blue, Green, Red, Near IR (4)
SkySat-1	2013	0.9	2.0	Blue, Green, Red, Near IR (4)
WorldView-3	2014	0.31	1.24	Coastal, Blue, Green, Yellow, Red, Red Edge, Near IR, Near IR2 (8)
SkySat-2	2014	0.9	2.0	Blue, Green, Red, Near IR (4)
Kompsat-3A	2015	0.55	2.2	Blue, Green, Red, Near IR (4)
WorldView-4	2016	0.34	1.36	Not available at time of printing

* Panchromatic (Px) and Multispectral (Mx) resolution at nadir.

Other important platforms than the ones mentioned above are SPOT 6,7 (1.5m pan resolution), RapidEye (5m pan resolution), SuperView-1 (0.5m pan resolution), and Jilin-1 (0.7m pan resolution). The Copernicus global monitoring programme by ESA (European space Agency) deserves special mention, since the Sentinel satellite family features various sensors (optical and radar) on a twin system with a high revisit rate and 12 multispectral band imagers (Thales Alenia Space, 2017). The data are freely available for users and can be retrieved from the ESA, NASA, NOAA, and USGS websites. ESA also presents free software tools for the analysis of the Sentinel data (STEP/SNAP) ready for download on their website (ESA, 2020b). More recent developments in satellite technology comprise the further launch of flocks of nano satellites with a planned revisit rate of 12 per day. They are called SkySat with a multispectral spatial resolution of 1 m and operated by Planet Labs. Other advances in the spaceborne remote sensing business involve the improved sensor agility to allow for stereo capture of the imagery (i.e., 3D-modelling), as well as shorter revisit times due to tandem (e.g., TanDEM-X / TerraSAR-X) or flock constellation.

Although multispectral sensors are more geared for the assessment of vegetation conditions (Xie *et al.*, 2008) the higher spatial resolution of the panchromatic band of VHR sensors now allows for digital and manual interpretation of (forestry related) features (Falkowski *et al.*, 2009). Since the first launch of VHR spacebourne sensors numbers of

related publications have been soaring. Regarding forestry application panchromatic imagery has been used to identify and discriminate dominant tree species (e.g. Mora *et al.*, 2010a, Astola *et al.,* 2010, Kravtsova, 2012, and Carleer and Wolff, 2004) stand height (e.g. Piermattei *et al.*, 2018, Beguet *et al.*, 2014, Mora *et al.*, 2010b, Mora *et al.*, 2013b, Goldbergs *et al.*, 2019, and Persson, 2016), and volume and biomass (e.g. Mauro, 2004, Hirata, 2008, Mora *et al.*, 2013a, Fuchs *et al.*, 2009, and Leboeuf *et al.*, 2007). Other forest structural parameters such as DBH, tree spacing, and tree crown diameter were successfully extracted from VHR imagery by authors like Lamonaca *et al.* (2008), Kayitakire *et al.* (2006), Banerjee *et al.* (2014), Brosofske *et al.* (2014), Gomes and Maillard (2016), and Gómez *et al.* (2011). Abdollahnejad *et al.* (2018) even used the correlation between Pléiades and extremely high resolution UAV data to derive tree height, crown diameter, DBH, and stem volume. Leboeuf *et al.* (2012) employed an intriguing shadow fraction approach on QuickBird images to estimate volume, basal area, height and crown closure of boreal forests in Canada. Interestingly, Mora *et al.* (2013a) found similar stand-level height estimates derived from VHR images to those generated from Landsat (Chen *et al.*, 2012b). This implies, that a very high spatial resolution is by no means a warrant for more accurate forest parameter determination. WorldView-2 image texture was analysed by Ozdemir and Karnieli (2011) to predict forest structural parameters (e.g. basal area, number of trees) in dryland forests in Israel. Their results clearly indicate that forest structural parameters are significantly correlated with image texture features. This is very much in line with a study conducted by Meng *et al.* (2016). According to them DBH related measures in particular can be reliably predicted using the spectral or textural measures extracted from SPOT-5 images. Tree canopy cover was assessed by Eskandari *et al.* (2020) on Sentinel-2 images. They found out, that a linear regression model appears to be a decent predictive model for canopy cover percentage based on NDVI (R^2 = 0.86). Wittke *et al.* (2019) also used (multitemporal) Sentinel-2 data to compare the extraction of forest structure parameters with higher resolution WorldView-2 and three-dimensional data from TerraSAR and airborne laser scanning (ALS). The outcomes indicate that higher spatial resolution data is correlated with more accurate forest inventory parameter predictions, with ALS performing best. These results affirm very well the findings of other authors (e.g. Hyyppä *et al.*, 2000, and Tuominen *et al.*, 2017b), that 3D features (e.g. ALS and stereo imagery) are superior to 2D spectral features of traditional image capturing. Apparently, imagery taken from satellites fitted with directable sensor heads are afflicted with certain deficiencies. Not only the angular conditions between the sun-surface-sensor is changed, but the different viewing conditions can also result in the occlusion of trees in the imagery taken from a different vantage point (Belouard *et al.*, 2015, Persson *et al.*, 2013, Poli *et al.,* 2010). In

addition, bidirectional reflectance properties of objects are altered atmospheric effects between object and sensor aggravated (Pacifici *et al.*, 2014).

Hyperspectral remote sensing

This fairly recent development most certainly opens up new application fields by meeting demands for improved radiometric resolution of imaging systems. As opposed to acquiring imagery only with a limited number of spectral bands, hyperspectral sensors allow for data capturing with up to 300 spectral channels. The graph below (Figure 4.3) reflects some of the major characteristics of a hyperspectral system.

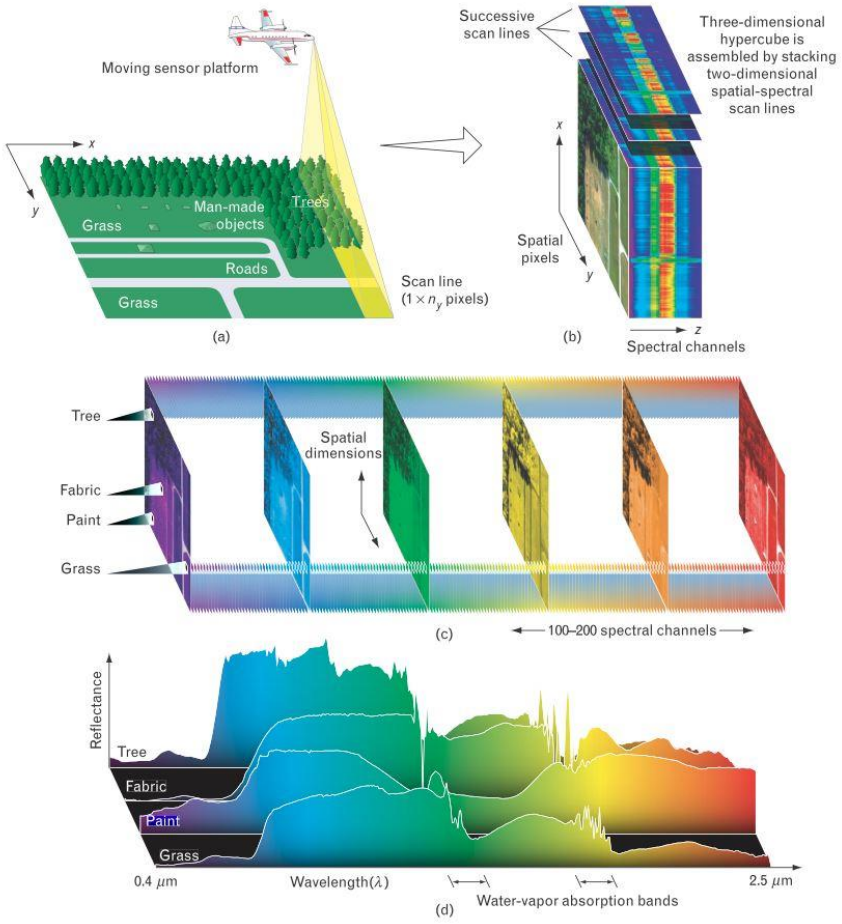

Figure 4.2: Structure of the hyperspectral data cube: (a) push-broom sensing from air-, or spaceborne platform; (b) successive scan lines are stacked to obtain a three-dimensional data cube; (c) each of the stacked narrow-band images can be treated as an individual item; (d) alternatively, each individual pixel can be analysed as a separate class member – features can be more easily distinguished than by using only a few spectral bands (Shaw and Bourke, 2003).

Examples for spaceborne systems are NASA's Hyperion and HyspIRI, China's Jilin-1 satellite, as well as ESA's CHRIS, and Germany's (DLR) HIS sensor onboard the EnMap satellite (see also ITC's satellite and sensor database: ITC, 2020). Due to their advantages

of better spatial resolution airborne platforms still play a vital role in remote sensing. Imagers such as HyMap (Hyperspectral Mapper), AVIRIS (Airborne Visible/Near-Infrared Imaging Spectrometer), CASI (Compact Airborne Spectrographic Imager), and AHS (Airborne Hyperspectral Scanner) have become very popular in the remote sensing community (Jia *et al.*, 2020). With the miniaturisation of sensing units even unmanned aerial vehicles (UAVs) can now carry hyperspectral payloads like the ones manufactured by Headwall and Cubert (see also chapter 6.2.). Successful applications in forestry are described for example by Adão *et al.* (2017), and Lin *et al.* (2019) for UAV based operations. They describe the possible identification of individual trees, the discrimination of plant species, as well as the detection of bark beetle infestations. The stability of the platform, as well as issues with image registration apparently still need to be explored (Honkavaara *et al.*, 2017). Airborne solutions are reported by Alonzo *et al.* (2014), Dalponte *et al.* (2014) and Dalponte *et al.* (2013) for tree species discrimination and tree detection, the latter describing a better detection rate for the laser scanning system that was used in comparison. Based on their observations spatial resolution has a strong effect on the classification accuracy. According to Ghosh *et al.* (2014) and other authors the combination of hyperspectral and LiDAR data seems to be very rewarding for mapping tree species.

Airborne and terrestrial laser scanning

Laser scanning technology has been extremely successful for the last few decades not only for creating digital terrain models (DTM), but also for providing information on forest structure (Hyyppä *et al.*, 2008). The development of new data analysis tools and sensors has brought about significant insights in vertical forest structures in particular. Laser technology has gained laurels in many fields and as such has become indispensable in forest inventory, namely in the Scandinavian countries (Kangas *et al.*, 2018, Næsset, 2014, Nilsson *et al.*, 2017, Tomppo *et al.*, 2008, Tomppo *et al.,* 2014). By now LiDAR (Light Detection And Ranging) systems are widely available from space (e.g. GLAS on ICESat) to terrestrial systems, with aerial platforms being better suited for forestry applications because of the limiting character of the laser pulse in terms of range and data rate (Maltamo, 2014: 2–3, Toth and Jóźków, 2015). Airborne Laser Scanning (ALS) is an active technology to fathom the three-dimensional distribution of vegetation features (Lefsky *et al.*, 1999). LiDAR systems are categorised by the mode they record the energy returned to the sensor. Single or even multiple returns are recorded for each emitted laser pulse by discrete return systems. In contrast, full-waveform systems record the returned energy as a continuous return or waveform to allow for the derivation of much more detailed spatial patterning of data points, hence supporting the identification of tree positions and even species (Jones and Vaughan, 2010: 144-115, Reitberger *et al.*, 2009, Wulder *et al.*, 2008, Yu *et al.*, 2014).

A common approach for identifying tree positions is to segment the laser point cloud (Canopy Height Model) by applying the so-called watershed algorithm, where in analogy with hydrology reversed areas identified as tree tops are filled first (see also chapter 4.6.). Examples of software to carry out laser point cloud analysis are: GRASS GIS, ENVI LIDAR, ArcGIS, VR Mesh, Global Mapper, FUSION, and LASTools (QGIS).

LiDAR systems commonly use a near-infrared light source, however, with four-band systems being already tested in forestry applications (Goodbody *et al.*, 2020, Wei *et al.*, 2012). ALS footprints range from 0.1 m to 2 m - depending on the flying altitude and the laser system used – with achievable vertical sub-decimetre accuracies (Næsset, 2015). The following graph (Figure 4.3.) shows the results of a flying mission employing ALS and aerial imagery to derive 3D models of a boreal forest area. Quite obviously, the photogrammetry point cloud (DAP) is denser than the ALS point cloud, however, fails on most of the vertical forest structures and terrain points.

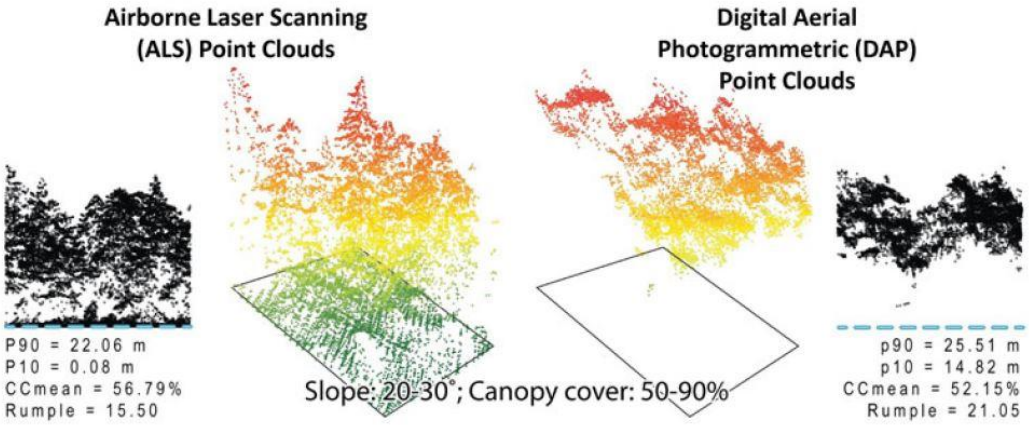

Figure 4.3: Comparison of ALS and digital aerial photogrammetry (DAP) point clouds in a forest in British Columbia (White et al., 2016).

While commercial and operational ALS-based forest inventories frequently are conducted according to the so-called area-based approach (ABA), methods targeting single tree characteristics (Individual Tree Crown - ITC) have also been proposed (Næsset, 2002b, Persson *et al.*, 2002, White *et al.*, 2016). The latter method usually requires ALS data with a high density – small footprint scanning systems can generate point clouds with densities ranging from 25 to 100 points m^{-2} (Hyyppä *et al.*, 2008). ABA depends largely on the statistical relationship between predictor variables extracted from the LiDAR returns and the ground-based evaluation. The predictive models are subsequently applied to the area covered by the ALS point cloud. ABA has become a standard procedure for large area assessments, such as National Forest Inventories, to predict variables comprising stem volume, basal area, and stand height (Holopainen *et al.*, 2010, Næsset, 2004, 2014). There

exists even a best practices guide for generating forest inventory attributes from ALS using ABA (White *et al.*, 2013b). In contrast, ITC based approaches exploit methods developed for high resolution imagery and involves individual tree detection form canopy height models (Gougeon, 1995). Other inquiries concern the determination of tree height, crown dimensions, and species. Finally, ITC information can be aggregated to estimates at plot or even stand level.

For the last two decades a wealth of literature has been published on LiDAR use in forestry, especially in the Scandinavian countries – even an entire book has been devoted to this promising technology (Maltamo, 2014). Some of the more prominent studies are outlined in the following.

The potential of estimating single-tree characteristics by ALS has been investigated in several studies, including stem volume (Maltamo *et al.*, 2004, Persson *et al.*, 2002, Sousa da Silva, 2019), stem diameter (Gobakken and Næsset, 2004, Popescu, 2007), crown base height (Popescu and Zhao, 2008, Vauhkonen, 2010), leaf area index (Pope and Treitz, 2013, Roberts *et al.*, 2005, Zheng and Moskal, 2009), and biomass (Hauglin *et al.*, 2013, Kankare *et al.*, 2013, Næsset and Gobakken, 2008, Popescu, 2007). In their investigation Straub and Koch (2011) found that tree height and crown diameter worked best for the determination of parameters for allometric models. Regarding tree species discrimination recent publications indicate strongly, that combining ALS and multi-, or hyperspectral data considerably improve classification results and also help reduce data acquisition costs (Dalponte *et al.*, 2014, Ørka *et al.*, 2012, Puttonen *et al.*, 2010). LiDAR systems are also profitable for derivation of fractional forest cover, which is a very common feature in semi-arid areas. Spectral methods (e.g., NDVI) fail in situations, when background tends to bare soil and understorey is highly vegetated. ALS can be an esteemed remedy by providing vertical profile information (Chen *et al.*, 2006, Danson *et al.*, 2007, Kaartinen *et al.*, 2012, Leiterer *et al.,* 2012).

For quite a number of years, there has been a fierce debate on whether ALS data can yield higher accuracies than terrestrial surveys and other parameter derivation methods or not. Results of various studies are contradictive and most of them concern the extraction of tree height as one of the essential parameters. The following graph represents the outcomes of an investigation conducted by (Nevalainen *et al.*, 2017). According to them: 'The profile plots revealed that the photogrammetric surfaces generally followed the structure that was visible in the ALS point cloud: individual trees seemed well-aligned and minor differences in canopy top level and ground level were observable'.

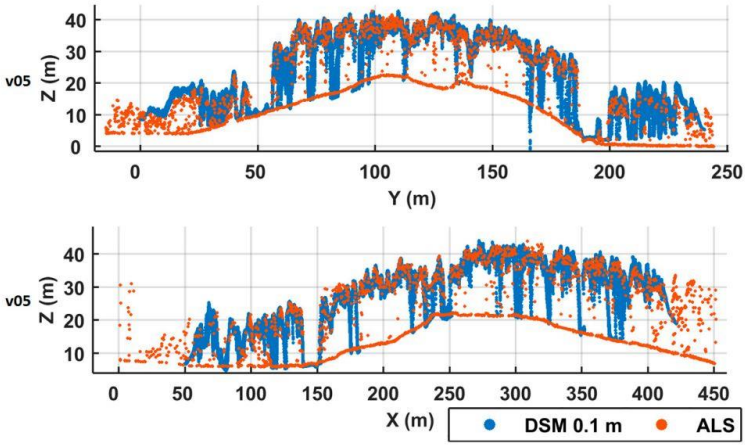

Figure 4.4: Comparison of photogrammetric (blue) and ALS (red) point cloud profiles for two different test sites (Nevalainen et al., 2017).

Andersen *et al.* (2006) state, that ALS derived measurements performed poorer than field methods, but the loss in accuracy was offset by the large-area coverage and the reduction in survey costs. Bias for plot height estimation with ALS data seems to be typically below 0.5m (Næsset, 2002a, Næsset, 2007). The observation made by Nevalainen *et al.* (2017), that height extraction from photogrammetric point clouds (DAP) yield similar accuracies to ALS measurements have also been confirmed by studies conducted by Ganz *et al.* (2019), Tuominen *et al.* (2017b) and Moe *et al.* (2020). Vastaranta *et al.* (2013) relate, that their investigation reflects a better suitability of DAP for deriving height metrics, whereas ALS performed better in stand density tasks. Research carried out by Mielcarek *et al.* (2020) showed a distinct tendency of both, DAP and ALS, to underestimate tree height, when put alongside terrestrial surveys. In addition, ALS complied slightly better with accuracy requirements than the heights taken from the aerial imagery point cloud. An important aspect is mentioned in the publication by Gatziolis *et al.* (2010), when looking into tree height estimations in a temperate forest in Western Oregon, USA. Not only the complexity of the terrain and its steepness, but also a high canopy cover appears to have great potential in diluting the accuracies (i.e., more than 10%) of tree height determination.

In summary, as being reflected by the studies, achievable accuracies seem to hinge on the technology used (i.e. scanning system and pulse rate), the software / algorithms applied for data analysis, the forest structure itself, but also allometry (Breidenbach *et al.*, 2008, Holopainen *et al.*, 2014, Jakubowski *et al.*, 2013, Korpela *et al.*, 2010, Lim *et al.*, 2003, Rahlf *et al.*, 2015, Vauhkonen *et al.*, 2012). One has also to bear in mind, that most ALS derived estimate accuracies are based on the comparison with terrestrial data. However, the recent revelations by Wang *et al.* (2019b) resting on length measurements of felled trees suggest the following: (i) field measurements tend to overestimate tree height, especially concerning tall trees in codominant crown class; (ii) ALS proved to be robust and accurate across all

stand conditions, with a few uncertainties related to trees in intermediate crown class due to difficult identification of tree tops; (iii) reliable tree heights for TLS measurements are only to be expected for trees lower than 15-20m in height, depending on the complexity of the forest stand. The authors also reason: 'The greatest challenges of the laser scanning (LS) techniques in measuring individual tree heights lie in the occlusion effects, which lead to omissions of trees in intermediate and suppressed crown classes in ALS data and incomplete crowns of tall trees in TLS data'.

Terrestrial laser scanning

The same laser ranging principles as in the ALS are also being applied in scanning from fixed positions on the ground, also referred to as terrestrial laser scanning (TLS). The use of TLS in forestry has not been as popular as of ALS, but the viewing geometry of ALS is not optimised for the assessment of specific forest components such as trunks, near-ground vegetation, and lower parts of the tree canopy (Hilker *et al.*, 2010). The following graph (Figure 4.5.) by Seidel (2011) illustrates the main parameters that can be extracted from laser point clouds these days.

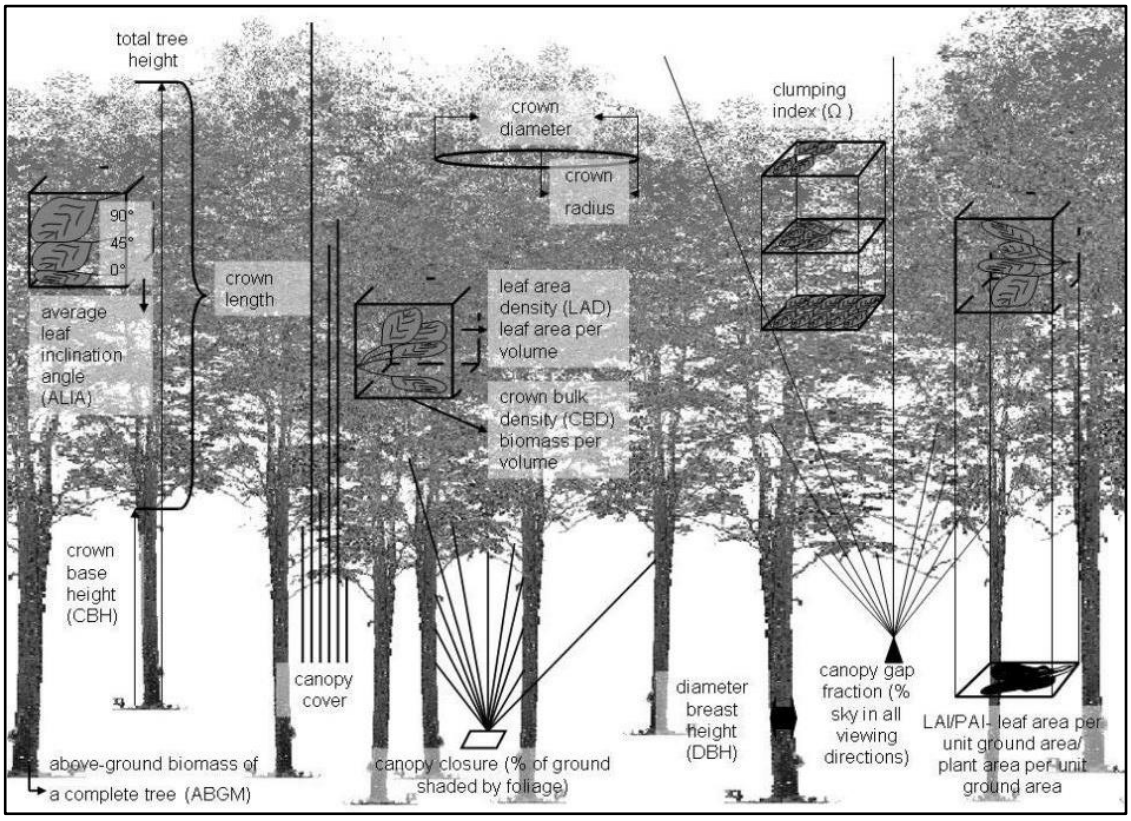

Figure 4.5: Extraction of main tree parameters with TLS (source: Seidel, 2011:59).

A number of successful applications of TLS comprise the estimation of tree position and diameter at breast height, as well as taper (Hauglin *et al.*, 2013, Hyyppä *et al.*, 2018, Maas

et al., 2008, Tansey *et al.*, 2009, Thies *et al.*, 2004). Reported errors for DBH estimation range from 1.3 to 3.3 cm. Tansey *et al.* (2009) mention an RMSE for DBH between 1.9 and 3.7 cm, but report a complete failure of tree volume estimation in a dense forest. There are also studies presenting procedures to determine above-ground biomass from TLS data (Hauglin *et al.*, 2014, Holopainen *et al.*, 2011, Muukkonen, 2006, Yu *et al.*, 2013). Biomass estimation commonly relies on a calculated relationship between TLS variables and allometric functions. Hauglin *et al.* (2014) showed that Norway spruce crown biomass estimates can be derived from TLS data with a higher accuracy than by conventional field measurements and existing allometric models. TLS derived variables can also be used to fit models to ALS data (Hauglin *et al.*, 2014). The authors constitute, that their analysis showed better accuracies for TLS acquired parameters than for employing allometric estimations. Recent investigations also concern the description of more complex forest structures to extract the entire morphology itself (Côté *et al.*, 2011, Seidel, 2018, Seidel *et al.*, 2019, Strahler *et al.*, 2008). Other studies even have focused on gap fraction and LAI determination (Danson *et al.*, 2007, Zhao *et al.*, 2012). An interesting approach was taken by Piermattei *et al.* (2019): they used photographs taken on the sampling plot to derive a 3D point cloud and to further extract tree parameters. The tree detection rate varied between 65% and 98% (depending on the forest structure), and a mean error for DBH of -0.77cm for the photogrammetry point cloud and -1.13cm for the TLS point cloud in comparison. Current undertakings are related to the fusion of TLS and ALS data to model the below-canopy structure with the goal to retrieve the complete canopy structure across an entire landscape (Hilker *et al.*, 2010, Holopainen *et al.*, 2014, Paris *et al.*, 2017). In addition, the combination of 3D models created from (UAV) aerial photos with laser scanning point clouds seem to be gaining a lot of interest these days for improving the knowledge on forest canopy structures (Kato *et al.*, 2015, Paris and Bruzzone, 2015, Tian *et al.*, 2019). Despite TLS's potential to succeed, or at least complement conventional forest inventory cruising (by providing improved allometric equations), some issues still remain to be solved: (i) TLS data analysis is far from being trivial and has not reached operational level for automatic parameter extraction yet; (ii) a relatively high number of scans is required (5 – 13) to capture groups of more than three trees, resulting in (iii) foliated trees cause many obstruction effects in the upper canopy (i.e. poor reconstruction); (v) the high level of detail afforded by TLS (millions of data points) demands for superior computational power; (vi) fusion with ALS and photogrammetric point clouds (co-registration) remains a challenge (Newnham *et al.*, 2015, White *et al.*, 2016). A lot of research is being conducted on these issues, with for example propositions being made for mobile and 'airborne' TLS (Innovatek, 2020, Liang *et al.*, 2014).

Highlights of the laser scanning technology (ALS, TLS):

- Provides unprecedented insights into vertical forest structures and terrain characteristics.
- Has proven to achieve accuracies congruent with or even better than traditional terrestrial surveys.
- Excellent bedrock for modelling tree architecture and forest structures; big potential to improve species specific allometric formulas.
- As opposed to many other remote sensing applications a best practice guide for employing ALS for forest inventory purposes exists.
- Fusion with multi- (hyper) spectral and /or photogrammetry data yields exemplary information on vertical structures, species discrimination, and ecological parameters.
- Data analysis is by no means a trivial task, and computing-intensive.
- (Co)Registration of point clouds to be merged is most challenging.
- Expensive technology, but also renders high area coverage (ALS).

Digital aerial photogrammetry

Traditional photogrammetry has experienced a true paradigm shift not only in terms of new algorithms (e.g. Structure from Motion (SfM)) for the generation of 3D models, but also in the devise of novel sensor platforms (Baltsavias, 1999, Baltsavias *et al.*, 2008, Leberl *et al.*, 2010, Waser *et al.*, 2007). With satellites equipped with a tiltable sensor system, stereo image capturing to cover huge areas has become feasible. Classic airborne missions, by contrast, carry a big price tag, and as such, are only embarked on to meet special demands. The galloping advances in unmanned aerial vehicle (UAV) technology have set out to by and large supersede piloted surveys and revolutionise the fashion forest inventories are being conducted today and in future (St-Onge *et al.*, 2008, Vega and St-Onge, 2008, White *et al.*, 2013a). On that account, I decided to dedicate an entire chapter (i.e., chapter 6. in relation with chapter 4.5.) to this topic.

Radar imaging systems

Radar, as an active air-, or spaceborne sensoring technology, is a century old concept. The cloud penetration ability makes these systems particularly suitable for areas with high cloud coverage. However, most of the equipment is rather expensive, and data analysis far from being trivial. SAR (Synthetic Aperture Radar) sensors on satellite platforms carry big names

like ALOS, TerraSAR-X/TanDEM-X, KOMPSAT, and Sentinel-1. Recent publications show very reasonable accuracies for the estimation of structural parameters (RMSE of 15% for stand height and 32% for stem volume – see also: Erasmi *et al.*, 2019) and the determination of forest above ground biomass / growing stock for carbon sequestration appraisal (Shao and Zhang, 2016, Wilhelm *et al.*, 2014). Thiel *et al.* (2006) used JERS-1 SAR data to achieve high accuracies (90%) for delineating forest cover and detecting deforestation activities. Forest canopy structure was assessed by Chen *et al.* (2017b) by deploying a UAV radar system. Their analysis confirmed that the profiling radar measures a clear signal form the canopy structure. However, image backscatter and saturation of radar signals over forests still require some research to get a better understanding on the interpretation of the signal response to forest structure (Joshi *et al.*, 2017).

These days, web-based analysis and data retrieval tools for remote sensing applications are becoming increasingly popular. Although a number of limitations are apparent (e.g., for regional and/or local projects), in specific cases analysis of the data can be carried out extremely efficiently, saving a lot of time and financial resources. A splendid example for such an analysis tool is Google Earth Engine (GEE), which is a powerful web-platform for cloud-based processing of remote sensing data on large scales (Google, 2020). Its repository provides the most common satellite imagery and makes it available online with tools for scientists, independent researchers, and other individuals and institutions to detect changes, map trends and quantify differences on the Earth's surface. The database holds imagery and derived products such as Landsat, Sentinel, MODIS, and SRTM (DEM). Applications include: detecting deforestation, classifying land cover, estimating forest biomass and carbon, and mapping the world’s inaccessible areas. In this context a very well-known project has been initiated by the University of Maryland, led by Matt Hansen, to survey the global tree cover extent indicating gains and losses (Galiatsatos *et al.*, 2020, Hansen *et al.*, 2013). The University's website and the related database are updated frequently and can be accessed through: http://data.globalforestwatch.org/datasets/14228e6347c44f5691572169e9e107ad. Other examples of very useful sites are those operated by NASA (FIRMS (Fire Information for Resource Management System) – for fire detection and mapping), the European Open Science Cloud (EOSC), or USGS’s (United States Geological Survey) Earth Explorer. Another beneficial user tool is provided by ESA called the Sentinel Hub. This cloud-based hub not only provides a global archive of earth observation data, but also offers opportunities for multi-temporal and statistical data analysis and easy integration with desktop and webGIS software.

4.2. Image interpretation

The interpretation of remotely acquired imagery seems rather outdated, considering the fact, that the last decade has seen substantial progress in computer aided pattern recognition and artificial intelligence (Beyerer *et al.*, 2018: 2–3, Bishop, 2009: 1, Theodoridis and Koutroumbas, 2009: 3–5) . However, in a number of well-defined situations the faculty of a human being to accurately detect and interpret patterns in imagery has proven to be superior to modern sophisticated algorithms (Ke and Quackenbush, 2011a). One of the truly salient discovery is, that the human brain has been trained to recognise patterns in our environment as part of the survival strategy, which we also share with most of the living creatures on this planet. It took evolution hundreds of thousands of years to bring this skill to almost perfection in humans.

With the advances in the neurosciences, we gradually begin to understand the underlying principles of cognition involving the 'eye – brain' processing scheme. Nevertheless, processes related to (e.g.) size, brightness and position invariance of objects, pattern confusion, shape segmentation, complexity reduction of scenes, and scene abstraction still require more in-depth consideration in research (Jiao *et al.*, 2020: 1–3, Sutherland, 1968).

Image interpretation encompasses all intellectual processes related to imagery acquired from all sorts of sensors and platforms (CCD cameras, aerial, satellite imagery, laser scans, etc.) provided that it renders sufficient information for the interpreter, either involving basic technical equipment and/or even benefitting from modern computer vision and pattern recognition algorithms. The more sophisticated, technical approach is illustrated in chapters 4.3., 4.5. and 4.6., whereas this specific section focusses on the values and merits of the human interpreter.

The first accounts on employing aerial imagery for forestry purposes date back to 1887 and as early as 1920 the first pursuits were undertaken to utilise this new technology for forest inventory purposes (Albertz, 2009: 165). Ever since, a whole array of imagery has been playing a pivotal role in a variety of forestry applications (Hildebrandt, 1996: 349-355,565,622). In practice, advances related to forest inventories (large and small-scale), forest disturbance detection (pests, wildfires, etc.), forest ecology, and forest infrastructure, would be unthought of. Inter alia, the following features and phenomena (only forestry related) can be extracted or derived from airborne and most spaceborne imagery:

- shape and size of forested land
- health status of the trees (with multi-, or hyperspectral imagery)
- extend and quality of forest disturbances
- tree species, the related distribution and percentage
- tree crown size and shape
- tree density (number of trees)

- age structure of a forest stand
- canopy closure
- tree and stand height (Albertz, 2009: 165–167, Hildebrandt, 1996: 360–368, Troycke *et al.,* 2003).

The identification of objects and phenomena in aerial and satellite imagery requires explicit familiarity with factors, which determine the quality of the interpretation process. The *brightness* of a specific area is an indication of the reflective properties of the object, but is also determined by illumination conditions, atmospheric effects, sensor characteristics, etc. *Colour hue* and *saturation* allow inferences on object differences (e.g., birch usually appears in bright green, spruce in a dark, saturated green). The *shape* of an object is easy to identify, if sudden changes in brightness result in edges and lines. The *size* of an object can also help to more easily get background information on its function and origin (e.g., a big tree is more suitable for timber, than a young, small tree). The *surface texture* can be an important indicator for the correct classification of tree species in a forest, since many species reveal typical structures of their crown. The emergence of *shadows* largely depends on the object characteristics and the illumination conditions (sun angle, terrain). The length and shape of the shadow itself allows to draw conclusions on the object properties (e.g., size, height) and for example the *location* within a specific population or environment (single tree / tree in a confined forest). In addition, o*bject patterns* are great to identify feature systems (Albertz, 2009: 107–112). Drainage systems or river networks make great examples for the underlying terrain fabric and the pertaining geological structure. Another good example is the branch structure of a tree, which tells a lot of what tree species to expect.

Having dealt with the physical attributes above, it is also important to elucidate the process of interpretation itself more specifically. Image interpretation in humans is based on perception (as an unconscious process) as well as on apperception (i.e., conscious process). Physiological and psychological processes embody intrinsic factors (Albertz, 1970, Guski, 1996: 5-8,75, Schneider, 1974: 168–170). Vision and discrimination are determined by the physical faculties of the interpreter and the photographic qualities of the image to be interpreted. However, the conscious perception of what was seen in which context can be considered an intellectual proficiency. This process demands for professional knowledge, as well as for the mental ability to recognise, analyse, and to conclude (Hildebrandt, 1996: 287). Image content attributes such as proximity, symmetry, concision, similarity, depth (stereoscopic), and continuity of objects and structures are essential for our brain to detect and interpret patterns (Goldstein and van Hooff, 2018: 59,368-370) . The following diagram represents the main procedures involved in image interpretation.

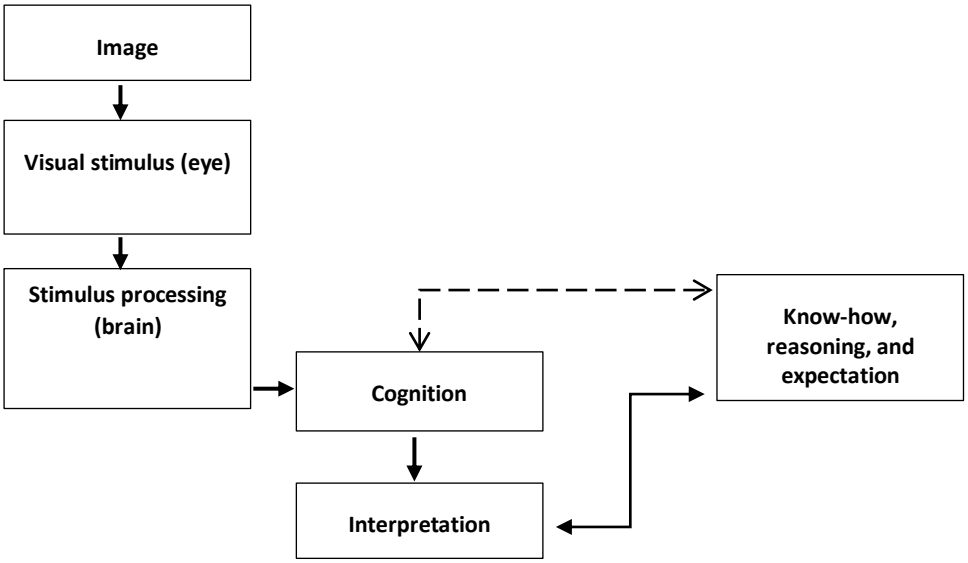

Figure 4.6: Image interpretation process (based on Schneider, 1974).

Various technical and analytical tools are available to support the interpreter in the difficult and demanding interpretation task. In particular, when working in a GIS environment, utensils for image enhancement, stereo viewing, distance and area measurement, object segmentation, and object counting can be a real blessing. Interpretation procedures can be either based on the human's visual faculty alone, but also semi-automatic, or even fully automatic employing machine learning and computer vision technology. Tree species identification remains one of the most important and challenging endeavours when being faced with forestry related investigations. Despite the successes in computer aided image classification, in some instances the achieved accuracies are extremely low. This happens quite often, when dealing with poor image quality and/or imagery featuring extremely high spatial resolution. In a study Durisova and Asche (2013) reported Kappa values (i.e. measure of agreement) of 0.69 (object-based classification) and 0.58 (pixel-based classification) when using 0.2m resolution RGB aerial photographs for a land cover classification comprising five basic classes. Visual interpretation value was close to 1.0, indicating almost full agreement with the reference data. In a Swedish study Erikson (2004b) achieved an overall accuracy of 77% for the identification of boreal tree species (spruce, pine, birch, aspen) based on 0.03m resolution colour-infrared imagery (CIR). Sophisticated image segmentation was applied for classification. Carleer and Wolff (2004) report an overall accuracy of 82% when employing IKONOS imagery (1m resolution) for identifying seven tree species in a forest in Brussels. Franklin (2018) details the identification of nine tree species in a mixed wood forest in Ontario, Canada, based on 0.12m multispectral UAV imagery. Pixel-based classifiers yielded an overall accuracy of 50-60%, whereas object-based and machine learning algorithm methods achieved 80% correct classification. In another forestry related study Komárek *et al.* (2018) notice overall accuracies of about 77%,

when looking at tree species identification. Geographic object-based image analysis in conjunction with Support Vector Machine algorithm was used to extract tree species specific information from RGB, multispectral and thermal imagery and their various fusion combinations - a method that is rated as one of the most sophisticated ones in current remote sensing applications. Quite interestingly it is to notice, that most of the more recent studies rely on the visual interpretation of very high-resolution imagery as data reference, when ground data are not available. Despite all progress in modern computer technology, Zhang (2008) constitutes in his review on modern classification techniques, that: 'The capability of current classification techniques is still far behind the ability of the human interpretation…'. As such, especially in cases, when sophisticated classification algorithms are not in hand, visual interpretation can pose a feasible option. Moreover, when ground truthing data are not available, or when budget constraints defy further engagement, visual interpretation can serve as a valuable reference in accuracy assessments in tree detection and crown delineation exercises (Ke and Quackenbush, 2011a, Park *et al.*, 2014).

For a well-trained expert with in depth knowledge on forestry and the associated local or regional conditions, obtainable outcomes can be quite impressive, of course depending on the level of the desired detail and prerequisites, such as quality of the imagery, spatial and spectral resolution (Hildebrandt, 1996: 303–305). Unfortunately, there are only a few studies specifically dealing with the achievable accuracies on visual interpretation issues, such as tree species identification. Most of them date back to the 1990s. Inter alia, Münch (1993) and Ahrens (2001) report identification accuracies for the most common European tree species of between 80 and 90%. Investigations in the USA have shown, that 14 different conifer and deciduous tree species could be identified on large-scale aerial photographs with a fidelity of about 95% (Heller *et al.*, 1964). With respect to the enormous variety of tree species in rainforests, one would expect unsatisfactory results. Nevertheless, Myers and Benson (1981) were able to detect 55 different species, with 24 of them being classified as more than 75% correct, eleven out of the 55 were identified with 100% accuracy. Similar outcomes have been confirmed by other authors, like Valérie and Marie-Pierre (2006). Of the 12 major canopy species groups 87% were correctly identified. In addition to the identification of the species as such, the high-resolution imagery provides insight in a great variety of ecological parameters. This holds great potential in particular for imagery acquired by UAVs, which can work as a magnifying class, with image resolutions of a few centimetres.

The interpretation of specific object features (e.g., trees) asks for some sort of guidelines and/or instruction. Many decades ago, interpretation keys based on morphological features and object-related reflection properties have been devised for this particular purpose

(Arbeitsgruppe Forstlicher Luftbildinterpreten, 2012, Bernhard, 2003, European Commission, 2001, Rhody, 1983, Sayn-Wittgenstein, 1978, Troycke *et al.,* 2003). Interpretation standards do not just quicken the process, but also have the potential to keep the interpreter's bias and subjectiveness at bay. The following table details some of the typology criteria that can be used for tree species identification by image interpretation – criteria are just exemplary. These criteria need to be adapted to the specific growing conditions (site) and varieties in phenotype as well as development stage.

Table 4-3: Criteria for tree species identification (based on Valérie, 2006).

Classes of criteria	Sub-classes	Definition of criteria
Crow size	Small, medium. large	Diameter 5-10m, etc.
Crown status	Dominant, co-dominant, suppressed	Above the mean canopy, etc.
Crown contour	Round, elliptic, irregular, elongated	
Crown architecture	Flat, rounded, tufted, layered, segmented, multiple	More or less horizontal surface, etc.
Foliage cover	Opaceous, light	Nothing visible through foliage, etc.
Foliage texture	Smooth, grainy, dotted	No textural design discernible, etc.
Colour	Green, yellow, dark, light	
Phenology	Flowering, leaf shed, flushing	Species specific
Bark	Grooved, smoothed, flaking, white, brown	Species specific

Exhaustive information on various interpretation keys can be found in: European Commission, 2001, Heller *et al.*, 1964, Rhody, 1983, Sayn-Wittgenstein, 1978, and Valérie and Marie-Pierre, 2006. The following graphs provide a few examples of interpretation guidelines.

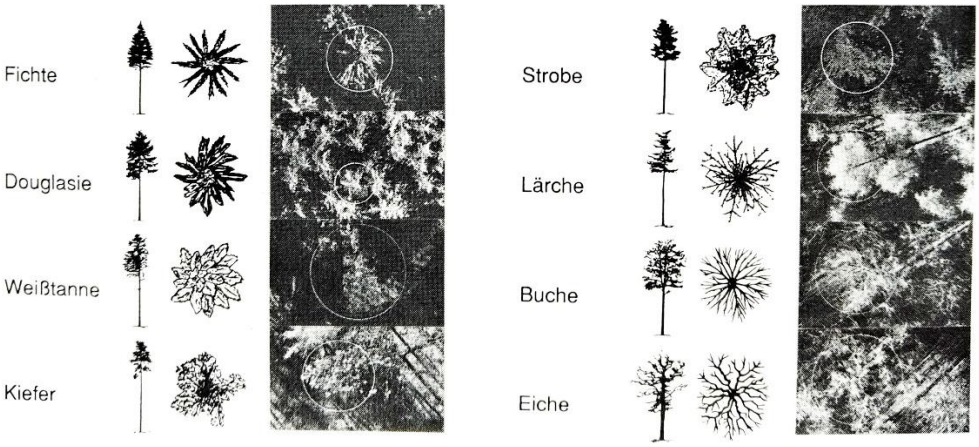

Figure 4.7: Interpretation key for European tree species (Fichte – spruce; Douglasie – Douglas fir; Weißtanne – silver fir; Kiefer – pine; Strobe – soft pine; Lärche – larch; Buche – beech; Eiche – oak); depicted are tree crowns in front and vertical view and the associated aerial photo (source: Rhody, 1983).

CIR imagery can provide some substantial increase in interpretation accuracy over common RGB imagery, in particular when assessing health status:

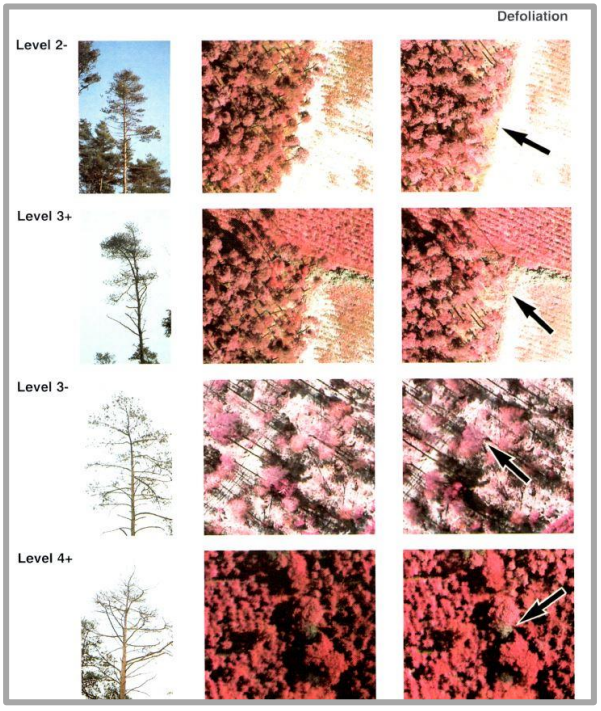

Figure 4.8: CIR aerial photography showing levels of defoliation in Scots pine (source: European Commission, 2001).

Criteria for the interpretation of Scots Pine (Pinus sylvestris) on the basis of CIR- Aerial Photographs (Abbreviations: p.b.= primary branches, +/- = more or less, occ.= occaisonal(ly))

Level	Shape Characteristics				Colour characteristics
0	Form	outline of crown or crown sections complete ; evenly smooth or +/- thickly corrugated ; sharp contours	Colour distribution		even
	Coarse structure	Ranging from crowns divided into large and/or smaller spheres to crowns divided into large and/or smaller spheres consisting of small spheres	Saturation Brightness		generally intensive dark, occasionally bright
	Fine structure	ranging from structural elements that are homogeneously dense ; without gaps ; sharply contoured ; marked by a surface dominated by coarse grains to structural elements that are homogeneously dense ; without gaps ; generally sharply contoured ; characterized by a surface which is clearly marked by coarse grains.	Tone	general specific	brown-red or brown
1	Form	outline of crown or crown sections mainly without gaps ; +/- evenly smooth of finely corrugated ; +/- sharp contours.	Colour distribution		mainly even
	Coarse structure	ranging from crowns divided into large and/or smaller spheres, or spheres consisting of small spheres to small spheres which do no longer form spheres.	Saturation Brightness		usually as in level 0, variation may occur dark, often bright
	Fine structure	ranging from structural elements that are mainly densely patterned, showing no or only a few small or single large gaps; generally sharp in contours ; grainy to structural elements partly interspersed by small or single large gaps ; generally blurred in contours ; grainly or partly amorphous.	Tone	general specific	brown-red or brown
2	Form	outline of crown or crown sections dispersed ; irregularly corrugated or serrated ; some isolated elements ; blurred contours	Colour distribution		generally uneven or jumbled
	Coarse structure	ranging from numerous smaller and/or single large gaps (shadow furrows) which structure crown into large and/or smaller spheres to crowns consisting of small spheres ; small spheres showing no patterning or in some instances small and/or large gaps (shadow furrows) which structure small spheres into small lumps.	Saturation Brightness		less intensive mostly bright
	Fine structure	ranging from dispersed structural elements ; numerous small and/or large gaps ; generally blurred in contours ; +/- grainy and/or amorphous to diffuse structural elements ; numerous small and/or few large gaps ; blurred in contours ; mostly amorphous.	Tone	general specific	brown-red or brown

Figure 4.9: Interpretation criteria for health assessment in Scots pine (Source: European Commission, 2001)

Despite all the praise, visual interpretation can be quite cumbersome and time-consuming (expensive). This method is thus not well-suited for the interpretation of huge forest areas (Heller *et al.*, 1964). With the gaining popularity of extremely high-resolution UAV imagery, however, visual interpretation has the potential to come into fashion again. For interpretation key of Mongolian taiga tree species and extraction of other forestry related parameters, please consult Chapter 7.3.4.1.

4.3. Image classification

The classification of imagery represents a vital part of the pattern recognition process, which has become a focus of research in computer vision recently (Förstner and Wrobel, 2016: 2, Theodoridis and Koutroumbas, 2009: 1–2). The subsequent chapter details only the essential methods, and skims well-known basics, and algorithms, being too complex for hands-on approaches suited for practitioners (e.g., deep learning). As such, the interested reader is referenced to excellent reading for instance from Gonzalez and Woods (2018), Beyerer *et al.* (2018) and Theodoridis and Koutroumbas (2009) for pattern recognition and image processing in a broad context, and from Mather (2011), Tso and Mather (2009),

Lillesand *et al.* (2015), Jones and Vaughan (2010), Liu and Mason (2009) and Jensen (2016) for image classification associated with remote sensing technologies in particular. A detailed account on the comparison of the most popular classifiers (i.e., RF, SVM, k-NN) and their merits and demerits in practice is provided at the end of the pertaining subchapters.

The human eye – brain linkage is considered to be the most sophisticated pattern recognition system in the biological world, leaving contemporary recognition machines pale in contrast (Gonzalez and Woods, 2018). However, recognition machines have become important in everyday life (e.g., barcode readers, speech recognition). The four main stages involved in pattern recognition are: (1) sensing, (2) pre-processing, (3) feature extraction, (4) classification, and (5) accuracy assessment. Image classification requires the user to carry out the (i) determination of the number and nature of the categories to be classified (e.g. land cover), and (ii) the assignment of numerical labels to the pixels based on their properties employing a decision rule (Mather, 2011: 167–168). Classification methods are commonly categorised as being *unsupervised* (i.e. systems learn the pattern classes themselves without almost no a priori conditions, and are entirely based on data distribution statistics), or *supervised*, the latter using training data representing various ground objects (Liu and Mason, 2009). They can be applied to segment imagery into regions with similar attributes such as land cover classes (e.g., water, forest, buildings). Supervised approaches vary from designer-fixed feature forms to systems, that utilise deep learning to learn on their own. The crucial steps for describing objects of the real world and their inherent patterns are (i) the selection of a feature set that best reflects the pattern, and (ii) the selection of a suitable method for the comparison of the pattern. Subsequently, the accuracy assessment of the allocation process is mandatory. The goal of the classification process is to generate a thematic information layer with little or no user intervention (i.e., semi-, or fully automatic). As a standard procedure, statistical concepts are applied to exploit the spectral fingerprint of a specific object or object class. In addition, spatial information such as *context* (the relationship of a pixel to a neighbouring object) and *texture* (a measure of homogeneity of neighbouring pixels) can help improve the classification outcomes considerably, when integrated in the classification algorithm (see also object-based classification) (Khatami *et al.*, 2016).

Very high-resolution imagery with enormous amount of detail requires specific algorithms, which are able to make use of the full potential of the radiometric and spatial resolving capacity. Resolutions of only a few centimetres or decimetres now reveal individual component parts of plants such as branches and leaves, thus, mixed pixels with great variation and high contrast differences between features have evolved into a new challenge

for image classification. Most of the classifiers, that have been used decades ago, become superseded by more sophisticated algorithms, which are to a much higher degree able to manage big and complex data sets such as UAV and hyperspectral imagery. One of the consequences is, that a shift from pixel-, to object-based classifiers becomes noticeable (Hajek, 2004, Laliberte *et al.*, 2010, Nussbaum *et al.*, 2013, Whitehead and Hugenholtz, 2014, Whiteside *et al.*, 2011). According to Lu and Weng (2007), not only the image characteristics, but also the choice of an appropriate classifier sizably determines the success of an image classification operation. Classification methods range from unsupervised algorithms (e.g., ISODATA and K-means) to parametric supervised approaches (e.g., maximum likelihood, or parallelepiped). Modern non-parametric machine learning algorithms comprise approaches such as *decision trees* (DT), *Support Vector Machines* (SVM), *k-Nearest Neighbours* (kNN), *Neural Networks* (NN), and *Random Forest* (RF). Thanh Noi and Kappas (2017) carried out some exhaustive literature search to conclude, that SVM and RF have by far received the most attention in the remote sensing community in recent years.

4.3.1. Pixel-based classifiers

A *decision tree* (Yes/No type) is a nonlinear, supervised classifier and multistage decision system, in which classes are sequentially reject until a finally accepted class is reached (Theodoridis and Koutroumbas, 2009: 215–219). The hierarchically structured tree consists of nodes (a value for a certain attribute is assessed here), branches (corresponding to the result of a test and connecting to other nodes or leaves), and leaf nodes (as terminal nodes predicting the outcome like class label). Decision trees are constructed that way, that during an iterative process data are split into partitions with subsequent further splitting on each branch, also known as binary recursive partitioning. A vital part of the process is the a priori definition of a set of questions and the splitting criteria. The size of the decision tree is a crucial part of the design, and has to be chosen with care. Another factor to be considered is the high variance, with small changes in the training data set to cause a very different tree structure (Theodoridis and Koutroumbas, 2009: 220–221). Nevalainen *et al.* (2017) used decision trees among other classifiers for the detection and classification of trees from UAV-based photogrammetric point clouds. However, other classifiers such as RF and Multilayer Perceptron (MLP) outperformed DT. In contrast, Sharma *et al.* (2013) found out, that DT (90%) provided much better overall land use classification results on Landsat imagery than other classifiers like ISODATA (57.5%) and Maximum Likelihood (76.7%). Sankey *et al.* (2017) deployed an unmanned aerial vehicle with LiDAR and hyperspectral sensors onboard to look into tree density and canopy cover in a forest in Arizona. By using a DT approach, they managed to fuse both sensor data to achieve much better results than with an isolated analysis of the data layers. A comprehensive study on various classification

schemes was conducted by Prasad *et al.* (2006) for predictive tree species mapping. According to them, DT turned out to be too sensitive to small changes in the training dataset and exhibited a tendency to overfit in the model.

A *random forest* (RF) classifier can be considered a variation of the decision tree approach, consisting of a large number of individual decision trees that operate as an assemblage. As such, the prediction by committee is more accurate than that of each individual tree. The low correlation between the models is a key component for achieving maximum output accuracy. Another prerequisite is that features with at least some predictive power are needed. How does RF work? In an image to be classified a sufficiently high number of datasets (object classes) need to be defined for training and testing the classifier. RF allows each individual tree to take random samples from the dataset to result in different trees, also known as 'bagging' or 'bootstrap aggregation' (Theodoridis and Koutroumbas, 2009: 221). Instead of sub-setting the training data into smaller components, random samples of size N are taken with replacement to get an unbiased estimate of the classification error as trees are added to the forest (Cutler *et al.*, 2012). Picking only from a random subset of features causes more variation amongst the tree models to result in lower correlations across the trees. This is in contrast to a conventional decision tree, where every possible feature is considered and the one selected, that produces the most separation between the observations in the left vs. the right node. After the construction of each tree, all data are trickled down the tree, and proximities computed for each pair of cases to train the tree. Subsequently, each tree of the forest ejects a predicted class. A final decision is taken through a majority rule, i.e. by measuring which prediction was made by most of the trees (Breiman, 2001, Liaw and Wiener, 2002, Wang *et al.*, 2019a). The following graph provides a simplified depiction of the process portrayed above.

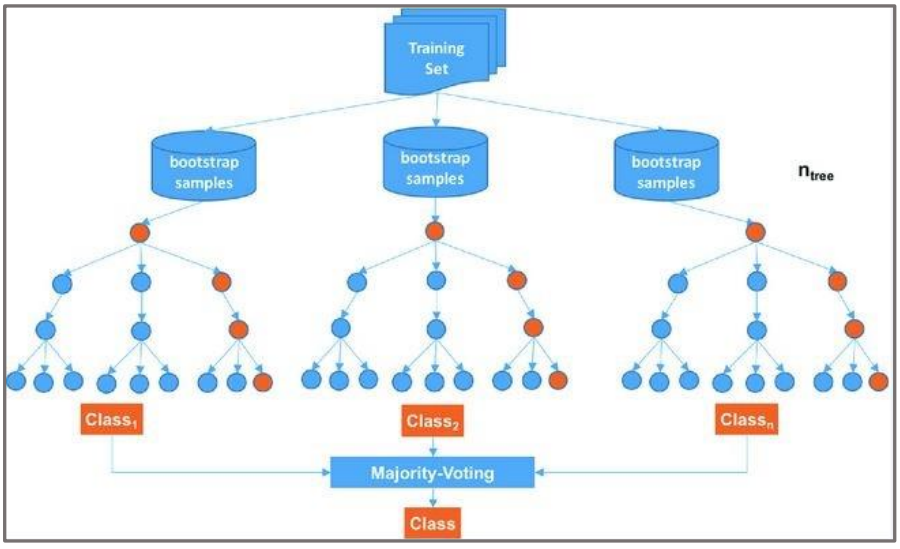

Figure 4.10: Simplified view of the Random Forest classifier (Wang et al., 2019).

Numerous authors have recently looked into the application of RF, including a comparison with other machine learning algorithms in particular (Khatami *et al.*, 2016). Conclusions have transpired quite differently. For better comparison of the RF, SVM, and k-NN classifiers, a comprehensive account is given at the end of this subchapter. A specific section dealing with classifying UAV imagery is dedicated to chapter 6.8 with reference to chapter 4.7.

Advantages of RF:

- Maintains accuracy for missing data.
- Does not overfit the model.
- Can handle large datasets with higher dimensionality.
- There is no need for cross-validation, since the test error is estimated internally.

Disadvantages:

- Very sensitive to small changes in training data.
- User has very little control over the model (black box) (Belgiu and Drăguţ, 2016, Khatami *et al.*, 2016).

Support Vector Machines (SVM) is a machine learning concept based on the objective to find a *hyperplane* in an n-dimensional space to distinctly classify data points. Hyperplanes are decision boundaries and defined as being a subspace of dimension n-1in the n-dimensional space (i.e., Euclidian, affine, or vector space). For the separation of two (training)data point classes, there is a choice of a multitude of hyperplanes. The goal is to find a plane with a maximum margin, i.e. the maximum distance between data points of both classes (Ghandi, 2018). The following graph provides an account on this undertaking:

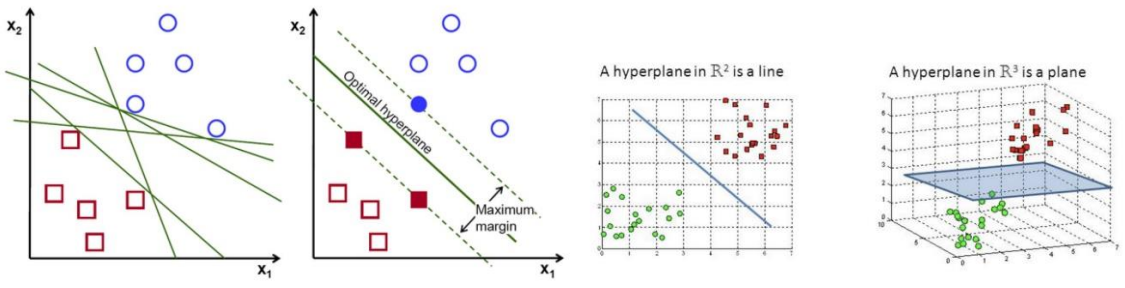

Figure 4.11: Possible hyperplanes to separate classes (both left) – support vector data points are indicated as bold points; both right: hyperplane in 2-dimensional (R^2) and three-dimensional space (R^3). Source: Ghandi, 2018.

SVM supports both, the linear and non-linear separability of objects, using the kernel trick for the latter to transfer the separation vectors into higher dimensional spaces. The separation vectors, also known as *support vectors*, are data points being closer to the

hyperplane than other data points, and, as such, effect the position and orientation of the hyperplane. By using those support vectors, we are able to maximise the margin of the classifier (Theodoridis and Koutroumbas, 2009: 119–125).

Recently, Support Vector Machines have become real superstars in the remote sensing community (Khatami *et al.*, 2016). As with all classifiers, there are merits and demerits to disclose:

- SVM work well in high dimensional spaces with a clear margin of separation between classes.
- SVM works in a memory efficient fashion.
- SVM have superior performance with respect to small training sample sizes.
- The risk of overfitting is less than in other algorithms.
- Unlike in neuronal networks, SVM is not solved for local optima.
- SVM algorithm is not well suited for large datasets.
- The algorithm does not perform well with overlapping classes.
- The final model is rather veiled; thus, replication of the results is difficult.
- Finding a good kernel function is not trivial (Mountrakis *et al.*, 2011, Sothe *et al.*, 2020).

Neural networks mimic the visual cortex of mammals by using a multitude of elemental non-linear computing elements called artificial neurons (Lee *et al.*, 1998). New training algorithms for multilayers of the perceptron-like concepts (learning machines) are based on methods, called backpropagation (Jiao *et al.*, 2020: 9–11, Mather, 2011: 185–188). Most approaches of pattern recognition rely on human-engineered techniques to translate raw data into computer processing suitable formats. Divergent from these methods, neural networks use backpropagation to learn representations suitable for recognition. Starting with raw data, each layer of the network refines the representation into more abstract levels (Gonzalez and Woods, 2018). This kind of multi-layered learning has also become known as *deep learning (LeCun et al., 2015)*. However, human intervention is still required for the specification of parameters, like the number of layers and the number of artificial neurons per layer. Despite the recent overwhelming success of the deep learning strategy, considerable knowledge and experimentation is required on the part of the designer, thus making deep learning quite challenging and as such not very suitable for everyday use. For analysing imagery, a specific class of deep neural networks, referred to as *convolutional neural network* (*CNN*), has become quite popular. Convolution is a specific kind of linear operation in CNN, which replaces general matrix multiplication in at least one layer. The following graph demonstrates the architecture of a typical CNN for image analysis.

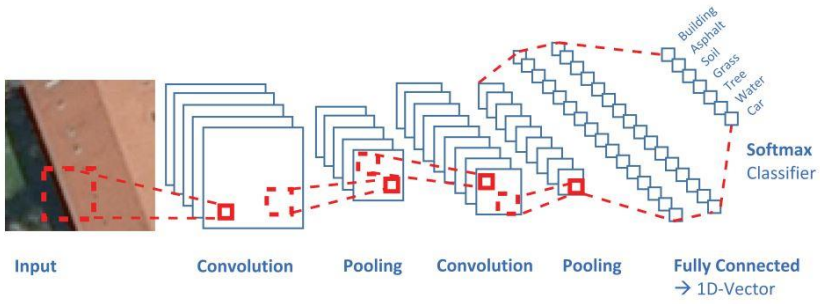

Figure 4.12: Successive steps of a convolution and pooling are shown to generate a feature vector which is classified in the final step (source: Heipke and Rottensteiner, 2020).

In an initial step, a set of digital filters is applied to an image of fixed size (convolution). In the subsequent pooling from a larger group of filtered pixels only one pixel is retained (the one with the maximum entry). The remaining set of pixels is then subjected to a non-linear function. Processing is pursued through densely connected layers, resulting in a feature vector representing the entire input image. This feature vector is finally classified with an arbitrary classifier (Heipke and Rottensteiner, 2020).

Literature on neural network applications is rapidly evolving (Ma *et al.*, 2019). Successful applications in UAV remote sensing have been reported by Fromm *et al.* (2019) for the detection of conifer seedlings (precision of 81%), and by Morales *et al.* (2018) for the identification of palm trees in the Amazon rainforest (overall accuracy of about 97%). Miyoshi *et al.* (2020) also inform about extremely high identification rates (about 96%) for single tree species extracted from hyperspectral UAV imagery. WorldView2 imagery was analysed in a study by Braga *et al.* (2020) for identification and delineation of tree crowns in a rainforest, yielding accuracies of around 92% when employing CNN algorithms. Li *et al.* (2017) also report high detection rates (96%) of oil palms extracted from Quickbird imagery.

Despite all the merits, limitations of the CNN classifier need to be related:

- A CNN needs a sufficient number of training data.
- A CNN cannot learn the unseen.
- Reasoning associated with human behaviour has not materialised in CNN.
- A CNN is largely a black box, and as such, classification results are almost impossible to replicate (Heipke and Rottensteiner, 2020).

The *k-nearest neighbour* algorithm (*k-NN*) is a non-parametric supervised machine learning method, not to be confused with the k-means clustering classifier (Chirici, 2012). The k-NN

method was initially developed to carry out the national forest inventory (NFI) in Finland more efficiently and has also proven to be very successful in Norway and Finland (Baasan, 2010, McRoberts and Tomppo, 2007). As a variant of the regression technique, k-NN helps to cut down on inventory costs and labour by “extrapolating” measurement values (e.g. timber volume) from sampling plots to the neighbouring areas (Tomppo *et al.*, 2008). As such, this technique has proven to be very useful for wall-to-wall inventories of huge areas. It is based on the idea to transform and link specific forest attributes, such as timber volume, forest cover type, or DBH, to individual pixels. As the name suggests, the nearest neighbour concept is a prerequisite for this approach. It thus assumes, that similar objects exist in close proximity. For the calculation of the distance between data points the Euclidian distance is being used most commonly. With N training vectors given, k-NN identifies the *k* (i.e., amount of) nearest neighbours of the data point to be classified. The training vector itself defines a region in space to partition the entire feature space (e.g., Voronoi partition).

In the following graph the most critical steps of the classification process are represented, which are: (i) load dataset; (ii) define k (use various *k*s to find best fit); (iii) calculate distance between any two points; (iv) find the nearest neighbour based on these pairwise distances; (v) get majority vote on class labels based on nearest neighbour ranking; (vi) create confusion matrix for classification accuracy results.

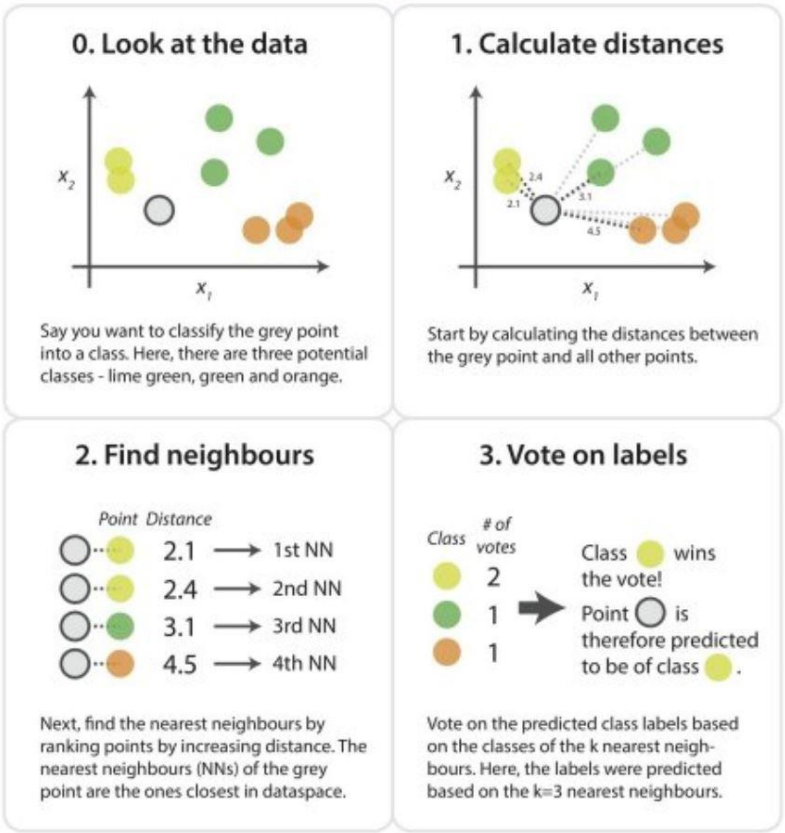

Figure 4.13: Major tasks to be accomplished for k-NN classification (Latysheva, 2016).

The real challenge of this classification method is in finding the most suitable *k* for optimal classification results, since *k* determines the accuracy of the prediction output (Naidoo *et al.*, 2012). As such, it is an iterative process of applying various *k* values to the dataset. If *k* is too low, the prediction of the new class data point is too noisy and subject to effects of outliers. Choosing a *k* being too big will be at the expense of computing time, and causing an excessive leverage of dominating data classes.

Advantages of k-NN:

- It is simple to implement.
- No need to build a model and tune several parameters.
- The algorithm makes no prior assumption of the data.

Disadvantages:

- The prediction time is high for high numbers of data and/or predictors.
- K-NN features drawback of majority voting in skewed class distribution (can be overcome by weighting the classification).
- K-NN is considered a lazy learner (Latysheva, 2016, Stümer, 2004, Wilson *et al.*, 2012).

Literature review:

In studies by Adam *et al.* (2014) and Ghosh and Joshi (2014), RF and SVM performed almost equally well, when considering classification of RapidEye and WorldView-2 imagery. In a meta-analysis Khatami *et al.* (2016) found clear indications of SVM, kNN, and RF being clearly superior to other supervised classifiers and other image spectral information manipulation and feature extraction such as vegetation indices and Principal Component Analysis (PCA). They also constitute, that SVM has achieved the best overall performance in all studies investigated. Pouteau *et al.* (2011) compared the six most popular machine learning algorithms applied to different satellite datasets (Landsat 7, SPOT, airSAR, TerraSAR-X, Quickbird, and WorldView-2) for tropical ecosystem classification. They testify, that SVM outperformed all other tested classifiers in 75% of the situations. Heydari and Mountrakis (2018) examined the effects of the classifier selection, reference sample size, reference class, and scene heterogeneity in per-pixel classification accuracy on 26 Landsat test sites employing five favoured classification algorithms. Obviously, SVM and kNN performed much better, when concentrating on edge pixels bordering adjacent object classes. The authors also state, that , with the exception of Naïve Bayes (NB), all classifiers performed similarly well for the entire image block. Thanh Noi and Kappas (2017) compared

SVM, k-NN and RF for classifying Sentinel-2 imagery showing the Red River Delta in Vietnam. An overall high accuracy was obtained for all classifiers (90 to 95%) for designating six various land use classes. Albeit, the SVM delivered better results for smaller sample sizes. However, not only the sample size seems to be crucial for the performance of classifiers, but also the selection of the spectral bands of the imagery. For example, Adelabu *et al.* (2014) achieved an increase of the overall accuracy of about 20% by integrating the red-edge band of RapidEye images. They conclude, that RapidEye has the potential to considerably improve insect defoliation classification. By applying CNN, SVM, and RF to fused hyperspectral and photogrammetric data, Sothe *et al.* (2020) discovered, that all classifiers generated satisfactory results for tree species determination. However, CNN was between 22% and 26% more accurate, when only the hyperspectral bands were employed. Interestingly, Ghosh *et al.* (2014) found out, that tree species classification results do not necessarily improve with spatial resolution of the imagery using the same classifier (i.e. RF). RF performed better with 8m resolution images, than with 4m – even the 30m resolution of the hyperspectral data produced sound results. WorldView-2 and Landsat 8 images were analysed with SVM and CNN to detect bark beetle outbreaks in the investigation conducted by Stych *et al.* (2019). They found SVM to be the best method used in their study. Immitzer *et al.* (2016a) employed a RF algorithm on WorldView-2 imagery for wall-to-wall mapping of growing stock for a national forest inventory. The satellite data was used as auxiliary information for the RF modelling approach, and was considered to be acceptable in the overall performance with an R^2 of 0.44. To improve estimations of forest attributes like basal area, Landsat and hyperspectral imagery was employed by Stümer (2004). The k-NN analysis revealed overall accuracies for basal area of being between 35% and 67% for Landsat, and values of 65% to 67% for the HyMap data. Scheuber (2010) also applied the k-NN method to look into the estimation of parameters such as basal area, stem volume, and trees per hectare in a mixed forest in southwest Germany. For the tree species determination, he found an overall accuracy of 52.2%. However, accuracies deteriorated for timber volume, being an RMSE of 30.9% for k = 5 and 22.6% for k = 20. This behaviour of the algorithm clearly demonstrates the circumstance, that the value for k has to be chosen with extreme care. In a similar survey Abedi and Bonyad (2015) analysed IRS satellite imagery to achieve sufficient estimates for forest attributes. They observed accuracies between 80% and 94%, with k between 5 and 8 being the most suitable values. Beaudoin *et al.* (2014) mapped Canadian forest attributes through k-NN and MODIS imagery to conclude, that k-NN predictions at pixel level deviated from ground sampling especially in mountainous regions with low biomass, and that spatial aggregation of pixels can help improve accuracies. A relevant disclosure was made by Eskelson *et al.* (2009) by finding out, that k-NN approaches can turn out to be very useful in imputing missing data for forest

inventory. The authors also stress, that methods to minimise the registration error of the various sources (e.g., aerial photographs, LiDAR point clouds, satellite data) employed require further investigation.

4.3.2. Object-based image classification

An alternative to essentially pixel-based analysis has been devised in the early 2000s, when trends to higher spatial resolution of imagery had become obvious (Blaschke, 2010, Li *et al.*, 2016). Object-based strategies (also known as OBIA (Object Based Image analysis)) amalgamate pixel groups into discrete objects based on their spectral, size, textural, and shape characteristics. Such methods can deliver very useful results, if the classified objects represent meaningful units, such as individual trees (Whitehead and Hugenholtz, 2014). Analogous to the supervised classification, the ancillary information makes this classifier particularly efficient when searching for objects occupying small areas, such as trees, thus avoiding a complete classification of the entire image (Jones and Vaughan, 2010: 156). Object-based classification is a three-step process: (i) pre-processing of the imagery (i.e., geometric and/or atmospheric/radiometric correction); (ii) subsequently the image is segmented into discrete objects or features and (iii) then each object is classified. This kind of classification is quite similar to the type of analysis done by humans during visual interpretation and as such mimics pattern recognition processes (Nussbaum *et al.*, 2013). Most of the segmentation algorithms are based on the image intensity value properties *discontinuity* and *similarity*. In the first case, the image is portioned into regions featuring abrupt changes in intensity, such as edges. Whereas in the latter, the image is portioned into regions that are similar according to a set of predefined criteria (e.g., thresholding, region growing, splitting, and merging). Some approaches even combine both approaches for exploiting image content to a maximum (Gonzalez and Woods, 2018). The *scale* of the objects plays an important role in the segmentation process. It defines the minimum number of pixels to be contained in a group to become an image segment or object and thus determines the size of the resulting image objects. Most studies dealing with OBIA reveal, that finding the right scale parameter can be a very time consuming trial and error undertaking (Niemeyer *et al.*, 2012, Yang *et al.*, 2019). Once the image objects have been created the classification is carried out based on rule set defined by the user. The underlying criteria for the rule set reach far beyond spectral characteristics (e.g., colour) and encompass feature factors such as shape, size, texture, as well as neighbouring relationships like connectivity and proximity. To ease the decision on the most appropriate rule set and feature selection a statistical tool (SEaTH) was devised by Nussbaum *et al.*

(2013). It calculates the separability for each class combination and determines the best threshold for class separation (see also eCognition software). The following graph (4.14.) presents an example of the outlined object-based classification procedure.

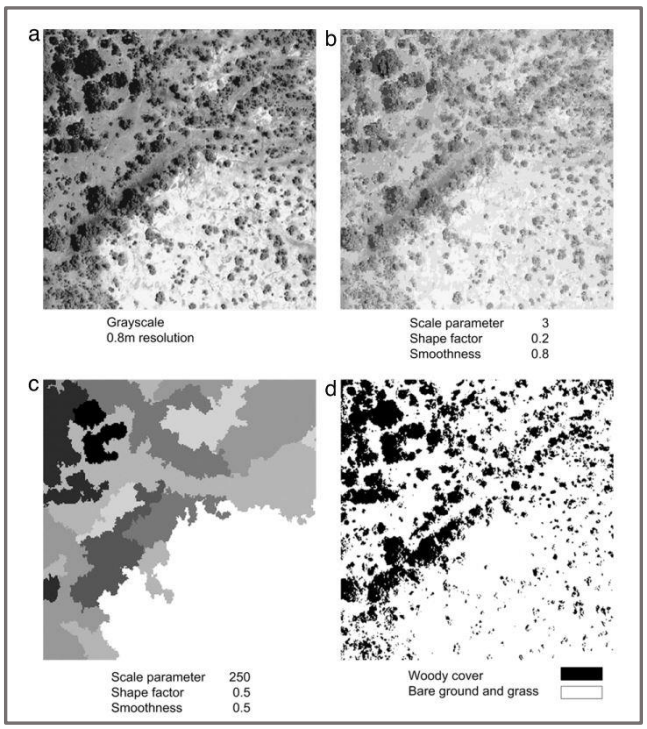

Figure 4.14: (a) aerial photograph of heterogenous landscape; (b) fine scale segmentation; (c) coarse scale segmentation; (d) OBIA based classification of woody cover. Source: Blaschke, 2010.

Another method is described by Tong *et al.* (2012). They applied a supervised and fuzzy-based approach to determine optimal multi-resolution segmentation parameters. Unfortunately, as with above-mentioned SEaTH, this tool has not been integrated into object-based image analysis software packages yet, although segmentation accuracies are reported to increase considerably, and operation times (processes are operator-independent) reduced drastically.

Successful classification of satellite imagery is reported by Aguilar *et al.* (2013). The analysis of GeoEye-1 and WorldView-2 images yielded overall accuracies of 89% and 83%, respectively, when looking at urban environments. According to them the accuracy of the classification is driven by three main factors, namely (i) sensor used, (ii) sets of image objects employed, and (iii) the size and quality of the training samples to feed the classifier. Deng *et al.* (2014) found improvements of up to 34% compared to pixel-based classification of WorldView-2 imagery for the identification of tree tops in the Purple Mountain National Park close to Nanjing, China. Yan *et al.* (2006) found even a higher gain (36.77%) when classifying land cover from 15m ASTER datasets. In his investigation on tree species determination from multispectral UAV imagery Franklin (2018) reports classification accuracies of 50% to 60% for pixel-based classifiers, and 80% for OBIA. Hajek (2004) confirms excellent classification results (i.e. 95%) for tree species discrimination extracted from 4m Ikonos imagery. OBIA was also applied to WorldView-2 images in the study presented by Karlson *et al.* (2014). The overall detection rate for individual tree crowns in a managed forest in Burkina Faso was 85.4%, with lower accuracies in areas featuring high tree density and dense understorey vegetation. Increased classification performances (Kappa index of 91.6 %) have been conveyed by Ke *et al.* (2010), when synergistically using

high-resolution Quickbird satellite imagery and LIDAR point clouds. However, this finding is in contrast to the results published by Machala and Zejdová (2014), who applied OBIA for forest classification of aerial imagery. According to them the overall accuracy of almost 90% deteriorated to a mere 70% by integrating tree height information into the classification process. The authors address high tree density (i.e. low object separation) and poor tree height class definition as major culprits for mediocre outcomes. Kavzoglu and Yildiz (2014) report good OBIA classification accuracies for aerial and Quickbird-2 imagery to discriminate several land use features. An important observation of the authors was, that segmentation parameters have a direct effect on the classification accuracy, with low scale-shape combinations generating the best results. This view is supportingly extended by Karakis *et al.* (2006), who suggest to also consider sun elevation and topography, when selecting segmentation parameters. In an extensive survey Myburgh and van Niekerk (2014) investigated the performance of various classifiers in an OBIA environment in relation to the size of the training set. They deduce that: (i) the performance of all the classifiers (i.e., SVM, Nearest Neighbour, Maximum Likelihood) improved significantly as the size of the training set increased, and (ii) SVM was the superior classifier for all training-set sizes. Although multi-scale segmentation seems to be working very well for very high-resolution imagery, authors like Jing *et al.* (2012) do not fail in stressing, that forests consist of multi-scale branches, complex tree crowns, and tree clusters causing an over-segmentation of the imagery.

Advantages and disadvantages wrapped up:

- The majority of the studies confirm, that OBIA clearly outperforms most pixel-based classifiers, except for sophisticated classification methods based on machine learning (e.g., SVM, RF).
- Increasingly complex OBIA classification rule-sets and workflows become real challenges.
- Not as user friendly as other classification strategies.
- Most methods either produce over-, or under segmentation, requiring a lot of editing.
- Automatic object extraction is still in its infancy.
- Segmentation process is complex and no single method performs consistently well on different regions of the world and in varying image acquisition circumstances.
- Future discussions on epistemological and ontological aspects of objects as well as their methods of derivation are required (Blaschke, 2010, Liu and Xia, 2010, Mallinis *et al.*, 2008, Niemeyer *et al.*, 2012, Vatsavai, 2013).

4.3.3. Spectral indices for image classification

Apart from the above-mentioned classifying approaches vegetation indices (VI) have proven to be very apt tools for analysing imagery in a remote sensing context. The subsequent section focuses solely on a few fundamentals, as well as a selection on specific indices employed in the forestry context. Exhaustive material on VIs is provided for example by Bannari *et al.* (1995), Huete (2012), Jones and Vaughan (2010: 168–176), and Xue and Su (2017).

VIs are simple, dimensionless and effective algorithms for quantitative as well as qualitative assessments of vegetation cover, vigour, growth dynamics, Leaf Area Index (LAI), fire scars, and many other applications. VIs exploit the reflectance properties of electromagnetic radiation in vegetation and as such allow inferences on their chemical and morphological traits. Vegetation indices have been designed that way, that confounding factors such as soil background reflectance, directional, or atmospheric effects are minimised. They have become very popular and widely used in the remote sensing community, with sensor platforms including space-, and airborne carriers, and with UAV based imagers as a fairly recent 'disciple'. Owed to the complexity of variations in instrumentation, spectral and spatial resolution, band combinations, and environmental conditions, no unified mathematical expression to encase all VIs exists (Xue and Su, 2017). As such, VIs are commonly tailored to the specific application requirements. As a consequence, far more than one hundred different indices are being offered to the user these days.

According to Broge and Leblanc (2001) vegetation indices can be categorised as follows (with examples provided below):

- Ratio indices (e.g., NDVI, RVI, MSI); these VIs tend to enhance the contrast between soil and vegetation .
- Orthogonal indices (e.g., PVI, TC, GVI); compared to ratio indices, the greenness isolines do not converge in the origin, making them perform very well at low LAI values.
- Hybrid indices – i.e., the fusion of ratio and orthogonal VIs (e.g., SAVI, TSAVI, MSAVI); these VIs attempt to decouple vegetation reflectance from soil reflectance for better vegetation – soil (background) discrimination. They are particularly geared for arid and semi-arid environments.
- Hyperspectral indices (focussing on the red edge reflectance pattern); these VIs are better suited for hyperspectral sensors to account for subtle changes in vegetation traits.

A selection of the most common VIs and their formulas is given below in Table 4-4.

With regard to the vast number of published studies the *NDVI* (Normalized Difference Vegetation Index) has been as popular as ever to detect plant vitality, despite of a few shortcomings (Muhsoni *et al.*, 2018). Apparently, NDVI shows a distinct saturation tendency for LAIs greater than 2 (Gitelson, 2004, Liang and Wang, 2020: 405–445). This property can result in a grave underestimation of biomass in lush vegetation such as tropical rainforests (Jiang *et al.*, 2008, Tesfaye and Awoke, 2020). In addition, sensitive reactions to ground reflections have been observed. NDVI values range from -1 to +1, with negative values indicating shadow areas, water, snow, or bare soil. Low values reveal either low vegetation cover, or deteriorated vigour. In contrast, high NDVI values denote a high level of photosynthetic activity and as such suggest elevated quantities of biomass. The *DVI* (Difference Vegetation Index: DVI = NIR-R) also seems well suited for low LAI, however, appears to be more sensitive to soil background than the NDVI (Jackson and Huete, 1991). The *SAVI* (Soil Adjusted Vegetation Index) was established to improve the sensitivity of NDVI to soil backgrounds. The adjustment factor *L* (see also formula) was introduced to equally deal with dark and light soils. However, the SAVI was modified (MSAVI) recently, since the *L* factor depends on the level of vegetation cover prior to classification and as such, is subject to speculation, when vegetation cover is not known .

Table 4-4: Examples of common vegetation indices and possible applications (Hatfield,2010).

Vegetation Index	Formula and Wavebands	Crop Parameters
Ratio	R_{NIR}/R_{Red}	Biomass, LAI, cover
Normalized Difference Vegetative Index (NDVI)	$(R_{NIR}-R_{Red})/(R_{NIR}+R_{Red})$	LAI, intercepted radiation
Green NDVI (GNDVI)	$(R_{NIR}-R_{Green})/(R_{NIR}+R_{Green})$	LAI, intercepted radiation
Red Edge NDVI (NDRE)	$(R_{NIR}-R_{Red\ edge})/(R_{NIR}+R_{Red\ edge})$	LAI, intercepted radiation
Soil Adjusted Vegetation Index (SAVI)	$(R_{NIR}-R_{Red})(1+L)/(R_{NIR}+R_{Red}+L)$ Where L is an adjustment parameter typically equal to 0.5	LAI
Enhanced Vegetation Index (EVI)	$2.5*(R_{NIR}-R_{Red})/(R_{NIR}+6*R_{Red}-7.5R_{Blue}+1)$	LAI
Normalized Pigment Chlorophyll Ratio Index (NCPI)	$(RED_{660}-BLUE_{460})/(RED_{660}+BLUE_{460}$	Leaf chlorophyll
Green Chlorophyll Index (CI_{green})	$(R_{NIR}/R_{Green})-1$	Leaf chlorophyll
Red Edge Chlorophyll Index ($CI_{Red\ Edge}$)	$(R_{NIR}/R_{Red\ edge})-1$	Leaf chlorophyll
Plant Senescence Reflectance Index (PSRI)	$(RED_{660}-GREEN_{510})/NIR_{760}$	Plant senescence

The *GNDVI* (Green NDVI) performs better than NDVI at higher LAIs, and has been found to be more sensible than NDVI to identify differences in chlorophyll content. A variation of the NDVI, the so-called NDRE (exploiting the red-edge bands), also seems to be more geared for the observation of vegetation with low chlorophyll content (Boiarskii and Hasegawa, 2019). In general, modern sensors also acquiring the red-edge part of the electromagnetic spectrum seem to be having some edge over conventional sensors, when applied to vegetation indices such as the NDVI Red-edge, or the NBR (Korhonen *et al.*, 2017). The *EVI* (Enhanced Vegetation Index) was especially designed for MODIS products

to account for negative atmospheric effects. *EVI* (Enhanced Vegetation Index) is considered to feature an improved sensitivity to vegetation differences from uncovered to dense vegetation conditions (Glenn *et al.*, 2008). More recently developed VIs attempt to fully exploit the potential of hyperspectral imagery. Indices like the *MSARVI* (Modified Soil and Atmospherically Resistant Vegetation Index) or the *PRI* (Photochemical Reflectance Index) apparently show very high sensitivity for vegetation pigments, allowing improved assessment of photosynthesis activity and biomass (Broge and Leblanc, 2001). With the development of thermal remote sensing technology, canopy temperature as related to transpiration and stomatal conductance in plants can be measured. This notion is reflected in the so-called *CWSI* (Crop Water Stress Index) to monitor changes in water content of vegetation. With the advent of sophisticated multispectral sensors, indices especially geared for the assessment of burn severity of burnt areas have been designed and successfully applied. One of the salient indices is referred to as *NBR* (Normalised Burn Ratio: NBR = (NIR-SWIR)/(NIR+SWIR)). This index exploits the near-, and short-wave infrared reflectance of the fire affected areas and as such renders the assessment of pre-, and postfire incidents possible (Keeley, 2009, Lutes *et al.,* 2006).

Other than the well-reputed and conspicuous NDVI, the *LAI* also deserves special attention due to its relevance in determining plant vigour and biomass estimation. Leaf Area Index (LAI) is one of the most widely used indices for describing plant canopy structure, and for getting a better understanding of the biosphere-atmosphere exchange of mass and energy at the leaf surface. As such, the determination of LAI has become a crucial index in biochemical, hydrological, and ecological modelling, as well as for measuring forest growth and productivity. By definition, LAI is the ratio of one-sided leaf area per unit ground area (e.g., sqm). Since it is a ratio of areas, LAI is unitless – an LAI of 3 would thus have a ratio of 3:1 of leaf to ground area. Common LAI values range from 1 for desert ecosystems to 9 for very lush tropical forests, with mid-latitude forests assigned values between 3 and 6. However, seasonality, phenology, leaf characteristics (needle vs broad leaf), canopy structure, and transpiration rate can exhibit large variations in LAI and thus the associated values need to be interpreted with great care (see graph on the left). In the light of this it is also important to stress that LAI derived from remote sensing also comprises all green contributors, i.e., the understory under forest canopies.

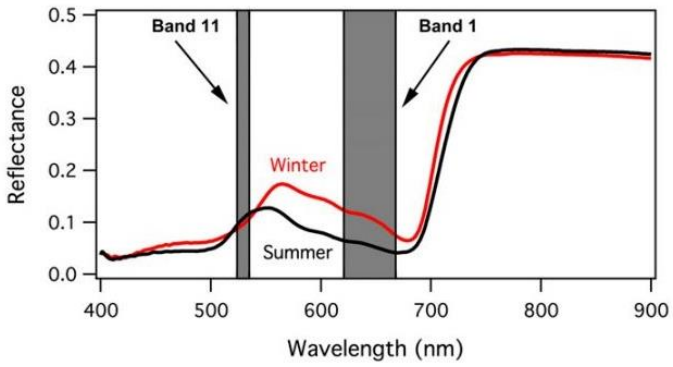

Figure 4.15: Seasonality effects: Needle reflectance spectra of Pinus contorta exposed to winter (red line) and summer (black line). MODIS bands indicated in grey. Source: Gamon, et al., 2016.

The following graph presents some of the underlying principles for accurately measuring LAI (Campbell, 2012, Campbell and Norman, 1998: 247–248).

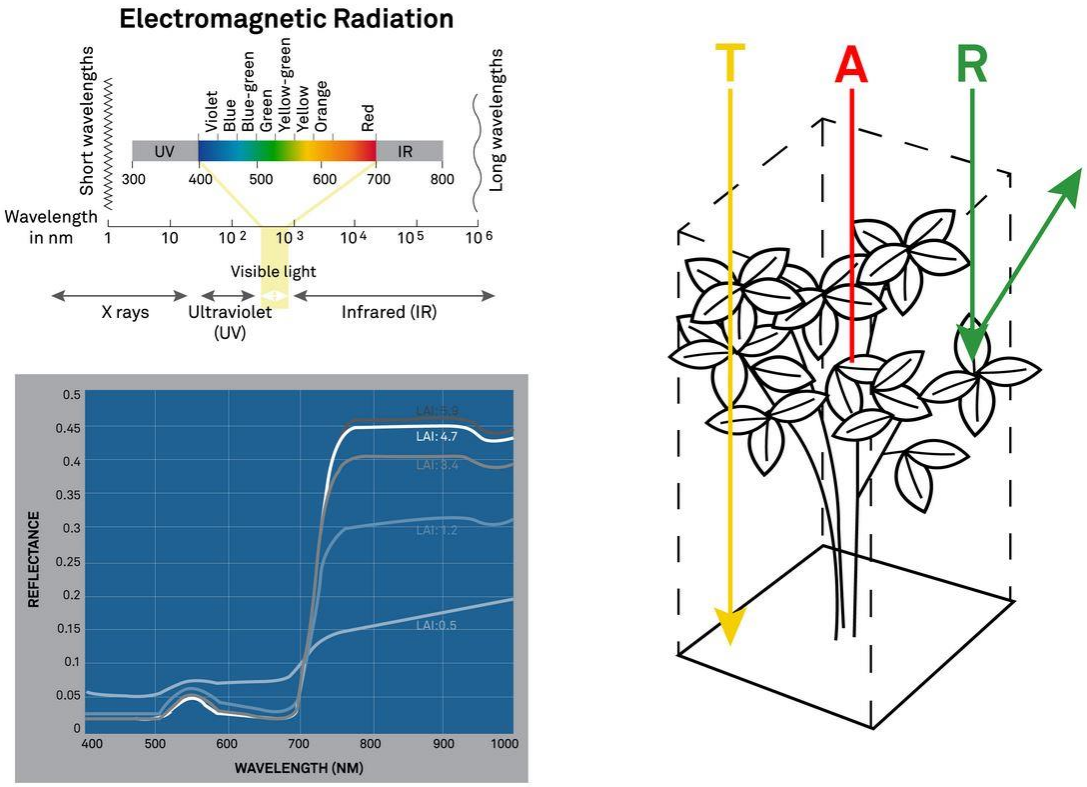

Figure 4.16: The plot at the bottom left shows clearly, that reflectance is wavelength dependent – increase in LAI shows decrease in the visible spectrum, whereas near infrared values increase. The sketch on the right illustrates major effects of ambient radiation interacting with the plant canopy as either being transmitted (T), absorbed (A), or reflected (R). High LAI displays low light transmittance, high absorptance, and low visible, but high NIR reflectance (Source: Campbell, 2012).

LAI can be measured directly by harvesting all leaves from a plot to employ flatbed scanners to calculate the total leaf area. Albeit being very time consuming and destructive, this method yields the most accurate results. Indirect measurements entail the determination of related variables dealing with the reflectance or transmittance of light by or through the canopy, or the use of hemispherical photography (i.e. fisheye lens) to differentiate between vegetated and non-vegetated pixels in the imagery (Chianucci, 2016). Two different approaches have become very common to determine LAI from surface reflectance, namely (i) (semi-) empirical relationships between vegetation indices and LAI, and (ii) the inversion of radiative transfer models to mimic surface reflectance from canopy structural characteristics such as LAI (Kappas and Propastin, 2012). Commercially available instruments such as LICOR's LAI 2200 estimate LAI by using the amount of light energy

transmitted by a plant canopy and are based on Beer's law describing the relationship between LAI and light interception: PAR*t* = PAR*i exp (-kz)* , where PAR*t* denotes the transmitted photosynthetically active radiation (PAR) near the ground, PAR*i* is PAR incident at the top of the canopy, *k* is the extinction coefficient, and *z* the path length of the photons through the attenuating medium (i.e. the leaves) (Rautiainen *et al.*, 2005). Additional variables include solar zenith angle, beam fraction, and leaf angle distribution. By calculating z, it is possible to obtain a veritable estimate of LAI (so-called PAR inversion technique). PAR inversion technique is non-destructive, but requires measurements of both transmitted (i.e., below canopy) and incident (above canopy) PAR. Above canopy measurements can be very cumbersome, however, large canopy gaps or clearings are appropriate to capture radiation of an unobstructed sky. Identical or at least similar light conditions are a prerequisite to obtain proper radiance readings. An alternative for estimating LAI is the use of reflected rather than transmitted light. It has become very common to exploit the spectral properties of the reflected radiation on the red (also red-edge) and NIR bands for this purpose. Either wavelength combinations, the pertaining ratios, or the employment of various vegetation indices (e.g. NDVI (Normalised Difference Vegetation Index), the MSAVI (Modified Soil Adjusted Vegetation Index), and the EVI (Enhanced Vegetation Index)) are now routinely used as proxies for LAI (Coops *et al.*, 1997) (see also graph below).

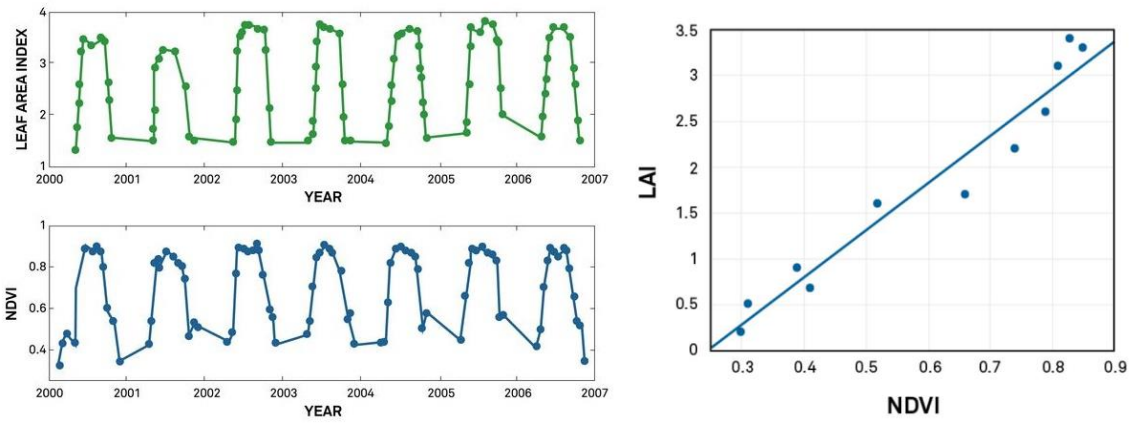

Figure 4.17: Strong relationship between LAI and NDVI (left); for each canopy a specific LAI – NDVI correlation can be established (right) – source: Campbell, 2012.

These days handheld spectrometers offer a relatively inexpensive and practicable technique to measure and monitor vegetation reflectance patterns. In addition, most earth-observing satellites (e.g., Landsat, MODIS, Sentinel-2, SPOT) are equipped with sensoring systems to capture spectral signatures of various land cover schemes and allow for the calculation of vegetation indices (VIs). The derivation of LAI from spacebourne platforms usually is based on the employment of neural networks with top of canopy reflectance and

geometry of acquisition (i.e., sun zenith and azimuth angle) used as algorithm inputs. However, a few caveats apply, bearing the potential to gravely impinge the determination of the indices. A number of studies indicate that the measurement methods are prone to awry performances (Campbell, 2012, Goude *et al.*, 2019, Korhonen *et al.*, 2006). The following graph provides an excellent account on this issue.

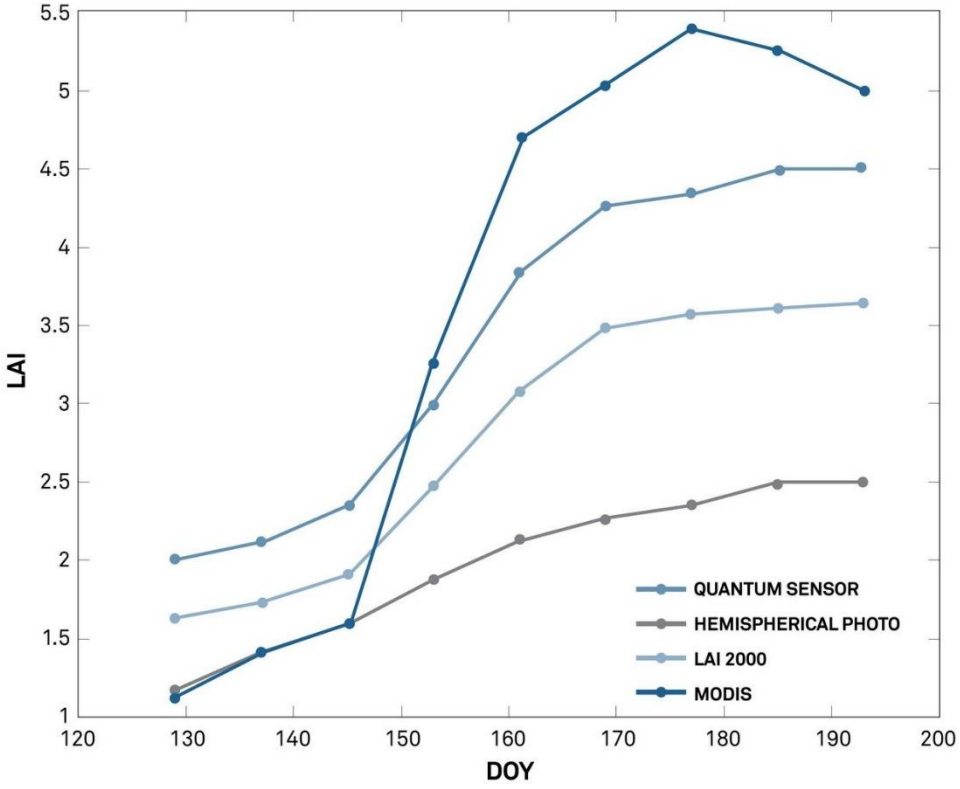

Figure 4.18: Disparities in measurement performances of various methods. The graph shows LAI values in a deciduous forest canopy in spring (DOY – Day Of Year). Source: Campbell, 2012.

All LAI derivation algorithms are based on specific radiative transfer models associated with specific assumptions of the canopy architecture. Since they are developed to be applied to any type of vegetation, the devised algorithms are inherently generic. They are also best suited for landscape patches presenting enough homogeneity at pixel scale, and as such, have to be treated with care when applied to forest areas, which show a high degree of heterogeneity (Weiss and Baret, 2016).

Literature review:

Banerjee *et al.* (2014) investigated the combination of several vegetation indices (i.e. Canopy Shadow Index, Advance Vegetation Index and Bare Soil Index) for the extraction of forest canopy cover from Landsat images in an old growth forest in northern India. The overall accuracy yielded a respectable value of 80%, however, the authors did not fail to point out, that the integration of terrain parameters (e.g., slope, aspect) into the classification

process have the potential to considerably improve the overall outcomes. When considering the wildfire situation in Australia, Boer *et al.* (2008) found, that NDVI, LAI, and the NBR proved to be very suitable candidates for the accurate post-fire assessment of eucalyptus forests in south-western Australia. Carvajal-Ramírez *et al.* (2019) also used NBR, but in addition NDVI and the NDRE (Normalised Difference Red Edge) for the determination of burnt areas from multispectral UAV imagery. According to them the difference between pre-, and post-fire NDVI worked best for the UAV flight conditions and sensor specifications. Moving away from the destructive forces of wildfires, Freitas *et al.* (2005) attempted to find potential relationships between forest structure and vegetation indices in the Atlantic Rainforest, Brazil. They used NDVI and moisture vegetation indices (Landsat's band 5 (MVI5) and 7 (MVI7)) for a linear regression analysis to learn, that MVI5 and MVI7 show the best performances in dense humid forests, whereas NDVI seems to be a good estimator of green biomass in deciduous and dry forests. Karnieli *et al.* (2006) carried out an interesting investigation on the combination of NDVI and brightness temperature, both derived from the NOAA AVHRR sensor. The conclude, that, opposed to common assumption, NDVI and land surface temperature showed a positive correlation for six different ecosystems in Mongolia (i.e., rising temperature positively affects vegetation activity). They further infer, that the Vegetation Health Index (combination of NDVI and brightness temperature) should be used with caution, particularly in high latitude areas. Shifting the focus to boreal forests in Canada, McDonald *et al.* (1998) scrutinised various vegetation indices (e.g. NDVI, SAVI, TSAVI) for their potential applicability in determining forest inventory parameters. They found out the following for the analysis of Landsat images: (i) all indices were not linear with respect to forest cover because of shadowing effects, (ii) the indices were greatly affected by perturbations caused by solar zenith angle, background reflectance, stand structure, and LAI, and (iii) at high canopy covers SAVI and TSAVI performed best, since they show large dynamic ranges and are less susceptible to atmospheric perturbations. When looking at logging activities in a Polish forest, Pałaś and Zawadzki (2020) found that the MERIS Terrestrial Chlorophyll Index (MTCI[2]) and the Brightness Index (BI[3]) performed best when employing Sentinel imagery, followed by NDVI and the Ratio Vegetation Index (RVI[4]). Another interesting discovery was made by Mayer and Scribner (2002), who found that NDVI preferentially detects the greenest vegetation, whereas SWIR NDVI (NBR) shows a tendency to highlight vegetation residing in shadowed areas. When investigating biophysical properties of boreal forests in Finland based on field data and Sentinel-2

[2] $MTCI = \frac{(Near\ Infrared - RedEdge)}{(RedEdge - Red)}$

[3] $BI = \sqrt{\frac{Red^2 + Green^2}{2}}$

[4] $RVI = \frac{Near\ Infrared}{Red}$

imagery Majasalmi and Rautiainen (2016) found that the estimation of fPAR and LAI performed best when using bands 7 and 9 (R^2 of 0.93 for both). However, they also conclude that performance can decrease considerably (i.e., R^2 of 0.3), when wrong vegetation indices are applied for approximation of the vegetation traits.

Validation processes are crucial to all relevant remote sensing activities – the determination of vegetation indices and the derived correlations related to the 'true' phenomena are not exempt from such procedures. Most commonly in situ measurements (destructive and non-destructive) are conducted to gain insight in vegetation cover, LAI, biomass, growth, and vigour (Xue and Su, 2017). More sophisticated, but effortful approaches assess VIs by monitoring sentinel plants to be compared with the VI values for calibration (allometric measurements). A considerable number related of studies were undertaken to gauge LAI in particular. For example Dufrêne and Bréda (1995) detail an overall underestimation of the LAI in the range of 6 to 37% when applying indirect methods (i.e. LAI-2000 plant canopy analyser; needle method; Demon light sensor) in a temperate forest. They hypothesise that local clumping of architectural canopy components is a reasonable explanation for this phenomenon, thus violating the underlying principle of random distribution of the plant structural elements (the so-called Beer's law) being used in most indirect appraisals. Clumping of foliage and the negative impact on LAI measurements have also been described by Chen *et al.* (2005), Gower and Norman (1991), Peng *et al.* (2018), Kappas and Propastin (2012), Ryu *et al.* (2010), Whitehead *et al.* (1990), and Zhao *et al.* (2012). Moreover, Goude *et al.* (2019) found LAI underestimates of 30 to 73% for boreal forests in Sweden, finding stand-level LAI largely depending on species composition, management schemes and site conditions. In addition, Garrigues *et al.* (2008) found variation in illumination conditions to be one of the major drivers for LAI discrepancies when comparing LAI-2000 plant canopy analyser, the Decagon AccuPAR ceptometer, and digital hemispherical photography. A similar survey was carried out by Hyer and Goetz (2004) on a boreal forest site to yield commensurable results. The research team also found variability in LAI measurements to be attributable to spatial heterogeneity within forest stands, particularly in sparse canopies. Kappas and Propastin (2012) found that all algorithms for the derivation of LAI are empirical and tend to over-simplify the relationship between recorded signal and the pertaining plant parameters, thus leading to potentially low accuracies. They further state, that more research is required to address this issue.

At this point, I should like to make a last note on the literature reviewed: based on the scientific discussion on VIs, it should be needless to say, that satellite derived indices should ideally be derived from corrected 'at-surface' reflectance values. Yet, many reported studies use the 'at-sensor' reflectance or the DNs (Digital Numbers) instead, making outcomes of

vegetation assessments very hard to compare. This finding is very much in line with the one reported by Jones and Vaughan (2010: 167) and Xue and Su (2017).

Wrap-up of this section:

- Vegetation indices (e.g., NDVI, NBR, LAI) have become indispensable tools in remote sensing for the analyses of vegetation surfaces such as canopy density , burnt area determination, and vigour.
- Those indices have shown to be correlated with variables such as chlorophyll content, biomass, leaf nitrogen, photosynthesis, productivity, and LAI.
- Proper image pre-processing (radiometric, atmospheric, and geometric correction) is crucial prior to the calculation of vegetation indices.
- Factors such as seasonality, phenology, leaf characteristics (needle vs broad leaf), canopy structure, and transpiration rate can exhibit large variations in VI behaviour, and need to be considered as such.
- The selection of an appropriate measurement method is also pivotal for the exploitation of vegetation traits.

4.3.4. Image pre-processing

It is not the author's intention to overly expand on this subject (i.e. georectification, image co-registration, mosaicking, spectral and spatial enhancement, etc.) since there is a plethora of publications available (e.g. (Cracknell and Hayes, 2007: 162–175, Jones and Vaughan, 2010: 128–151, Liu and Mason, 2009: 265–271, Mather, 2011: 67–96). However, since sensor-specific correction algorithms can have grave impacts on the outcomes of classification procedures and the magnitude of various vegetation indices, they deserve special attention as such.

The quantity as well as quality of a signal received by a satellite sensor largely depends on the following factors:

- the reflectance properties of the target,
- the nature of atmospheric interactions (i.e., scatter, attenuation, absorption, transmission, refraction, reflection),
- the viewing angle of the sensor,
- the solar azimuth, and
- the aspect and slope (terrain effects) of the target relative to the solar angle (Mather, 2011: 90).

Prior to all image processing procedures, the electromagnetic radiation striking the sensor (Top of Atmosphere - TOA) needs to be converted to quantities of surface radiance (Bottom of Atmosphere – BOA) to be able to assess the genuine characteristics of the ground target. Many satellite products are at the customer's disposition on a so-called 2A level, meaning, that geometric, radiometric, and atmospheric correction are inherent to this imagery (BOA). In contrast, level-1C products (like imagery covering Mongolia) only provide TOA reflectance, thus requiring further processing. For this purpose, a fair number of correction algorithms have been devised to account for atmospheric and even for terrain effects - e.g., 6S, ATCOR, Sen2Cor, iCOR, COST, DOS, MODTRAN, just to mention a few. Three of these will be detailed in the following section as provided by most image processing software packages.

The *Dark Object Subtraction Model* (DOS) is considered to be the most simple model to eliminate relatively uniform atmospheric effects such as haze. It is solely based on the digital image itself without requiring in-situ field measurements and additional information like solar elevation angle. The procedure is to look for values in areas of known zero reflectance (e.g., deep water, dark shadow) - assuming that any value greater than zero must result from atmospheric scattering - and to subtract this value from each pixel in the specific band. Albeit, finding zero value pixels in the imagery is an elementary prerequisite, which is rarely met (Chavez, 1988, Jones and Vaughan, 2010: 139).

To compensate for the shortfalls of the DOS Chavez (1996) developed a model exploiting the cosine of the solar zenith angle (*COST*) as an approximation of the atmospheric transmittance. Among other correction models (e.g. 6S) this approach seems to yield corrections as nearly as accurate as in-situ field measurements (Chavez, 1996, Mahiny and Turner, 2007).

Sen2Cor (Sentinel-2 Correction) is a processor tailored for the Sentinel-2 imagery to perform atmospheric-, terrain-, and cirrus correction of TOA level 1C input data. Additionally, aerosol optical thickness, water vapour, scene classification maps and quality indicators for snow and cloud probabilities are generated. The Sen2Cor model comprises:

- the detection of dark pixel values of the S2 bands B2, B3, B4, B8, B11 and B12 for cloud shadow calculation,
- the geometric parameters such as sun position, sun elevation, and an empirical model for top-cloud height distribution for creating cloud masks,
- and a DEM (e.g. SRTM) and an empirical BRDF (Bi-directional Reflectance Distribution Function) model to compensate for terrain effects (Main-Knorn *et al.*, 2017).

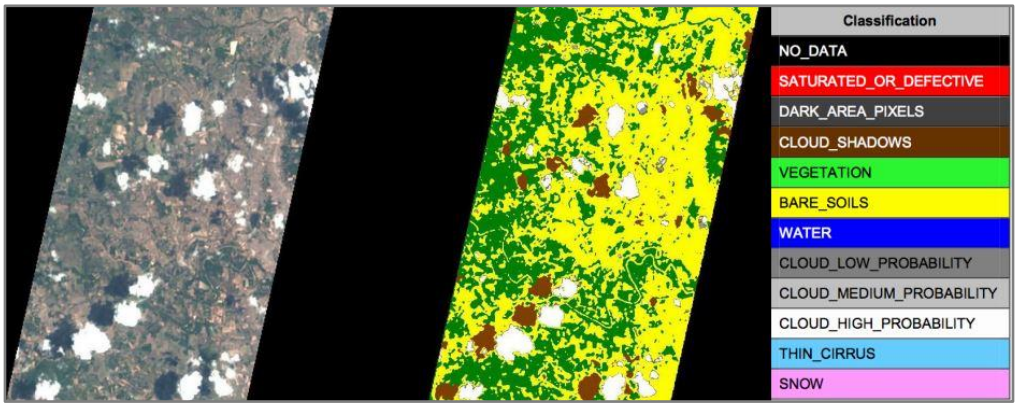

Figure 4.19: Example of a scene classification map (here: cloud mask) generated by Sen2Cor (Müller-Wilm, et al., 2014).

A growing number of publications deal with the impact of atmospheric and topographic correction models on image classification outcomes and the determination of vegetation indices. For example, Buho *et al.* (2009) looked in to the NDVI values of marsh land on Hokkaido Island, Japan, before and after atmospheric correction. They conclude, that the NIR of the ASTER satellite sensor was mostly affected by scattering, and that NDVI values were larger after performing the correction algorithm (i.e., ATCOR). These findings are line with the outcomes published by Xie *et al.* (2010). According to them the NDVI derived from Landsat 7 images was more sensitive to the atmospheric correction (i.e. 6S[5]) in dense vegetation, with an overall increase of the NDVI values and its range after applying 6S. Keukelaere *et al.* (2018) assessed the performance of the iCOR atmospheric correction approach for coastal and inland waters to reason that the algorithm shows an overall very satisfactory correlation between the Landsat 8 and Sentinel-2 data and in-situ measurements. However, in a few instances iCOR under-corrected in the NIR wavelengths. Pflug *et al.* (2015) report satisfactory results for the classification of various land cover types, with NDVI performance excelling after Sen2Cor correction. In contrast, Li *et al.* (2018) found Sen2Cor surface reflectance to be overestimated when assessing 40 different test sites in North America, but with NDVI performing extremely well with a correlation coefficient of 0.973 against the surface data. However, Sen2Cor has been subject to continuous improvement, with version 2.8. being the latest release (ESA, 2020a), and with further validation reports to be expected. An interesting observation was made by a team around Vanonckelen *et al.* (2015) when studying the effect of atmospheric and topographic correction on image composites for forest cover detection in mountainous areas. They ascertain, that not only the choice of an adequate classifier has a stronger impact on the classification accuracy than topographic correction, but in turn the topographic component

[5] **S**econd **S**imulation of a **S**atellite **S**ignal in the **S**olar **S**pectrum

had a higher influence on classification accuracy than the atmospheric component. The team also states very clearly, 'that it is worthwhile to invest in both atmospheric and topographic corrections in a multi-temporal study' (Vanonckelen *et al.*, 2013). Studies like the ones by Huang *et al.* (2016) and Weirather *et al.* (2018) suggest, that atmospheric correction largely affects the visible wavelength bands. For own findings regarding the application of SenCor to Sentinel-2 imagery, please refer to section 8.3.1. of this thesis.

4.3.5. Presentation and interpretation of image classification results

As indicated in the bulk of the literature, the most common way to assess the accuracy of any classification, we need to set the classification output against ground reference data (Jones and Vaughan, 2010: 266–269). The creation of an error matrix (synonyms are: confusion matrix, classification matrix) has become common practice these days with the key information detailed below. The following example shows the classification results of three different classes compared to the pertaining ground truth.

		Reference image			
		A	B	C	Total
Classified image	a	37	3	7	∑a = 47
	b	9	25	5	∑b = 39
	c	11	2	43	∑c = 56
	Total	∑A = 57	∑B = 30	∑C = 55	N = 142

Figure 4.20: Example of a simple error matrix (source: www.50northspatial.org).

The most common measure of accuracy is referred to as the ***overall accuracy*** (OA), which is calculated as the sum of the diagonal values (in blue) divided by the total number of samples (OA in this case is: 0.74, or 74%). Another common indicator is the so-called ***producer's accuracy*** (PA) describing the number of correctly identified pixels divided by the total number of pixels in the reference image (PA is: aA / ΣA = 0.65). The **error of commission** is calculated as the complimentary of PA (i.e., 0.35), denoting the assignment of pixels to a certain class that don't belong to it. ***User's accuracy*** (UA) in contrast is the number of correctly identified pixels of a class, divided by the total number of the class in the classified image (UA is: aA / Σa = 0.79). The **error of omission** occurs, when pixels belonging to one class are included in another class (wrong assignment) – in our case resulting in a value of 0.21 (i.e., 1 – UA). In addition to above mentioned descriptive evaluations the ***Kappa statistic*** as a measurement of agreement has become very popular.

It characterises the degree of matching between reference data (e.g., ground truth) and the classification outcomes by comparing two matrices. Kappa (κ) is calculated as: $\hat{\kappa} = (p_o - p_c) / (1 - p_c)$ with $p_o = \Sigma\, p_{ii}$ (i.e., sum of relative frequency in the diagonal of the error matrix (total accuracy)), and $p_c = \Sigma\, p_{i+}\, p_{+j}$ (i.e., relative frequency of a random allocation of observations to the cells). $\hat{K} = 0$ indicates, that the agreement equals chance agreement, a value of 1 meaning a perfect agreement.

In general, classification and their evaluation results have to be treated with caution, since there is plenty of room for manipulation. For example, the less classes are defined, the less the confusion possibilities are. Furthermore, the number and quality of the reference data play an important role, and higher accuracies can be achieved by including huge areas with easily identifiable features (Foody, 2002, Jones and Vaughan, 2010: 268, Olofsson *et al.*, 2013). With reference to the difficulty in interpretating the Kappa index, some authors even plea for the abandonment of this index. Comparisons of the Kappa index seem to be particularly challenging if the classes vary in their prevalence (i.e. properties of the of the population) (Foody, 2020). In summary, the decision on what can be considered a good classification result cannot be of a generic character, since each classification has to be seen in the light of the classification purpose, as well as the quality of the image and the reference data.

By wrapping up the chapter dealing with image classification and spectral indices, the main findings are:

- The pick of the “wrong” classifier can significantly affect the classification outcomes.
- Proper image pre-processing (i.e., atmospheric, radiometric and topographic correction; resampling; sub-setting) is crucial prior to image classification and derivation of vegetation indices, especially when looking at temporal analyses and comparing different sensors.
- There seems to be no such thing as an atmospheric correction tool to serve all purposes.
- In very high-resolution imagery (e.g., UAV imagery) object-based classifiers have proven to be more suitable than other approaches.
- Although image resolution matters, an extremely high spatial resolution does not necessarily lead to superior classification results.
- In most studies undertaken, SVM and RF classifiers have managed to live up to their expectation and reputation.
- A lack of radiometric resolution and number of spectral bands cannot be compensated with higher spatial image resolution.

- Most machine learning classifiers present themselves as black boxes, being sensitive to small changes in the training datasets and thus leading to differing classification results.
- The proper selection of the training data is pivotal for the attainable classification accuracies.
- The evaluation of classification accuracies has to be conducted with great care.
- Neural networks provide great new opportunities, but have not reached a very practicable level yet.
- Estimation parameters such as *k* for the k-NN method have to be chosen painstakingly.
- This is old news, though: classification results are difficult to upscale and even harder to be applied to other environmental and sensoring conditions.
- Vegetation indices, in particular the NDVI and the NBR, have proven to be salient indicators for plant vigour, tree species discrimination, forest cover and biomass determination, fire scar detection, and vegetation succession.
- Appraisal of many indices is subject to variations in illumination conditions, saturation effects, species composition, plant (tree) architecture, site quality, and the measurement methods applied.

4.4. Digital photogrammetry

Digital photogrammetry has come a long way from transferring the basic concepts of 3D extraction from imagery to embracing the realm of bits and bytes. Before the nineteen fifties either very basic instruments (e.g., stereoscopes) or delicate, sophisticated machinery (stereo plotters) were state-of-the-art in this field. The advent of computer technology then caused a real paradigm shift also in photogrammetry, when analytical instruments were hooked up to increase processing speed and quality of the yet analogue imagery (analytical plotters) (Hildebrandt, 1996: 182, Kraus, 2003: 207-214;338). However, it was not until the mid-nineteen-nineties, that fully-fledged systems (e.g. Leica Helava DPW 770) to handle image data in an entire digital environment were available on the market (Chapuis, 1995, Leberl and Thurgood, 2004, Petrie and Walker, 2007, Vogt, 2000: 1–3). This progress would be unthinkable without the advancements in hardware technology and the plethora of algorithms we have at our fingertips these days. Caveats have to be considered when dealing with software black boxes, since they thwart and obfuscate a deeper understanding of the underlying concepts and algorithms. As such, at times it is very hard to pursue critical analyses of photogrammetry products such as elevation models (DEMs) and canopy height models (CHMs).

In the following chapter the pillars of digital photogrammetry are presented and new concepts in computer vision, like Structure from Motion (SfM), elaborated. Potential pitfalls and shortcomings are considered. Exhaustive accounts on (digital) photogrammetry are provided by e.g. (Albertz, 2013, Förstner and Wrobel, 2016, Heipke, 2017, Hildebrandt, 1996, Kasser and Egels, 2002, Kraus, 2003, Linder, 2016, Luhmann and Schumacher, 2019, McGlone, 2004, Mikhail *et al.*, 2001).

Fundamentals of digital photogrammetry

According to Förstner and Wrobel (2016: 1): '*Photogrammetry* is the science and technology of obtaining information about the physical environment from images, with a focus on applications in mapping, surveying and high-precision metrology'. In contrast, *computer vision* does not focus on specific applications, but rather aims at mimicking intelligent human behaviour. It is also deeply linked to cognitive science (Förstner and Wrobel, 2016: 1, Theodoridis and Koutroumbas, 2009: 1). Modern digital photogrammetry reflects the pursuit of amalgamating various technologies for best results. As depicted in the following graph, internal processing of 3D reconstruction of objects straddles various disciplines such as remote sensing, photogrammetry and computer vision. Thus, an intimate understanding of all related processes is required to derive a maximum of information from specific scenes.

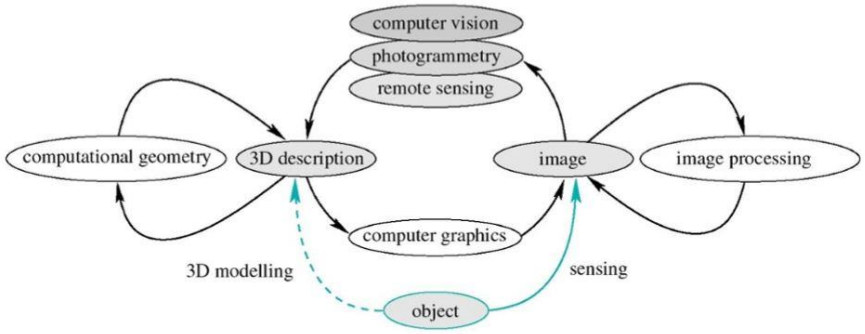

Figure 4.21: Computer internal processing of 3D descriptions of objects (source: Luhmann, et.al., 2013)

The primary purpose of photogrammetry is the three-dimensional reconstruction of an object. For the reconstruction of an object the elements contributing to the optical process such as light sources, surface properties, sensor and camera technology, and image processing have to considered (Luhmann and Schumacher, 2019: 2). The following graph depicts the determining photogrammetric process from object-to-object model:

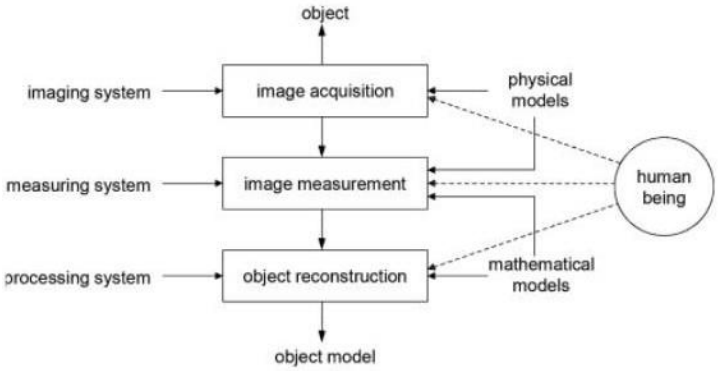

Figure 4.22: The photogrammetric process (source: Luhmann and Schumacher, 2019:3)

This graph shows also very clearly, that the human being is still required for the creational and interventional process flow.

In order to get an idea on the what current technologies are able to achieve in terms of obtainable and required accuracies the following figure is trying to furnish some particulars, although subject to rapid changes.

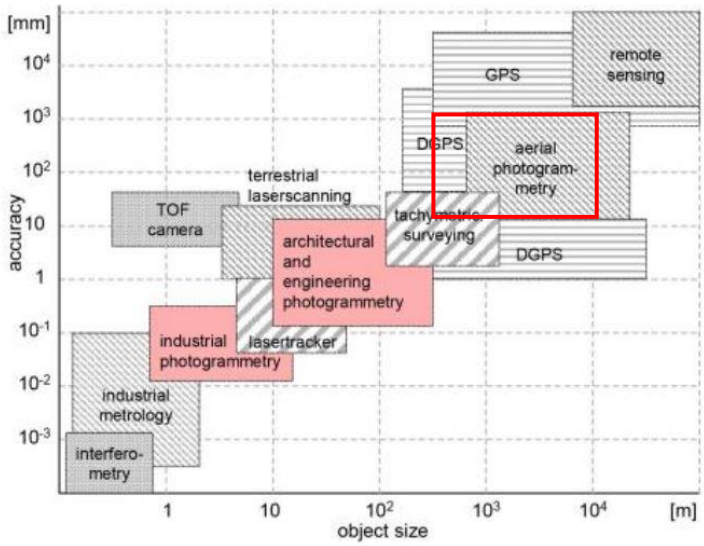

Figure 4.23: Relationship between measurement methods and object size and accuracy (Source: Luhmann, et.al., 2013)

This graph provides a good indication that, when it comes to object definition and reconstruction, attainable geometric accuracies of aerial photogrammetry are increasingly getting closer to (aerial) laser scanning fidelity. This holds even more true for very high - resolution imagery acquired by UAVs flying low altitudes as compared to conventional aerial flying missions. This observation has also been strongly supported by various publications in recent years (e.g.Colomina and Molina, 2014, Edson and Wing, 2011, Gobakken *et al.*, 2015, Goodbody *et al.*, 2017b, James *et al.*, 2019, Lim *et al.*, 2003).

Before we get to the nitty gritty of an object reconstruction pipeline in a photogrammetry suite it is indispensable to focus on a few fundamentals of the geometric characteristics of imagery and sensors, as well as the concepts of orientation of the imagery.

The main image acquisition systems comprise photographic, scanner, and radar. The former is characterised by central projection causing radial distortion of high elevation objects (see also figure 4.24). Scanner systems feature a parallel projection in the line of flight, however, perpendicular to the flight line central projection prevails. Radar systems generate parallel projected images in the line of flight, whereas the perpendicular component is determined by the angular distance between object and the active radar sensor causing a displacement of high elevation objects towards the line of flight.

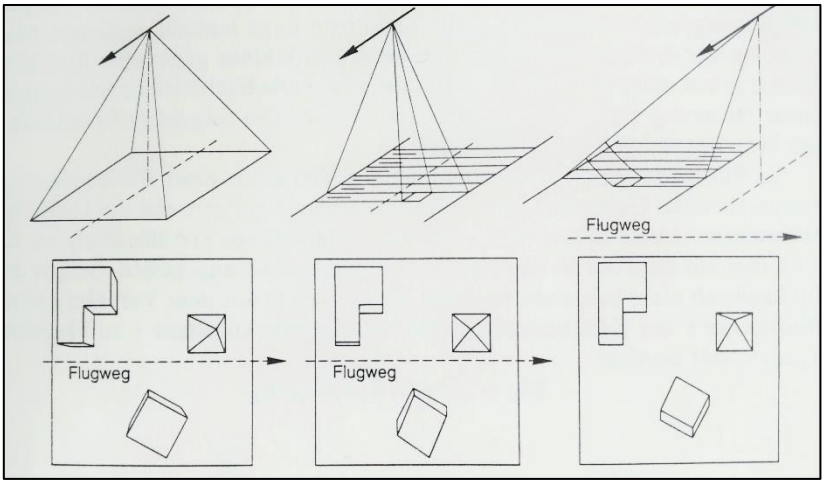

Figure 4.24: Projection geometry of photographic (left), scanner (middle) and radar systems (right). The associated object displacements are indicated below – 'Flugweg' meaning flight direction (source: Albertz, 2013:65).

Since most of the imagery we deal with in digital photogrammetry originates from photographic systems the subsequent procedures will be centred on this acquisition system. As mentioned above a very common effect we observe with central projection is radial displacement of objects. This can have grave implications on the reconstruction of objects in the photogrammetric workflow, especially when dealing with wide-angle lenses and low flying altitude platforms (e.g., UAVs). The following graph reveals such an effect in the case of a forested landscape.

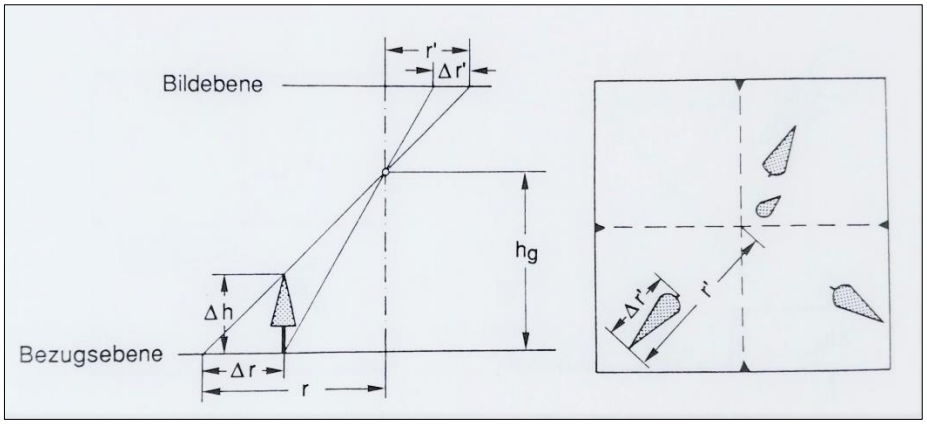

Figure 4.25: Central projection: radial displacement of trees due to object height difference. The reference plane('Bezugsebene') features a tree with a specific height (Δh) and the associated plane distances (Δr;r). The projected reference plane distances on the image plane ('Bildebene') are denoted Δr' and r'. The higher and the further away an object is from the image centre, the more it gets displaced in the image plane (source: Albertz, 2013:67).

The effect of radial displacement can clearly be detected in a real-life image taken during one of the flying missions at the test area at Thunkel, Mongolia.

Figure 4.26: The tree at the image centre is rendered perpendicularly, whereas trees further away feature an oblique view (image taken by Vogt, 2017).

In order to be able to extract three-dimensional coordinates form images the so-called stereoscopic viewing is essential: if we have at least two photos from the same object, taken from different positions, the exact position of any point being shared in at least both photos can be determined. The following graph depicts the representative situation of aerial photogrammetry.

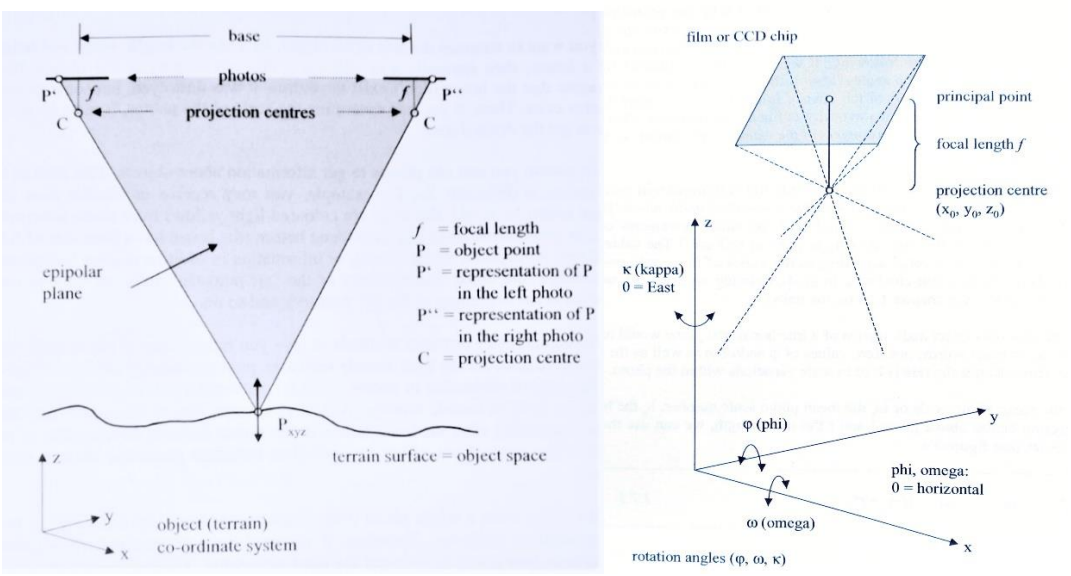

Figure 4.27: Geometry in an oriented stereo model (left) and focal length, projection centre and rotation angles (right) (source: Linder, 2016:2).

As part of the reconstruction and orientation of each photo, not only the exact positions of all photos within the terrain coordinate system have to be known ('exterior orientation'), but also the relationship between the image plane (i.e., pixel coordinate system) and the projection centre of the camera (i.e., camera internal coordinate system) have to be established ('interior orientation'). For *interior orientation* the camera calibration data (e.g., focal length, distortion parameters) is required. If digitised aerial photos are used the measurement of the fiducial marks need to be carried out and translation vectors as well as rotation angles computed prior to transformation. However, these days direct digital image sources are preferred. For digital cameras, the relationship between pixel and image coordinate system is almost constant and determined during the calibration procedure (Linder, 2016: 35–37). For *exterior orientation* the camera position in the object coordinate system is determined in each photo. The camera position can be described as the location of its perspective centre and the camera attitude. The pertaining six orientation (i.e., X,Y,Z and the rotation angles ω, φ, κ) parameters are usually established by using a collinearity model. Exterior orientation can be resolved by either using real-world coordinates of ground control points, the GPS coordinates of the aerial photos (stored as metadata in the EXIF image file), or by tapping the inertial navigation system (INS) of the aerial platform (Cramer *et al.*, 2016).

When working with big sets of imagery collected during a flying mission, the orientation has to resolved for the entire image block. In order to achieve this, we need to find and measure object coordinates that will be used to connect all images (so-called 'tie points'). The following graph demonstrates the principle of the block adjustment.

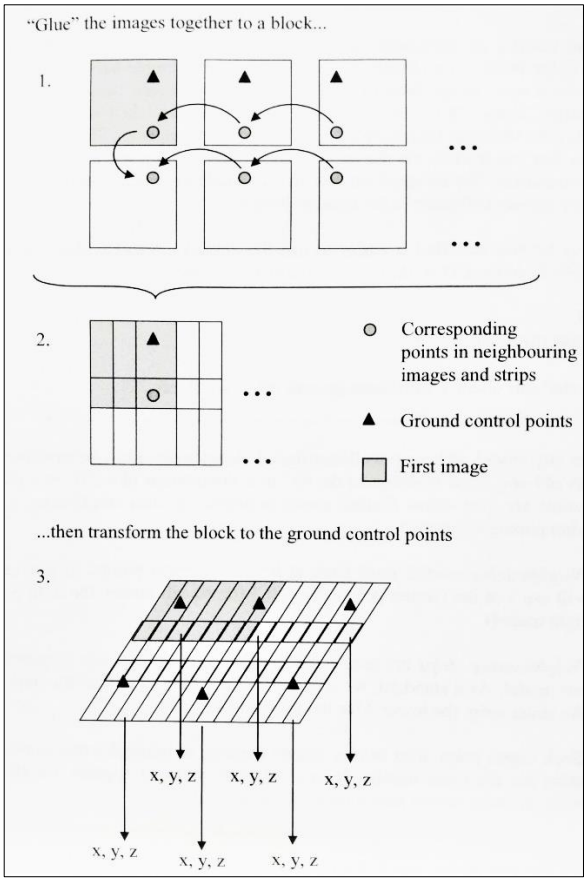

Figure 4.28: Scheme of a block adjustment (source: Linder, 2016:77).

Without block triangulation (adjustment), every stereo model would require two horizontal, three vertical control points plus check points, that need to be measured during filed survey. Instead, independent model algorithms are used to simplify the computation process. Currently, most block adjustment is carried out using the *bundle method.* This allows the integration of additional geometric or navigational information such as Ground Control Points (GCPs) and attitude information of the aerial platform. Images consist of bundle of rays converging at the perspective centre with an unknown position and orientation. With block adjustment, the position and orientation of each bundle is resolved by using the rays in each bundle and the ground control information (Mikhail *et al.*, 2001: 123). The entire adjustment process consists of a translation of the X, Y and Z coordinates and the rotation of ω, φ and κ, until the image rays meet accurately at the tie points and control points (Kraus, 2003: 268–271). The pertaining algorithm is based on collinearity equations, with self-calibration parameters and high-quality GPS data added to correct for systematic errors and to increase overall accuracy of the adjustment. Formerly, camera calibration was carried out as a disjoint procedure. Now, principal point coordinates and focal length can be treated as additional unknowns in the block adjustment solution (Förstner and Wrobel, 2016: 674-676,696). However, care has to be taken, when choosing the self-calibration parameters to avoid introduction of additional errors. For this purpose, sophisticated self-

calibration models account for lens distortion, principal distance error, or principal point offset, as well as for other deformation effects (Mikhail *et al.*, 2001: 124–125). Evaluation of the block adjustment can be performed by examining a graphical representation of the adjustment's output. The resulting image residual plot can help to diagnose and rectify problems such as unadjusted image parameters or systematic errors. Removal or re-measuring inaccurate points can substantially increase the bundle adjustment solution. Once the outcomes reflect an acceptable error tolerance, the resulting model can be used for further processing, like the creation of elevation models or ortho-mosaics. The following figure represents the more traditional workflow, which seems to be still in use. However, with the advancements in computer vision, a game changer appears on the stage (Goodbody *et al.*, 2019).

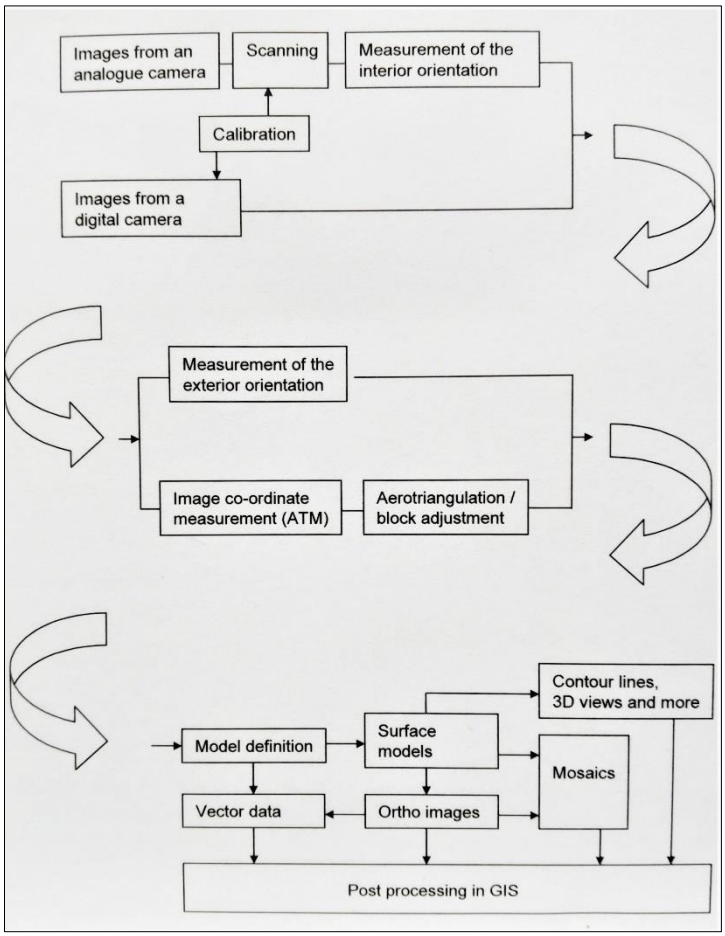

Figure 4.29: Workflow of traditional photogrammetry (source: Linder, 2013:17).

Computer vision can be considered one of the first applications of artificial intelligence. Imagery is used to recognise objects or navigate through an entire scene (Mikhail *et al.*, 2001: 169–173). A great number of various algorithms have been developed in the last couple of years to deal with tasks such as surface representation and *feature extraction*, however, no such thing as a perfect allrounder seems to exist. A computer vision algorithm starts with an application goal, like to recognise an object, to attain precise measurements

of this specific object. The algorithm is based on the description of a model of the object and its context in the scene. In addition, potential object occlusions have to be considered. Models for a large number of objects have already been described for applications such as Computer Aided design (CAD). In computer vision the specific object representations are generated from image data and matched against a reference model. The type of imagery plays an important role in the subsequent processes. The resolution and the spectral characteristics of the imagery determine the geometry, amount of detail and type of feature that can be exploited for recognition. Image features such as edges, textures, colour, shading and stereo disparity are common basic concepts in computer vision.

Other than object recognition and feature extraction *stereo image matching* has proven to be crucial for certain applications, like the generation of digital elevation models. The image matching procedure is far from being a trivial task because of intrinsic problems such as occlusion and noise. A matching algorithm needs to be robust, but also flexible enough to deal with varying viewing angles, object scales and radiometric variance in the imagery. The most popular algorithms use the following approaches: in *area matching*, the grey levels within a window are matched against the corresponding grey levels in other images; in *feature matching*, extracted features such as line segments are matched between images (Mikhail *et al.*, 2001: 188–189). Normalised correlation between the windows in the two images to be matched is a typical procedure with area matching. The differences in brightness and variance between the images are considered by correlating a pixel within a specified window in the so-called master image with a window in the slave image. A large window proves to be more noise resistant in the computational process, but is subject to glitches due to sudden changes in stereo disparity. This problem can be overcome by performing matching at multiple scales and resolutions (image pyramids). In general, image characteristics have a substantial effect on the quality of the correlation quality. Image noise, uncorrected lens distortion, and atmospheric refraction can potentially degrade the matching properties (Förstner and Wrobel, 2016: 696, Fryer and Mitchell, 1987, Mikhail *et al.*, 2001: 190–191, Wackrow and Chandler, 2008).

A fairly recent development is marked by the appearance of largely automated photogrammetry pipelines for the production of 3D point cloud data from large sets of overlapping digital photos. The entire processes as described above can now be solved within one software suite with hardly any user interference required. An increasingly popular approach, referred to as *Structure from Motion* (SfM) – *Multi View Stereo* (MVS), is rooted in traditional stereo-photogrammetry and is able to recover 3D structure form projected 2D imagery of moving objects or scene (so-called motion parallax). SfM techniques initiates by detecting 2D features in every input image and matching those features between pairs of

images, resulting in a coarse mesh as output. When many matches are found between the images, a 3D transformation matrix between the images can be computed. This process determines the relative 3D position between the two camera poses. Subsequently, the MVS algorithm is used to refine the mesh retrieved by the SfM technique, generating a dense reconstruction point cloud**.** MVS requires the camera parameters of each image as input, which is generated by the SfM algorithm.

In short, the 3D reconstruction process entails the following steps:

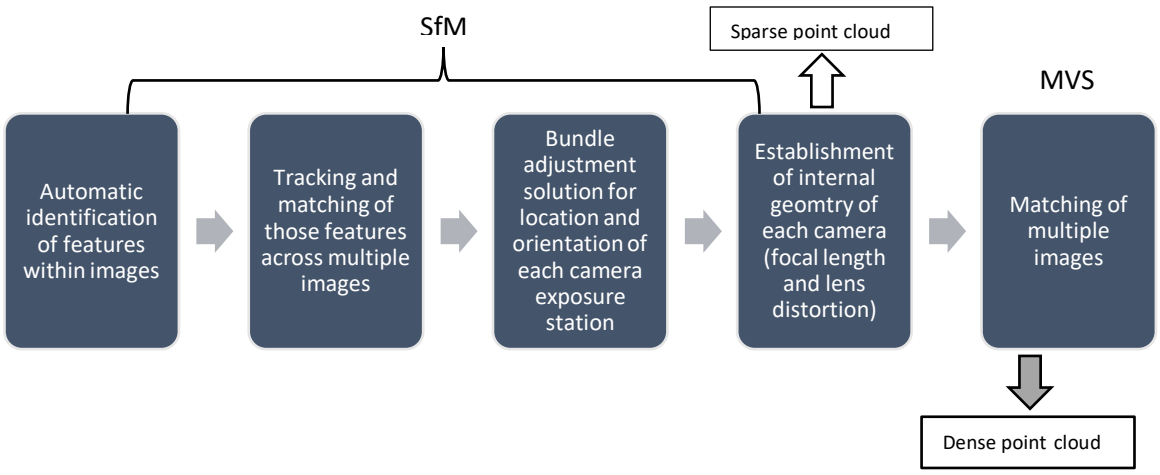

Figure 4.30: SfM – MVS pipeline for 3D reconstruction from multiple images

For a more detailed account on the SfM technique and the pertaining characteristics the reader is referred to chapters 4.5. and 7.3.4.2.

Some of the major merits of the SfM – MVS approach are that the methods operate largely invariant with respect to scale, viewing angle and illumination of the depicted features (Jensen and Mathews, 2016, Westoby *et al.*, 2012). In addition, even imagery acquired with uncalibrated cameras can be used, since the process of camera calibration is integrated in the photogrammetric solution workflow. However, in order to achieve the highest possible reconstruction results, the following factors have to be scrutinised:

- image quality (i.e., high contrast, no image blur, high resolution, colour fidelity),
- geometric characteristics of the camera (focal length, lens distortion, etc.),
- nature of the depicted scene (image features and texture).

Despite the ease and achievable accuracies of the SfM – MVS technique, a few major issues remain unresolved, particularly concerning flying missions in forested terrain. Automated image matching relies on the algorithms used to identify and reliably measure corresponding pixels in a set of images. Incorrect or inaccurate matching become very likely especially with a low degree of image overlap, occluded features and high variations in radiometric traits. The most substantial crunches, however, occur, when abrupt vertical

changes either in terrain geometry, or within a tree canopy surface (open stands) exist. This can cause the resulting 3D model to be flawed or render even unusable (Greiwe, 2018, Kunneke, 2019, Ludwig *et al.*, 2020, Osborn *et al.,* 2017, Seifert *et al.*, 2019, Seifert, 2019, Semyonov, 2011, van Aardt, 2019).

4.5. Structure from Motion (SfM)

This user-friendly, fairly recent photogrammetric technique is dedicated an entire sub-chapter, since SfM represents the core of 3D feature extraction in a sophisticated photogrammetry environment. An excellent detailed account on SfM can be found in Carrivick *et al.* (2016).

SfM was developed in the 1990s by the computer vision community and has hugely gained from the development of automatic feature-matching algorithms (Westoby *et al.*, 2012). This technique has become one of the standard schemes in the earth sciences and a potential alternative to other 3D rendering platforms such as laser scanning or GPS, in particular in remote and inaccessible areas (Iglhaut *et al.*, 2019). SfM shares the same basic tenets with stereoscopic photogrammetry, however, instead of a single stereo pair, it requires multiple, overlapping photographs as input to feature extraction and 3D reconstruction. In contrast to conventional photogrammetry, the geometry of the scene, the camera positions and orientation is determined automatically without a priori knowledge of 3D positions of certain features. Rather, a redundant, iterative bundle adjustment procedure is exercised with prior automatic feature extraction from manifold overlapping images (Förstner and Wrobel, 2016: 450–452).

As follows the SfM workflow is detailed to elucidate the process from photograph to point cloud (see also figure 4.31):

In a first step, multiple images, taken from different angles are employed to identify features (*key points*) in individual images to be used for image correspondence. The so-called Scale Invariant Feature Transform (*SIFT*) object recognition system is a common approach to identify features in each image that are not variant to scaling and rotation, as well as camera viewpoint and to some extent to varying illumination conditions (Lowe, 2004). It locates certain key points and then furnishes them with quantitative information (so-called *descriptors*). Best results are achieved by using high resolution, complex images with good image texture. Factors such as resolution, sharpness and richness of texture are crucial for the quality of the resulting point cloud data. In addition, special care should be taken to ensure high overlap of the imagery by adopting short camera baselines (Lowe, 2004).

Having identified the required key points and assigned the pertaining descriptor, a bundle adjustment strategy is employed to estimate camera pose and generate a *sparse point cloud*. For enhancement of this point cloud Clustering View for Multi-View Stereo (CMVS) and Patched-based Multi-View Stereo (PMVS2) algorithms are viable options (Furukawa and Ponce, 2007). Nearest neighbour and random sample consensus or Hough transform algorithms are subsequently applied to match key points in multiple images and to establish so-called tracks to link specific key points in the pertaining image stack (Lowe, 2004, Westoby *et al.*, 2012). Tracks of at least two key points in three corresponding images are required for point-cloud reconstruction. Finally, a triangulation process is applied to estimate 3D positions and reconstruct scene geometry. However, since a relative coordinate system is generated, the transformation into a 'real-world' coordinate system has to be accomplished at a later stage.

The last step of the workflow entails the assignment of absolute coordinates to the relative system via transformation procedures. This transformation involves the creation of a transformation matrix with the relevant rotation and scale factor information and is similar to the absolute orientation procedures in common photogrammetry. Real-world coordinates can either originate from map readings, GPS readings of a ground survey (Ground Control Points), or by integration of the on-board GPS logfiles (i.e., EXIF files) into the point cloud. For best results it is crucial to carry out GPS measurements with best possible accuracy (e.g., DGPS, RTK), since this has grave implications on the quality of the 3D model. Ground Control Points (GCPs) also need to be easily identified on the imagery. These can be represented either by clearly defined, unambiguous objects such as buildings or road crossings, or by artificial targets with maximum visibility (Westoby *et al.*, 2012). By completing the georeferencing step the referenced point cloud can now be further processed for mesh generation and exported for advanced analysis in a GIS suite.

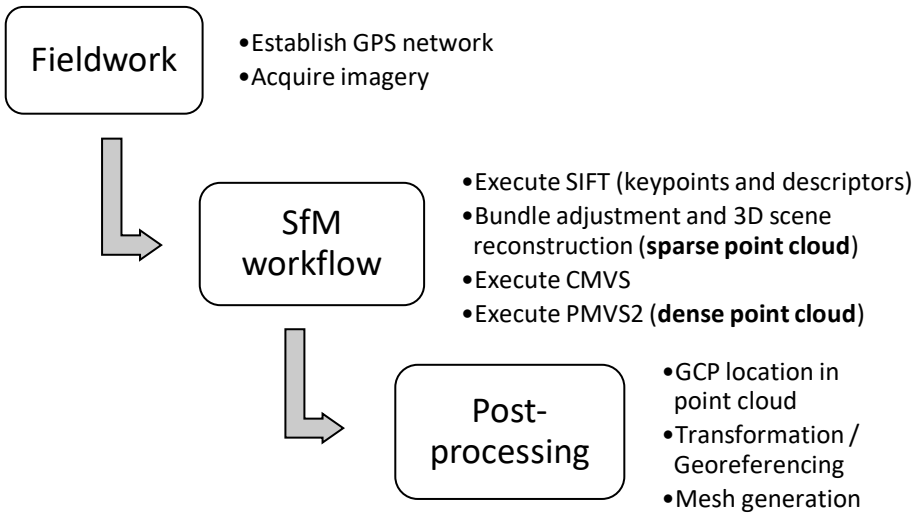

Figure 4.31: From image to 3D point cloud (with reference to: Westoby, et.al., 2012)

The main advantages of SfM are as follows (see also: Carrivick *et al.*, 2016, Goos *et al.*, 2000, Iglhaut *et al.*, 2019, James *et al.*, 2019, Piermattei *et al.*, 2019):

- can be used with a variety of sensor platforms
- is able to handle big image blocks with imagery of varying scale, resolution and viewing angles
- SfM enables surveys at relatively low cost
- does not require specific technical expertise
- allows for the successful orientation of complex and unconventional image blocks
- provides flexible and robust workflow
- delivers results comparable with LiDAR surveys .

Despite the merits as described above, some caveats require attention. Even though some software packages like Agisoft Metashape allow automatic camera calibration within interior orientation during bundle adjustment, some open issues remain such as the effect of camera autofocus and the implications of inaccurate pre-calibration. In conjunction with other factors, like number and distribution of GCPs, the derelict handling of camera specifications can have grave implications on the orientation results and lead to deformations of the reconstructed 3D model (Dall'Asta *et al.*, 2015, Kraus, 2003: 466, Sanz-Ablanedo *et al.*, 2018, Zimmerman *et al.*, 2020).

4.6. Extraction of inventory data from imagery

The extraction of information from remotely sensed data on forested areas has a long tradition starting with the most simple identification and delineation of forest areas from imagery taken from blimps and airplanes (Hildebrandt, 1996: 1; 286; 349). With the advancements in sensor and computer technology, as well as in data processing and modelling, environmentalists and forest managers are faced with a plethora of options of how to retrieve useful information from various data sources. The reader will find a detailed account on contemporary sensors and platforms in chapters 4.1. and 6.2.

Forest inventory parameters can either be gathered on a stand, or individual tree level (Guimarães *et al.*, 2020). Stand-level criteria such as basal area, average stand height or volume, are better derived using an area-based approach (ABA). Whereas for stem density, tree height, and crown length, the individual tree crown (ITC) approach appears to be the method of choice (Yu *et al.*, 2010). The former approach derives the response variable results form a combined value over a sample plot, whereas the latter considers the direct estimation of tree the related attributes. Both approaches are given justice in the subsequent chapter, however, with a focus on technical aspects on image manipulation.

Some forest structure attributes such as tree number, crown diameter, tree species, canopy closure, tree height, and NVDI (for tree vigour) can be derived directly from the imagery or point clouds, whereas parameters like DBH, age, basal area (BA), LAI (Leaf Area Index), and biomass require sophisticated modelling approaches as indirect methods (e.g., Artificial Neural Networks (ANN), linear regression, nearest neighbour imputation (k-NN), decision trees). In the following the most prominent structure attribute extraction techniques are presented and the merits and caveats outlined, with below mentioned table (Table 4-5) reflecting the most common forest structure attributes and their source of prediction.

Although most of the forestry related publications have dealt with forest attribute extraction from 2D imagery, the manipulation of 3D point clouds (e.g., from LiDAR, UAV imagery) has made an enormous contribution to the knowledge base on forest structure in the last four decades. Thus, the subsequent chapters account for both, the 2D as well as the 3D realm.

Table 4-5: Common predictors of forest inventory attributes (source: Brosofske et al., 2014). Ancillary variables refer to variables related to climate, topography, soil, and land cover; image derivatives refer to e.g., band ratios (indices), or textures.

Response	Frequent predictors
Composition	
Forest/vegetation type	Ancillary variables[1]
	Multispectral imageries and/or derivatives[2]
	Hyperspectral imageries and/or derivatives[3]
Species composition	Ancillary variables[1]
	Multispectral imageries and/or derivatives[2]
	Hyperspectral imageries and/or derivatives[3]
	LiDAR metrics[4]
	High-resolution imageries[5]
Structure	
Age/successional stage	Ancillary variables[1]
	Multispectral imageries and/or derivatives[2]
	LiDAR metrics[4]
	High-resolution imageries[5]
Basal area	Ancillary variables[1]
	Multispectral imageries and/or derivatives[2]
	LiDAR metrics[4]
	Inventory variables[6]
	Aerial photos[7]
Canopy cover/crown closure	Ancillary variables[1]
	Multispectral imageries and/or derivatives[2]
	LiDAR metrics[4]
	High-resolution imageries[5]
Diameter	Ancillary variables[1]
	Multispectral imageries and/or derivatives[2]
	LiDAR metrics[4]
	Inventory variables[6]
Density	Ancillary variables[1]
	Multispectral imageries and/or derivatives[2]
	LiDAR metrics[4]
	Inventory variables[6]
	Aerial photos[7]
Height	Ancillary variables[1]
	Multispectral imageries and/or derivatives[2]
	LiDAR metrics[4]
	High-resolution imageries[5]
LAI	Ancillary variables[1]
	Multispectral imageries and/or derivatives[2]
	LiDAR metrics[4]
	High-resolution imageries[5]
Volume	Ancillary variables[1]
	Multispectral imageries and/or derivatives[2]
	LiDAR metrics[4]
	Inventory variables[6]
Biomass/AGB	Ancillary variables[1]
	Multispectral imageries and/or derivatives[2]
	LiDAR metrics[4]
	Synthetic aperture radar (SAR)[8]

4.6.1. ‘Direct’ approaches for extracting forest structure attributes

Tree identification / tree count

The basic units of forest management are represented by the individual trees, and as such, they constitute the essential elements of forest stand knowledge (Gougeon and Leckie, 2003, Le Wang *et al.*, 2004). The number of trees in the field and the related identification of the tree species provide utile information for forest inventories, forest management, and the creation of growth models. The analysis of the tree density may also imply timely management and silvicultural interventions such as thinning or regeneration procedures (Zöhrer, 1980: 144, 164). Modern high-resolution imagery now allows for cost-efficient acquisition of tree information. Sophisticated image analysis exploits the reflectance characteristics of trees, which vary pursuant to tree species, crown shape, hierarchical status, and vigour (Culvenor, 2002, Gougeon, 1995, Le Wang *et al.*, 2004, Leckie *et al.*, 2005, Pouliot *et al.*, 2002). Since delineation and detection of trees based on visual inspection is very cumbersome, research in automation of such processes already started in the mid-1980s. According to Gougeon and Leckie (2003) the multiple approaches can be categorised as follows: (i) tree location detection (i.e. identification of the tree top); (ii) tree location detection and crown dimension parameterisation; and (iii) full crown delineation. All categories share the same necessity for accurate individual tree detection prior to crown delineation, since it greatly impinges the accuracy of the delineation process. The application of such efforts involve imagery captured by passive and active sensors alike, namely LiDAR, SAR, airborne and spaceborne multi-, thermal, and hyperspectral sensors. However, such imagery has to meet the requirement of sufficient spatial and radiometric resolution for the recognition of individual trees. Recently, UAV based imagery, as well as LiDAR and SAR have become increasingly popular to furnish three-dimensional information on tree traits and forest structure (Erasmi *et al.*, 2019, Goldbergs *et al.*, 2018, Gougeon and Leckie, 2003, Karila *et al.*, 2015, Ke and Quackenbush, 2011b, Kwak *et al.*, 2007, Magnussen *et al.*, 2013, Næsset, 1997, Nevalainen *et al.*, 2017, Park *et al.*, 2014, Popescu *et al.*, 2002, Vauhkonen *et al.*, 2012).

In the most simple way, trees can be identified and their numbers counted on very high resolution imagery through visual interpretation (Kangas and Maltamo, 2009: 343–344)(see also chapter 4.2. for more details). What initially seems a straightforward and quick task in forest plantations with a single tree species and equal spacing, turns out to be far from being trivial, when it comes to interpreting complex-structured multi-species and multi-storey forests. Image quality needs to be near to perfect, with excellent illumination conditions prevailing (Sayn-Wittgenstein, 1978). In addition, the interpreter’s skills and experience, as

well as the quality of the provided auxiliary information (e.g., inventory maps, management plans) have far-reaching implications on the counting results. Ideally, the identification of the tree species is being conducted in the course of tallying the tree individuals. The following graph (Figure 4.32) represents the spatial resolution of various sensors to convey the snags and eases of interpreting aerial and satellite imagery. Apparently, the identification of individual trees can be carried out with ease in the UAV and WorldView-2 images, whereas in the Pléiades, and in the Sentinel-2 images in particular, tree identification becomes sheer speculation. Even in the extremely highly resolved UAV images it remains a challenge to identify trees not being dominant or co-dominant, although those trees may contribute considerably to the biomass of a forest stand. As mentioned in chapter 4.2. tree identification results can range from 55% up to more than 95%, depending on the quality of the imagery and the training level of the interpreter (Ahrens, 2001, Carleer and Wolff, 2004, Heller *et al.*, 1964, Ke and Quackenbush, 2011b, Myers and Benson, 1981). Apparently, an image segmentation prior to interpretation bears the potential to improve the results of defining ad identifying single objects (trees) (Ardila *et al.*, 2012, Erikson, 2004b).

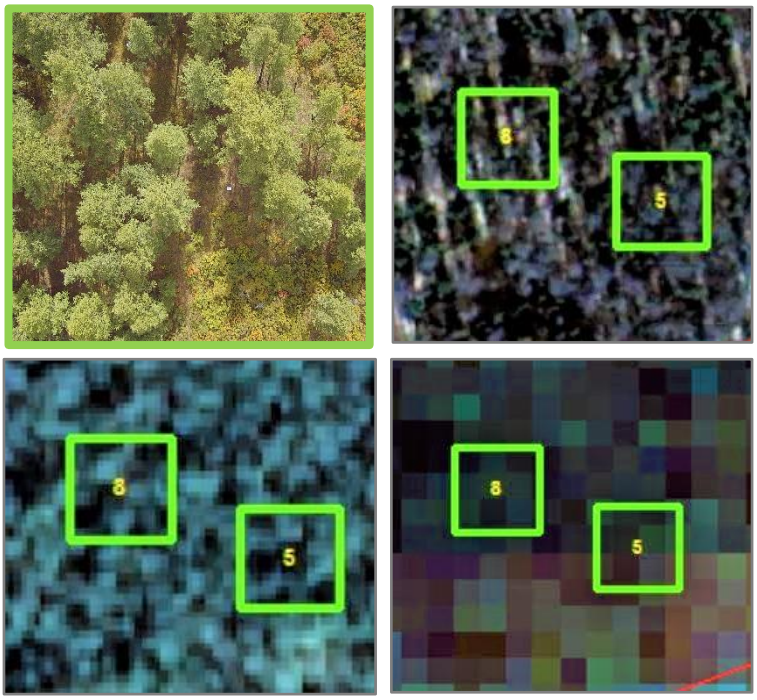

Figure 4.32: Spatial resolution of various imaging sensors – the green boxes represent an area of 30x30m. Top left: UAV image (5cm); top right: WorldView-2 pansharpened (46cm); lower left: Pléiades (2m); lower right: Sentinel-2 (10m).

In order to avoid the cumbersome process of manually identifying tree individuals, the automatic extraction of trees has gained momentum in the last few decades. Some of the approaches for individual tree isolation are portrayed in the subsequent section. Since the determination of tree position is closely associated with the detection and measurement of tree crowns, the reader will find an amalgamation of both approaches below.

The crown diameter as the circle enclosing the projection of the tree crown represents another relevant stand parameter. It helps to estimate tree development, space requirements of the specific species, evaluate carbon sequestration and determine crown radius – DBH relationships (Miranda *et al.,* 2018, Panagiotidis *et al.*, 2017, Yilmaz *et al.*,

2017). As such, crown diameter, among other structural parameters, serves as an indicator for silvicultural treatment and logging management. The diameter reflects the average of the measurement of the crown in two perpendicular directions (usually N-S; E-W). Ideally, the resulting value represents the longest and shortest spread of the tree. Crown diameter can be obtained through the manual measurement on the orthophoto in a GIS environment, or by extracting the corresponding figures from a 3D point cloud. These 3D models (CHM) can either be generated by applying LiDAR technology, or by creating dense point clouds form overlapping UAV or high-resolution satellite imagery (e.g., WorldView-2). Subsequently, segmentation techniques (e.g., region growing, or multiresolution segmentation) are exercised to delineate the shapes of the tree crowns and to calculate crown metrics automatically. It has become very common these days to perform the determination of the tree crown metrics in unity with the identification of the tree tops and the calculation of the tree heights. The following graph presents an example of a delineation process and potential errors, such as over-, or under-segmentation and the resulting split of tree crowns.

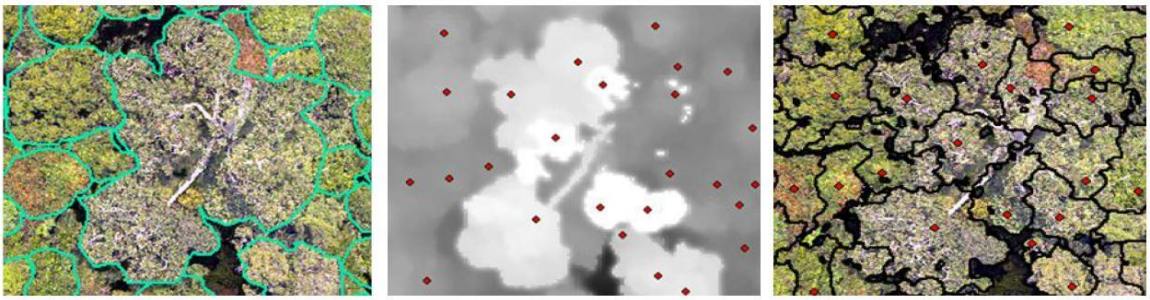

Figure 4.33: Example of a split match case of a big tree (centre of images). (a) visual delineation; (b) result of tree top detection; (c) result of region growing process featuring a multi-segmented tree crown. Source: Nurhayati, 2015.

The following table provides an excellent synopsis of commonly used individual tree crown detection (ITCD) methods. The main advantages and disadvantages are also being mentioned. Despite the focus being on LiDAR point cloud manipulation, the authors (Zhen *et al.*, 2016) do not fall short in additionally bringing up raster-based approaches.

Table 4-6: Characteristics of the four methods using LiDAR data for ITCD (Zhen et al., 2016).

Method Group	Example of Specific Algorithms/Methods	Advantages	Disadvantages
Raster-based method	Treetop detection: local maximum, image binarization, template matching Crown delineation: valley-following, region-growing, watershed segmentation GEOBIA-based method	• Well developed; • Easy to be used and improved; • Easy to use multiple data sources if using GEOBIA-based method; • Easy to use multiple scales if using GEOBIA-based method.	• Missing information or causing potential errors from extraction, interpolation and smoothing procedures.
Point cloud-based method	K-means clustering technique Voxel-based single tree segmentation	• Easy to use 3D information; • Easy to reflect canopy structure; • Could detect understory trees or small trees.	• Harder to implement than raster-based method; • Greatly depend on point density of LiDAR data.
Methods combining raster, point, and *a priori* information	Classic ITCD algorithms + prior information (crown size/stand density) Imagery + point cloud	• Benefit to use historical data; • Easy to integrate remotely sensed data and GIS data; • Could use both spectral and height information.	• Depend on prior information; • May have difficulties in registration of different data sources.
Tree shape reconstruction	Convex hull Alpha shape Superquadrics Hough transform	• Further delineation of crown; • Provide 3D individual tree profiles; • Provide information for estimating foliage and photosynthetic activity; • Allow further application of modeling tree growth	• Difficult to implement; • Sometimes depend on successful segmentation of single trees; • Difficult to collect field data for validation

The most common tree detection and crown delineation algorithms are described and delimited to:

- Local maximum filtering.
- Image binarization.
- Scale analysis.
- Template matching.
- Valley following.
- Region growing.
- Watershed segmentation (Ke and Quackenbush, 2011b, Park *et al.*, 2014, Theodoridis and Koutroumbas, 2009: 481–483, van Herk, 1992, Zhen *et al.*, 2016).

According to literature, the most favoured algorithm for tree detection seems the *local maxima*. Hereof, the highest pixel value in an image is identified by comparing the height value of any given pixel with its neighbours. This is based on the underlying assumption, that the tree top represents the highest digital number due to its convex shape. Thus, the size of the search window proves to be important for the performance of the algorithm. Wulder *et al.* (2000) introduced a novel approach by using semi-variance to determine optimal window size and Culvenor (2002) developed a contextual scheme without prior definition of window size. In some studies, a smoothing strategy is applied prior to the

detection process to account for spurious maxima (Wallace *et al.*, 2014). To eliminate noise a threshold tolerance based on mean and standard deviation computations is also applied (Eick and Villaverde, 1996). In the following graph the concept of local maxima is depicted.

Figure 4.34: Tree top detection of a canopy height model with local maxima filtering (Demir, 2017).

The *image binarization* algorithm uses various image transformations for the extraction of tree top values by enhancing pixels. Albeit, sufficient contrast between crown and non-crown areas is mandatory. Inconspicuous boundaries between tree crowns can easily bring about omission errors and as such dilute the accuracy of the detection undertaking (Park *et al.*, 2014). *Scale analysis* engages image smoothing. Usually, imagery is acquired with a pixel size small enough to detect the smallest required object. This approach minimises omission errors, but in turn leads to commission errors in large tree crowns. Pouliot and King (2005) managed to devise an optimum global scale approach, where the appropriate local scale can be defined to identify a tree as a single object. In contrast, Culvenor (2002) exhausted the (local) radiometric maxima and minima as the primary image features used for the crown delineation process, being indicative of crown centroids and boundaries. Their algorithm was developed for application to imagery of native Eucalypt forests in Australia, and uses a 'top–down' spatial clustering approach involving key steps designed to reduce the effects of crown segmentation. *Template matching* is a method providing information about the likelihood of pattern presence prior to the segmentation step. Complex patterns combining pixels of varying brightness and colour are a real challenge of the object-based approach of image analysis. As a possible remedy image texture templates are created to find and identify similar patterns (trees) in the entire image (Erikson, 2004a: 12–13). Different algorithms are in common use for this method, with the measurement of similarity carried out by using the squared differences between a template and an image region being one of the most simple approaches (Jasvilis *et al.*, 2016). Template matching has been successfully applied such as for the detection of individual trees of palm plantations featuring accuracies of almost 90% (e.g. Li *et al.*, 2017).

Other algorithms for automatic tree detection comprise the *valley-following*, *region growing*, and *watershed segmentation* method (Gougeon and Leckie, 2003, Park *et al.*, 2014). These

approaches are also viable options for the automatic delineation of individual tree crowns (Miranda *et al.,* 2018):

The *valley following* algorithm is based on work by Gougeon (1995). This approach attempts to extract local minima as valleys, which are considered to be crown edges. Subsequently, pixels are searched for that are located between pixels of higher value. However, there is a risk of diluting the crown boundaries, when overlapping effects conceal the minima pixels (Leckie *et al.*, 2005).

A *region-growing* algorithm defines a seed pixel for growing regions based on specific criteria. A successful region growing process draws on the assumption, that neighbouring pixels belong to the same tree crown region as the seed pixel, provided, their characteristics (reflectance values) are sufficiently similar to those of the seed pixel (Culvenor, 2002).

Watershed segmentation considers an image as a topographic surface, with grey levels representing altitude. It has become a standard procedure to apply watershed segmentation to an inverted image, with local maxima to be transformed to local minima. The regions within the crown now correspond to catchment basins, whereas the edges (shaded areas between the crown) depict the watershed lines. The segmentation process aims at generating lines that isolate each region as an inner crown. The difficulty lies in the definition of the segmentation threshold for each region and as such has the tendency to either over-, or under-segment regions. Spatial variations in intensity are found to be the main culprit for this phenomenon (Park *et al.*, 2014). Le Wang *et al.* (2004) attempted to overcome this deficiency by introducing a marker-controlled watershed segmentation to further differentiate touching and clumping trees. However, the outcomes of the study showed very clearly, that scale effects (i.e., tree crowns differ in size) can considerably hamper segmentation, and tree crown boundaries are sometimes inconsistent with grey-scale boundaries. They suggest to employ 3D-based methods to overcome such crunches. To improve the performance of the watershed segmentation method specific smoothing filters can be applied. In most cases the Gaussian filter have yielded better results than the Laplacian filter (Ke and Quackenbush, 2011b). Having said this, both filters considerably increase the quality of the approach by avoiding over-segmentation bias (Abdullah S *et al.*, 2019, Brieger *et al.*, 2019, Goldbergs *et al.*, 2018, Zhen *et al.*, 2016).

The following figure depicts typical segmentation and delineation scenarios and errors.

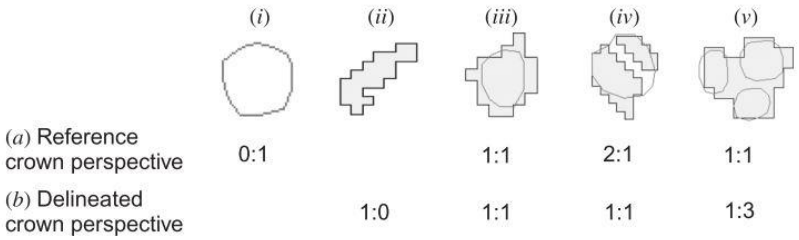

Figure 4.35: Examples of detection scenarios from (a) reference and (b) delineated crown. Reference crown shown as circles, delineated crowns as filled pixels. (i) omission error; (ii) commission error; (iii) exact match; (iv) commission error through over-segmentation; (v) omission through under-segmentation (Ke and Quackenbush, 2011a).

All the previously portrayed algorithms reveal certain limitations. Inaccurate tree detection is often caused by the restricted window size of the local maxima algorithm, the dilemma in finding the appropriate thresholds, and when dealing with a lack of altitude variation (flat tree crowns) when employing the watershed approach.

So far, no existing study has reported detection rates of 100% (Larsen *et al.*, 2011). The type of vegetation (i.e. height, shape, tree density, separation of individuals, branching structure, etc.), image contrast, and the accuracy of the used CHM / point cloud are important determinants for the performance of the algorithms applied (Park *et al.*, 2014). Other sources of error are trees in the shade, tree intermingling, and smaller trees concealed by more dominant individuals (Gomes and Maillard, 2016). Goldbergs *et al.* (2018) report detection rates of about 70% for dominant and co-dominant trees in the Australian savannahs. Local maxima and watershed segmentation algorithms were employed. Nevalainen *et al.* (2017) observed an individual tree identification varying between 40% and 95% related to the characteristics of the flown area (e.g. tree distribution). In their study Mohan *et al.* (2017) give account of 312 trees out of 367 being detected correctly, with an omission error of 55 and a commission error of 46 individuals of the applied local maxima algorithm. Gomes and Maillard (2016) report an average performance rate of 82% for detecting trees in an urban environment and a rate of 90% for orchards using a variation of template matching algorithms. WorldView-2 imagery was the choice in this investigation. Gebreslasie *et al.* (2011) also chose very high resolution satellite imagery (here: Ikonos) to identify tree individuals in a *Eucalyptus grandis* plantation in South Africa. The local maxima algorithm yielded 80% of correctly spotted trees with a fixed window size, whereas a variable window size increased the detection rate of 5%. Looking at aerial imagery, Erikson and Olofsson (2005) report detection rates of 80% when applying region growing and template matching strategies. Ramalho de Oliveira *et al.* (2021) used UAV-derived LiDAR and photogrammetric data to find out, that, although LiDAR technology performed best for tree detection and height measurement, photogrammetric point clouds

proved to be more than sufficient by exhibiting slight under-estimates of the inventory parameters. WorldView-2 images were employed for the detection of trees in a tropical environment in the investigation conducted by Gomes and Maillard (2013). In this very complex situation, watershed segmentation, region growing and template matching had to compete against each other, authoring region growing algorithm as the favourite with an accuracy of 80%. Local maxima and valley-following algorithms were administered by Gougeon and Leckie (2006) on Ikonos imagery to detect individual trees in a conifer plantation in Canada. The low detection rate of overall 67% was explained by the difficulties for the algorithms to identify trees with various degrees of maturity. In addition, visual inspection revealed that tree crown clusters are challenging to segregate. Katoh and Gougeon (2012) combined individual tree crown delineation with tree top detection technique to improve the detection rate of conifer trees in aerial imagery. Tree top detection rate was 67%, with an increase of 22%, when amalgamating both approaches. Larsen *et al.* (2011) compared six individual tree crown detection algorithms evaluated under varying forest conditions to find out, that 'None of the algorithms alone could successfully analyse all different cases.' The authors strongly advice to partition the imagery into homogenous forest stands prior to the tree detection analysis. In addition, they postulate, that for complex forest types, monoscopic imagery might not yield best results, and thus, 3D models (CHM) would be much better suited. Wulder *et al.* (2000) looked at tree detection in 1-m resolution imagery to conclude, that a tree crown radius of 1.5m seems to be the minimum size for reliable tree identification using local maxima filtering. A more sophisticated approach was used by Li *et al.* (2017) to detect individual oil palms in a plantation in Malaysia. They took a number of manually interpreted samples of Quickbird imagery to train the convolutional network (CNN) as a deep learning effort, to achieve a remarkable detection rate of 96%.

In their review Zhen *et al.* (2016) scrutinise the trends in automatic tree detection and crown delineation algorithms. Their main finding is that active data (SAR, and LiDAR in particular) and the fusion of active and passive sensoring technologies become more and more prominent in tree crown detection and delineation (ITCD) studies. Since the common 2D imagery reflects certain limits, the novel approaches of active sensors provide much better insights in the 3D structures of the forests. This of course implies, that algorithms developed for passive data sources have to be adapted to or even redesigned for three-dimensional analysis. Another finding is, that algorithms, which might have worked well for hardwood or mixed forests, fail to present satisfactory results in softwoods (e.g. (Ke and Quackenbush, 2011a, Larsen *et al.*, 2011).

Since there seems to be no standardised accuracy assessment procedure, comparison of the results achieved by the various techniques becomes speculative to some extent. However, there seems to be consensus, that the applied ITCD algorithms had greater success, when analysing even-spaced, even-aged, and even-sized softwood forests (Ke and Quackenbush, 2011b). A number of authors report, that tree crown delineation proves to be very difficult in mixed-species forests of complex structure because of varying reflectance characteristics, the multi-storey character, and shadowing effects within and between tree crowns (Bunting and Lucas, 2006).

There is great potential by fully exploiting the information content of remotely sensed data, especially when sensors are mounted on the same air-, or spacebourne platform. In recent studies, multi-, or even hyperspectral imagery in unity with LiDAR seem to be holding great promise for great advancements in ITCD. Authors, such as Breidenbach *et al.* (2010), Chen *et al.* (2012a), Hyyppä *et al.* (2018), Katoh and Gougeon (2012), and Suárez *et al.* (2005) found, that ITCD was greatly improved by integrating tree height from ALS (LiDAR) into conventional imagery.

Tree identification, with tree (canopy) density being the associated measure, can also be derived from medium resolution imagery (e.g., Sentinel-2, Landsat) by applying modelling approaches (see also section above) such as nearest neighbour imputation, regression trees (CARTs), Kriging, or Random Forest (RF). For instance, in their study Pierce *et al.* (2009) found prediction accuracies for the number of live trees ranging from $r^6 = 0.29$ to $r = 0.59$ for the two best models (i.e. linear models; nearest neighbour imputation). For more details on indirect methods please refer to chapter 4.6.2.

Identification of tree species

The identification of the various species is imperative for generating valuable information on the forest ecosystems as such, the estimation of the forest's economic value, and the derivation of the requirements with respect to the site conditions. In addition, growing characteristics are very species specific and are used as input variables for growth and yield models and forest management practises. The assessment of forest composition employing remote sensing technologies is rested on the principle that every tree species reflects, transmits and absorbs electromagnetic radiation in a specific manner (Jones and Vaughan, 2010: 19–22). This species specific fingerprint is a valuable aid in species discrimination and quantification (Lisein *et al.*, 2015). The consideration of seasonal effects such as senescence (leaf discolouration; leaf-on, leaf-off) ,flowering, and knowledge on site quality

[6] Pearson correlation coefficient

also contribute largely to the identification accuracies (Getzin *et al.*, 2012). For tree identification specific software providing classification techniques is mandatory (Goodbody *et al.*, 2017a, Sperlich *et al.*, 2014). As mentioned before, (very) high resolution imagery requires specific classification algorithms to deal with the very detailed spatial and radiometric information inherent to that imagery. As such, a shift from pixel-, to object-based classifiers becomes noticeable. Modern classification algorithms comprise: Classification Trees, Support Vector Machines, k-Nearest Neighbour, Neural Networks, Random Forest, and Maximum Likelihood estimation (for details on classifiers see also chapters 4.3.1 and 4.3.2.). Apart from determining various tree species or species groups (coniferous, broad-leafed), all mentioned classifying techniques also serve more generic purposes in the sense to help work out the extent of forested areas (i.e., classes: forest, non-forest) as well as their general structure (e.g., clumped, dense, sparse), and the plant vigour (e.g., NDVI). In the last few decades, an enormous amount of studies have been conducted related to image classification. However, in the following, only a few relevant publications with respect to high-resolution imagery are presented.

An excellent showcase for tree species discrimination is presented by Immitzer *et al.* (2016b), who attempted to identify seven different tree species in test sites located in Bavaria, Germany. They employed imagery from WorldView-2, Sentinel-2 and Landsat 8 to perform classifications based on image segmentation and Random Forest (RF). Overall accuracies for the various sensors are 0.74 for WV-2, 0.68 for Sentinel-2, and 0.49 for Landsat 8, thus proving the leverage of high spatial resolution on classification results. Further analysis yielded, that the spectral signature of pine and spruce appeared to be similar. Although the spectral band characteristics of Sentinel-2 and Landsat 8 show very little difference, the coarser spatial resolution of Landsat seemed to result in the poorer overall discriminatory performance. Best results for species identification were achieved in Landsat 8 and Sentinel-2 in the RedEdge (RE) and Short Wave Infrared (SWIR) bands. Quite recently, some more authors explored Sentinel-2 images to find the best time period and optimal spectral bands and indices for gaining best results. For example, Mirończuk and Hościło (2017), Ma *et al.* (2019), Wang *et al.* (2018) and Wittke *et al.* (2019) detected the Sentinel-2 bands B5 (RedEdge 1), B7 (RedEdge 3), B8 (NIR), B11 (SWIR 1), as well as the NDVI to best suited for forest classification in late summer imagery in the temporal and boreal biomes by applying modern machine learning algorithms (i.e. RF and SVM). Immitzer *et al.* (2019) favour Sentinel-2 band B4 (Red) for the identification of conifers in Central European forests, B11 (SWIR 1) for broad-leafed forests, as well as a mix of B4, B5, B11, NDVI and NDWI for mixed forests. In their review of studies on tree species classification, Fassnacht *et al.* (2016) also found the green band (B3) very useful to exploit the traits of phenology. Since phenology usually varies with species, the specific knowledge

on phenology (e.g., leafing period, senescence) can be a sharp tool to determine species discrimination. The authors stress, that machine learning algorithms have significant advantages over more traditional classifiers, but they also observed, that most of the considered studies miss a clearly set target by only pursuing the optimisation of the classification accuracy. In their meta-study Ma *et al.* (2019) found indications, that a combination different sensors (e.g. optical and radar), as well as the exploitation of multi-temporal imagery sems to yield best results (see also Elatawneh *et al.*, 2013). The improvement in classification accuracy (here: 5-10%) by utilising Sentinel-2 images of various time series instead of focusing on a single image is also confirmed by authors like Grabska *et al.* (2019), Persson *et al.* (2018), Wessel *et al.* (2018) and Denisova *et al.* (2019). In contrast, Wittke *et al.* (2019) found only a miniscule improvement of the prediction accuracy, when adding multidate imagery.

There are also recent examples concerning the fusion of 2D and 3D technology. For instance, reasonable results of classification procedures have been reported by Nevalainen *et al.* (2017) with an accuracy of 95% (Random forest classifier) and St-Onge *et al.* (2015) with 83% accuracy for LiDAR and 79% for the derived photogrammetric point cloud (PPC) for boreal forests. The outcomes not only prove, that contemporary remote sensing technology (e.g., LiDAR, UAV) is able to yield decent species identification, but also provides added value, when canopy height models and tree detection algorithms (segmentation techniques, local maxima filers, etc.) are part of the identification process. The following graph shows an example of a detection exercise by analysing hyperspectral imagery in unity with a CHM.

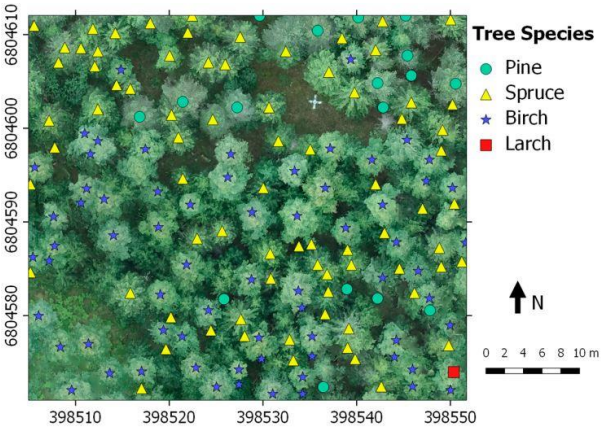

Figure 4.36: Example of detected and classified trees of a boreal forest (Nevalainen et al., 2017).

Tree height determination

Tree height is considered one of the main forest inventory parameters, since it reflects the productivity of a specific site and species, and allows for inferences on forest biomass and carbon stock (Gadow, 2003: 31–33, Panagiotidis *et al.*, 2017, van Laar and Akça, 2007: 1–3). The extraction of the heights is typically carried out by deriving the pertaining height values from a canopy height model (CHM = DSM – DTM) or by getting the readings from a LiDAR point cloud. CHM are created from passive sensor imagery in a photogrammetry process, whereas active sensor LiDAR data are processed in specific software environments to derive forest structural parameters.

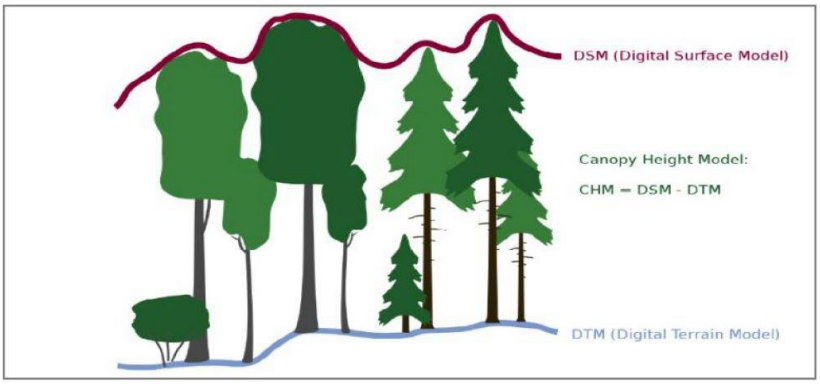

Figure 4.37: Canopy Height Model (CHM) defined as DSM values subtracted from DTM values (Miranda, et al., 2018).

As mentioned above the mostly used algorithms for the height extraction are local maxima and watershed segmentation algorithms.

With respect to attainable height determination accuracies, Birdal *et al.* (2017) report a value of 90% for coniferous trees in an urban forest sensed with a UAV based RGB consumer grade camera. The following figures shows some of the results obtained by Birdal et al., 2017.

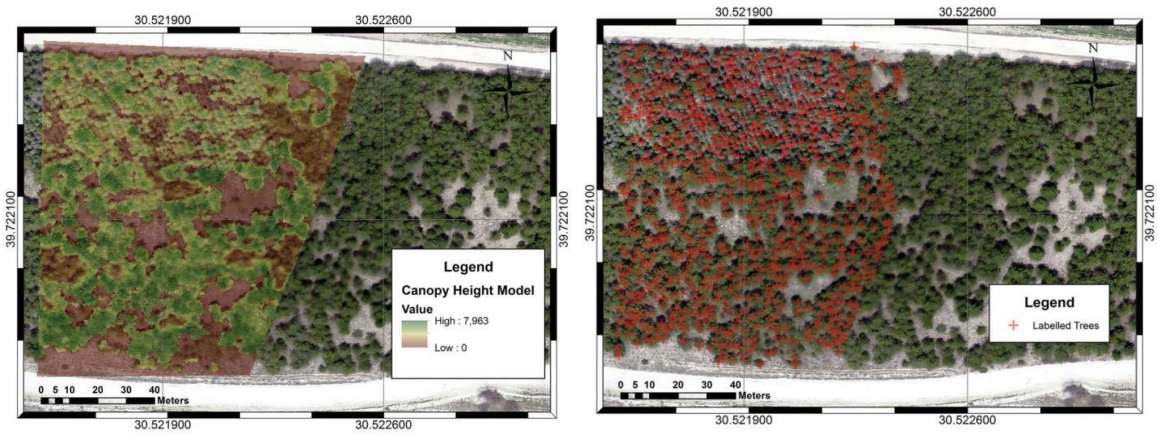

Figure 4.38: Canopy Height Model (left) and individual trees (right) extracted as point features (red crosses) from CHM by applying local maxima filtering (Birdal et al., 2017).

In a study conducted by Zainuddin *et al.* (2016), tree heights were extracted from a *Cocos nucifera* CHM with an R^2 of 0.80 and an RMSE of 69.9cm, when employing UAV based RGB imagery. Nurminen *et al.* (2013) also looked into digital photogrammetry as an alternative to laser scanning to conclude: 'Our results confirmed that digital aerial photographs were about as accurate as ALS in forest resources estimation as long as a terrain model was available.' Krause *et al.* (2019) also generated CHMs form UAV point clouds for a Scots pine forest in Brandenburg, Germany. Interestingly, the team observed an overestimate of tree heights in the field measurements compared to the length of felled trees, and a slight underestimate of the CHM derived height values. In contrast, Stereńczak *et al.* (2019) found, that terrestrial tree heights showed an underestimate, when set against length measurements. In their investigation the authors felled 2388 sample trees from 299 stands in Poland, representing eight tree species. They also learned, that factors such as tree length, species, and terrain are among the most influential factors on correct height estimation. A similar study was conducted by Sibona *et al.* (2017) by comparing field-based measurements, direct metering on 100 felled trees, and heights derived from an ALS point cloud. They postulate, that height estimates originating from ALS showed a better approximation to real heights, than compared to the field data. The authors also stress, that terrain and the crown architecture seem to be major determinants for field measurement errors. Their finding is underpinned by the fact, that height approximations were best for larch with a conical crown architecture, followed by spruce and by pine - the latter exhibiting a non-monopodial, flat crown architecture at a higher age. Despite the shortfalls of in situ measurements they conclude, that field data will remain a standard reference for comparison with tree heights obtained from other sources. A meta-study conducted by Guimarães *et al.* (2020) revealed, that UAV-based data provided good estimations for tree height metrics set against field data. However, in most cases UAV-LiDAR sensors

performed better than height metrics gained from off-the-shelf RGB sensors (e.g. Cao *et al.*, 2019, Wallace *et al.*, 2016).

The extraction of forest structure attributes like tree height and crown metrics, as well as the determination of tree location can even be subjected to a single workflow as proposed by Guerra-Hernández *et al.* (2016) to streamline and optimise the process:

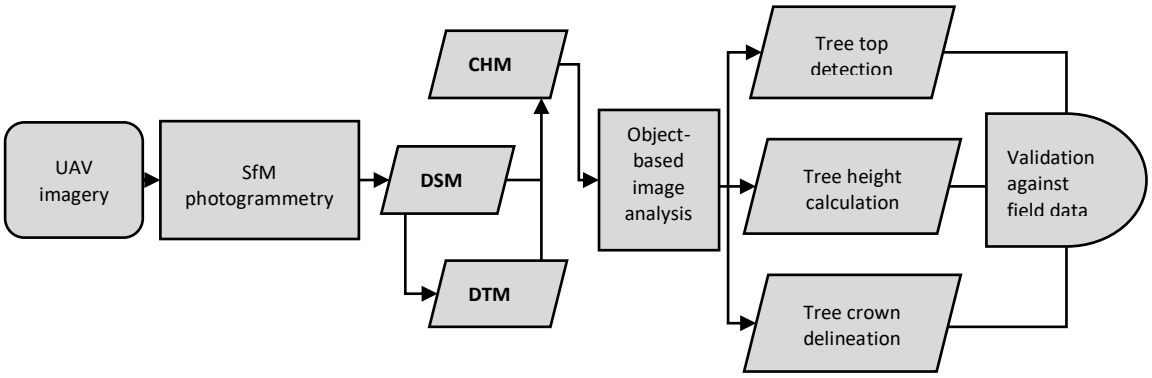

Figure 4.39: Flow chart of the proposed process (according to Guerra-Hernández et al., 2016)

Overlapping UAV imagery is used to generate a high-density point cloud in a photogrammetry suite. The resulting digital surface model (DSM) is normalised (DSM – DTM) to obtain a 3D model of the canopy (CHM). In the next step tree position, height, and crown width is retrieved form the canopy height model (CHM). Canopy delineation is carried out by applying CHM smoothing (with mean and median filters), segmentation, and classification within the object-based analysis process. Parameters have to be tuned and tailored in an iterative process with reference to the various crown shapes. Crown width and the location of the tree tops (including height attributes) are exported as shape files and further analysed in a GIS environment. Crown width is measured in perpendicular directions (N-S; E-W) employing the specific GIS tools. Subsequently, RMSE and regression fits are computed with imagery data set against the estimations of the field survey.

With respect to the creation of Canopy Height Models (CHMs) achievable accuracies seemingly largely depend on factors such as forest structure, terrain, and algorithm parameter settings. In addition, the quality of a CHM can be marred by a lack of image texture, object discontinuities, moving objects (e.g. leaves, shadows), occlusions, and multi-layered or transparent objects (Lisein *et al.*, 2013). Chapter 6.8.1. provides further details on the most relevant studies on UAV applications, with accuracies achieved, and error sources described. Relevant studies comprise works for instance by Alonzo *et al.* (2018), Cao *et al.* (2019), Giannetti *et al.* (2018), Jaakkola *et al.* (2017), and Puliti *et al.* (2015) .

An interesting literature review was published by Holopainen *et al.* (2015) . They condense the experience with 3D techniques (i.e., laser scanning, stereo imagery, radargrammetry) for forest attribute estimation to conclude with the findings for even-aged, single canopy layer stands in boreal forests: '… the main predicative power comes from 3D, i.e., the inclusion of the tree height information, and it does not matter so much what is the final point density.' The table below (table 4-8) provides an overview of the most relevant studies undertaken and accuracies achieved.

Table 4-7: Obtained accuracies in forest attribute estimation using various 3D remote sensing methods in study sites around Finland (Holopainen et al., 2015).

	Stem volume	Above-ground biomass	Basal-area	Mean height	Mean diameter
Airborne laser scanning	**RMSE-%**				
Vastaranta et al. 2013a	23.4	24.7	***	***	***
Vastaranta et al. 2013b	17.9	17.5	17.8	7.8	19.1
Nurminen et al. 2013	20.7	***	***	6.6	11.4
Hyyppä et al. 2012	20.3	***	***	6.1	16.1
Yu et al. 2010	20.9	***	***	6.4	10.9
Aerial imagery	**RMSE-%**				
Järnstedt et al. 2012	40.4	***	36.2	28.2	25.3
Nurminen et al. 2013	22.6	***	***	6.8	12
Vastaranta et al. 2013b	24.5	23.7	23.6	11.2	21.7
SAR radargrammetry	**RMSE-%**				
Karjalainen et al. 2012	34		29	14	19.7
Vastaranta et al. 2013a	29.9	30.2	***	***	***
Vastaranta et al. 2014	16.3	16.1	12	6.7	***
SAR interferometry	**RMSE-%**				
Karila et al. 2015	32	***	29	20	***

Gathering from the outcomes ALS appears to be performing best in all disciplines with aerial imagery ranking next (for further findings on the accuracies of laser scanning point clouds please refer to chapter 4.1.). However, radargrammetry also seems to be a good choice regarding mean height estimation. In the context of the investigation, it is also important to point out, that boreal forests, which were targeted in the studies mentioned above, do not share the lower level of complexity compared with forests of the temperate zones or even tropical forests. Nevertheless, even boreal forests can be a real challenge for forest attribute estimation in very densely populated natural forest systems such as the dark taiga. The presented study above in fact reflects a nice transient from directly extracted forest attributes to the indirect methods (see next sub-chapter) for estimating parameters such as timber volume or AGB.

A wrap-up of this chapter indicates the following:

- Many forest structure attributes like tree species identification, tree density, canopy diameter, and tree height can be directly retrieved form spectral imagery or 3D point clouds. Other parameters (e.g., timber volume, biomass, DBH) require modelling approaches as indirect methods involving ancillary data (e.g., climate, topography).
- Forest inventory parameter extraction is either focused on individual tree traits, or on forest stand characteristics (e.g., mean height, mean DBH).
- Identification of tree individuals (also including tree species) in very high-resolution imagery (i.e., <1m) yields excellent results by visual interpretation due to superior pattern recognition capacity of the brain; automatic retrieval is more efficient and advantageous in stands with even-aged, sparsely spaced forests with conical crown shapes. Poor results in both approaches for very complex forests with mix of many species and multi-storey structure.
- Object-based classifying approaches prior to image classification are best for very high-resolution images (e.g., UAV imagery, WorldView-2), however, tending to over-, or under-segment tree individuals.
- Modern machine learning classification methods like SVM or RF have proven to outperform traditional classifiers for tree species and forest (land-cover) identification.
- Image quality (i.e., high contrast, no clouds) and pick of best season (phenology) is crucial for achieving useful image classification results.
- Most salient and successful spectral bands of multispectral imagery for classification purposes are: Red, Red Edge, Near Infrared, Shortwave Infrared, as well as vegetation indices like NDVI (Normalised Difference Vegetation Index), and NDWI (Normalised Difference Water Index).
- Field estimates of tree heights, being a standard reference, proved to create either under-, or over-estimates compared to length measurements of felled trees. Most critical factors are experience and skill of field worker, and tree crown architecture.
- In many instances tree heights extracted form laser scan clouds tend to be more accurate than heights derived from 3D point clouds generated from stereo imagery (e.g., UAV).
- Laser scan clouds provide an expensive, but excellent tool for deriving many forest structure attributes such as tree height, tree volume, DBH, and crown diameter.

4.6.2. ‘Indirect’ methods for extracting forest structure attributes

In their meta-study Guimarães *et al.* (2020) point out, that for stand-, and tree-level studies, tree height metrics had a strong focus, followed by basal area (BA) and above-ground biomass (AGB) estimations. Since attributes such as BA, AGB, and DBH cannot be directly estimated from 2D imagery and 3D point clouds, they depend either on allometric equations, or on other indirect methods such as regression algorithms, the latter being presented below.

The most sophisticated and widely used methods for mapping and predicting forest inventory attributes comprise regression, decision trees, nearest neighbour, and neural networks. Some of these techniques have become standard and fairly straightforward practise in image classification, but the prediction of forest inventory attributes itself requires much more attention to the methods, the selection of parameters, and the characteristics of the data. In a meta-study carried out by Brosofske *et al.* (2014), the authors conclude, that no single technique has proven to be superior for predicting forest inventory attributes, which comes to no surprise considering the unfathomable variety of forest types and structures (stretching from desert to rainforest), the possible combinations of platforms and sensors, as well as the myriad of options relating to data analysis techniques. Today, multivariate techniques predicting a suite of forest attributes simultaneously become more and more popular to reduce analysis time. In addition, nonparametric approaches receive much more attention to account for the nature of forest characteristics not meeting the assumptions of linearity and normal distribution. The following table below (table *4-6*) provides an excellent account on the various methodological approaches on how to extract forest structure parameters (Brosofske *et al.*, 2014). Since techniques such as Neural Networks (NN) and Random Forest (RF) have been dealt with in detail in chapter 4.3. already, the focus of this chapter will be on methods (e.g., Nearest Neighbour) employed for the analysis of the remote sensing data gathered within the framework of the presented study.

Table 4-8: Advantages and disadvantages of methods for modelling and predicting forest inventory attributes (Brosofske et al., 2014).

Method	Advantages	Disadvantages
Regression	Most techniques are familiar to analysts and users Robust predictions when assumptions are valid Efficient variable selection Extendable across sites with similar conditions Easy to implement/included in most statistical packages	Assumptions are often violated Linear variable relationships are usually assumed Collinearity among predictors complicates model building Cannot easily handle missing values Does not explicitly consider the spatial structure of the data Variable interactions must be prespecified
CART	Distribution free Nonlinear variable relationships allowed Relatively unaffected by multicollinearity and outliers Easily handles both categorical and continuous data Relatively simple to implement and interpret Can handle variable interactions without prespecification	Model structures of a single decision tree can be unstable given small changes to input data Some algorithms suffer from selection bias Does not explicitly consider the spatial structure of the data
MARS	Better at detecting global and linear data structure Models nonlinearity and interactions among variables Computationally efficient Both continuous and categorical predictors	Model tuning is cumbersome Extensively guided by local nature of data, predictions with new data are unstable
ANNs	Distribution free Underlying processes do not need to be defined/known Easily handles nonlinear data Can effectively handle very complex problems Collinearity among predictors is not a problem Effective with multisource data	"Black box" approach Steep learning curve Risk of overfitting Determination of optimal parameters can be difficult/time consuming (trial and error) Greater number of predictors may lead to poorer predictions Can produce values outside the data range Does not consider the spatial structure of the data
RF	Retains the benefits of CART and addresses many limitations Reduces tendency to overfitting and bias compared to CART Can estimate variable importance from cross-validation Can be combined with nearest neighbors (i.e., RF imputation)	Less interpretable than CART because many trees are averaged Potentially sensitive to the inclusion of too many predictors Careful variable selection may be important Does not explicitly consider the spatial structure of the data
NN	Distribution free Concept of "nearest neighbor" is intuitive Easy to implement Variants allow explicit incorporation of the relationships between predictors and response into the weights and distance measures Easily handles multivariate responses	Can be time consuming (search process) with large data sets Selection of appropriate parameters (k) is not always straightforward; may require trial and error Does not explicitly consider the spatial structure of the data without using spatial distance-based weight

Regression, as an essentially parametric technique, has traditionally been used to predict forest attributes such as basal area or tree height from ancillary data and other structure variables, since many forest variables have shown to be highly correlated (e.g. height, DBH, age, volume, LAI, NDVI) (Pocewicz *et al.*, 2004, Pretzsch, 2010: 3–10, van Laar and Akça, 2007: 271–273, Wolter *et al.*, 2009). As an example, Hudak *et al.* (2006) used regression modelling to predict basal area and tree density in temperate coniferous forests from LiDAR and multispectral satellite imagery. LiDAR by far outperformed multispectral imagery by explaining more than 90% of the variance in the forest attributes analysed. Le Maire *et al.* (2011) employed multiple linear regression to predict stand dominant height and timber volume from age, NDVI, and bioclimatic variables. Best results were achieved for timber volume with $R^2 = 0.9$, and $R^2 = 0.92$ for dominant height in eucalyptus plantations in Brazil. In their study, Fuchs *et al.* (2009) looked into the aboveground carbon and phytomass in a catchment of the Siberian forest tundra. They combined ASTER, Quickbird, and field data to assess the spatial variability of above-mentioned parameters by applying the kNN distance-weighted classifier and linear regression technique to find only small differences in predictions. Many authors have successfully used regression techniques, especially in conjunction with LiDAR technology, to predict tree height, basal area, timber volume, biomass, and density (Bergseng *et al.*, 2015, Næsset, 2004, 2007, Næsset *et al.*, 2011,

Næsset, 2014, Noordermeer *et al.*, 2019). The bulk of regression analyses in the literature is performed by applying the so-called ordinary least squares (OLS) technique to estimate the unknown parameters in a linear regression model (Le Maire *et al.*, 2011, Næsset, 2007). OLS assumes that there are either no measurement errors in the explanatory variable , or the errors are independent and Gaussian. However, in many cases these assumptions are hardly met in reality (Berterretche *et al.*, 2005, Sokal and Rohlf, 2012: 472–474). Despite some demerits of the regression technique, it is easy to implement, with predictions being robust, when assumptions are found to be valid.

Classification and Regression Trees (CARTs) '…work by recursively subdividing training (i.e., reference) data into more and more homogenous subgroups' (Brosofske *et al.*, 2014: 735). In a classification environment the trees predict a categorial response, whereas when applied to regression analysis, the trees predict a continuous response like timber volume. A splitting rule is determined at each level to partition the observations, leading to a hierarchical tree (Moisen and Frescino, 2002). Decision trees have been extensively employed in classification procedures for identifying and specifying forested areas, as well as for predicting forest structure attributes (Falkowski *et al.*, 2005, Gómez *et al.*, 2012, Mora *et al.*, 2010a, Rogan *et al.*, 2002). Decision trees feature some compelling advantages such as being non-parametric and being able to accommodate nonlinear responses. In addition, they are relatively unaffected by outliers and can handle both categorial, as well as continuous variables (Brosofske *et al.*, 2014). Nevertheless, there are limitations to report, namely the potential instability of the models (different tree structures), and thus high sensitivity towards miniscule changes in the input data (Prasad *et al.*, 2006).

Artificial Neural Networks (ANNs) pursue the attempt to mimic the problem-solving structures of the (human) brain. The ANN model has to be trained in that way, that it has to 'learn' the patterns based on observations, thus acquiring cognition capacities. Because of its black box nature, ANN applications are still fairly scant. Nevertheless, a few successful classification results exist. For example, Braga *et al.* (2020) achieved promising outcomes when detecting and delineating tree crowns in a rainforest in Brazil. In their survey, Chen *et al.* (2014) applied deep learning algorithms on hyperspectral data for classifying forested areas in the USA and Italy outperforming other approaches like SVM. This observation is very much in line with the findings by Lee *et al.* (2020), when investigating land use classification performed on Landsat imagery. Their Convolutional Neural Network approach yielded much better outcomes compared to SVM and RF, in particular, when training sampling sizes were small. Rogan *et al.* (2008) confirm similar observations, when assessing land-cover modifications in California. According to them, the ANN outcomes showed similar accuracies to human-interpreted map, however, featuring much higher

efficiency. In contrast, Abdi (2020) found the highest overall accuracies for Sentinel-2 classification of a boreal landscape achieved by SVM, followed by RF, with deep learning ranking last. Another positive example is given by Ingram *et al.* (2005) - they used ANN to model basal areas from Landsat imagery in a tropical forest to achieve a correlation of r = 0.79 for this relationship. However, all authors mentioned do not fall short in stressing, that careful variable selection is crucial when applying ANN. Apparently, variables that lack a relationship with the response can largely affect the predictive power of the model.

By combining myriads of decision trees, **Random Forest (RF)** has become one of the most popular classification and prediction ensembles of forest related subjects (Belgiu and Drăguţ, 2016, Brosofske *et al.*, 2014, Tso and Mather, 2009: 215). RF uses bootstrapping for the selection of samples, which are subsequently subjected to fitting of the model (see also chapter 4.3.1 for more details). Since only a random selection of predictor variables are used for finding the best split at the nodes, correlation between trees, and as such, bias is reduced (Breiman, 2001, Cutler *et al.*, 2012, Hastie *et al.*, 2009: 587–604). One of the big merits of RF is the fact, that this algorithm is not subject to overfitting (Breiman, 2001, Prasad *et al.*, 2006). Applications of RF are abundant these days. For example, Grossmann *et al.* (2010) created an RF model featuring 13 explanatory variables to classify forest ecological systems in the West Cascades (USA) region. The dominant system (North Pacific dry-mesic Western Hemlock – Douglas fir forest) was classified with a User's Accuracy of 97%. Tree cover and species presence was investigated by Evans and Cushman (2009) by looking at the distribution of conifer species in a forest area in Northern Idaho, USA. Their RF model involved predictor variables such as topography, climate, solar insolation, NDVI, and Landsat image values. The classification resulted in an overall accuracy (OA) of 86%. Immitzer *et al.* (2016a) employed stereo WorldView-2 imagery to map growing stock of a forested area in Bavaria (Steigerwald). Their RF regression approach (combination height and spectral data) explained 56% of the variability (R^2) in the growing stock when compared to Management Forest Inventory (MFI) field data. Falkowski *et al.* (2009) developed a framework for supporting Canada's National forest Inventory based on the analysis of VHR satellite imagery (e.g. WorldView-2, Quickbird). The authors ascertain, that by applying image segmentation for the extraction of tree crowns and other forest structural parameters in combination with sophisticated regression algorithms (e.g., RF) National forest Inventories can be carried out with much higher efficacy and at lower cost. Despite all the merits of RF, caveats do apply: authors like Evans and Cushman (2009), Falkowski *et al.* (2009), and Murphy *et al.* (2010) conclude, that the process of identifying a parsimonious set of variables can significantly minimise noise and improve the performance of the model.

Another notable technique, namely the **Nearest Neighbour (k-NN)** approach, has gained substantial momentum in the last couple of years. In plain words, in k-NN the reference and target (i.e., dependent) samples are being linked via ancillary (i.e., independent) variables, usually being obtained from satellite or aerial imagery. The response variable (e.g., timber volume) is predicted in an unsampled pixel by computing a distance metric (e.g., *Euclidian*) between the target and neighbouring reference samples, and successively assigning the value of the closest neighbour to the target pixel. The distance metric is determined from the ancillary variables (e.g. NDVI, spectral bands) being common to reference and target samples (Chirici, 2012, McRoberts, 2012). K-NN can attain any number (*k*) of nearest neighbours to impute the target value.

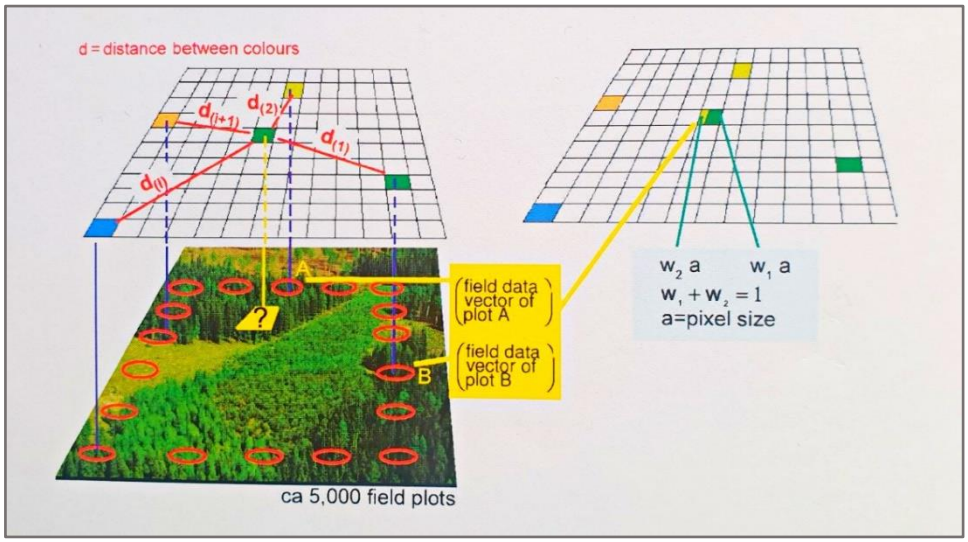

Figure 4.40: A simplified demonstration of the k-NN method with k = 2; Kangas and Maltamo, 2009:204.

Several distance metrics (e.g. *Euclidian*, *Mahalanobis*, *most similar neighbour* (*MSN*), *Kriging*) have been tested by various authors (e.g. Hudak *et al.*, 2008, Eskelson *et al.*, 2009, Chirici, 2012, Räty and Kangas, 2012) to find out, that the simple *Euclidian* distance (i.e. shortest distance between two points) works best in many instances (McRoberts, 2012). K-NN boasts a lot of benefits, such as being nonparametric (i.e., disregarding the underlying distribution of the data), the ability to predict multiple response variables simultaneously, and being easy to apply. This technique has proven to be very successful especially when dealing with huge forested areas to be inventoried. Thus, the Nordic countries, such as Finland and Norway, have favoured k-NN to support their National forest Inventories (NFIs) for many years (Kangas *et al.*, 2018, McRoberts *et al.*, 2010, Tomppo, 1991, Tomppo *et al.*, 2009, Tomppo *et al.*, 2010). Various applications of k-NN comprise the successful classification (Overall Accuracy (OA) of 91%) of boreal forests in Finland (Haapanen *et al.*, 2004), the determination of biomass outperforming RF and SVM (López-Serrano *et al.*, 2016), the imputation of tree-level stem volume and basal area resulting in small RMSE (Root Mean Square Error) (Falkowski *et al.*, 2009), or the determination of forest structure

attributes (basal area, tree density) from LiDAR data (Hudak *et al.*, 2008). However, there are examples of mediocre performance of k-NN, like the ones reported by Gjertsen (2007), who found an OA of only 63% for the classification of Norwegian forests from Landsat imagery. In his study, Baasan (2010) found accuracies for basal area for a forest area in the in the Khan Khentii, Mongolia, ranging from 26.94 to 76.94%, depending on the number of satellite spectral bands used as ancillary data.

In a number of investigations useful suggestions are to be found on how to improve the quality of the k-NN outcomes and how to avoid glitches: Jung *et al.* (2013), and Eskelson *et al.* (2009) for instance point out very clearly, that image registration (positional) errors need to be shunned. Gjertsen (2007) suggests the use of image band ratios (indices) as additional input for ancillary data, whereas Franco-Lopez *et al.* (2001) ask for more research on multi-sensor k-NN approaches. Koukal *et al.* (2007) dedicated an entire study on the possible ramifications of radiometric calibration on the k-NN predictions of forest attributes to ascertain, that image calibration is vital for achieving good k-NN results. McRoberts (2008) found the selection of the optimal feature space crucial for his study on stand density and basal area derived from Landsat imagery, and suggests in another investigation to either use a high amount of sampling plots, or stratify the field data prior to further analysis (McRoberts *et al.*, 2002). Good results on k-NN derived basal area of a forest in the Kyiv region (Ukraine) were yielded in a study conducted by Myroniuk *et al.* (2019). The authors conclude, that the pixel size of the satellite imagery proved to be less important than a high temporal resolution to capture the variation in spectral response.

The authors of the above mentioned meta-study legitimately complain of the difficulties in interpreting accuracy assessments and model outputs (Brosofske *et al.*, 2014). This is by far no recent phenomenon, since errors associated with the modelling process, the variability in the datasets, spatial mismatches in data, and flawed reference data are generally arduous to deal with. As a possible remedy, Riemann *et al.* (2010) proposed a set of guidelines for the assessment of model outputs:

- Compare the empirical cumulative distribution functions of the observed and predicted data set for several scales.
- Examine the overall agreement across several scales (e.g., scatterplots).
- Assess spatial and distributional patterns of local discrepancies.
- Analyse local variability via chloropleth maps (standard deviations) of the modelled estimates.

Unfortunately, only few of these suggestions have materialised in studies in the subsequent years.

In the following, some more outstanding *publications* dealing with the modelling techniques for predicting forest characteristics are outlined. Five modelling techniques were scrutinised by Moisen and Frescino (2002) to gain responses for biomass, average tree age, mean DBH, and crown cover for forest test sites in Montana and Arizona in the USA. Predictor variables for the models comprised spectral data from satellite imagery, vegetation cover type maps, topographic data, and NDVI. Of the five models, linear models performed better in a few instances, but in real data runs, adaptive regression splines (MARS), and generalised additive models (GAMs) gave the best results for predicting forest characteristics. Pierce *et al.* (2009) also investigated various methods for the imputation of forest structure variables for forests in Washington and Oregon, USA. They also confirm, that simple linear models have the potential to outperform more complex models such as Kriging and CART. Overall best performance, however, was attributed to nearest neighbour imputation for predicting forest canopy and structural variables. In general, best results were achieved for even-aged old forests with little variation in DBH and tree height. Landsat imagery with a 30m resolution, as well as ancillary data such as topography and climate were employed throughout as predictor variables. Franco-Lopez *et al.* (2001) applied the k-NN method to estimate stand density, timber volume, and cover type for forest areas in Minnesota, USA. Landsat imagery in combination with climatic, geologic, soil, vegetation, and hydrologic data were used as model inputs. The overall satisfactory results for basal area (RMSE of 9.02 sqm/ha), and for timber volume (RMSE of 54.58 qm/ha) clearly indicate a recommendation for applying the kNN method on a regional scale. Powell *et al.* (2010) exercised multitemporal Landsat imagery in conjunction with spectral indices like NDVI and tasselled cap transformations to estimate and monitor above ground biomass for several forested areas in the USA. According to the authors, the Random Forest (RF) approach yielded the best outcomes. However, they also state, that biomass estimates with optical remote sensing data '…will never be as accurate as estimation by active remote sensing approaches (e.g., LiDAR and interferometric radar)'. Another team of authors also used Landsat imagery depicting forest areas in Alberta, Canada, to estimate canopy closure and biomass. Multivariate regression techniques formed the basis for the pursuant models, resulting in an R^2 value of 0.57 for crown closure, and an RMSE of 4 qm/ha for biomass estimates, when set against field data. The authors mention field plot distribution, error propagation, and extending models over multiple images as factors asking for further scrutiny. Falkowski *et al.* (2010) applied k-NN on LiDAR point clouds to generate a forest

growth model. Very good results were achieved for basal area (BA) and timber volume estimation (RMSE of 5 sqm/ha, and 16 qm/ha respectively).

One of the few publications on forest structure parameter estimations for Mongolian forests has been conducted by Klinge *et al.* (2020). The team employed satellite imagery (i.e., Landsat 5/8, Sentinel-2) and ancillary data such as NDVI, soil data, allometric formulas, climate and topographic data to model forest biomass and potential forest area for the forest-steppe ecotone of Central Mongolia. The authors found topographic and climatic parameters to be the driving factors of the spatial extent of the forests. Biomass was reduced at forest edges, and small, fragmented patches, as compared to large forest stands. Interestingly, no significant correlation between NDVI and tree biomass was detected.

By wrapping up this section we conclude, that:

- There is no analytical technique (be it regression, RF, ANN, k-NN, etc.) perceived to be superior for all cases.
- Variable selection plays a pivotal role in achieving useful results and can be more rewarding than simply focussing on the modelling method.
- Data characteristics such as non-Gaussian and non-linear relationships are best dealt with decision trees, nearest neighbours, or ANNs.
- Decision trees and nearest neighbour approaches are better suited for the incorporation of a big set of ancillary variables, and for the handling of categorial and continuous predictors.
- K-NN method has shown to deliver very useful results for mapping big areas on a regional, or even country-wide scale (wall-to-wall).

5. Wildfires

Wildfires have been intrinsic to the boreal ecosystems for millennia and as such also affect forest structure, species composition, timber markets, and forest management (Stocks *et al.*, 2001). In this chapter the main drivers of fire occurrences, the possible ramifications, the potential remedies, and the role of remote sensing technology are discussed in general as well as for the conditions in Mongolia in particular (5.2.).

5.1. Fire and ecosystems

The occurrence of fire usually triggers associations in humans such as destruction of assets and peril to human health. However, fire has always been an important ecosystem scheme deeply impacting terrestrial, aquatic, and atmospheric processes (Bonan and Shugart, 1989). These days our changing climate seems to be the culprit for exacerbating or at least altering disturbance regimes like wildfire (Bonan, 2008). In this context General Circulation Models (GCMs) have been used extensively by teams around the globe to investigate fire season intensities, and to generate outlooks for future fire scenarios and appropriate management measures. According to findings reflected in the literature fire severity levels will rise most in the Northern hemisphere with increased frequency and length of the fire season, as well as a decrease of the effectivity of conventional fire management approaches (Coogan *et al.*, 2019, Flannigan *et al.*, 2009, Flannigan *et al.*, 2013, Goldammer, 2013: 13–15, Kukavskaya *et al.*, 2013, Moritz *et al.*, 2005, Soja *et al.*, 2007, Stocks *et al.*, 2001, Stocks, 2013). Studies such as by Pechony and Shindell (2010) imply that global fire regimes were strongly driven by precipitation during the pre-industrial period, whereas in the 21st century a marked shift to temperature-driven regimes is becoming a reality. Their models suggest that the associated impact of a changing climate on driving fire trends seems to outweigh direct human influence like ignition and suppression. Scientific reports even allude a doubling of burned area …'along with a 50% increase in fire occurrence in parts of the circumboreal by the end of this century' (Flannigan *et al.*, 2009, Jolly *et al.*, 2015).

What are the driving processes and the associated scales behind the occurrence of wildfires? The following graph (Figure 5.1) provides a simplified model of the main factors influencing the magnitude and severity of a wildfire.

At the smallest scale fuel particles are ignited at a critical temperature. The resulting fire then transfers energy to its direct environment. Depending on weather conditions and topography combustion events can spread within a short period of time to affect huge areas. At the largest scale, regional and even global climatic conditions have an impact on the fire situation even up to the point that wildfires create their 'own weather' (Soja *et al.*, 2007). In

addition, particular vegetation types support a characteristic fire in terms of recurrence, intensity, seasonality and biological effects, implying that a change in vegetation (species composition and condition (living or dead)) type can potentially alter the fire regime (Moritz *et al.*, 2005).

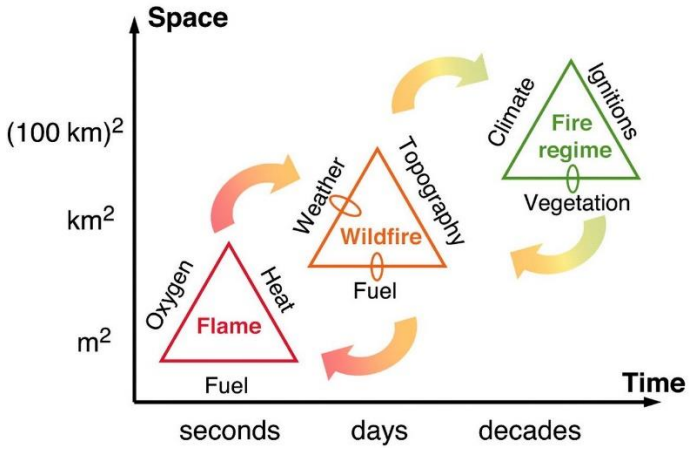

Figure 5.1: Dominant factors that influence fire at the scale of a flame, a wildfire, and a fire regime (based on concept of fire triangle). Loops indicate the feedbacks of the fire on the controls themselves; arrows indicate the feedbacks between processes at different scales (Moritz et al., 2005).

Causes of wildfires are both, natural and human-induced (negligence, arson, etc.), with varying involvement. According to Tymstra *et al.* (2020) human-caused fires account for around 50% of fires occurring in Canada, with lightning being the major contributor to area burned in the boreal forests. Areas scorched annually are huge, with estimations of the size of Belgium destroyed in Siberia alone (Jones and Vaughan, 2010: 303). The massive fires raging in Australia from the end of 2019 until spring 2020 apparently left between 13 and 17 million hectares of land being torched (Australian Bureau of Agricultural and Resource Economics and Sciences, 2019: 258–267, Granwal, 2020, National Council for Fire and Emergency Services, 2020). The Australian Bureau of Meteorology reported a fatal 'alliance' of a breakdown of the Southern polar vortex with a positive Indian Ocean Dipole as a major driver of the gout of flames, reverberating in an inadvertent contribution to global warming due to gas and aerosol emissions (Goldammer, 2013: 251). One of the most destructive cases of a single event in 2016 at Fort McMurray, Canada, destroyed almost 590,000 ha of boreal forest and more than 3,200 buildings. A natural El Niño cycle significantly contributed to the dry and hot conditions as a perfect precondition for an explosive wildfire (Kahn, 2016).

Wildfires are categorised according to the kind and location of the fuel they affect: (i) *crown fires* combust the entire length of a tree from base to top, and are the most intense fires raging with extreme speed at high wind velocity; (ii) *surface fires* only scorch surface litter

and duff, causing the least damage to the forest; (iii) *ground fires* occur in thick layers of humus, peat and dead vegetation, moving very slowly with the potential to smoulder for months (Lutes *et al.,* 2006). Crown fires are considered to be the most destructive and difficult to fight type of wildland fire.

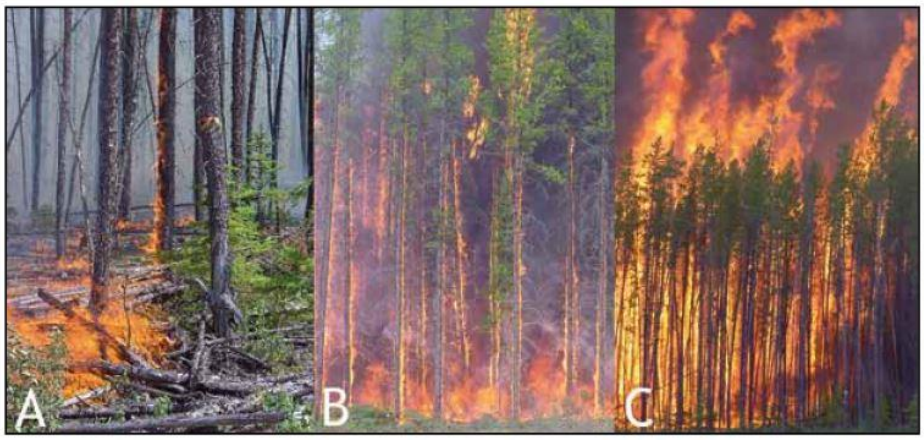

Figure 5.2: Fire behaviour in a jack pine/black spruce forest: (A) surface fire; (B) passive crown fire; (C) active crown fire (Werth et al., 2011).

At a local scale, fire can stimulate soil microbial processes, promote germination, seed production, but also combust biomass to effectively alter the structure and composition of vegetation and soil (Lentile *et al.*, 2006). At larger scales, the varying fire intensity creates a mosaic of different habitats to be populated by a variety of species. High-severity wildfire often creates a complex early seral forest habitat with some of the highest levels of native biodiversity compared to an unburned old forest (DellaSala and Hanson, 2015).

Since ecosystems have been exposed to wildfires for millions of years, many species have adopted very successfully to ramifications of thermal impacts. For example, birch developed the ability to survive by sprouting shortly after a fire, and pine and larch species protect themselves from scorching by growing a thick, robust bark. Forest fires show immediate effects, but also long-term trajectories on the surface energy and water budget. While removing the insulating organic layer during a fire, the permafrost layer near to the surface begins to thaw in a first stage. Subsequently, deeper removal of the permafrost takes place to the point that this water reservoir depletes and soils become increasingly dry, forcing the vegetation to adapt (Goldammer, 2013: 79–81).

The intensity and frequency of wildfires have severe repercussions on the structure and spatial distribution of forests. From a fire ecology perspective, a distinction is made between three main forest types (Crisp 2004):

Disturbance maintained forests are shaped by fire of high frequency and feature an open, parc-like structure with transitional zones towards the forest steppe.

Disturbance driven forests are created by high intensity mass fires resulting in even-aged, low structured systems.

Gap driven forests are characterised by destructive disturbances in small areas (gaps), where regeneration processes are induced. Those forests are highly structured vertically and horizontally, and typically occupy sites with a good supply of water resources.

Fighting wildfires has become very sophisticated and professional, and has been subject to many research studies over the last few decades. Activities in the field routinely comprise the establishment of fire breaks, prescribed burnings, creating backfires, and the application of silver iodide (to encourage precipitation) and fire retardants. For more details on how to successfully fight wildfires please refer to excellent sources for the pertaining codes of practice and manuals like Beebe *et al.* (2020), Goldammer (2013), Heikkilä *et al.* (2010), and Hirsch and Fuglem (2006). However, fire management tools are also part of an effective fire strategy. Useful 'gadgets' of this tool-box can be a forest fire weather index system (like in Canada), a fire behaviour prediction model to estimate fire spread and intensity, and fire effects models to analyse the physical effects of fire on stands and the ecosystem. These days fire databases (e.g. Canadian National Fire Database (CNFDB), and Canadian Wildland Fire Information System (CWIS)) have become very useful tools to support modern monitoring systems for getting useful and tangible information for wildfire risk management (Lutes *et al.,* 2006). This is the moment, when remote sensing technology comes into play (see section below).

Satellite based fire detection and monitoring

Remote sensing can be considered an ideal tool for:

- The identification of conditions prior to fire events (prediction).
- The detection of live fires and the post-fire succession (monitoring)
- The mapping of the destroyed area (Jones and Vaughan, 2010: 303).

Pre-fire event conditions may involve land use and (tree) species classification, terrain analyses, the assessment of biomass, the detection of the proximity of settlements and industrial areas, the retrieval and integration of weather data, and information on the management regime of the specified range. Most of the common earth observation satellite and UAV sensors have proven to be suitable for these tasks. However, the detection of wildfires requires specific spatial, spectral (i.e., sensors), and temporal resolution to ensure quick and appropriate response to imminent damage to natural resources, livelihood and lives. The systematic detection and monitoring have been operational since the early 1980s with the launch of the AVHRR (Advanced Very High Resolution Radiometer) sensor onboard the NOAA (National Oceanic and Atmospheric Administration) satellite. However,

the infrared sensors proved to hit a saturation point very quickly, thus making the NOAA product less suitable for the detection of active fires. With the MODIS (Moderate Resolution Imaging Spectroradiometer) instrument piggy backed by NASA's TERRA and AQUA satellites a sensor has come into orbit in the late 1990s specifically designed for the detection of fires. Live fires can be accurately detected through the mid and thermal infrared bands (MIR, TIR) with an extent of more than 1 km^2. The MODIS fire products are freely retrievable from NASA's Distributed Active Archive Center (DAAC) with a spatial resolution of 1 km and a temporal resolution of 24 hours. NASA's Fire Information and Resource Management System (FIRMS) now provides a web-based tool to visualise and download (as shape files) MODIS hotspots in almost real-time[7] including a host of archived data. The user of those products, however, has to consider, that most global products are based on a coarse pixel size, thus affecting the potential detection area size and leading to grave under-estimates (Roteta *et al.*, 2019). The provision of data acquired by the Visible Infrared Imaging Radiometer Suite (VIIRS) sensor (375m resolution) on the same website essentially complements the MODIS products. Other fire reporting initiatives comprise the European Forest fire Information System (EFFIS[8]), and the South African based Advanced Fire Information System (AFIS[9]). Various other satellite systems also feature fire detecting capacities, however, with lower temporal, but higher spatial resolution. Popular, still operational examples comprise: Landsat 8 (bands 10 and 11 of the TIRS sensor), NOAA's GOES-16 and 17, ESA's Meteosat fleet, China's Fengyun, and Japan's Himawari 8. A different approach has been pursued by NASA by mounting their newly developed CTI (Compact Thermal Imager) sensor onboard the International Space Station (ISS). Crisp imagery with a spatial resolution of 80m has been successfully transmitted since 2019 aimed at succeeding Landsat's TIRS sensor[10]. A real paradigm shift is to be expected with the population of the Earth's orbit with so-called 'Cube Sat' nanosatellites. Rocking the traditional satellite industry, cube satellites provide a low-cost solution with additional merits such as high temporal resolution (especially in swarm formations), high versatility, low weight (below 3 kg), and tailoring to specific requirements. A representative of this new satellite generation was launched in December 2018 by the name of LUME-1. The platform is part of the European Fire Remote Sensing (FireRS)[11] project especially designed for the detection and monitoring of wildfires to provide almost real-time information, GPS positioning, fire perimeter, infrared images, and propagation prediction. However, at this stage it remains unclear when the data will be available to the public.

[7] URL: https://earthdata.nasa.gov/earth-observation-data/near-real-time/firms
[8] https://effis.jrc.ec.europa.eu/
[9] https://www.afis.co.za/#home
[10] URL: https://earthobservatory.nasa.gov/images/146547/taking-temperatures-from-iss
[11] URL: https://alen.space/lume-1-launch/

Forest cover change can also be an indication for a loss of forest areas caused by wildfires. These phenomena can be of transitory or irreversible nature. The team around Matthew Hansen of the University of Maryland[12] in collaboration with institutions such as NASA, Google, and the USGS (United States Geological Survey) designed an internet platform (Global Forest Watch[13] (GFW)), from which information on forest loss and gain are retrievable on a global scale. The observations are all based on Landsat 7/8 and VIIRS data, and stringent definitions[14] are exercised to ensure consistency (i.e., tree cover > 60% canopy cover; vegetation taller than 5m). GFW data are used by institutions worldwide because of their reliability, ease of access, and high update rate (twice a day).

Prior to engaging into monitoring and mapping of fire related phenomena it is vital to become aware of the definition of technical terms that are being used interchangeably in the literature, thus causing confusion in the user community. *Fire intensity* is referred to the amount of energy released during the incineration process, whereas *fire* or *burn severity* are related to the loss of organic matter also including ecosystem responses such as soil erosion, vegetation regeneration, and faunal recolonisation (Keeley, 2009).

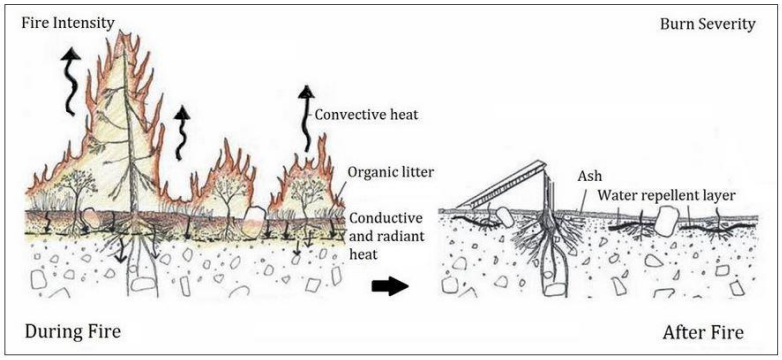

Figure 5.3: Illustration of fire intensity versus burn severity. Source: U.S. Forest Service (Parsons et al., 2010).

Hotspot or fire detection (*fire intensity*) is commonly carried out by exploiting the measurements of thermal infrared sensors onboard air-, or space-borne platforms (e.g., AVHRR[15], MODIS[16], TIRS[17]). Several methods have been developed (e.g., Dozier method, threshold method, fuel mask method) based on radiance functions to account for specific fire scenarios and regional specifics (temperate, boreal, tropical forests, etc.). In order to avoid false results due to saturation effects, additional information from other spectral bands

[12] URL: https://earthenginepartners.appspot.com/science-2013-global-forest
[13] URL: https://www.globalforestwatch.org/map
[14] Tree cover loss is defined as 'stand replacement disturbance', or the complete removal of tree canopy cover at the Landsat pixel scale. Tree cover loss may indicate a number of potential activities, such as timber harvesting, fires or disease, the conversion of natural forest… (https://earthenginepartners.appspot.com)
[15] **A**dvanced **V**ery **H**igh **R**esolution **R**adiometer
[16] **MOD**erate-resolution **I**maging **S**pectroradiometer
[17] Landsat 8 **T**hermal **I**nfra**R**ed **S**ensor

(e.g. NIR, SWIR) is used to minimise false hot spots (Keeley, 2009, Lentile *et al.*, 2006, Li *et al.*, 2003). In addition to thermal bands SWIR bands are also able to penetrate smoke plumes and as such are most suitable for the detection of fire spots and fire-lines. During the combustion of wood, a drastic decrease in visible to NIR and a sharp increase in SWIR reflectance can be observed (see figures below). However, the deposition of a large quantities of white ash has the potential to increase surface reflectance (Lentile *et al.*, 2006). Authors of numerous studies also report confusion between recently charred areas and shaded surfaces (Said *et al.*, 2015).

For the assessment of burned areas (*burn severity*), the application of a variety of vegetation indices has become second nature. The favourites as listed in many studies are NDVI, NBR (RBR), and NDWI (see figures below).

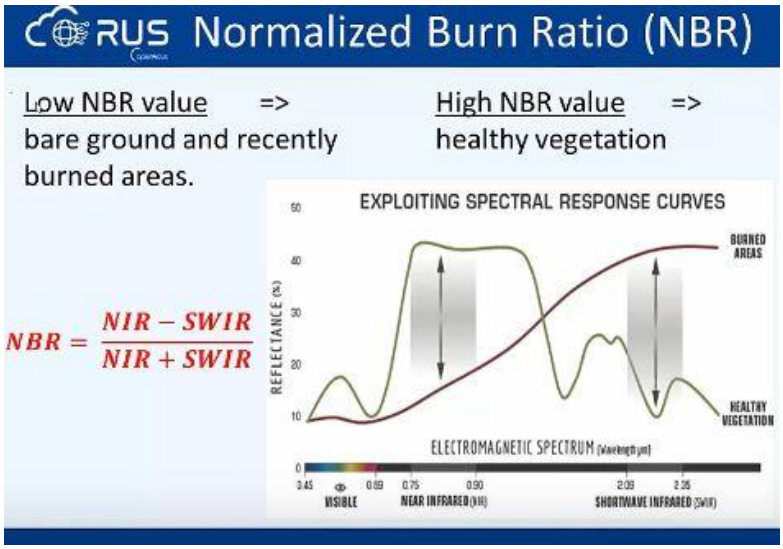

Figure 5.4: Characteristics of the Normalised Burn Ratio (source: ESA, 2017).

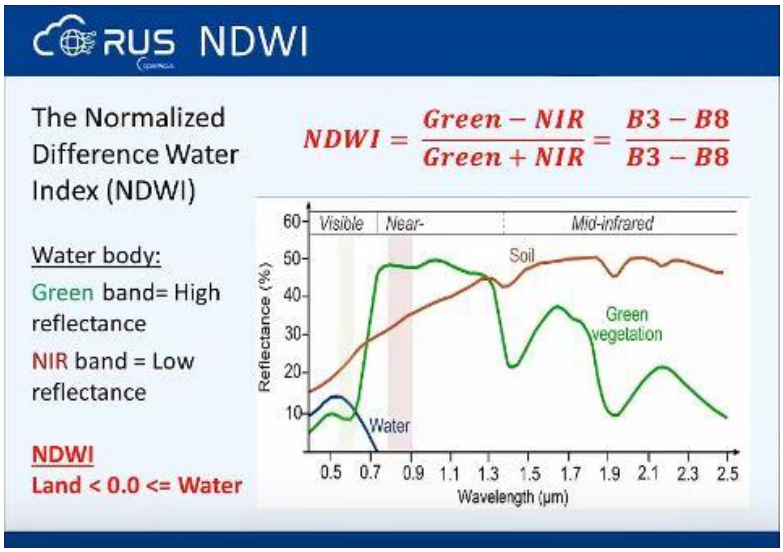

Figure 5.5: Characteristics of the Normalised Difference Water Index (source: ESA, 2017).

The associated formulas are as follows (band indications (e.g., B8) refer to Sentinel-2 bands):

$$RBR = \left(\frac{dNBR}{NBRpre + 1.001}\right) \qquad NDWI = \frac{Green-NIR}{Green+NIR} = \frac{B3-B8}{B3+B8} \qquad NBR = \frac{NIR-SWIR}{NIR+SWIR} = \frac{B8-B12}{B8+B12}$$

$$NDVI = \frac{NIR-Red}{NIR+Red} = \frac{B8-B4}{B8+B4}$$

A standard procedure for the evaluation of areas affected by fires is to compare pre-, and post-fire conditions (e.g., difference of NBR (dNBR)). Based on the exhaustive assessments of burned areas by institutions like the United States Geological Survey (USGS), and the United States Department of Agriculture (USDA), reference tables have been devised to reflect certain degrees of severity levels. The table below shows such values, being applied by many forest researchers and practitioners these days.

Table 5-1: Burn severity levels with related dNBR ranges calculated from satellite imagery (source: USDA, Lutes et al., 2006: 256)

Severity Level	dNBR Range (scaled by 10^3)	dNBR Range (not scaled)
Enhanced Regrowth, high (post-fire)	-500 to -251	-0.500 to -0.251
Enhanced Regrowth, low (post-fire)	-250 to -101	-0.250 to -0.101
Unburned	-100 to +99	-0.100 to +0.99
Low Severity	+100 to +269	+0.100 to +0.269
Moderate-low Severity	+270 to +439	+0.270 to +0.439
Miderate-high Severity	+440 to +659	+0.440 to +0.659
High Severity	+660 to +1300	+0.660 to +1.300

In numerous studies (relating to boreal forests in particular), the NBR index has demonstrated its ability to attain good correlation with field-based methods and its transferability across multiple landscapes and multitemporal surveys (Allen and Sorbel, 2008, Chen *et al.*, 2011, George *et al.*, 2006, Navarro *et al.*, 2017, Soverel *et al.*, 2011). Mallinis *et al.* (2018) found out, that the dNBR even outperformed NDVI, when assessing large fires in pine forests in Thasos, Greece. In addition, the classification accuracy was slightly higher for the Sentinel-2 imagery compared to Landsat 8 OLI. This finding was confirmed by Fernández-Manso *et al.* (2016) for the Sierra Grata (Spain) wildfire in 2015. When assessing burned areas in coniferous forests in the Western USA, Parks *et al.* (2014) discovered, that the RBR (formula see above) corresponded better to field-based measurements than dNBR (R^2 for RBR: 0.786 and for dNBR: 0.761). Despite the overall success of the NBR, this index has proven to be less effective with a considerate time lag between the fire event and the assessment of post-fire conditions with vegetation regrowth starting immediately after the fire (i.e., higher reflection in the NIR). It is also important to know, that this index is very sensitive to water, thus causing misclassified pixels. This

requires a creation of a water mask and/or consideration of a NDWI calculation prior to classifying the imagery (Keeley, 2009, Polychronaki and Gitas, 2010).

Undoubtedly, the choice of the right sensor seems crucial for successful fire detection and monitoring missions, but also the right timing for detection and interpretation. In forests in particular, survivorship of trees, the delayed mortality of individuals, and the resprouting capacity of certain species can lead to over-, or underestimates of fire severity. In addition, the sampling intervals have to be chosen with care accordingly. Recovery (succession) intervals of the vegetation can be very long, depending on species adaptation to fire, and interactions with climate and soil conditions (Key, 2006).

Not only the way how to effectively fight fires has changed in the few last decades, but also how forests need to be managed in the future to achieve forest ecosystems with a much higher degree of resilience towards fire risks and hazards. A growing number of researchers in the Northern hemisphere seem to support the idea that forests need active manipulation to achieve more fire-tolerant structures. This idea would involve thinning activities, prescribed burning, and removal of fuel from forest areas in a specific pattern to gain a broader landscape scale management perspective (Bowie *et al.,* 2015, Pollet and Omi, 2002, Tymstra *et al.*, 2020). In addition, the mix of tree species, the silvicultural practices, and the age structure of the forests need to be reconsidered for risk distribution and the alleviation of fire damages (Adams, 2013, Beck *et al.*, 2011, Bergeron *et al.*, 2017, Reich *et al.*, 2001, Terrier *et al.*, 2013).

Wrap-up of the section:

- Fire has always been an important ecosystem scheme deeply impacting terrestrial, aquatic, and atmospheric processes, however, with climate change exacerbating the destructive character.
- Remote sensing with a variety of sensors (TIR, NIR, etc.) has become crucially important for the detection, monitoring, and assessment of fires and their aftermath related to changes in the environment and ecosystems.
- NDVI and NBR are favoured by the remote sensing community for burned area mapping.
- Image pre-processing (atmospheric, geometric, radiometric correction) and creation of water and cloud masks is vital prior to applying the indices to avoid confusion with areas burned (Weirather *et al.*, 2018).
- The right choice of sensor, the radiometric, temporal, and spatial resolution, as well as the appropriate assessment scheme (timing) are determinants for getting useful results for fire and forest managers.

- Silvicultural and fire suppression management practices need to be reconsidered for creating higher fire-resilient forests (e.g., thinning, tree species selection, prescribed burning) in the future.

5.2. Wildfires in Mongolia

Apart from timber logging, insect pests, livestock grazing, and climate change related phenomena, wildfires are the major influencing factors on the landscape ecosystems of the taiga and the forest steppe (Altrell and Erdenejav, 2016, Dulamsuren *et al.*, 2011, Dulamsuren *et al.*, 2014, Goldammer, 2013, Klinge *et al.*, 2020). Rising levels of wildland fire incidents, increasing temperatures, and land use change have coincided in many forested regions, making it difficult to parse causes of elevated fire activity (Klinge *et al.*, 2014). According to a report by Byambasuren (2018) wildfires account for more almost 90% of forest degradation, and as such, also thwart all efforts to contribute to the global programme of reducing carbon emissions (see also REDD+[18] programme of the United Nations (www.un-redd.org)). High intensity forest fires can be a major cause for the degradation of the taiga forests and bear the potential to irreversibly induce a shift to the steppe grassland ecotone (Mühlenberg *et al.*, 2004). Between 2011 and 2013 around 1 Mio. ha of forested land were affected by wildfires (Ministry of Environment and Tourism, Mongolia, 2020). Crown fires are known to be the most destructive form, whereas fires of low intensity (ground fires) promote the growth of fire tolerant tree species such as larch (Goldammer and Furyaev, 2010). Nonetheless, not only the intensity of the fires greatly determine the composition of the vegetation, but also the sequence of the occurrence. Goldammer and Furyaev (2010: 168–185) report intervals ranging from 10 to 33 years for the Western part of Siberia, whereas Byambasuren (2011) found intervals of 11.6 years for parts of the Khentii mountains in Mongolia. Fire regimes with short intervals apparently are favourable for pioneering tree species, like birch and poplar (Makoto *et al.*, 2007, Wyss, 2007). In Mongolia, human-induced fires represent about 95% of all wildfires recorded, with lightning being the major natural cause (Byambasuren, 2018, Goldammer and Furyaev, 2010: 186–190, Schmidt-Corsitto, 2016, Tsogtbaatar, 2004a). Many people in rural areas are accustomed to gathering non-timber products such as berries, pine kernels, firewood, and antlers, and as such tend to leave fireplaces either unattended or not properly put out. Steppe fires, which are laid to extract pasture land, also pose a risk to neighbouring forests, favourable weather conditions provided.

[18] ***R****educing* ***E****missions from* ***D****eforestation and Forest* ***D****egradation*

The following table retrieved from the official National Forest Inventory report (Altrell and Erdenejav, 2016: 85) provides an account on the fire incidents of recent decades:

Table 5-2: Proportion of forest area affected by wildfire, by forest Inventory Region (NFI report, 2016).

Proportion of forest area affected by wildfire, by forest Inventory Region %		
Region	**Recent Wildfire**	**No evidence of Fire**
Mongolia	**18.6**	**81.4**
Altai	1.4	98.6
Khangai	8.3	91.7
Khuvsgul	13.2	86.8
Khentii	34.7	65.3
Boreal buffer zone	13.0	87.0

The Khentii region, where the Thunkel test area is located, shows the largest impact of wildfire with almost 35%. However, above mentioned observations are not based on the wildfire assessment of satellite imagery, but rather on the evidence of burn marks on tree stems found in the inventory sampling plots. Yet, these figures provide a useful clue on wildfire hotspots and potential fire management scenarios.

Most of the forest stands surveyed show marks of historic or recent wildfire events and thus have a substantial impact on the species composition, the growth rate, and the structure of the forests (Goldammer and Furyaev, 2010: 186, Gradel, 2017, Gradel and Mühlenberg, 2011). Gunin *et al.* (1999) suggest regeneration periods of up to 200 years to be realistic because of the short vegetation period. Even-aged, huge forest stands show a typical low-structure type induced by high intensity fires (Goldammer and Furyaev, 2010: 1–20). Tree species such as birch, poplar and larch are to be found in these light taiga forests. In contrast, gap-driven disturbance regimes are characteristic for dark taiga (Siberian pine, Siberian spruce) areas featuring a small-scale mosaic of varying tree age, DBH, and tree height (Gradel *et al.*, 2015, Gradel, 2017, Gradel and Mühlenberg, 2011, Schulze *et al.*, 2012). Disturbance intensity has turned out to be an important determinant of interspecific species competition. Fire intensity, but also regeneration and protection potential of the various tree species either favour species such as aspen and birch (coppicing) after stand replacing fires, or are conducive to larch and Scots pine due to their ability to better cope with ground fires thanks to their thick bark. Short intervals of ground fires apparently put a lot of strain on the thin-barked birch, thus giving pine and larch a competitive edge. Yet, soil and crown fires burning with high intensity are also dangerous for thick-barked tree species (Gradel, 2017, Pausas, 2015, Pellegrini *et al.*, 2017). Interestingly, Undraa *et al.* (2015) observed no drastic changes in species composition about 10 years after big fires in the

Central Khangai in 1996 and 2002. According to the authors, grazing seemed to have a much larger impact on larch regeneration than long-term effects of wildfires.

Climate also plays a pivotal role in driving disturbance regimes. According to Dulamsuren *et al.* (2011) extremely low temperatures and absent precipitation during the winter season seems to favour larch, since these climatic conditions keep insect populations low. In addition, sufficient rainfall towards the end of the vegetation period of the previous year and in the initial phase of the growing season of the current year proved to be particularly important for the growth increment of the trees. Current reports of the IPPC suggest rising temperatures for the main part of Mongolia, with grave impacts on the productivity of the light taiga species, and with an increasing rate of wildfires in the future (IPCC, 2020, Jolly *et al.*, 2015, Ministry of Environment and Green Development of Mongolia, 2014, Ministry of Environment, Japan, 2014). As water availability and soil moisture are higher in the dark taiga ecosystems, these higher elevations are expected to be less affected by a changing climate. After all, with the thaw of the permafrost as a dwindling water resource, even the dark taiga vegetation will have to tune in, and adaption strategies in terms of forest management need to be devised in general (Goldammer and Furyaev, 2010: 366–371).

Fire detection, monitoring, and reporting in Mongolia

Reliable data concerning the occurrence of wildfires have been on hand for North America, Canada, and Scandinavia for many years. As for Mongolia information on wildfires are

published through governmental platforms such as the website maintained and populated by the Mongolian Ministry of Environment and Tourism (see Figure 5.6 below). However, individual checks convey the impression, that the fire reporting and/or publishing system seems rather dubious. In 2017 I witnessed at least six huge fires in the Thunkel area, but only one incident was being indicated on the above-mentioned website for the whole of the Selenge province.

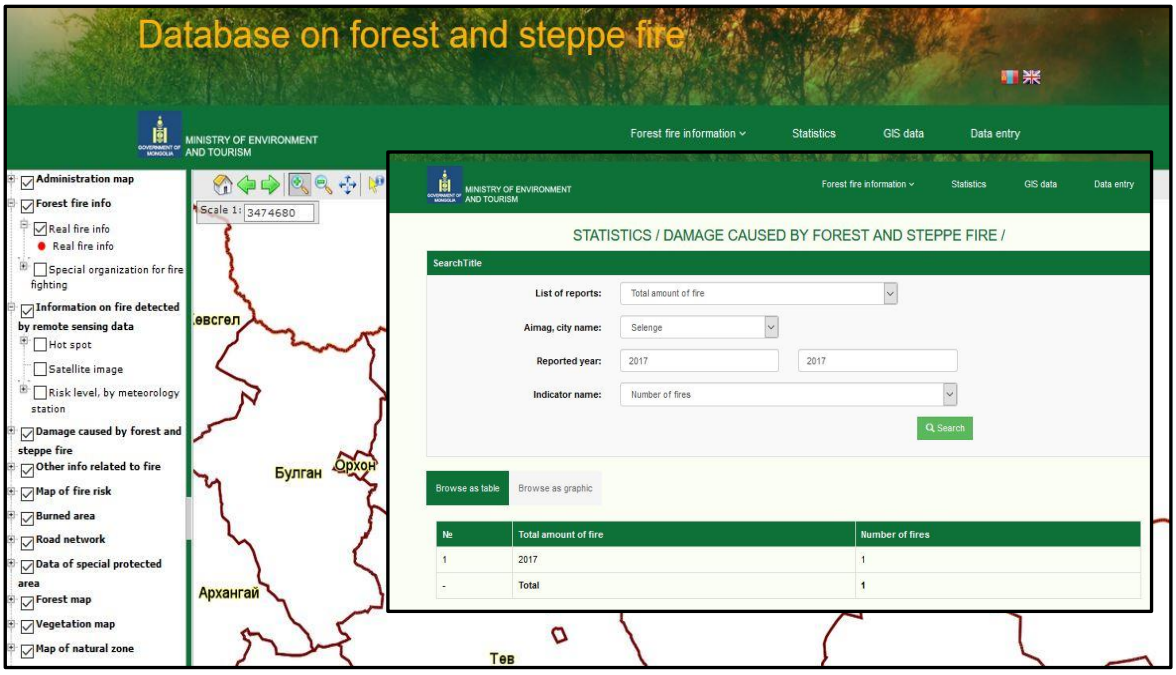

Figure 5.6: Mongolian database on forest and steppe fire – data retrieval in September 2020 (source: Ministry of Environment and Tourism (www.mne.mn), Ulaanbaatar, 2020).

Retrieval of data from the FIRMS (MODIS satellite data) platform for the specified year however suggests many more fire hotspots (see also chapter 5.1 for FIRMS).

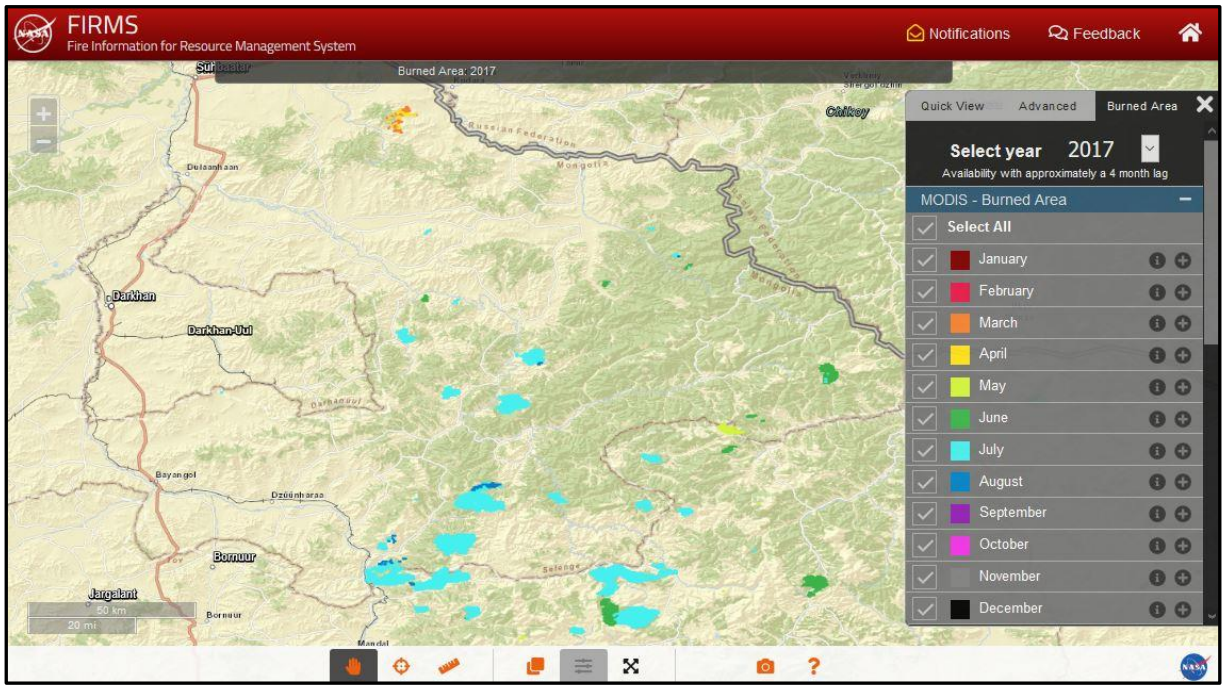

Figure 5.7: Retrieval of wildfire occurrences for the Selenge Aimag for the year 2017. Source: FIRMS database, 2020.

Pursuant to the FIRMS database for the period from 2000 to 2019 the Selenge Aimag was hit by destructive wildfires almost every year, with 2009 being one of the most salient. The database also indicates the season the wildfires occurred – for the Thunkel area in 2017 it was July and August, being in line with weather reports highlighting an extremely dry summer. The landscape around Thunkel (including the GIZ school forest as test area) has been affected very hard in the years 2002, 2008 and 2017, with a number of areas having been scorched twice within one decade. These extremely short fire intervals hardly leave any time for the vegetation to recover, thus causing irreversible damage to the forest resources. The Global Forest Watch (GFW) data repository (www.globalforestwatch.org /map) exhibits a loss of forest cover for the Selenge Aimag for the 2001-2019 period of nearly 140,000 ha (i.e., 12% of total tree cover). However, the indicated loss can be attributed to a variety of causes, such as wildfires, logging activities, and land degradation (for details see also GFW website).

According to the UN-REDD report 2018 (UN-REDD, 2018) more than 52,000 ha of forest land were lost in Mongolia due to wildfires and other disturbances in the period between 2005 and 2015, leaving another 1.4 Mio ha degraded due to illegal logging and grazing activities (around 35% of livestock graze in or near forests). In 2017 more than 80,000 ha of forest are reported to have been torched. Once again, the presented figures have to be seen in the light of different definitions of the term forest and the data used for analysis. GFW indicates the tree cover being 3.55 Mio ha for the entire country of Mongolia, whereas the UN-REDD report claims the forest area comprising 14.2 Mio ha. The general trend to surrender forest land has been confirmed by a study undertaken by Teusan (2017), who analysed MODIS and Landsat imagery for the 2000-2015 timescale. He observed severe wildfires particularly in the years 2000, 2003, and 2007-2009, with a substantial decline of the Scots pine for the Selenge Aimag. He also found that fire incidents predominantly take place in April and May (when soil moisture reaches a low), with another peak in September, when summer rainfalls recede. This observation has been generally supported by Wyss (2007), who analysed MODIS and NOAA imagery for the period from 2000 to 2005. By visually comparing the results with Landsat ETM+ scenes he found out that fire delineation with MODIS matched with a 70% accuracy, and NOAA only with a mere 20% accuracy, strongly indicating that MODIS sensors seem to be much better geared for fire detection. Since forests are mainly to be found to occupy northern slopes, the fuel load is much bigger and as such generate a higher fire risk with higher fire intensity than the steppe ecosystems on southern slops. MODIS sensors are only able to detect fire hotspots beyond a certain temperature threshold (i.e., greater than 10 Megawatt), and thus primarily record forest fire activities. The assessment of the fire incidence – altitude relationship also revealed, that forests at lower altitudes are more prone to wildfires in spring (higher temperatures at the

slope foot) than the dark taiga at higher altitudes due to the extended snow melting period. Teusan (2017 111-115) does not fall short in mentioning, that: (i) the MODIS sensors can only detect hot fires with a huge extend, (ii) a low sun angle can potentially impede the classification of the satellite imagery (i.e., fire severity on Northern slopes gets easily underestimated) , and (iii) areas classified as “burnt” may as well indicate dead wood caused by insect attacks or drought, since the spectral signatures show many similarities. Time line analysis of the ICC NOAA imagery reflects a steady positive trend in fire incidents since the 1980s, with a sharp increase of cases in the 1990s associated with higher intensities and longer duration (Wyss 2007). Fire hotspots have been located at the Aimags Bulgan, Tov, Selenge, and Khentii, showing a clear association with socio-economic activities, particularly along the railway line connecting Ulaanbaatar with the Russian border. However, the results of the ICC have to be consulted with caution – for the year 2000 a total of 7.9 Mio ha was indicated for the whole of Mongolia, whereas Goldammer (2002) calculated an effected area of 2.9 Mio ha for the same period. In contrast to the general observation of rising fire incidents over the last few decades, Hessl et al., 2016 observed no change in fire return intervals post-1900. They analysed 20 multi-century fire scar chronologies (464 fire scar samples) to further conclude that drought remains an important driver of fire, and that ‘…limited fire activity in recent decades may be due to the coincidence of drought and intensive grazing that have synergized to reduce fuel continuity and fire spread’.

Fire-fighting infrastructure and activities in Mongolia

Since the early 1950s the Mongolian government has been pursuing an aggressive policy of wildfire suppression. In 1969 the Mongolian Fire Protection and the Aerial Patrol Service were founded to work efficiently until the collapse of the socialist system in 1992. With the grounding of the Aerial Patrol Service in 1992 and the substantial decline of financial aid the Mongolian fire-fighting system came to a halt, causing wildfire damages to soar (Goldammer, 2013: 69–72, Wyss, 2007: 39). Even with recent incentives of the FAO or the GIZ (‘Integrated Fire Management Project’), there has been no presentable improvement of the situation (Schmidt-Corsitto, 2017, Teusan, 2018: 113–115). Even though the Mongolian forest act (Articles 18 and 19) demands that no fires are to be started from 20 March until 10 June, there is a severe lack of financial and infrastructural resources to monitor, survey, and prosecute any misdemeanour. Early warning systems have been established on a local scale, yet, communication has turned out to be an incumbent problem. As early as the late 1980s the Mongolian government realised that remote sensing technology has proven to be a useful tool for detecting wildfires, especially in areas, which

are difficult to access. In 1987 a satellite receiving station (Information and Computer Centre - ICC) for NOAA/AVHRR data was established at Ulaanbaatar to provide the relevant fire-fighting and managing institutions with timely and accurate information on fire incidents, and to further work out fire risk scenarios. Once again, getting the information to the people in the field remains an enormous challenge. An essential step towards resolving the major issues was undertaken by establishing the Fire Management Resource Center – Central Asia Region (FMRC-CAR) in 2015 based at the National University of Mongolia (NUM) at Ulaanbaatar. Being a subsidiary and partner of the Global Fire Monitoring Center (GFMC), hosted by the Fire Ecology Research Group, Max Planck Institute for Chemistry, c/o Freiburg University, Germany, the training of people and the knowledge transfer on fire ecology and fire-fighting is considered the domain of this institution. With the recent appointment of Dr. Oyunsanaa Byambasuren as General Director of the Department of Forest Policy and Coordination at the Mongolian Ministry of Environment and Tourism (MET), an experienced fire ecologist has been endorsed the opportunity to considerably improve the Mongolian wildfire management scheme.

Synopsis of this section:

- Causes of forest fires and their propagation are difficult to designate to a single factor, but can be seen as a coincidence of: rising temperatures, drought, changing precipitation patterns, thawing permafrost, human action (negligence, illegal logging, hunting and gathering), expanding grazing activities, lack of trained people and infrastructure, inadequate communication.
- Wildfires significantly affect forest structure and tree species composition. Stand replacing fires occurring in short intervals seem to favour pioneering tree species (e.g., birch), whereas thick-barked species (e.g., larch) are more resilient to ground fires.
- Fire suppression activities can induce higher fire risks in the long term (e.g., accumulation of fuel load).
- The increase of severity and interval of fires during the last few decades has been discussed controversially in the scientific community, however, with a few indications of a positive trend linked to climate change.
- Main forest fire seasons are late spring and late summer.
- Forest fires have been part of the ecosystem for many millennia and as such been shaping the landscape.
- Near-real time fire detection has become operational through the MODIS Rapid Response System and the associated Web Fire Mapper.

- The recently established Fire Management Resource Center – Central Asia Region (FMRC-CAR) at Ulaanbaatar helps to address shortcomings in training of managing and fire-fighting personnel.
- Despite all efforts, the lack of infrastructure and proper equipment, the low number of professionally trained people in combination with deficits in communication still result in an impaired fire management in Mongolia.

Rest of page intentionally left blank

6. Unmanned Aerial Vehicles (UAVs)

For the last couple of years, the acronym ’UAV’ (Unmanned Aerial Vehicle; with the terms ‘UAS’ and ‘drone’ being used interchangeably) has become the new buzzword in the remote sensing community per se. This hype is not only being reflected in the sales figures of the systems, but also in the various new application fields and the skyrocketing numbers of publications. The following sections provide some fundamental knowledge on the technical advances of unmanned aerial vehicles, their potential in various applications, image acquisition and processing workflows, as well as regulatory related issues. For the sake of simplicity and to remain consistent with a large proportion of the literature published, the term UAV is being used interchangeably with all other denominations related to unmanned aerial vehicles.

6.1. Definitions and classifications

The technical advances in robotics and computer systems have created new opportunities regarding remote sensing operations and also have acted as an impetus for the development of novel data analysis approaches. The advent of unmanned aerial vehicles seems to have heralded a new era of the acquisition of more timely data with unprecedented spatial resolution, however, without putting a pilot’s life at risk. Initially earmarked for the so-called ‘D3 operations’ (i.e. dirty, dull and dangerous), remotely-piloted aircraft systems (**RPAS**) have shaken the traditional remote sensing markets providing an almost unlimited variety of applications, in the civilian environment in particular (Salamí *et al.*, 2014).

The term **UA** (Unmanned Aircraft), as well as the acronym **UAV** (Unmanned Aerial Vehicle) in a narrow sense refer to the air vehicle itself. To distinguish it from the aforementioned, the term **UAS** (Unmanned Aerial System) was coined to emphasise that an aircraft, no matter, if piloted remotely, or flying autonomously, requires a *control station* and *data links* for proper operation (Colomina and Molina, 2014, Gupta *et al.*, 2013). UAS are also known under names, such as ‘**aerial robot**’ and ‘**drone**’, with the latter having been ascribed a rather negative connotation because of the association with military missions (e.g. the deployment of the ‘Predator’ during the Gulf War in 1991) (Eisenbeiss, 2009: 2, Gupta *et al.*, 2013, Sabins, 2020: 225–226, Salamí *et al.*, 2014, Toro and Tsourdos, 2018). The first UAV dates back to 1916 and is known as the beginning of attitude control for automatic steering of an aircraft. The further developments were clearly driven by a military context, but as early as the nineteen-seventies, the potential of UAVs were recognised by research groups (Colomina and Molina, 2014). In particular during the last fifteen years a large number of manufacturers of platforms and sensors have tried to establish their products on the military and civilian markets, leaving the customers with a sheerly unfathomable number of choices. Hence, classification systems for UAVs have been devised as rough guidelines

to bring order into chaos. However, there is no such thing as a unique and universal classification until now (Watts *et al.*, 2012).

These days, most of the categories are based on size, weight, operating range, endurance, and aerodynamics. Others also consider the nature of propulsion (powered, non-powered, combustion engines, electrical, fuel cells, solar power, etc.), payload and being lighter-than-air (e.g. blimps) or heavier-than-air (Colomina and Molina, 2014, Eisenbeiss, 2009: 34–37). Categories range from 'high altitude long endurance' (HALE) platforms resembling medium-sized commercial airplanes to 'nano air vehicles' (NAV) with a size of a beetle (own observations).

Figure 6.1: Example for a HALE UAV (General Atomics MQ-1 'Predator' - left) and a NAV (AeroVironment 'Hummingbird' - right). Source: manufacturer's photos.

The bulk of UAVs is represented by the categories 'Mini UAV' (MUAV), with payloads below 20kg and operating ranges of about 30km, and the so-called 'Micro UAV' (MAV), featuring a weight below 2kg and operating at low altitudes and short ranges (Colomina and Molina, 2014, Jeziorska, 2019). Another popular way of categorising UAV platforms is the distinction between: 'fixed-wing' (requiring a runway or catapult for take-off and landing), 'rotary-wing' (vertical take-off and landing), 'blimps' (airships and balloons), and 'flapping-wing' (morphing small wings, inspired by birds and insects) (Büchi, 2018: 2–4, Gupta *et al.*, 2013, Petrie, 2013, Sabins, 2020: 227–229). More details on the various platforms and the sensoring systems are provided in the subsequent section (6.2.).

6.2. Platforms, navigation and sensors

Leaving aside powered airships, blimps, balloons, parafoils and tethered kites, the majority of UAVs are based on the airframes fixed-, and rotary-winged aircraft. Based on the specific requirements on a survey, a choice has to be made for the best platform – sensor compound. Rotary-based versions (single, or multiple rotors) have become the favoured pick, whenever hovering capabilities are required, the survey area is not bigger than a few hectares, and taking-off and landing sites are confined. Traditional fixed-wing platforms are much better suited for large-scale operations (e.g., 1 km^2), when high endurance and energy efficiency are paramount. However, these platforms call for very well-trained

personnel and sufficient space for operation. Sometimes even specific equipment such as launching catapults and salvaging devices are prerequisites. A combination of fixed-, and rotary-winged systems (hybrid), like the Skyports, the ATMOS Marlyn, or the Hi-Tec Trinity, are ready for the market, however, are difficult to manoeuvre due to the tilted rotor constellation. The figure below depicts some of the popular fixed-winged products with a flying wing, or a conventional fuselage design.

Figure 6.2: Examples of a fixed-wing UAV design: (a) QuestUAV Q-Pod; (b) SenseFly eBee; (c) Trimble UX5; (d) MaVinci Sirius Pro; (e) PrecisionHawk Lancaster (source: Padua, 2017).

Rotary-winged platforms can be single-rotor driven with a high payload capacity, such as the Mikado Logo 600, feature coaxial rotors with two contra-rotating rotors (e.g., DraganFlyer X6), or are fitted with multiple rotors, requiring no specific pitch control. Manufacturers of the latter are legion, like DJI, Yuneec, Aibotix, HiSystems, Microdrones, Droidworx, and Topcon, just to name some of the more popular brands. Examples are given below (Figure 6.3).

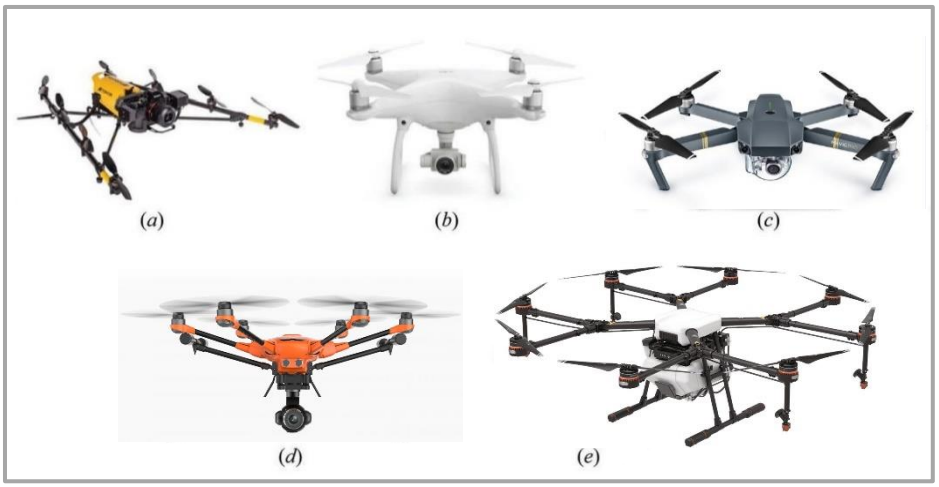

Figure 6.3: Rotary-winged UAVs: (a) Topcon Falcon 8 (octocopter); (b) DJI Phantom 4; (c) DJI Mavic (quadrocopter); (d) Yuneec H 520 (hexacopter); (e) DJI Agras MG 1S (octocopter with mounted spraying tank for pesticides). Source: manufacturer websites.

The main merits and demerits of the major platform systems are detailed in the following table (6-1).

Table 6-1: (Dis)advantages of different platforms (source: Tmusic, et.al., 2020, and Jeziorska, 2019).

Platform	***Advantages (+) and disadvantages (-)***	***Flight time / coverage***
Rotary-wing	+ flexibility and ease of use + stability + possibility for low flight heights and low speed + possibility to hover + small landing/take-off zone + greater manoeuvrability - lower area coverage - wind may affect vehicle stability	Flight time typically 20-40 minutes Coverage 5-30 x 10^3 m^2 depending on flight altitude
Fixed-wing	+ capacity to cover large areas + higher speed and reduced time of flight execution - take-off and landing require dedicated space, equipment and experienced pilot - fast vehicle may have difficulties in mapping small areas or establish sufficient image overlap	Flight time up to hours Coverage >20 km^2 depending on flight altitude
Hybrid VTOL (Vertical Take Off and Landing)	+ entails all advantages of rotary and fixed-winged systems - complex mechanical system (tilting rotors); difficult to operate	Flight time up to hours, but less than fixed-winged systems Coverage similar to fixed-winged system

The *navigation* of an aerial platform consists of the calculation of its location, velocity, as well its orientation (attitude). This process relies on input from various sensors and subsystems to provide specific output for the control system, which in turn determines the required signals for the engines and control surfaces (pitch, roll, yaw). In addition, those internal sensors make certain, that semi-, or even fully automatic flying mission can be pursued and that the platform can react adequately in situations, when immediate intervention is required (e.g., wind gusts, collision with other objects). The so-called inertial navigation system (*INS*) - often also referred to as inertial measurement unit (*IMU*) - uses motion (*accelerometers*) and rotation sensors (*gyroscopes*) to continuously calculate the direction and speed of movement of an aerial platform without requiring external references. More robust and accurate (i.e., more expensive) systems are augmented by additional sensors, such as *barometric altimeters* and *magnetic sensors* (compasses). Most of the relatively inexpensive UAVs are fitted with low sensitivity INS sensors and are notably subject to integration drift, resulting in progressively larger positional errors. INS inaccuracies can be compensated for by integrating highly accurate GPS receivers (e.g. RTK – Real Time Kinematic), thus allowing direct georeferencing of aerial imagery without the need for ground control point measurements (Büchi, 2018, Sabins, 2020: 229). The achievable high positional accuracies naturally come with a big price tag. Sensor fusion (INS) technology has become available through manufacturers of autopilot devices, like

Pix4, MicroPilot, Euroavionics, ArduPilot, and Pixhawk (Colomina and Molina, 2014, Galar and Seneviratne, 2020: 141–142).

Ground control stations represent another crucial part of an unmanned aerial vehicle system and can be considered an interface with human intelligence. They are either stationary or mobile equipment to command and monitor the aircraft. The most predominant technology for the wireless communication is based on Wi-Fi electronics transmitting at 2.4 GHz. The two-way communication between ground control (pilot) and aerial platform ensures the provision of the pilot with real-time information on the UAVs performance and position (e.g., battery status, flying altitude, bearing) in a virtual cockpit. In addition, new mission parameters can be uploaded and live video streams form the onboard camera monitored (Colomina and Molina, 2014, Galar and Seneviratne, 2020: 141–144, Salamí *et al.*, 2014).

Sensing payloads have to be chosen very carefully and tailored according to the required goal of a flying mission (sensing bandwidth, accuracy, resolution, etc.) (Komárek *et al.*, 2018, Pádua *et al.*, 2017, Petrie, 2013, Tmušić *et al.*, 2020). Thanks to the advances in minimisation of the once very bulky and heavy sensors, passive as well as active sensing systems, ranging from visible, to Near Infrared (NIR) up to the Thermal Infrared (TIR) and microwave systems can be integrated into UAV platforms these days. The remote sensing community has benefited from mass-markets offering off-the-shelf products, as well as from markets especially geared for the UAV industry. The following table (6-2) lists a selection of some of the more popular sensing systems. However, sensing markets develop so rapidly, that it is almost impossible for the consumer (user) to keep up with. Although considerable progress has been made with many sensor types, some issues have not been resolved. Hyperspectral cameras and LiDAR systems still require a big lifting capacity of the aerial platform and costs are still enormous (up to 100,00 Euros). There are also trade-offs between performance and the size of the systems (e.g. low resolution of TIR cameras), and UAV SAR radar systems still represent a miniscule market segment struggling with integration hitches (Catapano *et al.*, 2020, Colomina and Molina, 2014, Ludeno *et al.*, 2018, Manfreda *et al.*, 2018).

Table 6-2: Common sensing payloads for UAVs (source: manufacturer's website).

Sensor type	Manufacturer / Model	Resolution	Weight	Spectral range	Range
Small and medium format visible band cameras	Sony Nex-7 Hasselblad H4D-60 Sony α 6600 Lumix DC-GX9	24.3 MPix 60.0 MPix 24.2 MPix 20.0 MPix	0.35 kg 1.80 kg 0.53 kg 0.45 kg	450-750 nm 450-750 nm 450-750 nm 450-750 nm	
UAV mounted visual band cameras	DJI Zenmuse Xz SenseFly S.O.D.A Yuneec CGO3+ DJI Hasselblad L1D-20	24.0 MPix 20.0 MPix 12.0 MPix 20-40 MPix	0.45 kg 0.11 kg 0.25 kg 0.07 kg	450-750 nm 450-750 nm 450-750 nm 450-750 nm	
UAV multispectral cameras	Tetracam Mini MCA-6 Parrot Sequoia MicaSense RedEdge	1.3 MPix 1.3 MPix 1.3 MPix	0.70 kg 0.07 kg 0.18 kg	450-1050 nm 550-790 nm 475-840 nm	

Sensor type	Manufacturer / Model	Resolution	Weight	Spectral range	Range
Hyperspectral cameras for UAV	Headwall Nano-Hyperspec Cubert Ultris 20 Quest Hyperea 660 C1 Resonon Pik L	Not available 1600 px 1024 px 900 px	1.20 kg 0.35 kg 1.44 kg 0.60 kg	400-1000 nm 450-850 nm 400-1000 nm 400-1000 nm	
Thermal cameras for UAV	FLIR Tau 640 Optris PI400 Thermoteknix MIRICLE 370K Yuneec E10T	640x512 px 382x288 px 640x480 px 640x512 px	0.11 kg 0.32 kg 0.17 kg 0.37 kg	7.5-13.5 µm 7.5-13.0 µm 8.0-12.0 µm 8.0-14.0 µm	
Laser scanners for UAV	Harris Aerial Puck Velodyne HDL-32 E RIEGL VUX 240 YellowScan Mapper II		2.00 kg 1.30 kg 3.80 kg 2.10 kg		100 m 100 m 1400 m 75 m
Radar sensors for UAV	Echodyne EchoFlight Pulson P440 radar system IMSAR NanoSAR B		0.81 kg 0.04 kg 1.58 kg	24.45-24.65 GHz 3.1-4.8 GHz	6000 m >750m on UAV 1000 m

Off-the-shelf consumer cameras often feature low quality lenses and sensors resulting in effects such as barrel or pincushion distortion, image noise, vignetting and scatter (Carbonneau and Dietrich, 2017, James and Robson, 2014). However, with the correct choice of camera settings, good illumination conditions, and flying parameters (e.g., speed), a high number of these detriments can be remedied. In addition, sophisticated image analysis and photogrammetry software exploiting Structure from Motion (SfM) and Multiple ViewStereo (MVS) algorithms (for details also see chapter 4.6.) can handle even low quality imagery for mapping and monitoring purposes with acceptable yields (Jeziorska, 2019, Tmušić *et al.*, 2020) . In the following figure (6.4)some examples of popular sensing systems are provided.

*Figure 6.4: Popular imaging systems: **RGB**: (a) GoPro Hero3; (b) Canon G9X; (c) Panasonic Lumix DMC; (d) Sony Alpha 7; **NIR**: (a) Canon S110; (b) Panasonic Lumix 7; (c) Fujifilm X-M1; **Multispectral**: (a) Parrot Sequoia; (b) multiSPEC 4C; (c) Tetracam ADC; (d) MicaSense RedEdge; **LiDAR**: (a) Routescene LiDAR Pod; (b) Yellowscan Mapper; (c)Velodyne PUCK. Source: manufacturer's website and Padua, et.al., 2017.*

The following list shows in brief some potential application areas, grouped by sensor size, to facilitate sensor choice (Adão *et al.*, 2017, Barbedo, 2019, Cracknell and Hayes, 2007: 281–285, European Space Agency, 2009: 171–175, Howard, 1991: 311–318, Jones and Vaughan, 2010: 297–305, Lillesand *et al.*, 2015: 632–638, Manfreda *et al.*, 2018, Pádua *et al.*, 2017, White *et al.*, 2016):

- RGB: biomass monitoring, vegetation identification and segmentation, dead wood inspection, tree age class definition.
- Thermal: water status assessment, fire detection, heat stress in plants.
- Multispectral: vigour maps (vegetation indices), biomass estimation, pest detection, species classification, nutrient deficiency estimation.
- Hyperspectral: biomass estimation, species discrimination, water status assessment, early detection of plant diseases, chlorophyll estimation.
- LiDAR: forest canopy mapping, creation of terrain models, forest inventory and structural properties, tree parameter assessment (e.g., tree height, crown diameter, crown height).
- Radar (can penetrate clouds, rain, vegetation, soil): soil moisture assessment, species discrimination, land cover (change) mapping, disaster evaluation, DEM generation.

In addition to above mentioned appliances, UAVs equipped with very specific sensoring systems have already been tested and proved successful. Sensors such as particle counters, radiation gauges, gas detectors, and spectrometers are used to measure gas emissions from volcanoes and power plants, to assess the distribution of aerosols, and to gauge radionuclide contamination of nuclear power plants and detect ground-based radiation anomalies in naturally occurring geological features (Pajares, 2015). In GPS denied environments (i.e. indoors, between buildings, etc.) specific sensors employing *optical flow*[19] technology have become state-of-the-art for navigation and collision avoidance (Chao *et al.*, 2013, Ding *et al.,* Raudies, 2013, Tchernykh *et al.*, 2006). This concept was first introduced by an American psychologist to describe the visual stimulus inherent to animals to navigate through any scenery. In more simple terms this specific field of robotics attempts to mimic the movement of flying insects in a visual scene and as such contributes to safe operation of the UAV.

A detailed account on UAV applications can be found in chapter 6.3.

[19] For various definitions see also Raudies, 2013

6.3. Applications

The spatio-temporal richness of UAV systems make the application so transformative (Manfreda *et al.*, 2018). In particular, when immediate response and live imagery or video footage is required in specific situations (e.g., accidents, disasters), UAVs can be deployed very rapidly and without putting the operator's life at peril. In addition, UAV operations can be conducted in fairly adverse weather (some UAVs are weather proof) for collecting data in cloudy or hazy conditions. Another big advantage compared to traditional aerial or satellite image missions is the capability of specific timing and frequent acquisition of data (e.g., change detection, plant phenology), provided that flying conditions are suitable. More than a thousand peer reviewed studies and manifold projects make it almost impossible to provide a complete referencing of the subject. Thus, the following list of potential and proven applications is by no means meant to be exhaustive:

- Policing duties
- Traffic spotting
- Fisheries protection
- Pipeline survey
- Wind and solar power plant inspection
- Precision agriculture
- Surveillance
- Military operations
- Disaster management (e.g., spills, avalanches)
- Archaeology (site mapping)
- Cadastral mapping
- Geomorphological assessments
- Façade inspection of buildings
- Search and Rescue (SAR)
- Fire fighting
- Communications relay
- Environmental monitoring
- Aerial mapping
- Meteorology
- Wildlife management
- Events film coverage
- Forestry
- Engineering
- Soil erosion assessment
- Land cover mapping
- Volume determination of landfills
- Contamination missions
- Archaeology.

In many cases the smaller, cheaper and easier-to-operate platform paradigm has gained an increasing appreciation in the remote sensing community (Colomina and Molina, 2014). An interesting twist and recent feature is the deployment of UAV swarms in the context of SAR operations, disaster management, communications improvement and environmental monitoring (Campion *et al.*, 2018, Tahir *et al.*, 2019). In addition, the integration of multiple imaging sensors onto the aerial platform also offers new application opportunities (Grenzdörffer and Niemeyer, 2011, Pajares, 2015, Wierzbicki, 2018). As examples of recent environmentally related UAV missions, work has targeted (a) land cover and rangeland

mapping (Akar, 2017, Laliberte *et al.*, 2011); (b) vegetation phenology and health (Dell *et al.*, 2019, Ludovisi *et al.*, 2017, Pajares, 2015); (c) agriculture (Daponte *et al.*, 2019, Urbahs and Jonaite, 2013); (d) invasive species infestation (Alvarez-Taboada *et al.*, 2017); (e) disaster mapping (Stone *et al.,* 2017); soil erosion (James R. Frankenberger *et al.*, 2008); and change detection (Niethammer *et al.*, 2012). UAV applications in the forestry sector (as is in part focus of this thesis) have reached such big numbers, with publications being abundant, that an entire chapter (6.8.) is dedicated to this subject.

Future trends will certainly see more of the fusion of various sensors and the collaboration and coordination of swarms of UAV platforms. In particular with advances in battery life (i.e., increased flying times) and a legally sound integration of UAVs into air space, there will be virtually no limits for the potential application of this technology. First trials in areas such as crop pollination and traffic control sound quite promising (Pajares, 2015). Miniaturisation of UAVs ('Micro-drones') also hold great promise for a variety of operations. With a rising awareness of UAVs in the pubic, as well as in the industry, the annual growth rate in the UAV remote sensing market will certainly see a sharp increase. However, as has happened in other areas of remote sensing, the current hype is expected to also lead to some disillusionment, or a rather a level-headed dealing with emerging new technologies. In addition, especially concerning the proliferation of AI integrated algorithms in sensor and data analysis, more discussions and reconciliation is needed with respect to 'big data' issues and the protection of the privacy of individuals.

6.4. Regulations and organisations

In the last few years, the booming UAV market has increasingly induced issues concerning personal rights, but also air traffic safety. The 'see – and – avoid' and 'see – and – be - seen' routines once developed for visual flight rules are not deemed practical anymore, since UAVs with a size of less than one meter, flying at high speeds, cannot be detected early enough to avoid collisions. Thus, there's been many initiatives to get UAVs integrated into air traffic under the 'Sense and Avoid' strategy (see also chapter 6.4. for regulatory requirements). Technology for operation in shared airspace asks for: detect conflicting air traffic, determine right of way, analyse flight path, manoeuvre, and communicate (Gupta *et al.*, 2013, Yu and Zhang, 2015). As yet, only systems such as TCAS (Traffic Alert And Collision Avoidance System) engineered for commercial air traffic seems to be meeting the technical and regulatory requirements. A great variety of sensing systems based on microwave, radar, laser, acoustic and thermal technology bear the potential of becoming perfect candidates for 'Sense and Avoid' (Orefice *et al.*, 2010, Skowron *et al.*, 2019). As of now, UAV manufacturers such as DJI and Yuneec offer anti-collision sensors in their

portfolio, however, there's still a long way to go for getting UAVs perfectly integrated into air traffic.

The integration of UAV operations into existing air traffic demands for meticulous procedures to ensure safety and ease of use. As such, a lot of technicalities for certification and commercialisation of unmanned aerial vehicles need to be considered and harmonised by a large group of stakeholders and contributing agents (Colomina and Molina, 2014). Regulations are galore as are actors and initiatives to achieve acceptable standards. In the USA, representing one of the biggest markets and drivers for commercial UAVs, the Federal Aviation Administration (FAA – www.faa.gov) issued specific rules in June 2016, which are updated at intervals (Federal Aviation Administration, 2016). Within the federal system of Germany, the detailed regulation of flights by UAVs and the related permissions (if required – see below) is given by the 'Niedersächsische Landesbehörde für Straßenbau und Verkehr' as the authority in charge for Lower Saxony affairs (Niedersächsische Landesbehörde für Straßenbau und Verkehr, 2019). As a subordinate authority it acts on behalf of the Federal Ministry of Transport and Digital Infrastructure (BMVI) located in Berlin. It specifies the conditions under which flights can be made (see also the relevant regulations such as LuftVO (Luftverkehrs Verordnung – Air Traffic Regulation), LuftVG (Luftverkehrs Gesetz – Aviation Act) and LuftVZO (Luftverkehrs Zulassungs Ordnung – Air Traffic Admission Regulation)). In broad terms, flights are only allowed below 100m above ground under line-of-sight conditions (see also Figure 6.5 below). To enter airspace beyond this level, permissions need to be obtained and pilot's qualifications to be presented. UAVs with a take-off weight under 0.25kg are to be labelled (pilot's name and address). For UAVs exceeding 2kg of weight, pilots are required to proof that they are able to operate the unmanned platform safely and also show the relevant technical and juridical expertise. In addition, UAVs piloted beyond the 5kg bracket call for special permissions granted by the concerned air traffic authority. Under all circumstances, the no-fly zones (e.g., airport control areas, residential areas, military facilities, nature conservation areas) stipulated by the International Civil Aviation Organisation (ICAO) and other authorities have to be observed (provided in some flight planning software and apps).

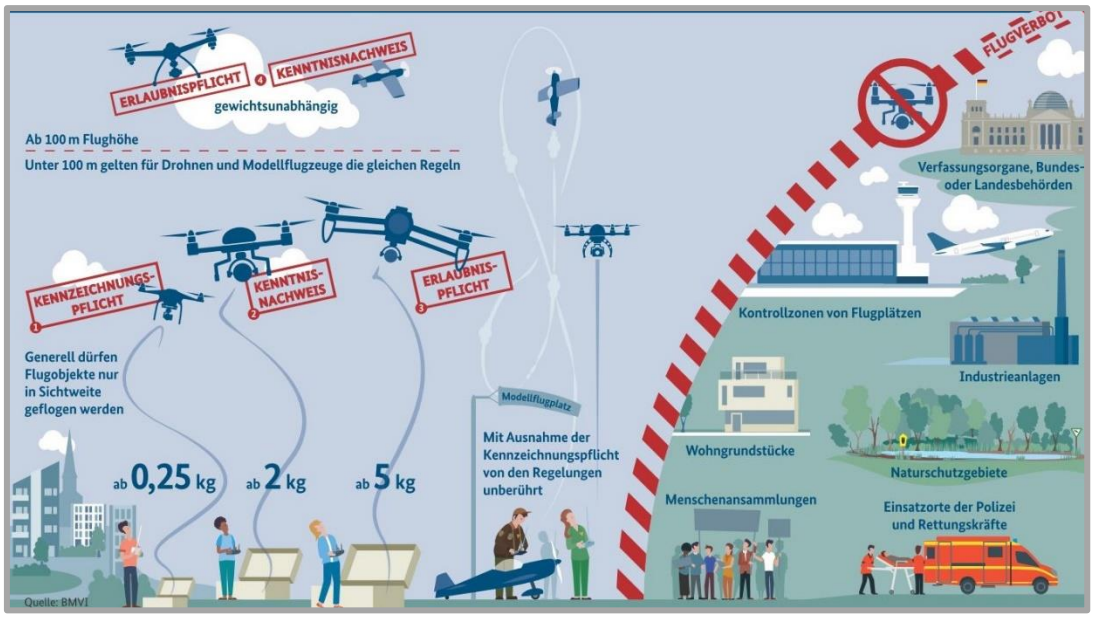

Figure 6.5 Current general regulations concerning UAV operation in Germany (source: Niedersächsische Landesbehörde für Straßenbau und Verkehr).

Regulations pertaining the operation of UAVs in Germany are currently subject to revision, since a generally valid solution for the members of the European Union is under way to harmonise legal provisions (European Union Aviation Safety Ageny, 2018). The new regulations, also permitting flights beyond visual line of sight, are expected to enter into force by mid of the year 2021. Airworthiness (design, functionality, construction and safety) for UAVs is issued by the European Unmanned Systems Centre (EuroUSC). However, new standards are currently being developed by the Institute of flight Guidance (DLR) as commissioned by the EASA.

To the best of the author's knowledge, no specific regulations for the operation of UAVs in Mongolia seem to exist.

A considerable number of organisations have been founded in the last decade to promote UAV markets in terms of technical innovations, possible applications and guidance with respect to regulations and training. Most of the existing platforms work as an interface for industry, academia, and government. The world's largest non-profit organisation, AUVSI (Association for Unmanned Aerial Vehicles International – www.auvsi.org), has committed itself to advance technology in UASs and robotics by bringing together its members from the civil, defence and commercial markets. In addition, AUVSI organises conferences, which have gained a lot of attention in the UAV community. For Europe, the DACH (Association for unmanned aviation – www.uavdach.org), founded by the DLR, Diehl Defence, RUAG and Airbus, shares similar goals with the AUVSI. With the expertise of its members, it also advises regulatory bodies and its subsidiaries such as the European Union

Aviation Safety Agency (EASA). Smaller organisations, like the 'Verband unbemannte Luftfahrt' (www.verband-unbemannte-luftfahrt.de), or the ‚BUVUS' (Bundesverband für Unbemannte Systeme e.V. – buvus.de) cater for clients and users in Germany in particular.

6.5. Image acquisition and mission project workflow

Despite all spatiotemporal merits, UAVs suffer from their operational and processing problems. Image blur due to forward motion, varying resolution caused by variable flying heights, and geometric distortion attributed to camera lens quality shortcomings and inadequate image overlap are just some of the numerous factors, that can affect the derived products (Gerke and Przybilla, 2016, Manfreda *et al.*, 2018, Whitehead and Hugenholtz, 2014). In order to achieve the best possible results of a flying mission, the following best practice factors need to be accounted for: mission and flight planning; sensor configuration and calibration; in-flight data collection; ground control and radiometric calibration; geometric and atmospheric correction; orthorectification and image mosaicking; generation of the desired products (e.g. DSM, CHM) (Manfreda *et al.*, 2018). The following graph (Figure 6.6.) depicts all relevant aspects related to an UAV mission.

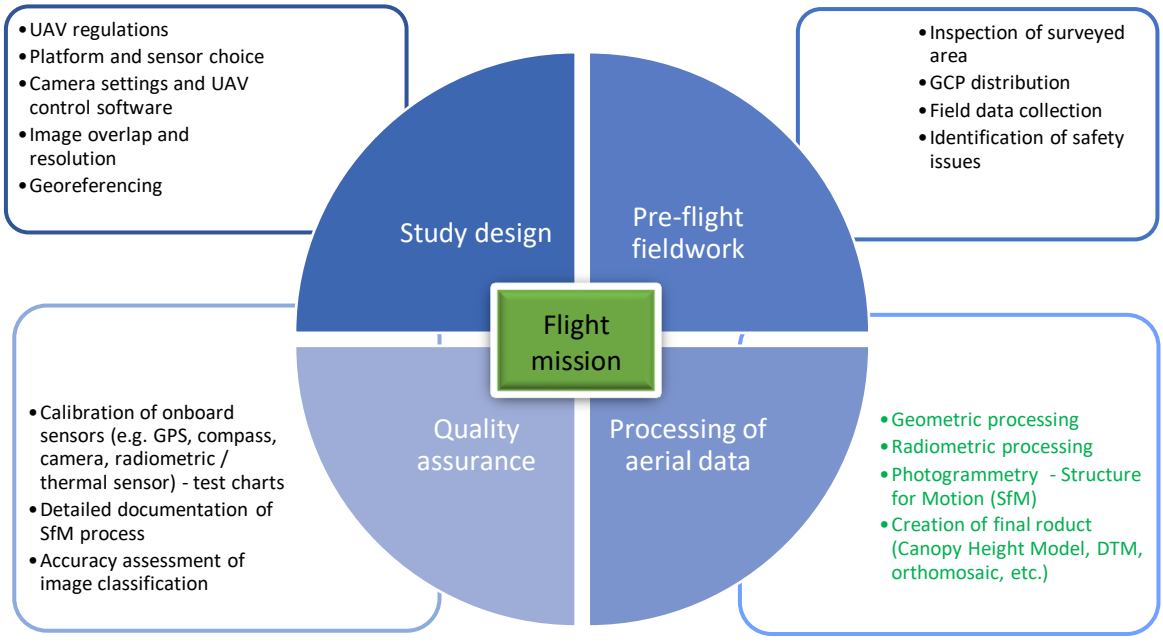

Figure 6.6: Activities involved in UAV mapping and basic workflow (according to: Tmusic, et.al., 2020)

As opposed to stable satellite trajectories and the use of premium sensors and components, off-the-shelf UAV products are geared for the consumer market with a limited lifetime and

relatively low quality standards. However, even with equipment under 1,000 Euros, presentable results can be achieved (e.g. DJI Mavic Air2 (UAV Campus Group, 2020)). Many aspects determine success or failure of an UAV survey and as such compel the user to gain background knowledge on the influencing factors (see Figure 6.7.). These can be simple factors such as flying height, target distribution, sensor choice, or image overlap, but interactions are complex. Although some of those aspects defy the user's control, others require just a bit of fine-tuning and tweaking for satisfactory outcomes. In the subsequent sections the most relevant and feasible options and directives are detailed. Excellent resources to extract information from on how to perform a formidable flying mission are provided by Bosak (2011), Büchi (2018) and Wich and Koh (2018).

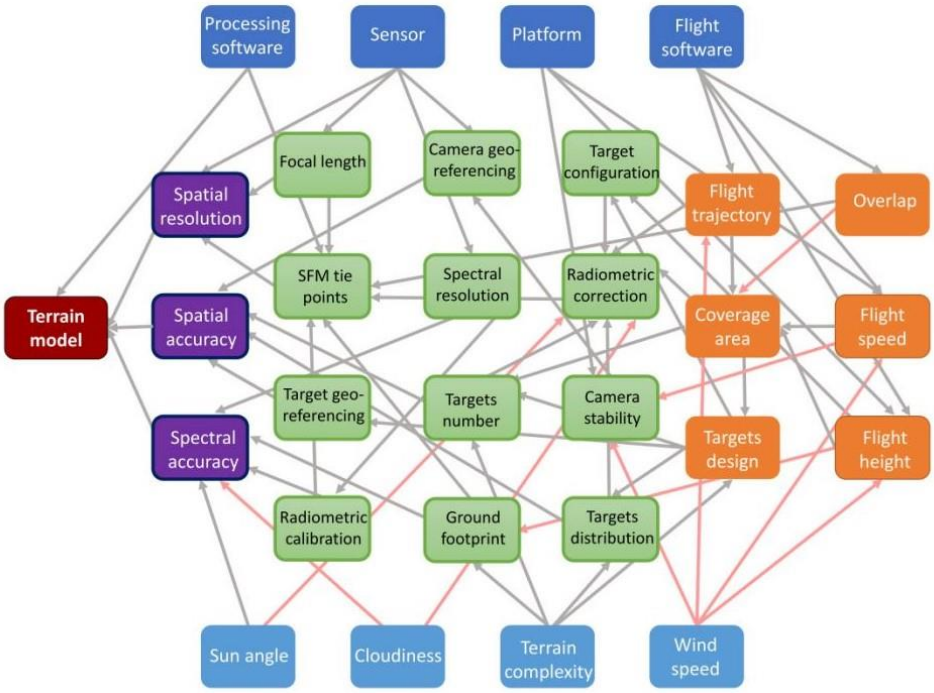

Figure 6.7: The influence of various conditions on the output quality of an UAV flying mission: red – output product; purple – quality parameters; blue – software/hardware; orange – experiment design; light blue – environmental conditions; green – internal parameters. Arrow colours: grey – direct dependence, orange – inverse dependence (source: Tmusic, et.al., 2020).

Pre-flight planning is the first essential step in a sequence of other actions for UAV data acquisition. This involves setting up of a study goal, the inspection of the area of interest for obstacles and topography, dealing with weather forecasts (including Kp index for GPS signal inaccuracies), complying with air traffic regulations and considering no-fly zones, sensor calibration (e.g., compass, accelerometer), considering number and distribution

pattern of the GCPs, making decisions on a suitable platform (fixed-, or rotary-winged) and imaging sensors (see also chapter 6.2. for decision support), and not to forget the skill level of the pilot and other crew members (Manfreda *et al.*, 2018, Tmušić *et al.*, 2020). Field data (e.g., forest inventory parameters) also need to be collected, if specific data analyses are contemplated. Planning the mission itself has become very straightforward, since very sophisticated software (e.g., Pix4Dcapture, DroneDeploy, Mission Planner, UAV Toolbox) is at the user's disposal these days. A background map or satellite image (e.g., Google maps, Bing maps) is used to define the confines of the mission area (placing of waypoints). In addition, parameters are set, such as camera shutter speed (should be short to avoid image blur), flying height, focal length, orientation of the camera, and image overlap (forward overlap of about 90% and side overlap of at least 60% are proven to be optimal (see also: (Dandois *et al.*, 2015, Lisein *et al.*, 2013, Mosbrucker *et al.*, 2017, Seifert *et al.*, 2019, Whitehead and Hugenholtz, 2014)).

In most instances, missions are carried out either semi-, or fully automatically. For this purpose, the pre-defined flying parameters are uploaded to the UAV for the onboard autopilot to conduct and control the survey. During the flight operation, relevant flight information is displayed on the ground control station for the pilot to monitor the campaign, upload new mission parameters, or abort the flight in justified cases. On completion of the flight, a log file with all relevant positional data is downloaded from the aircraft autopilot, or the data gets directly integrated in the image EXIF file. This information is subsequently used to provide initial estimates for camera orientations and image centre positions within the photogrammetry pipeline.

If further processing of the resulting imagery is intended to take place within a photogrammetry environment, special caution has to be taken when employing consumer-grade cameras, since they do not meet the very strict standards of metric imagers. Poor camera performance potentially leads to error propagation in UAV DEMs (James and Robson, 2014). Manufacturers of professional cameras (frame cameras and DSLRs) furnish calibration protocols to be used as a reference when initialising a photogrammetry workflow. However, efforts would be out of proportion to carry out calibration with each camera in the consumer grade segment. Well-known biases are enhanced vignetting (pixels on the outside of the images receive less light than the centre pixels), attenuation and chromatic aberration (separation of colours at the edges of the image). Fast detector saturation and waveband overlaps also contribute to difficulties in obtaining proper spectral signatures of objects. Some of the most common image artefacts are depicted in Figure 6.8. based on Whitehead and Hugenholtz (2014). Aforementioned downsides have

prompted authors such as Lebourgeois *et al.* (2008) to conclude, that consumer-grade cameras are to be considered unsuitable for photogrammetric operations.

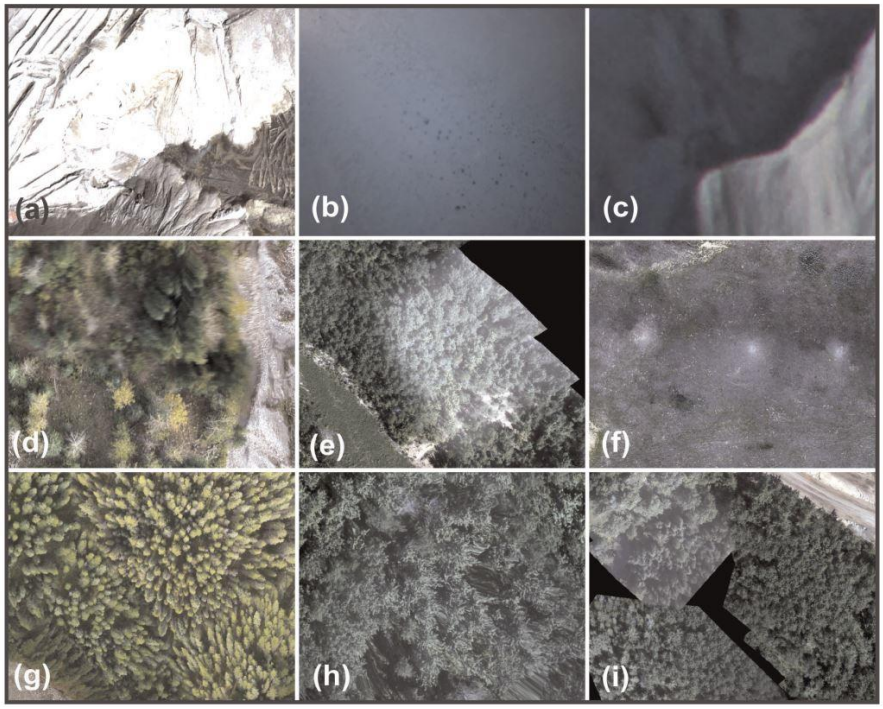

Figure 6.8: Common image artefacts of UAV remote sensing: (a) saturated image; (b) vignetting; (c) chromatic aberration; (d) mosaic blurring in image overlap; (e) incorrect colour balancing; (f) hotspots due to bidirectional reflectance; (g) relief displacement (tree lean); (h) image distortion due to DSM errors; (i) mosaic gaps caused by incorrect orthorectification ormissing images. Source: Whitehead and Hugenholtz, 2014.

Nevertheless, some of the major issues can be resolved by:

- using camera calibration software (freeware or proprietary) or test panels
- mounting appropriate filters
- avoiding extreme wide-angle lenses or fly high to avoid too much radial distortion
- flying in favourable weather conditions (no clouds if possible; time around solar noon)
- averting illumination conditions with extreme or too low contrast
- using camera lenses with a fixed focal length (i.e., no zoom lenses)
- keeping a constant flying altitude above ground to avoid imagery scale leaps
- executing calibration schemes for multi-, hyperspectral and thermal sensors as provided by the manufacturer
- capturing imagery from different viewing angles (multi-camera configuration, oblique views, varying flight line pattern, high image overlap),
- and by employing modern photogrammetry software featuring SfM and MVS algorithms, which can handle non-metric imagery much better, than conventional

photogrammetry suites (Assmann *et al.*, 2019, Colomina and Molina, 2014, Greiwe, 2018, Kunneke, 2019, Manfreda *et al.*, 2018, Næsset, 2016, Salamí *et al.*, 2014, Seifert, 2019, UAV Campus Group, 2020, van Aardt, 2019, Vogt, 2020, Wich and Koh, 2018: 24–26).

6.6. UAV data processing

In the following a typical processing pipeline is presented irrespective of the software package being used. The acquired imagery can be processed in different ways, depending on the defined goals of the mission. Possible outcomes are terrain (DTMs) or canopy height models (CHMs), orthophotos, or maps featuring classified objects. The analysis of this imagery requires specific software and can be performed either in a remote sensing and/or GIS environment (e.g. ArcMap, QGIS, ENVI, TerrSet, SAGA, ECognition), or in a digital photogrammetry suite (e.g. Agisoft Metashape, Pix4D, DroneDeploy, Open Dronemap, MicMac, RealityCapture - for details also see: 3D Natives, 2019). For a more detailed and refined account on the project workflow employing Agisoft's Metashape/Photoscan, which was used in the presented study, see also chapter 7.3.4.

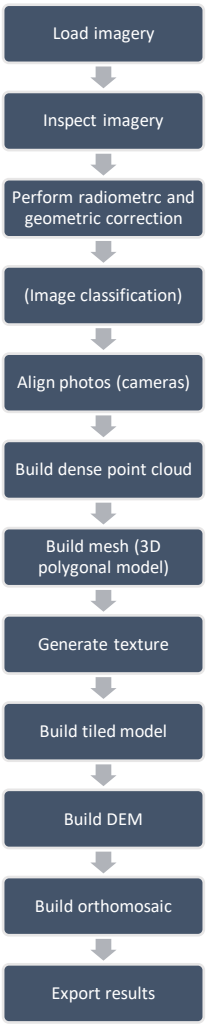

Figure 6.9: Typical UAV image processing workflow

Upon a successful completion of a flying mission, the imagery gets uploaded into the selected software programme and visually inspected for blunders and redundancies for potential disposal. The subsequent steps of performing *radiometric* and *geometric* correction of the imagery are crucial for the achievable accuracies of the final products. During the acquisition process the radiometric signal of the object to be captured is effected by the viewing geometry (sun-object-sensor), the illumination conditions, and atmospheric responses such as scattering and attenuation (Tu *et al.*, 2018). These effects get exacerbated by sensors, which do not present a radiometrically reliable signal. To compensate for such ramifications, sensor calibration has to be carried out either prior

or during image processing. For this purpose, radiometric reference targets, calibrated colour charts (e.g., XRite), and/or additional onboard sensors for irradiance measurements (e.g., Parrot Sequoia) are employed. The resulting correction function transforms the digital numbers (DNs) recorded by the sensor to linear radiometric coefficients (Tmušić *et al.*, 2020). Measurement geometry gets accounted for by assessing the object's bidirectional reflectance distribution function. The pertaining information from each image is either averaged, or just the geometries close to nadir considered (Aasen and Bolten, 2018). A nifty approach was designed by Honkavaara and Khoramshahi (2018) to radiometrically correct geometry effects and changes in illumination conditions during bundle block adjustment.

The determination of image orientation and location is pivotal for the photogrammetry process, as well as for the correct assignment of *geometry* attributes (coordinates) for further processing in a GIS workflow (Jurjević *et al.*, 2020). The UAV's onboard navigation system (IMU) usually provides sufficient information on the 'position-velocity-attitude' solution, but low-cost platforms are hardly accurate enough to satisfy the ambitious requirements of a photogrammetry system. Although direct sensor orientation with cm-level positioning seems possible in modern photogrammetry environments (Cramer *et al.*, 2016, Rehak *et al.*, 2013), the consideration of highly accurate Ground Control Point (GCP) measurements still prevails as a 'gold standard' (Assmann *et al.*, 2019, Colomina and Molina, 2014, Tmušić *et al.*, 2020, Zimmerman *et al.*, 2020). Only in very specific constellations (e.g. fusion of imagery from different flying missions into one point cloud), the involvement of GCPs can be waived (Cook and Dietze, 2019). However, with the integration of differential GPS, real-time kinematic georeferencing (RTK-DG) or post-processed kinematic direct georeferencing (PPK-DG) into the UAV platform, the GCP standard will gradually be superseded (Gerke and Przybilla, 2016, Grayson *et al.*, 2018, Jeziorska, 2019, Tmušić *et al.*, 2020). Unfortunately, RTK and PPK services are not available around the globe, thus georeferencing of the products has to be carried out manually by matching map coordinates with image features. The evaluation of the geospatial products can subsequently be accomplished by using independent checkpoints, reference surfaces, or length measurements (James *et al.*, 2019).

In many ways *image classification* techniques have to be different from the analysis of satellite or other aerial imagery (see also chapter 4.3.), since, with UAV images featuring spatial resolutions of a few centimetres, the amount of detail presents new challenges. Even high-resolution satellite images exhibit relatively homogenous clusters of pixels, whereas in UAV imagery, individual component parts of plants (branches, leaves) become apparent. This results in high contrast differences between and high variation within objects,

and as such, pixel-based classification algorithms seem overwhelmed in many instances. For a number of years, the object-based analysis strategy (OBIA) has proven to be a viable alternative. Pixels are amalgamated into groups to represent discrete objects, based on spectral, textural, shape properties and topological relationships. This process is also widely known as image segmentation. In many recent studies, the superiority of OBIA over pixel-based approaches has been reported (Calderón *et al.*, 2013, Dunford *et al.*, 2009, Nebiker *et al.*, 2008, Pádua *et al.*, 2017, Rango *et al.*, 2009, Salamí *et al.*, 2014).

A classified UAV image represents one possible option for a final product. Having said this, the generation of other outputs, like terrain models, orthomosaics, and surface representations, require further data analysis within the 3D realm. This is accomplished by importing into and processing the UAV images in a digital photogrammetry suite, like Agisoft's Metashape. Since the subsequent workflow is identical with the one outlined in chapters 4.5. and 4.6. (SfM and MVS), no further information is furnished in this section.

In many cases UAVs have demonstrated to be a cost-effective and promptly to deploy monitoring technique for survey areas smaller than about 20 ha – beyond that aerial or satellite platforms might be a better option. Despite all merits, some fundamental issues and related challenges with UAV surveys are evident:

- Government regulations restricting flying missions become more and more strict.
- The huge variability in methodologies, sensors, and data analysis strategies makes it very intricate to compare outcomes of studies and missions.
- Technical limits (sensor size, radiometric resolution, battery life) still prevail.
- The high spatial resolution of UAV imagery demands for high processing and storage capacity.
- There are no standards for sensor calibration routines, error propagation assessments, and quality management.
- It remains very hard to get hands on information regarding data processing algorithms, even though there is a growing number of open source software becoming available (Beck, 2019, Haala and Rothermel, 2012, Manfreda *et al.*, 2018, Pádua *et al.*, 2017, Poley and McDermid, 2020, Remondino *et al.*, 2014, Salamí *et al.*, 2014, Shakhatreh *et al.*, 2019, Tang and Shao, 2015, Tmušić *et al.*, 2020, UAV Campus Group, 2020, Vogt, 2020, White *et al.*, 2016, Whitehead and Hugenholtz, 2014).

6.7. UAV photogrammetry

So, why dedicate an entire section to UAV photogrammetry, when all relevant traits have been dealt with in chapters 4.5. and 4.6. already? A number of studies, as well as own experiences suggest, that, although having performed a (near) perfect flying mission, the outcomes of a photogrammetry workflow can be far from being satisfactory. Apparently, the specific characteristics of the vegetation observed (i.e. trees) in combination with the photogrammetry algorithms and the associated parameters hugely effect the quality of the final products (e.g. CHMs, orthomosaics) (Dandois *et al.*, 2015, Fankhauser *et al.*, 2018, Hugenholtz *et al.*, 2013, Nex and Remondino, 2014, Puliti *et al.*, 2015, Seifert *et al.*, 2019, UAV Campus Group, 2020). A flawed object reconstruction bears the potential to inaccurately quantify the distribution, spatial extent and volume of the trees.

The three-dimensional reconstruction of features seems to be working best for objects, which are stationary, solid, well-lit and show distinctive textures and patterns (Mostegel *et al.*, 2016, Nex and Remondino, 2014, Przybilla *et al.*, 2019a, 2019b). However, most vegetation objects are complexly structured (branches, leaves), with low opacity (e.g., due to defoliation) and a rough surface. Even in calm conditions, the reflective properties and the varying geometric arrangement exacerbate the situation with divergent orientations and sizes. In addition, due to the similarity of the shape of thousands of leaves, the proper identification and matching of key features seems an almost vain endeavour. As a result, errors get disproportionately inflated during the recursive camera positioning calculations (bundle adjustment). With such error propagation introduced into the photogrammetric workflow, artificial discontinuities and artefacts become prevalent features in the point cloud generation process and need to be assessed painstakingly before the reconstructed object surface is submitted to further analysis (Alidoost and Arefi, 2017, James R. Frankenberger *et al.*, 2008, Schöning and Heidemann, 2015, Seifert *et al.*, 2019, Sona *et al.*, 2014).

The selection of a specific photogrammetry suite, as well as the settings of the workflow parameters also greatly affect the achievable accuracies of the reconstructed output. In a very elaborate recent study carried out by Probst *et al.* (2018), the most relevant findings were - when assessing six popular photogrammetry software packages:

- '…all software trials yielded object representations clearly identifiable as trees…'.
- All of them showed inaccuracies and artefacts manifested as errors of commission and omission, with incomplete representations (holes, discontinuities).
- Floating artefacts in particular require laborious and costly manual clean-up of the point cloud.
- In some cases, background features were attached to the foreground.
- Errors within the foliage are very difficult to identify.

- Vertical disparities (in the tree crown) in particular contribute to the failure of algorithms during bundle adjustment.
- The parametric configuration of the software tested appears to be rather static and thus fails to adapt to local conditions.

In the following graph some of their major findings are illustrated.

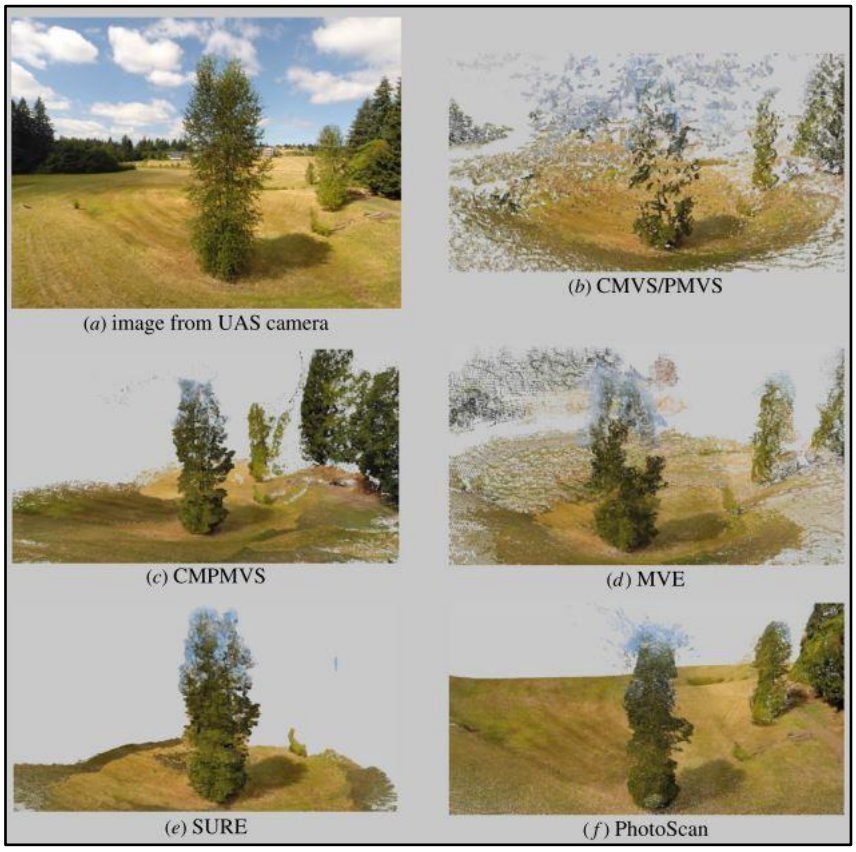

Figure 6.10: UAV scene image (a), and software generated 3D-reconstructions (b-f). Source: Probst, et.al. 2018.

The subsequent graph illustrates the discrepancies between a synthetic reference tree and the models derived from the imagery itself.

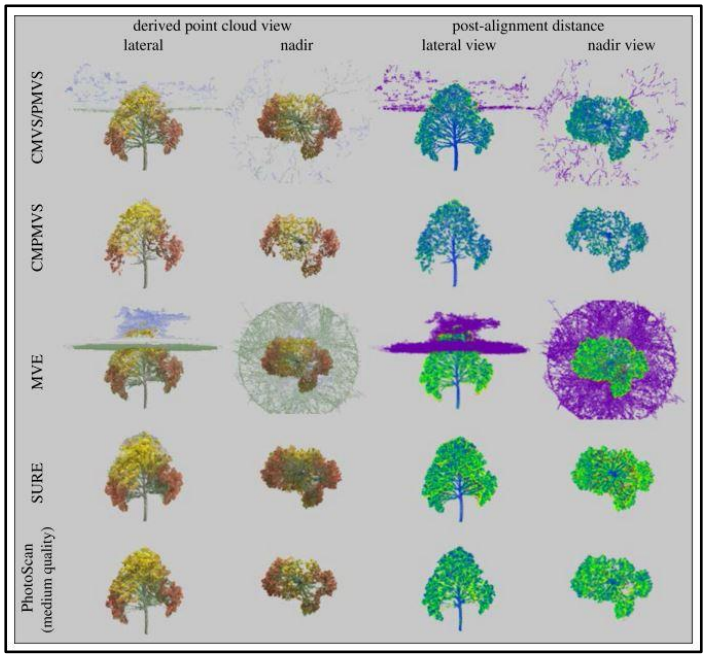

Figure 6.11: Derived point clouds aligned to reference synthetic tree in lateral and nadir views (first two columns); local distance discrepancies are indicated in colour (blue: zero discrepancy, purple and red for larger distances) – columns three and four. Source: Probst, et.al., 2018.

Another interesting finding of above-mentioned authors is, that the settings in the software (here: Agisoft Metashape) to achieve point clouds in a much higher density (i.e., highest quality), can have a detrimental effect on the fidelity of the reconstructed object. They presume, that the highest-quality settings filter out scene components with a representation frequency below an internally defined image number threshold. All of the before-mentioned revelations are perfectly in line with my own observations during data analysis and the study we carried out in 2019 (Seifert *et al.*, 2019). In addition, we also found out, that extreme image resolution, resulting in a very high number of detail, does not necessarily lead to better results. In one case, the highest resolution imagery depicting a lime tree yielded the worst number of tie points instead. In essence, the findings support the idea, that SfM and MVS algorithms are designed for opaque objects with more or less Lambertian surface reflectance properties. The algorithms seem more geared for gradual changes in object parallax and illumination geometry.

Before concluding this section, I should like to make a final remark – this concerns the conspicuous absence of technical documentation applying to most of the software packages. Even with the vendor's or manufacturer's support, the user is quite often left to his own devices. This issue is partly mitigated by online forums. However, some of the shared information can be deemed speculative, or is only suited for specific conditions.

6.8. UAVs in forestry

The last decade has seen a substantial proliferation of the application of UAVs in the forestry sector. This is attributed to the fact, that UAV platforms have become much more affordable, and advances in sensor technology now allow payloads, such as LiDAR and hyperspectral imagers, which were limited to sizeable (manned) aerial and spacebourne platforms before. In this chapter the array of actual and potential applications is sketched first, with a subsequent, more detailed account of an arbitrary selection.

In the literature researched the following applications are reflected:

- Forest fire detection (single operation or swarms of UAVs)
- Post-fire monitoring
- Inspection of harvesting operations
- Monitoring and change detection within natural forests
- (Tree) species identification
- Assessment of silvicultural treatment
- Forest health
- Biodiversity and habitat assessments
- Appraisal of seasonality in vegetation
- Forest pest detection and analysis
- Wildlife management
- Extraction of forest structural parameters
- Examination of forest / canopy gaps
- Mapping below canopy features
- Detection of forest regeneration / succession
- Soil disturbance assessment
- Tree stump detection
- Tree specific parameter extraction
- Tree planting
- Applying fertilisers and pesticides from UAVs
- 3D mapping beneath tree canopy
- Post-harvest waste assessment
- Agroforestry
- Invasive species detection.

In this respect, excellent examples are provided by: Banu *et al.* (2016), Berni *et al.* (2009), Brovkina *et al.* (2018), Chisholm *et al.* (2013), Desale *et al.* (2019), Getzin *et al.* (2012), Getzin *et al.* (2014), Grenzdörffer *et al.* (2008), Guimarães *et al.* (2020), Innovatek (2020), Iost Filho *et al.* (2020), Nex and Remondino (2014), Niemann (2020), Pajares (2015), Puliti *et al.* (2015), Pádua *et al.* (2017), and Suomalainen *et al.* (2014).

When considering a UAV based forest survey, specific challenges need to be taken into account. Firstly, sufficient and level space is required for safe take-off and landing of the system, which is a very demanding task in closed forests. Secondly, atmospheric conditions above the canopy vary greatly, resulting in turbulences and thus affecting the stability of the UAV platform. Thirdly, line-of-sight operation of the vehicle is only possible within a short range, because of the obstruction of the UAV by big trees. However, in a growing number of cases the situation will be alleviated with strict regulations to be eased in the future to allow for automatic UAV missions (see also chapter 6.4.). Last, but not least, salvaging a stranded aerial vehicle in a forest environment is far from being trivial and requires some precautionary measures and dispositions.

6.8.1. Forest structural parameters estimation

Forest inventory reflects a continuous activity to appraise physical, chemical and biological parameters over time. UAVs now offer an economical and highly accurate alternative to satellite-, or aerial-based platforms, as well as to copious and labour-intensive field work. Forest inventory parameters can either be gathered on a stand, or individual tree level (Guimarães *et al.*, 2020). Stand-level criteria such as basal area, average stand height or volume, are better derived using an area-baes approach (ABA). Whereas for stem density, tree height, and crown length, the individual tree crown (ITC) approach appears to be the method of choice (Yu *et al.*, 2010). All of the studies investigated either use ALS point cloud data or ground-truth measurements as a reference to compare the outcomes. Statistical methods are applied and the related coefficients (e.g., coefficient of determination (R^2) and Pearson's correlation (r)) indicated. A detailed account on the extraction of forest inventory parameters from imagery is given in chapter 4.6.

In the following a selection of the most cited and notable peer reviewed studies is presented considering the extraction of inventory parameters at stand, as well as tree level. Prior to attending to the outcomes in detail, the distinguished reader has to be advised of specific aspects:

i. The determination of tree height (aside from tree species) is legitimately one of the most relevant actions in the assessment of forest characteristics. Most of the other determinants (e.g., DBH, volume) are derived from tree height using allometric

formulas or some kind of regression function. As such, great care has to be taken, when judging tree height outcomes.

ii. In their recent study Stereńczak *et al.* (2019) found out, that field surveys in general underestimate tree height compared to the length measurement of felled trees. However, this is contrasted by Krause *et al.* (2019), who observed slight overestimates in field surveys.

iii. In Kitahara *et al.* (2010) it is concluded, that inexperienced surveyors cause big errors in tree height estimations, in particular in broad-leaved trees.

iv. Tompalski *et al.* (2014a) and other authors ascertain, that blunders in tree height estimation result in grave inaccuracies in tree/stand volume calculation, just as with generic allometric formulas (i.e. non tree species specific).

v. Other research (e.g. Sibona *et al.*, 2017) revealed, that LiDAR estimates of tree heights are closer to actual values than field survey mensuration results. This seems particularly true for tree crowns with a conical shape.

In **stand-level** studies *height parameters* play an ever so important role when assessing forest structure. The results in most of the investigations were coherent, featuring strong correlations (see also table 6-3 below). In addition, there is broad agreement, that outcomes depend on the sensor payload, and the forest characteristics and species configuration (Cao *et al.*, 2019, Guo *et al.*, 2017, Ota *et al.*, 2017, Puliti *et al.*, 2015, Xu *et al.*, 2020). In most cases UAV-LiDAR seem to obtain better results than those acquired by UAV RGB sensors. This sounds explicable, since RGB point clouds are limited to the upper part of the canopy, as opposed to LiDAR technology. Nevertheless, RGB derived CHM exhibit a higher point density than the laser point clouds and thus are more tuned for the extraction of higher detail. When considering various forest types, Puliti *et al.* (2015) suggest that boreal forests are easier to assess due to less variation in tree species and height. Broad-leafed forests, in comparison, typically are more complex and more dense. These findings are very much in line with discoveries made by Cao *et al.* (2019), who notice, that most coniferous trees have a more regularly shaped crown. Wallace *et al.* (2016) account the comparison between LiDAR and UAV RGB height metrics in a sclerophyll eucalypt forest. Since SfM photogrammetric technique is not able to properly model the terrain for CHM derivation, LiDAR showed a much better performance (RMSE of 0.92m for LiDAR and 1.30m for SfM).

The derivation of *stem number* (S_n) appears to be a real challenge, especially in dense forests and with species characterised by irregular height and crown (Gobakken and Næsset, 2004). This explains the relatively poor, but still acceptable accuracies with good correlations (Brieger *et al.*, 2019, Cao *et al.*, 2019, Puliti *et al.*, 2015).

Stem volume (S_v) is also reflected in a number of studies, with strong correlation obtained, irrespective of the sensors being used (Chen *et al.*, 2017a, Giannetti *et al.*, 2018, Goodbody *et al.*, 2017b, Puliti *et al.*, 2015). Once again, the more open and less complex structure of boreal forests seem to contribute to the good results (Goodbody *et al.*, 2017b).

For the determination of *basal area* (BA) the investigations conducted by Alonzo *et al.* (2018) yielded a strong correlation (R^2 = 0.79). This is, however, in dissent with the findings by Puliti *et al.* (2015) and Cao *et al.* (2019), who only achieved a good correlation (R^2 = 0.60 and 0.61). Apparently, better results can be achieved by incorporating variables representing crown height, colour and shape (Alonzo *et al.*, 2018).

Diameter at breast height (DBH) was explored by Cao *et al.* (2019). Good correlation was reported for UAV LiDAR (R^2 = 0.69) and RGB (R^2 = 0.50) derived point clouds. However, LiDAR and RGB derived estimations were almost on par when considering forest structural attributes.

Results are quite promising for the estimation of stand *volume* (V). Cao *et al.* (2019), Jayathunga *et al.* (2018b) and Ota *et al.* (2017) inform about a strong correlation (R^2 between 0.78 and 0.84), with a slightly higher correlation for LiDAR derived metrics. Apart from that, respectable outcomes can also be achieved by combining LiDAR-DTM and RGB DSM metrics (Jayathunga *et al.*, 2018b).

Above ground biomass (AGB) estimations showed good correlation in the study carried out by Cao *et al.* (2019). Better results were achieved by Alonzo *et al.* (2018) and Guo *et al.* (2017). All studies indicate, that acceptable estimations can be obtained using LiDAR or RGB sensors. Apparently, all outcomes can be related to the type of forest assessed.

Table 6-3: Sensing payloads and results from stand-level studies (based on Guimarães, 2020).

Studies	***Sensor type***			***Results (R^2)***							
	RGB	**LiDAR**	**CIR**	**H_L**	**H_M**	**H_{dom}**	**S_n**	**BA**	**S_v**	**DBH**	**V**	**AGB**
Puliti et al., 2015			•	0.71		0.97	0.60	0.60	0.85			
Giannetti et al., 2018	•		•						0.80-0.83			
Chen et al., 2017a	•								0.91			
Cao et al., 2019		•		0.90			0.56	0.64		0.69	0.78	0.68
Cao et al., 2019	•			0.82			0.50	0.61		0.50	0.70	0.63
Jayathunga et al., 2018a	•										0.84	
Guo et al., 2017		•				0.81						0.84
Goodbody et al., 2017b	•								0.93			
Ota et al., 2017	•			0.93	0.93	0.91					0.75	
Surový et al., 2018	•						50%-80%					

Studies	*Sensor type*	*Results (R^2)*					
Medvedev et al., 2020	•		60%-87%				
Brieger et al., 2019	•			67%			
Gülci, 2019	•	0.78		0.87			
Xu et al., 2020	•	0.58-0.95			0.24-0.52	0.29-0.71	0.27-0.64
Thiel and Schmullius, 2017	•			93%			

CIR: Colour Infrared; **H_L:** Lorey's Mean Height; **H_M:** Maximum Height; **H_{dom}:** Dominant Height; **S_n:** Stem Number; **BA:** Basal Area; **S_v:** Stem Volume; **DBH:** Diameter at Breast Height; **V:** Volume; **AGB:** Above Ground Biomass.

Considering **tree-level** studies, RGB sensor derived *height* metrics reveal the full potential of this technology. Strong correlations are reported by Ni *et al.* (2015), Guerra-Hernández *et al.* (2016), Guerra-Hernández *et al.* (2017), Hao *et al.* (2021) and Lin *et al.* (2018). R^2 values range from 0.81 to 0.95. Other authors used UAV-LiDAR to also obtain a strong correlation (Jaakkola *et al.*, 2017, Yin and Le Wang, 2019). Sankey *et al.* (2017) achieved an R^2 of 0.90 when using LiDAR, multi-, and hyperspectral sensors. In their investigation, Wallace *et al.* (2016) found that LiDAR performed much better (R^2 = 0.84) than SfM derived height information (R^2 = 0.68). According to them, the poorer performance can be blamed on the fact, that mid- and understorey parts of the forest are not well represented. In contrast, when looking at Eucalyptus plantations in Portugal, Guerra-Hernández *et al.* (2018) conclude, that UAV generated point clouds are as good as ALS derived point clouds for estimating individual tree height. The authors achieved even good results in high-density eucalypt forests. However, they point out, that landscapes featuring a canopy cover exceeding 60% and with slopes steeper than 20% must be considered with caution. Their findings is very much in line with the outcomes of a study conducted by Dandois and Ellis (2013). The achieved performance of the UAV derived CHM was similar to the LiDAR 3D point cloud height estimates. When assessing UAV imagery-derived stand parameters for pine tree plantations in Turkey Gülci (2019) found out that tree density, crown shape, and branching structure considerably effected the achieved accuracies. Kameyama and Sugiura (2021) deployed a DJI Phantom3 UAV to assess imagery of 20 different flight conditions to be processed in three different digital photogrammetry software packages. They conclude, that a low flying altitude is conducive to an overall accurate creation of the 3D tree models, and that image artefacts, wind speed and light conditions are to be meticulously considered. According to their analysis of the pertaining point clouds, the tree height showed an overall RMSE of 5-6m, with the Pix4D software performing best, followed by Agisoft's Metashape. As such, the selection of an appropriate photogrammetry software seems imperative.

Crown diameter (CD) estimation with strong correlation (R^2 from 0.72 to 0.85) with regard to LiDAR systems can be found in Sankey *et al.* (2017) and Yin and Le Wang (2019). Panagiotidis *et al.* (2017) employed an RGB sensor to obtain crown metrics from conifer dominated forest plots. The correlation ranged from 0.63 to 0.85 for R^2. Most of the authors conclude, that better results can be obtained in more open forests, whereas poor performance is expected in denser vegetated areas (Guerra-Hernández *et al.*, 2016, Panagiotidis *et al.*, 2017, Sankey *et al.*, 2017).

Table 6-4: Sensing payloads and results from tree-level studies (based on Guimarães, 2020).

Studies	***Sensor type***					***Results (R^2; *r)***				
	RGB	**LiDAR**	**CIR**	**MSP**	**HSP**	**H**	**CD**	**DBH**	**S_v**	**AGB**
Ni et al.	•					0.87				
Wallace et al., 2016		•				0.84				
Wallace et al., 2016	•					0.68				
Guerra-Hernández et al., 2018	•					0.61-0.69*				
Chen et al., 2017a	•					0.76*				
Carr and Slyder, 2018	•							0.82*		
Surový et al., 2018	•									
Dandois et al., 2015	•					0.86				
Chisholm et al., 2013		•						0.45		
Sankey et al., 2017		•		•	•	0.90	0.72			
Guerra-Hernández et al., 2016	•					0.81	0.95			
Lin et al., 2018	•					0.92				
Panagiotidis et al., 2017	•					0.75-0.72	0.63-0.85			
Yin and Le Wang, 2019		•				>0.9	0.83-0.85			
Otero et al., 2018	•					0.6				
Guerra-Hernández et al., 2017	•					0.96		0.79		0.86
Zarco-Tejada et al., 2014			•			0.83				
Peña et al., 2018	•					0.6				0.25-0.54
Krause et al., 2019	•					0.97				
Dandois and Ellis, 2013	•	•				0.63-0.84				

CIR: Colour Infrared; **MSP:** multispectral; **HSP:** hyperspectral; **H:** Tree Height; **CD:** Crown Diameter; **DBH:** Diameter at Breast Height; **S_v:** Stem Volume; **AGB:** Above Ground Biomass.

DBH estimations showing consistently strong correlation are covered by various authors, such as Carr and Slyder (2018), Iizuka *et al.* (2018) and Guerra-Hernández *et al.* (2017) (R^2 of 0.82, 0.79 and 0.79). All of them used RGB sensors as UAV payload. LiDAR performances were inconsistent. Jaakkola *et al.* (2017) obtained a strong correlation (r =

0.88), whereas Chisholm *et al.* (2013) report an R^2 value of 0.45. The latter used an UAV mounted LiDAR system to fly below the forest canopy. The GPS denied environment shows several limitations, in such the point cloud cannot easily be referenced in space. Nonetheless, DBH estimates were positively correlated with the human-based values, and thus holds the potential for further advancements. Innovatek (2020) reports the first successful attempts of autonomous UAV flights under a forest canopy in a *Pinus radiata* forest in New Zealand. The system consists of a localisation and 3D mapping laser scanning system to create point clouds with no GPS signal.

Strong correlation on *stem volume* (S_v) estimation are recorded by Jaakkola *et al.* (2017) and Abdollahnejad *et al.* (2018) with values for r of 0.88 and R^2 of 0.71, respectively. Jaakkola et al. used a UAV LiDAR system, while Abdollahnejad deployed an RGB based platform.

Literature on *AGB* estimation is still scant. However, the results of the few existing studies are promising. RGB sensors were used in surveys conducted by Lin *et al.* (2018), Guerra-Hernández *et al.* (2017) and Otero *et al.* (2018). Correlations varied from 0.75 to 0.96 for R^2. Jaakkola *et al.* (2017) achieved a strong correlation of 0.89 for R^2. All studies have in common, that flying missions were performed in forests with fairly low tree density. In addition, it is concluded, that good AGB estimates sorely hinge on accurate individual tree height extraction (Lin *et al.*, 2018). Above findings clearly demonstrate, that the consideration of stand-, as well as individual tree traits play a major role in the adequate analysis of canopy height models.

6.8.2. Tree species classification

Besides the determination of tree height, the identification of tree species is another crucial factor in forest inventory. Nonetheless, this task requires a rigorous selection of the relevant variables and classification technique, as well as a strict error assessment (Belgiu and Drăguţ, 2016). Tree species can either be identified by their spectral response, or by their structural parameters, or by the combination of both approaches. In most of the reviewed studies RGB, CIR and hyperspectral sensors were employed, contrasting to the determination of structural parameters, where LiDAR sensors and UAV image derived CHMs were the preferred choice. Because of the high resolution properties of the UAV imagery, individual tree detection and OBIA algorithms were applied in the majority of the studies (Guimarães *et al.*, 2020). Of the classification approaches RF appears to be the favourite candidate, since RF is able to handle high data dimensionality and has proven to be insensitive to overfitting (Belgiu and Drăguţ, 2016, Nevalainen *et al.*, 2017). In addition,

the extra introduced randomness is reported to increase performance considerably (Theodoridis and Koutroumbas, 2009: 221). In contrast, when dealing with multiple features and limited records, SVM appears to be the better choice (Pádua *et al.*, 2019). The following table provides a concise survey of the findings in the literature.

Table 6-5: Sensing payloads and classifiers used for tree classification (based on Guimarães, 2020).

Studies	***Sensor type***				***Classification method***					***Accuracies***
	RGB	**LiDAR**	**CIR**	**HSP**	**k-Nearest Neighbours**	**RF**	**SVM**	**MaxL**	**CNN**	
Sothe et al., 2019				•		•	•		•	72.4%
Nezami et al., 2020	•			•					•	94.8-99.6%
Nevalainen et al., 2017				•		•				95%
Miyoshi et al., 2020				•					•	95-97%
Lisein et al., 2015	•		•			•				64-84%
Laliberte et al., 2010	•								•	83-88%
Goodbody et al., 2018a	•					•				86-95%
Brovkina et al., 2018	•		•		•					75-78%
Michez et al., 2016	•		•			•				79.5-90.6%
Röder et al., 2018	•					•				60.7%
Cao et al., 2018				•	•		•			82-88%
Sá et al., 2018	•		•			•				96%
Fromm et al., 2019	•								•	81%
Gini et al., 2014	•		•					•		80%
Sankey et al., 2017		•		•		•				76%
Tuominen et al., 2018				•	•	•				82%
Komárek et al., 2018	•						•			77-91%

CIR: Colour Infrared; **HSP:** Hyperspectral; **RF:** Random Forest; **SVM:** Support Vector Machine; **MaxL:** Maximum Likelihood; **CNN:** Convolutional Neural Network.

Good examples of the application of RF on RGB imagery are given by Goodbody *et al.* (2018a) and Röder *et al.* (2018). Goodbody *et al.* explored the forest regeneration in clear-cut stands by using orthophoto mosaics, dense point clouds and vegetation indices to apply OBIA and RF for classification. The overall accuracies ranged from 86% to 95%. Röder *et al.* looked into the disturbances caused by *Ips typographus* (European bark beetle). Random forest algorithm was exercised to correctly delineate affected trees. The overall poor performance (i.e. 60.7%) was explained by the complex structure of the test areas. Michez *et al.* (2016) also applied RF method, but in addition to a RGB sensor they employed CIR imagery to survey riparian forests. The combination of RF and OBIA yielded overall accuracies of 79.5 to 84.1%. Komárek *et al.* (2018) applied OBIA and SVM algorithms to RGB and multispectral imagery to find out, that multispectral imagery was substantially superior to RGB sensors (77-91% vs 67-80%). Other important findings were, that the overall classification accuracy decreased with the increasing complexity of the vegetation,

and that higher spatial resolution can in no way act as a surrogate for the lack of spectral bands. To investigate the potential of UAV RGB and NIR imagery for mapping the invasive *Acacia longifolia* Sá *et al.* (2018) used RF and CHM to achieve an overall accuracy Cohen's Kappa value of 0.95. Nevalainen *et al.* (2017) deployed an UAV with hyperspectral and RGB sensor onboard to exploit the data fusion of both sensors. The highest accuracies (95.2%) were achieved by applying RF when classifying pine, spruce, larch and birch stands in a boreal forest. Other classifiers, such as k-NN and SVM were tested on UAV hyperspectral imagery to distinguish various different tree species in mangrove forests. Cao *et al.* (2018) found that SVM outperformed k-NN (82.39% vs 76.12%). However, the best results were achieved by combining spectral and height information (i.e., CHM) – the accuracies increased to 82.09% for k-NN and 82.39% for SVM.

Other classifiers, such as CNN and the more traditional maximum likelihood were also noted in investigations. Gini *et al.* (2014) observed overall accuracies for tree species discrimination in a park in Italy for ISODATA classifier a value of 50%, whereas the supervised classification (i.e. maximum likelihood) yielded a sheer 80%. A comprehensive study was carried out by Sothe *et al.* (2020) to contrast more sophisticated classifying algorithms such as SVM, CNN and RF. The data extracted from hyperspectral and photogrammetric technologies were subsequently subject to the classification process. The results showed very clearly, that the inclusion of the CHM to the hyperspectral data substantially improved the classification results in general. The machine learning classifier CNN was found to be up to 26% more accurate than the SVM and RF when only the hyperspectral bands were considered. In general, all authors were able to achieve satisfactory results with the classifiers used. Tuominen *et al.* (2018) applied a RF and a k nearest neighbour (k-nn) classifier on hyperspectral imagery for the distinction of 26 tree species in an arboretum in Finland. In their investigation the k-nn classifier provided consistently better results than RF. However, best results were achieved by combining hyperspectral with 3D point cloud features and k-nn, yielding an overall accuracy of 82% for tree species and 87% for tree genus.

6.8.3. Forest health and biomass estimation

The control of biophysical variables, such as chlorophyll content and biomass are of particular interest, when assessing potential treatments of forest sites (e.g. fertilisation, irrigation), the calculation of fuel for forest fires, and the determination of funding within the scope of a REDD+ programme (Puliti *et al.*, 2015, Salamí *et al.*, 2014, Wallace *et al.*, 2012). In a specific study, the deployment of a helicopter-based UAV proved to be very successful, when thermal and narrowband multispectral sensors were used to determine LAI,

chlorophyll content and water stress parameters. The outcomes showed on par accuracies with aerial based sensoring platforms, however, at lower cost and with higher flexibility (Berni *et al.*, 2009). A similar study was carried out by Zarco-Tejada *et al.* (2012). They conclude: 'The work presented in this manuscript demonstrates the feasibility of thermal, narrow-band indices and fluorescence retrievals obtained from a micro-hyperspectral imager and a light-weight thermal camera on board small UAV platforms for stress detection in a heterogeneous tree canopy where very high resolution is required'. Dell *et al.* (2019) proved in their study, that even plain RGB imagery has the potential to detect necrotic foliage. They combined a generated CHM and the so-called VARIgreen index to enhance the subtle discoloration effects of *Eucalyptus pellita* caused by a fungus infection. Hernández-Clemente *et al.* (2012) employed a multispectral camera onboard a fixed-wing platform to successfully obtain chlorophyll and carotenoid content of a pine forest effected by decline processes. Disregarding the very costly sensoring systems, CIR imagery also remains very qualified for the determination of forest health. However, as is true for all stress detection approaches, the spectral signature, or rather the response of an afflicted forest or tree can be hardly linked to a specific cause such as water or nutrient deficiency, or a pest attack (Jones and Vaughan, 2010: 271–272).

An example for calculating biomass in a Malawi woodland is provided by Kachamba *et al.* (2016). Here, the authors used the UAV imagery derived canopy height and the spectral variables of the RGB sensor to successfully model a biomass value of 38.99 $Mg.ha^{-1}$. Jayathunga *et al.* (2019) also derived biomass from canopy height models, in this case, however, considering leaf-on and leaf-off conditions in a mixed conifer-broadleaf forest in the University Hokkaido Forest. They found out, that image downscaling had a negative impact on the biomass estimation and the accuracy of the CHM. In addition, leaf-off biomass estimation performed poorer for broadleaf trees, with a better performance for conifer biomass. Interestingly, the biomass estimation apparently varied with statistical approaches (e.g. parametric, non-parametric) as well as data sources (i.e. different image resolutions, vegetation metrics). Peña *et al.* (2018) investigated the estimation of biomass of poplar plantations for lignocellulose production. Correlation between field measurements and CHM derived values were found to be acceptable (i.e. $R^2 = 0.599$), with an unsatisfactory outcome of R^2 of 0.247 when correlating biomass with NDVI derived form a multispectral camera. Lin *et al.* (2018) had much greater success, when determining tree biomass in a sparse subalpine coniferous forest on the banks of the Minjiang River, China. They deployed a fix-winged UAV with an onboard RGB camera to take oblique imagery. The resulting CHM yielded biomass estimates with an R^2 of 0.96 and 54.9 kg for individual trees.

6.8.4. Forest wildfire and pest detection

In their study Merino *et al.* (2012) demonstrate the successful deployment of a fleet of three UAVs equipped with TIR sensors to observe stages in the evolution of a fire, which is crucial for effective fire-fighting, without putting people's lives at risk. This is a an excellent example, on how UAVs can communicate, collaborate, and cooperate, especially, when it comes to the assignment of a portion of a global goal to each aerial platform (Pajares, 2015). Forest burn severity was assessed by Shin *et al.* (2019) by deploying a RedEdge multispectral camera UAV to classify the impact of a wildfire in South Korea. Maximum Likelihood, spectral angle mapper, and thresholding of an NDVI were used as classifiers to determine the burned surface, as well as the degree of tree damage. Not only thermal infrared sensors are most suitable for UAV applications in wildfires, but also RGB and multispectral cameras, to estimate forest canopy fuels and tree densities (Guimarães *et al.*, 2020). Although most of the forest fire studies focus on post-fire phenomena, UAVs are also suited for monitoring wildfires on a regional scale. NASA's high payload Ikhana UAV seems to be perfectly cut out for this task.

Tuominen *et al.* (2018) and Näsi *et al.* (2018) compared hyperspectral imagery taken by an UAV and a traditional aerial platform to detect damage in a boreal forest in Lahti, Finland, caused by *Ips typographus*, L. The finer resolution of the UAV imagery yielded better results (overall accuracy of 81% vs 73%) than the aircraft imagery. Minařík and Langhammer (2016) declare, that dead trees were only separable in the red and red-edge portion of the infested trees. In a different study, the infestation with *Agrilus biguttatus* (Fabricius) on oak was assessed by Lehmann *et al.* (2015). With a combination of CIR and NIR sensors the various infestation levels were determined with an overall Kappa Index of 0.81 and 0.77 for each study site, respectively. Cardil *et al.* (2019) and Otsu *et al.* (2018) employed RGB sensors to determine the level of defoliation in pine trees by the pine processionary moth. The mission yielded an overall accuracy of 79% for the three different defoliation classes. Lin *et al.* (2019) employed LiDAR and hyperspectral sensors to detect damage in pine forests caused by the pine shoot beetle. The LiDAR approach proved to be more rewarding, but the detection rate improved considerably when combining both technologies ($R^2 = 0.83$). Goodbody *et al.* (2018b) melded structural and spectral (NDVI) information for predicting cumulative defoliation caused by spruce budworm *(Choristoneura fumiferana* ,Clem.) to find out, that spectral metrics outperformed structural metrics by far (R^2 0.79 vs 0.49). In case the spraying of the forest/crop is required as a last resort, Desale *et al.* (2019) and Iost Filho *et al.* (2020) recommend the deployment of UAVs for specific treatment of the vegetation.

6.8.5. Biodiversity

Fallen trees were surveyed by Inoue *et al.* (2014) in eastern Japan as an indicator for biodiversity (e.g. colonisation with fungi and saproxylic insects) and biogeochemical cycling. DEMs were generated from imagery taken by a consumer-grade RGB camera mounted on an unmanned helicopter flying at low altitude. About 80-90% of the bigger fallen trees were identified correctly. Getzin *et al.* (2012) used very high resolution UAV imagery to detect forest gaps for the assessment of floristic biodiversity of the forest understory. They found a strong dependency between gap shape metrics and plant diversity with an R^2 of up to 0.74. Listopad *et al.* (2015) reported, that structural elements helped assess hardwood encroachment and determine diversity changes in vegetation due to wildfires. The study was carried out by analysing UAV-borne LiDAR point clouds. Plot-level biodiversity indicators (e.g. amount of dead wood) and structural metrics were extracted from UAV point clouds and hyperspectral images by Saarinen *et al.* (2018) in a boreal forest. They conclude, that structural diversity can be reliably predicted by fusing the 3D point cloud with hyperspectral information for biodiversity monitoring.

In summary, the presented studies have attested, that UAVs have the potential to supersede, or at least complement the more traditional remote sensing technologies (aerial and satellite-based sensor platforms). The extraction of the most relevant forest inventory parameters seems to be working with acceptable accuracies, however, with lower costs and higher flexibility involved in comparison with conventional forest inventory strategies. With the advent of light-weight LiDAR and hyperspectral systems, UAVs also become more and more competitive with aerial or satellite-based systems in areas such as vegetation vigour, species determination, and plant canopy modelling. Having perused more than 250 publications on UAV technology and its application in practice, all resources reveal, that, not only the parameters of a flying mission and the resulting imagery are pivotal for the obtained accuracies, but also the algorithms and parameter settings of the data analysis – with the latter being ‘old news’ in remote sensing, though. The assessment of the outcomes becomes even more complex and devious, when dealing with black-box software systems.

7. Material and Methods

7.1. Study area

7.1.1. General characteristics

It is more than a half-day's drive (about 100 km) northbound to reach the Thunkel test area form the capital of Ulaanbaatar. The study area presents itself being part of the western Khentii mountain range reaching altitudes of up to 2000 m (a.s.l.). The Thunkel area is located on the border between the *aimags* Töv and Selenge to occupy a forested area with a good infrastructure (i.e., railway line) close to the Russian border. Activities in the area surrounding the research site reflect intensive agricultural production, animal husbandry (cattle, goats, horses), mining for gold (mostly illegal),and timber logging (also mostly illegal (see Tsogtbaatar, 2013)). Being part of the *Kharaa* River catchment, all water runs north(western)wards to feed bigger systems such as the *Orkhon* River. The Khentii mountains were formed by terrain attachment in the early mid-Palaeozoic, featuring Permian intrusions and Mesozoic volcanoes, with speckles of flysch sediments. The landscape shows marks of former glaciation such as rock streams and moraines, with evidence of solifluction and cryogenic processes (Dulamsuren, 2004, Lehmkuhl *et al.*, 2011, Meng *et al.*, 2020).

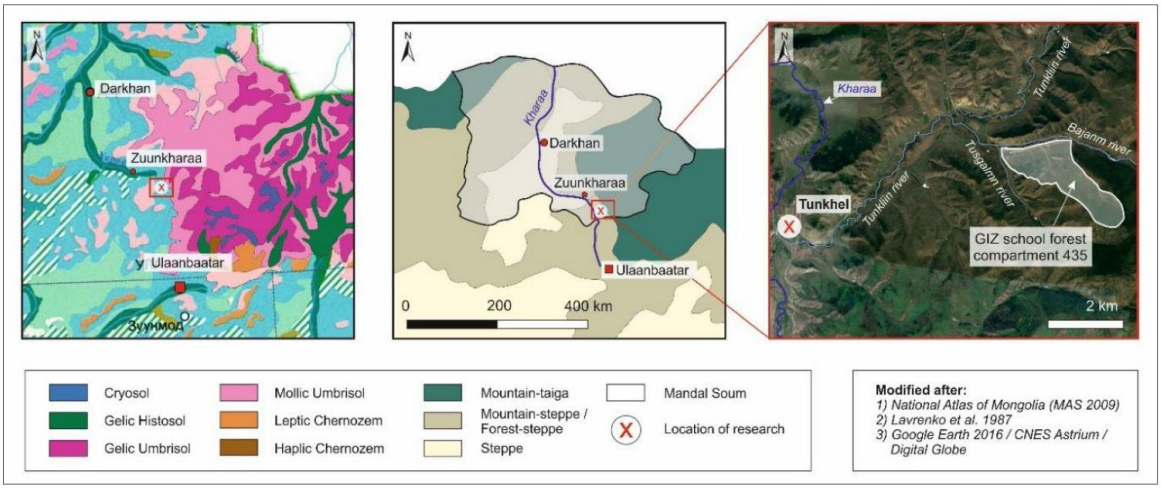

Figure 7.1: Location of the test area featuring geology (left), vegetation zones (middle), and forest compartment 435 at Thunkel. Source: Wecking, 2017.

The ecosystems of the Thunkel area show high variability with small-scale variations and are considered to constitute a transition zone between forest steppe and steppe (Mühlenberg, 2012). According to Dulamsuren (2004) the Khentii mountain range features two distinct altitudinal belts, namely the lower mountain belt (900 m to 1200 m), and the upper mountain belt exceeding 1200 m (see also Figure 7.2). As mentioned earlier, the

southern slopes are occupied by grassland in the lower belt, whereas riparian areas and northern slopes are populated with taiga forest of varying species.

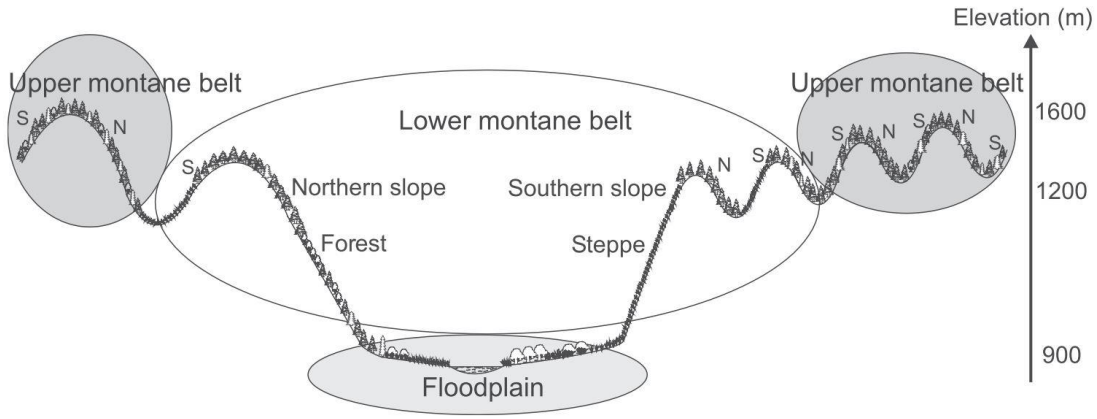

Figure 7.2: Altitudinal characterisation of the Khentii mountain region (Dulamsuren, et al., 2005).

Climatic conditions are harsh with limited precipitation (around 300 to 400 mm/annum) and temperatures ranging from -45° C in the winter to up to 50° C in summer (Batima *et al.,* 2005, Dulamsuren *et al.*, 2010a). The precipitation maxima have been observed in early and late summer, and snow cover can last up to 124 days per year (Dulamsuren, 2004, Dulamsuren and Hauck, 2008). As opposed to the relatively high solar input of the southern slopes, the northern slopes receive much less radiation resulting in a temperature being 15% lower. In addition, a gradual decrease in temperature of about 0.6° C has been measured to occur per every 100 m (a.s.l.) (Dulamsuren, 2004). Rising temperatures for the winter and summer periods have been observed since the 1940s leading to declines in overall precipitation and the thawing of the permafrost (Bohannon, 2008, Dashtseren *et al.*, 2014, Dulamsuren *et al.*, 2010a). Drastic implications of this development are for instance the large-scale diebacks of the Siberian larch in the Khentii area (Dulamsuren *et al.*, 2009, Dulamsuren *et al.*, 2010b, Dulamsuren *et al.*, 2011, Dulamsuren *et al.*, 2014, Juřička *et al.*, 2020, Khansaritoreh *et al.*, 2017, Kharuk *et al.*, 2019, Klinge *et al.*, 2018). In addition, a rise in the rate and intensity of fire incidents and attacks by harmful insects have also been confirmed in recent years (Bussler and Walentowski, 2011, Byambasuren, 2018, Misheel, 2019, Munkhzorig, 2009, Otoda *et al.*, 2013, Schmidt-Corsitto, 2017, Teusan, 2018).

Soils play a crucial role in forest growth as they provide nutrients and are an important supply of water to safeguard survival and flourishing in these prevailing harsh conditions. The soil temperature in Mongolia is subject to enormous seasonal variation. Dulamsuren

and Hauck (2008) found temperatures dropping to -52° C in winter, and summer extremes of a scorching 65° C. Soil moisture also varies greatly and largely depends on the precipitation pattern and existence of permafrost. There are distinct dry phases in spring (depending on the snow layer) and autumn, with recharge taking place in summer. However, summer recharge has been decreasing with numerous droughts occurring in the last few years throughout Mongolia. As for latitudinal effects north-eastern soils show a higher level of moisture as compared to soils in the southwest when considering the north - south gradient. For successful tree growth, however, a constant supply of water would be optimal – especially precipitation of autumn of the previous year seems to be crucial in this context (Nandintsetseg and Shinoda, 2011). In the western Khentii mountain area soils can be classified as soils of mountains and soils of plains. In most cases Proterozoic and Palaeozoic rocks (granite) serve as the parent material. According to Dulamsuren *et al.* (2010b) mountain forest soils are classified as: (1) mountain taiga cryomorphic ochro soil, (2) mountain taiga cryomorphic peat-muck humic soil, (3) mountain taiga podzolic soils, (4) mountain taiga derno-taiga soil, (5) mountain forest dark coloured derno soil, and (6) forest soils with slightly podzolic sandy soil. The mountain steppe soil types comprise: (1) high mountain steppe raw humic soil, (2) mountain chernozem, and (3) mountain kastanozems. In an extensive study Wecking (2017) conducted a mapping of the soils of compartment 435, which also served as my test area – further details on the results are provided below.

The classification of the forest areas vary amongst researchers (Dulamsuren, 2004, Maximovich, 2004, Mühlenberg *et al.*, 2012b). However, in this study the more recent approach by Dulamsuren (2004) is favoured based on the altitudinal position, exposition, and the prevailing tree species (see also chapter 2.1.4 and 2.1.5 of this thesis). Consensus seems to exist, when describing the '*dark taiga*' as being populated with shade-tolerant tree species (i.e., Siberian fir, Siberian spruce, Siberian pine, with Scots pine), whereas the '*light taiga*' definition commonly comprises light-demanding species such as Siberian larch, White birch, as well as various poplar and willow species. After forest disturbance incidents like forest fire the light taiga species usually form the prime stage of succession (Bergeron *et al.*, 2017, Bonan and Shugart, 1989, Byambasuren, 2011, Otoda *et al.*, 2013, Schulze *et al.*, 2005, Teusan, 2018). The co-occurrence of light and dark taiga, and forest steppe vegetation is a key feature of the Khentii mountain area with a high percentage of broad-leafed tree species. In addition, the Khentii mountain region boasts on accommodating the largest concentration of pure *Pinus sibirica* and the largest proportion of dark taiga in Mongolia (Dulamsuren *et al.*, 2005c). The small-scale pattern of the Khentii topography appears to be the main determinant for the density of taiga forests and the occurrence of a great floristic diversity (Mühlenberg *et al.*, 2004). The light taiga apparently prefers the lower and medium elevations, whereas the dark taiga preferably occupies the upper montane belt

beyond the 1200 m (a.s.l.) contour lines (Dulamsuren *et al.*, 2005a, Mühlenberg *et al.*, 2004, Mühlenberg *et al.*, 2012a). Higher elevations feature higher precipitation rates and also higher air humidity with decreasing temperatures, causing a species shift towards the more moisture demanding and cold-resistant tree species of the dark taiga (Dulamsuren, 2004, Dulamsuren and Hauck, 2008). Dark taiga populations also appear to be less prone to forest disturbances due to a higher moisture content of the soils and the retarded melting of the snow. Interesting observations were made by Gradel and Mühlenberg (2011) regarding the dark taiga forest structure. According to them the dark taiga research plots exhibited a rather random tree distribution resulting a better mingling with other tree species. They further state, that …'in the progress of undisturbed succession, taiga may start with irregular tree distribution, rather low basal area and low tree species number'. Although current disturbance regimes were observed to favour pioneer tree communities (e.g. White birch, Siberian larch), successional dynamics between light and dark taiga remain not to be fully understood (Gradel and Mühlenberg, 2011, Mühlenberg *et al.*, 2012a).

7.1.2. The test site - Forest Compartment 435

The test site, also known as the GIZ school forest compartment 435, is situated about nine kilometers east of the village of Thunkel. The surrounding area is characterised by more or less legal timber logging and mining for gold activities (Ministry of Agriculture, Forestry and Fisheries, 2009, Teusan, 2018: 50–51, Wyss, 2007: 28–29). The GIZ has leased the area as a research site and capacity building camp and as such has been authorised to conduct specific activities such as timber logging and silvicultural practices (Schmidt-Corsitto, 2017). The altidunal stretch of the 608 ha area ranges from about 1100 meters at the Bayanm river to the highest point with 1758 meters a.s.l. The light taiga dominates the lower altitudes, whereas a distinct transition zone with mixed-forest stands between about 1300 m and 1500 m is conspicuous. The dark taiga area is limited to the top range of the compartment beyond 1550 m (Wecking, 2017: 29).

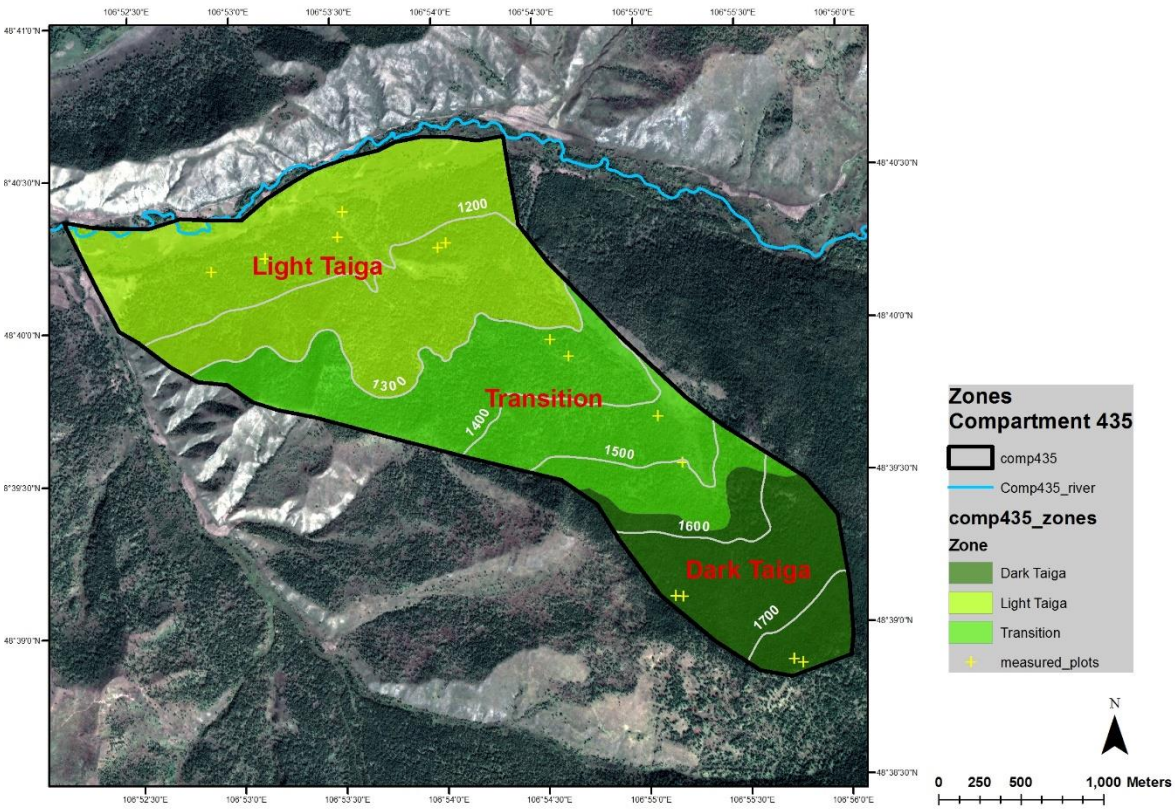

Figure 7.3: Zones of compartment 435 (according to GIZ, 2017, and Wecking, 2017).

The following graph conveys a good impression on the compartment 435, which almost entirley faces north – the photographs were taken after the devastating fires took place in the area in 2017 (Vogt, 2017).

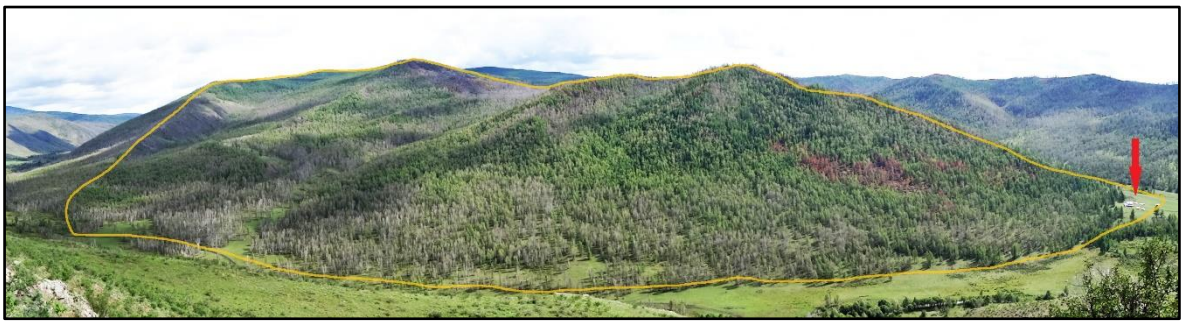

Figure 7.4: Panoramic view of school forest compartment 435 with view facing south. The compartment boundary is indicated in yellow, the GIZ camp marked with a red arrow; numerous burn marks are noticeable (Vogt, 2017).

Except for the almost inaccessible dark taiga parts of compartment 435 the impact of human activity is visible throughout. Damages caused by animal husbandry (bark stripping and bite), and extensive (mostly illegal) logging have paid a high tribute. The formerly prospering hamlet of Thunkel has seen much better days – now, being faced with a faltering wood

industry the population is compelled to gather non-timber forest products and to sustain its needs for fire wood and construction timber (Schmidt-Corsitto, 2017, Wyss, 2007: 28). As one of the dire repercussions tall trees with a high DBH have almost disappeared in accessible areas. Skidding paths in the lower parts of the forests and remaining stumps are silent witnesses of this development. To make things worse, wildfires and insect pests have afflicted the forests in recent years – at least the greater part of the dark taiga has remained unscathed featuring an impressive diversity in species and structure (Schmidt-Corsitto, 2017, Vogt, 2017, Wecking, 2017: 30, 31).

Most parts of the school forest are faced north-east, north, or north-west, with slope gradients usually not exceeding 25 degrees. As expected, the climate is harsh, with a vegetation period of 108 – 145 days, and an annual mean precipitation of 240 mm (Teusan, 2018: 50). The geological map of Mongolia indicates Lower Palaeozoic rocks for the lower parts of the forest compartment 435 and Upper Pre-Cambrian bedrock material for the higher altitudes. The current geomorphology lends its character through cryogenic processes, weathering and denudation (Wecking, 2017: 28). The soil distribution (see Figure 7.5 below) shows the following features: (i) in the lower parts colluvial soils were found with humus enrichment and anthropogenic impacts; (ii) further up soils of Gneissic parent rock with intensified weathering and soddy topsoil prevailed (eutric and leptic cambisols); (iii) going further uphill the soils get more shallow, showing signs of distinct charcoal incorporation and less chemical and physical properties (mollic umbrisols); (iv) with reaching the dark taiga lower limit line the organic matter accumulation on the forest floor becomes apparent with soil formation on consolidated rock (leptic cabisols); (v) within the dark taiga stands soil depth increases again (Gneiss), with thick organic layers, initial podzolisation and appearance of permafrost (haplic leptosols and cambisols) (Wecking, 2017: 83). Wecking (2017) also found that: 'Soil-vegetation interactions were found to be tight, particularly supported by pyrogenic organic matter incorporation, mycorrhization and freeze-thawing dynamics' (Wecking, 2017: 10).

According to Gaschick (2013), White birch and Siberian larch dominate compartment 435 with a timber volume per hectare of 47.83 m^3 and 40.98 m^3. The dark taiga patches on the hilltop present themselves as almost pristine stands, however, Siberian fir does not occur. As specified in the management plan, compartment 435 does not excel with an average growing stock of 95.70 m^3 per hectare, being well below the Mongolian average of 140 m^3 per hectare. At this point it is important for me to point out, that the inventory data for compartment 435 are based on a 6^{th}-tree sampling method showing a very large coefficient of variation (see also chapter 3.1.2). In combination with the survey not carried out by

professionals, this might have resulted in a few discrepancies compared to my own findings and calculations.

As pointed out before signs of over-exploitation, at least in the lower parts of compartment 435, are prominent. The forest management plan of the school forest stipulates the following management goals (Gaschick, 2013):

- Increase growing stock and improve natural regeneration.
- Improve stand stability and timber quality.
- Collect dead wood.
- Preserve biodiversity, protect soils, prevent clear cuts.

In the light of talks with the GIZ experts Altrell (2017) and Schmidt-Corsitto (2017), as well as in conjunction with my own observations, compartment 435 reveals the following characteristics:

- The lower parts of compartment 435 are over-exploited in most part.
- Recent drought incidents (die-back) and insect attacks (Gypsy moth, *Lymantria dispar*, L.) have caused massive defoliation in birch and partly in larch in the lower parts of the compartment.
- Dense forest floor consisting of mostly grass (e.g., Calamagrostis) and shrub is omni-present, particularly in the sparsely populated stands.
- The White birch population shows many signs of multi-stem appearance (coppicing).
- Tee quality in general is mediocre in the best of consideration.
- There is a considerable amount of hanging and leaning trees indicating a lack of stability.
- Stand density is not uniform with a rather clumped (mottled) or scattered appearance.
- In the lower part close to the river and to the east no clear forest boundaries can be determined because of the transitional character of the forest towards the steppe vegetation.
- Old trees with big stem diameters are limited to inaccessible areas of the compartment and the dark taiga.
- Dark taiga patches are in excellent condition, with many tree species present, rich forest floor flora, and excellent vertical and horizontal structure.

- Older larch trees exhibit broken crowns and very por timber quality.
- Throughout the compartment there are signs of fire incidents – recent and historical.
- In the most part forest stands are overaged with a lack of vertical structure; pure stands (birch) also occur quite often.
- In the lower parts White birch is kilned for charcoal production; traditionally, birch is not being utilised in any way by the local population.

In view of above-mentioned stand characteristics, the stated management goals appear to be reasonable.

Rest of page intentionally left blank

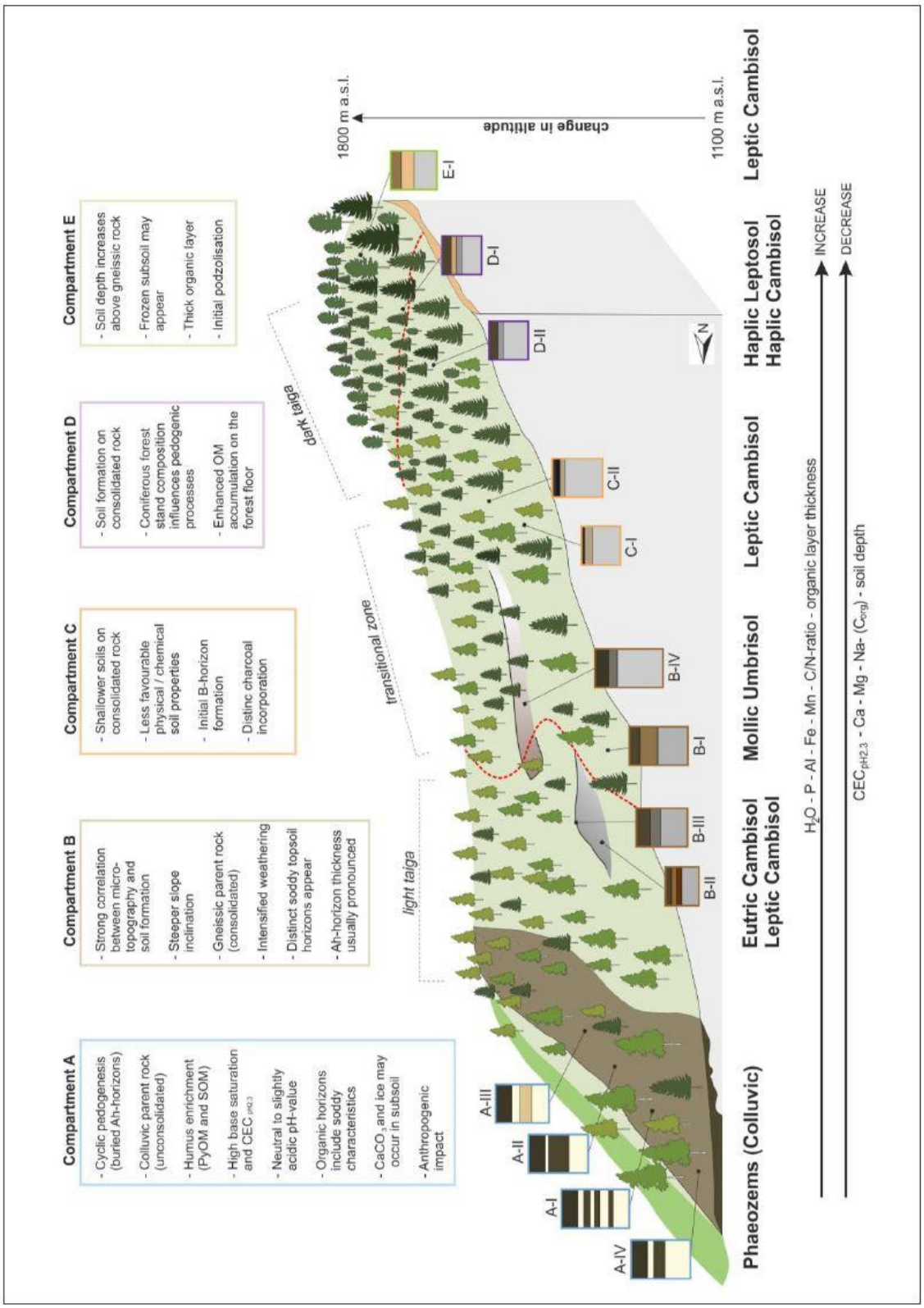

Figure 7.5: GIZ forest compartment 435 main pedogenic characteristics. The coloured boxes at the top summarise the pedogenic characteristics of each research compartment (A to E). The arrows at the bottom indicate the course of physical and chemical soil parameters in dependence on elevation rise. Soil profiles investigated are to describe as: (AI-AIV) Chernic Phaeozems (Colluvic), (BII) Leptic Cambisol (Ferric), (BIII) Mollic Umbrisol, (BI) Eutric Cambisol, (BIV) Mollic Umbrisol (Gleyic), (CI-CII) Leptic Cambisol, (DI-DII) Haplic Cambisol and (EI) Leptic Cambisol (Gelic). Source: Wecking, 2017 p.83.

The following graphs are intended to convey an impression on the scenery and stand structure the visitor would most likely encounter when entering compartment 435 and surrounds.

Figure 7.6: Aspect-related distribution pattern of forest (i.e. forests on northern slope, grassland on southern slope aspect). Terelj area.

Figure 7.7: Typical light taiga (i.e. birch – larch mix) appearance in the lower part of compartment 435 (left). Dense and lush forest floor vegetation (right). Both stands are partly defoliated.

Figure 7.8: Birch – larch mix in plot no.31 – the mean age is about 70 years (left). Pure birch stand at plot no.60 (right) – most of the birches show signs of defoliation caused by Lymantria dispar (inset – insect not true to scale).

Figure 7.9: In contrast to the light taiga, the dark taiga is dominated by coniferous tree species (left). The dark taiga features complex vertical and horizontal structure, as well as rich forest floor flora (right). The pictures were taken at plot no. 8.

In the lower part of compartment 435 defoliation of the trees is conspicuous throughout, whereas in the upper part populated by the dark taiga the forest seems perfectly intact, making every forester's heart leap.

7.2. Material, equipment and software

Prior to the field trip to Mongolia our cooperation partner GIZ kindly provided data as follows:

- DEM with resolution of 8 metres (based on Russian topographic map 1:100,000).
- Satellite imagery (RapidEye, WorldView-2, Pléiades) – more information is provided in chapter 7.3.5.
- Field data of the last survey of compartment 435 (based on 6th tree sampling).
- GIS shapefiles with compartment and sub-compartment boundaries.

The GIZ also saw about transport to and from the Thunkel area, on site accommodation, and supported the organisation of horse-riding capacities. Furthermore, a hardcopy of a topographic map of Russian origin was provided: TUV (TÖV) ЖАНЖИшТАЪ M-48-130; 1:100,000, dating from 1969 – the map is also part of the digital data repository of our institute at the University of Göttingen.

The following equipment for gathering data in the field was employed (application in parentheses):

- Nikon Forestry Pro laser rangefinder (tree heights)
- Garmin GPSmap 64s (coordinates; navigation)
- Kramer dendrometer (basal area estimation)
- DBH measuring tape (tree diameter)
- Suunto inclinometer (slope and tree heights)
- Li – COR LAI 2000 (LAI)
- Crown mirror with pegs (crown diameter)
- Canopy App & Habit App (canopy closure)
- Chalk (for marking trees measured)
- 2 m - pole (for marking plot centre)
- Barrier tape (for marking plot boundary)
- Measuring tape (distances)
- Lacing cord and bubble level (for slope compensation)
- Small poles (marking of corner points of test plot)
- Eschenbach precision compass (cardinal point - aspect)
- Sony DSC-HX50V camera - GPS integrated (photo documentation)
- Lenovo Thinkpad 230i Notebook

Figure 7.10: Field equipment (selection). Starting from top left: Suunto inclinometer, Kramer dendrometer, measuring tape; bottom left: bubble level, lacing cord, Garmin GPSmap 64s, Nikon Forestry Pro laser rangefinder.

For the UAV flying mission equipment and material was as listed:

- Yuneec Typhoon H with CGO3+ camera
- Checkerboards (ground control points (GPS))
- Garmin GPSmap 64s (GCP measurement)
- Printout of flight pattern
- Landing pad
- UAV forecast App (weather data, solar storms)

Figure 7.11: Yuneec Typhoon H hexacopter with remote control.

CGO3+ camera specifications according to the manufacturer's specifications sheet are:

- Focal length 14 mm
- Fixed aperture of F 2.8
- Field of view 94 degrees
- Sensor resolution 12.4 Megapixel CMOS – sensor size ½.3"

For data analysis and preparation of the field trip the listed software programmes and applications (Apps) were used:

GIS / Remote Sensing:

- Terrset 2020, Clark labs
- QGIS 3.10 A Coruña (incl. SAGA, GRASS, OTB)
- ArcGIS Pro 2.6.3
- ArcMap 10.8.1
- SNAP (Sentinel Application Platform) 8.0.3
- eCognition Essentials 1.3
- eCognition Developer 10.0.2
- ENVI 5.4 & IDL 8.6

Digital Photogrammetry:

- Agisoft Metashape 1.6.5
- UAV Editor (flight planning)

Statistics:

- R Studio 4.0.3
- Microsoft Excel 2019

Other software:

- MS Office 2019
- Exif Viewer (to extract metadata from photos)
- Garmin BaseCamp 4.6.2 (to load maps on GPS)
- Google Earth Pro 7.1.8 (to visualise photo locations)
- Hugin Panorama Stitcher (to create panorama photos)
- Microsoft Movie Maker (for UAV video footage editing)
- Datacolor Spyder4 Pro 4.5.9 (for monitor calibration)

7.3. Methods

7.3.1. Overall concept

The overarching concepts for the extraction of forest inventory attributes from high-resolution imagery are based on the assumptions, that: (i) there is sufficient spectral information immanent to the imagery to result in a satisfactory classification of tree species, and (ii) the spatial resolution of the images is high enough to allow for the identification of trees and to further extract useful height information form stereo imagery. In order to achieve the best possible outcomes a thorough and meticulous planning and implementation of the various methodologies can be assumed to be pivotal for the success of such undertaking.

The most relevant stepping stones of the overall concept are:

- Gather and scrutinise material and equipment that is available and still required.
- Set up a sampling design for the field work and the flying missions prior to field trip.
- Gather necessary data as reference (validation) for accuracy assessment of remote sensing data and adapt the field work strategies according to on site conditions.
- Decide on the most appropriate data analysis technique and apply it accordingly.
- Set the findings of remote sensing data analysis against the reference data.
- Distill the results for future applications and variations, and make inferences and recommendations for further research.

A well-designed sampling strategy (including contingency plans) for gathering the required reference data in the field is one of the determinants for the quality of the resulting accuracy assessments. As outlined in chapter 3.1.2. a sampling strategy based on a random design, ideally in combination with a stratification approach, appears to be very rewarding when considering smaller sampling areas. Stratified sampling is known to have the following advantages over other sampling strategies: (i) it can provide data of known precision for subgroups of the population, (ii) it can be more convenient to carry out and is less expensive, and (iii) it often gives more precise estimates for population mans and totals (Lohr, 2010: 73–75). Fortunately, compartment 435 was surveyed before, and as such at least provides a fairly good idea on the species distribution pattern and the age classes to be expected. Based on this information a 35m buffer layer was created in ArcGIS to account for possible edge effects of adjoining other sub-compartments and forest edges (see Figure 7.12.).

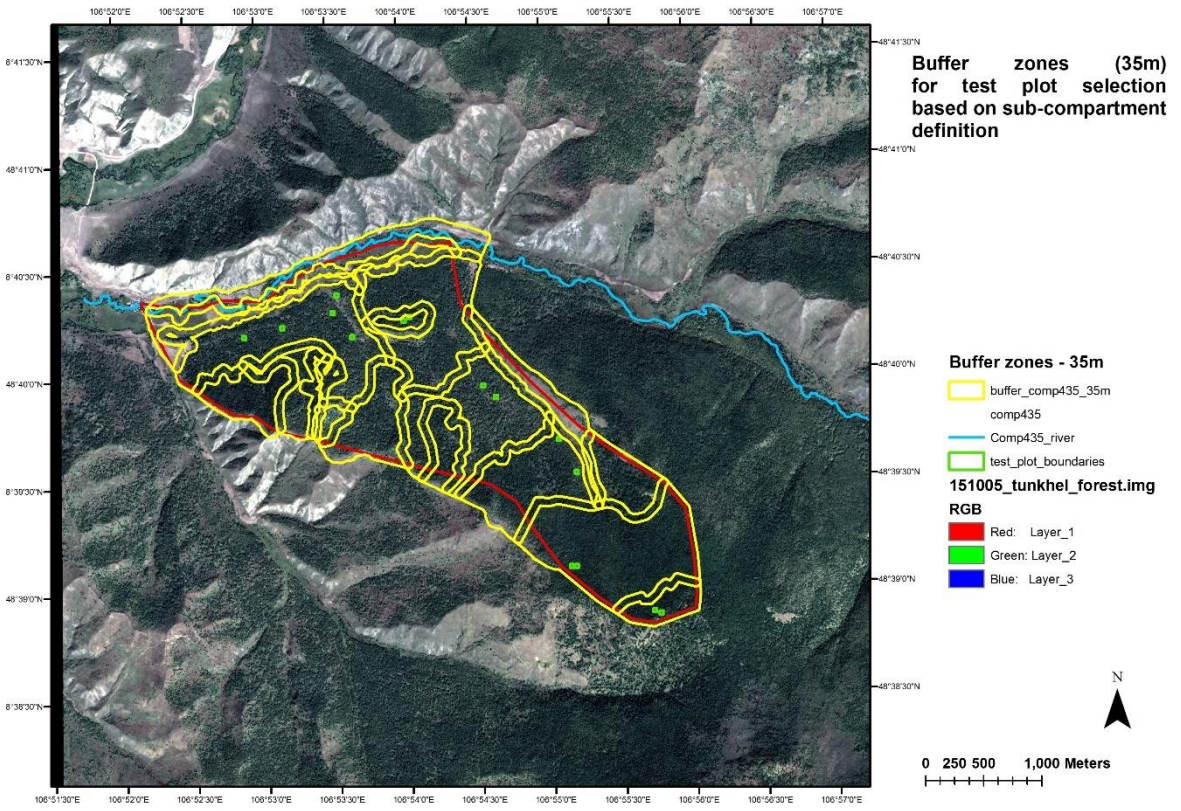

Figure 7.12: Buffer areas (35m) around sub-compartment boundaries.

For getting a good estimate on the required sampling size a sample size calculator was exhausted (https://www.calculator.net/sample-size-calculator.html). Input data: estimated 700 trees per hectare (figure from other field surveys) x 608 hectare (size of compartment 435) = 425,600 trees for total population. The confidence level was set to 95%, the margin of error to 5%. The resulting sample size as calculated was 384 (trees). With an intended plot size of 1000 m^2 this would translate into a number of between 5 and 6 test plots. However, in order to take the great variety in forest structure int consideration a much higher plot number was decided on. Random sampling points were generated in ArcMap within the sub-compartments to fulfil the requirements of randomness for the sampling design. Unfortunately, due to the severe wildfire situation in the surrounds of the GIZ forest school, the initial plans on conducting surveys on more than 60 plots were foiled to end up with 15 plots to be explored. In addition, time had been forked out for extra measurements on single trees and for the UAV flying missions. The resulting number and distribution of the sampling plots, however, reflect a good compromise between the achievable accuracies for the inventory and the diverse appearance of compartment 435 (see also Figure 7.11. and Figure 7.12.).

The shape and orientation of the sampling plot was chosen to be congruent with the satellite image structure, i.e., squared shape (pixel) and aligned to the north. As for the plot size an area of 1,000 m^2 (i.e., a square of 31.6m x 31.6m) seemed sensible, since it covers a bit

more than a Landsat 8 pixel of 30m x 30m and Sentinel-2 pixels of 10m x 10m. In addition, the suggested plot size is big enough to gather representative data for the forest stand surveyed, and is small enough for a time-efficient inventory for plots in higher numbers when dealing with limited resources. A compensation for the slope also needed to be accounted for, since distances measured along the slope causes a bias due to the fact, that the plot being projected to the horizontal will feature an under-represented area (Kangas and Maltamo, 2009: 61).

The *UAV flying mission* concepts were primarily driven by the curiosity on : (i) how accurate are tree height values with respect to single trees, and (ii) how useful are Canopy Height Models (CHMs) to determine stand height to replace or at least augment field survey? In order to shed light on these issues flying areas were identified on a GIS basemap in combination with the GIZ survey data to ensure that launching and landing of the UAV is safe (i.e., either outside the forest or in forest gaps) and the flown areas are large enough to extract useful height information for individual stands. A number of potential flying areas were pinpointed and the missions planned using the UAV Editor online tool (https://www.uaveditor.com/de/). The mentioned planning tool allows for automatic waypoint flying for attaining best results in subsequent photogrammetry processing. The flying parameters were set to get a forward image overlap of 95%, a side overlap of 65%, and a flying altitude of 70 metres above ground for catching enough tree details, but also ensure good area coverage (for optimal flying parameters see also Seifert *et al.*, 2019). For more information on the flying missions and the extraction of the relevant forest and tree attributes please refer to chapter 7.3.4.

The most relevant data gathering and analysis concepts are portrayed in the following chapters.

7.3.2. Ground truthing and mensuration

Fieldwork was conducted on-site in the period from mid of July to beginning of September 2017. However, due to the wildfire situation in the test area fieldwork had to be suspended for more than two weeks. With reference to the process of determining the location of the test plots and single trees (see also Figure 7.11) the locations were identified on site using the coordinates stored in the GPS instrument. After having marked the plot centre with a pole the four corner points of the test plot were found by using compass, measuring tape, and lacing cord. To compensate for the slope effects on length measurements a level bubble was attached to the lacing cord (see also Figure 7.14.).

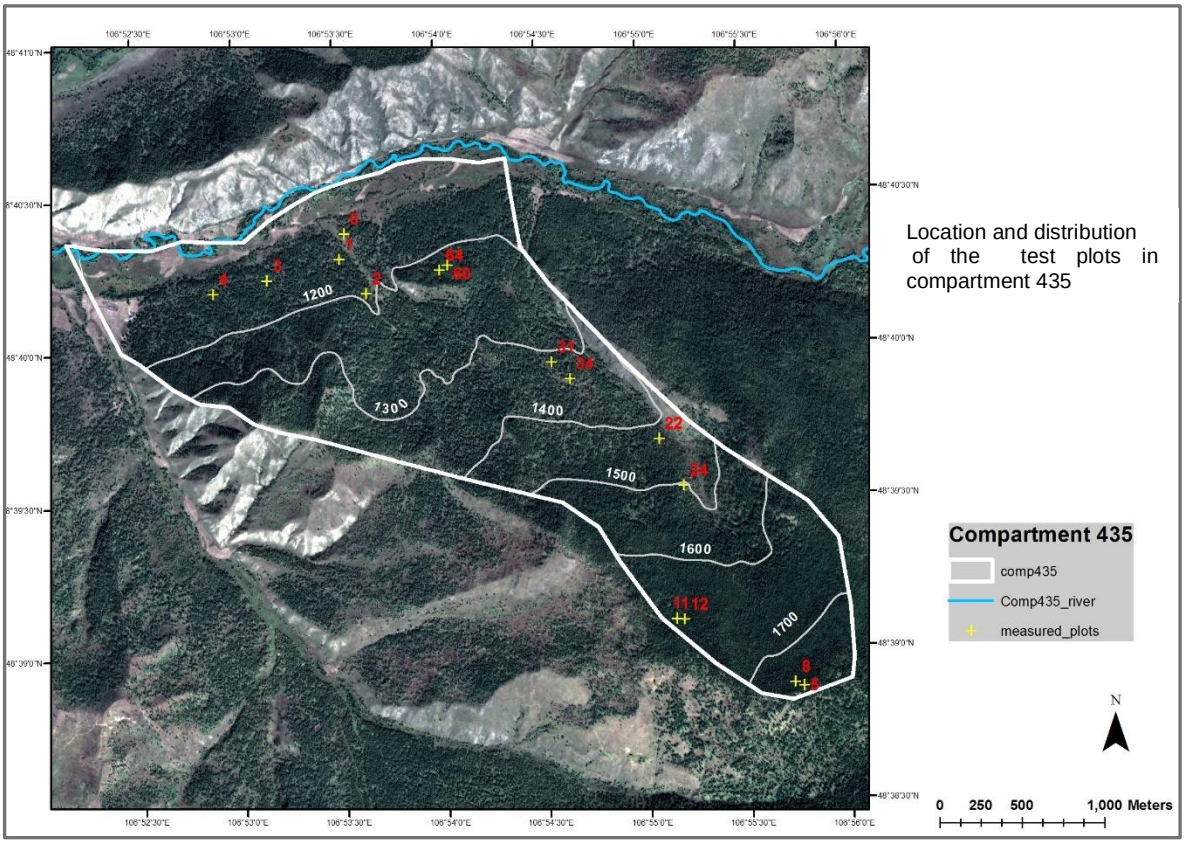

Figure 7.13: Location and distribution of the test plots in compartment 435 (yellow crosses).

The four corner points were then marked and the barrier tape tightened between the points for getting an easily identifiable plot boundary. All trees within this boundary were then subjected to various measurements.

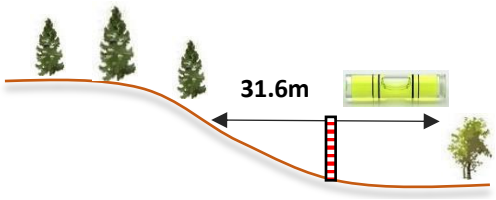

Figure 7.14: Compensation of slope effect.

Subsequently, the following tree and stand attributes were gathered:

- Tree height
- Diameter Breast Height (DBH)
- Tree species
- Crown diameter
- Leaf Area Index (LAI)
- Slope / aspect
- Canopy closure
- Number of trees
- Timber quality
- Remarks (e.g., forest floor flora).

At this point I would like to footnote that the author of this thesis has worked in the forest inventory business for many years, thus has gathered sound experience by measuring thousands of trees. Having said this, it be can be assumed that measuring errors were kept to a minimum. The author's assistant Enkhbat also underwent extensive training and was given detailed instructions on site. For extensive studies it is not unusual to have the surveyors work in turns to minimise systematic errors in measurements. However, my Mongolian assistant had only limited practical experience, and as such, it was decided to make him focus just on the determination of the DBH.

Tree *height*, *DBH*, and *crown diameter* were measured in compliance with the methods portrayed in chapter 3.1.3. The surveyor employed the Nikon laser rangefinder (especially designed for carrying out height measurements), the DBH measuring tape, as well as the crown mirror for readings in S-N and E-W distances of the crown extent. *Aspect* was determined by getting the pertaining compass bearing. *Slope* was gauged by getting an eye level reading (marking tape attached to a pole at 1.70m height at a distance of 30m from the plot centre) in fall line using the Suunto inclinometer. *Tree species* identification was based on personal experience and descriptions found in the technical literature (see also chapter 7.3.4.1.). The assessment of *timber quality* and identification of *forest flora* are retrieved form the author's experience and also from the information provided by experts. *Tree number* could easily be established by counting the measured and chalk-marked trees within the plot. For the *LAI* measurements a diagonal transect was chosen within the test plot with readings taken every 2 meters with the LICOR LAI 2000 to achieve an average value for the plot. The identical pattern was used for measuring *canopy closure* (crown cover) with the Canopy App (for Android mobile phones). *Basal Area* was gathered by a full 360° sweep with the Kramer dendrometer (gauge width of 1) on at least four representative points within the test plot.

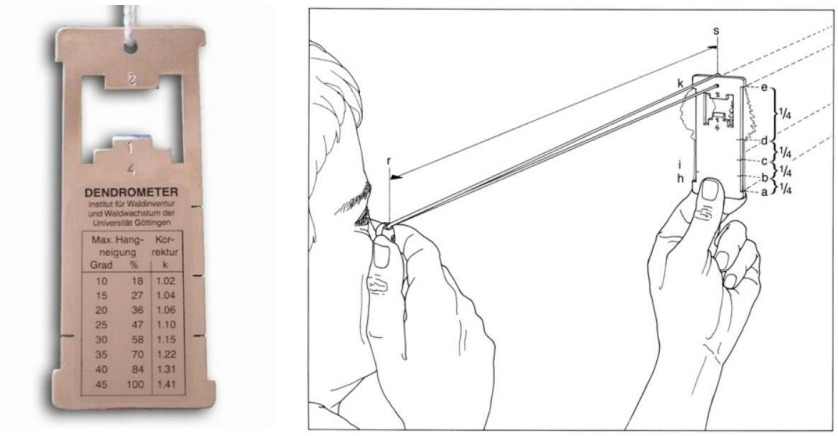

Figure 7.15: Kramer's dendrometer for determination of stand basal area (van Laar and Akça, 2007: 39-40).

7.3.3. Analysis of field data

Tree and *stand heights* were retrieved and calculated for single trees and per test plot per tree species. In addition, the stand heights were aggregated for light taiga and dark taiga to determine disparities. In the professional literature several definitions of stand height are used. As such, it is vital to get a decent understanding on the various rationales.

Stand height determination variants are:

- Arithmetic mean: mean of the height of all trees in the stand (it represents a measure of stand height in more uniform, even-aged stands, but is affected by thinning and mortality).
- Predominant height: mean height of the tallest trees in a stand (to account for thinning and tree mortality).
- Top height: mean height of the trees with the largest DBH in a stand.
- Dominant height: mean height of the dominant trees in a stand.
- Lorey's mean height: weights the contribution of trees to the stand height by their basal area (mostly used in Europe and the USA).

In order to be consistent, stand heights in the presented study are calculated as arithmetic mean, since most of the investigated forest stands are rather uniform in the selected strata, except for the dark taiga areas (they are not affected by thinning). In addition, values calculated by applying the variants as described above cannot be extracted from the satellite image pixels by using regional or local statistics methods.

Diameter Breast Height (DBH) can be derived for a forest stand most commonly as (i) arithmetic mean of all DBHs measured, or (ii) calculated as the diameter of the tree representing mean basal area. The latter was computed by using the following formula:

$$dg = \sqrt[2]{\frac{\Sigma\, di^2}{n}}$$

The calculated mean d_g is less susceptible to extreme values than the arithmetic mean and as such is the most commonly used measure for mean DBH (Prodan, 2014: 148–149). Mean d_g was used throughout the mean DBH calculations for this thesis. DBH distributions were established for drawing conclusions on the structure as well as on the treatment (e.g., thinning) of the forest stands.

Other forest stand attributes like *LAI*, *Basal Area* (stand density index), *canopy closure*, and *crown diameter* were calculated as arithmetic means. *Timber volume* (for details see section below) was derived for each species per plot and as plot average (mean). The *Shannon index* was worked out per plot using the index formula as follows:

$$H' = \sum_{i=1}^{R} pi * \ln pi$$

where p_i is the proportion of individuals belonging to the *i*th species in the dataset.

The calculation of *timber volume* is a task being far from trivial. Commonly, allometric formulas are applied per species and site-specific conditions (i.e., soil, climate, etc.). However, this undertaking requires the exhaustive (destructive) measurement of thousands of trees to attain a sound basis for the construction of such formulas. In cases resources (time, money, personnel) are limited the outcomes tend to reflect a more generic character as is the case for Mongolia. The required allometric formulas were devised by the Mongolian Botanical Institute (Altrell and Erdenejav, 2016). They are referred to as the 'Mongolian national volume function of a tree stem including bark'.

The generic model is as follows: **Volume = a * DBH^{b} * Height^{c}** , with **a** being a species-specific factor; **b** being a species specific DBH exponential factor; **c** being a species-specific Height exponential factor (for all factors see table below).

Table 7-1: Species specific factors for Mongolian volume function (NFI report, 2016).

Factor	Tree species						
	Larch	Pine	Cedar	Spruce & Fir	Birch	young Larch	
						Central Khangai	Eastern Khentii
a	0.229067	0.356149	0.422366	0.407192	0.121815	0.6624588	0.2094661
b	1.75631439	1.91061797	1.93511358	1.94199866	1.79633106	1.981094	1.7602414
c	1.04530318	0.96807707	0.94402384	0.94744137	1.24762399	0.7989367	1.0522551

All timber volumes were computed based on the factors given above. In the naming convention of above table, the term 'pine' refers to Scots pine, whereas 'cedar' denotes the species of Siberian pine.

The scientific community in forest mensuration and growth & yield does not get wary of emphasising that the *relationship between DBH and tree height* allows for substantiated inferences on the structure and management of forest stands (Corona *et al.*, 2003, Kangas and Maltamo, 2009, Kleinn, 2014, Pretzsch, 2010, Prodan, 2014, van Laar and Akça, 2007).

Once a close relationship is established the individual tree height can be deduced from the reading for DBH and vice versa. It is for this reason the height/DBH relationships were calculated for each test plot and each species employing liner regression.

Further statistical analysis

One of the most intriguing questions related to this work is in my opinion, whether there are distinct differences in the field data between the dark and the light taiga or not. Most obviously there is variation in the species composition, but will the specific traits also be reflected in the species shared by both dark and light taiga – the Siberian larch? To resolve this 'plight' a two-pronged approach was taken, namely (i) the *box plot* analysis, and (ii) the *Mann-Whitney U test* (also referred to as Mann-Whitney-Wilcoxon, or Wilcoxon rank sum test).

Creating a box plot in Excel is very straightforward, once the field data have been sorted according to each category (i.e., tree height, DBH, dark taiga, light taiga). The standard statics (e.g., mean, median, standard deviation, variance) for both, height and DBH, were also computed. Prior to taking a decision on an appropriate statistical test the nature of the distribution of the data needed to be looked into. The calculated skewness and kurtosis values already reveal a good trend, but this analysis was taken a step further by conducting a so-called *Q-Q* (quantile – quantile) plot analysis. This particular method is a graphical representation of the properties of distributions (location, scale, skewness) to be perfectly cut out for the comparison of data collections by plotting their quantiles against each other. As for the interpretation of the resulting Q-Q plots two distributions being compared can be regarded as identical, if the plot follows the 45^{o} line. Once the plot shows an arced ('S') shaped graphical representation of the quantiles, one of the distributions is more skewed, thus not following a normal distribution (Lorenz, 2020, Thode, 2002: 21–22, Wilk and Gnanadesikan, 1968). Anticipating the outcome of the Q-Q plot analysis the graph reveals that DBH distributions are skewed, thus not showing the characteristics of a normal (Gaussian) distribution (for results see chapter 8.1.3.). This information was a prerequisite for further statistical testing.

Since DBH distributions for the light taiga set against the dark taiga do not meet the requirements to be Gaussian, a non-parametric statistical test had to be chosen. The selection of a specific test was based on the decision tree designed by Groner and Wartburg (2020) for testing the hypothesis, whether there is a difference between the DBH populations for dark and light taiga. Following the decision tree (https://etools.fernuni.ch/entscheidungsbaum/index.html) the Mann-Whitney U test appeared as the most appropriate (see figure 7.16.).

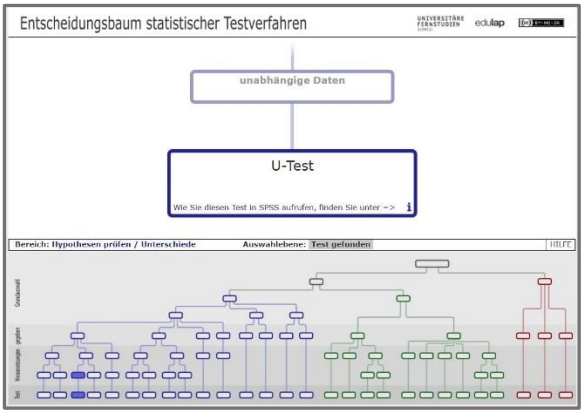

Figure 7.16: Decision tree for statistical testing (Groner and Wartburg, 2020).

The *Mann-Whitney U test* is a non-parametric test for independent samples to determine, if there are differences in medians between two groups. Instead of using the concrete values the dependent variable is ranked accordingly, thus exhibiting an ordinal character. Further assumptions are:

- The null hypothesis H_0 stipulates the distributions of both populations to be equal.
- The alternative hypothesis H_1 is that the distributions are not equal.

Test following statistics need to be calculated to be able to draw conclusions:

$$U = n_1 n_2 + \frac{n_1 (n_1+1)}{2} - R_1$$

with n_1 = sample size of the group with the bigger rank sum; n_2 = sample size of the group with the smaller rank sum; R_1 = the bigger of the two rank sums. For a sample size bigger than 30 the calculated U values need to be standardised by using:

$$z = \frac{U - \mu_U}{\sigma_U} = \frac{U - \frac{n_1 \cdot n_2}{2}}{\sqrt{\frac{n_1 \cdot n_2 (n_1 + n_2 + 1)}{12}}}$$

with μ_U = median of the U distribution; σ_U = standard error of the U value. The resulting z value is now tested against the critical value of the z distribution, which for the two-tailed significance level is $\pm$ 1.96 for extremely big sampling sizes. Once the calculated z value proofs to be greater than the critical z value the null hypothesis has to be rejected, thus the difference between the two groups can be considered to be significant. The results of these calculations can to be found in chapter 8.1.4.

7.3.4. Aerial (UAV) imagery

From the UAV imagery the following main tree/forest attributes can be derived:

- Tree species
- Tree location
- Tree/stand height
- Crown delineation and crown diameter

All attributes mentioned above were extracted from the UAV imagery. Further attributes can also be determined, such as tree vitality/health status using multispectral imagery (with NIR band), horizontal structure (distribution of the trees being single, clumped, scattered, etc.), counting of tree stumps for cutting control, or post-disaster analysis (windfall, pest attacks). However, such extended investigation would have been beyond the scope of this work.

In total eight missions were planned, but due to access restrictions (wildfire) only two missions could be implemented for the single tree height measurements and another two for gaining height information of forest stands. Flying time was between 11:00 and 13:00 in favourable weather conditions (low wind speed, little cloud coverage) to get imagery with good contrast and ‘sharpness’. The locations of the flying missions are depicted in Figure 7.17. below.

Rest of this page intentionally left blank

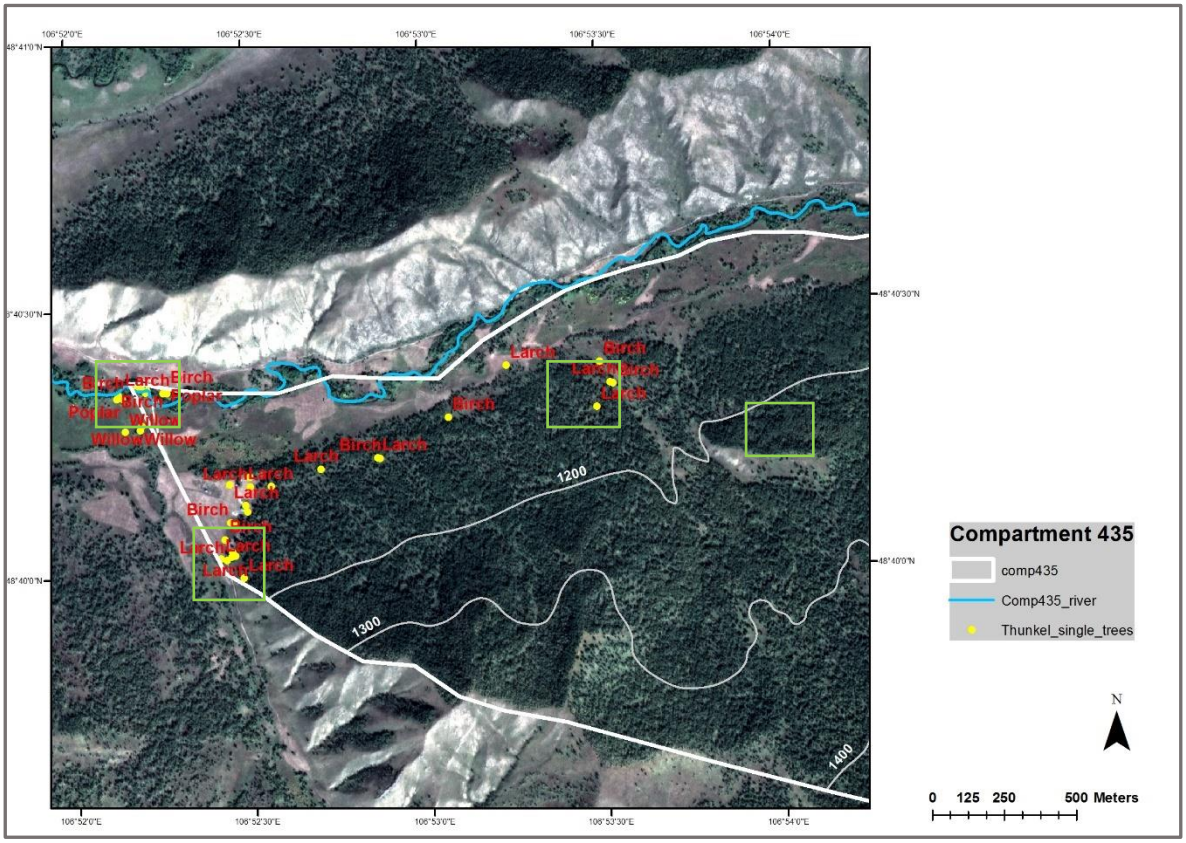

Figure 7.17: Location of the single trees measured (yellow dots). The locations of the flying missions are indicated with boxes in green. Trees outside compartment 435 were also measured and captured during flying mission 14 (riparian area top left of map).

7.3.4.1. Photointerpretation for *tree species* identification and *tree location* (number)

In this subchapter only the visual interpretation of the UAV imagery is dealt with. However, some automatic tree species classification was also carried out as a trial to be found in chapters 7.3.4.6. and 8.8.1.

Based on the interpretation keys by Sayn-Wittgenstein (1978) and the European Commission (2001), but foremost, on own observations, the following guideline was devised for the interpretation of the most salient tree species to be found in Mongolian taiga forests. To the author's knowledge, no such an interpretation key is assumed to exist up to date. The descriptions are embellished with photographs (Figure 7.20) showing the corresponding species in the field and from above.

Table 7-2: Interpretation key for the most abundant tree species of the Mongolian taiga.

Tree species	Characteristics in aerial imagery
Larix sibirica (Siberian larch)	Narrow, open, symmetrical, conical crown, when young; broad, irregular in old trees; old trees often skeletonised, crown wrecked, damaged (lightning); twigs slender; foliage very fine; deciduous – changing colour from green to yellow; in general lighter tone than spruce.
Pinus sibirica (Siberian pine)	Crown dense, narrow, symmetrical and conical; branching symmetrical ; wavy outline; branches horizontal, reaching ground, when in the open; foliage denser and darker than Scots pine; trunk darker than Scots pine; as member of the dark taiga residing at higher altitudes.
Pinus sylvestris (Scots pine)	Crown irregular, in young trees more conical, flattened in old trees; crown furrowed, lumped; larger branches very prominent; star-shaped outline of crown; thinner foliage than Spruce; lighter colour than spruce; foliage more sparse in old trees (less opaque than spruce).
Picea obovata (Siberian spruce)	Crown conical, pointed top, symmetrical; outline corrugated or smooth; dense, dark foliage; branching prominent; single, straight, central, dark trunk; homogenous colour, intensive saturation; residing at higher altitudes (dark taiga), but also at riverine areas.
Abies sibirica (Siberian fir)	Crown narrowly conical (young trees), symmetrical, crown flattening, when ageing (stork's nest); crown structure step-shaped, densely lobate; serrated outline in old trees; dark foliage; branches less prominent than those of spruce; to be found at higher altitudes (dark taiga).
Betula platyphylla (Siberian silver birch)	Pure or in mixed stands; young trees: small, conical crown; old trees: crown more rounded, irregular, multiple; trunk WHITE, often forked and multiple (due to coppicing); ascending branches; often leaning or crooked; foliage bright, light green in spring, darker in summer; deciduous.
Populus laurifolia (laurel-leaf poplar)	Crowns medium or large; trunk dark; crown tufted, broad; branches and twigs coarse; grows along rivers, associated with willow; dark, big foliage; deciduous; height up to 15m.
Salix spec.(Willow)	Often appears as blankets in imagery, along rivers; trees fairly low, fine foliage texture, light-toned foliage; crown mostly spherical; deciduous; height up to 8m.

Based on afore-mentioned interpretation key, the distinction between larch and birch was very straightforward, since leafage appears sufficiently different (needle vs leaf). In addition, in many instances the white bark of the birch rendered very conspicuously and thus eased the identification considerably.

Figure 7.18: Left: close-up of aerial photo (flying altitude 70m above ground) illustrating birch (yellow dot) and larch (blue dot); right: GCP chequer target for georeferencing of the imagery.

However, high flying altitude of the UAV and a related incremental coarseness (graininess) of the imagery can hamper an accurate classification markedly. In addition, varying illumination conditions and so-called hot spots (i.e., very bright areas) constitute a real challenge to every image interpreter. The mentioned circumstances are illustrated in the following aerial image, which was taken at an altitude of 150m above ground with a wide-angle lens camera (Figure 7.19).

Figure 7.19: Left: high altitude UAV image with hot spot (yellow ellipse); right: close-up of same image.

Since proper tree species discrimination appeared to be almost impossible, imagery taken at 150m above ground was ruled out for further visual interpretation. Focus was on imagery taken at 70m above ground – no further image processing was required prior to interpretation.

The following tree species were considered for an interpretation assignment (see also figure below): Siberian birch, Siberian larch, poplar and willow. Unfortunately, no acceptable aerial imagery was available for Siberian pine, Siberian spruce and Siberian fir (dark taiga). For reference single trees were selected in the research area, with the location coordinates determined (GPS) and tree species and further parameters (DBH, height, crown diameter) specified. Although some of the GPS coordinates were found to be up to five meters off the true location, the visual assignment of the correct tree individual turned out to be smooth. The results of the comparison between visually interpreted species and ground truthing are detailed in chapter 8.8.1. The figure below demonstrates the appearance of the most relevant tree species from a vantage point above and a view from the ground. If tree species can be attributed to single trees it is also possible to determine the Shannon index from UAV or other very high-resolution imagery (see also chapters 7.3.3. and 8.11.).

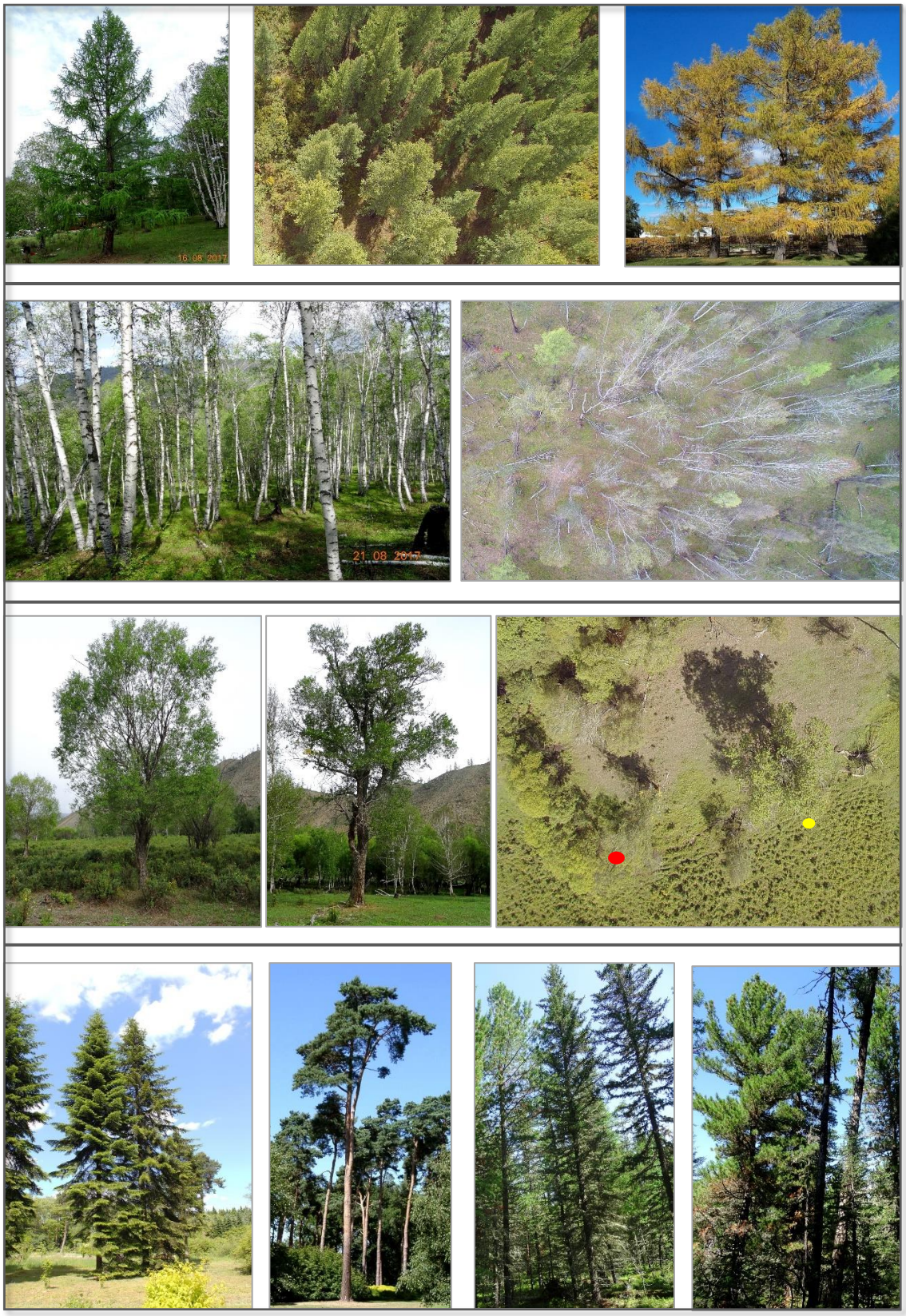

Figure 7.20: Tree species - top left to right: larch (ground view, aerial, larch in autumn colours (source: Wikipedia)); below: birch (ground view, aerial (partially defoliated)); below: willow, poplar (ground view, aerial: willow red dot, poplar yellow dot); bottom: Siberian fir (source: Wikipedia), Scots pine (source: Wikipedia), Siberian spruce, Siberian pine.

7.3.4.2. Tree height extraction preparation - Photogrammetry workflow in AgiSoft Metashape

As detailed in chapter 4.6. tree height, being one of the most important forest inventory parameters, can be extracted indirectly (modelling, regression, etc.) or directly by analysing 3D point clouds (laser, photogrammetry). The following section details the photogrammetry pipeline in Photoscan (now called 'Metashape'). All individual settings are described pertaining the relevant workflow actions (see Figure 7.21) to ensure transparency and replicability. Parameter settings have been extracted from the AgiSoft Metashape manual (Agisoft, 2018), various tutorials (Agisoft, 2015, Endicott, 2018, James, 2017, level 80, 2015, Malory, 2015) and based on recommendations (Greiwe, 2018, Kunneke, 2019, Seifert, 2019, UAV Campus Group, 2018, Unger, 2018, van Aardt, 2019) as well as personal experience and trials. In a few comparative studies the Agisoft software performed better than other photogrammetry packages (Jaud *et al.*, 2016, e.g. Sona *et al.*, 2014), but other studies point out, that the accuracy of the outcomes also largely depends on the characteristics of the objects scrutinised. As such, there is no clear winner (Alidoost and Arefi, 2017, Kunneke, 2019, Probst *et al.*, 2018, UAV Campus Group, 2020).

According to the Agisoft support Dmitry Semyonov (2011) in Metashape algorithms similar to SIFT and Bundle are executed. For dense surface reconstruction pair-wise depth map computation as well as multi-view approach (see also CMVS) is utilised. Regrettably, more current information on the algorithms used was not available.

In the following the steps of the CHM (Canopy Height Model) and orthophoto generation are detailed. Various parameter settings were tested and the results optimised.

Rest of this page intentionally left blank

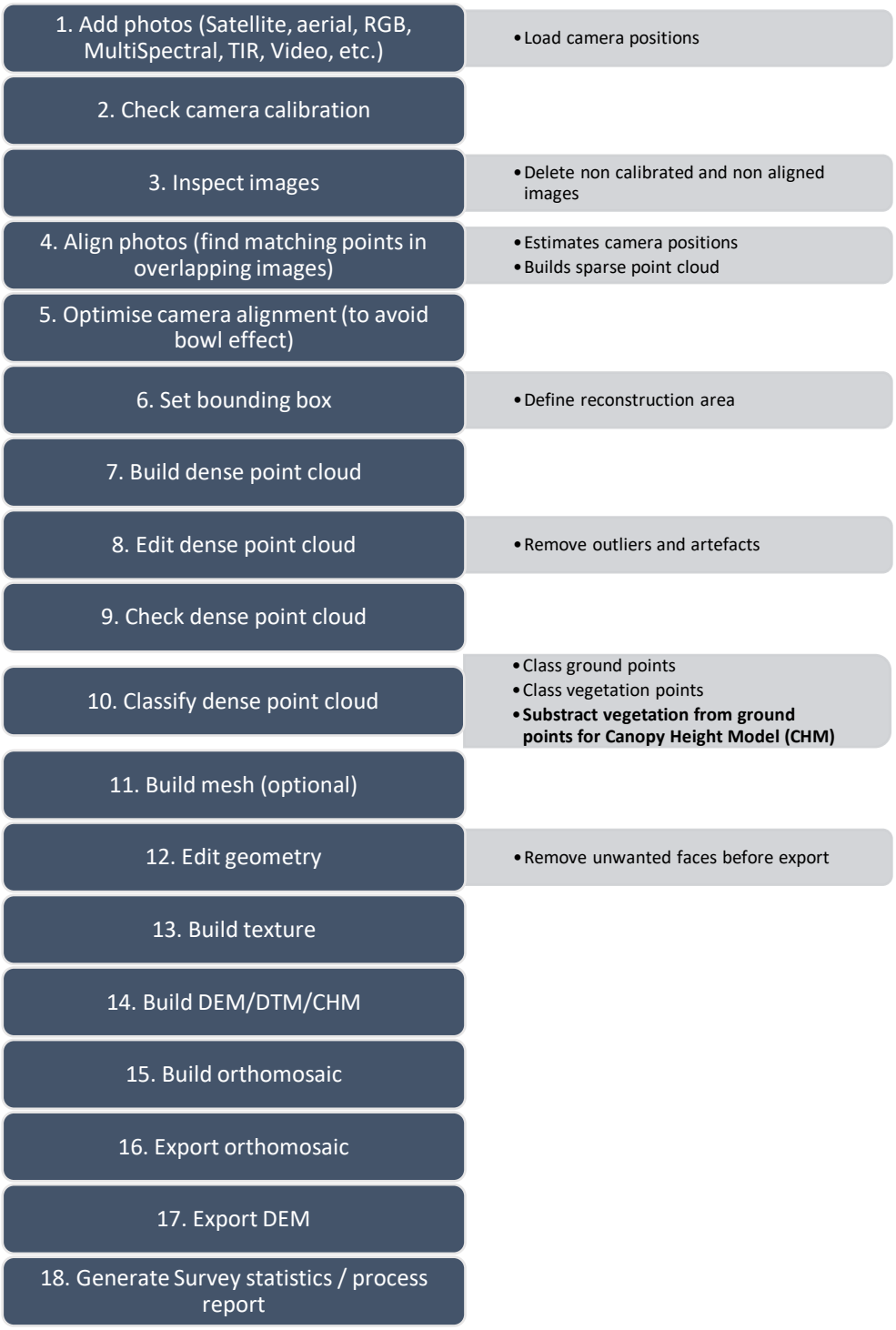

Figure 7.21: Project workflow in AgiSoft Metashape

Metashape supports the following imagery (aerial, spacebourne and near ground) :

- scanned photos
- multispectral imagery
- thermal imagery
- satellite imagery
- conventional RGB imagery

Camera positions can either be loaded directly or are imported from the EXIF files of the UAV imagery (images linked with GPS data of the camera positions determined during mission). Prior to loading the UAV RGB imagery, the stack was checked for flaws and the EXIF files selected randomly for inspection – no major issues were detected for all Thunkel flying missions.

Camera calibration is either extracted automatically from the EXIF metadata file of the images (as carried out here) or available in the Camera Calibration dialog for individual parameter settings. As a preceding step Agisoft's Lens module can be used to determine camera parameters such as focal length, principal point coordinates and radial distortion coefficients. According to the Lens manual: *'Agisoft Lens is an automatic calibration software, which uses LCD screen as a calibration target. It supports estimation of the full camera calibration matrix, including non-linear distortion coefficients'* (Agisoft, 2011: iv). Unfortunately, the Lens module failed in each trial, thus I relied on the correct estimation of the camera parameters within the alignment process using the EXIF information. However, to get an impression on the quality of the Typhoon H camera lens I took a few test photos using a professional test template (see also Figure 7.22) and discussed the outcomes with a professional photographer (Klawunn, 2018). According to him, no grave effects such as barrel distortion, vignetting, colour aberration and lack of resolution were observed.

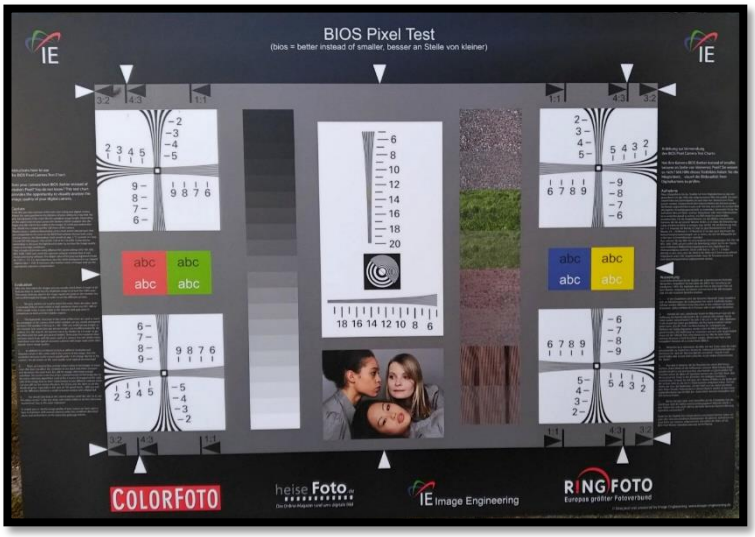

Figure 7.22: Template for testing camera parameters and image quality.

In addition, a distortion plot and a residual graph was generated in Metashape and subsequently evaluated. The performance of the Typhoon camera was considered surprisingly good for a consumer grade camera.

The assessment of the image quality is another crucial step for the subsequent creation of the 3D forest model. Imagery was checked visually, and blurred, non-calibrated and poorly

exposed photos discarded. In addition, Metashape's image quality metric (mainly based on contrast estimates) was employed to expel photos with a quality score smaller than 0.5.
For precise georeferencing of the model *Ground Control Point* (GCP) data are mandatory prior to running the alignment procedure. Since I experienced location shifts of up to five meters for my GPS ground survey, the idea of incorporating this inaccurate information was scrapped. Consideration of the GPS GCPs would have introduced major strain and thus distortion of the 3D model. Instead, the georeferencing process was carried out during further processing in a GIS environment. Rather, a highly precise internal 3D model was targeted at this stage of the photogrammetry workflow. The EXIF metadata of the UAV imagery determining the positions of the UAV camera now serves as a critical input to find matching points in multiple, overlapping images. Intrinsic and extrinsic camera parameters are estimated. The following settings were applied throughout the project:

Table 7-3.: Parameter settings of the UAV project. Numeration corresponds with workflow details.

Parameters	Settings
4.Align photos	
Accuracy	High
Pair preselection	Reference
Key point limit	0 (i.e., no limit)
Tie point limit	0 (i.e. no limit)
Adaptive camera model fitting	Enabled
Coordinate System	WGS84 EPSG: 4326
Camera accuracy	0.5 m
Marker accuracy	0.005 m
Scale bar accuracy	0.001 m
Marker accuracy	0.1 pixel
Tie point accuracy	1.0 pixel
7.Build dense point cloud	
Quality	High
Depth filtering	Mild
11.Build mesh	
Surface type	Height field & Arbitrary
Source data	Dense cloud
Face/polygon count	High
Interpolation	Enabled
13.Build texture	
Mapping mode	Orthophoto
Blending mode	Mosaic
Enable hole filling	Yes

Parameters	Settings
14.Build DEM/CHM	
Projection	WGS 84
Source data	Dense cloud
Interpolation	Enabled
Point class	Ground,vegetation, canopy height
Resolution	5 cm
Total size	25 Mio. pixel
15.Build orthomosaic	
Projection	WGS 84
Surface	DEM
Blending mode	Mosaic
Enable hole filling	Yes
Pixel size	3 cm
16.Export orthomosaic	
Coordinate system	WGS 84
Pixel size	3 pixels
Region	Model area
TIF compression	LZW
JPEG quality	90
17.Export DEM/CHM	
Coordinate System	WGS 84
Raster pixel size	3 pixels
No data value	0
Region: total pixel size	25 Mio.
Write world file	*Enabled*

After completion of the alignment process a *sparse cloud* indicating the 3D tie points of the model are displayed. The next processing step entails the assessment and refinement of the tie point quality. For this purpose, all images were sorted by RMS tie point image residual and photos exceeding an RMS of 3 pixels excluded from further processing. Furthermore, all images taken at unusual angles (e.g., taken during banking manoeuvres) had to be removed. Obvious tie point outliers were also good candidates for elimination. Agisoft's *Gradual Selection* tool provided another option to expel images, where tie points were only observed in three or fewer photos. Further quality metrics were applied to select flawed imagery such as *Reprojection Error* (represents image residuals based on image matching; critical value: > 0.2 pixels), *Reconstruction Uncertainty* (possible variation in point placement - indicating vertical and horizontal precision; critical value: > 10 pixels) and Projection Accuracy (accuracy of point placement from local neighbour points; critical value: > 10 pixels). Unfortunately, no information on the algorithms used for the determination of these quality metrics was provided by Agisoft's tech support Alexey Pasumansky or Dmitry Semyonov.

To achieve higher accuracy in calculating internal and external camera parameters the *Optimize Camera Alignment* procedure was run and additional distortion coefficients calculated to be displayed in a distortion plot for quality check. Compensation of rolling shutter was also considered. This procedure resulted in a slight improvement of the camera model.

In the model pane of Metashape a bounding box was determined for definition of the reconstruction area to avoid inclusion of unsound tie points in the model.

Based on the estimated camera positions the program calculates depth information for each image to generate a *dense point cloud*. The reconstruction quality is specified by the individual choice of quality settings. Higher settings result in more detailed and accurate geometry, however, to the expense of computing time. Since forests represent a highly structured surface, the modes 'High' and 'Very high' were chosen – the mode 'Very high', however, did not yield a huge gain of 3D information over the slightly lower resolution. The depth filtering mode 'Mild' was selected to account for the complex structure of the landscape. The mode 'Aggressive' is more appropriate for rather untextured surfaces, like roofs, to sort out outliers. Disabling filtering at all entails a lot of noise in the point cloud.

The resulting dense point cloud of step 7 might still feature some blunders, which can be manually selected and deleted. After a meticulous check of the now refined point cloud the 3D model is posed for further processing.

The entire 3D model was subsequently split up to create models representing ground as well as vegetation points. A set-off of 0.5m was applied to generate an elevation plane to portray the terrain and exclude low vegetation, like shrub, from further consideration of tree canopy heights. Serendipitously, there was sufficient spacing between the trees to obtain satisfactory

results. The *interpolation* option was selected to fill the holes in the train model. Unfortunately, no information on the interpolation algorithms was disclosed by the Agisoft support team. The following graphs show an example of the split of the point cloud into terrain model (DTM), interpolated, and surface model (DSM).

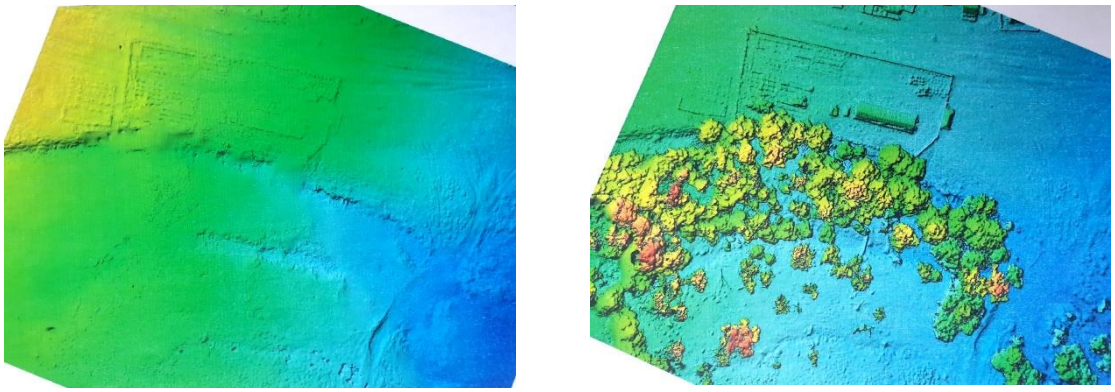

Figure 7.23: DTM (left) and DSM (right) of flying mission 14.

Albeit these circumstances, a visual check of the terrain model revealed suitable outcomes. The complement of the initial 3D model now contains all height information pertaining the forest. In order to ease further assessment of the canopy height model, relative heights were generated by subtracting DTM values from the vegetation model values.

Mesh construction is an optional step in the Metashape workflow. Both surface type options were assessed for best results. 'Height field' option is more geared for planar surfaces, thus 'Arbitrary' was chosen for mesh construction, since this algorithm does not make any assumptions on the type of object to be modelled.

Before building texture and exporting the model it is sometimes required to take action concerning geometry. Metashape tends to generate 3D models with excessive geometry resolution. However, close inspection of the geometry did not expose features to be rectified.

Building *texture* is imperative, if a more realistic appeal of the 3D model is favoured. In addition, it also helps to inspect the model and to place markers more precise for measurements. In our case 'orthophoto' mapping was selected, since the entire surface is textured in the orthographic projection. Alternative mapping options did not amount to acceptable results.

Having finalised all required steps to obtain a representative, correct 3D model of the specified object, the dense point cloud is used as the basis for the *DEM* generation process. DEMs can be then used for further topographic analysis in a GIS suite. The coordinate system has to be specified in accordance with the system used for the modelling reference (in our case: WGS84). Metashape allows to set up the DEM boundaries and define DEM resolution. The creation process was undertaken for both, DTM and DEM(CHM). The results were visualised in Metashape for inspection.

The construction of *orthomosaics* can be useful for subsequent analysis in a GIS package. Rectified imagery in an orthogonal projection can help identify specific objects and their related precise location. Projection, colour correction, hole filling and desired resolution can be specified in Metashape.

Subsequently, the generated orthomosaic image was exported with high raster resolution and low image compression to avoid model deterioration. In a subsequent step, the same applied to the export process for the DTM/DEM/CHM. Because of the complex structure of forests, it is advisable to retain as much model information as possible at reasonable cost and processing time. For outcomes of the DTM/CHM creation process please refer to the 'Results' section (chapter 8.3).

For a conclusive and thorough assessment of the quality of the 3D model the statistics of the survey, as well as a process report were generated (for discussion see also section 8.3.).

In the following the resulting model parameters of the various flying missions are detailed.

Table 7-4: Flying and model parameters of the various missions.

	Mission 1	Mission 1 low profile	Mission 2	Mission 3	Mission 14
Number of photos	74	74	427	224	147
Total error (m)	0.66	0.71	1.33	1.16	2.53
Image quality index	0.85	0.85	0.85	0.86	0.85
Reprojection error (pixel)	0.248	3.29	0.99	1.15	0.80
Number of tie points	139,566	13,493	852,316	691,825	468,483
Ground resolution (cm)	2.92	2.78	3.04	4.93	3.64
Flying altitude above ground (m)	(70) 59	(70) 56	(70) 71	(70) 114	(70) 87
DEM resolution (cm/pixel)	5.57	5.89	6.09	9.85	7.29

As extracted from above table, the total error as calculated by Metashape is within a range of 0.66 to 2.53 – however, mission 14 with the highest error value was only used for tree species identification and a few height measurements. All crucial canopy height model creations were carried out only on the missions 1,2 and 3, all featuring acceptable errors. The image quality index seems to be also in the acceptable range (Semyonov, 2011) – photos with higher values than 0.86 were eliminated prior to model construction. The reprojection error for 'Mission 1 low profile' is due to the fact, that the parameter settings were all set to the lowest possible values

to show the difference in outcome between various setting scenarios. This is also indicated by the low number of tie points, which were at least ten times for the other mission models. The calculated ground resolution of about 3 cm is impressive, given the fact that the flying altitude was moderate and the camera lens featuring an extreme wide lens characteristic. With a resolution of around 3 cm even small features such as bigger leaves are detectable. The calculated flying altitude above ground seems somewhat odd, since the flying height was set to 70 m above ground in the flight planning software (i.e., UAV Editor). However, the flying height (70 m) was carefully chosen to capture enough detail of the features (trees), while retaining enough area coverage.

The figure below illustrates some resulting 3D representation of the terrain flown.

Figure 7.24: Example of a resulting high-resolution 3D model of flying mission 14 (riparian area). The photo locations are indicated with blue squares hovering above the scenery. All features in the model seem precisely represented, especially non-tree objects.

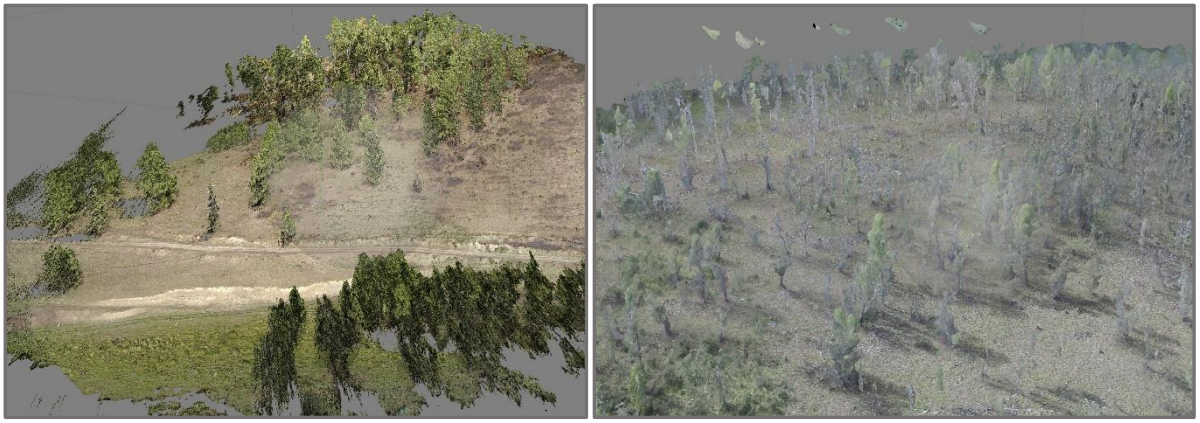

Figure 7.25: Resulting point high-density clouds for flying mission 1 (left) and mission 2 (right). Some parts of the tree crowns seem detached, whereas in the right image the matching algorithm struggles with low contrast imagery and low image texture due to massive tree defoliation.

Since the aerial images were taken in a perpendicular mode the representation of the forest canopy lacks detail of tree stems and lower parts of the crowns. This constellation is reflected in the resulting models with tree parts seemingly being detached ad hovering (see figure above). The results of the height extraction (elevation model) for the various missions are indicated in the map below.

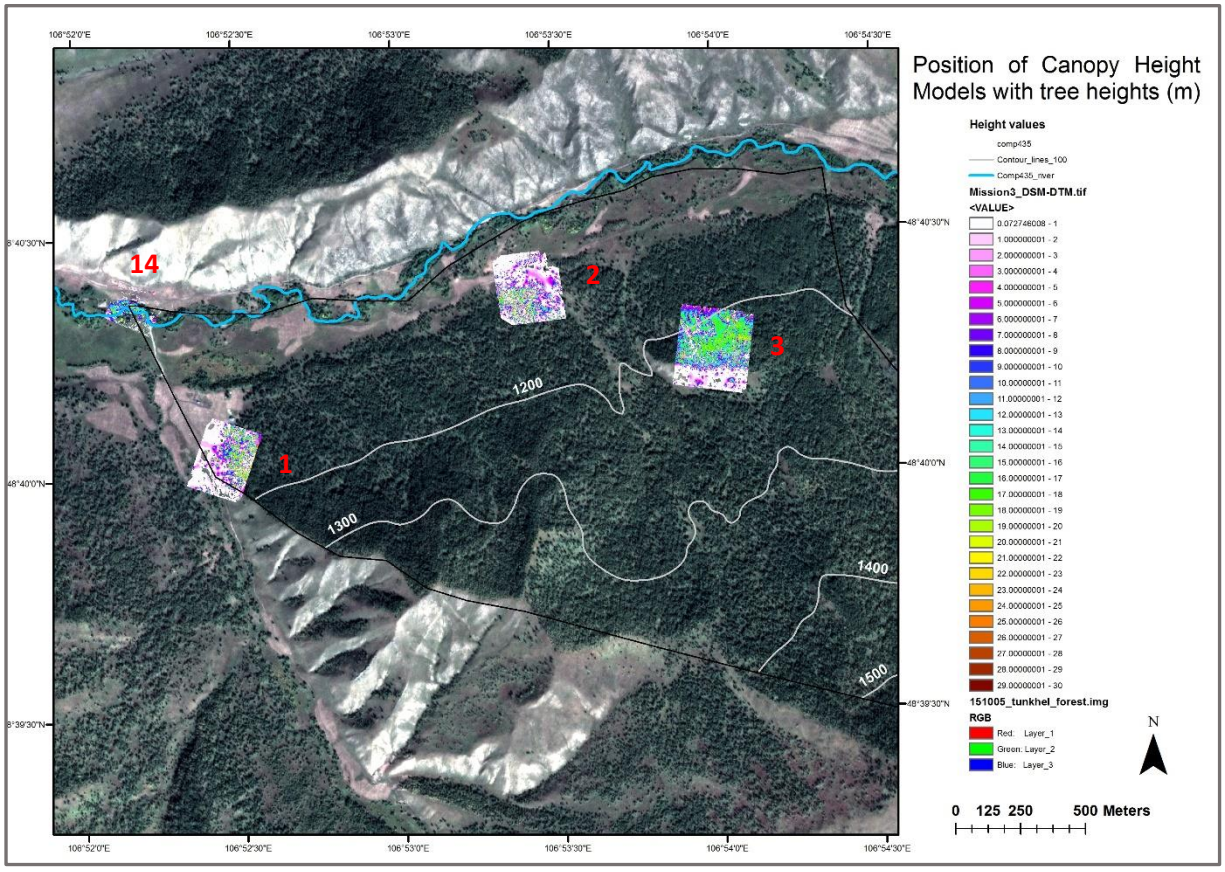

Figure 7.26: Location of the resulting Canopy Height Models (CHMs) with associated tree heights.

The resulting models were exported as orthophotos and elevation models for further analysis in a GIS environment. Individual tree heights were extracted and compared with the reference

data originating from the field measurements. This procedure can turn out to be very cumbersome when height information for entire forest patches is called for. Automatic extraction options for obtaining stand height have been portrayed in chapter 4.6.1. already. The detailed workflow for the application of one of the various methods is given below.

7.3.4.3. Tree height extraction - concrete

The workflow below depicts a standard procedure for the extraction of aggregated tree heights for a forest stand.

Figure 7.27: Workflow for the flying missions conducted at compartment 435, Thunkel.

The QGIS SAGA software was used to carry out the required steps. Gaussian filtering was employed to account for graininess of the height model. An example for an inverted CHM is provided below. The minimum height for the seed points was set to 3 metres to avoid inclusion of the shrub layer in the subsequent stand height calculation process. The outcomes of the statistical analysis are presented in chapter 8.3.

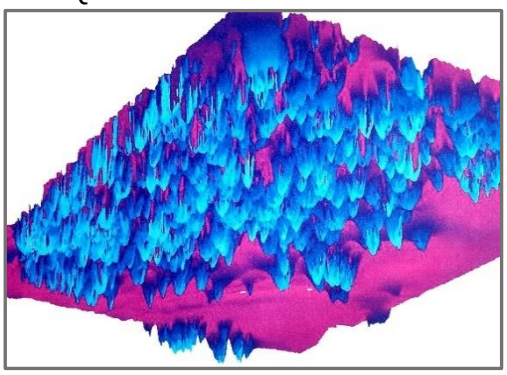

Figure 7.28: Inverted Canopy Height Model of flying mission 1.

7.3.4.4. Tree position determination

Figure 7.29: Orthophoto – flying mission 1.

After having finalised the Metashape workflow it is now possible to export and further manipulate the resulting orthophoto. Since the integration of the ground control points (GCPs) into the 3D model was discarded (i.e., GPS deviations – positional errors), the imported orthophoto was georeferenced in ArcMap using the (BING) Basemap and the Russian topographic map (TÖV M-48-130 1:100,000) as references. The orthophoto can now be used to relatively precisely

determine the position of single trees once identified. However, in many cases the bree base is concealed, so that only a good estimate of the tree location is possible. The picture below shows an example of an orthophoto – it depicts a subset of flying mission1. Conspicuous are blurred areas due to the orthorectification process, and data gaps indicated as white areas. Nevertheless, tree positions for most of the single trees can be identified with considerable ease.

7.3.4.5. Tree crown diameter estimation

The (semi) automatic extraction of the crown shapes and the associated diameter estimations is described in the workflow beneath (Figure 7.31). The CHM was resampled to 20 centimetres prior to further processing to increase efficiency, however, without sacrificing accuracy. In addition, a median filter (5x5) was applied for smoothing the CHM. The portrayed workflow was implemented for the extraction of tree crown diameter on the orthophoto of mission1 with a good mix of isolated and overlapping trees. The eCognition Essentials software package proved to be of great support in the extraction process.

In order to achieve a useful delineation of the tree crowns from very high-resolution imagery an image segmentation is essential.

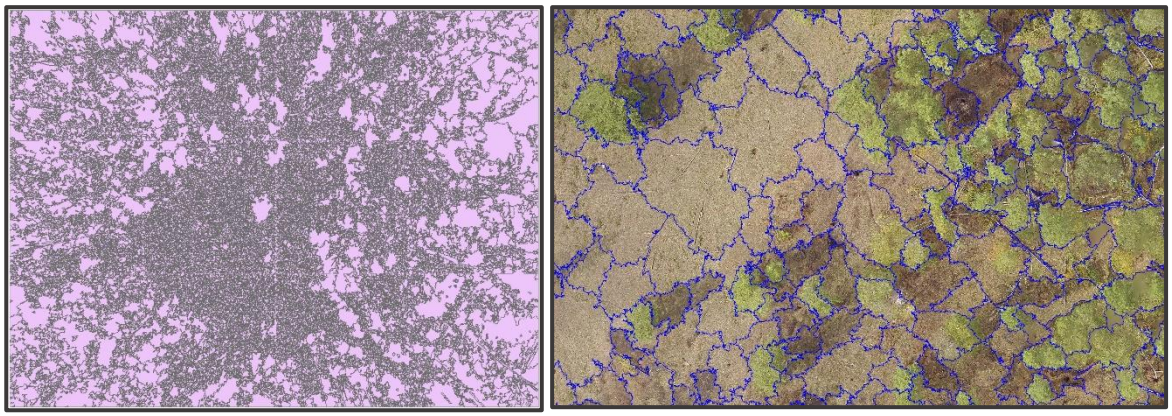

Figure 7.30: Image segmentation on orthophoto mission 1. Segmentation result for entire image (left) and a close-up (right).

The testing of various scale/shape combinations within the segmentation procedure resulted in a segmented image of a scale factor of 300. However, indications of over-, and under-segmentation are apparent. Best results are achieved for solitary trees with small enough crowns, whereas big tree crowns and clustered trees are not segmented well. As a possible remedy to compensate for these effects the integration of height information from the CHM was deemed sensible.

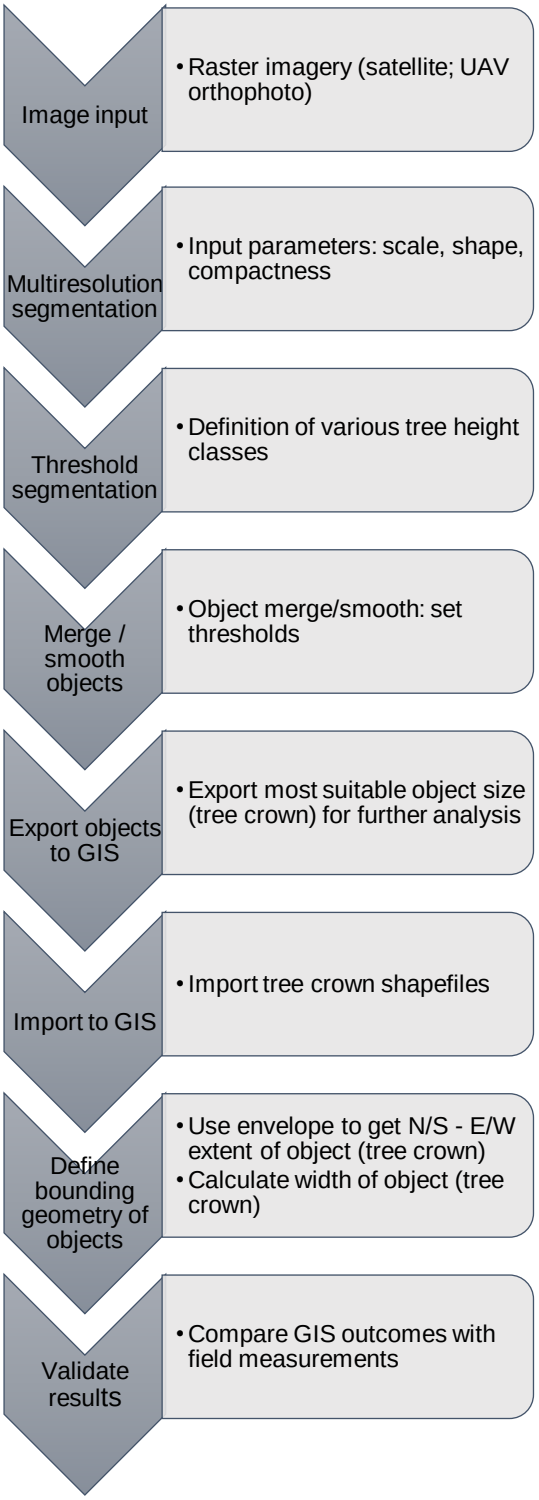

Figure 7.31: Crown diameter extraction workflow.

Having played around with various CHM heights for achieving best segmentation and thus crown delineation results a height of 9 metres was found to be number one. However, as the picture below demonstrates, once again solitary tree crowns get delineated almost perfectly, whereas tree clusters are virtually impossible to separate in a meaningful fashion.

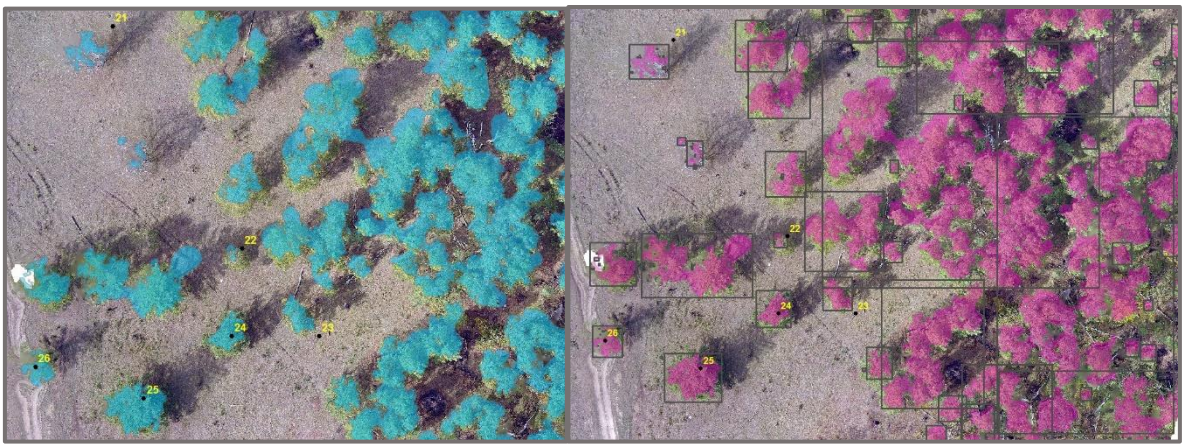

Figure 7.32: Tree crown segmentation and delineation in orthophoto mission 1 applying a Canopy Height Model (left). The resulting enveloping process for the extraction of crown diameter is demonstrated in the right image. Manually measured trees are indicated in yellow.

Having imported the delineated tree crowns derived from the segmentation process into a GIS the crowns were enveloped as a minimum bounding geometry ('envelope polygon') and the crown diameters calculated (rectangle by width/length). The outcomes of the comparison between the field data and the computer-extracted values are detailed in chapter 8.7.

7.3.4.6. Tree species classification in UAV imagery

The following classification trials were run just for interest's sake, since the combination of poor radiometric resolution (i.e., 3 spectral bands RGB) and extremely high spatial resolution were not expected to yield satisfactory results in species determination. As such, the classification validation is only based on visual interpretation of the classification results (chapter 8.8.1.).

Tree species classification in aerial CIR (colour infrared) imagery has a long tradition yielding excellent results. Thus, it was interesting to see whether a conventional RGB image would also create useful outcomes. For this reason, a flying mission 1 photo was chosen for subsequent analysis. Unfortunately, all generated orthophotos showed either blurring effects or data gaps due to the 3D modelling process. The 00242 image was loaded in ArcMap and training samples created as a prerequisite for the classification. Scatterplots for the tree species classes of Siberian birch and Siberian larch revealed that the separation of those classes would impose an extreme challenge on the classification algorithm (see Figure 7.33). The option of using an image segmentation prior to classification was discarded for the reason that no favourable object classes could be constructed. A commonly applied Maximum Likelihood classifier was singled out for tree class determination.

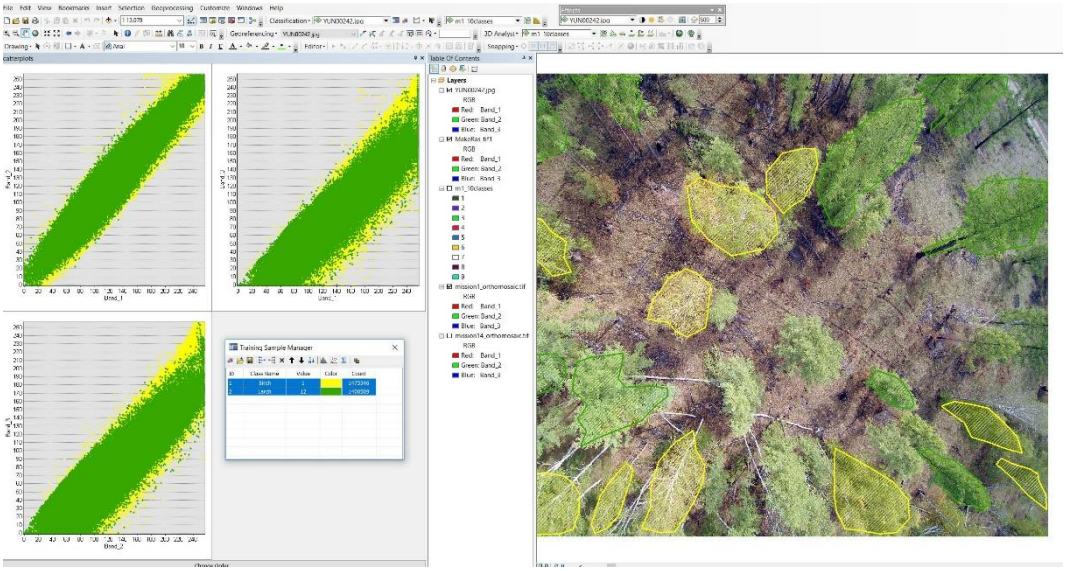

Figure 7.33: Scatterplot for RGB UAV image 00242. The classes for birch (yellow) and larch (green) appear to be inseparable.

7.3.4.7. Automatic tree count in UAV imagery

As outlined in chapter 4.6.1. the automatization of certain procedures helps to elude labour-intensive manual work – in this case the so-called template matching is offering an alternative to visually counting tree individuals in images. The template matching option is part of the eCognition software package. First of all, appropriate samples need to be selected in the (UAV) image using the Template Editor. A group size of 30, a ground truth tolerance of 30 and a threshold value of 0.4 was tested as an optimal constellation.

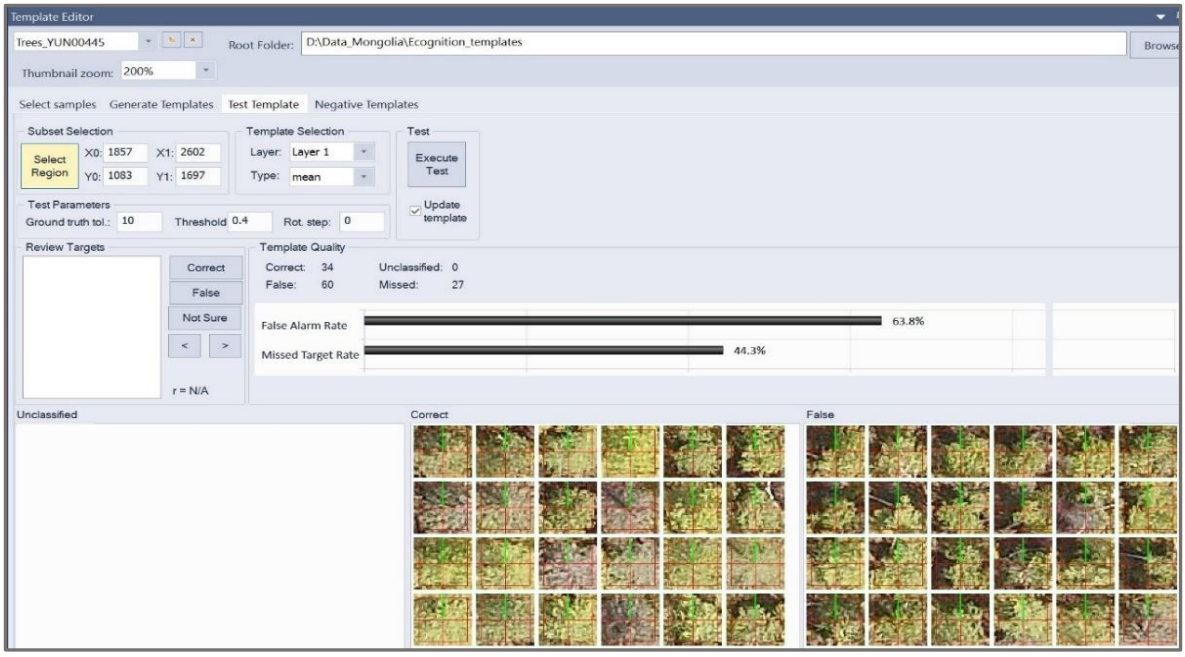

Figure 7.34: UAV image 00242 used for template matching. The picture demonstrates part of the template creation process.

Once an adequate number of samples is selected the template can be generated with test samples being subjected to the new template. Various thresholds are now applied to test for the best solution with the previous template being updated. This iterative process is carried out until the best template and its associated threshold is found (here: 0.4). The final template is then applied to the entire image and vector layers indicating the tree centres (tree tops) generated. The resulting shape file is now ready to be exported to a GIS for further inspection and analysis. The outcomes of this trial are presented in chapter 8.6.

7.3.5. Satellite imagery

Satellite imagery of various spectral and spatial resolution were employed to demonstrate the difference in performance related to specific tasks. The following table reflects the selection of all imagery used – Worldview 2, RapidEye and Pléiades images were provided by the GIZ. Although dubbed as SPOT 5 imagery by GIZ, investigation in the spectral characteristics and the spatial resolution resulted in Pléiades to be the accurate platform. All available imagery was checked for flaws (e.g., striping, pixel failures, clouds, haze, low contrast, geometric mismatch) and chosen according to the exclusion criteria. Unfortunately, Landsat 8 imagery proved only to be eligible and suitable for a single date, since all other imagery suffered from substantial cloud cover and striping. In addition, images with extreme snow cover also were considered unsuitable for not containing sufficient spectral information on the vegetation cover.

Table 7-5: Characteristics of the satellite imagery employed (own compilation).

Platform / Sensor	Number of spectral bands	Spatial resolution	Acquisition date	Season (Mongolia)	Revisit rate	Orbit altitude
WorldView-2	8 MS	0.46 m pan[20] 1.85 m MS[21]	30/10/2015	Winter	1.1 days at 1 m GSD	770 km
RapidEye	5 MS	5.0 m MS	17/09/2015	Autumn	5.5 days	630 km
Pléiades	4 MS	0.5 m pan 2.0 m MS	10/05/2015	Early spring	1 day	695 km
Sentinel-2	13 MS	10 – 20 (60 m)	14/03/2017	Winter	5 days	790 km
Sentinel-2	13 MS	10 – 20 (60 m)	03/04/2017	Early spring	5 days	790 km
Sentinel-2	13 MS	10 – 20 (60 m)	13/05/2017	Spring	5 days	790 km
Sentinel-2	13 MS	10 – 20 (60 m)	09/07/2017	Summer	5 days	790 km
Sentinel-2	13 MS	10 – 20 (60 m)	12/07/2017	Summer	5 days	790 km
Sentinel-2	13 MS	10 – 20 (60 m)	29/07/2917	Summer	5 days	790 km
Sentinel-2	13 MS	10 – 20 (60 m)	07/09/2017	Autumn	5 days	790 km

[20] pan Panchromatic
[21] MS Mutispectral

Platform / Sensor	Number of spectral bands	Spatial resolution	Acquisition date	Season (Mongolia)	Revisit rate	Orbit altitude
Sentinel-2	13 MS	10 – 20 (60 m)	10/09/2017	Autumn	5 days	790 km
Sentinel-2	13 MS	10 – 20 (60 m)	17/10/2017	Winter	5 days	790 km
Sentinel-2	13 MS	10 – 20 (60 m)	25/10/2017	Winter	5 days	790 km
Sentinel-2	13 MS	10 – 20 (60 m)	01/11/2017	Winter	5 days	790 km
Landsat 8 OLI	11 MS	15 m pan 30 – 100 m MS	09/07/2017	Summer	16 days	702km

As the table above suggests Landsat 8 and Sentinel-2 (twin system) provide one the best spectral resolution capabilities of all commercial earth observation satellites. In particular, the spectral bands representing the RedEdge (RE) and Short Wave Infrared (SWIR) spectrum have proven to be extremely useful in vegetation classification and for detecting and delineating burned areas. Although other satellite platforms feature higher spatial resolution, they have not been made freely available to the public like before-mentioned.

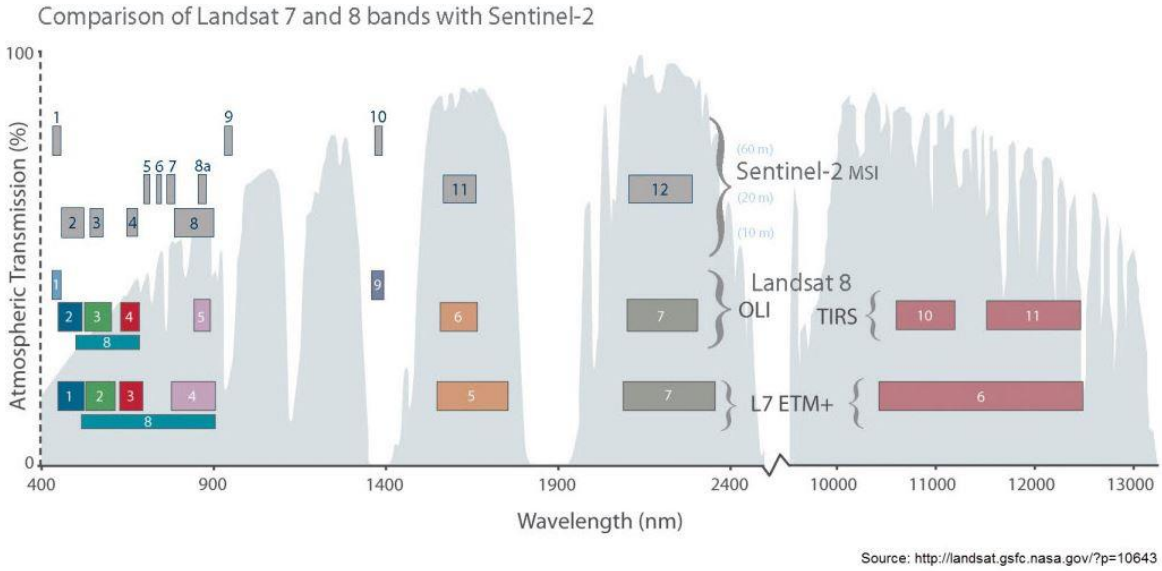

Figure 7.35: Comparison of spectral and radiometric resolution between Landsat 7/8 and Sentinel-2. Source: https://landsat.gsfc.nasa.gov/wp-content/uploads/2015/06/Landsat.v.Sentinel-2.png.

Imagery from satellite platforms such as Landsat and Sentinel have been made available to the public free of charge. The scientific community also increasingly suffers from budget constraints and as such it has been looking into alternatives to commercially marketed satellite products. This motion has led to an increased use of this imagery and in the wake of this to a respectable body of publications.

7.3.5.1. Spectral separability

The extraction of precise spectral information is one of the key components for accurate vegetation classification. Spatial , temporal, as well as radiometric resolution determine the quality of the outcomes, but subsequently characteristics such as colour, shape and texture also reflect the traits of the various objects to be classified (Lillesand *et al.*, 2015, Tso and Mather, 2009, Xie *et al.*, 2008). In order to get a first impression on the potential separability of various object classes some of the above listed imagery was scrutinised in the SNAP software by employing the pin management and spectrum view tools. The graph below provides such an example.

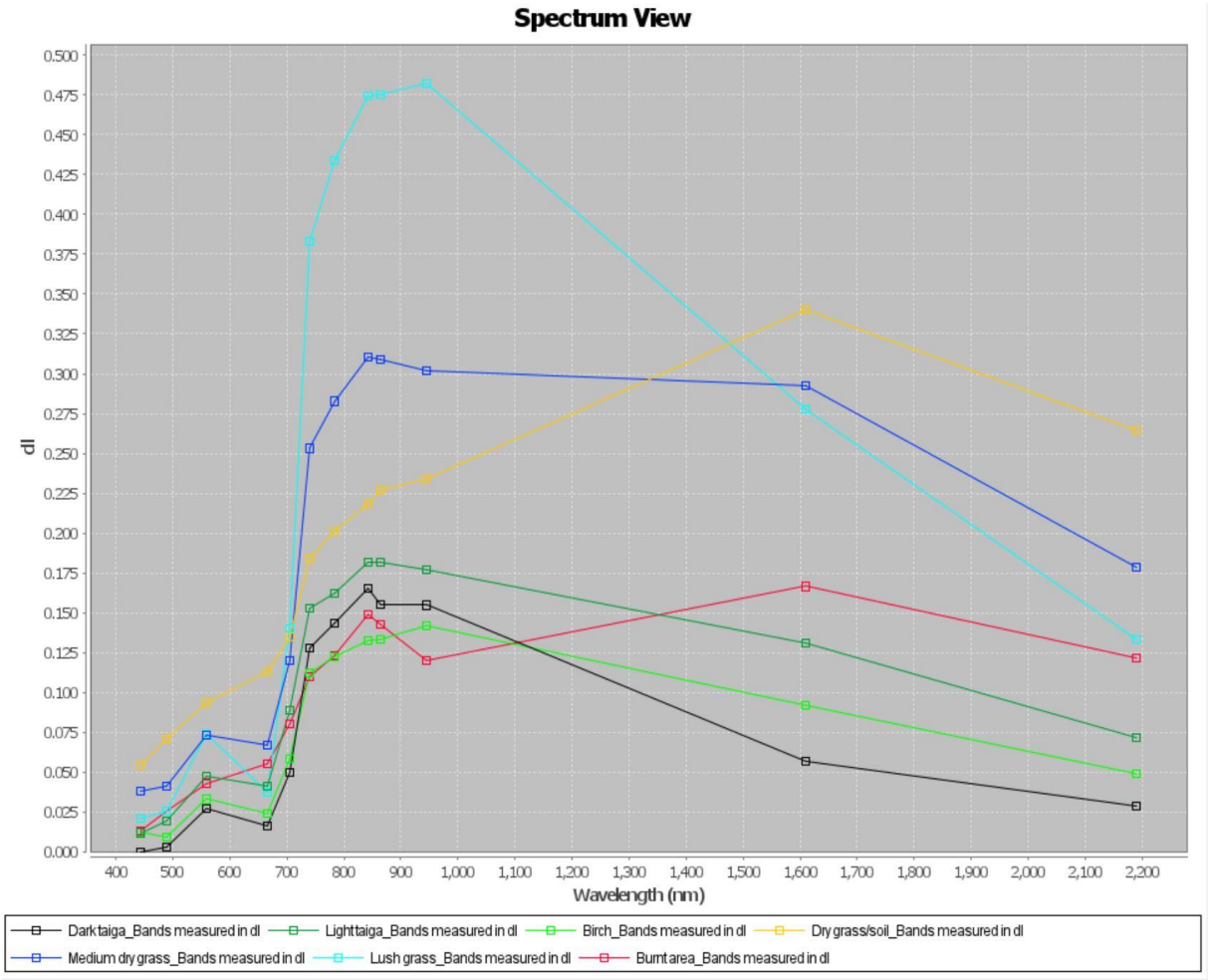

Figure 7.36: Spectral separability of various classes in compartment 435. Sentinel-2 image 10/09/2017.

A number of features were identified on the images either by visual inspection and/or by consulting the ground truth data. In the analysis above the classes are as defined: dark taiga, light taiga, Siberian birch, dry grass/soil, medium dry grass, lush green grass, and burned areas. It was expected that the classes dry grass/soil (high values in the visible and SWIR) and green grass (highest values in the NIR) would show typical reflectance patterns, which they did. Conifers and broad-leafed trees usually reflect considerably less radiation in the green spectrum, thus appearing darker in the wavelength around 650 nm (Ciesla, 2000). Although

categorised as a conifer the Siberian larch shows a lighter green colour in leaves as compared to spruce or pine for example. In addition, *Larix* is deciduous and as such sheds its needles in autumn, turning yellow prior to that. Thus, the temporal scale also needs to be considered before classification (Jensen and Mathews, 2016). The graphs below demonstrate seasonal effects of the major tree classes dark taiga, light taiga (i.e., mix of birch and larch) and birch.

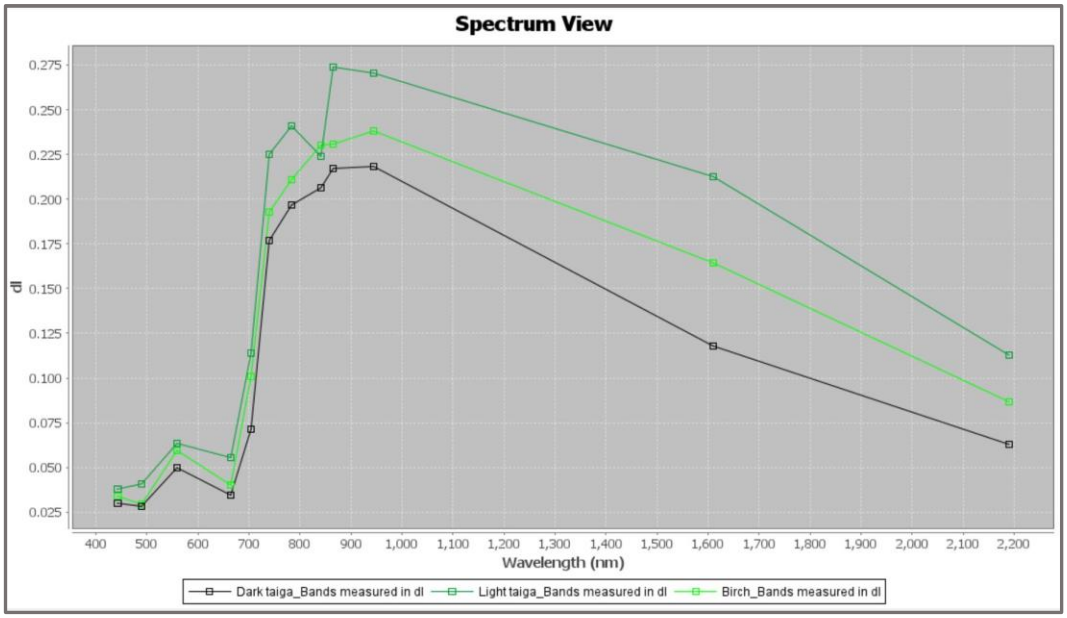

Figure 7.37: Spectral separability of taiga classes in Sentinel-2 image 29/07/2017.

The summer image of Sentinel-2 in general shows higher reflectance values compared to the autumn image below. Dark taiga (black line) generally reveals lower reflectance in the visible as well as in the NIR and SWIR set against birch (bright green line) and light taiga (green line). The birch class shows a distinctive dip in the NIR and particularly in the Red Edge (700 – 800 nm) in the autumn image, with the senescence period having started in Mongolia. This finding is very much in line with the ones by authors like Cipar *et al.* (2008) , Jensen (2016: 339) and Jones and Vaughan (2010: 271–272).

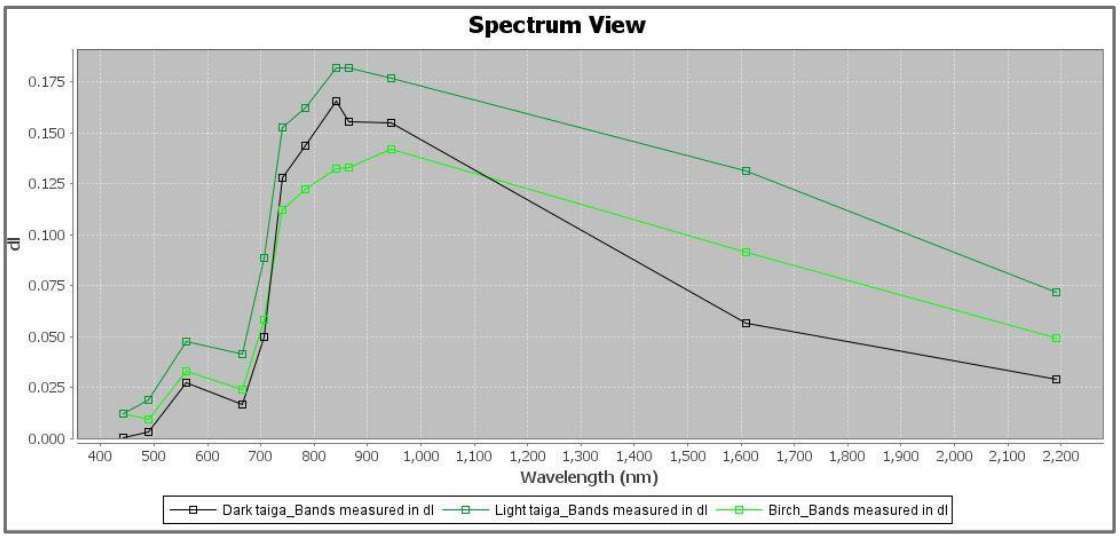

Figure 7.38: Spectral separability of taiga classes in Sentinel-2 image 10/09/2017.

A different way of visualisation of the separability of certain classes for the compartment 435 was taken below. The scatter plot graph clearly shows a better distinction of the classes in the SWIR (right) than in the visible part (left) of the electromagnetic spectrum.

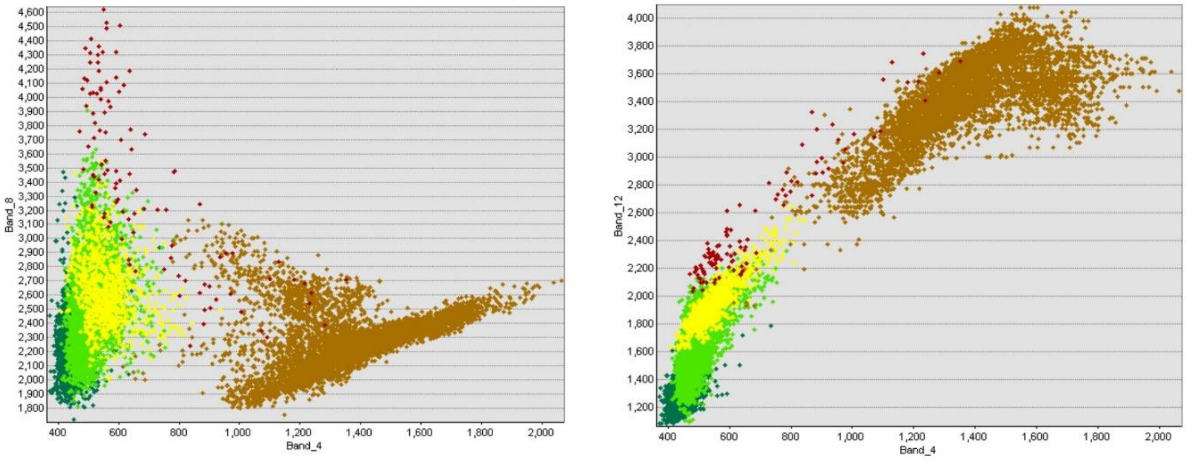

Figure 7.39: Scatter plot. Spectral separability in Sentinel-2 image 29/07/2017 for the classes: dark taiga (dark green), light taiga (bright green), birch (yellow), dry grass/soil (brown), green grass (red). Left image shows S-2 bands B8 vs B4; right image shows B12 vs B4.

The segregation of the various classes is even more refined when looking at the mean and the standard deviation of the Digital Numbers (DN) of the reflectance patterns. These values were calculated and are graphically represented in the figure below. This analysis was done for the summer Sentinel-2 image acquired on 09/07/2017. This image was chosen for further image classification for specific reasons outlined in chapter 7.3.5.3. The statistical analysis exposes distinct clumping effects in the visible part of the spectrum for all five classes defined. As such, class separation solely based on spectral analysis does not seem a rewarding venture. In contrast, the class separation in the SWIR bands (indicated as bands 12 and 13) holds much

better promise. The dark taiga class presents itself with very low reflectance with a decent spectral distance to the other forest classes light taiga and birch.

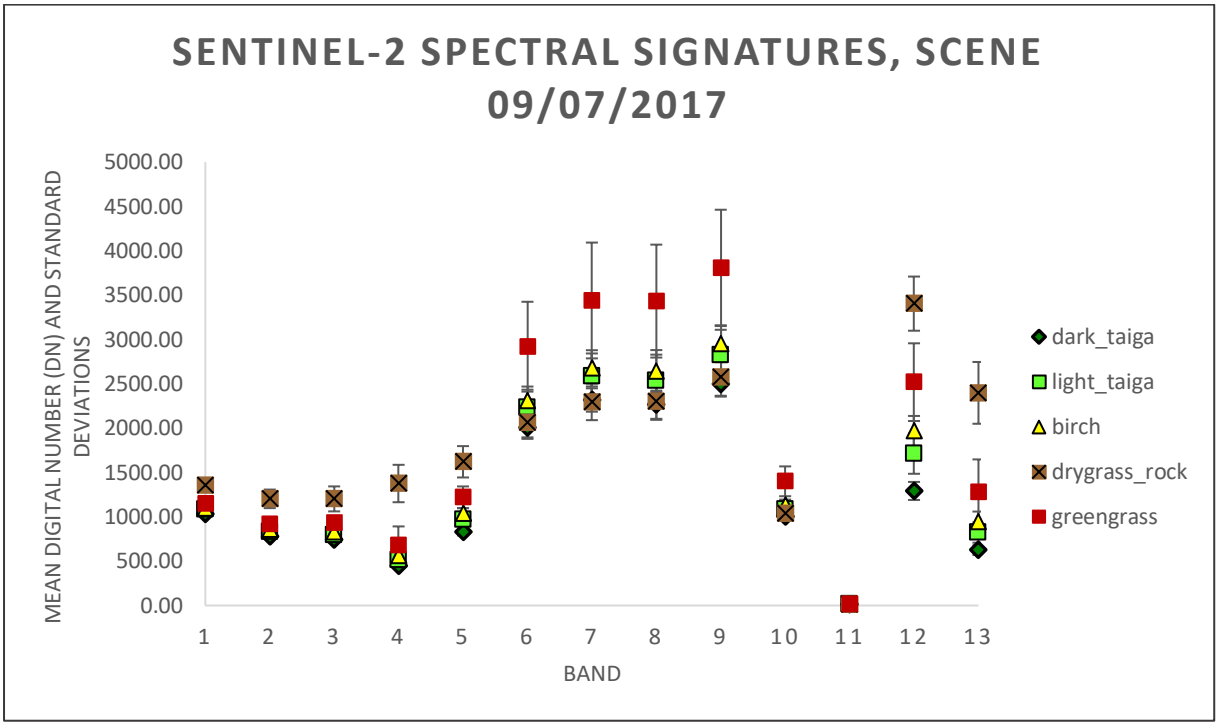

Figure 7.40: Spectral signature separation for Sentinel-2 image 09/07/2017. Best separation qualities show bands B7 (RedEdge 3), B8 (NIR), B9 (8A) (Narrow NIR), and as best B 12 (B11) (SWIR 2). Mean digital numbers and standard deviations are portrayed for the five different classes.

The separability of the classes in the NIR (bands 8 and 9) and part of the RE (band 7) regions also appear to be useful, however, is not as pronounced as in the SWIR region. The spectral variability for the dark taiga is very low throughout most of the spectral bands, whereas light taiga and birch show higher standard deviations in comparison. The class of green grass is characterised by the highest variability in the NIR and RE spectrum bracket in correlation with the highest reflectance in those ranges due to its high chlorophyll content and supreme vigour. Based on above findings the choice for specific spectral bands (i.e., bands 7,8,9,12) to be primarily utilised in subsequent image classification processes was not difficult to be made. Nevertheless, the graph above also brings to light that forest class separation would not be a smooth task.

7.3.5.2. Image pre-processing

As outlined in chapter 4.3.4. specific image management prior to further processing is a crucial step to be taken. All imagery to be utilised in the presented study was tested for geometric and geometric fidelity with no flaws being detected. However, effects of atmosphere and terrain have to be taken seriously, especially when dealing with multitemporal imagery, the application

of vegetation indices, and the consideration of sun angles at high latitudes. Regarding the afore-mentioned caveats, atmospheric correction of the imagery was given preference for all imagery used. The Sentinel-2 tailored Sen2Cor 285 (using SRTM for terrain compensation) was applied in SNAP to all Sentinel-2 images, whereas all remaining imagery was subjected to Dark Object Subtraction (DOS). The resulting spectral values now reflect the bottom of atmosphere characteristics (BOA). Given below are graphical representations on the effect of atmospheric correction performed on Sentinel-2 imagery.

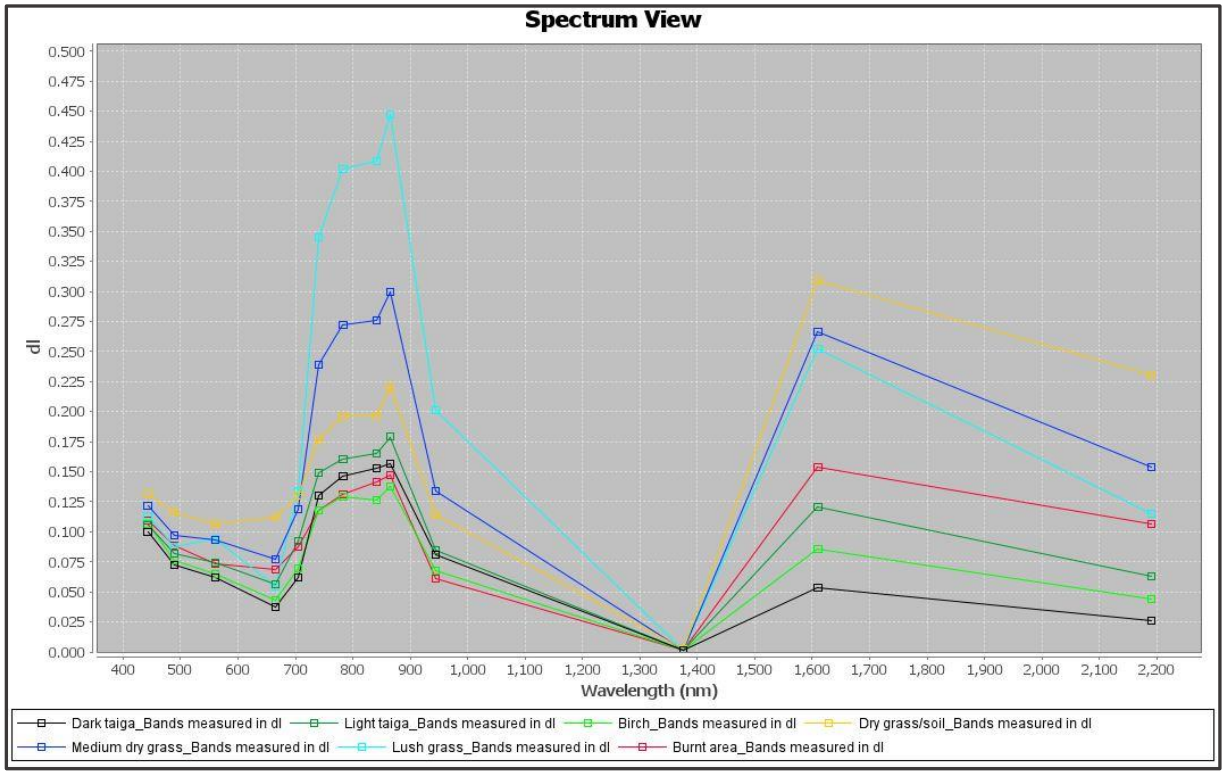

Figure 7.41: Sentinel-2 image 10/09/2017 prior to atmospheric correction. The intensity values are set against the wavelengths of the Seintinel-2 specific spectral bands.

The comparison of the two graphs (i.e. before – after correction) confirms the findings in the literature that atmospheric correction has the severest impact on the visible spectrum of the image signature (e.g. Chavez, 1996, Buho *et al.*, 2009, Main-Knorn *et al.*, 2017, Vanonckelen *et al.*, 2015). The reflectance intensities are lower in the corrected image, but class separation in turn seems to have slightly increased. Total absorption (i.e., value 0) in the cirrus band at 1400 nm was eliminated by excluding this band from further processing. The spectral curves in the visible part of the spectrum display a much more 'natural' shape for vegetation after application of Sen2Cor, i.e., a distinct peak at the green band. To get a much clearer picture on the precise effect of Sen2Cor on the imagery a specific class (forest) was used for a pixel-to-pixel comparison for the associated reflectance values (Figure 7.43). Once again, the visible

part of the spectrum (blue, green) showed the most severe discrepancy, whereas the wavelengths beyond the red band do not reveal any significant change.

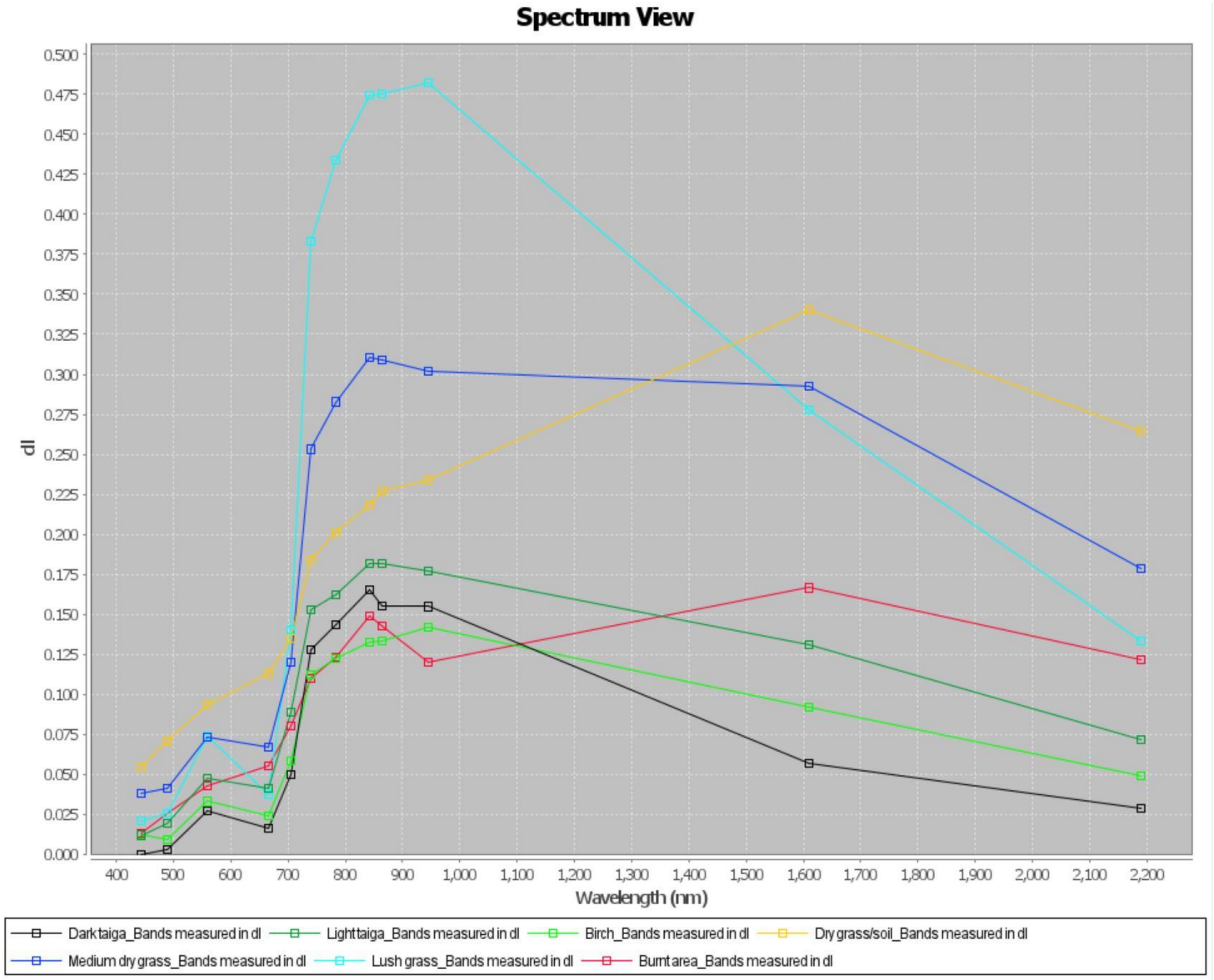

Figure 7.42: Sentinel-2 image 10/09/2017 after Sen2Cor atmospheric correction. The intensity values are set against the wavelengths of the Seintinel-2 specific spectral bands.

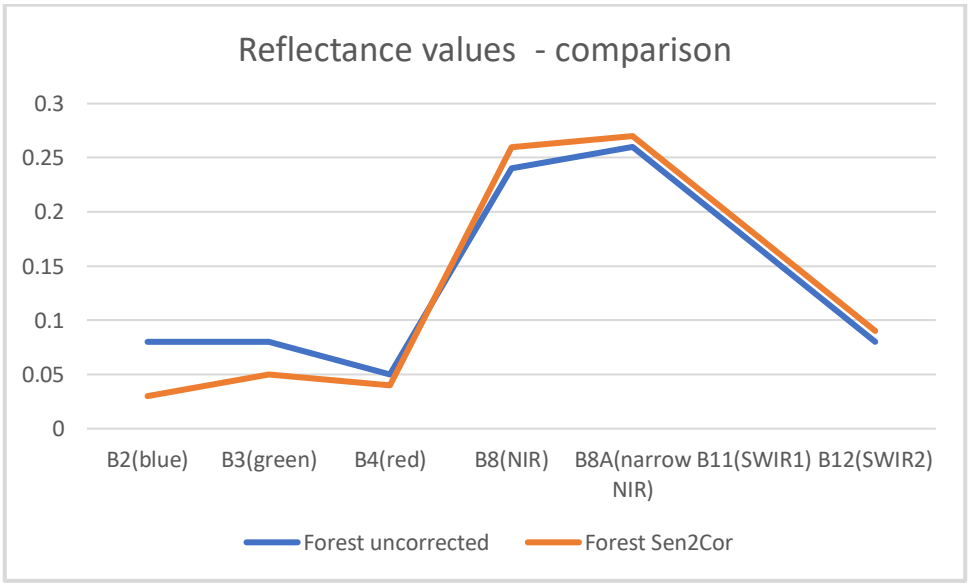

Figure 7.43: Sentinel-2 image 10/09/2017 after atmospheric correction. Comparison of before (blue line) and after correction (orange line) reflectance intensity values for the class forest. The blue (B2) and green (B3) spectral bands show the greatest effects.

All above findings are in conformity with the respective scientific literature, and as such, arguments for performing atmospheric correction on all images used were compelling.

7.3.5.3. Principal Component Analysis (PCA)

Principal component analysis (PCA) has been a standard procedure in the remote sensing community for many years for attaining a dimensionality reduction in the image data. The computed first principal component can be considered as the direction that maximises the variance of the projected data, and as such it is perfectly suited for a decision on what band combinations or which temporal aspect exhibits the most rewarding approach by retaining the best efficiency. More details on the characteristics and the computation of the components are featured in for example Jones and Vaughan (2010: 147–148) and Lillesand *et al.* (2015: 522–529). The PCA in the case of this study was employed for finding the Sentinel-2 image with the biggest variety (variance) in spectral appearance for subsequent image classification. The figure below shows the first principal component for Sentinel-2 imagery taken at various dates.

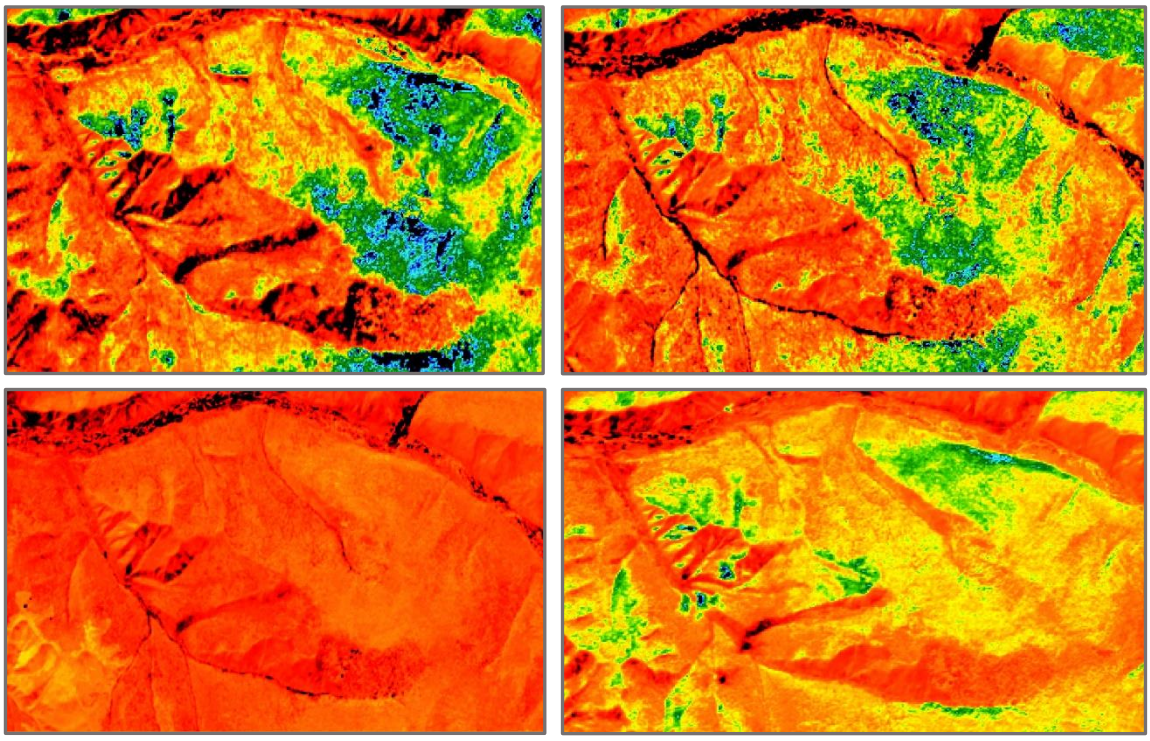

Figure 7.44: Principal Component Analysis (PCA) performed on various Sentinel-2 images. The images exhibiting the greatest variance are for 13/05/2017 (top left) and for 09/07/2017 (top right); the least variance shows the image taken on 29/07/2017 (bottom left); image acquired on 07/09/2017shows medium variance (bottom right).

The outcomes of the PCA are depicted in the figure above using a highly diagnostic colour scale – the more colourful the presented values, the higher the variance as computed in the PCA. Even though the results for the spring image (13/05/2017) looked the most promising,

this image was excluded for subsequent classification, since in May 2017 broad-leafed trees only started leafing shortly before. This seasonal phenomenon was confirmed by local experts and was amplified by the findings for the NDVI seasonal timeline (see chapter 8.4.). As a consequence, the spectral interference with the forest floor flora (shrub, grass, etc.) was most likely to happen. The next best PCA result in line was for the 09/07/2017 summer image, making it the prime candidate for vegetation classification. Interestingly, the other summer image (29/07/2017) features hardly any variance.

7.3.5.4. Image segmentation

Image segmentation techniques have received a lot of attention in the remote sensing community with respect to analysing (very) high-resolution imagery. Not only single trees or other homogenous units (tree clusters, stands, tree crowns) can be extracted, but segmentation also provides an unvaluable tool for improving classification accuracies. Successful applications have been reported earlier in chapters 4.3.2. and 4.6.1. Major determinants in the segmentation process are scale, colour, and compactness, with scale being the most relevant of the three. The example below shows the World View-2 winter image used for tree number extraction.

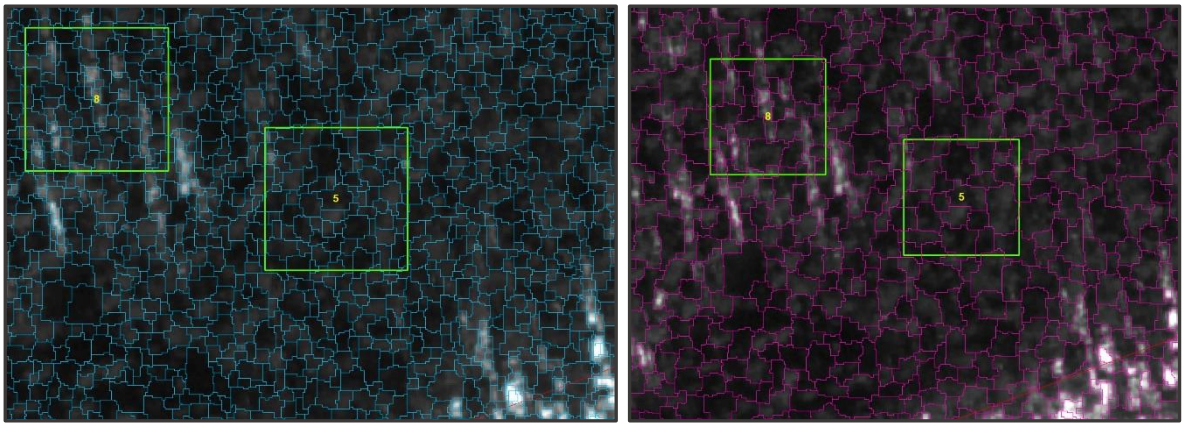

Figure 7.45: Image segmentation performed in a World View-2 winter image. The scale factor for the left image was 10, for the right image it was chosen to be 20. The green boxes denote the boundaries of test plots no.5 and no.8.

Apparently, the scale factor has the most significant impact on the size of the objects created. For the procedures of counting trees and classifying vegetation, where image segmentation was conducted, a diverse combination of values for the parameters scale, colour, and compactness were tested for the imagery used. The pertaining values are detailed in the corresponding chapters.

7.3.5.5. Template matching for tree count

The template matching process has been portrayed for the UAV imagery in chapter 7.3.4.7. already – it is only marginally different for the application in satellite imagery. Tree detection requires a certain spatial resolution in the underlying images. The satellite platforms of World View-2 and Pléiades were the only ones qualifying for this task by supporting a pixel size small enough to identify single trees. However, the creation of the pertaining templates turned out to extremely demanding. In both images the presence of shadows within the tree clusters imposed a real challenge to the interpreter for the proper identification of tree individuals. An excellent case of this 'imbroglio' is illustrated below. The panchromatic World View-2 winter image shows little contrast particularly in areas with tree clumps, thus making it very arduous to select ideal candidates for the template creation procedure. In addition to the template matching approach an image segmentation with a scale factor of 10 was used for the WV-2 image for comparison. The centre of each segment was subsequently defined as representing an individual tree within the regarded test plots 5 and 8. The outcomes of the template matching and image segmentation used for tree count are detailed in chapter 8.6.

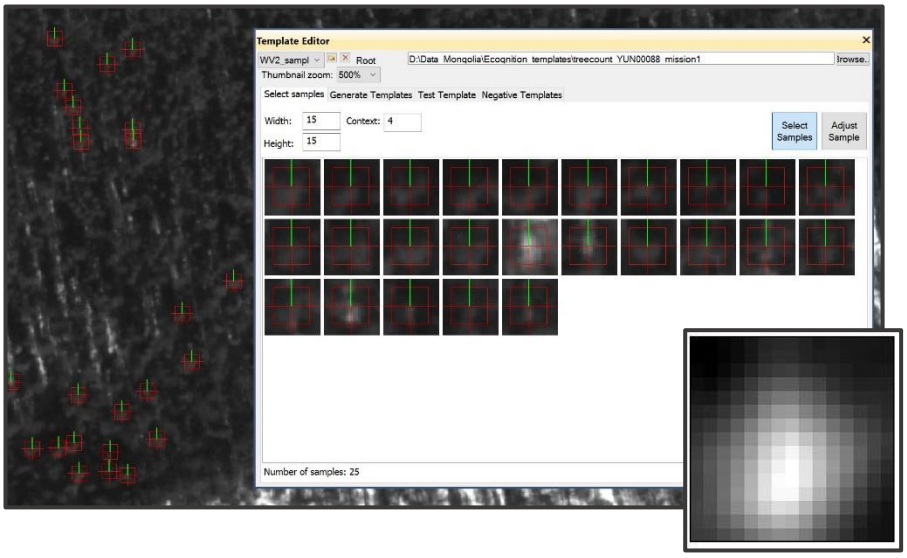

Figure 7.46: Template matching procedure in the World View-2 winter image. The resulting image template is shown in the lower right as an inset.

7.3.5.6. Image classifications and accuracy assessments

Image classification was conducted on various sensors with the objective to assess their suitability for species discrimination and to test for correct delineation related to class definition. Moreover, it is attempted to answer the question, if (i) the object-based method is superior to the pixel-based, and (ii) which classifier performs better (i.e., Random Forest or Support Vector Machine).

The table below illustrates the sensor platforms employed and the classification techniques exercised.

Table 7-6: Sensor platform and classification technique combinations related to the study.

Sensor platform	*Sentinel-2*	*RapidEye*	*Pléiades*	*WorldView-2*	*UAV imagery*
Classification technique					
Object-based (OBIA)	x		x	x	
Single tree species			X		X
Dominant tree species	X		X	X	
Support Vector Machine	X		X		
Random Forest	X		X		
Pixel-based	x	x	x		
Dominant tree species	X	X	X		
Support Vector Machine	X	X	X		
Random Forest	X	X	X		
Maximum Likelihood					X

The following graph provides an account on the steps taken for image classification:

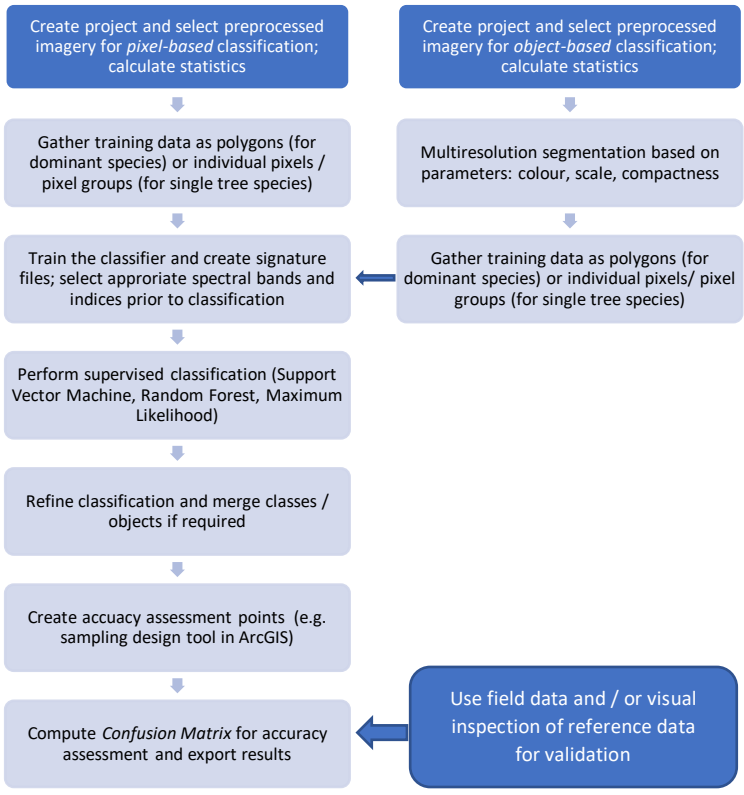

Figure 7.47: Workflow for pixel-based (left) and object-based (right) image classification.

Most of the satellite imagery (i.e., RapidEye, Pléiades, WorldView-2) was kindly provided by the GIZ for further analysis. All Sentinel-2 and Landsat 8 images listed in table 7-5 in chapter 7.3.5. were downloaded from the USGS Earth Explorer website for subsequent use (https://earthexplorer.usgs.gov/). Atmospheric correction was carried out on all images, except for the RapidEye image, which was furnished as a level 3A product (i.e., including geometric,

radiometric, and sensor correction). The choice for specific spectral bands and indices was based on the spectral separability assessment conducted before. The PCA also contributed to finding the appropriate Sentinel-2 image with the highest seasonal spectral variation (i.e., 09/07/2017). The definition of the areas for training the classifiers rested on the field data analysis, personal experience of the surveyor on site, as well as the visual inspection of sources such as the BING base map. The figure below illustrates the location of the training areas with five designated classes. Despite the fact it has become a standard procedure to create a forest mask for attaining better classification results, this option was dismissed for the reason, that it was decisive for me to also explore the performance of the classification methods beyond the forest boundaries.

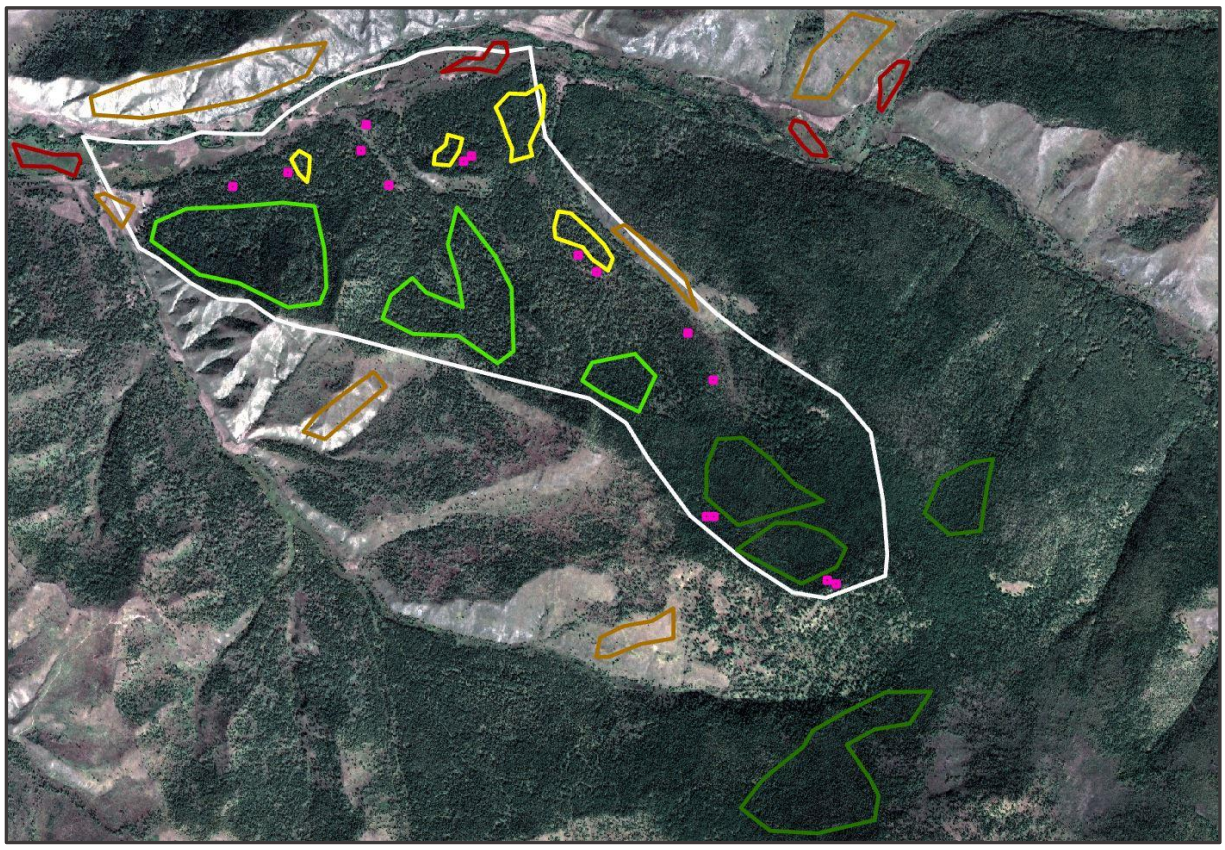

Figure 7.48: Location and extent of the training areas for training the various classifiers. The test plots are marked with squares in magenta. The training areas represent the classes birch (yellow), light taiga (bright green), dark taiga (dark green), dry grass/soil (brown), and green grass (red).

This demand is reflected in the definition of the training classes and the accuracy assessment being extended to a bigger area. More than that this pathway provides an opportunity to be better prepared for a judgement on a potential up-scaling of the proposed methods to other regions in Mongolia. It has also been decided to go without a subsequent refining and merging process in the classification to avoid a dilution of the classification accuracies. The individual settings for the classification procedure are listed below.

Table 7-7: Settings for the object-based and pixel-based classification for the various sensor platforms.

Sensor platform	*Sentinel-2*	*RapidEye*	*Pléiades*	*Pléiades – single trees*	*WorldView-2*
OBIA settings					
Colour	*0.15*		*0.95*	*0.95*	*1.0*
Scale	*20*		*300*	*40*	*300*
Compactness	*0.95*		*0.2*	*0.2*	*0.9*
Classifier settings					
Support Vector Machine (Kernel type linear; C = 2)					
Mean difference to neighbours	*See variants 1-4 below*	*All bands*	*All bands, NDVI*	*All bands, NDVI*	*All bands, NDVI*
Standard deviation	*See variants 1-4 below*	*All bands*	*All bands, NDVI*	*All bands, NDVI*	*All bands, NDVI*
Means	*See variants 1-4 below*	*All bands*	*All bands, NDVI*	*All bands, NDVI*	*All bands, NDVI*
Random Forest					
Tree depth	*4*	*20*	*5*	*15*	*5*
Minimum samples per node	*20*	*20*	*1*	*20*	*1*
Maximum categories	*16*	*16*	*16*	*16*	*16*
Active variables	*0*	*0*	*0*	*0*	*0*
Maximum trees	*50*	*50*	*50*	*50*	*50*
Forest accuracy	*0.01*	*0.01*	*0.01*	*0.01*	*0.01*

All mentioned preferences for finding the most relevant parameter combinations are resting on verbose trials, on suggestions provided by colleagues in the scientific community, and on clues in the literature (e.g. (Aguilar *et al.*, 2013, Dezsö *et al.,* 2012, Hajek, 2004, Kavzoglu and Yildiz, 2014, Mallinis *et al.*, 2008). Several variants for the refinement of the classification process were devised to give credit to the enormous amount of spectral variety available these days. For instance, the Sentinel-2 multispectral instrument stands out for delivering imagery with 13 different bands. The following band combination settings might seem arbitrary, but they are based on the spectral separability assessments and on references.

Table 7-8: Band combination variants used for classification per sensor platform.

Selection of spectral bands and indices	
Band combination variants for sensor platform:	
Sentinel-2	
Variant 1	*B8, B11, NBR, NDVI*
Variant 2	*B8, B11*
Variant 3	*B11, NDVI, NBR*
Variant 4	*B3, B8, B11, NBR*
Variant all	*All bands, no indices*
RapidEye	*All bands, no indices*
Pléiades	*All bands, no indices*
WorldView-2	*All bands, no indices*

With respect to the segmentation process the following examples are provided to convey a realistic impression on the challenges in finding the most suitable object size.

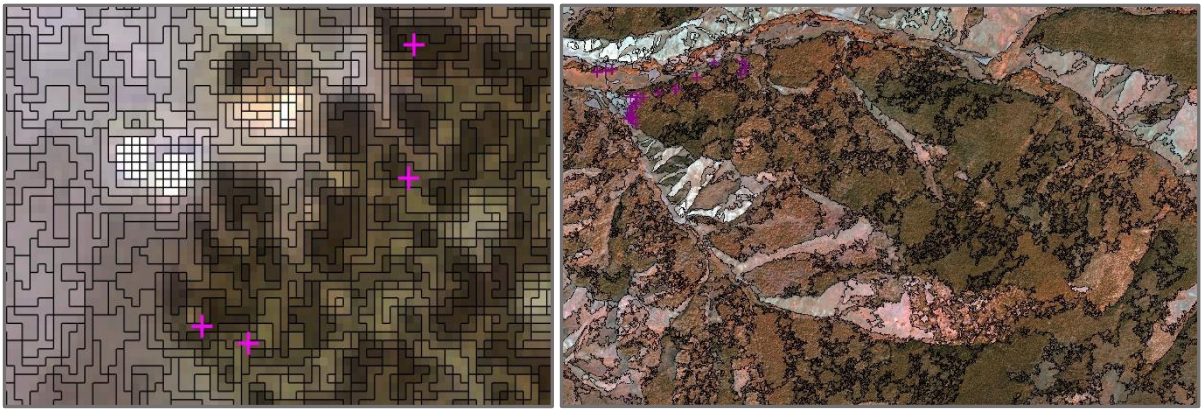

Figure 7.49: Image segmentation results for Pleiades imagery (10/05/2015) with a 2 m resolution - for single tree identification (left) and dominating tree species classification (right). Single tree locations are marked with crosses in magenta. Dominant (big) trees are only just recognisable.

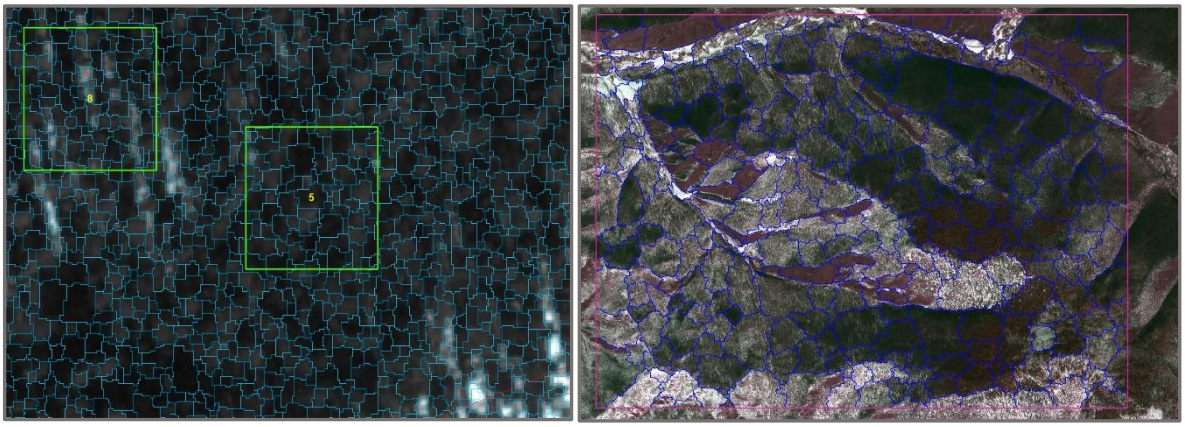

Figure 7.50: Image segmentation results for World-View 2 imagery (30/10/2015) with a 1.6 m resolution - for single tree identification (left) and dominant tree species classification (right). The green boxes on the left indicate the boundary of the test plots. Dominant (big) trees are barely recognisable.

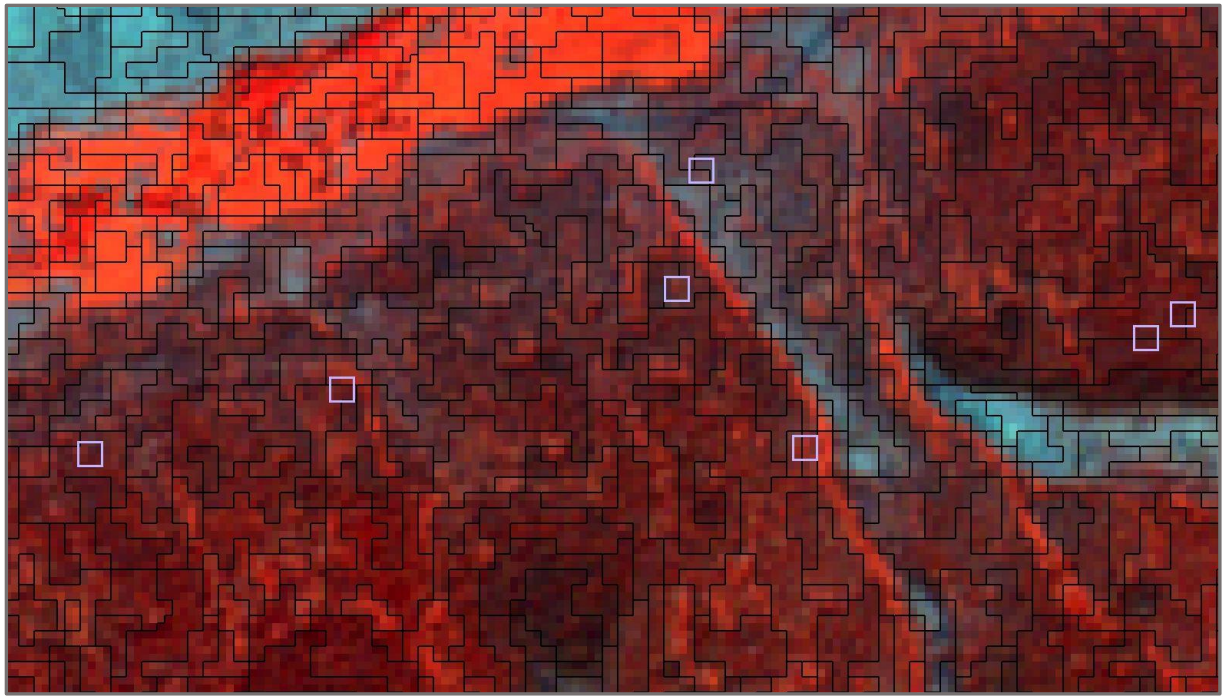

Figure 7.51: Image segmentation results for Sentinel-2 imagery – IR false colour - (09/07/2017) with a 10 m resolution (resampled) for dominant tree species classification. Test plot boundaries are marked with white boxes. Individual trees cannot be identified in this image.

Above graphs demonstrate quite compellingly, that the segmentation strategy (scale factor) has to be adjusted according to the classification purpose, in this case to single tree or dominating tree species determination. It is furthermore demonstrated, that spatial resolution has its inherent limitations when it comes to identification of individuals trees or well-defined clusters.

Accuracy assessment requires a lot of attention in terms of proper selection of the number and location of the assessment points, since this can affect the outcomes of the classification considerably. Subsequent to the successful classification a stratified random sampling design was applied in ArcGIS to generate the required accuracy assessment points – a number of 130 points was considered to be sufficient. The accuracy assessment points perfectly reflect the accurate character of the associated class, since field data and on-site observations were used for verification. The products of the various classification processes and the related conclusions are detailed in chapter 8.8.2.

7.3.5.7. Wildfire analysis

The occurrence of fires has been part of the Mongolian ecosystems for thousands of years (see also chapter 5.2.). During my fieldtrip I experienced massive scorching of huge parts of the landscape with substantial impacts on the taiga forests. The pictures below are intended

to provide a glimpse of the incidents. When investigating the extent and severity of such fires it is crucial to keep I mind that fire intensity can vary greatly within areas (from ground fires to crown fires) causing different levels of damage (i.e., ranging from trees being intact to total destruction). In addition, retarding effects of damage and also swift regeneration of the vegetation can be observed (see also chapters 5.1. and 5.2.).

Figure 7.52: Raging fires in the Thunkel area (left). Rapid regeneration of the forest floor flora after the fire (right).

Several remote sensing approaches have been taken to assess the extent and severity levels of fires with the listed ones below being the most commonly applied methods:

- Calculate pre-, and post-fire NDVI ((NIR – Red) / (NIR + RED)) for delta.
- Calculate pre-,and post-fire NBR ((NIR – SWIR) / (NIR + SWIR)) for delta. A variation of the NBR is constituted by the RBR as suggested by Parks *et al.* (2014) (see also chapter 5.1.).
- Calculate pre-, and post-fire NDWI ((GREEN - NIR) / (GREEN + NIR)) for delta.

The following graph illustrates the timeline for the occurrence of the wildfires in the Thunkel area. A band combination of SWIR 2 (B 12) / SWIR 1 (B11) / NIR (8A) for the Sentinel-2 imagery was chosen - SWIR is able to penetrate haze and thin clouds in contrast to the visible spectral bands.

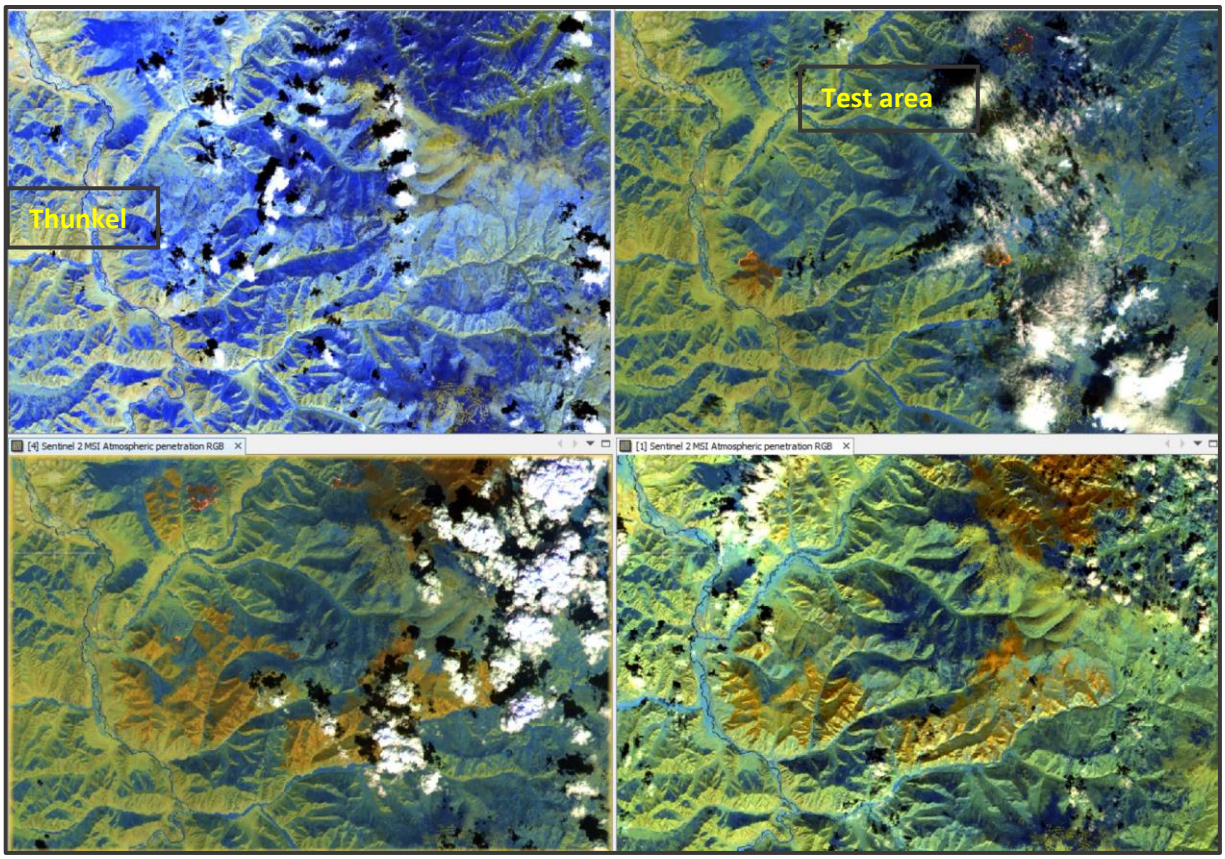

Figure 7.53: Timeline for the wildfire occurrence in the Thunkel area in 2017. The band combination of B12/B11/B8A was used for illustration in the Sentinel-2 images. Image from 02/06/2017 (top left) with no indication of fire. First fires (bright orange) appearing in image 12/07/2017 (top right). Fire extent for 29/07/017 in bottom left image and for 07/09/2017 in bottom right image.

The workflow for the extraction of the burned area is demonstrated below. As pre-fire image the Sentinel-2 scene 09/07/2017 was selected, with the Sentinel-2 scene 07/09/2017 for post-fire analysis. The NDWI was calculated for the detection of water bodies, which could potentially impede the interpretation of the results (see also McFeeters, 1996). The same applies to the masking of the cloud coverage - cloud masks are automatically created in SNAP when applying atmospheric correction of the imagery (i.e., Sen2Cor).

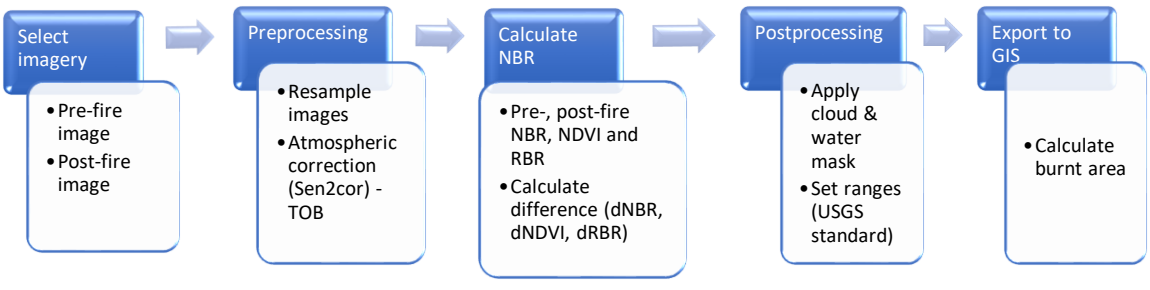

Figure 7.54: Workflow for the extraction of burned areas.

Having calculated the difference between pre-, and post-fire values, for the interpretation of the results the commonly used USGS standard was favoured. As a subsequent step the extent

of the burned area can be determined in a GIS environment. However, this part of the process was waived due to the fact that I was only interested in the inspection of the areas affected by the fires and the possible implications for managing compartment 435. Finally, the outcomes of the dNDVI, dRBR, and dNBR calculations were set against each other for visual assessment to attain indications on the best performance and suitability for burned area estimation. Part of the comparison between these indices the retrieval of burned area from some other source was also conducted – in this case the FIRMS database (Fire Information for Resource Management System) managed by NASA helped to verify the results of the Sentinel-2 image analysis. This database provides an excellent tool for the detection of fires incidents around the world (https://earthdata.nasa.gov/earth-observation-data/near-real-time/firms). The website not only provides the location of active fires, but also presents archived data in an extensive database repository. The user, however, has to be aware of the fact, that MODIS data represent a pixel size of 1 kilometre, whereas VIIRS data reflect an area of 375 metres per pixel (NASA, 2021).

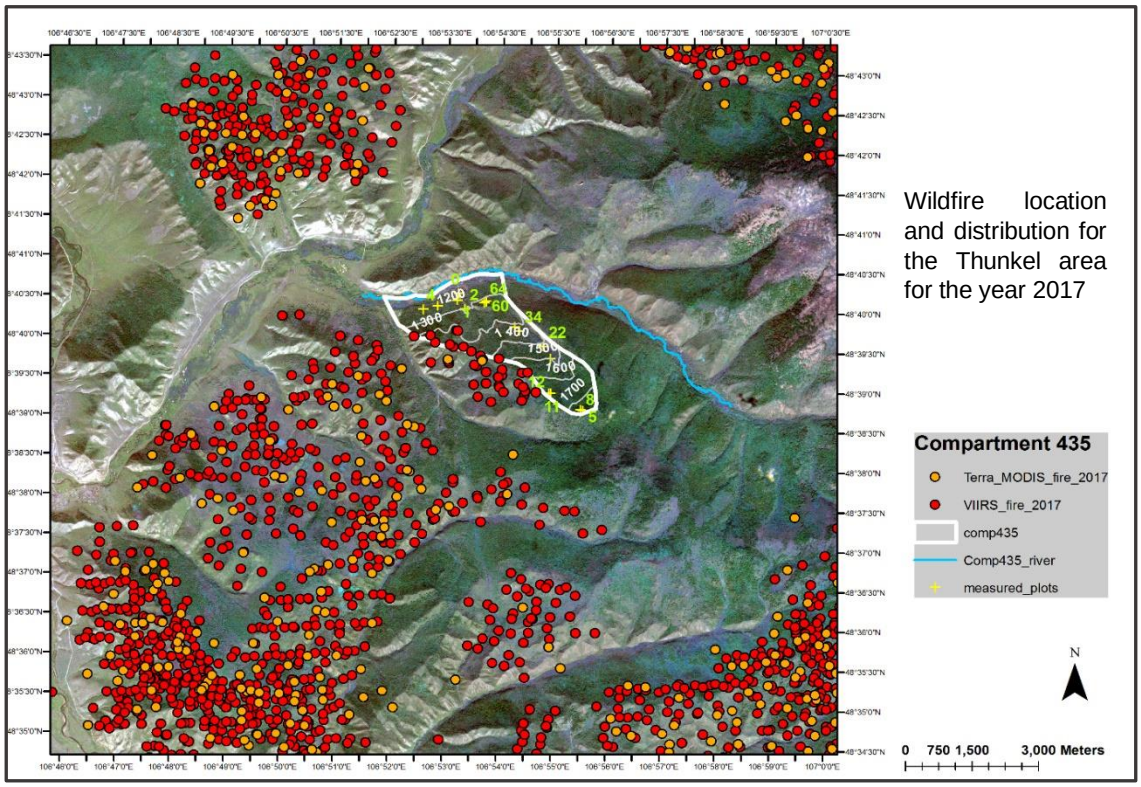

Figure 7.55: Extraction of areas affected by fires form the FIRMS database for the year 2017. Fires detected by the MODIS (orange spots) and VIIRS (red spots) sensors are indicated. Source: FIRMS, 2021.

7.3.5.8. Derivation of NDVI and LAI

NDVI and LAI are considered to be some of the most important biophysical variables for assessing vegetation cover, plant vigour, and vegetation density. With NDVI estimations in particular it is feasible to portray seasonal effects (phenology) and disturbances in the vegetation cover (e.g., fire, insect attacks). Various other applications have been illustrated in the respective chapters 3.1.4. and 4.3.3. for further reading.

Calculating NDVI in multispectral imagery is fairly trivial in most of the remote sensing software packages offered on the market. This procedure is based on direct retrieval of NDVI, or by using raster calculator operations by applying the formula NDVI = (NIR – RED) / (NIR + RED). The NDVI estimations were applied to achieve the following in this investigation:

1. Get a clear definition and delineation of the dark taiga conifer areas.
2. Show differences in NDVI results for the various satellite platforms.
3. Assess the relationship between NDVI and LAI.
4. Compare outcomes for the calculations of NDVI and the variant NDRE (NDRE = (NIR – RE) / (NIR + RE).
5. Illustrate seasonal effects for the year of 2017 (timeline).

The calculation of NDVI was conducted for all satellite imagery (i.e., WV-2, Sentinel-2, Pléiades, Landsat 8), with atmospheric correction, resampling, and clipping (area reduction) carried out prior to processing. An example for such NDVI estimation is provided in the figure below for the Sentinel-2 09/07/2017 summer scene with the associated NDVI values provided. As anticipated the green grass areas in the riparian areas (in red) show the highest values, whereas the sun-scorched rockfaces and bare soils appear in blue due to the lack of (live) vegetation cover.

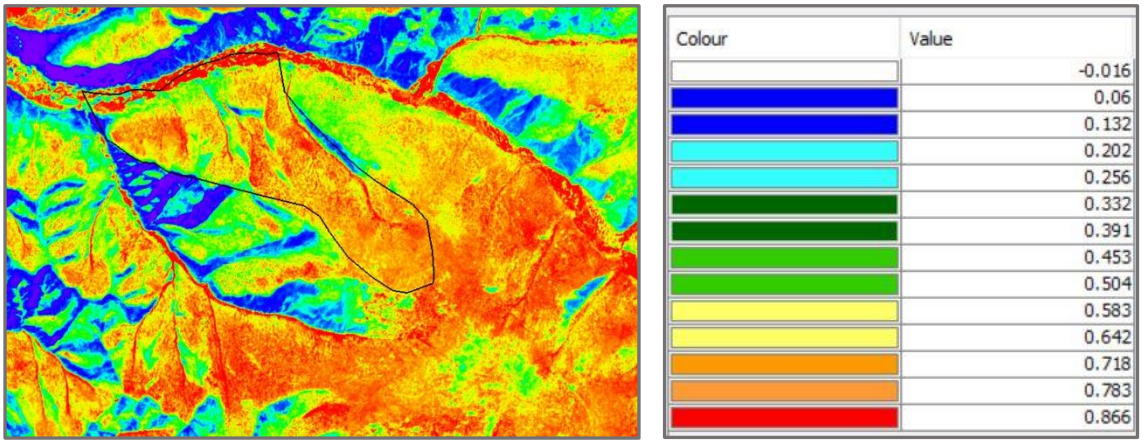

Figure 7.56: NDVI calculation of the S-2 image 09/07/2017 – associated values on the right.

The following procedures were implemented for finding adequate responses to the questions raised (enumeration numbers correspond):

1. Since the dark taiga conifer species are indeciduous a winter image (here:WV-2) with little snow coverage was selected for the identification of the related areas.

2. NDVI was calculated for the platforms of Landsat 8, Sentinel-2, and Pléiades with corresponding dates of acquisition. For comparison randomly chosen image pixels with their associated NDVI values were set against each other to be illustrated.

3. The NDVI/LAI relationship was investigated through linear regression of the same summer Sentinel-2 image.

4. NVI and NDRE were calculated for the same Sentinel-2 scene and displayed for contrasting results.

5. The seasonality analysis was performed in Terrset's Earth Trend Modeler (ETM) – a detailed workflow is given below. With ETM, it is possible to map long term trends, trends in seasonality and search for patterns in user-defined regions of interest .

In order to gain detailed insight in the seasonal trends for the test area in 2017 the most suitable Sentinel-2 images (in total 11) were selected to represent a winter-to-winter timeline (i.e., dates: 14/03, 03/04, 13/05, 09/07, 12/07, 29/07, 07/09, 10/09, 17/10, 25/10, 01/11). Prior to stacking of all imagery, they had to be checked for positional errors one by one to ensure a perfect match. Terrset's ETM also requires to define start and end of analysis, which was set to March and November, respectively. The series type was chosen to be monthly with the corresponding definition of the Julian day. The missing data interpolation option was enabled for accounting for time gaps. For inspection and examination of the image series a data cube is generated to explore the space/time dynamics.

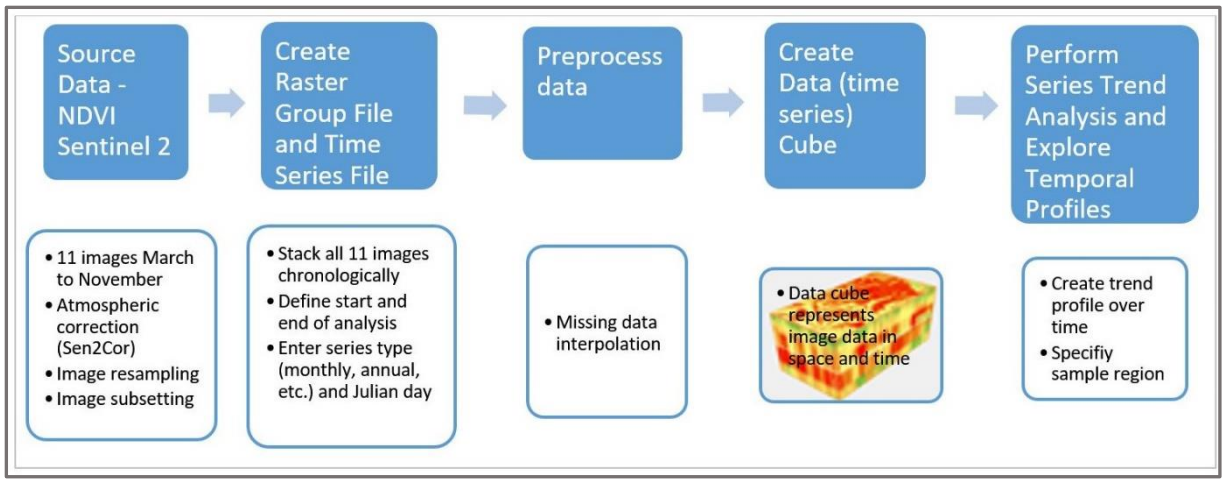

Figure 7.57: Illustration of the NDVI seasonal trend workflow in Terrset Earth Trend Modeler.

In a final step the temporal profiling is created by graphing the summary values of all pixels in a defined sample region. In this case regions of interest were specified for dark taiga, light taiga, burned areas, and the total area of compartment 435. Standard statistics like mean, median, minimum, maximum, range, sum or standard deviation summary values can now be graphed and trend lines added. The results of this analysis are detailed and illustrated in chapter 8.4. of this thesis. ETM offers much more options on trend modelling (Eastman, 2020: 275–301), however, further investigations would be beyond the scope of this work.

For the estimation of LAI, a measurement device was employed in the field, and LAI values derived in SNAP for the Sentinel-2 imagery. To ensure consistency in the measurements a diagonal transect was chosen within the test plot with readings taken every 2 meters with the LICOR LAI 2000 to achieve an average value for the plot. The LICOR instrument allows for the calculation of mean LAI values for a specific transect – the readings were taken accordingly for each test plot. A view cap with a 90^{o} angle was used to block the sun and the operator from the sensor's view. For further information please refer to the LICOR's user manual (Garrigues *et al.*, 2008, LI-COR, 1992).

The SNAP environment provides specific tools for the estimation of biophysical variables such as LAI (leaf area index), FAPAR (fraction of absorbed photosynthetically active radiation), and FVC (cover fraction). As an implementation of the Sentinel 2 Toolbox the variables are derived from top of canopy normalised reflectance data with neural networks trained to estimate the canopy characteristics from TOC reflectance along with corresponding angles defining the observational configuration (Weiss and Baret, 2016). However, it is important to know, that (i) the estimations are strongly scale dependant, (ii) all green contributors are included, i.e. all understorey vegetation, and (ii) the LAI estimation models are based on the assumption that leaves are randomly distributed (i.e. ignoring the clumping phenomenon) (Chen *et al.*, 2005,

Weiss and Baret, 2016, Yan *et al.*, 2019). As such the satellite derived LAI estimations have to be judged accordingly and treated with caution. More details on the LAI extraction algorithms in the S2Toolbox can be found in Weiss and Baret (2016). The estimation process in SNAP is very straightforward by choosing the 'Calculate biophysical variables (LAI, FAPAR)' in the Raster context menu and execute this on a specific satellite scene, which was corrected for atmospheric effects beforehand – in my case the 09/07/2017 Sentinel-2 image. The resulting raster is subsequently imported into a GIS for retrieval of the LAI values (zonal statistics) to be set against the field measurements for accuracy checks. In addition to the field / satellite LAI comparison, the relationship between LAI and NDVI , as well as for LAI and canopy cover was investigated in order to confirm or disaffirm the close correlation behaviour as indicated in the literature.

7.3.5.9. k-NN estimation for timber volume ad basal area (BA)

In publications KNN is often referred to as **K n**earest **n**eighbour *classifier* when it is used for classifying categorical variables such as in remote sensing projects. However, KNN is named K nearest neighbor *regression* when it is applied for predicting non-categorical variables (Meng *et al.*, 2007). The k-NN regression is based on the work of Chirici *et al.* (2008), which has been outlined in chapter 4.6.2. In 2012 a research group headed by Gherardo Chirici released a stand-alone programme for running k-NN regression in a Windows-based environment (Chirici, 2012). An email exchange with this group revealed, that in the meantime their development has been integrated as an improved version in Idrisi's Terrset software environment. The graph below portrays the workflow associated with the user interface in Terrset. In the presented study the Sentinel-2 image 09/07/2017 was chosen. A sample raster size was created to best possibly reflect the location of the test plots the timber volume and BA were calculated for – the plot raster pixels were indicated with their associated plot number, the surrounding pixel values were set as 0 as not to be considered in the subsequent calculations. For the database file the fields were populated with the corresponding values per test plot for timber volume, and BA respectively. The following satellite spectral bands were selected to be appropriate inputs: Blue, Green, Red, NIR, SWIR, with the calculated NDVI being an auxiliary input. According to the k-NN Manual (Chirici, 2012) the 'extraction type' was set to 'Minimum', the 'distance option' 'Euclidian' was chosen as proposed by a number of authors (see also chapter 4.6.2.). An example for populating the Terrset k-NN regression user interface, and the associated calculated K value is given in Figure 7.59.

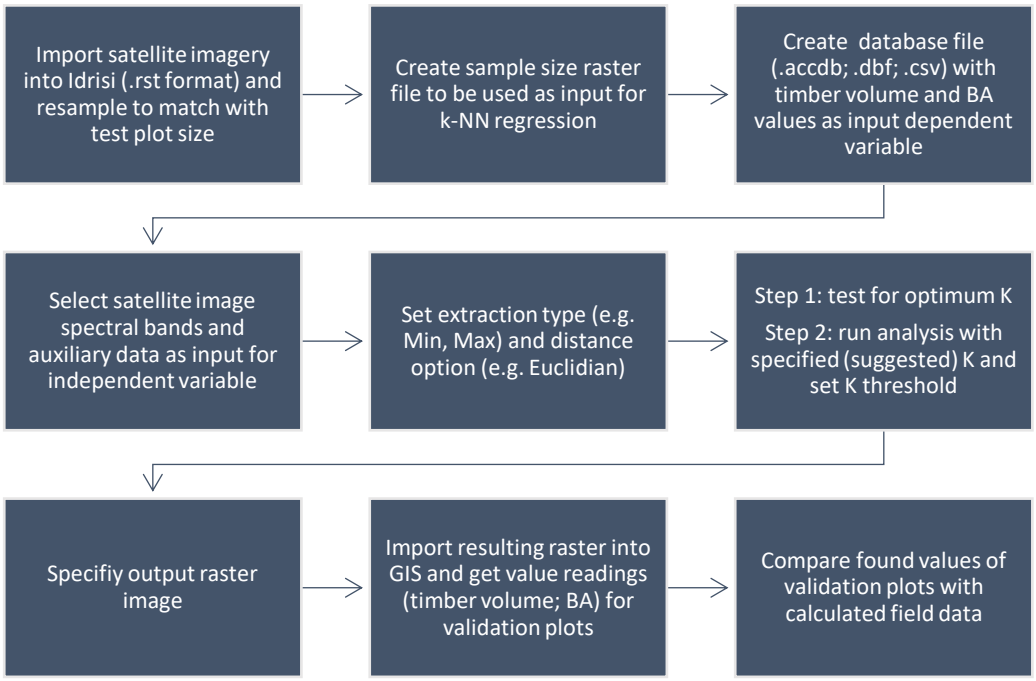

Figure 7.58: K-NN regression workflow (based on Chirici, 2012).

Since the k-NN output raster locations hardly perfectly match with the test plot boundaries used for the verification process, the zonal statistics tool was employed in ArcGIS to retrieve the related correct values for timber volume and BA. A direct comparison between volume and BA values as calculated during the k-NN regression analysis with the pertaining field data was conducted to find potential discrepancies.

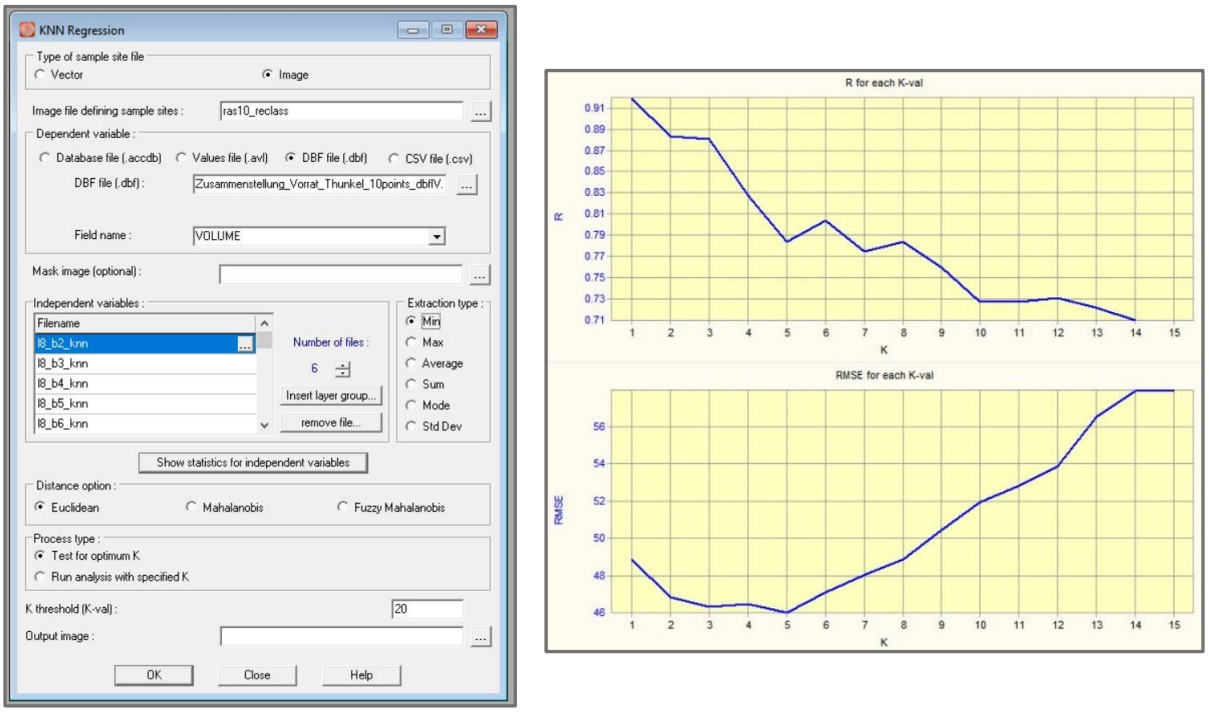

Figure 7.59: KNN Regression window in TerrSet2020 - left (Eastman, 2020); test for optimal K result – right.

8. Results and discussion

The following chapters details all findings related to the work conducted in the field as well as the subsequent analyses of the imagery employed. Since the presented work comprises the extraction of a huge bundle of forest attributes with various methods being associated, it was decided to merge the result description with interpretation in due consideration of the existing body of literature outlined in the preceding sections. The essence of all outcomes and their complementary ratings has been compiled in a 'results matrix' to be used as a 'vademecum' or even as a decision matrix for the best sensor / extraction method response to a specific query.

8.1. Field data

The analysis of data gathered either in a laboratory or in the field represents the very essence of any scientific investigation. Although the initially planned number of field surveys could not be implemented due to force majeure, almost 850 trees at 15 test plots were measured to provide a sound base for further analysis. The main objectives for the scrutiny of these data are manifold:

- Calculate specific values and statistics for various forest attributes for comparison with outcomes of other taxations carried out.
- Retrieve suitable information to set against the data extracted from the remotely sensed imagery (i.e., ground truthing reference).
- Try to find relationships between various parameters as described in the literature.
- Illustrate, if there is any difference between light and dark taiga traits.

The following subchapters and paragraphs are structured according to their relevance regarding comparison and correlation of the data, and their inherent information with respect to their characteristics concerning tree individuals and forest stands.

8.1.1. Main findings and calculations for single trees and all test plots

High resolution imagery qualifies for the extraction of certain parameters from individual trees as well as from tree communities. Based on this discovery the subsequent analyses were conducted regarding single trees and larger units, such as forest stands. The calculation procedures and underlying statistical methods for the data analysis have been previously detailed in chapter 7.3.3.

Randomly selected tree individuals were subject of the investigation on specific characteristics such as species, tree height, and crown diameter. The individuals reflect a large variety in

species and dimensions, and meet the requirement to be detectable in the imagery. The table below reflects the results of the calculations. The highest dimensions for DBH and tree height were determined for trees populating the riparian area, where excellent growing conditions prevail. The relationship between DBH and tree height is not being illustrated due to the small sample size.

Table 8-1: Measured and calculated parameters for the single trees survey.

Tree No	Species	DBH (cm)	Height (m)	Mean Crown Diameter (m)	Tree No	Species	DBH (cm)	Height (m)	Mean Crown Diameter (m)
1	Larch	44	17.4	9.20	19	Birch	45	11.4	6.75
2	Larch	42	19.6	7.60	20	Larch	37	17.8	7.30
3	Larch	80	22.0	11.90	21	Birch	40	16.4	9.60
4	Larch	57	21.8	10.10	22	Birch	25	13.0	4.90
5	Larch	39	18.4	7.35	23	Birch	35	16.0	5.55
6	Willow	18	7.6	5.20	24	Larch	46	15.4	9.90
7	Willow	29	8.0	4.80	25	Larch	63	18.5	13.85
8	Willow	22	6.6	5.85	26	Larch	34	16.4	7.10
9	Poplar	96	21.2	12.50	27	Larch	61	22.2	6.80
10	Birch	48	17.6	6.50	28	Larch	76	25.4	12.15
11	Birch	34	14.2	6.50	29	Larch	37	17.3	6.20
12	Larch	91	25.0	NA	30	Birch	27	14.0	7.05
13	Willow	61	8.6	5.00	31	Larch	39	18.8	4.70
14	Poplar	44	18.0	NA	32	Birch	25	14.0	4.60
15	Poplar	50	16.0	8.95	33	Larch	37	18.7	6.50
16	Birch	48	13.4	7.95	34	Birch	30	14.8	6.25
17	Willow	55	12.0	8.10	35	Larch	24	14.5	4.55
18	Poplar	87	19.9	11.50	36	Birch	26	16.0	4.35
					37	Larch	33	17.2	7.40

All data calculated above have been used as reference for the comparison between field data and the information extracted from the imagery to check for disparities.

In the following the calculations for the respective test plots are presented and set the calculations of the GIZ survey (i.e., Tables 8-2 and 8-3) side by side. The most relevant findings are elaborated, with a detailed comparison between light taiga and dark taiga features discussed in chapter 8.1.4. In order to gain more insights into the structure and characteristics of the taiga forests and for relativization purposes it would be sensible to set the outcomes of this study against some reference. However, only a few studies, namely by Gradel and Mühlenberg (2011), Gradel (2017), Gradel *et al.* (2017a), and Mestemacher and Doelle (2003) provide some clues on the growth development of the forests in the Khentii region. Some rough figures are also provided through the NFI report, though the forest inventory carried out on a national level pursues other goals. To the best of the author's knowledge, no other reliable sources seem to exist. There is of course a slight chance that Russian researchers conducted

investigations during the Russian – Mongolian collaboration period, however, since Dr. Gradel is in command of the Russian language and maintains correspondence with Russian experts, I imagine that he also perused the pertaining literature. In addition, reports on local forest taxations carried out by private companies are either not available or are based on ocular estimation, thus making any inferences based on sound scientific methods pure speculation (Altrell and Erdenejav, 2016: 107–108).

According to my surveys the tree heights range from 11.00m to 15.98m for the mean value, with a maximum height for an old larch with 24.8m. These outcomes are very much in line with the findings by Gradel (2017: 122) and the majority of the inventory results for compartment 435 assessed by Gaschick (2013). The number and variety of tree species found also correspondents with the classification definition for light and dark taiga. The number of trees per hectare varies greatly with figures of between 200 and 1010. Most of the more sparsely populated areas are to be found in the lower part of compartment 435, where marked indications of over-exploitation are apparent. In contrast, most of the dark taiga patches show high tree numbers, since no cutting activities seem to have taken place. The NFI report discloses an average of 444 N/ha for the Khentii inventory region, which is contrasted by Gradel (2017: 164), who found higher numbers for his test plots, even after thinning. In terms of diameter range and structure the DBH means straddle values between 15.5cm and 34.7cm. Once again, the dark taiga plots reflect the highest means. Unfortunately, the references mentioned above reveal no further information for comparison. The NFI report shows an average of 13.2 m^2/ha for the basal area related to the Khentii region (Altrell and Erdenejav, 2016: 51), whereas the value range associated with my survey shows a different picture, namely a mean from 13.25 to 29.40 m^2/ha. The dark taiga plots again yielded the highest values. Similar results are confirmed in the GIZ management plan, and in Gradel and Mühlenberg (2011). Gradel (2007) reports, that the BA of disturbed sites is on average lower compared to the undisturbed. This phenomenon could of course explain the poorer performance of the light taiga forest areas, since they are affected by causes such as wildfires much more often than the dark taigas, which occupy cooler and moister zones. In their study, Mestemacher and Doelle (2003) observed that the *Pinus sibirica* forest featured an average BA of 39 – 40 m^2 per hectare and the light taiga an BA average of around 19m^2/ha. These magnitudes are backed by Gradel (2007: 49) in his investigation. Canopy closure was found to be ranging from 10 to 60% in the school forest. Since the LAI values are correlated with the crown density to some extent, the lowest values can be reported for the light taiga areas in the lower part of compartment 435 and the higher LAI for the dark taigas. Some of the low LAIs, however, need to be seen in the context of the various levels of defoliation of the birch in the lower part of the school forest. The stocking levels can be considered as being quite low in general. This phenomenon can most probably attributed to the fact, that the growth and yield

tables used for the appraisal tend to gravely overestimate the stocking levels (Gradel, 2017: 164–165). The highest degree of controversy is to be reported on the determination of timber volume and the associated outcomes for the specific taiga types and regions. Although having applied the same allometric formulas, the results of my investigation are not commensurate with the findings in most of the other sources. The calculated values for compartment seem to be largely underestimated by Gaschick (2013) ranging from 20 to 48m^3/ha. The average volumes specified in the NFI report reflect a value of 96m^3/ha for the Khentii area, whereas my observations comprise a range from 58 to 332m^3/ha. The NFI calculations of course represent an average for the whole of the Khentii region. Gradel (2017: 164) also reports volumes to be much higher than in the NFI report. Thus, I consider my findings being closer to the real values, than those indicated by Gaschick (2013), however without claiming, that my observations are subject to the highest achievable accuracies.

As indicated above, there are a number of disparities to be reported between the GIZ management plan (i.e., Gaschick, 2013) and my survey data, of which some of them remain contentious. The table below (Table 8-3) bears testimony to the findings. The good news is that BA values are very similar and tree species allocations also match quite nicely. What stunned me most is an average tree height of 32m for the dominating tree species Siberian birch in stand no.5. Such tree height is already quite exceptional for a single birch to be found in Germany, but with respect to the growing conditions in Mongolia such an extreme value seems quite unrealistic. The number of trees found in the respective plots also raises a few concerns, since in a number of cases numbers were about 50% of the ones that were detected in my inventory. According to the management plan no excessive tree felling actions had been planned and executed prior to my field trip. The illustrated circumstances of course explain the variation in tree volume to a great extent. However, some of the volume discrepancies remain untold. In another instance the management plan reports a stocking level (BG) of (negative) –0.2, with a calculated number of trees per hectare of 1618 for plot no.16. Even though the growth and yield tables are known to overestimate stocking levels, this negative value comes to a great surprise. In order to obtain a stocking level value of zero in reality the corresponding forest area must present itself being almost void of trees.

In the light of the discrepancies mentioned above, it has been decided to discard the GIZ data as a possible reference for my ground truthing activities. This was also the reason for not taking tree age classes into account. Nevertheless, a few potential error sources should be noted for further consideration. Firstly, the GIZ survey was based on the 6th-tree method, which yields fairly useful, but not the most accurate results. Secondly, the training level of the surveyors play an important role in the gathering of the data, which the author can only speculate on. Thirdly, some inconsistencies in other inventory datasets were detected, such as an DBH of

30cm coupled with a tree height of zero. This critique is of course not meant to discredit any work related to the GIZ inventory, but rather taken as a suggestion for improving data analysis. However, it is quite unfortunate not having received any feedback on the points raised.

Rest of page intentionally left blank

Table 8-2: Calculated forest inventory attributes as surveyed by author (Vogt) in compartment 435.

Plot ID	**0**	**1**	**2**	**3**	**4**	**5**	**8**	**11**	**12**	**22**	**24**	**31**	**34**	**60**	**64**
Mean height (m)	15.81	14.52	14.58	12.06	11.00	11.52	14.89	12.45	11.47	12.50	13.40	12.85	13.96	15.47	15.98
Mean DBH (cm)	24.9	24.0	15.4	15.5	15.5	21.2	34.7	17.2	19.1	19.0	30.1	20.6	22.3	17.5	18.4
Trees/ha	200	340	520	530	920	860	450	1010	840	480	420	430	350	810	820
Species (%)															
Siberian birch	75	59	98	91	96	1	0	18	15	69	55	72	86	98	100
Siberian larch	25	41	2	9	4	26	31	63	54	31	45	28	14	2	0
Siberian spruce	0	0	0	0	0	44	38	9	14	0	0	0	0	0	0
Siberian pine	0	0	0	0	0	29	31	10	17	0	0	0	0	0	0
LAI	0.34	0.67	0.49	0.91	1.21	0.74	0.96	1.80	0.93	1.79	0.83	1.12	NA	1.12	0.71
Canopy closure (%)	10	15	24	41	64	46	38	60	37	27	29	37	NA	54	59
Timber volume (qm/ha)	66.40	84.70	86.00	58.10	78.70	223.50	331.80	157.30	153.00	80.20	239.40	94.40	93.60	188.10	165.20
Basal area (sqm/ha)	13.50	13.25	15.60	15.50	17.50	29.40	28.60	28.80	15.20	21.00	26.80	20.50	19.00	26.25	26.50
Stand density index	13.50	13.25	15.60	15.50	17.50	29.40	28.60	28.80	15.20	21.00	26.80	20.50	19.00	26.25	26.50
Shannon index	0.562	0.887	0.095	0.312	0.179	1.141	1.094	1.070	1.234	0.626	0.689	0.598	0.418	0.116	0.066
Slope (%)	25	22	21	22	20	15	10	20	10	25	19	25	23	30	41
Aspect	N	NNE	NNE	NNW	NNW	NW	NNW	NNE	NNE	NNW	NNE	NNE	N	NNW	NNW
Stand density index = BA/ha															

Table 8-3: Comparison of field data of compartment 435 as surveyed by GIZ (in green) and Vogt (in red). Field data Vogt were aggregated to accommodate GIZ zoning.

Stand no.	Area (ha)	Age (range)	Stocking level (BG)	Stocking level (BG)	Species	Tree species (%)	Tree species (%)	Number of trees (per ha)	Number of trees (per ha)	Mean tree height (m)	Mean tree height (m)	Volume (m^3/ha)	Volume (m^3/ha)	Basal area (m^2/ha)	Basal area (m^2/ha)
3	96.9	50-70	0.2	0.3	Birch	65	88	342	444	20.00	13.74	12.00	58.76	8.00	12.50
					Siberian larch	35	12	185	58	15.00	13.95	8.00	16.02	4.30	2.34
					total	100	100	528	502			20.00	74.78	12.30	14.84
5	8.4	50-70	0.5	0.6	Birch	94	98	758	790	32.00	15.74	25.00	149.80	16.90	23.70
					Siberian larch	6	2	72	15	5.00	12.55	2.00	25.10	1.00	3.75
					total	100	100	830	805			27.00	174.90	17.90	27.45
11	73.3	60-90	0.5	0.4	Birch	78	78	624	295	24.00	13.18	28.00	69.65	16.40	10.30
					Siberian larch	22	22	178	85	13.00	13.10	11.00	24.35	4.60	3.15
					total	100	100	802	380			39.00	94.00	21.00	13.45
14	57.9	50-150	0.4	0.3	Birch	42	62	577	270	15.00	10.85	12.00	41.75	8.40	8.10
					Siberian spruce	0	0	16	0	0.00	0.00	0.00	0.00	0.10	0.00
					Siberian larch	58	38	323	170	15.00	15.80	26.00	118.05	11.80	14.60
					total	100	100	916	440			38.00	159.80	20.30	22.70
16	97.5	60-130	**-0.2**	0.5	Birch	14	18	405	170	7.00	10.17	4.00	11.55	3.70	2.65
					Siberian larch	53	58	541	535	16.00	13.23	30.00	107.55	14.50	14.90
					Siberian pine	25	13	338	120	8.00	11.21	11.00	24.35	6.80	3.40
					Siberian spruce	8	11	334	105	5.00	9.99	3.00	11.30	2.30	2.10
					total	100	100	1618	930			48.00	154.75	27.30	23.05
17	14.6	40-130	0.3	0.4	Birch	2	2	67	10	1.00	9.90	0.00	1.30	0.40	0.40
					Siberian larch	21	26	107	165	8.00	17.06	11.00	147.00	5.20	20.00
			GIZ: green		Siberian pine	65	30	746	195	17.00	13.20	25.00	95.10	16.00	10.90
			Vogt: red		Siberian spruce	12	42	430	270	8.00	10.90	3.00	34.90	2.90	4.30
					total	100	100	1350	640			39.00	278.30	24.50	35.60

8.1.2. Relationship tree height to DBH per relevant tree species for all test plots

In the following the relationship between tree height and DBH is illustrated for the various tree species – a comparison between dark and light taiga attributes can be found in chapter 8.1.4. For testing similarity, the relevant coefficients of determination (R^2) were extracted from the National Forest Inventory Report (2016). Unfortunately, no information on the precise calculation process was available for the NFI values. In case of massive defects (e.g., broken crowns, leaning trees, etc.) a statistically sound correlation between DBH and tree height cannot be established. For this reason, both variants, i.e., with and without consideration of the defects are reported for compartment 435 for illustration. No distinction between the various levels of tree vitality was made.

Table 8-4: Relationship between DBH and tree height. R^2 values are extracted from the National Forest Inventory Report (NFI, 2016) and the field data for compartment 435. Data for the school forest (dubbed as 'Vogt') are presented including all trees measured and without trees with major defects ('outliers') to avoid potential bias.

DBH / Height relationship	R^2 NFI	Trees measured	R^2 Vogt incl. outliers	R^2 Vogt excl. outliers	Trees measured
Species					
Larix sibirica	0.676	6129	0.573	0.753	222
Betula platyphylla	0.702	4008	0.452	0.520	535
Pinus sibirica	0.688	2841	0.823	0.850	64
Picea obovata	0.753	365	0.651	0.692	77

The graphical representation of the DBH / tree height is provided below per species for all trees measured. In addition, the most relevant descriptive statistics are portrayed.

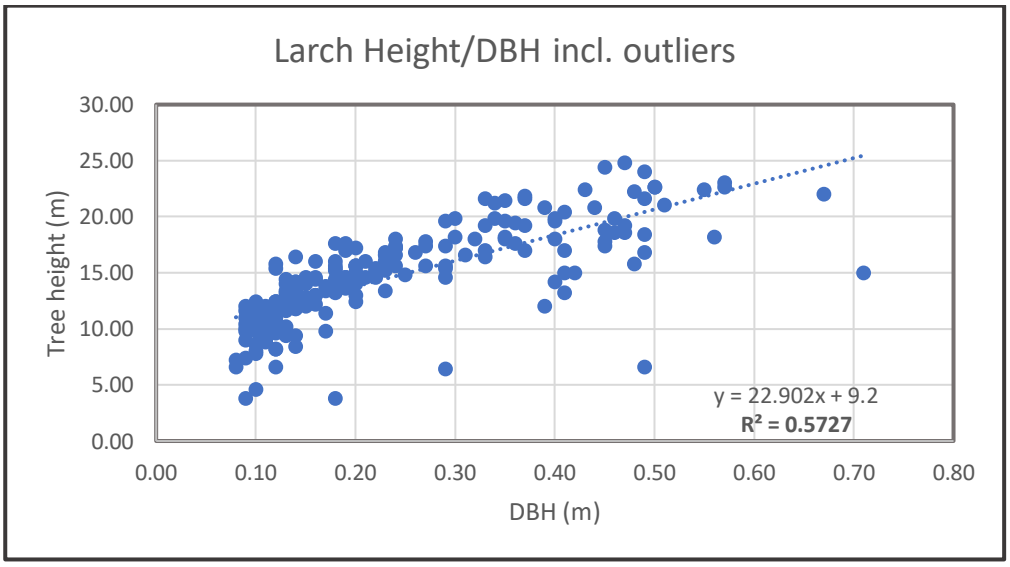

Figure 8.1: Tree height – DBH relationship for Siberian larch.

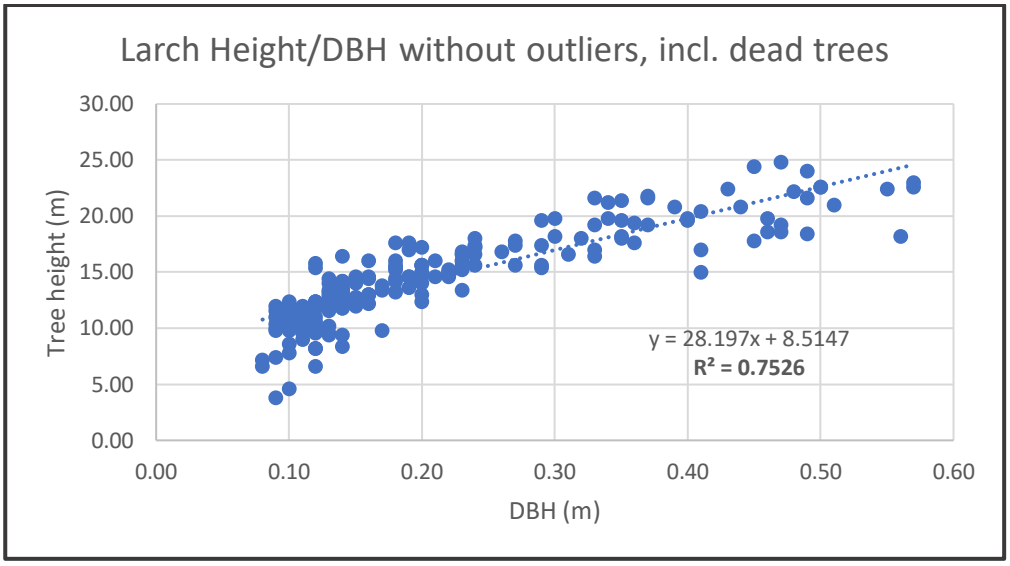

Figure 8.2: Tree height – DBH relationship for Siberian larch. Trees with broken crowns and heavily leaning trees are excluded from reckoning.

Since the larch stands feature a relatively high number of broken tree crowns it seems quite sensible to only consider the R^2 value for the height / DBH relationship disregarding the outliers. With a value calculated for my investigation the R^2 shows a better performance in comparison with the NFI findings, i.e., a higher proportion of total variation of outcomes are explained by the model. The main descriptive statistics are provided in the table below for which a detailed discussion related to the box plot interpretation for larch is provided in chapter 8.1.3.

Table 8-5: Main statistical parameters for Siberian larch (left) and Siberian birch (right) including outliers.

Statistics		
	Height (m)	**DBH (m)**
St.dev.	4.081	0.135
Variance	16.652	0.018
Mean	14.436	0.229
Median	14.300	0.180

Statistics		
	Height (m)	**DBH (m)**
St.dev.	3.765	0.059
Variance	14.181	0.004
Mean	13.300	0.170
Median	13.200	0.160

The tables above demonstrate, that due to the relatively high sampling size both - mean and median – are not that different for each species. As expected, the variances for DBH are low due to the fact, that the stands are quite uniform - a few exceptions of course exist in the dark taiga, where a high number of very old larches are still present. The variance for the tree heights is much larger in comparison, because the statistics also entail the outliers with broken and leaning trees considered.

When regarding the height / DBH relationship for the Siberian birch the low R^2 value in comparison with the NFI findings is obvious (i.e., 0.452 vs 0.702), even with outliers being discarded. Even though the number of tree individuals measured is high (i.e., 535), the

coefficient of determination shows a big discrepancy compared to the NFI figure. A possible interpretation is that many birch individuals exhibit a multi-stem characteristic – apparently, they were either felled or affected by fire with resprouting activities taking place afterwards. This phenomenon can lead to a skewed height / DBH relationship.

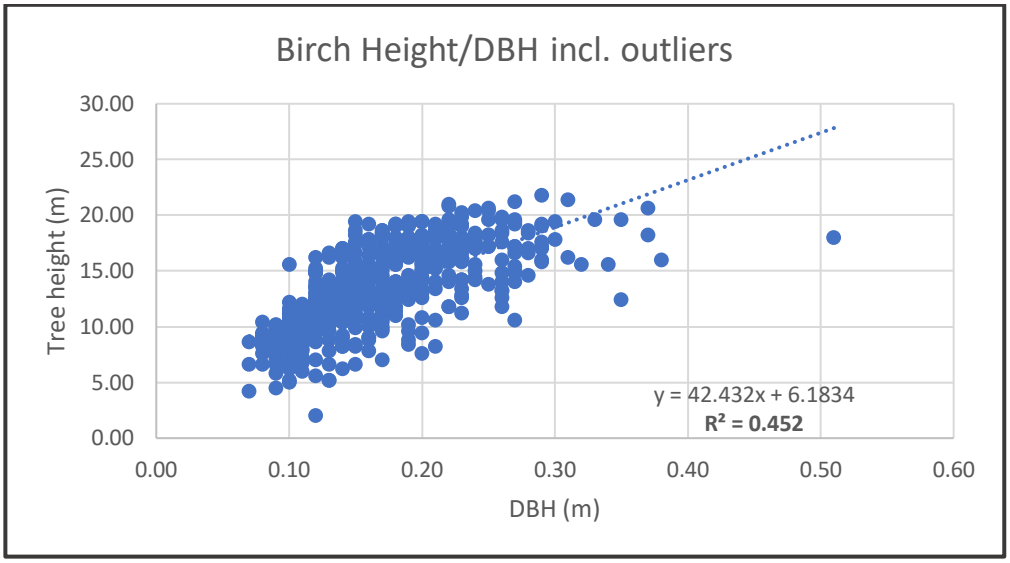

Figure 8.3: Tree height – DBH relationship for Siberian birch.

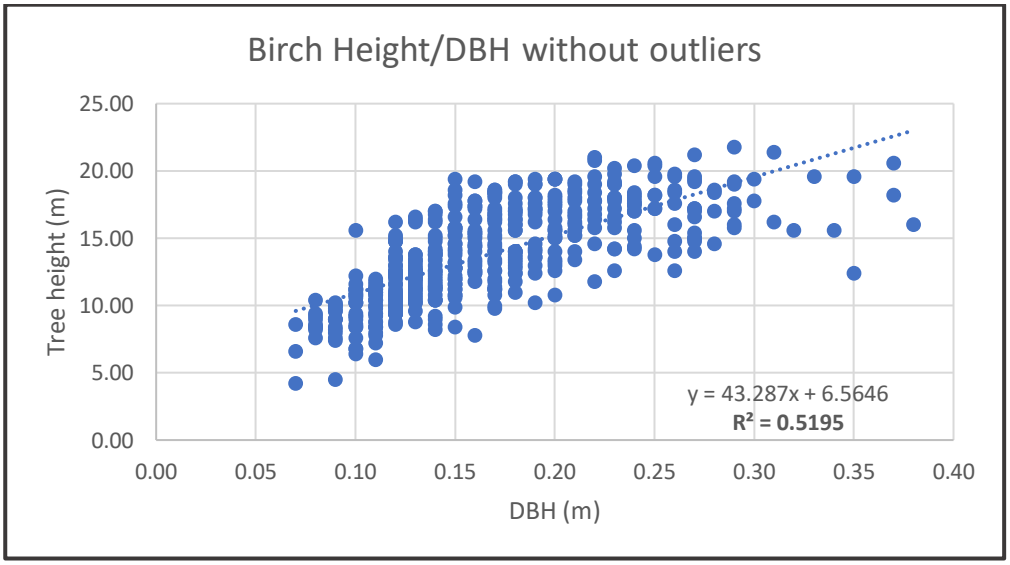

Figure 8.4: Tree height – DBH relationship for Siberian birch. Trees with broken crowns and heavily leaning trees are excluded from reckoning.

The analysis for Siberian pine shows an exceptionally high R^2 when set against the NFI result (i.e., 0.823 vs 0.688). This might have to do with the fact, however, that only a small number of pines were measured in this study.

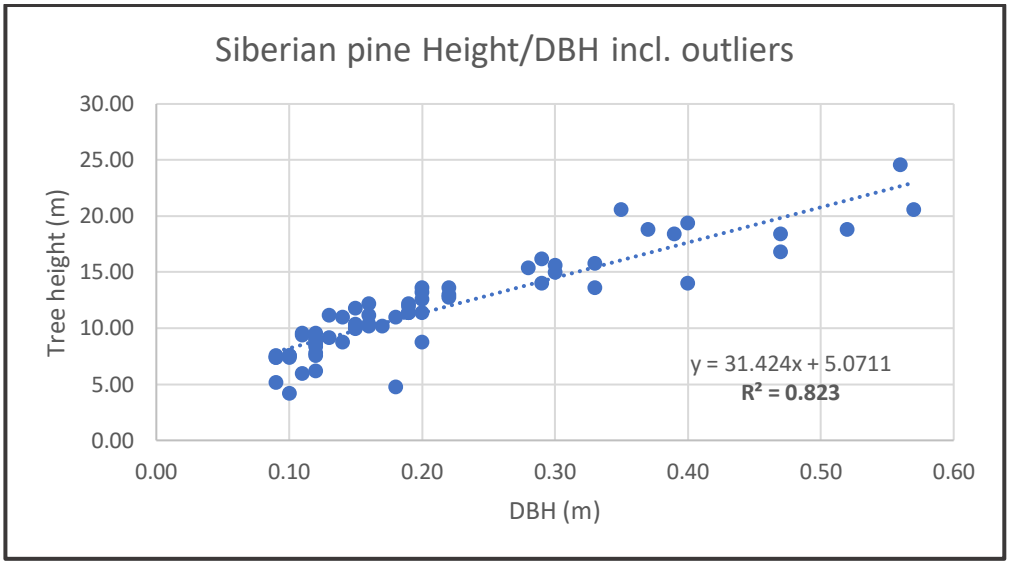

Figure 8.5: Tree height – DBH relationship for Siberian pine.

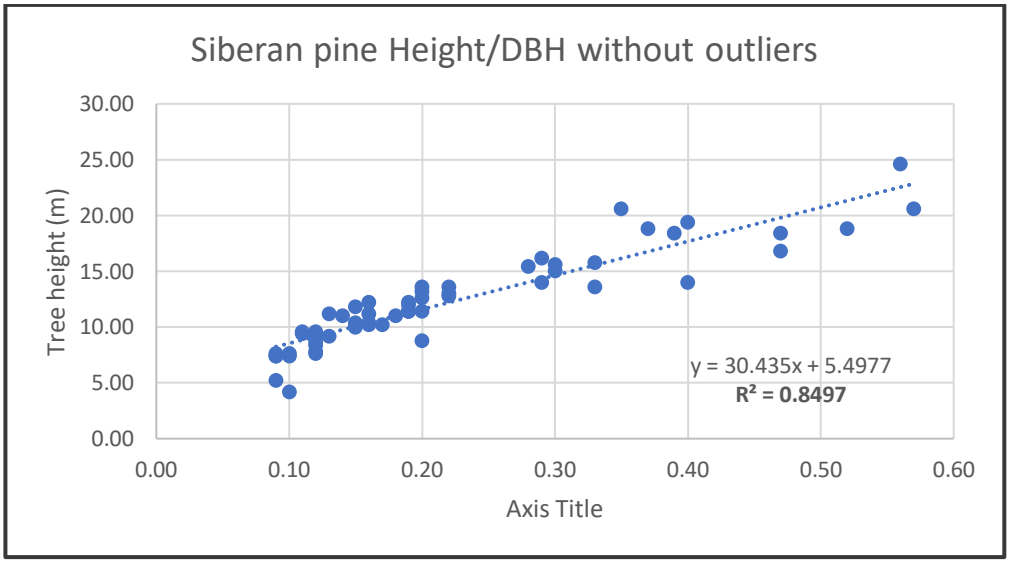

Figure 8.6: Tree height – DBH relationship for Siberian pine. Trees with broken crowns and heavily leaning trees are excluded from reckoning.

The consideration of the coefficient of determination for Siberian spruce shows a performance being quite similar to the NFI outcomes (R^2 0.692 vs 0.753). Nonetheless, with a sampling size this small (i.e., 77 trees) it is very difficult to establish a statistically sound height / DBH correlation.

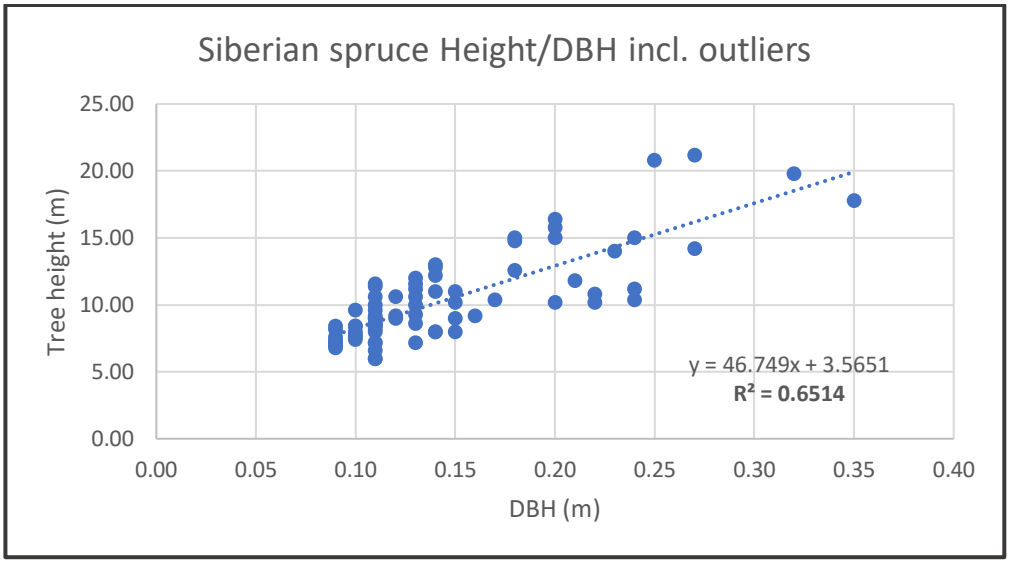

Figure 8.7: Tree height – DBH relationship for Siberian spruce.

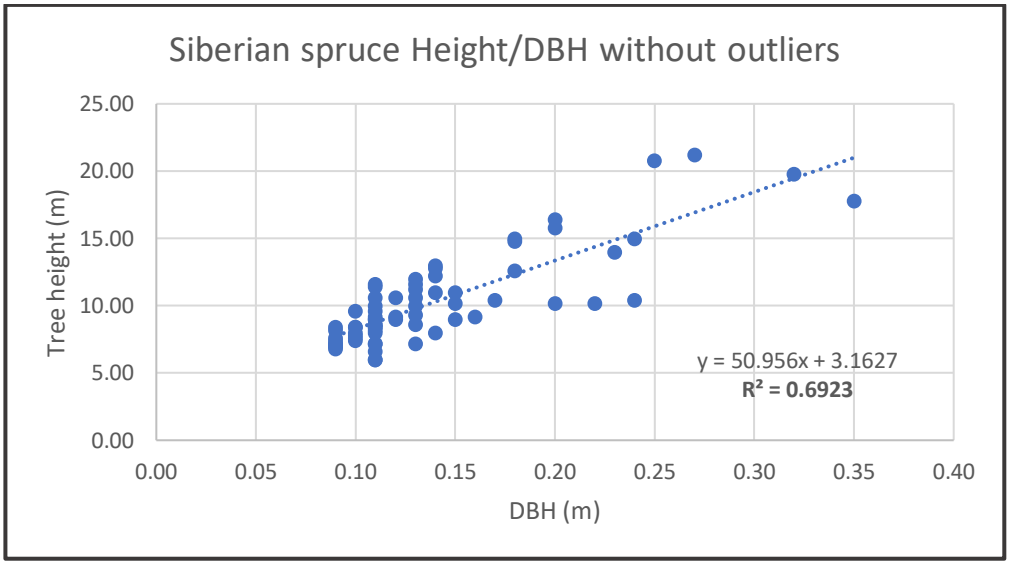

Figure 8.8: Tree height – DBH relationship for Siberian spruce. Trees with broken crowns and heavily leaning trees are excluded from reckoning.

The comparison between the descriptive statistics for DBH again shows a low degree of variance for both species. The mean and median values for the tree height, however, display a smaller variation for Siberian pine as for Siberian spruce – this outcome is hard to comprehend and might be linked to fact, that the sampling size for both species is rather limited (i.e., 66 trees vs 7 trees).

Table 8-6: Main statistical parameters for Siberian pine (left) and Siberian spruce (right) including outliers.

Statistics	Height (m)	DBH (m)
St.dev.	4.253	0.123
Variance	18.084	0.015
Mean	11.740	0.210
Median	11.200	0.180

Statistics	Height (m)	DBH (m)
St.dev.	3.322	0.057
Variance	11.034	0.003
Mean	10.350	0.150
Median	9.300	0.130

In conclusion it can be stated, that all tree species reveal a positive height / DBH relationship with no real anomalies compared to the NFI findings. It is, however, very unfortunate, that access to other data sources, such as the repository of the Mongolian Botanical Institute, was not possible.

8.1.3. Statistics for dominant tree species larch

These calculations and statistics are a prerequisite for the comparison between light and dark taiga features. Since no birch was found to be present in the surveys for the dark taiga, only the larch traits were subjected to further analysis.

As outlined in chapter 7.3.3. a quantile-quantile (Q-Q) plot had to be created to test the dark and light taiga features for a distribution deviating from the Gaussian principle.

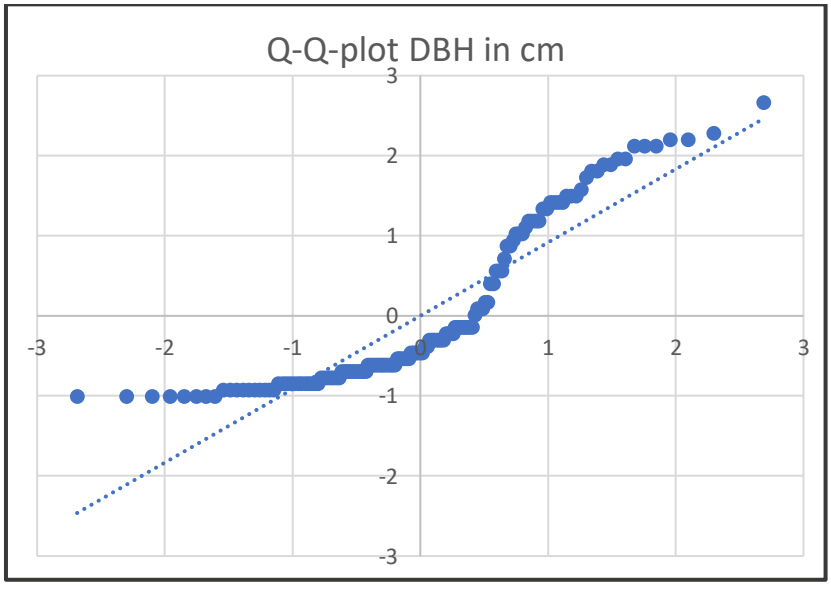

Figure 8.9: Q-Q-plot to examine distribution for DBH in Siberian larch (all plots).

The figure above features a clear S-shape for the two distributions regarding DBH (i.e., observed vs expected values). Once the plot shows such a graphical representation of the quantiles, one of the distributions is more skewed, thus not following a normal distribution

(Lorenz, 2020, Thode, 2002: 21–22, Wilk and Gnanadesikan, 1968). This outcome has grave implications on the further statistical testing, suggesting, a non-parametric test has to be chosen. In the figure below the same process is reflected for testing the height values for normal distribution.

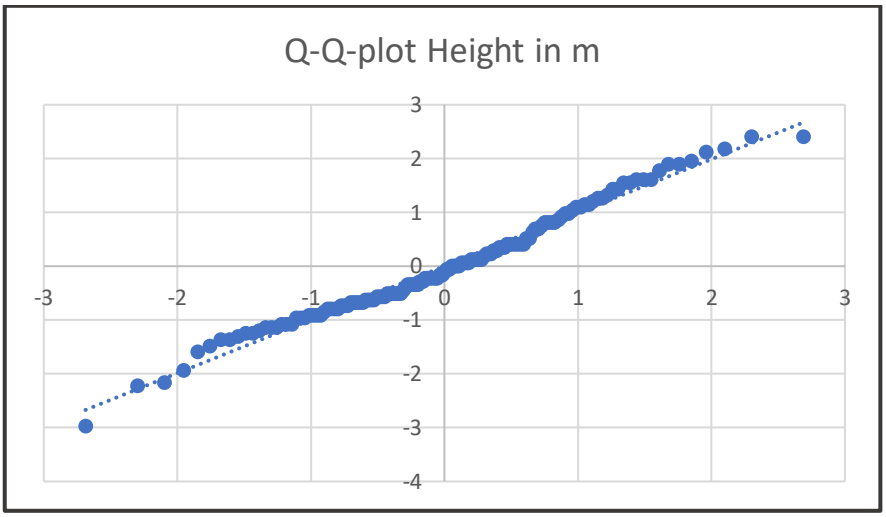

Figure 8.10: Q-Q-plot to examine distribution for tree height in Siberian larch (all plots).

As for the interpretation of the resulting Q-Q plots two distributions being compared can be regarded as identical, if the plot follows the 45° line. This most certainly is the case for the height distributions – thus, a parametric statistical test would be appropriate. However, since the biggest differences were expected to exist between the dark and light taiga DBH, the subsequent analysis (i.e., U-test) was only carried out for this forest attribute. In addition, the consideration of DBH was considered to be less prone to bias because of the occurrence of broken and leaning trees affecting the tree height analysis.

8.1.4. Comparison of statistics for dark and light taiga

In this subchapter the statistics for DBH and tree height are compared between dark and light taiga for Siberian larch, as well as for all tree species. Although the provided tables already provide a good insight in the disparities, the graphical representation as boxplots (for all species) make the analysis of the data much more tangible.

The first set of descriptive statistics reflects the dark taiga DBH set against the same attribute for the light taiga. The calculated DBH mean for the dark taiga is 2.5cm lower than for the light taiga, with the median being even 5cm different. The values for kurtosis and skewness are not very meaningful, since we already proved the DBH distribution not showing properties to be Gaussian. The minimum, but especially the maximum diameters – in consideration with the

mean diameter – already give an indication, that diameter growth appears to be more modest in the dark taigas.

Table 8-7: Dark taiga DBH for larch.

Larch dark taiga - DBH (cm)	
Mean	21.9064748
Standard Error	1.08524632
Median	16
Mode	14
Standard Deviation	12.7948654
Sample Variance	163.708581
Kurtosis	0.36605176
Skewness	0.99109195
Range	47
Minimum	9
Maximum	56
Sum	3045
Count	139
Confidence Level(95.0%)	2.14586139

Table 8-8: Light taiga DBH for larch.

Larch light taiga - DBH (cm)	
Mean	24.4698795
Standard Error	1.59195905
Median	21
Mode	12
Standard Deviation	14.5034372
Sample Variance	210.349691
Kurtosis	1.07481125
Skewness	1.27113054
Range	63
Minimum	8
Maximum	71
Sum	2031
Count	83
Confidence Level(95.0%)	3.16691369

When investigating the height disparities between the two populations the difference in mean is almost negligible. However, the difference in maximum tree height (i.e., 2m) in favour of the light taiga can be attributed to less favourable growing conditions in the dark taiga realm (cooler climate). In addition, it also needs to be taken into account, that the dark taigas are in average much older than the light taigas due to the lack of accessibility of the former. Unfortunately, the analysis of the tree rings is still in progress, with the GIZ data mostly being based on ocular estimations. Quite striking is the enormous height variance of the light taiga with a value of almost 24. This performance can be attributed to the fact, that large areas of very young taiga (i.e., lower part of compartment 435) are represented, as are older parts with a high number of so-called canopy emergent, I.e., old trees either not been cut (i.e., not accessible) and /or left as seed trees. Both, kurtosis and skewness values do not reflect a big discrepancy from the typical character of a normal distribution, which would ideally feature a value of 0.

Table 8-9: Dark taiga tree height for larch.

Larch dark taiga - Tree height (m)	
Mean	14.16115108
Standard Error	0.296849461
Median	13.8
Mode	15.6
Standard Deviation	3.499803531
Sample Variance	12.24862475
Kurtosis	0.037136771
Skewness	0.204029982
Range	18.8
Minimum	3.8
Maximum	22.6
Sum	1968.4
Count	139
Confidence Level(95.0%)	0.586961491

Table 8-10: Light taiga tree height for larch.

Larch light taiga - Tree height (m)	
Mean	14.8975904
Standard Error	0.53686593
Median	15
Mode	15
Standard Deviation	4.89108138
Sample Variance	23.922677
Kurtosis	0.53619037
Skewness	0.03360424
Range	21
Minimum	3.8
Maximum	24.8
Sum	1236.5
Count	83
Confidence Level(95.0%)	1.06799735

The following graphs provide a representation of the height / DBH relationship for light and dark taiga separately. The coefficients of determination are provided for the linear relationship, as well as for a polynomial 2nd order.

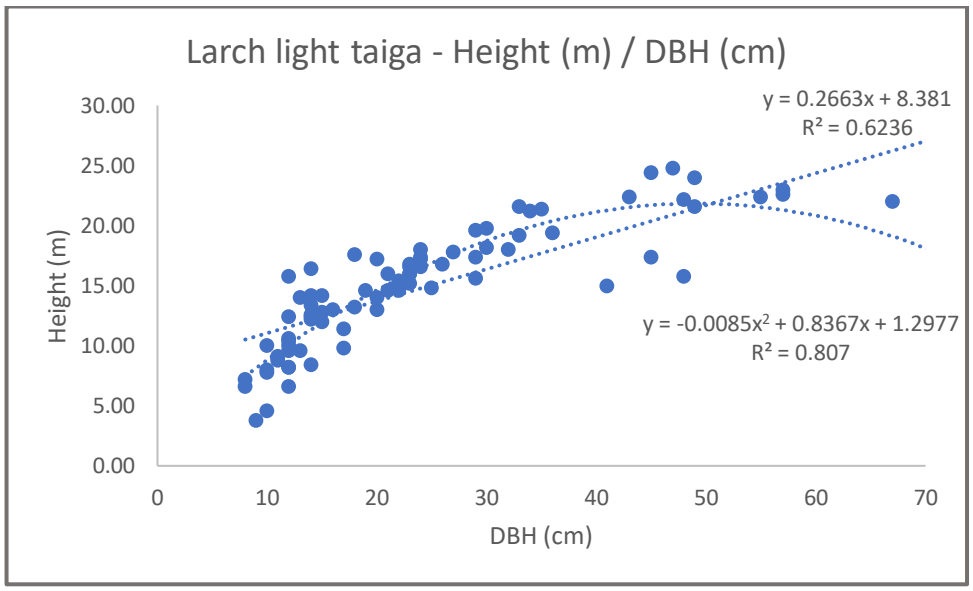

Figure 8.11: Relationship between tree height and DBH for Siberian larch, light taiga.

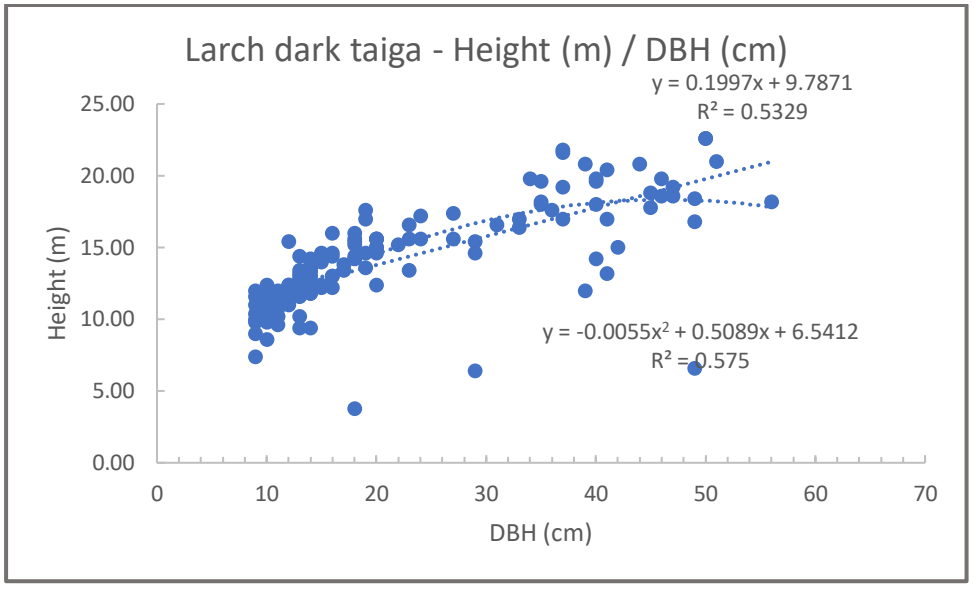

Figure 8.12: Relationship between tree height and DBH for Siberian larch, dark taiga.

The figures above show, that there is definitely a positive relationship between tree height and DBH, but with the light taiga variant revealing a higher coefficient of determination (for both, linear and polynomial). It is, however, quite unfortunate, that the NFI values provided for R^2 (see above in chapter 8.1.2.) do not allow a distinction between dark and light taiga height / DBH correlation. As such, an interpretation of the different performances is quite arduous. When looking at the graphical representation for the dark taiga relationship, it is at least apparent, that some more outliers exist. Since those extreme values can have a big leverage on the coefficient of determination, such a pull towards the poorer values can be assumed.

In the two bar graphs below a representation of the DBH class distribution is given.

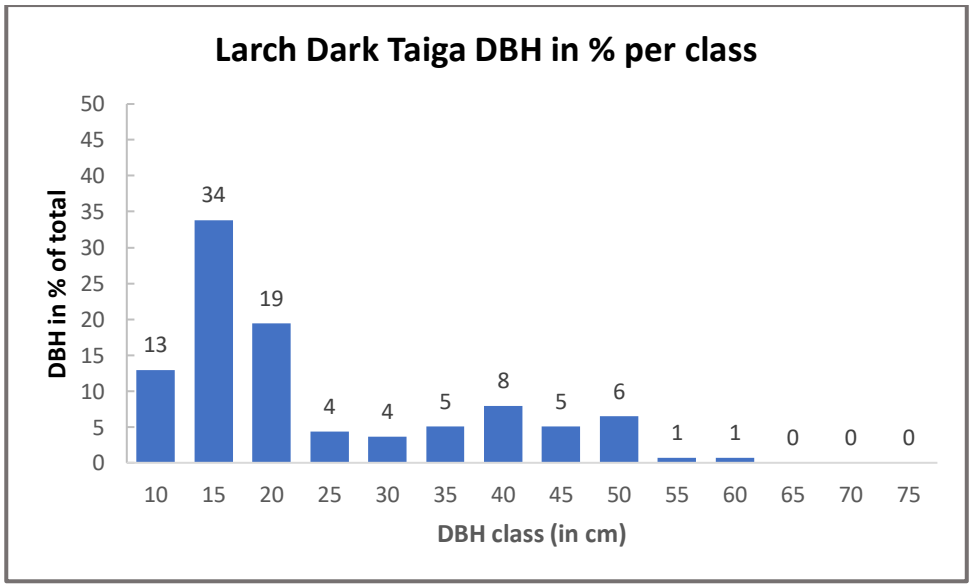

Figure 8.13: DBH distribution per class for the dark taiga Siberian larch.

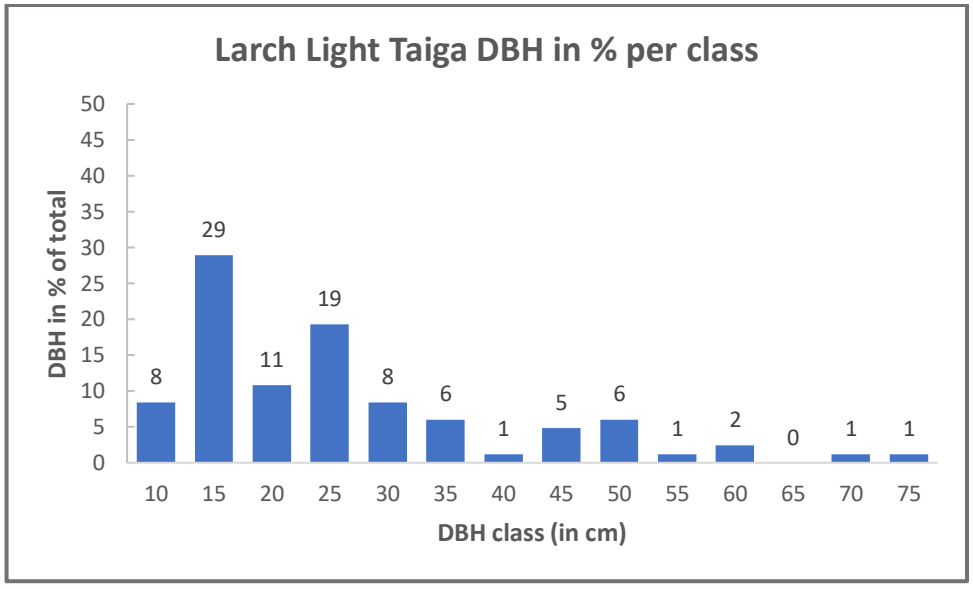

Figure 8.14: DBH distribution per class for the light taiga Siberian larch.

The figures above show for both variants a distribution with a slight skewness to the left, indicating that the lower diameters are dominating. The distribution of the DBH for the dark taiga, however, reveal that diameters beyond the 25cm class or more evenly spread. In turn, the light taiga class distribution indicates the existence of a few more trees with extremely high DBH. Both graphs also illustrate, that there seems to be a sufficient amount of trees of younger age to successively take a shift towards the higher diameters. This observation, however, is not quite in line with the one made by GIZ experts, who read a trend to an over-aging of the forest stands in the school forest (Schmidt-Corsitto, 2017).

In the following graphs the descriptive statistics have been converted into boxplots to improve interpretability. The first pair of plots represent the statistics related to the DBH for light and dark taiga, respectively, to represent all trees (i.e., all species) measured in the pertaining taiga class. Although the median values are identical for both taiga classes, the size of the box representing the interquartile area (i.e., 50%) is more extended for the dark, than for the light taiga. In addition, the mean value for the dark taiga (i.e., 21.51cm) exceeds the value for the light taiga by almost 3.5cm. According to the field data, the high average DBH of the Siberian pine largely contributes to this trend. For the dark taiga the range of the whiskers (i.e., 25th and 75th percentile, the so-called interquartile range) is more pronounced than for the light taiga indicating a higher variability. The maximum value for dark taiga is 52cm, whereas for the light taiga it is 37cm. On the other hand, outliers are much more abundant in the light taiga boxplot, but apparently exhibiting not much leverage.

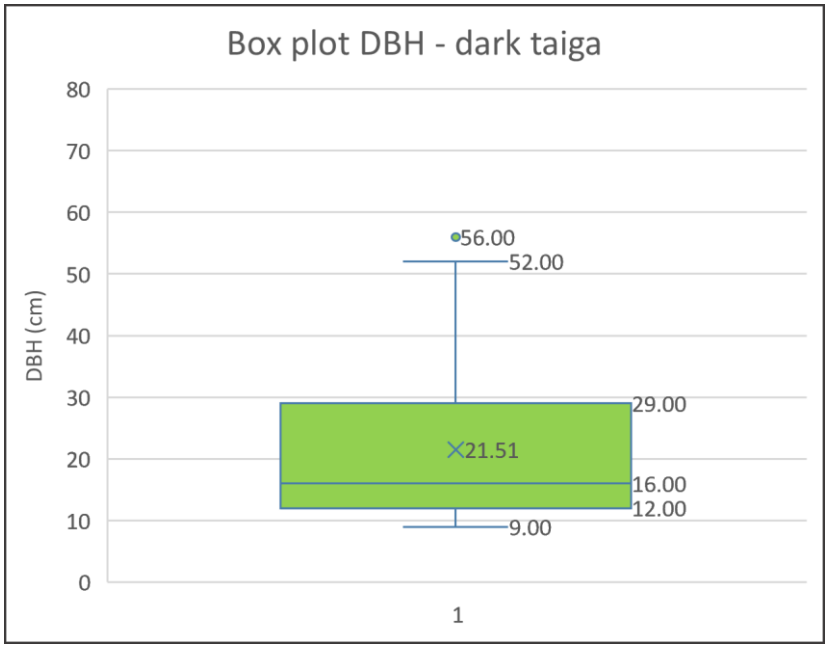

Figure 8.15: Box plot for DBH for dark taiga all species.

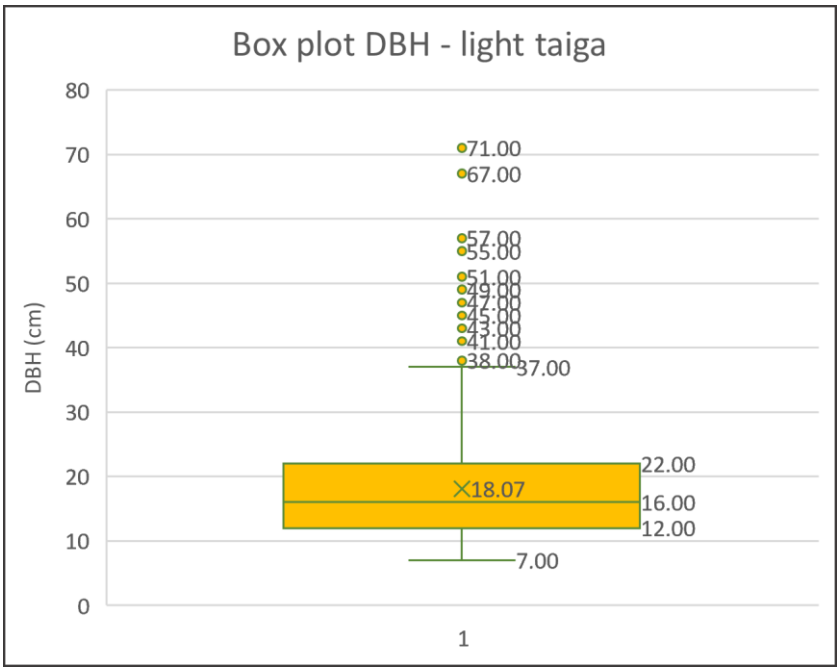

Figure 8.16: Box plot for DBH for light taiga all species.

The box plot for the tree height analysis reveals much more similarities between the taiga classes. The medians and the inter-quartiles very much look alike, as do the inter-quartile ranges. The value for the mean height is slightly higher for the light taiga, though. Thus, in conclusion, there are disparities for DBH in favour of the dark taiga, but there are also striking similarities in tree height for both taiga classes.

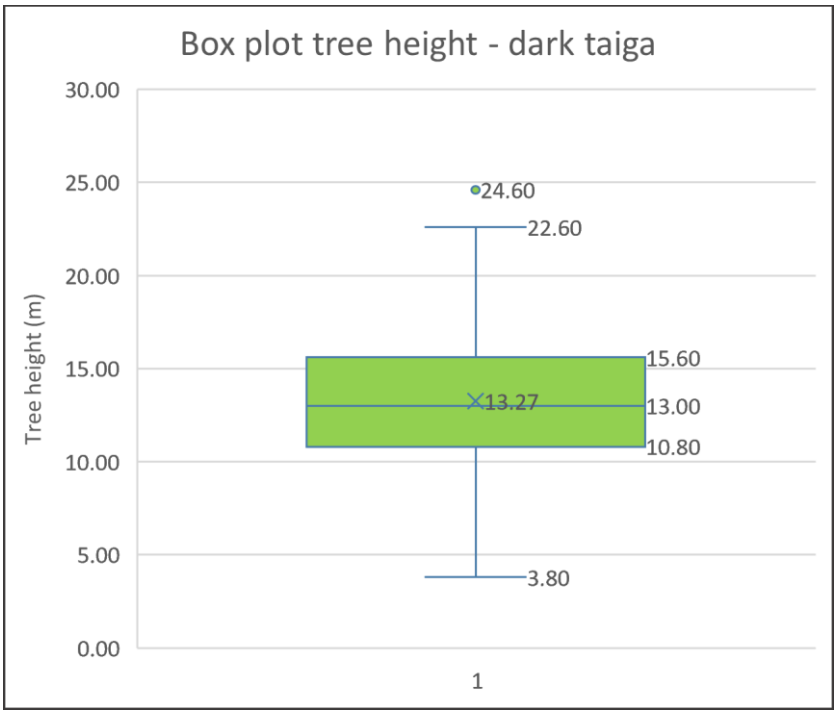

Figure 8.17: Box plot for tree height for dark taiga all species.

Figure 8.18: Box plot for tree height for light taiga all species.

The Wilcoxon rank sum test (U-test)

The descriptive statistics for the DBH in larch for light and dark taiga displayed some disparities. For instance, the calculated mean for the dark taiga DBH is 21.90cm, whereas the light taiga analysis yields a value of 24.47cm. Further above we also found the distribution for the DBH not complying with the normality standards (Q-Q plot). As a consequence, the Wilcoxon rank sum test had to be carried out for testing the following hypotheses: the null-hypothesis (H_o) was defined as there is NO difference between dark taiga and light taiga DBH. The alternative hypothesis (H_a), in contrast, considers the opposite.

The calculation of the U-test statistics is presented in the following table:

Table 8-11: Calculated values for the Wilcoxon rank sum test for testing difference between dark taiga and light taiga DBH in larch.

Wilcoxon signed-rank test		
R1	14417	dark taiga
R2	10336	light taiga
n1	136	dark taiga
n2	86	light taiga
U	6595	
Z	1.60228	
Critical value	**1.979**	

According to the literature for high sample numbers (i.e. *n* greater than 40) *Z alpha* equals *t alpha*, because with high sample numbers a normal distribution is approximated (Zar, 2010: 150–151). Thus, the critical values of the t-distribution apply. This results in a critical value for alpha 0.05 (5%) two-tailed test at n = 136 of **1.979**. Since the calculated Z value of 1.60228 is smaller than the t-table value of 1.979 the Null-hypothesis has to be accepted, i.e., there is no significant difference between the light taiga DBH and the dark taiga DBH in statistical terms.

Despite the fact, that there is no significant disparity between the dark and light taiga DBH, the assessment of the box plots above reveal, that there most certainly is a difference in DBH when considering all tree species. Thanks to the contribution of the Siberian pine to the outcomes of the DBH calculations a significant difference between the light and dark taiga is demonstrated.

8.2. DEM analysis

Topography and its related features (i.e., slope, aspect, elevation) is one of the prime factors controlling vegetation distribution patterns and species richness, but it also creates feedback effects on local climate. Mountain areas are expressly guilty for creating complex, very heterogenous relief characteristics, and as such very diverse microclimates and ecological niches (Begum *et al.*, 2010, Böhner and Antonić, 2009, Bonan and Shugart, 1989, Dobrowski *et al.*, 2009). Notwithstanding the fact that DEM analysis is not quite a focal point of this thesis, it can't be denied that the influence of slope, aspect, and elevation on the horizontal distribution of the forest areas is substantial. In addition, tree classification also entails a proper judgement and thus verification on the potential location of specific species. However, it is not intended to conduct an exhaustive investigation.

To the author's best of knowledge, the DEM employed is based on the extraction of elevation information from a Russian topographic map at a 1:100,000 scale. Quality checks revealed that the presented elevation model with an 8-metre resolution is almost perfectly true to the elevation data of the Russian map with a deviation of about 1 to 2 metres in elevation. The figure below illustrates the extent of the entire DEM for the Thunkel area.

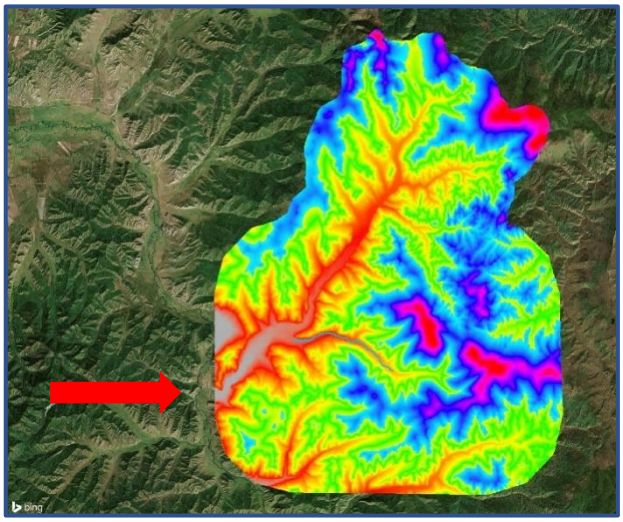

Figure 8.19: DEM for the Thunkel area featuring an 8m resolution. The village of Thunkel is indicated with a red arrow (tip). Source: GIZ, 2017.

The first analysis was carried out on the DEM to derive the aspect situation reflecting specified classes associated with common compass readings (see Figure 8.20). Compartment 435 is mainly oriented northwards with a few rockfaces sloping to the south. All forested areas follow the northerly bearing with some sparsely populated areas to be found southbound, but being restricted to the upper altitudes south of the of the compartment. All other areas facing south are not suited for tree cover with the exception of a few micro-relief pockets. This finding is very much in line with literature by authors such as Dulamsuren *et al.* (2005a), Dulamsuren and Hauck (2008), Dulamsuren (2004), Klinge *et al.* (2014) and Mühlenberg *et al.* (2012b). Although northern slopes receive less solar radiation this deficit is remedied with a higher moisture content and a much higher amount of permafrost areas as a potential water reservoir (Bonan and Shugart, 1989, Dashtseren *et al.*, 2014, Juřička *et al.*, 2020).

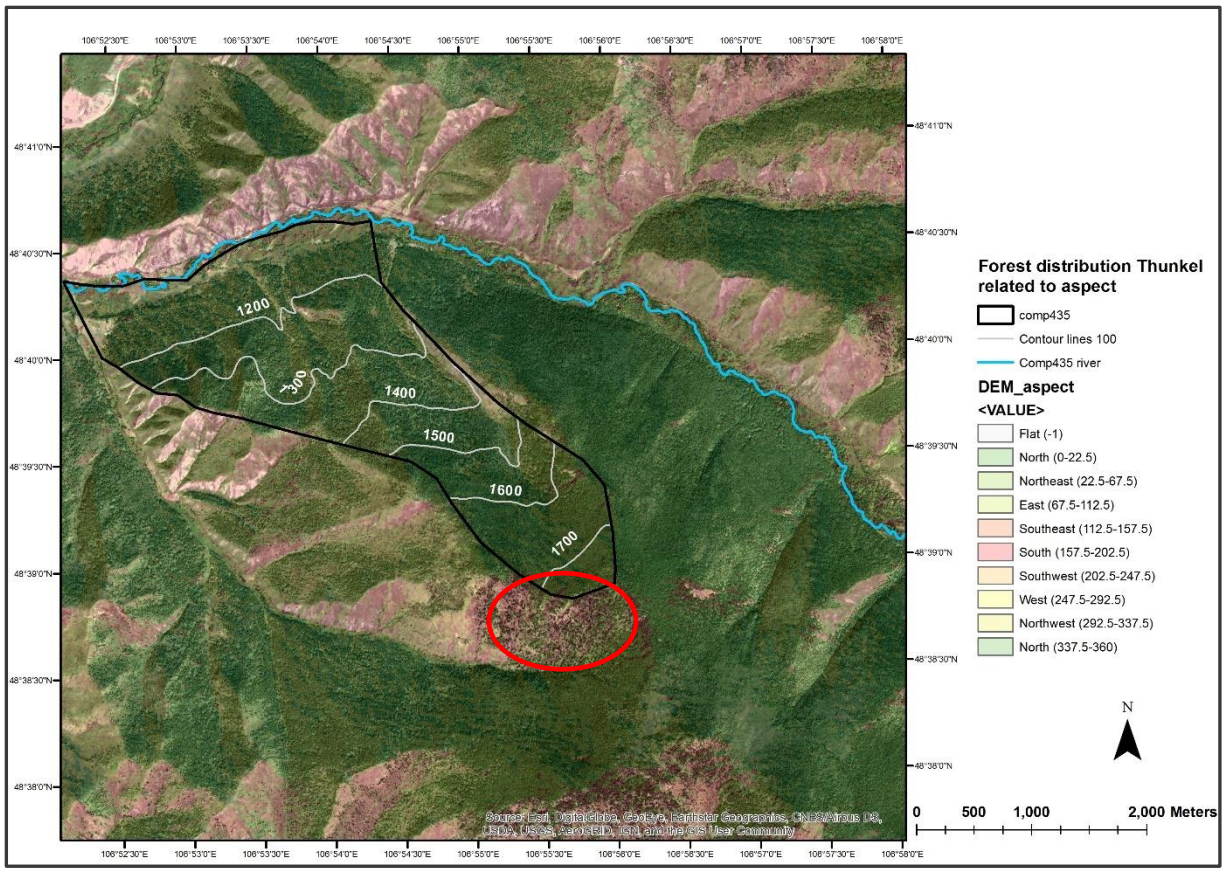

Figure 8.20: Forest distribution related to aspect. Most of the forested area is located on northern slopes; sparse forests are also to be found on slopes facing south (see ellipse in red), but only at higher altitudes.

Not only aspect appears a major driver for vegetation cover, but also elevation can be a limiting factor. In the graph below the DEM is plotted with the location of the dark taiga forest superimposed. The dark taiga is considered to be quite a rare commodity requiring protection with an overall proportion of about 7.4% of all forest stands in Mongolia (Altrell and Erdenejav, 2016). Apart from that this taiga variety is home to a great diversity of flora and fauna alike (Mühlenberg, 2012). The derived NDVI from the WV-2 winter image was used to identify the non-deciduous forested areas of the dark taiga - luckily, the snow cover was negligible and the dark taiga spectral signature was quite conspicuous. According to the map in Figure 8.21 the dark taiga seems to be primarily limited to the altitudes beyond the 1550 m contour line – this not only holds to be true for the compartment 435 confines, but also concerns other forest areas. Since the dark taiga areas do not appear as dense clusters, it can be fairly assumed that light taiga species (primarily larch) are intermingled with the dark taiga conifers at least to an elevation of up to 1700 metres. This conclusion is strongly supported by my own observations when conducting the fieldwork and by Wecking (2017: 53), who also assessed species distribution on site. However, this is in contrast to studies conducted by Dulamsuren *et al.* (2005c), who found the light taiga to be restricted to mid and low altitudes.

Most interestingly, the conifer forest of the dark taiga also populates certain parts of the riparian

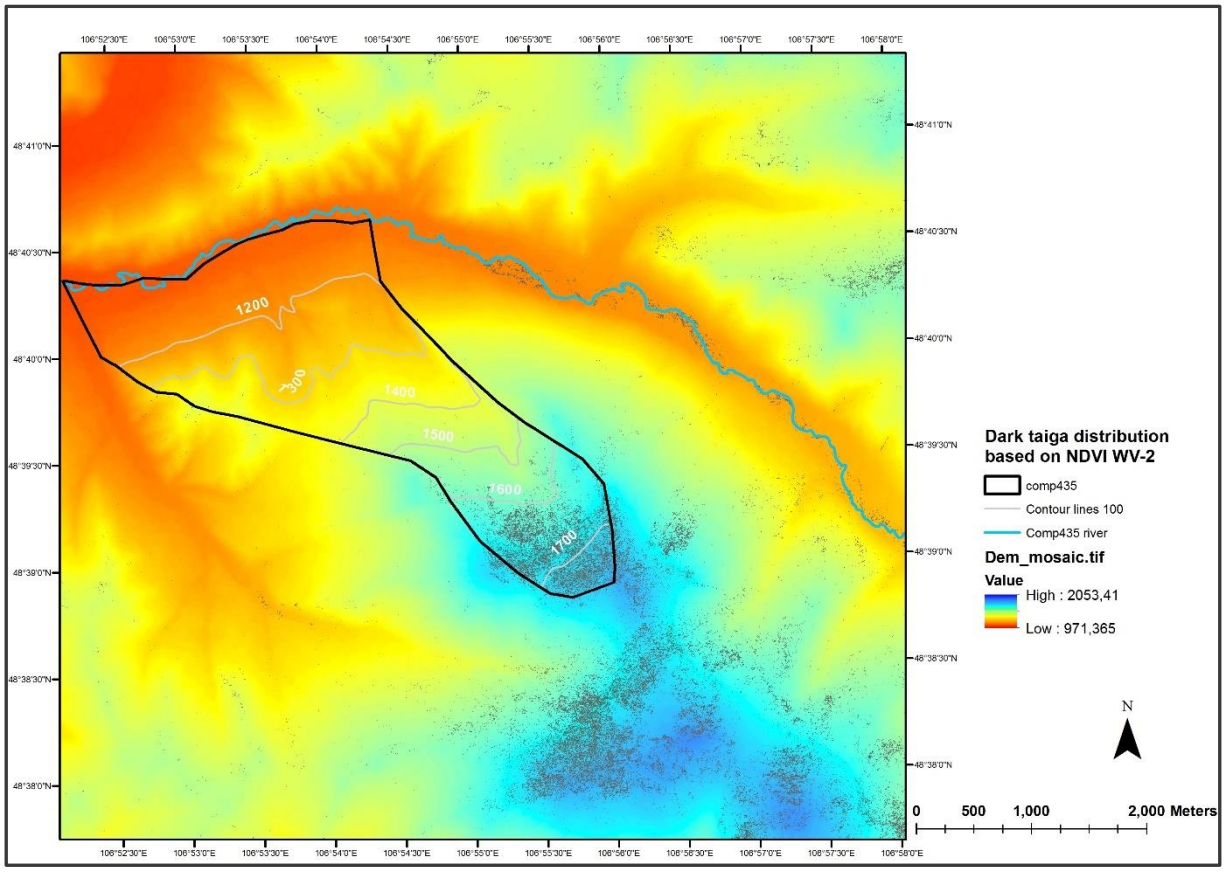

Figure 8.21: Distribution of dark taiga (point clouds in grey) in the Thunkel area. Dark taiga mainly populates elevations above 1550m, but is also found in riparian areas. The dark taiga delineation is based on the NDVI values derived from the WolrdView-2 winter image.

area. This phenomenon might be attributed to misclassifications at the first glance, but other authors also confirm the occurrence of dark taiga species at lower elevations (Altrell, 2017, Küstner, 2017, Schmidt-Corsitto, 2017, Zueghart, 2017: 71). This knowledge is mostly based on on-site inspections and is limited to locations stocked with Siberian spruce. Hypothetically, this species is able to cope with low temperature to be found in depressions of the riparian areas, and it can also be attributed to the high water and nutrient requirements of this dark taiga representative (see also Dulamsuren *et al.*, 2005a) - however, this assumption requires more in-depth research.

In her investigation on the spatial distribution patterns of dark and light taiga Zueghart (2017: 68–69) calculated an elevation mean value of 1605.9 metres for the dark taiga occurrence and 1364.1 metres for the light taiga proving the restriction to the upper altitudinal belt of the dark taiga. These figures, however, have to be considered in the light of the resources used – the Tandem-X DEM data constitute a slightly coarser resolution (i.e., 10m x 10m) in comparison with the DEM provided by the GIZ. Furthermore, the analysis of the RapidEye scene acquired in September 2015 with a radiometric resolution of five spectral bands revealed an area populated by the dark taiga that is different (here: smaller, with dark taiga appearance also in

the lower altitudes) from the findings of my own research. The almost perfect WV-2 winter image I used for assessment has proven to be an 'incorruptible' candidate for the delineation of the dark taiga, since no other vegetation than the non-deciduous dark taiga species shows NDVI values in the range of 0.3 to 0.5. Since the proportion of the Scots pine trees, which also representative for the non-deciduous plant species, is extremely low in compartment 435, the area populated with dark taiga can be delineated very precisely. Having said this, I ran into similar challenges concerning potential misclassifications when employing imagery other than the ones acquired in winter.

My terrain analysis also comprised the assessment of the dark taiga area in relation to the slope aspect. As outlined in previous chapters, the spatial distribution for forests in the Khentii mountain range is severely aspect-dependent with the dark taiga being restricted to the upper mountain slopes facing north (Dulamsuren, 2004, Dulamsuren *et al.*, 2005a, Dulamsuren and Hauck, 2008, Mühlenberg, 2012). The map below demonstrates very clearly, that the dark taiga seems to be limited to the northern slopes – light taiga also populates other areas (see figure above).

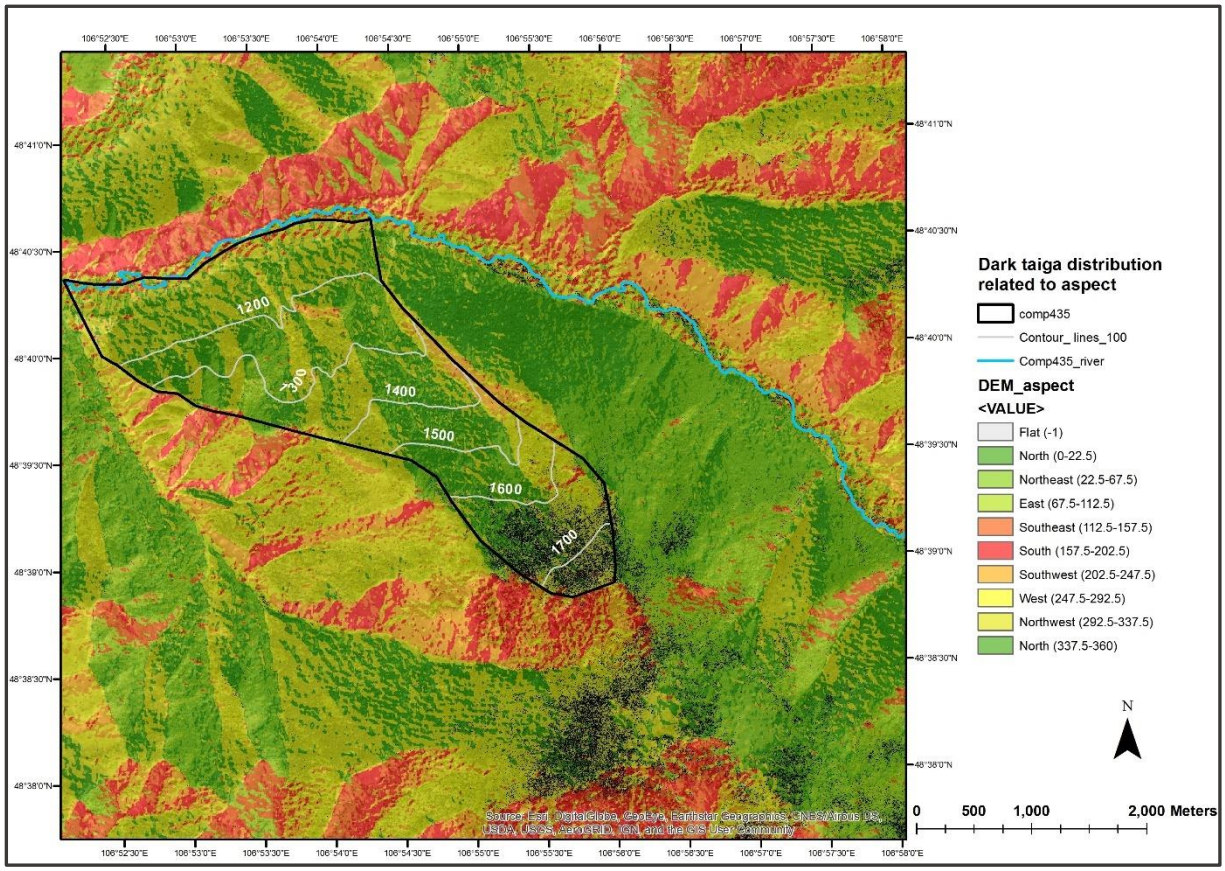

Figure 8.22: Location of dark taiga related to aspect. Dark taiga is mainly located on slopes facing north and northeast. Dark taiga locations are derived from NDVI values of the WV-2 winter image and indicated as a black point cloud.

This conclusion is very much in line with the results obtained by the authors mentioned above. In addition, Zueghart (2017: 70–71) also confirms that dark taiga mainly populates the north

and northwest aspects, whereas the light taiga habitat range is less restricted by also showing occurrences in areas bearing to the northeast and west. However, sparsely vegetated, open forests are conspicuous also in southern slopes, but at high altitudes, where water availability is not as limited as in the lower mountain range.

Slope gradient is another important determinant of the habitat range of vegetation, since it controls the amount of solar radiation received and the amount of water distributed. This effect has an increasing impact with a gain in slope gradient with the potential to amplify extremes when considering the various slope aspects. The situation reaches a level of much higher complexity when also taking the sun angle into account. Most of the forested areas are to be found within a range of 10 – 20^{o} slope gradient as being confirmed in the NFI report by Altrell and Erdenejav (2016: 96), and by Zueghart (2017: 76) . This is illustrated by the graph below, but it also exhibits the complex structure of the terrain of compartment 435 with pockets of very steep slope. In the north-western part of the compartment forested areas showing light taiga with a gradient exceeding 40^{o} are conspicuous.

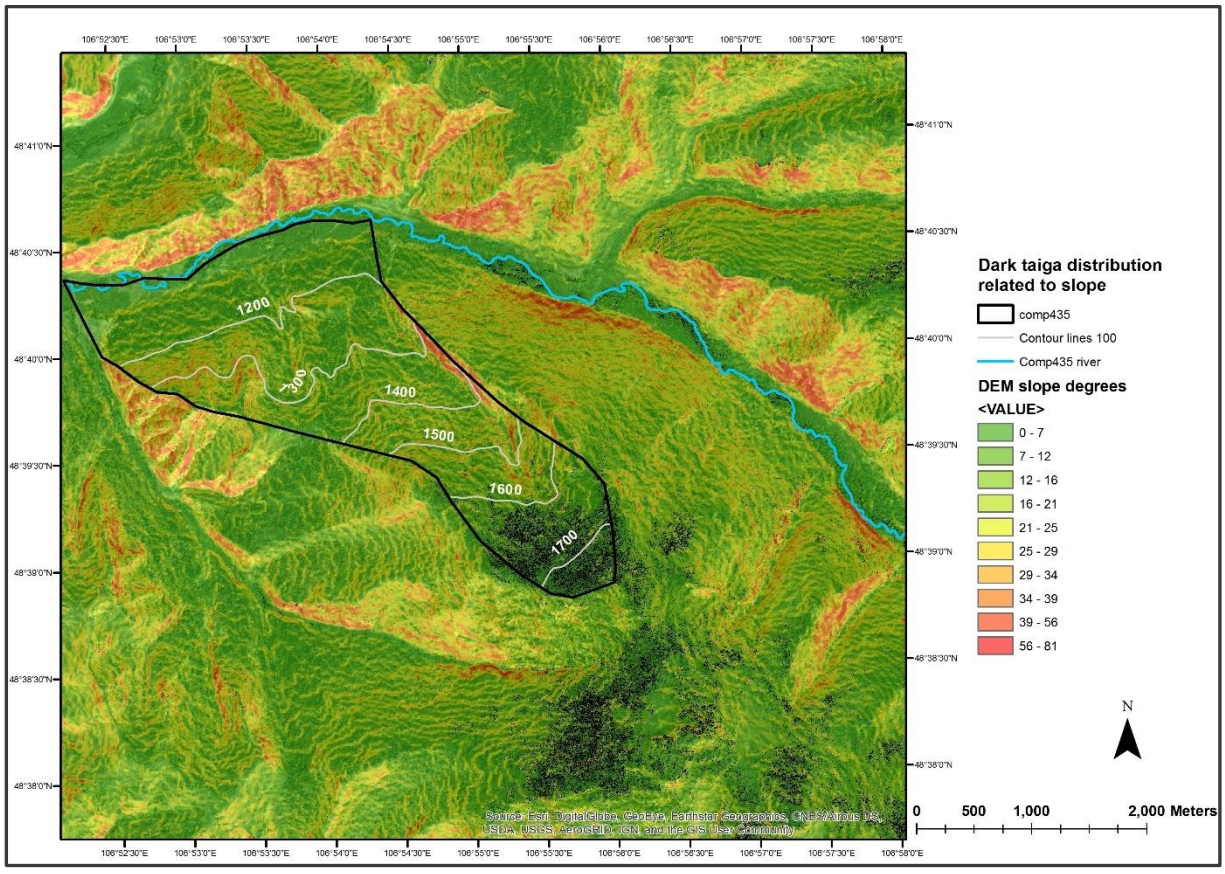

Figure 8.23: Dark taiga distribution related to slope inclination. These forests are located on slopes not exceeding 16^{o} . Dark taiga locations are derived from NDVI values of the WV-2 winter image and indicated as a black point cloud.

This is in contrast with the results reported in the literature, claiming that forests only occupy areas with a less pronounced slope gradient (Altrell and Erdenejav, 2016, Zueghart, 2017: 75–76). In her study Zueghart (2017: 76) observed a specific area populated by dark taiga on fairly steep slopes. A cross-check with my own findings, however, revealed that this phenomenon can be attributed to an area spuriously classified as dark taiga. This circumstance relentlessly discloses the predicaments, pitfalls, and the associated caveats when dealing with a limited data set – limited also in the sense of DEMs being too coarse not reflecting the complex nature of the terrain, and satellite imagery featuring limited radiometric and temporal resolution. Once again, it is old news that the quality of the input data determines the accuracy of the outcomes and not necessarily the method chosen. The results of the tree species classifications conducted by the author himself also unveil, that even with decent datasets utilised there is no warranty of achieving the best possible accuracy with reasonable effort (see also chapter 8.8.2.).

8.3. Extraction of tree height

Justifiably, tree height is considered to be a paramount forest inventory parameter per se, since it reflects the productivity of a specific site and species, and allows for inferences on forest biomass and carbon stock (Gadow, 2003: 31–33, Panagiotidis *et al.*, 2017, van Laar and Akça, 2007: 1–3). In the last few decades, advanced technologies such as LIDAR and radar, as well as progress in photogrammetric solutions have sparked an enormous interest in the scientific community. In the subsequent chapter the extraction of tree height regarding single trees and tree communities is being presented portraying a technique, that has become increasingly popular these days. The extraction procedure has been detailed already to be found in chapters 7.3.4.2 and 7.3.4.3.

Single tree heights

The derivation of the height of individual trees provides a good indication on the performance of the flying and calculation strategies employed and can be used for the fine tuning in conjunction with the generation of canopy height models for larger forest areas. The graph below demonstrates, that phenomenally good results are achievable for coniferous a well as for broad-leafed trees. The tree species selection comprises Siberian larch, poplar and willow, as well as Siberian birch.

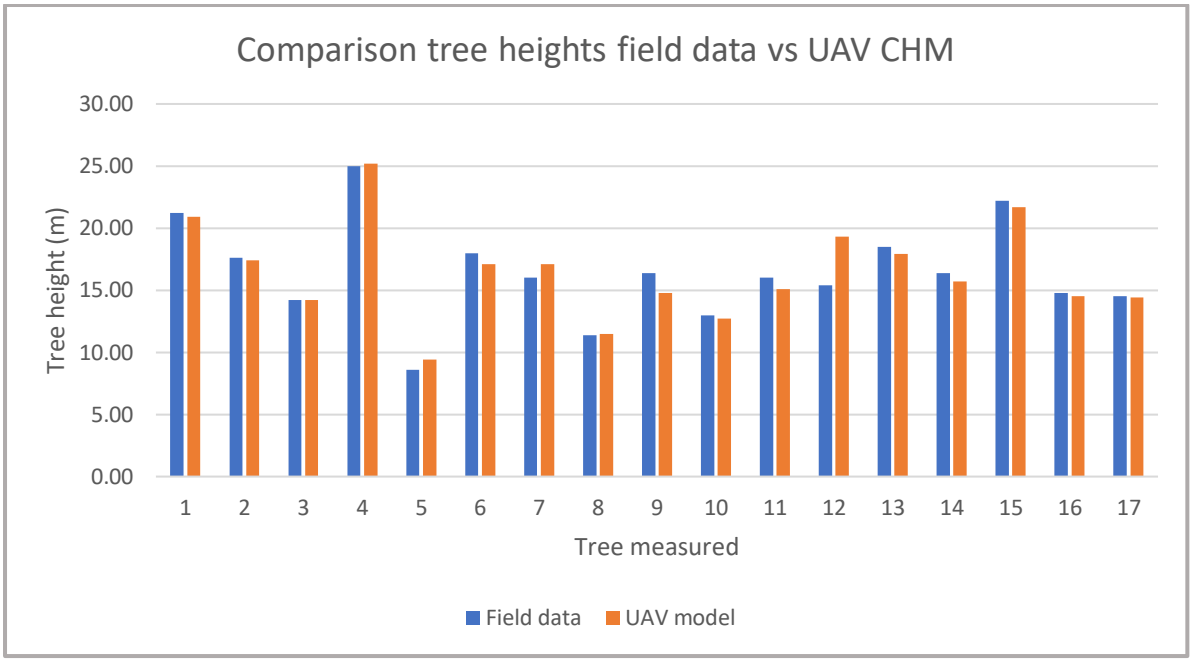

Figure 8.24: Comparison between tree height field data vs tree height derived from the Canopy Height Model of flying missions 1 and 14.

The bar chart above reveals, that the tree heights measured in the CHM are very close to the ones acquired in the field. The results also indicate a slight under-estimate of the CHM derived values. One outlier, however, needs to be noted – the grave CHM over-estimate of the height of tree no.12 defies any logical explanation, except for the fact, that the tree crown created in the 3D model shows some blurring. This indicates an inaccurate representation of the larch itself with an unclear source of error. When looking at the descriptive statistics the mean values for both strategies are almost identical. The same is true for the calculated standard error and the standard deviation.

Table 8-12: Descriptive statistics for the comparison tree height field data vs UAV CHM.

Tree height field data		*Tree height UAV CHM*	
RMSE	**1.156**		
Mean	16.42352941	Mean	16.405882
Standard Error	0.956346041	Standard Error	0.943845
Median	16	Median	15.7
Mode	16	Mode	17.1
Standard Deviation	3.943115743	Standard Deviation	3.8915727
Sample Variance	15.54816176	Sample Variance	15.144338
Range	16.4	Range	15.8
Minimum	8.6	Minimum	9.4
Maximum	25	Maximum	25.2

The following graph provides an even more detailed insight in the relationship between the field data and the CHM tree heights.

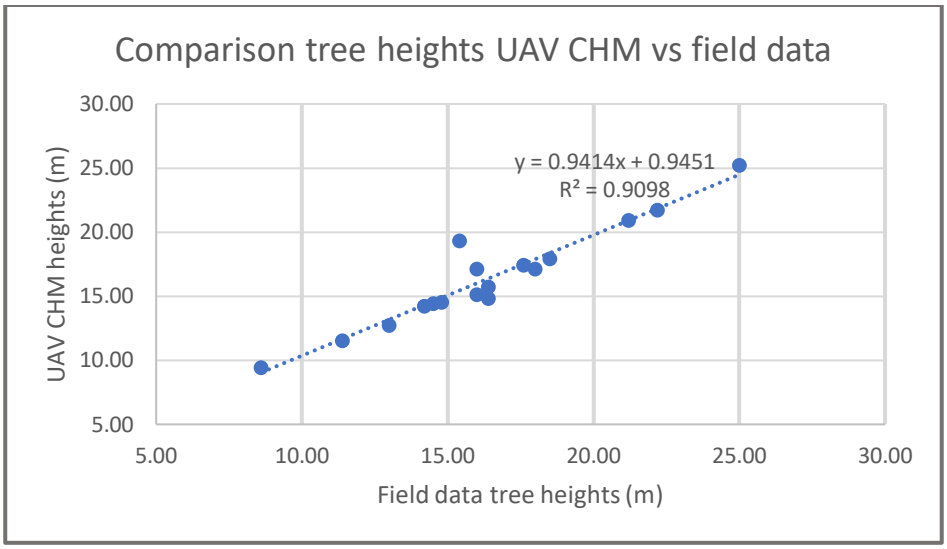

Figure 8.25: Relationship between tree heights field data vs UAV CHM heights.

With an R^2 of better than 0.9 and a calculated RMSE of 1.156m the presented manual extraction of tree heights from single trees proves very clearly, that this approach can yield extremely useful results.

Considering **tree-level** studies, RGB sensor derived *height* metrics reveal the full potential of this technology. Strong correlations are reported by Ni *et al.* (2015), Guerra-Hernández *et al.* (2016), Guerra-Hernández *et al.* (2017), Hao *et al.* (2021) and Lin *et al.* (2018). R^2 values range from 0.81 to 0.95. Other authors used UAV-LiDAR to also obtain a strong correlation (Jaakkola *et al.*, 2017, Yin and Le Wang, 2019). Sankey *et al.* (2017) achieved an R^2 of 0.90 when using LiDAR, multi-, and hyperspectral sensors. In their investigation, Wallace *et al.* (2016) found that LiDAR performed much better (R^2 = 0.84) than SfM derived height information (R^2 = 0.68). According to them, the poorer performance can be blamed on the fact, that mid- and understorey parts of the forest are not well represented. In contrast, when looking at Eucalyptus plantations in Portugal, Guerra-Hernández *et al.* (2018) conclude, that UAV generated point clouds are as good as ALS derived point clouds for estimating individual tree height. The authors achieved even good results in high-density eucalypt forests. However, they point out, that landscapes featuring a canopy cover exceeding 60% and with slopes steeper than 20% must be considered with caution. Their findings is very much in line with the outcomes of a study conducted by Dandois and Ellis (2013). The achieved performance of the UAV derived CHM was similar to the LiDAR 3D point cloud height estimates. When assessing UAV imagery-derived stand parameters for pine tree plantations in Turkey Gülci (2019) found out that tree density, crown shape, and branching structure considerably effected the achieved accuracies. Kameyama and Sugiura (2021) deployed a DJI Phantom3 UAV to assess imagery of 20 different flight conditions to be processed in three different digital photogrammetry

software packages. They conclude, that a low flying altitude is conducive to an overall accurate creation of the 3D tree models, and that image artefacts, wind speed and light conditions are to be meticulously considered. According to their analysis of the pertaining point clouds, the tree height showed an overall RMSE of 5-6m, with the Pix4D software performing best, followed by Agisoft's Metashape. As such, the selection of an appropriate photogrammetry software seems imperative.

Stand tree heights

The extraction of height estimates for tree clusters or stands as by far more complex than getting the height readings for individual trees in a 3D model. Some more steps are required in the derivation procedure, such as valley-following, region growing, and watershed segmentation (Gougeon and Leckie, 2003, Park *et al.*, 2014). With each additional component integrated in the process some further error sources ad potential biases are introduced.

The following table encapsulates the relevant statistics for the height estimations conducted in the various flying missions. In total two missions were considered suitable for the comparison between field data and heights derived from the CHM. The results for mission 3 were attained with consideration of a larger area and a subset created to represent just the size of the test plot no.60.

Table 8-13: Descriptive height statistics for the various flying missions and the field data.

Parameters	**Mission 1**	**Mission 2 Plot 1**	**Mission 3 Plot 60/64**	**Mission 3 subset plot 60**	**Field data Plot 1**	**Field data Plot 60**
Maximum	23.50	22.38	29.20	22.63	18.20	22.00
Minimum	3.00	3.00	3.00	3.00	NA	NA
Mean	18.55	**15.09**	13.99	6.61	**14.52**	15.47
Median	21.77	18.93	17.28	6.00	15.60	15.80
Standard deviation	5.84	5.72	5.22	3.03	3.10	
3rd Quartile	22.04	19.39	**17.71**	7.77	16.75	**17.60**

The results of above table indicate the following:

- The flown subset of mission 3 (equivalent to plot size no.60) shows, that the extraction of heights from the Canopy Height Model (CHM) of such a small area is not sufficient to reflect the average tree height of this specific area – i.e., the area to be flown needs to be much bigger than 30m x 30m. Tree density in plot no.60 is relatively high; the plot is stocked with birch for a 100%. Most of the birches were at least partially defoliated, which pose a potential problem to the 3D modelling algorithms in Agisoft Metashape.

- The figures for mission 3 (equivalent to plot no. 60 and 64) prove, that the flown area (about 150m x 150m) is big enough to get useful stand height results, especially for the 3rd quartile height (i.e., 17.71m vs 17.60m). The maximum height for mission 3 seems too far off (29.20m vs 22.00m).
- The extracted tree heights from mission 2 (representing plot no.1) also overestimate the maximum height (i.e., 22.38m vs 18.20m). The derived height values for the mean are fairly similar (15.09m vs 14.52m).
- With a sample size this small (i.e., 2 missions for individual tree height estimation, and 2 missions for the extraction of stand tree heights), however, there seems to be no golden rule on what height parameter always is the best option (mean height vs 3rd quartile height).

With respect to the studies on *stand-level* height parameters the results in most of the investigations were coherent by featuring strong correlations. In addition, there is broad agreement, that outcomes depend on the sensor payload, and the forest characteristics and species configuration (Cao *et al.*, 2019, Guo *et al.*, 2017, Ota *et al.*, 2017, Puliti *et al.*, 2015, Xu *et al.*, 2020). However, in most cases UAV-LiDAR seem to obtain better results than those acquired by UAV RGB sensors (McRoberts *et al.*, 2010, Mielcarek *et al.*, 2020, Noordermeer *et al.*, 2019, Tomppo *et al.*, 2008). This sounds explicable, since RGB point clouds are limited to the upper part of the canopy, as opposed to LiDAR technology. Nevertheless, RGB derived CHM exhibit a higher point density than the laser point clouds and thus are more tuned for the extraction of higher detail. Wallace *et al.* (2016) account the comparison between LiDAR and UAV RGB height metrics in a sclerophyll eucalypt forest. Since SfM photogrammetric technique is not able to properly model the terrain for CHM derivation, LiDAR showed a much better performance (RMSE of 0.92m for LiDAR and 1.30m for SfM).

These days a plethora of reviewed papers on tree height derivation form CHMs has been made available. There is quite a considerable number of authors having identified error sources and potential biases impeding the accuracy outcomes. The most common ones are listed as (non-specific order):

- Overlap of imagery
- Flying altitude
- Photo quality
- Camera specifications and settings
- Height extraction method
- Software used and parameter settings
- Application and accuracy of ground control points (GCP)
- Accuracy of reference data

- Distribution of the GCPs
- Ground Sampling distance (GSD)
- Tree morphology
- Forest structure
- Canopy density
- Seasonal effects
- Illumination conditions
- Tree species

The sheer number of imponderables, variables, and possible pitfalls is quite impressive and conveys the realistic image, that the entire workflow starting with flight planning, the execution of the mission, and the subsequent data analysis is far from being trivial. In the following the most talked about effects are briefly discussed and related to the flying missions conducted in this study.

The definition and setting of an appropriate image overlap prior to deploying the UAV seems to be a crucial factor determining the accuracy of the resulting 3D model. In most cases this setting is done by many pilots quite intuitively, but intimate knowledge on the correct forward and sideward overlap is conducive to the planning process. In an exhaustive study, I was involved in, it was found, that forward image overlaps >95% yield the best results (Seifert *et al.*, 2019). This was also confirmed by other authors, like Torres-Sánchez *et al.* (2018), Frey *et al.* (2018), Bayer (2018: 96–97), Ganz *et al.* (2019), Tuominen *et al.* (2015), Tuominen *et al.* (2017a) and Dandois *et al.* (2015), favouring very high forward overlaps. An sideward overlap of 60% was considered to be sufficient for most applications (Bayer, 2018: 99, Seifert *et al.*, 2019). The overlap settings for my flying missions were 95% for forward and 60% (65%) for sideward overlap, respectively.

For a number of years, there has been a number of controversial discussions concerning the optimal flying altitude, since this determines the ground resolution (GSD) and as such the achievable detail in the 3D model. The GSD of course is also dependent form other factors such as sensor size, image resolution, and focal length of the camera. Flying altitudes reported in the literature varied from about 40m above ground to around 150m. It is a golden rule, that the lower the flying altitude, the lower the area cover, and thus, the higher the flying time. Seifert *et al.* (2019) and Chen *et al.* (2017a) show, that drone flights at low altitudes dramatically increase the number of tie points and as such yield more reconstruction detail. Tuominen *et al.* (2015), Tuominen *et al.* (2017a) and Ganz *et al.* (2019) achieved reasonable results with a flying altitude between 85m and 150m above ground, but the authors propose a higher GSD (i.e., lower altitude) for better accuracies. In line of this, St-Onge *et al.* (2008) also talks about the lack of detail in high altitude imagery as a possible error source for the detection of tree apices, and Gobakken *et al.* (2015) support high-resolution imagery as well. In contrast, Pádua *et al.* (2019) and Pádua *et al.* (2018) conducted flying missions between 30m and 120m

above ground to find, that the best results for tree height and crown diameter extraction were achieved with the UAV flying maximum altitude. An off-the-shelf UAV (i.e., DJI Phantom IV) equipped with a 12.4 MP resolution camera was employed to mainly map chestnut trees in a rural area in Portugal. To be on the safe side, I chose a flying altitude of around 70 metres above ground for my flying missions. In my opinion this was a good compromise between area coverage and achievable reconstruction detail.

The focal length of the on-board camera also raises a few concerns. Most UAVs on the market are fitted with wide-angle cameras with short focal lengths, since they are actually designed for non-professional consumers and not for scientific purposes with specific requirements for photogrammetric analyses. However, apparently reasonably good results can be obtained with those platforms in various applications. Some authors have observed longer focal lengths working better for their specific purposes (e.g. Ganz *et al.*, 2019, Bayer, 2018: 106–108). In addition, the longer focal length also seems to contribute to better results in the image matching process (Bayer, 2018: 107–110). With respect to my study the accuracies of the created 3D models were considerably good, although having deployed a consumer UAV including a wide-angle camera. On visual inspection of the imagery, however, the resulting radial distortion of the photographs can impede a proper delineation of tree crowns, if no orthophoto is available.

Image quality also has an effect on the accuracy of the 3D point cloud. A decent sensor size and an image resolution of the camera of better than 12 MP have become standard these days for yielding acceptable model results. Most importantly, the variable settings of a camera seem to be of greater importance, than sensor size. Especially when conducting flying missions during difficult illumination conditions, the settings of a camera (i.e., aperture, white balance, shutter speed) need to be adjusted accordingly. Problems with image quality have been reported or improvements suggested for instance by Ganz *et al.* (2019), Jensen and Mathews (2016), Scher *et al.* (2019), and Tuominen *et al.* (2015). With respect to image quality the daytime and seasonal effects also require the pilot's attention. In order to avoid long shadows, flying missions should be carried out around noon (Krause *et al.*, 2019, Nevalainen *et al.*, 2017, Tuominen *et al.*, 2017a). In addition, a high image contrast contributes to the image matching process. This observation is also shared by me, with images taken during an overcast period around noon resulting in low contrast images and subsequently in a biased 3D model. Interestingly, Scher *et al.* (2019) report better image matching results with images acquired on an overcast day, as opposed to high contrast photographs taken in sunny conditions.

The positional accuracy, the number and distribution of ground control points (GCPs) is closely related to the accuracy of the 3D point clouds and as such to the tree heights extracted. This has been reported by authors like Birdal *et al.* (2017), Chen *et al.* (2017a), Dempewolf *et al.* (2017), Harwin and Lucieer (2012) Krause *et al.* (2019), Panagiotidis *et al.* (2017), and

Tuominen *et al.* (2017a), who managed to improve the model accuracy by using high precision GPS (e.g. RTK). Ganz *et al.* (2019) made an interesting observation, when including GCPs into the photogrammetry workflow. According to them the resulting accuracy of the 3D model was only slightly better, than without considering GCPs at all. I can fully subscribe to this conclusion, since the incorporation of GCPs did not make any difference, and even diluted the accuracy of the point cloud in a few cases – as such my models were calculated without these control points. However, it needs to be noted, that the positional accuracy of the GCPs was considerably poor in my case. In the countryside in Mongolia, it is virtually impossible to employ differential GPS or RTK[22] GPS with the lack of the required infrastructure – even upmarket GPS receivers feature positional discrepancies of about 3 to 5 metres, which is detrimental to the photogrammetry process.

Many researchers describe the performance of the photogrammetry software used as being not optimal, when imagery displaying dense forests, or big broad-leafed trees need to be modelled – this applies to all photogrammetry software available on the market. Apparently, conifer trees with a clearly detectable apice and a conical shape of the crown are much easier to be handled by the software algorithms (Bayer, 2018, Moe *et al.*, 2020, Röder *et al.*, 2018, St-Onge *et al.*, 2008, Tuominen *et al.*, 2017a, Vastaranta *et al.*, 2013). I can most certainly share this observation with confidence, since some of the tree clusters were not modelled properly and partly defoliated birches exhibit some artefacts. The difficulties in matching such imagery was even confirmed by Agisoft programmers (Semyonov, 2011). When considering various forest types, Puliti *et al.* (2015) suggest that boreal forests are easier to assess due to less variation in tree species and height. Broadleaved forests, in comparison, typically are more complex and more dense. These findings are very much in line with discoveries made by Cao *et al.* (2019), who notice, that most coniferous trees have a more regularly shaped crown.

The majority of the investigations on tree height derivation from CHM reveal an underestimate of tree heights in relation to the reference data (Dempewolf *et al.*, 2017, Ganz *et al.*, 2019, Krause *et al.*, 2019, Moe *et al.*, 2020, Noordermeer *et al.*, 2019). The findings in my research support this observation. Nonetheless, inconsistencies are also reported by Panagiotidis *et al.* (2017), who observed under-, as well as overestimates for individual tree heights for the various flying missions. A legitimate argument voiced by a few authors, however, needs to be taken into account regarding the accuracies of the reference data (Järnstedt *et al.*, 2012). Stereńczak *et al.* (2019) found, that terrestrial tree heights showed an underestimate, when set against length measurements. In their investigation the authors felled 2388 sample trees from 299 stands in Poland, representing eight tree species. They also learned, that factors such as tree length, species, and terrain are among the most influential factors on correct

[22] **R**eal **T**ime **K**inematics

height estimation. A similar study was conducted by Sibona *et al.* (2017) by comparing field-based measurements and heights derived from an ALS point cloud. They postulate, that height estimates originating from ALS showed a better approximation to real heights, than compared to the field data. Despite the shortfalls of in situ measurements they conclude, that field data will remain a standard reference for comparison with tree heights obtained from other sources.

Although above statements and explanations are not exhaustive, as a general conclusion it is legitimate to notice, that useful tree and stand heights can be extracted from Canopy Height Models (CHMs), in particular when single tree heights are considered. In order to gain more insight in possible shortfalls of the approach it would certainly be sensible to investigate the performance with higher flying altitudes (i.e., coarser ground resolution) and denser forest stands.

Rest of page intentionally left blank

8.4. Extraction of NDVI, MSI, NDWI, LAI

NDVI and LAI are considered to be some of the most important biophysical variables for assessing vegetation cover, plant vigour, and vegetation density. With NDVI estimations in particular it is feasible to portray seasonal effects (phenology) and disturbances in the vegetation cover (e.g., fire, insect attacks). Other indices have proven to be valuable indicators regarding water stress in plants such as Moisture Stress Index (MSI) and the Normalised Difference Water Indices NDWI (McFeeters, 1996) and NBR (Gao, 1996). Various other applications have been illustrated in the respective chapters 3.1.4. and 4.3.3. for further reading.

The associated formulas for the most relevant indices are as follows (band indications (e.g., B8) refer to Sentinel-2 bands):

$$NDWI = \frac{Green-NIR}{Green+NIR} = \frac{B3-B8}{B3+B8} \qquad NBR = \frac{NIR-SWIR}{NIR+SWIR} = \frac{B8-B12}{B8+B12} \qquad NDVI = \frac{NIR-Red}{NIR+Red} = \frac{B8-B4}{B8+B4}$$

The calculation of the vegetation indices was focused on NDVI to achieve the following in this investigation:

1. Show differences in NDVI results for the various satellite platforms.
2. Compare outcomes for the calculations of NDVI and the variant NDRE (NDRE = (NIR – RE) / (NIR + RE), as well as for MSI (SWIR / NIR).
3. Get a clear definition and delineation of the dark taiga conifer areas.
4. Illustrate seasonal effects for the year of 2017 (timeline).
5. Assess the relationship between NDVI and LAI (see the pertaining LAI subsection).

All satellite imagery was subjected to atmospheric correction, resampling, and sub-setting prior to the calculation procedures. The results of the estimation of the individual indices are presented below.

<u>NDVI portrayed for various satellite sensors</u>

NDVI was calculated for the platforms of Landsat 8, Sentinel-2, and Pléiades with corresponding dates of acquisition. For comparison randomly chosen image pixels with their associated NDVI values were set against each other to be illustrated. The first graph depicts the relationship between NDVI found in Pléiades imagery vs Senitnel-2. The coefficient of determination (R^2) value of around 0.6 indicates that there exists a relatively high degree of variance unexplained by the regression model. This is most likely due to the disparities in the

definitions of the band wavelengths for the Red and Near-Infrared. The band width for Sentinel-2 is 649 – 695 nm vs 590 – 710 nm for the Pléiades Red band. For the NIR it is 779 – 885 nm (Sentinel-2) vs 740 – 940 nm (Pléiades), showing, that the band width selection for the Sentinel-2 is much more narrow.

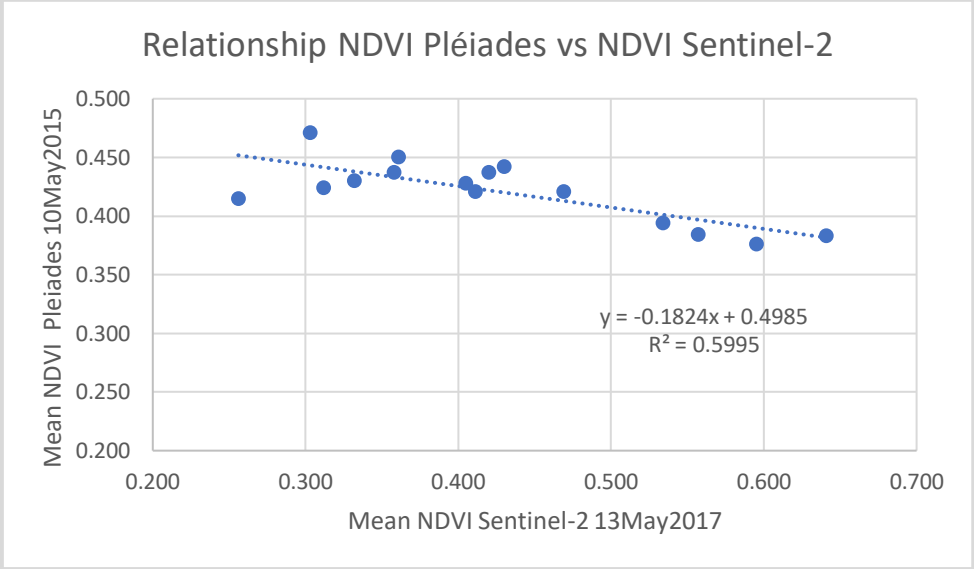

Figure 8.26: Comparison of mean NDVI values for Sentinel-2 and Pléiades sensors. The relatively low R^2 value indicates a relationship not being very strong.

In contrast, the calculated R^2 (i.e., 0.9368) for the relationship between the mean NDVI for Sentinel-2 and Landsat 8 demonstrates a very close affiliation. Although the spatial resolution is different (i.e., 10m vs 30m), the band wavelength width is fairly similar (i.e., S-2 Red 649 – 695 nm vs L8 640 – 670 nm; S-2 NIR 779 - 885 nm vs L8 850 – 880 nm).

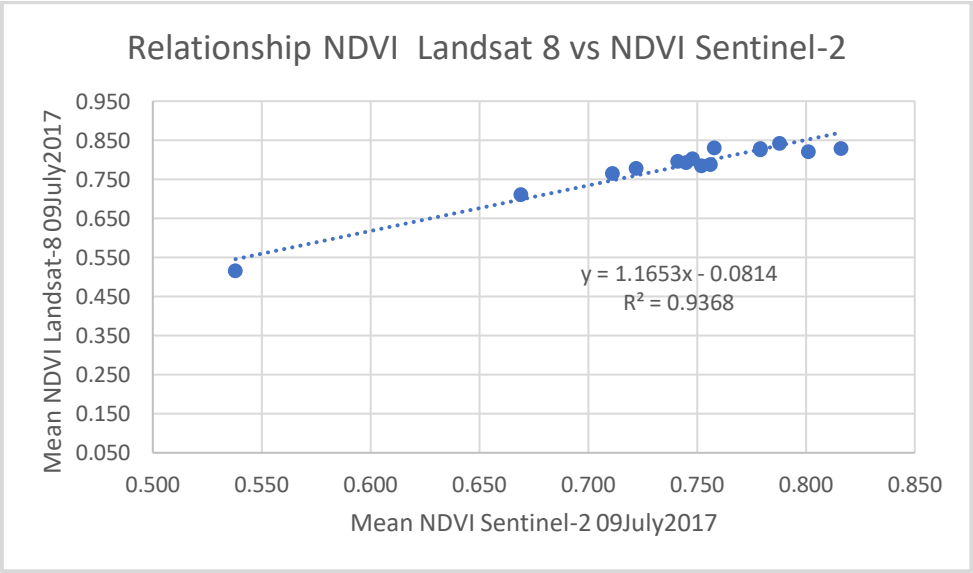

Figure 8.27: Comparison of mean NDVI values for Sentinel-2 and Landsat 8 sensors. The high R^2 value indicates a very strong relationship.

Since both sensors exhibit a very similar performance, the NDVI estimates can be performed on either of them interchangeably. This is also demonstrated in the graph below, where NDVI values derived from both sensors are set against each other.

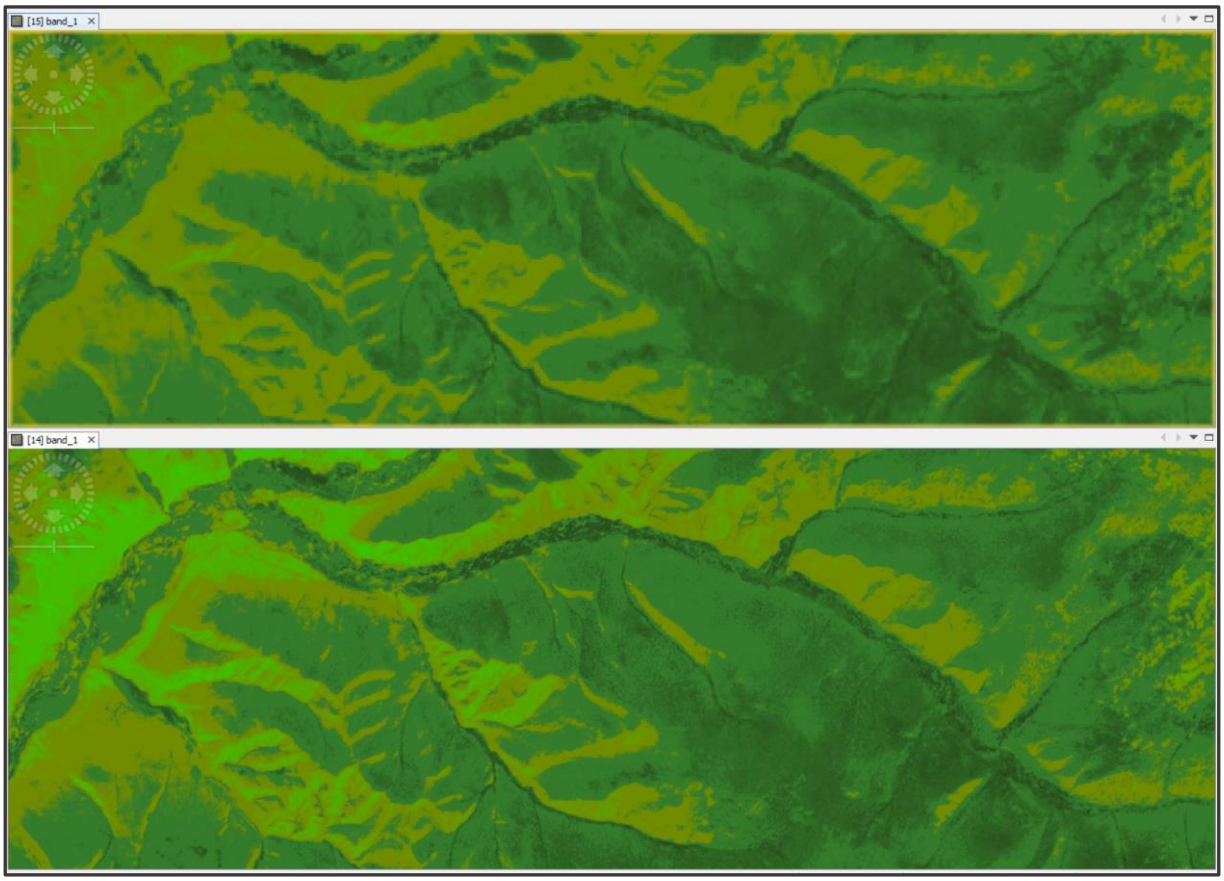

Figure 8.28: Comparison between NDVI derived from Landsat 8 image 09/07/2017 (above) and S-2 image 09/07/2017 (below). The S2-image shows higher spatial detail and higher variety in NDVI values.

The figure above, however, reveals subtle differences in that the Sentinel-2 data feature a higher spatial resolution, making the NDVI outcomes look more refined and detailed versus the Landsat 8 image. This finding is also confirmed by Korhonen *et al.* (2017), who used Landsat 8 and Sentinel-2 imagery for an investigation on forests in Finland. They found the performance of the Sentinel-2 MSI sensor superior to the Landsat 8 OLI due to its higher spatial resolution.

In the following graph the change in NDVI values in Sentinel-2imagery featuring different seasons (i.e., spring vs summer) is illustrated. The difference in NDVI between the seasons is remarkably high for most of the vegetated areas, whereas the dark taiga confines exhibit very little variation during the specified period. This provides a first indication on the seasonal trends in NDVI – more detailed analyses are demonstrated further below. A possible explanation is contributed by some further analysis shown below. The determination of NDVI, MSI, and NDWI indicate that the dark taiga components display the highest water content of the vegetation. The dark taiga species demand a decent water supply, which is found in higher elevations with

higher rates of precipitation. In addition, the evapotranspiration is lower in these areas compared to the lower mountain range forests.

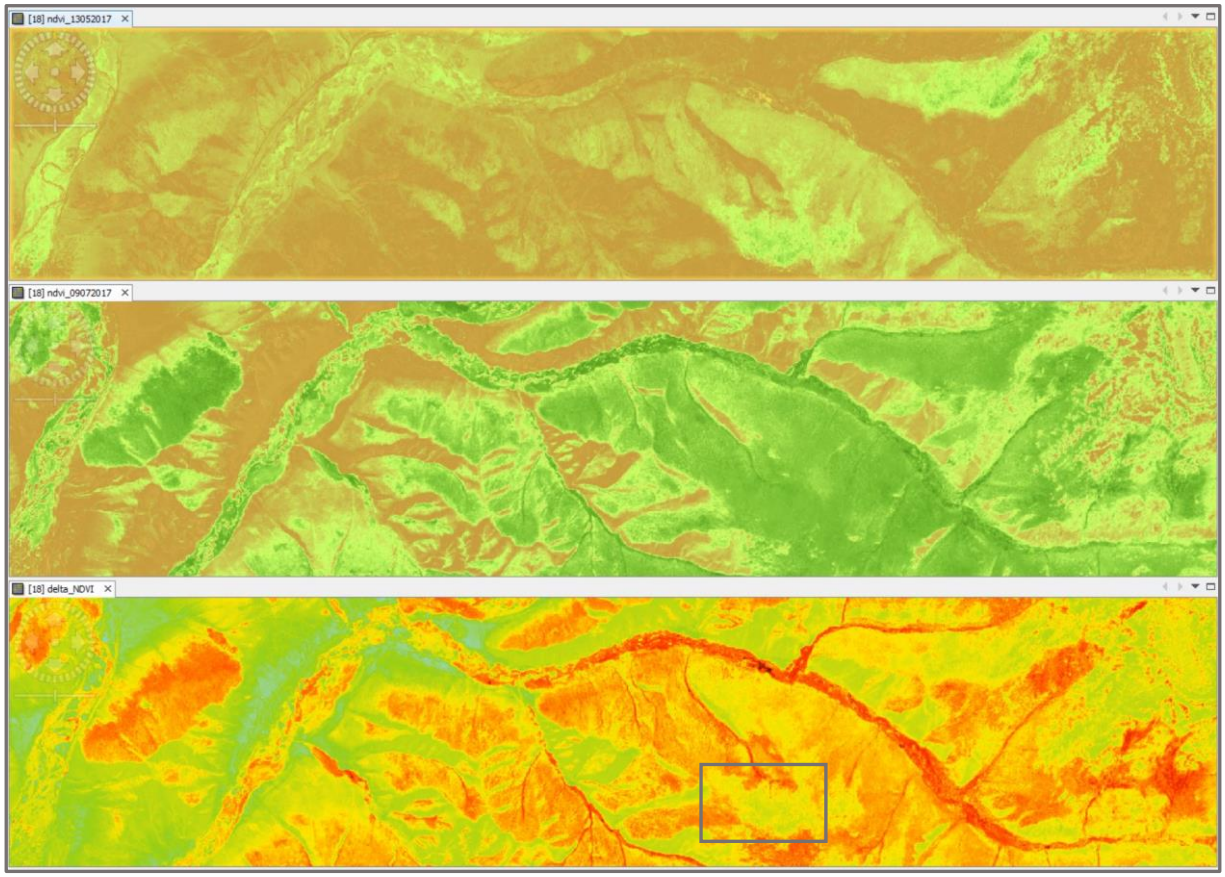

Figure 8.29:NDVI difference between S-2 13/05/2017 and S-2 09/07/2017 image. Dark taiga (black box) indicates very little change between spring and summer.

However, other vegetated areas as well reveal reasonable water content stored in their cell structure. This concerns the grass and shrub carpets, as well as the trees in the riparian area, and the light taiga zones in the northwest of compartment 435. The water supply varies with

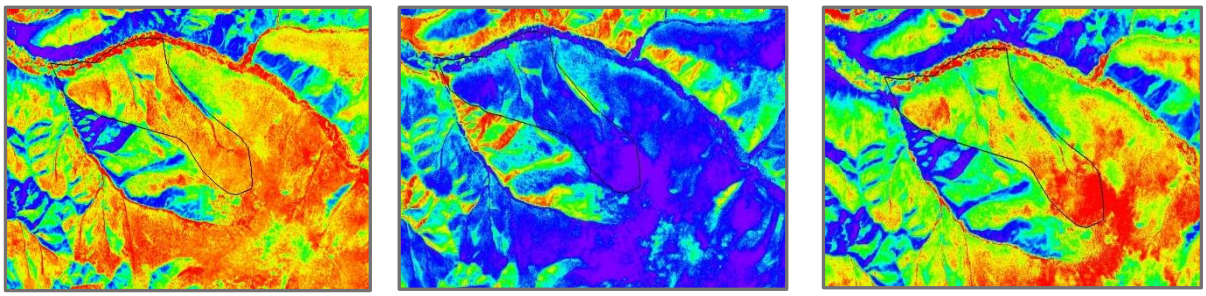

Figure 8.30.: Comparison of different vegetation indices in theS-2 09/07/2017 scene. From left: NDVI, MSI, NDWI. The dark taiga (bottom of image), the riparian area, and the light taiga area top left in compartment 435 show good water content in vegetation in MSI (crimson) and NDWI (red) image.

the water level in the riverbed, thus governing the stress level in the vegetation, whereas the phenomenon in the lower part of compartment 435 seems much more complicated. Unfortunately, there is very little information available on this specific area, other than it is

largely populated by Siberian larch (age between 60 and 149). The field data and the analysis of the DEM, however, provide an indication beyond speculation, that this area of compartment 435 is particularly afflicted with topographic irregularities. The elevation model shows slope inclinations exceeding a rate of 30 degrees, forcing the terrain into a corrugated landscape surface with many small depressions. This disturbance can easily create patterns to be picked up in a high-resolution imagery. Those revelations concerning water content will play an important role in the discrimination of tree species – a matter we will discuss in chapter 8.8.2.

A variation of the NDVI was proposed by Boiarskii and Hasegawa (2019) , who found a better suitability of the NDRE for their specific applications.

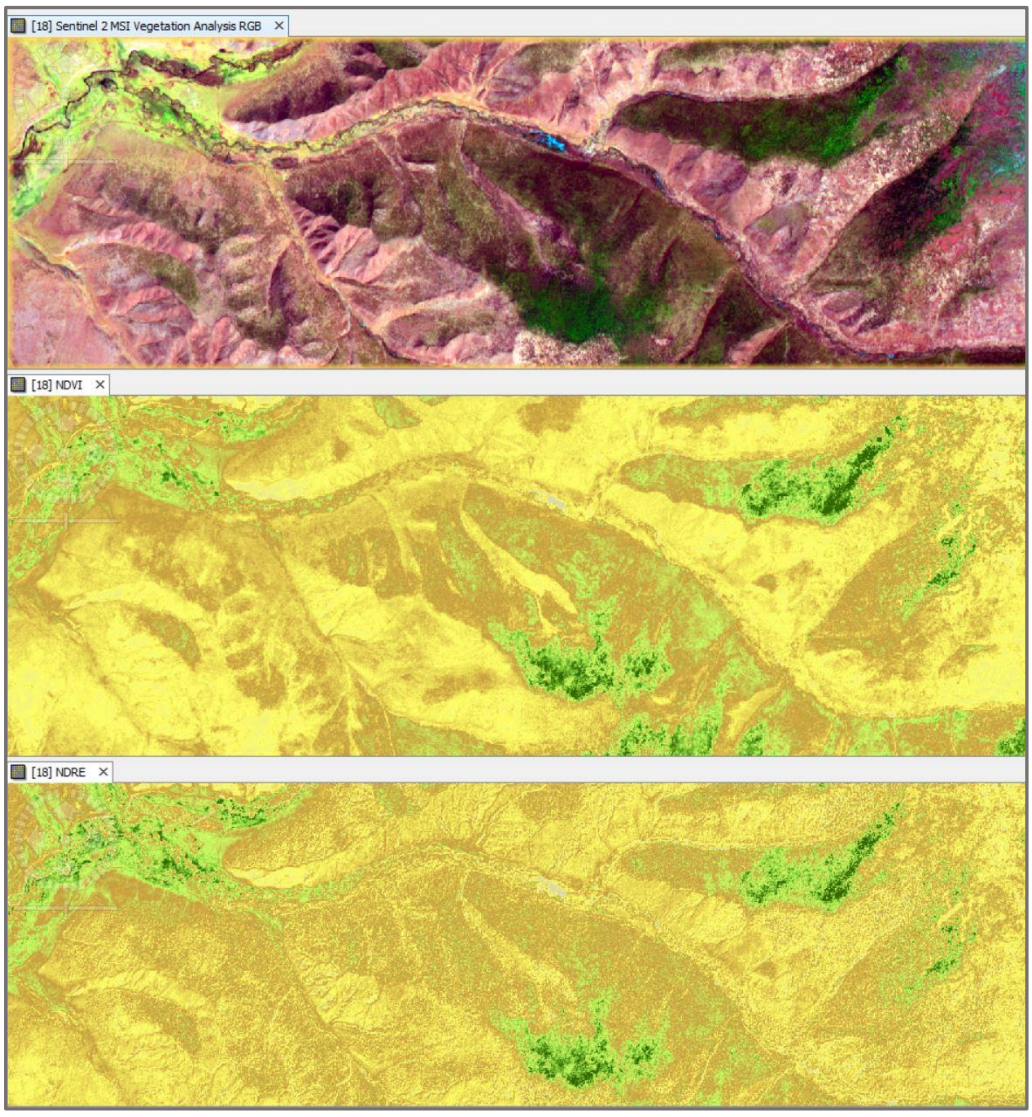

Figure 8.31: Comparison in S-2 13/05/2017 (top: RGB) between NDVI (middle) and NDRE (bottom). The NDVI shows better homogeneity and better identification of dark taiga areas (dark green).

The authors conclude, that NDRE has proven to be more sensitive for monitoring chlorophyll content than the common NDVI. Applied to the Thunkel test area, the NDRE calculation shows a speckled rendering suggesting a higher spatial differentiation. Albeit, as compared to the NDVI image, some of the detail seems to be lost. In addition, the dark taigas (shown in dark

green) represent a larger and more homogenous area than the NDRE variant. In order to retrieve more detail from the imagery the WV-2 scene was favoured because of its higher spatial resolution by comparison with the other imagery. Furthermore, the represented NDVI values also take advantage of the fact, that in the senescence period only non-deciduous trees (i.e., Siberian larch, Siberian pine, Siberian fir, and Scots pine) occupy a spectral signature to stand out as high NDVI values. The result of this calculation is demonstrated below.

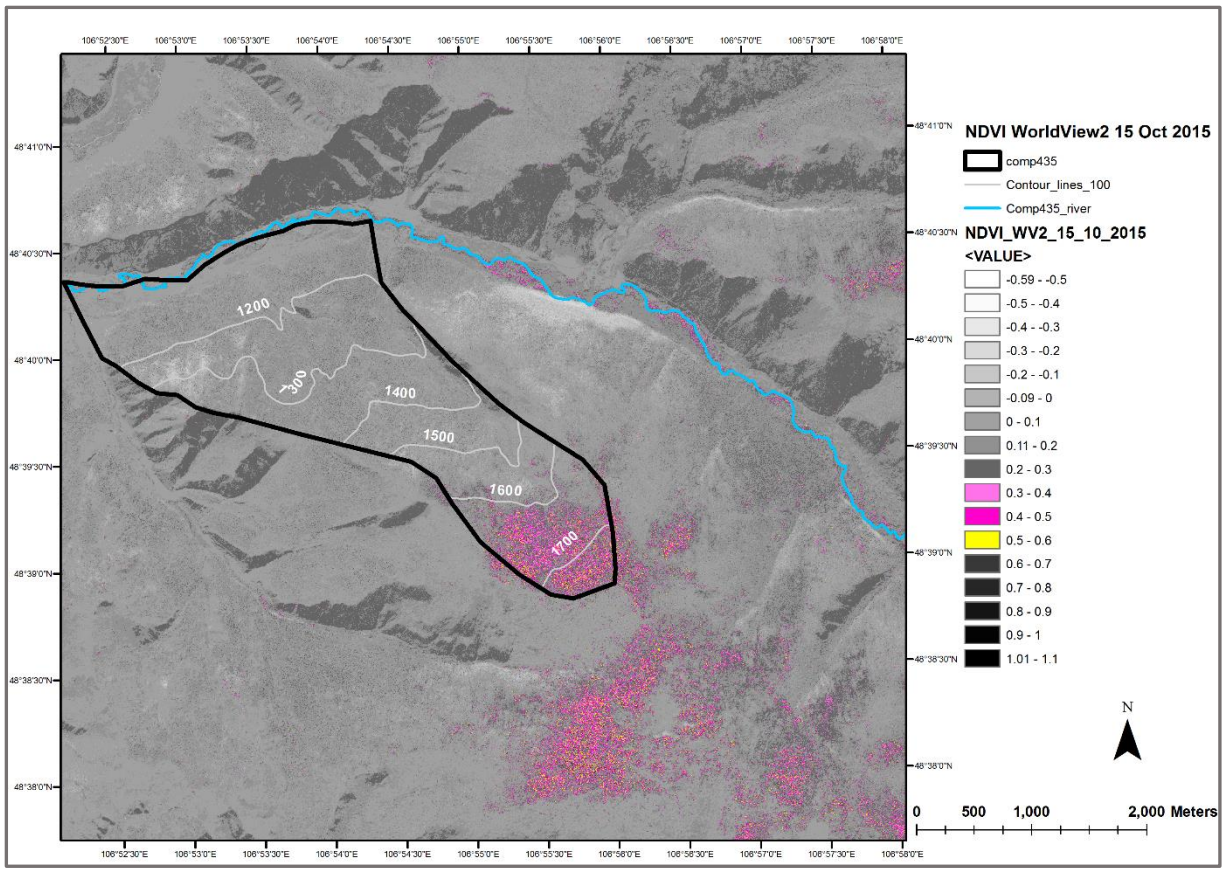

Figure 8.32: NDVI calculated for WV-2 winter image. The dark taiga areas are conspicuous with NDVI values ranging from 0.3 to 0.6.

The areas populated with dark taiga species can be clearly delineated and quantified. The good news is, that the snow cover was relatively thin, with the features exposed being relevant for NDVI estimation. Dark taiga areas reflect NDVI values higher than 0.3. By visual inspection the values between 0.2 and 0.3 apparently represent areas cleared from snow with some grass being exposed. One of the big surprises was to spot dark taiga species below their common altitudinal range of about 1600m. Initially deemed as a calculation error, the occurrence of the dark taiga at odd locations proved me right affirmed by my own observations, which were validated by other persons with on-site experience such as Altrell (2017), Küstner (2017), and Schmidt-Corsitto (2017).

One of the most interesting aspects of NDVI derivation of course is to see its change of the magnitude during all seasons. Seasonal effects can be reflected in the occurrence of

disturbances (e.g., fire, insect attacks), logging activities, post-fire succession, stress in the vegetation (e.g., water, nutrients), or of natural causes such as senescence. The Earth Trends Modeler offers a great opportunity to carry out detailed investigations on such effects. A number of 11 Sentinel-2 images acquired in 2017 were determined to be used as input for such assessment. The graphical representations below attempt to shed light on the major findings in the NDVI time profile. The first figure reflects an overall mean NDVI trend for the entire compartment 435 for the year 2017.

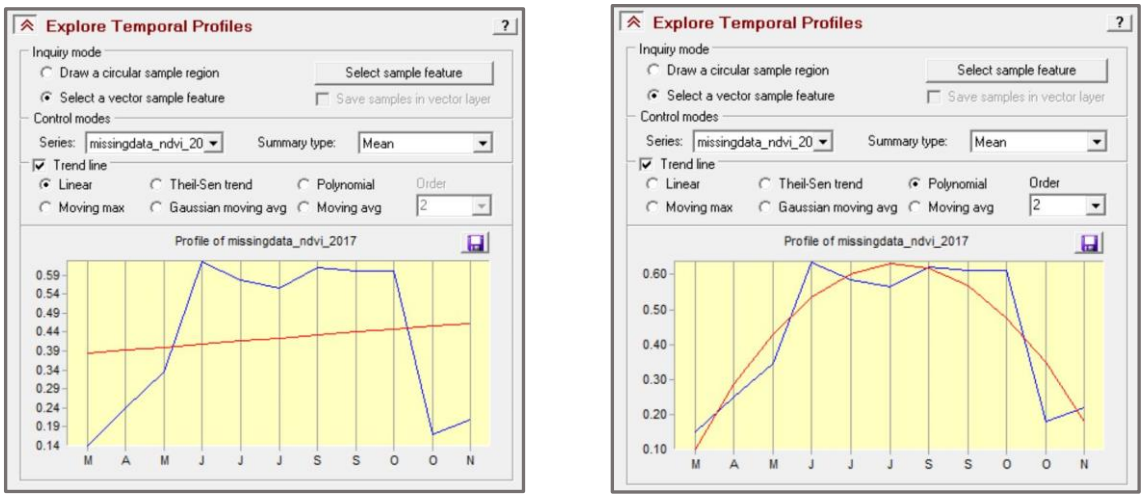

Figure 8.33: Overall temporal NDVI profile with linear trendline for compartment 435 (left) and with polynomial trend line (right).

The vegetation period takes a very sow start in March, with a real boost only experiencing in May. NDVI values then peak at the biginning in July showing the maximum in chlorophyll activity. Due to the lack of sufficient precipitation the NDVI curve takes a dip in July (i.e. drought) to rise again in September after replenishment of the water resources by rainfall. Leaf senescence period then starts in October with a massive plunge. In September the first snowfalls or showers of sleet are not uncommon. With the beginning of October the very short thriving period for the vegetation comes to an end with NDVIs decreasing and rising again in November, when vegetation gets exposed by the thawing snow.

This overall trend of course does not reveal enough detail for the comparison between the different taiga scenarios and the occurrence of disturbances such as wildfires. For this reason the calculation of the NDVI trend was conducted for dark and light taiga discretely, with an indidual consideration of the areas affected by the hugh fires taking place in July andAugust 2017. The following figure displays the temporal profile for dark and light taiga. At a glance the difference in NDVI maximum values is quite obvious – for the dark taiga it is 0.78, whereas the light yields only around 0.70. However, the picture becomes even more dramatic when reagarding the minumum values – for the dark taiga it is 0.54, and it is close to 0 for the light

taiga. The NDVI curves appear quite similar in shape from May unitl October with the summer drought inflicting an NDVI loss to both taiga types.

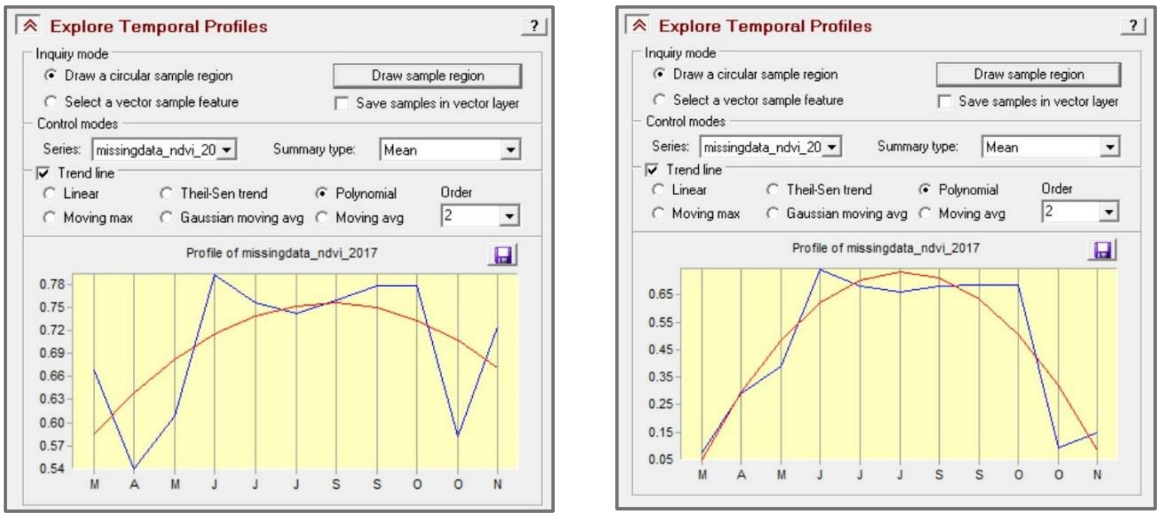

Figure 8.34: NDVI temporal profile for dark taiga (left) and light taiga (right).

For the dark taiga there is a sharp rise in NDVI noticeable at the end of October. This phenomenon usually goes hand in hand with the melting of the snow on the tree crowns in the winter season. Since there is hardly any green vegetation left in the light taigas in winter – except for some forest floor flora, their NDVI goes virtually unaffected. The trendline for the burned areas presents itself very divergently. Important for a precise and transparent interpretation is the start and the cessation point in time – according to the firefighters being onsite the fires raged from end of July until about mid of August 2017. This trend is very conspicuously reflected in the curve illustrated below. The NDVI timeline decreases continuously from July to the beginning of September to recover again. When I carried out some ground checks in the effected zones, I was stunned to see part of the vegetation regain ground with the grass creating carpets of bright green and some of the larch getting back to life. This episode of course explains quite comprehensibly the curve turning upward again to only subside again in late autumn.

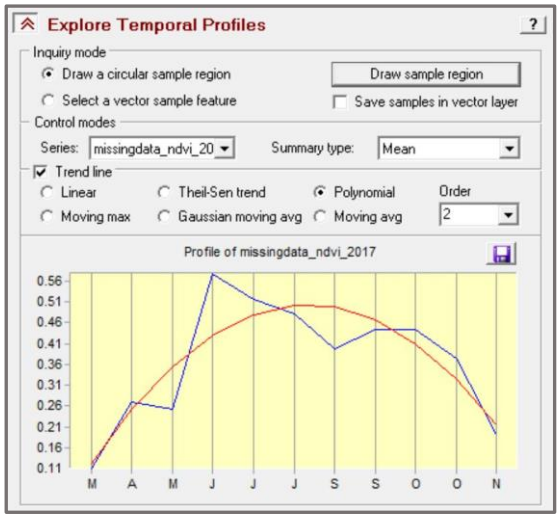

Figure 8.35: NDVI trendline for burned area. The trend shows a clear dip of NDVI during the fire (July 2017), but a recovery in September.

By taking a closer look at the literature published, Karnieli *et al.* (2006) carried out an interesting investigation on the combination of NDVI and brightness temperature, both derived from the NOAA AVHRR sensor. They conclude, that, opposed to common assumption, NDVI and land surface temperature showed a positive correlation for six different ecosystems in Mongolia (i.e., rising temperature positively affects vegetation activity). They further infer, that the Vegetation Health Index (combination of NDVI and brightness temperature) should be used with caution, particularly in high latitude areas. Another investigation deals with the NDVI trend regarding ecosystems in Mongolia. Lamchin *et al.* (2015) chose an observation period in MODIS data from 2002 to 2010 to analyse the trends in NDVI for the whole country. They found an average NDVI ranging from 0.3 to 0.4 for all vegetation, with a strong negative correlation with temperature, but a positive correlation with precipitation. Their assessment also revealed that the forested northern part of the country suffered a dramatic decrease of NDVI during the review period. High correlation was established between anomalies in rainfall and vegetation development, with a changing ENSO (El Niño Southern Oscillation) and a shift in climate exacerbating the situation. Lower rates of precipitation were detected especially during summer, which makes this finding to be much in line with my own observations made for the summer 2017. The authors also stress, that the observed NDVI decrease can be attributed to a combined 'effort' of natural causes and the effect of human activities. A similar study on the changing NADVI in Mongolia was conducted by Enebish *et al.* (2019). The team exploited data from various weather stations in Mongolia to explain the behaviour of the vegetation index as derived from NOOAA[23] satellite data. For the climate data they observed a rising maximum temperature for the last few decades, with NDVI showing lower values than the highs in the 1980s. The team also support the observation that rainfall has experienced a drop in its amount and now shows more irregular patterns. Their overall conclusion is, that despite some signs of local recovery, the biomass will suffer some further dramatic losses in the future. Another team of researchers assessed the change in NDVI to be used as an indicator of the growth status of the vegetation in Mongolia (Meng *et al.*, 2020). They scrutinised NDVI datasets from 1982 to 2015 retrieved from the so-called Global Inventory Monitoring and modelling System (GIMMS), which also uses NOOAA satellite imagery for data gathering. In addition to NDVI, climatic, topographical, soil and vegetation type information provided the required input to model the possible gains and losses of biomass (NDVI). Interestingly, the eastern part of the country shows a greening trend, whereas no clear trend with respect to the forest area was observed, with losses and gains bringing level. Nevertheless, according to the resulting map the Khentii area displays a massive decrease in NDVI in some areas. Once again, it became apparent, that natural as well as human factors are the driving forces of the change in vegetation cover. In another fairly recent study the NDVI

[23] NOAA = National Oceanic and Atmospheric Administration

derived from SPOT satellite imagery was considered by Klinge *et al.* (2018) to demonstrate the change in vegetation vitality and the shift of treelines in the boreal forests of Mongolia. Since the distribution of forest and steppe are highly dependent on the topographic and climatic parameters, this region is considered to be extremely sensitive to human impact and a changing climate. The reference period for the modelling process was from 1999 to 2013. Limiting parameters for tree growth were observed to be minimum temperature (6°C for the growing season) and the minimum of mean annual precipitation (230 – 290 mm/annum). Their findings also corroborate, that higher precipitation in coherence with higher temperatures lead to higher greenness in the vegetation as reflected in the NDVI values. The team concludes by stating, that with a rapid change in climate a spatial relocation of tree communities and an alteration in forest types associated with a shift in treelines are conceivable future scenarios. NDVI was used by Klinge *et al.* (2020) as a proxy for calculating biomass in Mongolian forest systems. Satellite imagery of Sentinel-2, Landsat 5 and 8, and Tandem-X (for DEM) were appropriated for the determination of NDVI for subsequent biomass estimation in Siberian larch forests. Due to a weak correlation between needle volume – as reflected in the NDVI value – and tree biomass the team found no significant correlation between tree biomass and NDVI. They also looked into a potentially useful correlation between LAI, biomass and NDVI to find, that relationship between NDVI and LAI was very weak (R^2 of 0.0052), and correlation between LAI and biomass was calculated to be also quite insignificant (R^2 of 0.1079). Another important discovery was to get some good insights to driving factors for tree vitality and growth, namely topography and climate. A complex constellation of drought occurrences, wildfire aftermaths, human impact, cold air masses accumulating in depressions, and cool conditions in higher elevations cause a melange almost impossible to disentangle and to resolve. In addition, low canopy closure (i.e., less than 53%) in association with lush understorey vegetation causes an amalgamation of plant vitality signals found in the NDVI, which is extremely difficult to interpret, let alone to quantify.

Shifting the focus to boreal forests in Canada, McDonald *et al.* (1998) scrutinised various vegetation indices (e.g. NDVI, SAVI, TSAVI) for their potential applicability in determining forest inventory parameters. They found out the following for the analysis of Landsat images: (i) all indices were not linear with respect to forest cover because of shadowing effects, (ii) the indices were greatly affected by perturbations caused by solar zenith angle, background reflectance, stand structure and LAI, and (iii) at high canopy covers SAVI and TSAVI performed best, since they show large dynamic ranges and are less susceptible to atmospheric perturbations. When looking at logging activities in a Polish forest, Pałaś and Zawadzki (2020)

found that the MERIS Terrestrial Chlorophyll Index (MTCI[24]) and the Brightness Index (BI[25]) performed best when employing Sentinel imagery, followed by NDVI and the Ratio Vegetation Index (RVI[26]). Another interesting discovery was made by Mayer and Scribner (2002), who found that NDVI preferentially detects the greenest vegetation, whereas SWIR NDVI (NBR) shows a tendency to highlight vegetation residing in shadowed areas. Another interesting aspect was portrayed by Sulla-Menashe *et al.* (2016), who investigated the possible sources of bias and variability in long-term Landsat time series over Canadian boreal forests. They conclude, that differences in sensor view geometry and radiometric disparities bear the potential to affect the integrity of satellite time series. A major cause for poor correlations between NDVI and forest related attributes (e.g., BA, biomass, canopy cover) has been identified to be saturation effect of the NDVI encountered in lusciously green forests. An impressive amount of publications exists on this particular issue. The good news is, however, that NDVI remains a good indicator of green biomass in deciduous and dry forests (Bannari *et al.*, 1995, Freitas *et al.*, 2005, Gitelson, 2004, Huete, 2012, Liang and Wang, 2020: 405–445).

In the light of above portrayed factors in the literature I can conclude, that, based on my findings, NDVI is very difficult to comprehend and to interpret with topography and climate proposing a conundrum. In parts of compartment 435 terrain is of such complexity associated with shadow effects and varying moisture content of the forest floor, so that there is no way in identifying a single factor as an underlying cause. The similarities with the study conducted by Klinge *et al.* (2020) are quite striking in the sense, that I also encountered forest stands with low to very low canopy closure, exposing a lot of green forest floor flora to the satellite sensor. As such, a high NDVI can be easily falsely attributed solely to the tree layer. Luckily, NDVI saturation effects cannot be reported of the test sites surveyed. To make things worse, the impacts of human activity (e.g., logging), and the occurrence of natural disasters (wildfire, insect attacks) have a huge impact on the NDVI performance – I found all mentioned factors to be true for compartment 435. Marks of fire impact, defoliation caused by insects (in larch and birch), and logging activities are apparent all over, except for some parts of the dark taiga. Although I have not carried out an NDVI study in extenso, the calculation of the MSI (see graph above) at least provided some indication on a positive relationship between plant water content and NDVI. I also detected hardly any change in NDVI in the dark taiga areas during the seasons, which is very much in line with Gamon *et al.* (2016). To conclude with, there seems to be a lot of room for further investigations on the NDVI related to the taiga forests in Mongolia.

[24] $MTCI = \frac{(Near\ Infrared - RedEdge)}{(RedEdge - Red)}$

[25] $BI = \sqrt{\frac{Red^2 + Green^2}{2}}$

[26] $RVI = \frac{Near\ Infrared}{Red}$

Leaf Area Index (LAI)

Where the NDVI shows its strengths in the assessment of plant vigour, the LAI is more geared for a slightly different realm. The Leaf Area Index (LAI) is one of the most widely used indices for describing plant canopy structure and forest growth, and for getting a better understanding of the biosphere-atmosphere exchange of mass and energy at the leaf surface. As such, the determination of LAI has become a crucial index in biochemical, hydrological, and ecological modelling, as well as for measuring forest growth and productivity. As portrayed in chapter 4.3.3. the LAI can be estimated in various ways. In the presented study it was measured on-site using the LICOR LAI 2000 instrument, but it was also directly derived from the Sentinel-2 imagery with the integrated SNAP tool for the extraction of biophysical variables (see also chapter 4.3.5.8.). The calculated LAI values for compartment 435 are illustrated below.

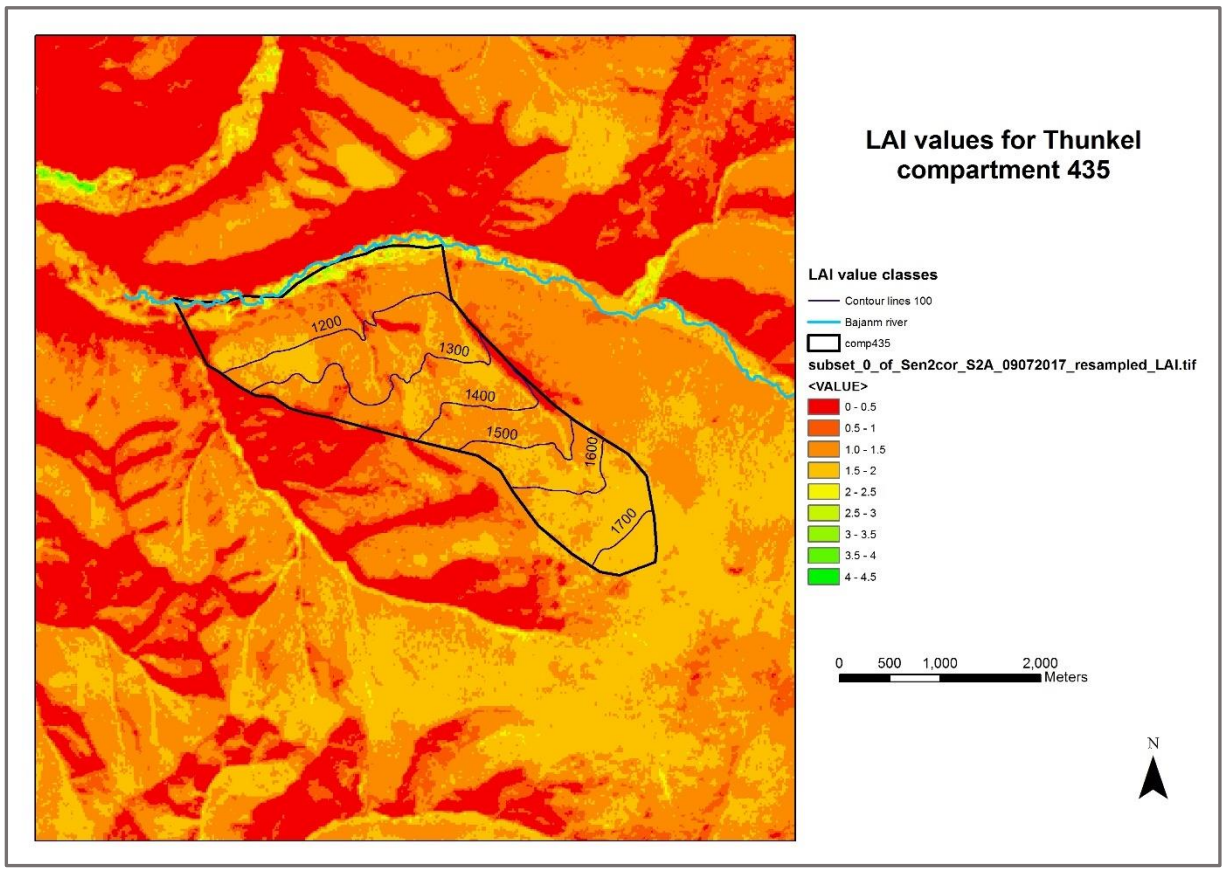

Figure 8.36: LAI values as calculated from Sentinel-2 image 09/07/2017. High values are only to be found in the lush vegetation of the riparian areas. Very low values are reflected by bare soil, rock, and dry grass.

The representation of the Seninel-2 image acquired in summer 2017 reflects the LAI values as being considerably low in general - only the riparian areas show values exceeding 2.5. The areas with dry grass and bare soil cover feature values of being close to zero, whereas the dark taiga areas, as well as some zones in the north-western part of compartment 435 are blessed with LAI values between 1.5 and 2.0; all other parts of the light taiga show values in the range of 1.0 to 1.5. In comparison, LAI measurements taken in temperate forests feature

a value range from 2 to 6 (own measurements carried out in the surrounds of Göttingen in summer 2020). However, it is important to accentuate the fact, that most of the forest stands assessed reveal a low canopy cover of around 30%. There is another factor that deserves attention, namely the fact, that, as being outlined in the S2Toolbox Manual, the LAI estimation comprises all green contributors, i.e., even forest floor vegetation. Since a dense forest floor flora is a fairly common feature in the taiga forests, any of the extracted LAI values from the satellite imagery reflect an amalgamation of both spectral signatures – for trees and understorey vegetation. In several other studies the importance of considering the effect of understorey on the LAI estimations is described. For instance, Chen and Cihlar (1996) found an improvement of the relationship between NDVI and LAI from R^2 0.42 to 0.52, by minimising the effect of the forest floor flora. The authors suggest to rather take late spring imagery (with little understorey vegetation) than satellite data acquired in summer with the flora being fully developed. They also stress, that the temporal variability of the (forest) vegetation needs to be taken into account. However, in the taiga forests a lush understorey is encountered almost all year round making it very difficult to mask out any effect on the LAI (and also NDVI) performance. In order to get a more detailed picture on a possible bias related to this phenomenon, some additional analyses were conducted. The first attempt of judging on potential causes was to set the LAI values gathered in the field against the related LAI estimates derived from the Sentinel-2 image (09/07/2017). The graph below demonstrates a missing linear relationship between the LAI satellite values and the field data with a calculated

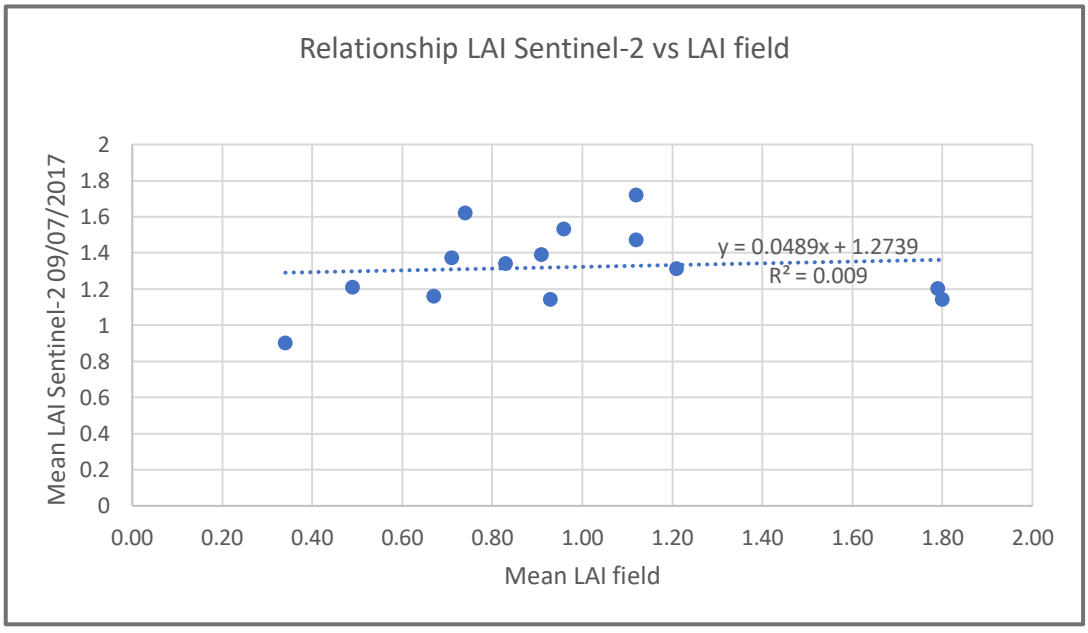

Figure 8.37: Relationship between mean LAI derived from Sentinel-2 image (09/07/2017) and the field data.

R^2 of 0.009. In this case the influence of the understorey can be characterised as substantial. This drastic outcome corroborates the observation, that the satellite derived LAI represents all vegetation contributors. Another scrutiny revealed, however, that at least a fairly clear trend

can be observed in the relationship. The graphical representation of the individual estimates below proves, that, with only few exceptions, the satellite derived LAI gravely over-estimates the LAI compared to the reference field data. This does not come as a real surprise, since almost all surveyed forest areas exhibit a lush understorey flora in combination with a low canopy cover, with many trees having been defoliated, at least partly.

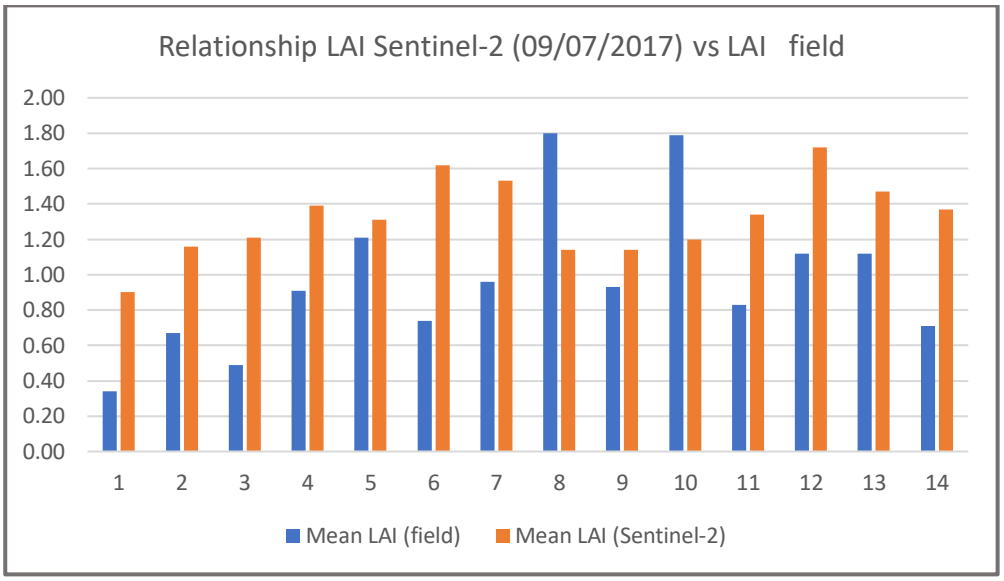

Figure 8.38: Relationship between Sentinel-2 (09/07/2017) LAI estimates and LAI field data.

Although LAI is commonly used as a proxy for the determination of various forest attributes, the literature on the relationship between forest canopy closure and LAI is scarce. I hypothesize, that LAI and canopy closure are correlated, since both estimations exploit the tree area obstructing the clear sky. However, these methods are based on different principles (see also chapter 4.3.3.). The figure below demonstrates the findings on such relationship for compartment 435. According to the graph the R^2 of 0.41 can be considered to be fairly mediocre, but this result was only achieved by some tweaking (i.e., using n-th power instead of linear). Thus, no strong correlation for the LAI and canopy closure can be established for this specific investigation.

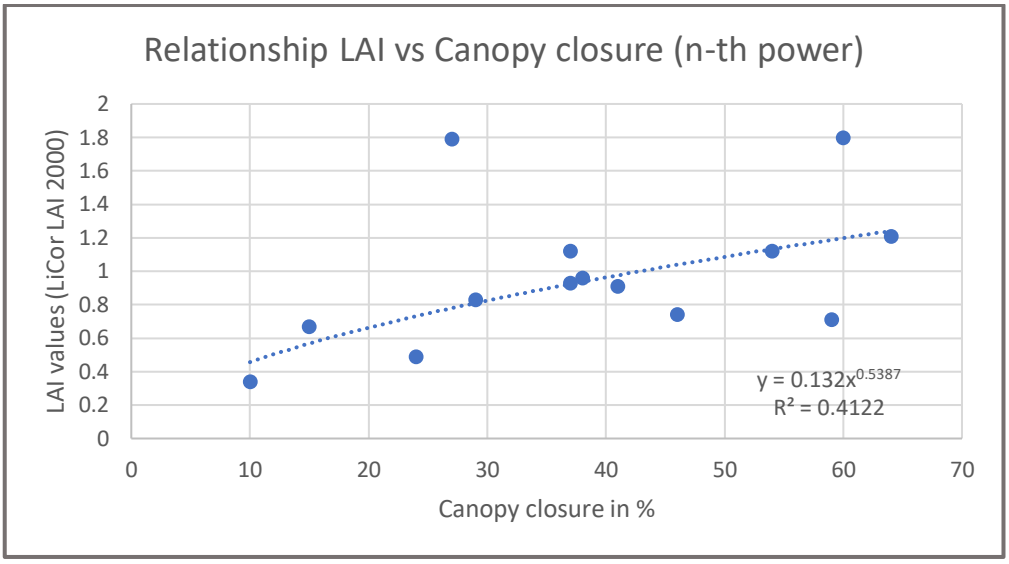

Figure 8.39: Relationship between LAI and canopy closure for compartment 435.

Another aspect found in the literature concerns the use of NDVI to estimate LAI and vice versa. For example, Wulder *et al.* (1998) found relationships between 0.01 (for mixed forest) and 0.61 (for deciduous hardwood) for R^2, with the best results achieved only by including image texture. The graph below illustrates the relationship between NDVI and LAI for compartment 435 with both variables extracted from the Sentinel-2 summer image. The amount of variation accounted for (R^2) is very low with a value of only 0.22.

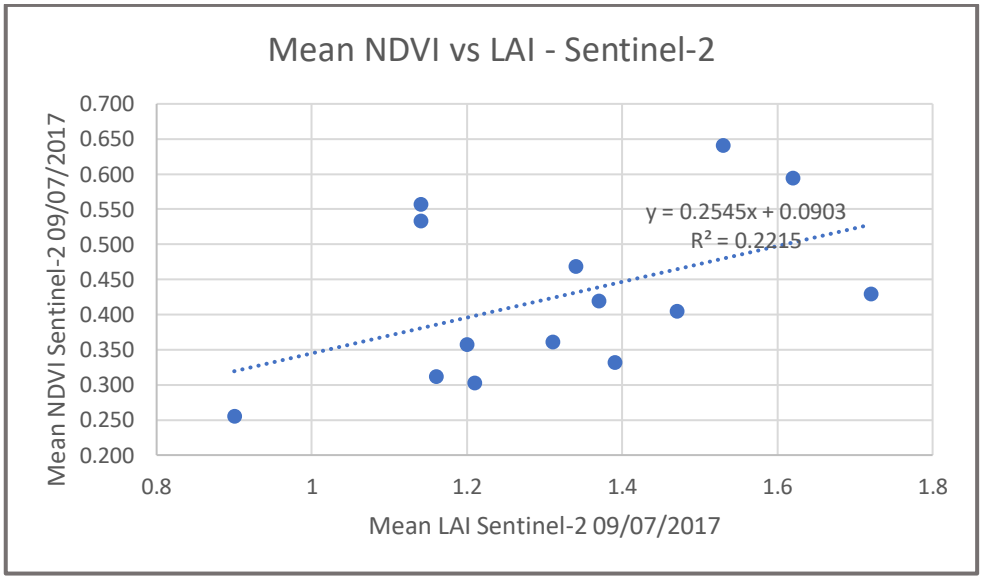

Figure 8.40: Relationship between mean NDVI and mean LAI derived from Sentinel-2 summer image (09/07/2017).

In above mentioned investigation the authors conclude, that except for the inclusion of texture parameters, the stratification of the forest stands proved to be conducive by accounting for the variation in tree species, tree densities, canopy closures, and successional regimes. For their study they chose a test area in New Brunswick, Canada, featuring a wide variety of forest species, forest structures, and age classes. An excellent correlation between NDVI and LAI is

reported by Davi *et al.* (2006). They assessed mixed forests in France by using SPOT imagery to find coefficients of determination to be between 0.73 and 0.82. The team of Coops *et al.* (1997) derived LAI and NDVI from Landsat images displaying Eucalypt forests in Australia. Their assessment yielded R^2 values ranging from 0.53 to 0.71. Moving north to Germany, Tillack *et al.* (2014) report about the NDVI derived from satellite imagery (RapidEye) set against the LAI gathered in the field (LICOR LAI2000). R^2 values range from 0.861 to 0.942 for the alluvial forests considered. The researchers observed, that seasonal effects, species composition, crown closure, and the background reflectance had an enormous impact on the outcomes. This observation is confirmed by Chen and Cihlar (1996), Gamon *et al.* (2016) and Spanner *et al.* (1990), who found it very hard to quantify the combined effects of temporal variability, the occurrence of understorey, the varying canopy closure, as well as soil spectral signature. Other authors also contribute to the detailing of various factors having an impact on the LAI and NDVI estimations. Banerjee *et al.* (2014) emphasize the critical influence of terrain (topography), whereas Yan *et al.* (2019) favour the LAI and NDVI estimation on a landscape over a pixel scale. In addition, they point out, that the clumping effect of leaves needs to be corrected, and that new technologies (e.g., LIDAR) bear the potential to greatly improve LAI estimations, especially, when considering non-continuous forest canopies. Another new approach was chosen by Zhang *et al.* (2019) for the improvement of the LAI estimate. Instead of exploiting LIDAR technology for this purpose, they combined canopy cover and height information extracted form a photogrammetry UAV point cloud to yield an R^2 of 0.833 for their LAI estimation.

Effects of over-, and underestimations of LAI are related by various authors. For a boreal forest in Sweden Goude *et al.* (2019) observed an underestimate between 30 and 73% depending on species and measurement technique. This is in line with Campbell (2012), who assessed various measurement methods to find large discrepencies in the outcomes. Chason *et al.* (1991) found the clumping of leaves to be the culprit for the measured underestimates of up to 45% compared to litter estimation. With regard to canopy closure and the related LAI estimates Olivas *et al.* (2013) and Baret and Guyot (1991) noticed a distinct saturation effect similar to the NDVI related plateauing of the values. According to their observations LAI was underestimated in all constellations with a high canopy closure in tropical forests. However, with LAI measurements not exceeding values of 3 this effect is very unlikely to occur in the Mongolian taiga forests. Dufrêne and Bréda (1995) detail an overall underestimation of the LAI in the range of 6 to 37% when applying indirect methods (i.e. LAI-2000 plant canopy analyser; needle method; Demon light sensor) in a temperate forest. They hypothesise that local clumping of architectural canopy components is a reasonable explanation for this phenomenon, thus violating the underlying principle of random distribution of the plant structural elements (the so-called Beer's law) being used in most indirect appraisals. Clumping

of foliage and the negative impact on LAI measurements have also been described by Chen *et al.* (2005), Gower and Norman (1991), Peng *et al.* (2018), Kappas and Propastin (2012), Ryu *et al.* (2010), Whitehead *et al.* (1990), and Zhao *et al.* (2012). In addition, Garrigues *et al.* (2008) found variation in illumination conditions to be one of the major drivers for LAI discrepancies when comparing LAI-2000 plant canopy analyser, the Decagon AccuPAR ceptometer, and digital hemispherical photography. A similar survey was carried out by Hyer and Goetz (2004) on a boreal forest site to yield commensurable results. The research team also found variability in LAI measurements to be attributable to spatial heterogeneity within forest stands, particularly in sparse canopies. Kappas and Propastin (2012) found that all algorithms for the derivation of LAI are empirical and tend to over-simplify the relationship between recorded signal and the pertaining plant parameters, thus leading to potentially low accuracies. They further state, that more research is required to address this issue.

Despite all shortfalls and imponderables mentioned above, there is also good news to be reported. When investigating biophysical properties of boreal forests in Finland based on field data and Sentinel-2 imagery Majasalmi and Rautiainen (2016) found that the estimation of fPAR and LAI performed best when using bands 7 (RedEdge) and 9 (water vapour) (R^2 of 0.93 for both) instead of exploiting vegetation indices like NDVI. However, they also conclude that performance can decrease considerably (i.e., R^2 of 0.3), when wrong vegetation indices are applied for approximation of the vegetation traits. Regarding the application of methods for LAI estimation a coefficient of determination of a phantastic 0.94 was discovered when comparing LICOR LAI2000 readings with direct LAI measures in mixed forests in Wisconsin, USA. A most interesting observation was chronicled by Baret and Guyot (1991). When they looked into the correlation between various vegetation indices and the LAI their sensitivity analysis revealed a clear trend for the Soil Adjusted Vegetation Index (TSAVI) being the best associate for lower LAIs (smaller than about 3), but reaching a saturation point at a certain level very much like other vegetation indices. In this context it also needs to be noted, that '…the noise due to soil background was amplified when combined with the noise due to leaf inclination' (Baret and Guyot, 1991: 168).

In conclusion it has to be put on record that the Sentinel-2 estimates for LAI are about 26.38% higher than the average of the LAI in-situ measurements. The latter is a clear indication of the effect of the universally occurring dense understorey vegetation diminishing the spectral response of the (partly) defoliated trees. In addition, the sparse population of the forested areas also contributes to the amplification of the understorey signal. At this stage it is extremely challenging to find a logical explanation for the missing correlation between the Sentinel-2 and the field LAI. With reference to the possible attributed factors detailed in the literature I can only speculate a combination of low canopy closure, topography, lush understorey, and the

underlying algorithm for the extraction of the LAI form the Sentinel-2 imagery. At least for the poor NDVI – LAI correlation it seems quite likely, that the NDVI was not the most suitable index for comparison, thus requiring further investigation.

8.5. Extraction of NBR (fire index)

Wildfires have been intrinsic to the boreal ecosystems for millennia and as such also affect forest structure, species composition, timber markets, and forest management (Stocks *et al.*, 2001). This is particularly true for Mongolia, where, apart from timber logging, insect pests, livestock grazing, and climate change related phenomena, wildfires are the major influencing factors on the landscape ecosystems of the taiga and the forest steppe (Altrell and Erdenejav, 2016, Dulamsuren *et al.*, 2011, Dulamsuren *et al.*, 2014, Goldammer, 2013, Klinge *et al.*, 2020). Rising levels of wildland fire incidents, increasing temperatures, and land use change have coincided in many forested regions, making it difficult to parse causes of elevated fire activity (Klinge *et al.*, 2014). According to a report by Byambasuren (2018) wildfires account for more almost 90% of forest degradation, and as such, also thwart all efforts to contribute to the global programme of reducing carbon emissions (see also REDD+[27] programme of the United Nations (www.un-redd.org)). High intensity forest fires can be a major cause for the degradation of the taiga forests and bear the potential to irreversibly induce a shift to the steppe grassland ecotone (Mühlenberg *et al.*, 2004).

In order to quantify the impact on the Thunkel region the most commonly applied burn indices were calculated (i.e., dNBR, dNDVI) to create a map showing the extent and severity of the fires in the year 2017. For safety reasons I was not allowed to enter, let alone survey the charred areas. As such, no cogent reference data could be gathered. However, based on own observations and photos taken from a few vantage points, at least a good impression on the extent could be received. The photograph below, which was taken in the vicinity of a burned area during a UAV flying mission, depicts features, which become an important reference when talking about burned area mapping and the assessment of the NDVI timeline. On the left of the image a cluster of birches were completely charred (i.e., crown fire). The centre depicts some larch trees, which survived, with the neighbouring larches being at least partly defoliated due to the fire (i.e., crown and surface fire). The black patches in the photograph represent areas affected by ground fires with some smouldering activities in parts. The image was taken two weeks after the fire came to an end and shows green vegetated patches, which quickly regained its former ground as an effect of a low-damage ground fire.

[27] ***R**educing **E**missions from **D**eforestation and Forest **D**egradation*

Figure 8.41: Burned area south of compartment 435 in the transition between light taiga and forest steppe.

Before getting into detail with respect to the achieved burn severity indices, a graph (Figure 8.42) is presented to illustrate the main differences between dNBR and dNDVI – both are used for the detection and delineation of burned areas. The resulting differences between the before-, and after-fire image reveal clearly recognisable disparities between the two indices applied. In this context two phenomena require some closer inspection. The NDVI has proven to be perfectly geared for the assessment of the health status (vigour) due to its capability in detecting photosynthetic activities. In contrast, the NBR with its smoke and haze penetrating capabilities of the SWIR, seems to be better suited for the moisture assessment of the vegetation. In numerous studies (relating to boreal forests in particular), the NBR index has demonstrated its ability to attain good correlation with field-based methods and its transferability across multiple landscapes and multitemporal surveys (Allen and Sorbel, 2008, Chen *et al.*, 2011, George *et al.*, 2006, Navarro *et al.*, 2017, Soverel *et al.*, 2011). Mallinis *et al.* (2018) found out, that the dNBR even outperformed NDVI, when assessing large fires in pine forests in Thasos, Greece. In addition, the classification accuracy was slightly higher for the Sentinel-2 imagery compared to Landsat 8 OLI. This finding was confirmed by Fernández-Manso *et al.* (2016) for the Sierra Grata (Spain) wildfire in 2015. When assessing burned areas in coniferous forests in the Western USA, Parks *et al.* (2014) discovered, that the RBR corresponded better to field-based measurements than dNBR (R^2 for RBR: 0.786 and for dNBR: 0.761). In another study, Veraverbeke *et al.* (2011) calculated a coefficient of determination (R^2) for the dNBR of 0.65 and an R2 of 0.46 for the dNDVI showing the superior

performance of the former in Mediterranean forests. A slight advantage of dNBR over dNDVI is also confirmed by Hudak *et al.* (2007), when investigating more than 50 huge fires in Montana, Alaska, and California. Tran *et al.* (2018) analysed the performance of various vegetation and soil indices for the evaluation of wildfires in Australia. They found the dNBR being a good choice for most of the forest types considered, but they also conclude, that there is no such thing as an overall best-performer of indices for each category. Despite the overall success of the NBR, this index has proven to be less effective with a considerate time lag between the fire event and the assessment of post-fire conditions with vegetation regrowth starting immediately after the fire (i.e., higher reflection in the NIR). It is also important to know, that this index is very sensitive to water, thus causing misclassified pixels. This requires a creation of a water mask and/or consideration of a NDWI calculation prior to classifying the imagery (Keeley, 2009, Polychronaki and Gitas, 2010). With respect to both factors mentioned, the time lag between the fire and my field visit was about two weeks, in which only a few smaller areas managed to recover with grass seed germinating. However, trees affected by the fire can still appear green for a few days before the leaves show the effects of tissue damage – as such, a time lag can also be advantageous. To account for the water sensitivity effect of the NBR a cloud/water mask was created.

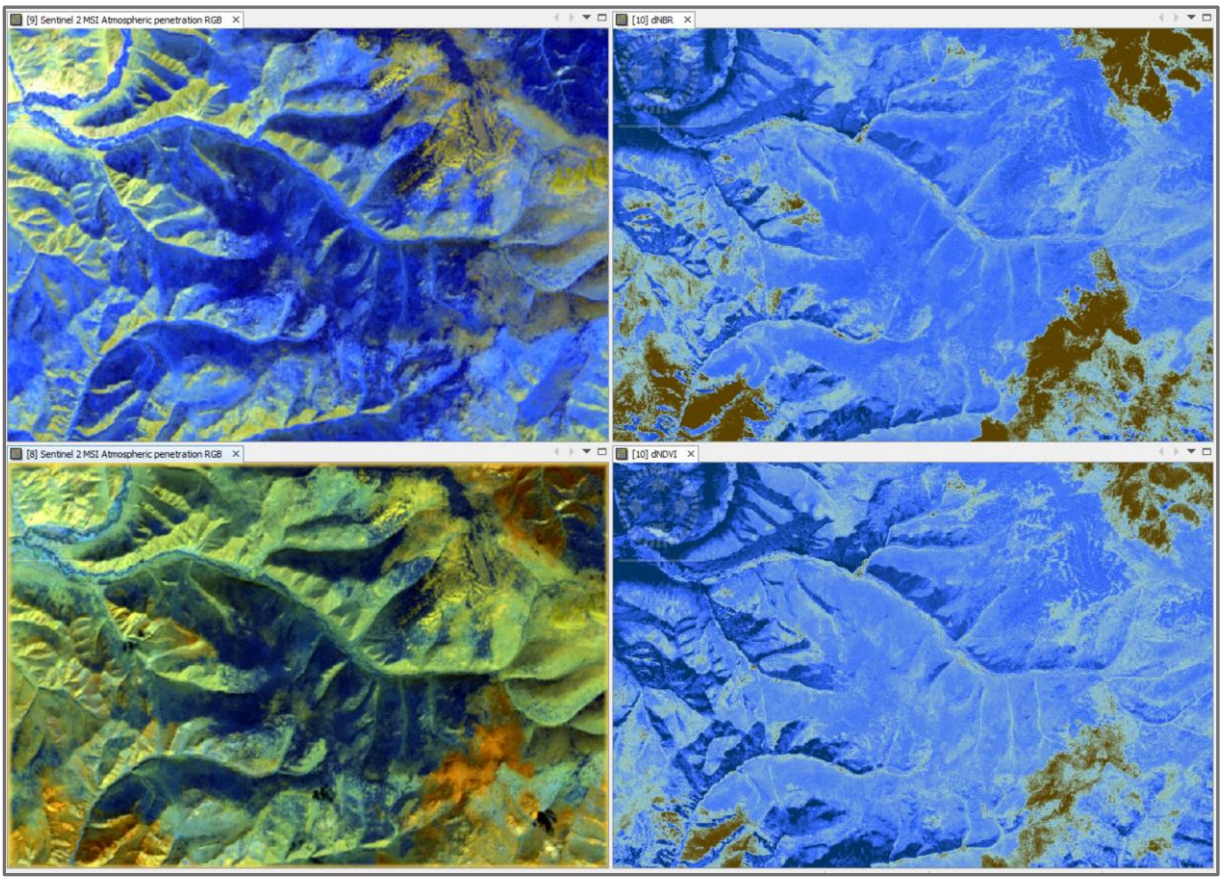

Figure 8.42: Comparison between dNBR (top right) and dNDVI (bottom right). S-2 image before (top left) and after the fire in 2017 (bottom left) – band combination B12 B11 B8A.

Getting back to the figure illustrating the difference between dNBR and dNDVI two observations can be made, namely (i) the calculated dNBR area is larger than for the dNDVI, and (ii) the dNBR shows a much more refined canvas of patches being affected by the fire. This impression gets even more manifested, when comparing the NDVI close-up of the compartment 435 with the dNBR calculations for the same area.

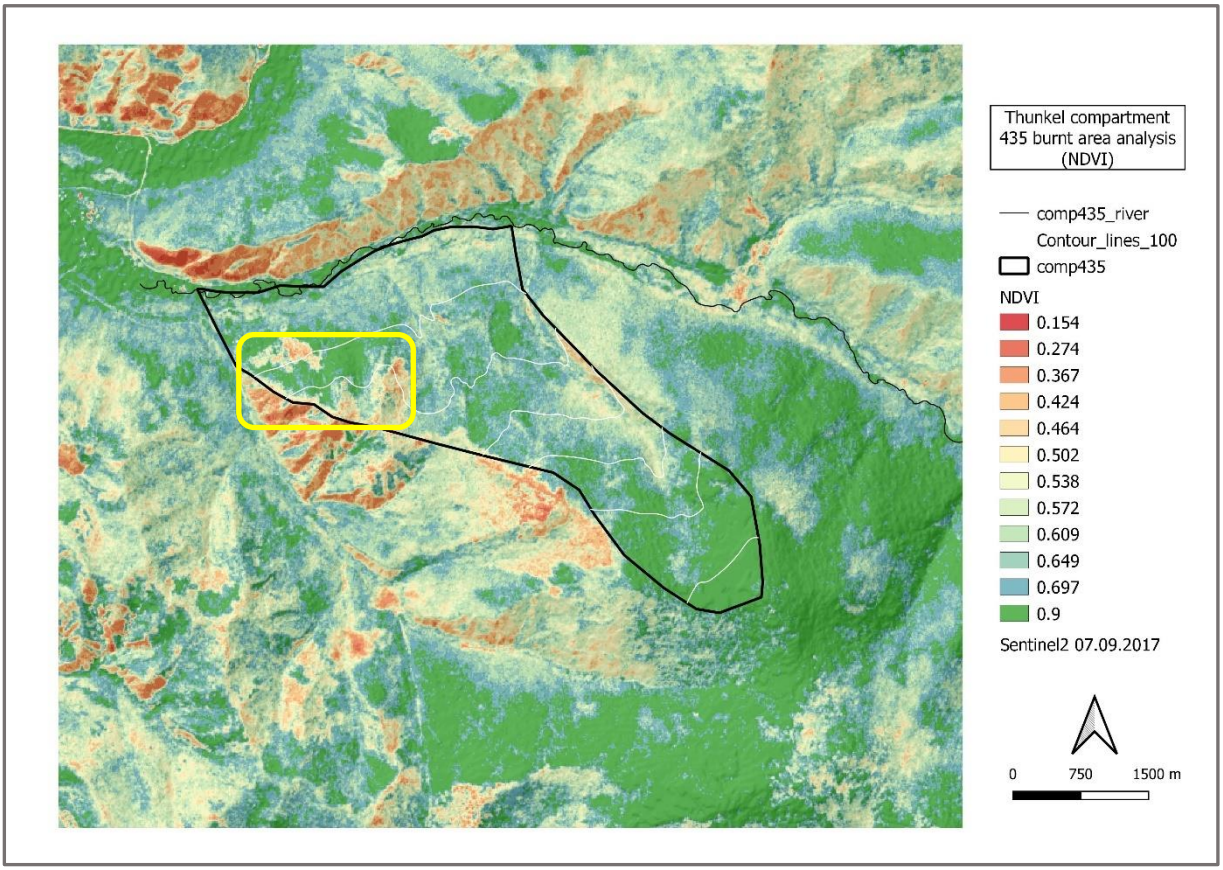

Figure 8.43: NDVI values for the S-2 07/09/2017 image (after fire). The affected areas in compartment 435 are indicated with a yellow box. The dark taiga area seems unimpaired (bottom of graph).

In the NDVI graph the absolute values are displayed, whereas in the dNBR graph below the dNBR values were transformed into the severity system used by the USGS. Although both scales are difficult to compare, an assignment to the affected areas is possible by visual interpretation. In the upper graph the area afflicted by the fire within compartment is indicated with a yellow box. In the NDVI image values for the index are relatively low, but the dNBR graph is much more precise concerning the severity of the fire – the upper part of the yellow box (it is white for the corresponding dNBR graph) shows a moderate to high severity of the fire, whereas in the NDVI graph it is very difficult to draw such conclusion. Based on my own observations I can confirm that the fires with a high impact occurred in this specific area. A similar inference can be made for the huge severely burned area south of the midsection of compartment 435 – the NDVI image shows a fairly low value, whereas the dNBR clearly

indicates a massive damage. Furthermore, the riparian areas reflect a vegetation being lush in the NDVI. In contrast, the dNBR reflects a low to moderate burn severity, which I can confirm.

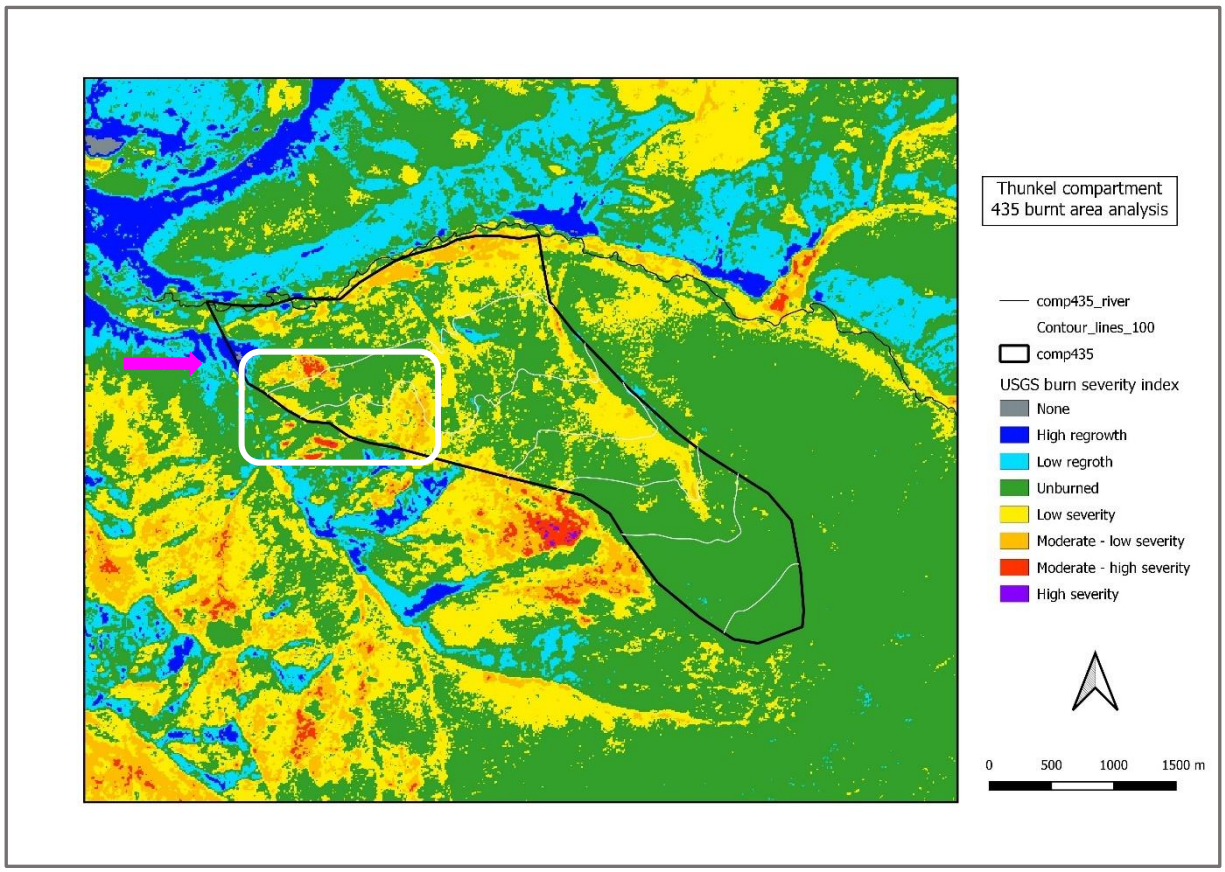

Figure 8.44: Burn severity indices for the Compartment 435 area and the vicinity. Fires were close to the GIZ Camp (arrow). Dark taiga in the south-east appears unaffected, but fires were at close quarters.

Nevertheless, both maps provide a clear indication, that the dark taiga area in the southeast of the school forest (compartment 435) remained completely intact. Even though the fire line was very close, the firefighters managed to stop, or at least retard the fire from entering the precious dark taiga. However, it needs to be pointed out, that due to the cooler and more moist condition in the dark taiga these areas seem to be less afflicted by the devastating fires. This conclusion can be drawn from the maps presented below and in chapter 8.4. (i.e., NDVI graph showing dark taiga zones), showing massive destruction in the entire Thunkel area, but sparing dark taiga. This phenomenon was also reported by the fire fighters and locals. It is unfortunate, though, that no exploitable ground truthing data is available for explicit verification. For cross-validation of the burned area mapping, the fire hotspots of the year 2017 were retrieved form the FIRMS database (see also chapter 7.3.5.7.). By comparing the affected areas in both maps the match is remarkable, albeit the dNBR illustration reflecting much more detail.

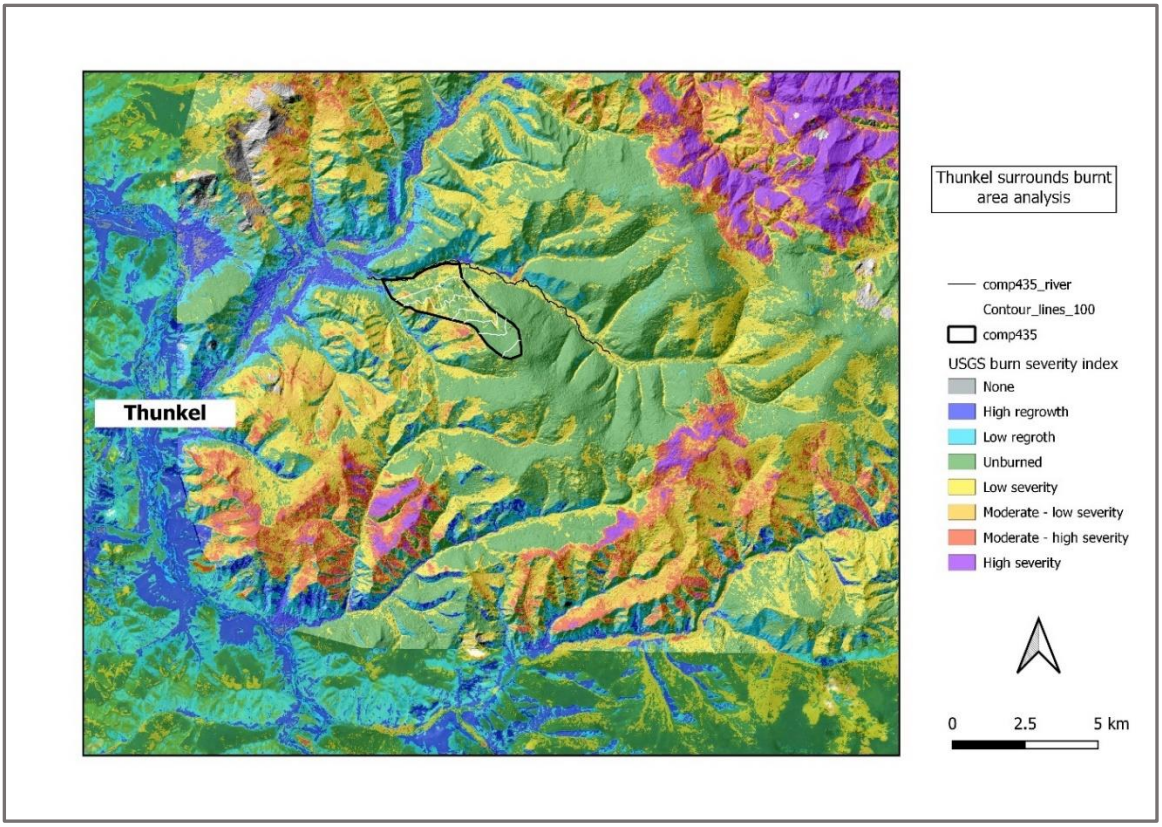

Figure 8.45: Burn severity indices for the greater Thunkel area. A huge forest area had been damaged severely.

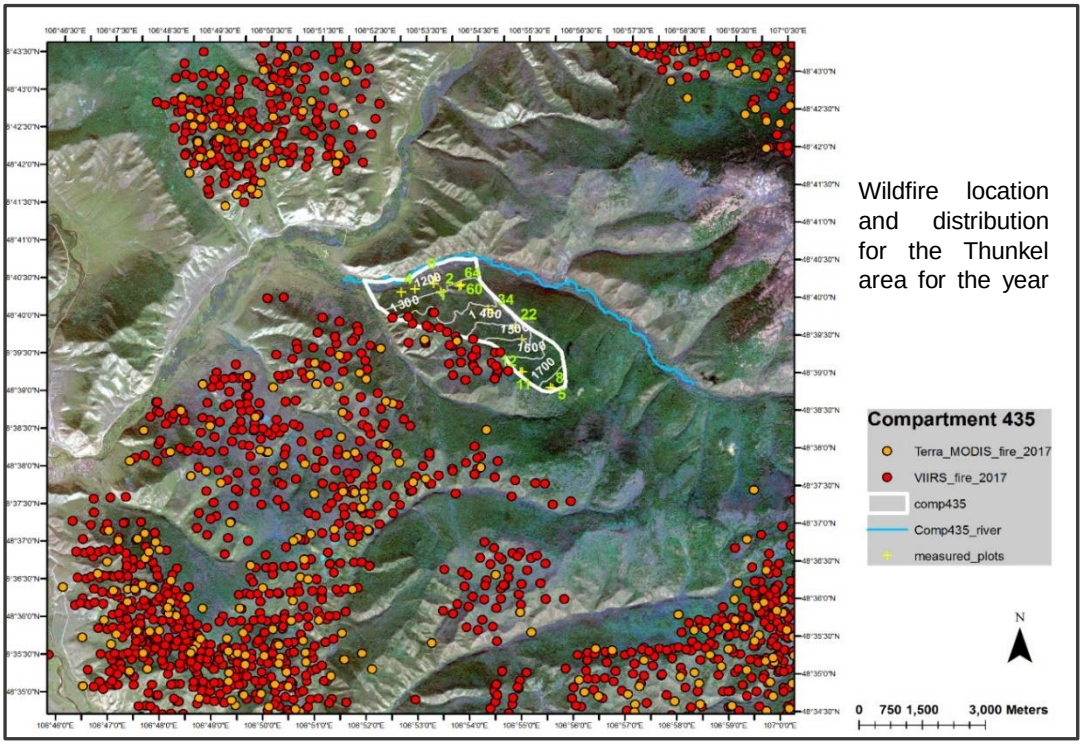

Wildfire location and distribution for the Thunkel area for the year

Figure 8.46: Extraction of areas affected by fires form the FIRMS database for the year 2017. Fires detected by the MODIS (orange spots) and VIIRS (red spots) sensors are indicated. Source: FIRMS, 2021.

Why is the analysis of the fire situation such an important issue to be considered, when talking about forest inventory and forest management?

In the pertaining literature several factors have been identified to cause long-term changes in the forest structures of the taigas with repercussions on the ecosystem as such. The main findings and hypotheses are:

- The occurrence of wildfires can potentially change the species composition and forest area distribution.
- Almost all forest areas within the Selenge Aimag have been subjected to fire and most certainly will be in the future with a changing climate happening. As such an increasing rate of the forests will turn from carbon sinks to carbon sources (see also REDD+).
- The effects of fires gravely influence the growth, yield, and timber quality.

In conclusion the impacts of fires in the past, present and future have to be take into account, when conducting forest inventories with the associated inferences for forest management practices.

High intensity forest fires can be a major cause for the degradation of the taiga forests and bear the potential to irreversibly induce a shift to the steppe grassland ecotone (Mühlenberg *et al.*, 2004). Between 2011 and 2013 around 1 Mio. ha of forested land were affected by wildfires (Ministry of Environment and Tourism, Mongolia, 2020). However, official figures need to be treated with caution. This is supported by observations by Teusan (2018: 31), Wyss (2007: 42), and myself – according to official records only a single fire occurred for the whole Aimag Selenge in 2017, whereas I experienced dozens of huge fires around Thunkel during my fieldtrip. In an exhaustive study Teusan (2018) looked into the gains and losses of forest areas due to wildfires occurring in the province of Selenge, Mongolia. Based on his analyses of satellite imagery in concerted action with data retrieval from credible sources (e.g., FIRMS, Hansen) he found, that not only fires have become a common feature in the Selenge province, but also that certain taiga areas get repeatedly afflicted within extreme short time intervals. For instance, forest patches around the test area of Bugant have been hit up to five times within a five-year period. The graph below illustrates his findings to also support the results of other undertakings, that about 30 to 50% of the total Selenge area are affected by wildfires annually (NFI report: Altrell and Erdenejav, 2016: 85). Teusan (2018) also states, that the northern slopes were generally more affected than the southern aspects. A possible reason for this clear ‘verdict’ is, that the MODIS and VIIRS satellite sensors require a certain amount of thermal radiation for fires to be detected. Since soil fires in grassland (mostly found on southern slopes

and representing little fuel load) are swift and emit relatively little thermal energy, those areas easily hit blind spots in the satellite thermal sensors.

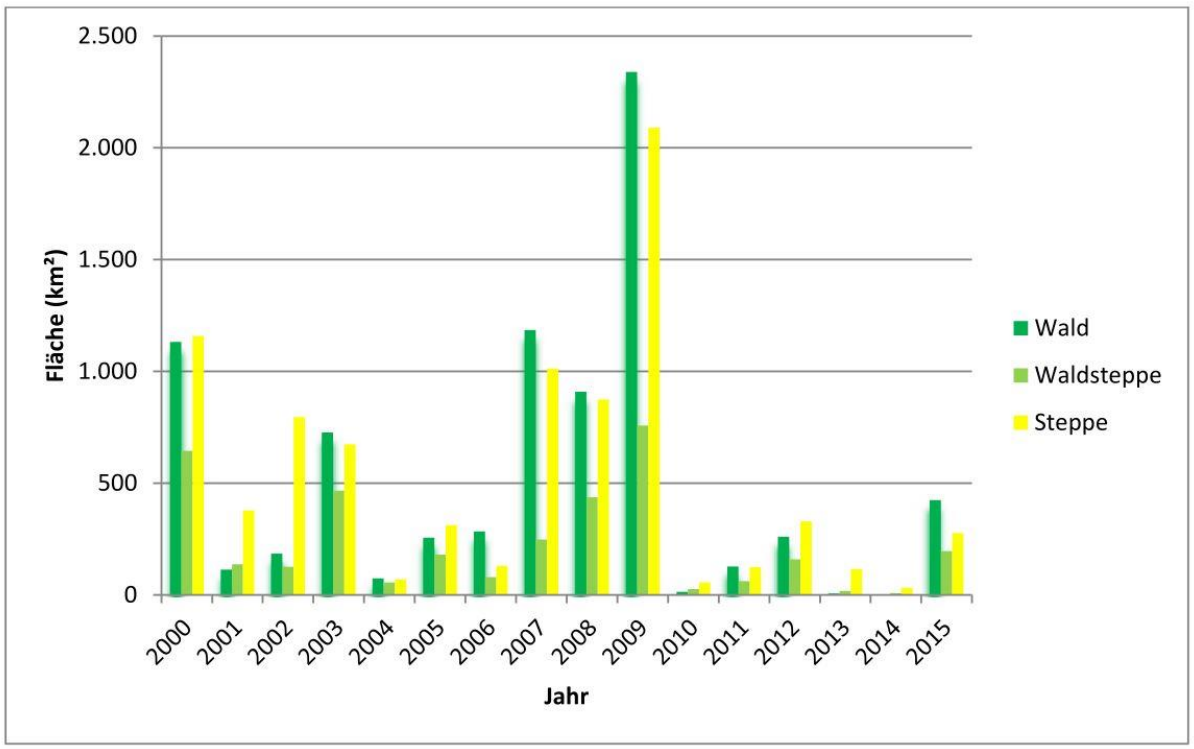

Figure 8.47: Fires detected by MODIS for the Selenge province with the associated affected areas calculated (source: Teusan, 2018:99). Designations are: Wald – forest; Waldsteppe - forest steppe; Steppe steppe; Fläche – area; Jahr – year.

Crown fires are known to be the most destructive form, whereas fires of low intensity (ground fires) promote the growth of fire tolerant tree species such as larch (Goldammer and Furyaev, 2010). Nonetheless, not only the intensity of the fires greatly determine the composition of the vegetation, but also the sequence of the occurrence. Goldammer and Furyaev (2010: 168–185) report intervals ranging from 10 to 33 years for the Western part of Siberia, whereas Byambasuren (2011) found intervals of 11.6 years for parts of the Khentii mountains in Mongolia. Several studies support the fact, that human-induced fires represent about 95% of all wildfires recorded, with lightning being the major natural cause (Byambasuren, 2018, Goldammer and Furyaev, 2010: 186–190, Schmidt-Corsitto, 2016, Tsogtbaatar, 2004a).

The marks of forest fires are not only conspicuous on the trees and on their remains, but also in the soil profile, where charcoal residues may remain. Wecking (2017: 51) conducted a study on the soil profiles in compartment 435 to find: ‘In opposition to GIZ assumptions that believed impact of wildfires to solely occur at light taiga sites (Schmidt-Corsitto, 2016), charcoal residues were identified at all C sites, as well as in the transitional zone (D) and dark taiga (E) further upslope’. A research team headed by Dr. Choima Dulamsuren took wood cores from

trees in compartment 435 in 2017. This investigation could shed some more light on the specific characteristics in the school forest; however, the analyses are still in progress. Nonetheless, Wecking's observations are quite in line with those made during my field survey in which I encountered fire marks on trees in virtually every sub-compartment (including dark taiga). Other authors report similar incidents. They state, that most of the forest stands surveyed show marks of historic or recent wildfire events and thus have a substantial impact on the species composition, the growth rate, and the structure of the forests (Goldammer and Furyaev, 2010: 186, Gradel, 2017, Gradel and Mühlenberg, 2011). Gunin *et al.* (1999) suggest regeneration periods of up to 200 years to be realistic because of the short vegetation period. Even-aged, huge forest stands show a typical low-structure type induced by high intensity fires (Goldammer and Furyaev, 2010: 1–20). Tree species such as birch, poplar and larch are very common in these light taiga forests. In contrast, gap-driven disturbance regimes are characteristic for dark taiga (Siberian pine, Siberian spruce) areas featuring a small-scale mosaic of varying tree age, DBH, and tree height (Gradel *et al.*, 2015, Gradel, 2017, Gradel and Mühlenberg, 2011, Schulze *et al.*, 2012). Disturbance intensity has turned out to be an important determinant of interspecific species competition. Fire intensity, but also regeneration and protection potential of the various tree species either favour species such as aspen and birch (coppicing) after stand replacing fires, or are conducive to larch and Scots pine due to their ability to better cope with ground fires thanks to their thick bark. Short intervals of ground fires apparently put a lot of strain on the thin-barked birch, thus giving pine and larch a competitive edge (Gradel *et al.*, 2015, Gradel and Mühlenberg, 2011). This is in contrast to the suggestions that regimes with short intervals apparently are favourable for pioneering tree species, like birch and poplar (Makoto *et al.*, 2007, Wyss, 2007). Yet, soil and crown fires burning with high intensity are also dangerous for thick-barked tree species (Gradel, 2017, Pausas, 2015, Pellegrini *et al.*, 2017). Interestingly, Undraa *et al.* (2015) observed no drastic changes in species composition about 10 years after big fires in the Central Khangai in 1996 and 2002. According to the authors, grazing seemed to have a much larger impact on larch regeneration than long-term effects of wildfires.

Climate also plays a pivotal role in driving disturbance regimes. According to Dulamsuren *et al.* (2011) extremely low temperatures and absent precipitation during the winter season seems to favour larch, since these climatic conditions keep insect populations low. In addition, sufficient rainfall towards the end of the vegetation period of the previous year and in the initial phase of the growing season of the current year proved to be particularly important for the growth increment of the trees. Current reports of the IPPC suggest rising temperatures for the main part of Mongolia, with grave impacts on the productivity of the light taiga species, and with an increasing rate of wildfires in the future (IPCC, 2020, Jolly *et al.*, 2015, Ministry of Environment and Green Development of Mongolia, 2014, Ministry of Environment, Japan,

2014). As water availability and soil moisture are higher in the dark taiga ecosystems, these higher elevations are expected to be less affected by a changing climate. After all, with the thaw of the permafrost as a dwindling water resource, even the dark taiga vegetation will have to tune in, and adaption strategies in terms of forest management need to be devised in general (Goldammer and Furyaev, 2010: 366–371).

In general, it is quite unfortunate, that only a very limited body of literature exists on the impact on wildfires on the taiga forests in Mongolia. Thus, many conclusions drawn on a limited number of samples and test plots remain somewhat speculative. The characteristics and the infrastructure of the GIZ school forest as being partly managed, over-exploited, or even untouched (dark taiga) presents this area as a perfect playground for the conduct of extended research, which is herewith encouraged.

The main objective of considering the wildfire aspect in the presented thesis has clearly not been to quantify in detail the damage caused in compartment 435, but to rather present a documentation on the situation back in 2017 to be exploited for further forest structure investigations. An in-depth assessment of the complex interaction between climatic conditions, topography, fire dynamics, forest structure, and human impact is proposed for future work to gain more insights into the nature of disturbances in the taiga forests.

8.6. Tree count

The number of trees in the field and the related identification of the tree species provide utile information for forest inventories, forest management, and the creation of growth models. The analysis of the tree density may also imply timely management and silvicultural interventions such as thinning or regeneration procedures. The various possible approaches of identifying and extracting tree numbers have been outlined in chapter 4.6.1. already. For the purpose of the presented study the (semi-) automatic methods of template matching and image segmentation were applied - for details on the methodology please see chapters 7.3.4.7. (UAV photos) and 7.3.5.5. (satellite imagery). The verification for the UAV photos was done on virtual inspection of the images (number of trees for photo 00445: 141, for photo 00088: 18). Satellite imagery verification was carried out on comparison with field data for the different test plots. The following graph represents quite impressively the ‘predicament’ of the template matching algorithms. With only the RGB bands available in an off-the-shelf UAV camera even the visual interpretation of the tree species and the segregation of the individual trees constitutes quite a challenge in the aerial photo of flying mission 007 – the flying altitude was 130 metres above ground. The photograph with the crosses superimposed shows the iteration procedure in finding the optimal template for the final matching. Apparently, the matching algorithm

struggles with the proper assignment of the crown structures to an individual tree – in most cases trees were identified as multiple objects.

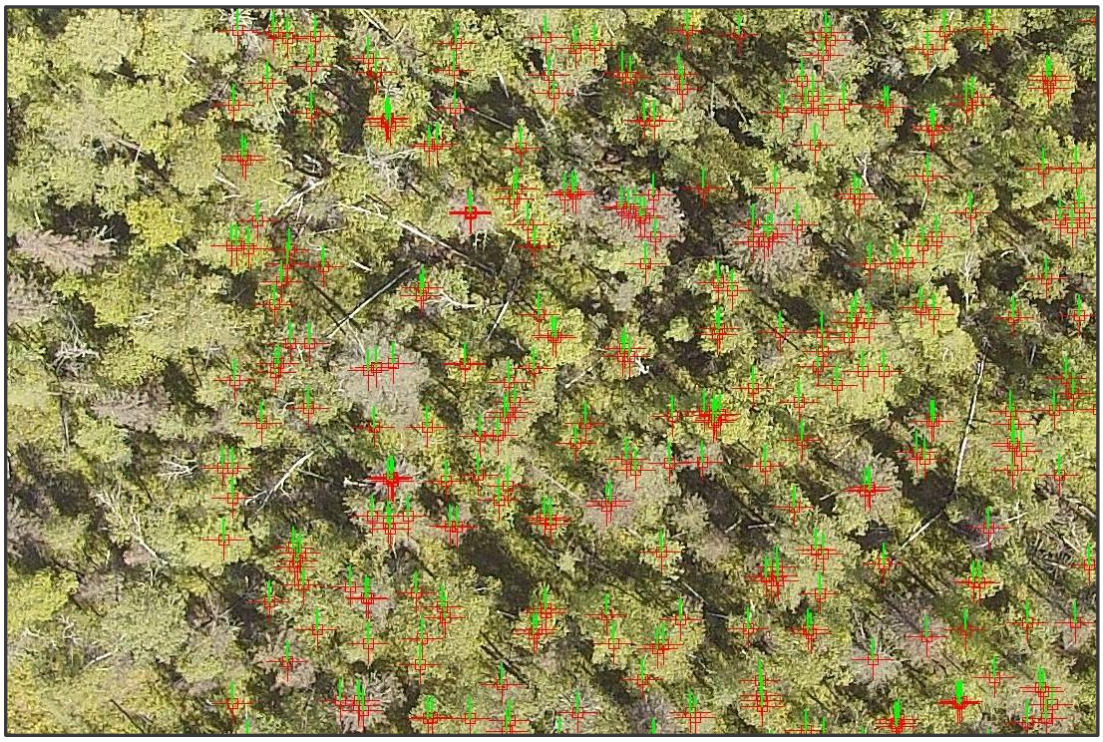

Figure 8.48: Template matching process illustrated in an UAV photo of flying mission 007 (flying altitude 130m above ground). Individual trees get identified as multiple objects (marked with crosses).

The graph below shows the application of the 'optimal' template matching constellation for the UAV photos of mission 1 (flying altitude 70m above ground) and mission 007 with a high flying altitude. Both images reveal, that some trees were correctly identified, others falsely designated, or even completely missed.

Figure 8.49: Template matching procedure applied for tree count. In both images (UAV image of mission 1 - left; image of mission 007 – right) trees are either correctly identified, falsely designated, or completely missed.

The results for all imagery used are portrayed in the bar chart below.

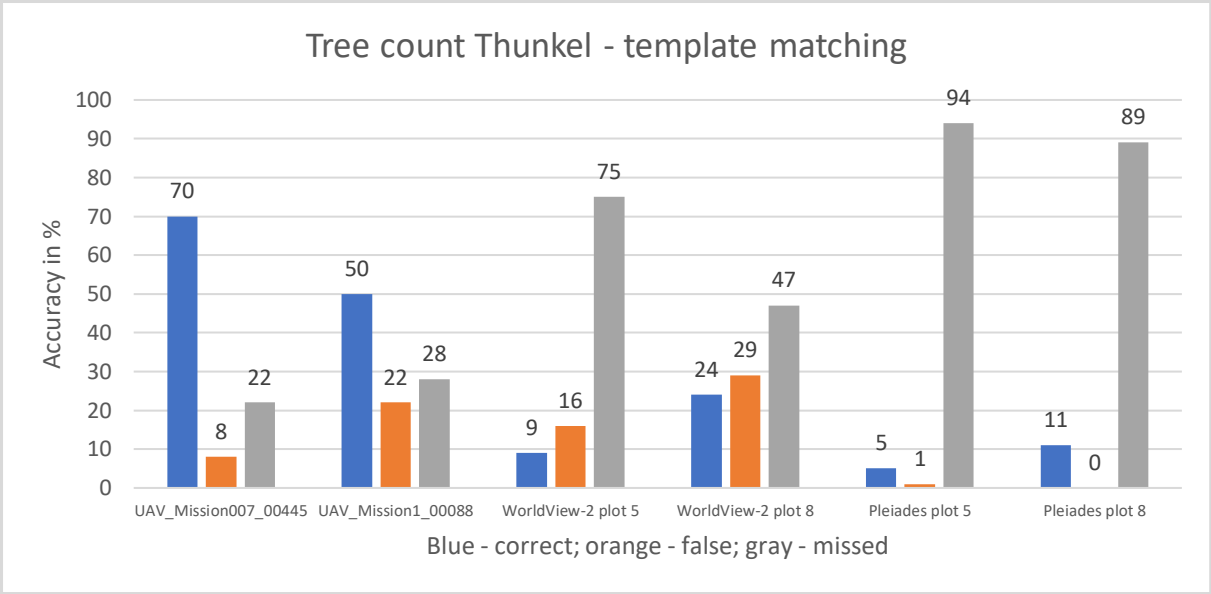

Figure 8.50: Template matching for tree count applied to UAV photographs, WorldView-2, and Pléiades satellite imagery.

Despite the relatively high spatial resolution the outcomes for the template matching in the satellite imagery are quite disillusioning. The rates for the missed tree individuals range from 75% to 94% in the WV-2 and the Pléiades images. Better detection rates can only be reported for the UAV photographs with an accuracy of 70% for the mission 007 image and 50% for the mission 1 photo. The higher identification rates for the high-altitude UAV image can be attributed to the fact, that (i) more trees are represented in the sample, and (ii) the mission 007 photo presents itself in an almost perfect nadir view, whereas the mission 1 image also depicts segments of trees (e.g., trunks) acquired form the oblique viewing angle. The off-nadir view might be conducive for a better tree species identification, however, makes it for the template matching algorithm extremely challenging to properly delineate tree crowns based on an unambiguous segregation process. The bar chart below depicts the outcomes for a different method applied, namely the image segmentation process. Segmentation was carried out using the scale factor of 10 for the WorldView-2 data. The corresponding figures for the field count are 86 individual trees for test plot no.5 and 45 trees for plot no.8. The difference between the outcomes for the template matching and the image segmentation approach is quite striking. For plot no.5 the performance of segmentation is 34% vs 9% for the template matching, whereas for plot no.8 the disparity is 91% vs 24%. The WV-2 image was acquired in winter featuring a low sun angle with long shadows, and trees not being represented in a nadir view. All in all, conditions were far from being perfect for a tree count. Nevertheless, the contrast of the outcomes makes the segmentation a clear winner over the template matching. The better performance in plot no.8 can be attributed to the fact, that the plot is more sparsely populated than plot no.5, thus facilitating object identification.

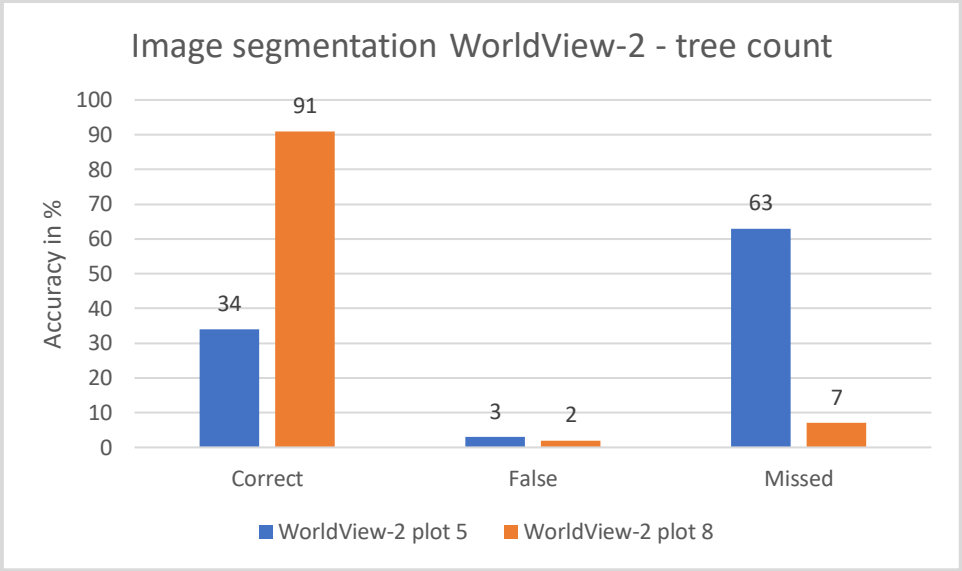

Figure 8.51: Image segmentation performed on WV-2 imagery for tree count.

Before we have a look at the existing publications related to the tree count methods applied and the results achieved, let us quickly wrap up the essentials of tree detection.

Commonly, tree detection is not being executed as a single measure, but rather in unity with (i) tree location detection and crown dimension parameterisation, and (ii) full crown delineation. All categories share the same necessity for accurate individual tree detection prior to crown delineation, since it greatly impinges the accuracy of the delineation process. In addition to the most simple way of identifying trees, namely the visual inspection, more sophisticated (semi-) automatic methods exist. Among the most important ones are:

- Local maximum filtering
- Image binarization
- Scale analysis
- Template matching
- Valley following
- Region growing
- Watershed segmentation.

A detailed description of these methods is given in chapter 4.6.1. In an extensive review by Larsen *et al.* (2011) the authors conclude quite unemotional, that so far no existing study has reported detection rates of 100%.

Several authors conducted studies on the detection and counting of oil palm trees by applying various methods. For instance, Daliman *et al.* (2015) favoured the template matching technique for extracting trees from a WV-2 image. The team achieved accuracies between 75.9 and 91.4% as compared to the reference data. The picture below illustrates an example of a tree count in oil palm plantations – the tree crowns with a distinct shape and regular spacing are much better suited for the template matching algorithms than irregularly shaped, overlapping tree canopies. Norzaki and Tahar (2019) looked into the performance of three different tree detection strategies. Oil palms in Malaysia were identified and counted with accuracies of 89% with the template matching process, 82% for using the Iso-cluster unsupervised classification, and with 96% for employing canopy tree segmentation. In contrast, Chemura *et al.* (2015) achieved only an accuracy of 69% for the correct detection of palm trees in WV-2 images by applying image segmentation. A slightly better result was obtained by Korom *et al.* (2014) for the WV-2 analysis – by using watershed segmentation procedures the accuracy was reported to be 77% as compared to the on-screen delineated tree crowns.

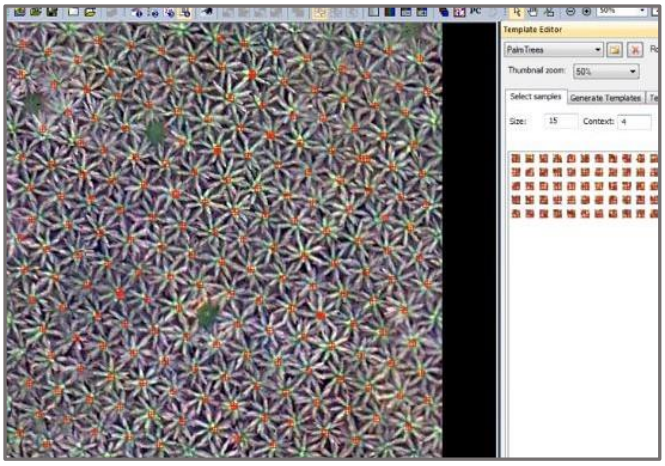

Figure 8.52: Template matching for oil palm tree detection. Example (WV-2 image) provided by Trimble eCognition (TemplateMatchingDemo, 2021).

With respect to the analysis of UAV imagery Nevalainen *et al.* (2017) observed an individual tree identification in a boreal forest varying between 40% and 95% related to the characteristics of the flown area (e.g. tree distribution). In another study Mohan *et al.* (2017) give account of 312 trees out of 367 conifers being detected correctly, with an omission error of 55 and a commission error of 46 individuals of the applied local maxima algorithm.

Moving to high-resolution satellite imagery Gomes and Maillard (2016) employed WV-2 images to correctly detect trees in (i) an urban environment and (ii) in orchards. Amongst other methods the team applied template matching for the identification process. The detection accuracies were 82% for (i) and 90% for (ii). They also conducted a review of other studies on the application of template matching to conclude, that (i) the performance of the algorithm is reduced in dense forests, and (ii) the recognition errors increase with the irregularity of the tree crowns. Local maxima and valley-following algorithms were administered by Gougeon and Leckie (2006) on Ikonos imagery to detect individual trees in a conifer plantation in Canada. The low detection rate of overall 67% was explained by the difficulties for the algorithms to

identify trees with various degrees of maturity. Another study was conducted by Gougeon *et al.* (2003) to favour Ikonos and Quickbird very high-resolution panchromatic imagery. It was subjected to valley following and local maxima filtering for tree detection in a boreal forest in Ontario, Canada. The detection rate was about 30% higher for the Quickbird imagery due to its higher spatial resolution.

Looking at aerial imagery, Erikson and Olofsson (2005) report detection rates of 80% in a boreal forest, when applying region growing and template matching strategies. Erikson (2004a) found that his segmentation results ranging from 73% to 95% largely depended on the segmentation strategy used and the type of forest flown. Katoh and Gougeon (2012) combined individual tree crown delineation with tree top detection technique and multispectral image classification to improve the detection rate of conifer trees in aerial imagery. Tree top detection rate was 67% for the local maxima filtering alone, with an increase of 22%, when amalgamating all three approaches.

An enormous number of studies has been published recently dealing with tree detection and crown delineation derived from LIDAR point clouds. Two of the most relevant ones are being considered in this chapter – for further reading please refer to chapters 4.1., 4.6.1., and 6.8.1.

Vauhkonen *et al.* (2012) carried out a comparative testing of single-tree detection algorithms under different types of forest employing airborne laser scanning (ALS). Considered were forests in the boreal zone, in the temporal zone, and the in the Brazilian tropics. For analysis applied were (i) k-means approach for cluster information, (ii) a voxel layer modelling algorithm, (iii) adaptive segmentation based on Poisson forest stand model, (iv) local maxima detection with residual height adjustment, (v) segmentation based on geometric tree crown models, and (vi) adaptive filtering based on CHM height values. The detection accuracies ranged from 45.2% to 100% with an overall average of 65%. The detection score was best for the plantation in Brazil (86%), followed by 75% for the mixed forest in Germany, 75% for the plots in Sweden, and 54% for the Norwegian test site. The authors conclude, that the algorithms showed similar performance, which was more attributed by forest structure (tree density and clustering) than by algorithm. A large-scale study (Kaartinen *et al.*, 2012) was conducted by a large team of researchers to assess various algorithms for the detection and extraction of trees using ALS (the so-called ‘tree extraction’ project organised by the EurSDR). Methods applied ranged from simple segmentation and manual extraction strategies to region growing and cluster analysis involving local maxima finding. In contrast to the study mentioned above, the authors ratiocinate, that the extraction method determines the accuracy, and that laser point density has lees impact on the detection success. In addition, they also state, that the structure of the forest assessed also plays an important role on the accuracies achieved.

There would be much more to relate and disclose in conjunction with findings on tree detection methods. The interested reader will find more on this subject in chapter 4.6.1. However, by having perused a substantial body of literature, it is with considerable ease to point out the most pivotal factors, when dealing with tree detection/count. Apparently, the type of vegetation (i.e. height, shape, tree density, separation of individuals, branching structure, etc.), image contrast, and the accuracy of the used CHM / point cloud are important determinants for the performance of the algorithms applied (Park *et al.*, 2014). Other sources of error are trees in the shade, tree intermingling, and smaller trees concealed by more dominant individuals (Gomes and Maillard, 2016). As a potential remedy for the outlined shortfalls and for attaining better results Zhen *et al.* (2016) suggest that active data (SAR, and LiDAR in particular) and the fusion of active and passive sensoring technologies become more and more prominent in tree crown detection and delineation (ITCD) studies. Since the common 2D imagery reflects certain limits, the novel approaches of active sensors provide much better insights in the 3D structures of the forests.

8.7. Extraction of crown diameter

The crown diameter as the circle enclosing the projection of the tree crown represents another relevant stand parameter. It helps to estimate tree development, space requirements of the specific species, evaluate carbon sequestration and determine crown radius – DBH relationships (Miranda *et al.,* 2018, Panagiotidis *et al.*, 2017, Yilmaz *et al.*, 2017). The diameter reflects the average of the measurement of the crown in two perpendicular directions (usually N-S; E-W). Crown diameter can be obtained through the manual measurement on the orthophoto in a GIS environment, or by extracting the corresponding figures from a 3D point cloud. Subsequently, segmentation techniques (e.g., region growing, or multiresolution segmentation) are exercised to delineate the shapes of the tree crowns and to calculate crown metrics automatically. It has become very common these days to perform the determination of the tree crown metrics in unity with the identification of the tree tops and the calculation of the tree heights.

Crown diameter extraction was only executed on the UAV imagery. The WV-2 winter image provides enough detail, however, only dark taiga areas are presented, where no crown diameter measurement took place. All other satellite imagery exhibits no features detailed enough for proper object indentification. As outlined in chapter 7.3.4.5. a combination of image segmentation and height extraction from a CHM was used for this study (eCognition). A manual extraction of the crown diameters in a GIS was not conducted. The segmentation process itself did not yield any satisfactory results. Having carried out a lot of trials with various CHM heights

for achieving best segmentation and thus crown delineation results, a tree height of 9 metres was found to be the most suitable to represent the bulk of the trees on the orthophoto. The graph below shows the results of the combined procedure.

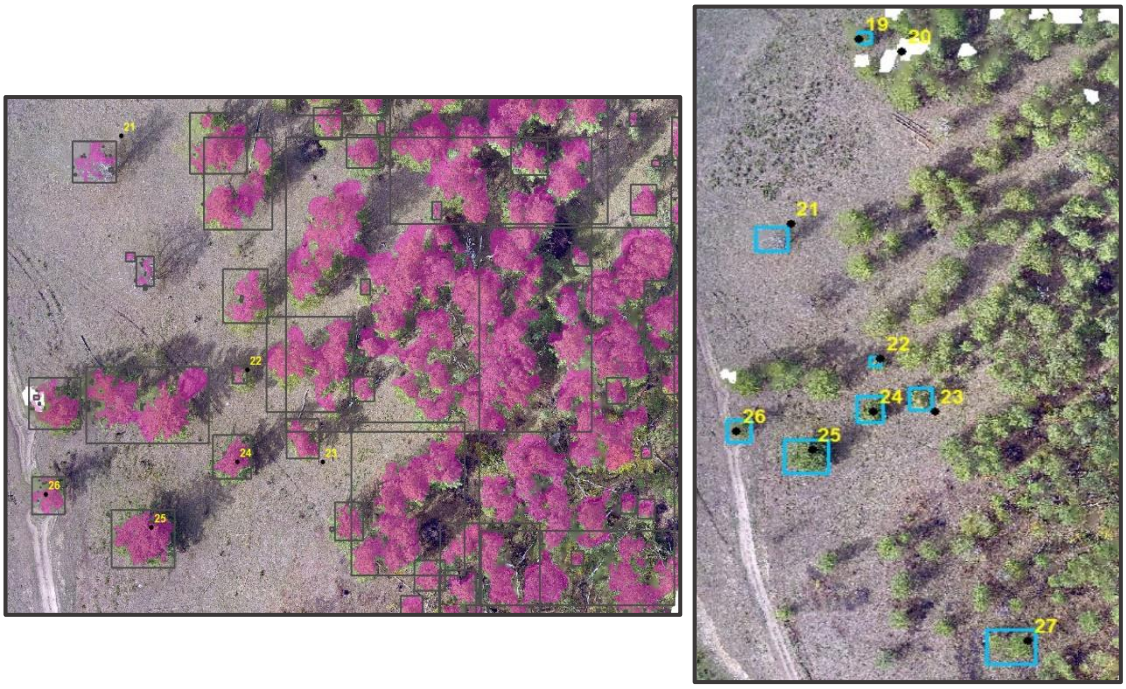

Figure 8.53: Results of the crown delineation and boundary boxing process for flying mission 1. The extraction procedure combined image segmentation with tree height extraction from the Canopy Height Model (CHM). Individual trees are well defined, whereas tree clusters are segregated not well (left). Resulting crown shape envelopes for individual trees are depicted on the right.

The left image proves without any doubt, that individual trees (e.g., tree no. 25, 26) can be identified and their crowns delineated very properly. A useful segregation of tree clusters, by contrast, is virtually impossible, especially when dealing with a wide range of tree heights and an intermingling forest structure. As a consequence, only the crown diameters of perfectly identifiable tree individuals were selected for comparison with the reference data. The tree crowns were then cloaked with rectangular boxes and the mean diameters calculated in ArcGIS. The graph below demonstrates the comparison between the automatic extracted crown diameter mean values from the orthophoto and the measurements carried out on site.

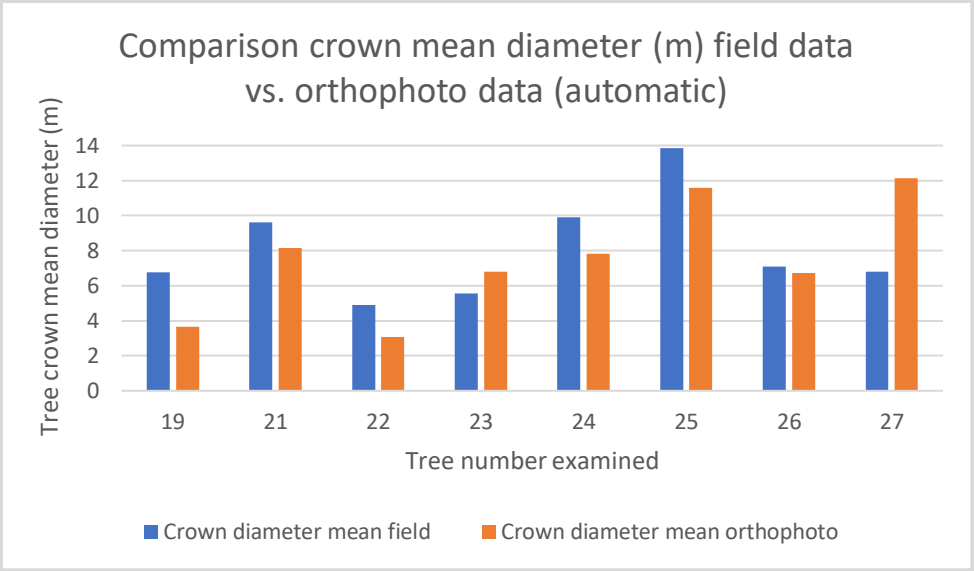

Figure 8.54: Comparison of mean crown diameter of selected trees as derived from the orthophoto of flying mission 1 with the calculated field data.

The outcome of above comparison shows a slight trend of underestimation of the mean crown diameter automatically derived from the orthophoto data. However, tree no.27 provides an example for a grave overestimate. This phenomenon could be partly explained on visual inspection by finding parts of the crown of the neighbouring tree reaching into tree no.27. The graphical representation below looks into the relationship between the mean diameter values for the field data and the derived data from the orthophoto. The calculated coefficient of determination (R^2) shows a value of 0.3783, which reflects a rather unsatisfactory performance. However, when deleting the outlier featuring the diameter pair of 12.12 / 6.8m, the R^2 value improves considerably to 0.7877. Although not being legitimate without good reason, the virtual deletion of an extreme outlier can result in a much-improved outcome demonstrating the leverage of such outliers. It must be taken into account however, that with the decision of considering the tree height (here: 9 metres) for the crown delineation procedure the true outline of the individual tree crowns gets truncated resulting in an overall smaller representation. Apparently, whenever automatic feature extraction is favoured, some part of the initial information has to be sacrificed as a compromise between efficiency and maximum accuracy.

As outlined in chapter 7.3.4.5. a manual extraction of the tree crown parameters had to be part of the assessment. The distance measuring tool in ArcGIS was used to determine the North-South and East-West diameters of the associated trees in the orthophotos to finally determine the mean diameter. The outcomes of the comparison with reference to the field data is provided below. The outlier in the graph can be attributed to the fact, that in the imported orthophoto the

tree itself appears rather blurred due to difficulties in the photogrammetric modelling process. As such, some guesswork was involved to precisely delineate the crown perimeter.

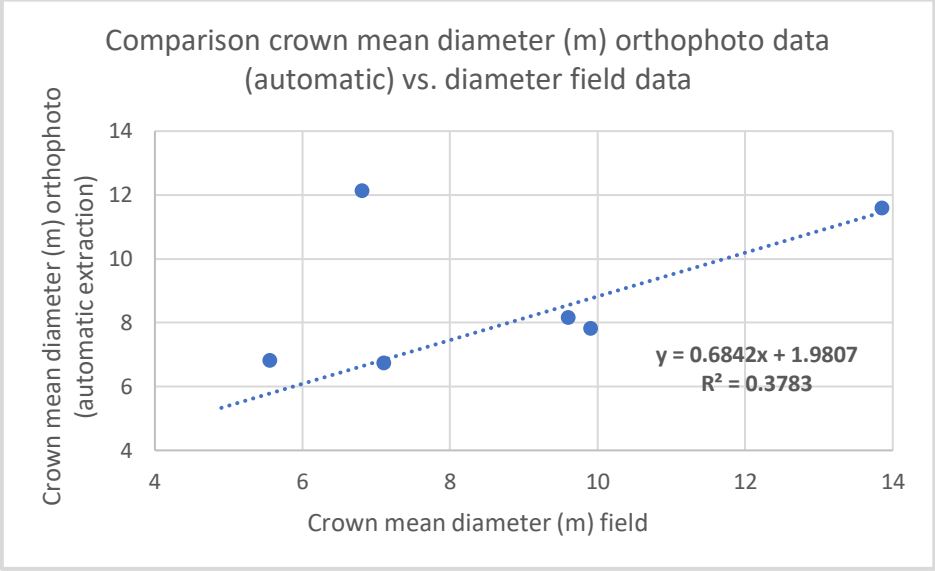

Figure 8.55: Tree crown diameter comparison between field data and orthophoto (automatic extraction) data.

With an R^2 value of almost 0.92 it is demonstrated, that the manual determination of the crown diameter is by far superior to the automatic extraction method discussed above.

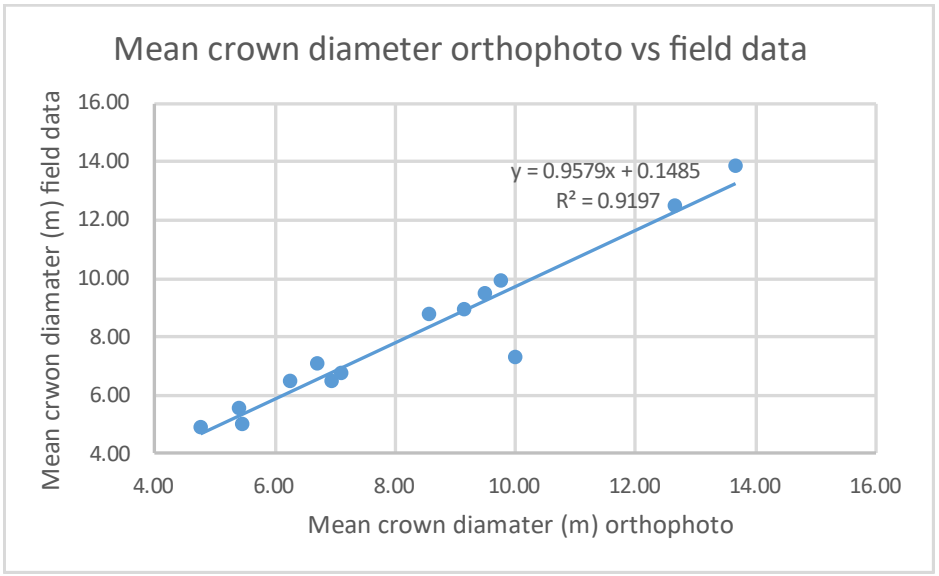

Figure 8.56: Tree crown diameter comparison between field data and manually extracted mean diameters from the orthophoto.

Despite the excellent results it needs to be taken into consideration, that the manual extraction might be more accurate, but it is most certainly more labour-intensive.

Let us now explore, what findings other authors have made in conjunction with the extraction of tree crown diameter.

Crown diameter (CD) estimation with strong a correlation (R^2 from 0.72 to 0.85) with regard to LiDAR systems can be found in Sankey *et al.* (2017) and Yin and Le Wang (2019). Panagiotidis *et al.* (2017) employed an RGB sensor piggy-backed on a UAV to obtain crown metrics from conifer dominated forest plots. Crown metrics were derived for a conifer forest in the Czech Republic using inverse watershed segmentation and height thresholds of 17m and 20m. The resulting crown boundaries were measured manually in a GIS resulting in an RMSE% between 14.29 and 18.56. The correlation ranged from 0.63 to 0.85 for R^2. The authors of this study reason, that their proposed method works well for homogenous (conifer) forest structures and larger tree crowns. However, they also realise that large tree crowns especially in deciduous trees feature several local height maxima resulting in a false attribution to an individual tree. Yilmaz *et al.* (2017) conducted an UAV flying mission over a small park in Turkey with trees in a regular array. They used multiresolution segmentation and region growing to extract crown diameters from the photogrammetric point cloud (CHM). This procedure resulted in RMS of 1.59m for the multiresolution segmentation and 1.76m for the region growing method. Pádua *et al.* (2018) also deployed an UAV aircraft to fly a patch of chestnut trees in a park in Portugal. They manually measured the crown diameters in a GIS to yield an excellent RMSE ranging from 0.60m (for the low flying altitude) to 0.37m (for the high flying altitude) – the associated R^2 values ranged from 0.91 to 0.96. High spatial resolution Quickbird imagery was employed by Ke and Quackenbush (2009) to calculate crown diameters. Their approach comprised an active contour segmentation method in combination with hill-climbing algorithms. The tree crown estimation errors were less than 0.5m for a Norway spruce plantation in Syracuse, New York. Another study on employing high resolution satellite imagery for tree crown delineation was conducted by Chemura (2012). His segmentation of WolrdView-2 imagery resulted in a delineation accuracy of 69% for an oil palm plantation located in Ghana. When examining other technologies, authors like Roberts *et al.* (2005) report on the performance of LIDAR used for the extraction of crown diameter in a loblolly pine plantation in the Mississippi area. They found an underestimate of 21% when deriving diameter from the point cloud. Popescu *et al.* (2003) also favoured LIDAR technology, when devising regression models for crown diameter estimation. Their calculated R^2 ranged from 0.62 to 0.63 for a mixed forest in the southeast of the UAS. Another team of authors made an attempt related to the automatic estimation of crown diameter in conifer trees. Their approach exploited the two-dimensional spatial wavelet analysis of LIDAR data to yield a coefficient of regression (*r*) of 0.86. The team assessed 30 individual trees within open canopy forests in the Moscow mountains, Idaho.

In the light of the findings by the authors mentioned above the outcomes of my crown extractions reflect a rather disappointing performance of the method used. This of course has to be seen in relation to the relatively small sample size used, the mix of conifer and deciduous trees, and the fact, that the tree height was integrated into the extraction model leading to an

underestimate of the crown diameter. Broad-leafed trees in particular impose an enormous challenge on the segmentation process. In a high number of cases I observed birch trees with split crowns during my survey. In my opinion a well experienced and trained image interpreter should be able to perform this task of crown delineation with much better outcomes as compared to automatic extraction techniques. Overall, I fully agree with most of the authors by concluding, that better extraction results can be obtained in more open forests, whereas poor performance is expected in denser vegetated areas (Guerra-Hernández *et al.*, 2016, Panagiotidis *et al.*, 2017, Sankey *et al.*, 2017).

8.8. Tree species determination

Tree species can be either be determined by visual interpretation, or by applying computer-aided techniques. Both approaches are outlined in the following.

8.8.1. Tree species extraction based on UAV imagery

First of all, the visual interpretation of the UAV imagery is dealt with. As described in chapter 7.3.4.1. UAV imagery taken at 150m above ground was ruled out for further visual interpretation due to the lack of quality of the photographs and the poor discernibility of the species. Instead, focus was on imagery taken at 70m above ground – no further image processing was required prior to interpretation. The following tree species were considered for the interpretation assignment: Siberian birch, Siberian larch, poplar and willow. Unfortunately, no acceptable aerial imagery was available for Siberian pine, Siberian spruce and Siberian fir (dark taiga). In total 36 trees were assessed based on the interpretation key devised and portrayed in chapter 7.3.4.1.

The trial yielded the following results:

Table 8-14: Classification result for visual interpretation of UAV imagery.

Classification result	**Correct**	**Incorrect**
Tree species		
Siberian larch	16	0
Siberian birch	11	0
Willow spec.	5	0
Poplar spec.	4	0
Total in %	**100**	0

The correct assignment of all tree species was expected with a ground resolution of a few centimetres and an image quality that high. However, the outcomes can be very different for aerial imagery taken at a high flying altitude. As mentioned in chapter 4.2. tree identification

results can range from 55% up to more than 95%, depending on the quality of the imagery and the training level of the interpreter (Ahrens, 2001, Carleer and Wolff, 2004, Heller *et al.*, 1964, Ke and Quackenbush, 2011b, Myers and Benson, 1981). For a well-trained expert with in depth knowledge on forestry and the associated local or regional conditions, obtainable outcomes can be quite impressive, of course depending on the level of the desired detail and prerequisites, such as quality of the imagery, spatial and spectral resolution (Hildebrandt, 1996: 303–305). Unfortunately, there are only a few studies specifically dealing with the achievable accuracies on visual interpretation issues, such as tree species identification. Most of them date back to the 1990s. Inter alia, Münch (1993) and Ahrens (2001) report identification accuracies for the most common European tree species of between 80 and 90%. Investigations in the USA have shown, that 14 different conifer and deciduous tree species could be identified on large-scale aerial photographs with a fidelity of about 95% (Heller *et al.*, 1964). Some authors also observed that the use of colour-infrared (CIR) or other multispectral imagery can also boost the correct identification of the tree species (European Commission, 2001) .

Secondly, the computer-aided classification was conducted with the outcomes presented. As mentioned in chapter 7.3.4.6. before this trial was based solely on personal interest, not so much to provide a sound scientific basis. The scatter plot below once again proves that a distinction between the classes (i.e., birch, larch, forest floor) is virtually impossible for the classifier to achieve.

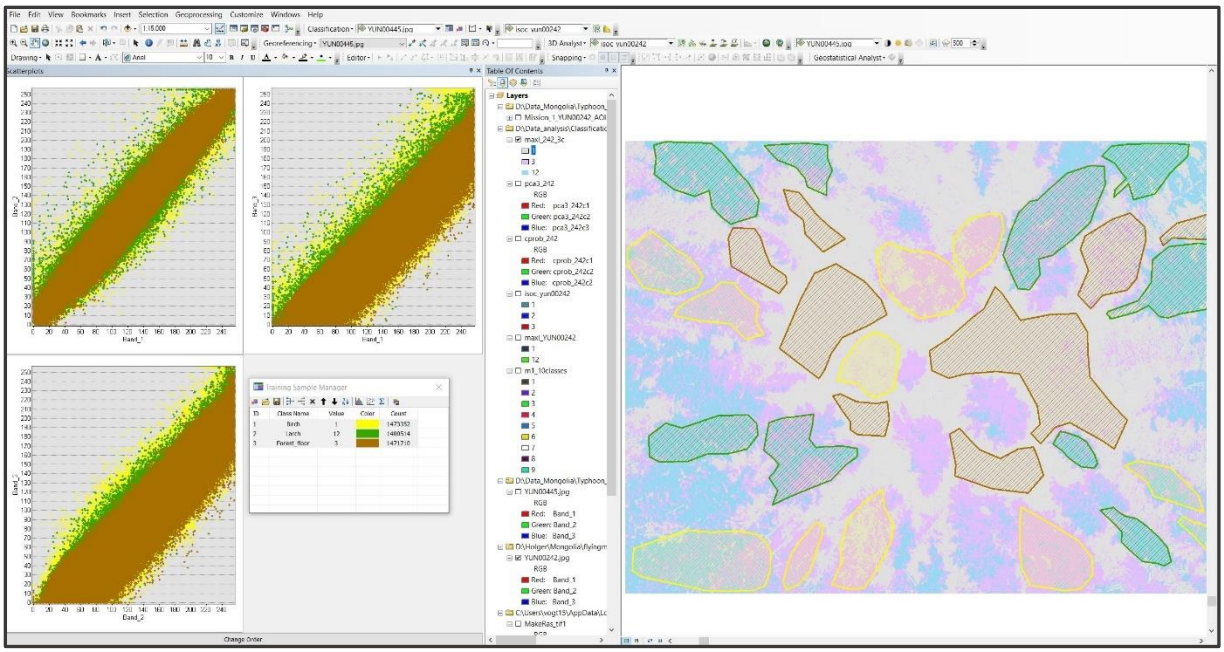

Figure 8.57: Flying mission 1 training areas. The scatterplot shows that no useful distinction between the classes birch (yellow), larch (green), and forest floor (brown) is possible in a standard RGB UAV image.

The classification result (Maximum Likelihood classifier) is furnished below.

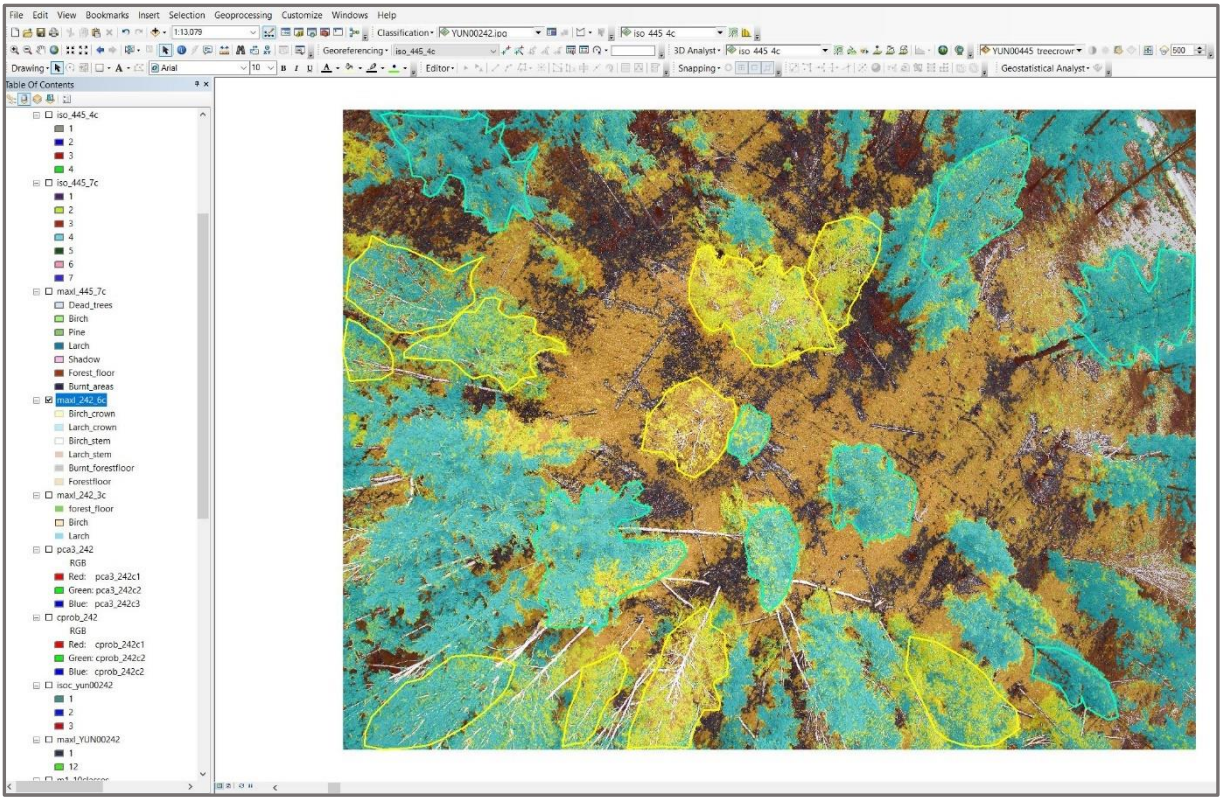

Figure 8.58: UAV very high-resolution image (60m altitude) of flying mission 1 classified using the Maximum Likelihood Classifier. The areas for training the classifier are superimposed. In most of the classified trees a mix of both tree species (birch – yellow; larch – green) is apparent.

Misclassifications are apparent – birches (in yellow) are classified as larches (in green) and vice versa. In addition, no clear assignment to any of the three classes materialised. In many trees there is a mix of all three classes, with forest floor characteristics found within the tree crowns. Due to the disastrous outcomes the creation of a classification accuracy matrix was spared.

The classification results of above UAV image demonstrate quite clearly the predicament of extremely high-resolution imagery, namely the failure to generate meaningful object discrimination, and to satisfactorily distinguish tree species based on a very limited number of spectral bands (i.e., RGB). The availability of at least a NIR band would most certainly yield much better outcomes, as demonstrated in various publications. Tree species classifications have been reported to be relatively successful, but those were performed on multi-, or hyperspectral imagery, which yielded good class separation in the spectral bands prior to classification.

8.8.2. Tree species extraction based on satellite imagery

As pointed out in previous chapters the correct classification of tree species is hinged on a variety of factors. The most relevant ones are (i) spectral separability of the defined classes, (ii) the quality and characteristics of the imagery with either a high spectral and/or spatial

resolution, (iii) the classification method applied, and (iv) the fidelity of the ground truthing reference data. In the following the outcomes are presented as tables and the explanations embellished with images corresponding accordingly.

As an important reference for the identification and delineation of the dark taiga the map below is provided, which is based on the NDVI analysis of the Sentinel-2 winter image. However, it needs to be noted that the WV-2 NDVI assessment is slightly more detailed due to the better spatial resolution and the less pronounced snow cover. According to the computation the dark taiga populates areas above about 1600m a.s.l., but it can also be encountered in specific depressions in the riparian zones.

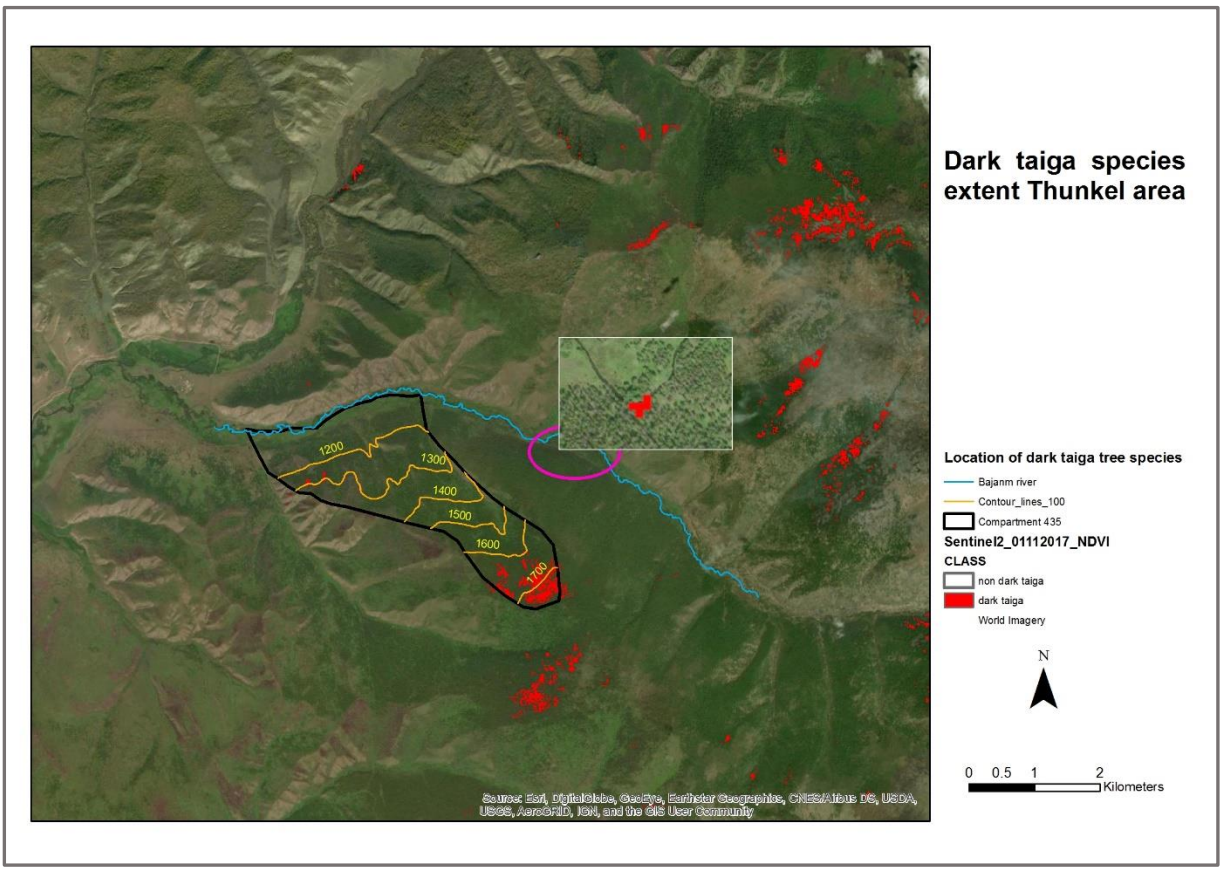

Figure 8.59: Distribution of the dark taiga in the Thunkel area based on the NDVI analysis of the Sentinel-2 winter image of 01.11.2017. The ellipse (magenta) and the inset highlight the occurrence of dark taiga in the riparian area.

8.8.2.1. Single tree species determination

The analysis of the very high-resolution satellite imagery was part of the initial classification trial. Based on the findings in the literature that image segmentation (OBIA) prior to the classification process largely improves the classification results, this method was applied first. Due to their salient spatial properties imagery of WorldView-2 and Pléiades were considered to qualify for the OBIA (object-based image analysis) approach.

The table below shows the results for WV-2 and Pléiades imagery for the less refined classes of light taiga (i.e., Siberian larch and Siberian birch) and dark taiga. All additional classes such as grassland, soil, etc. were introduced to reflect a much more realistic picture of the classification performance. However, as far as the calculation of the accuracy statistics is concerned, the accuracies are provided for the forest class solely, and the overall accuracy comprising all classes. In consideration of the table both classifiers (i.e., SVM and RF) perform equally well, showing only slight differences between WV-2 and Pléiades. Although the WV-2 features a better spatial resolution (1.8m vs 2.0m (resampled)), the broader bandwidth of the Pléiades sensor seems to have slight edge over the WV-2 in this case, with the bands Blue, Red, Green, and NIR used for both images. It is also quite enlightening to see, that although the WV-2 image was acquired in winter and the Pléiades scene in May, the spring image performs only marginally better than the WV-2 image. A much more interesting picture is reflected by the outcomes for the most specific assignment to the species, namely birch and larch. The results for both scenarios are entirely different, with the RF classifier outperforming the SVM by far (e.g., 64.28 % vs 35.71%). A closer look also reveals that the Siberian birch does not get well identified as such and is often misclassified as larch instead.

Table 8-15: Object-based classification of WorldView-2 and Pléiades imagery. The class definitions are more focused on tree specific traits.

OBJECT-BASED (OBIA)	Producer's Accuracy	User's Accuracy	**Overall Accuracy – Forest Classes**	Overall Accuracy – All Classes
WV-2 RF			**97.64**	98.79
Light taiga	100.00	98.32		
Dark taiga	94.89	100.00		
Grassland-soil	97.40	99.85		
WV-2 SVM			**97.64**	98.79
Light taiga	100	98.32		
Dark taiga	94.89	100		
Grassland-soil	97.4	99.85		
Pléiades RF			**98.34**	99.11
Light taiga	99.98	98.73		
Dark taiga	96.62	100		
Grassland-soil	97.83	99.92		
Pléiades SVM			**98.21**	98.64
Light taiga	99.79	98.25		
Dark taiga	94.42	100		
Grassland-soil	97.83	99.12		
Pléiades RF			**64.28**	64.28
Larch	70.58	80		
Birch	54.54	100		
Pléiades SVM			**35.71**	35.71
Larch	52.94	60.00		
Birch	09.09	33.33		

As discussed before, the spectral separability analysis already indicated a very challenging task for the classifiers to accurately assign the spectral signatures to specific classes. Since

birch and larch foliage features very similar reflectance properties the outcomes do not come to a surprise. The situation is even exacerbated by the fact, that due to defoliation processes in both tree species the spectral signatures represent a mix of tree and forest floor flora pixels. Moreover, only four spectral bands were available for the examination.

8.8.2.2. Dominant tree species determination

Since not all satellite imagery meets the requirements for single object (i.e., tree) identification, the tree species classes were extended to dominating classes, i.e., tree species such as larch and birch were merged. Apart from that, no pure larch stands or even smaller clusters could be distinguished during the field survey. The various results are illustrated in the table blow with the following denominations applied:

RF – Random Forest classifier
SVM – Support Vector Machine classifier
WV-2 – World View 2
S-2 – Sentinel-2

Var 1 – Sentinel-2 bands NIR, SWIR1, NDVI, NBR
Var 2 – Sentinel-2 bands NIR, SWIR1
Var 3 – Sentinel-2 bands SWIR1, NDVI, NBR
Var 4 – Sentinel-2 bands Green, NIR, SWIR1, NBR

Table 8-16: Object-based classification of Pléiades and Sentinel-2 imagery for dominant tree species.

OBJECT-BASED (OBIA)	Producer's Accuracy	User's Accuracy	**Overall Accuracy – Forest Classes**	Overall Accuracy – All Classes
Dominant species				
Pléiades RF				
Light taiga	76.50	27.13	**66.22**	66.22
Birch	57.17	89.09		
Dark taiga	100	100		
Pléiades SVM			**38.79**	38.79
Light taiga	66.11	15.24		
Birch	25.35	94.58		
Dark taiga	56.35	86.13		
Sentinel-2				
S-2 RF var 1			**87.23**	87.23
Light taiga	100.00	64.28		
Dark taiga	84.61	100.00		
Birch	85.71	100.00		
S-2 SVM var 1			**63.12**	63.12
Light taiga	50.00	20.93		
Dark taiga	100	100		
Birch	48.80	82.00		
S-2 RF var 2			**76.59**	76.59
Light taiga	50.00	36.00		
Dark taiga	100.00	100.00		
Birch	71.42	36.00		
S-2 SVM var 2			**54.60**	54.60
Light taiga	50.00	16.36		
Dark taiga	69.23	100.00		
Birch	48.80	82.00		
S-2 RF var 3			**87.23**	87.23
Light taiga	100.00	64.28		
Dark taiga	84.61	100.00		
Birch	85.71	64.28		
S-2 SVM var 3			**34.04**	34.04
Light taiga	00.00	00.00		

OBJECT-BASED (OBIA)	Producer's Accuracy	User's Accuracy	**Overall Accuracy – Forest Classes**	Overall Accuracy – All Classes
Dark taiga	100.00	81.25		
Birch	10.71	50.00		
S-2 RF var 4			**82.97**	82.97
Light taiga	100.00	52.94		
Dark taiga	100.00	100.00		
Birch	71.42	52.94		
S-2 SVM var 4			**54.60**	54.60
Light taiga	50.00	16.36		
Dark taiga	69.23	100.00		
Birch	48.80	82.00		

The table above reveals the following:

- In all presented cases the Siberian birch is by far the greatest underperformer in terms of correct assignment.
- The RF classifier shines out as the best classification approach.
- The band combination of NIR, SWIR1, NDVI, and NBR (i.e., variant 1) proves to be the most suitable.
- The results for the Pléiades imagery compared to the S-2 image suggests that the higher radiometric resolution of the latter is superior to the better spatial performance of the former.
- The application of the SVM on the S-2 imagery with variant 3 in place completely fails to properly identify the light taiga class.

In the following screenshots of the achieved classification results are provided and subjected to further discussion.

*Figure 8.60: Object-based classification of Pléiades image (10/05/2015). Random Forest (**RF**) classifier for dominant tree species classification was used. Classes depicted in graph: birch (yellow), light taiga (bright green), dark taiga (dark green), and grassland/soil (brown).*

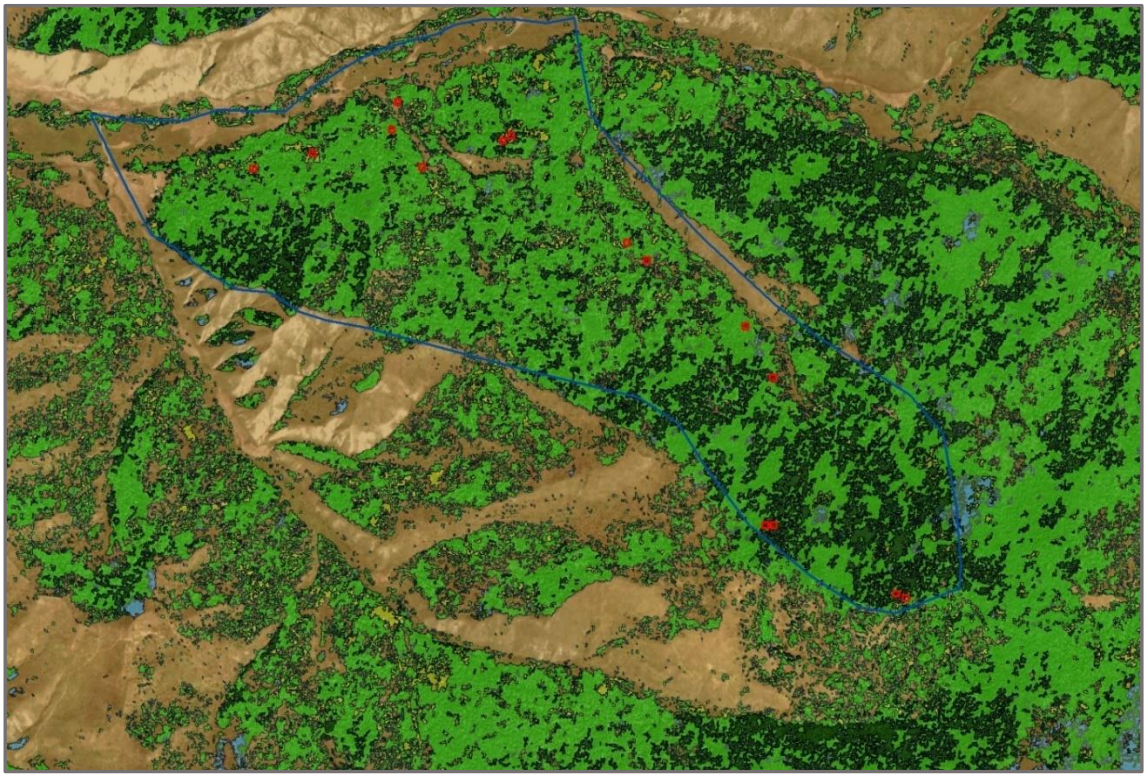

*Figure 8.61: : Object-based classification of Pléiades image (10/05/2015). Support Vector Machine (**SVM**) classifier for dominant tree species classification was used. Classes depicted in graph: birch (yellow), light taiga (bright green), dark taiga (dark green), and grassland/soil (brown).*

Both classification results set against each other demonstrate quite impressively, what huge difference the choice of an appropriate classification method can make. In the S-2 image with the SVM applied the birch areas have almost completely disappeared. This phenomenon is also reflected in the data above. Quite striking is also the evidence in finding the light taiga intermingled with and 'infiltrated' by patches of dark taiga. Right from the outset it was a major impetus and ambition to reveal all weak spots and snares of the various classification methods involved. For this reason, no tweaking and fine-tuning of the classifications was performed to avoid potential misinterpretations. It would have been easy to just introduce an altitudinal bracket for the correct identification of the dark taiga areas. However, the outcomes above prove without any doubt, that the segregation between dark and light taiga is far from being trivial.

In the images below the outcomes of the Sentinel-2 object-based classification is illustrated as an example. The lack of detail in comparison with the Pléiades imagery is apparent, however, the classes look more homogenous. At this point it is very important to advert to one of the pitfalls in accuracy assessment execution. Although 130 ground points were applied for verification, the calculated deviations from the 'true' value can be quite deceptive by potentially drawing an all-advised conclusion. For this reason, it is also crucial to cross-check with other sources representing the character of the object to be assessed.

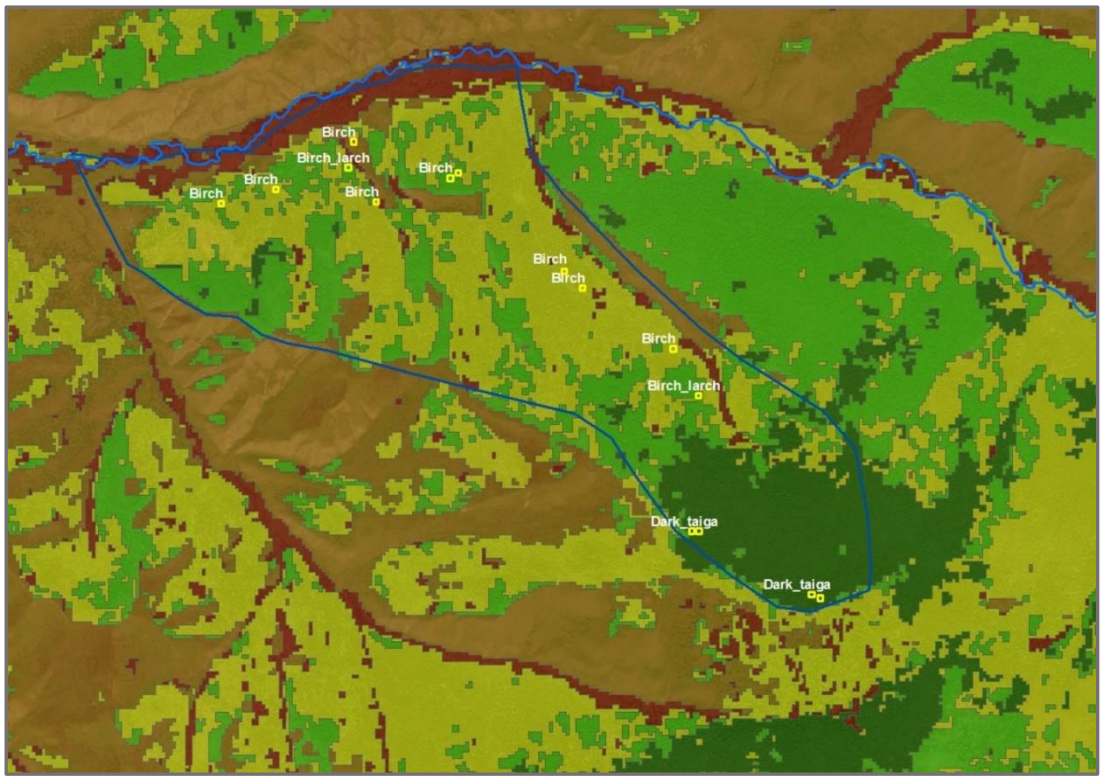

Figure 8.62: Object-based classification of Sentinel-2 image (09/07/2017). Random Forest (RF) classifier for dominant tree species classification was used. Classes depicted in graph: birch (yellow), light taiga (bright green), dark taiga (dark green), and grassland/soil (brown). Band selection of variant 4 (B12, B8, B3, NDWI) was used for image classification.

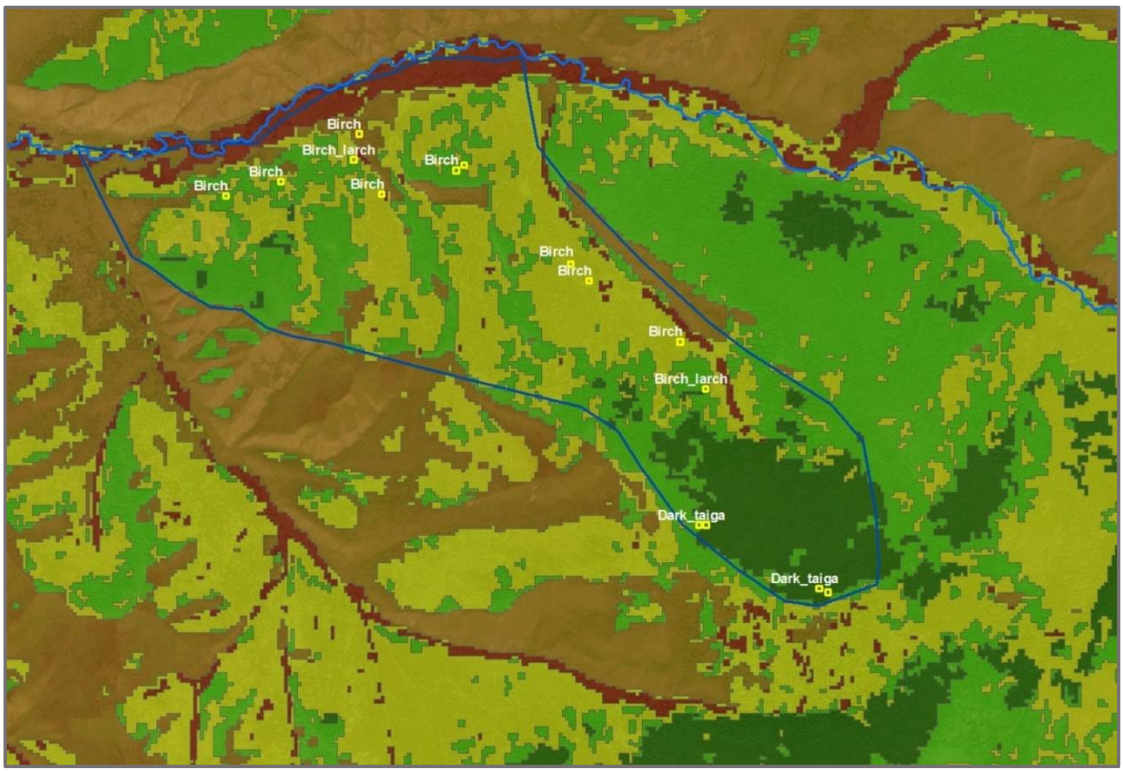

Figure 8.63: Object-based classification of Sentinel-2 image (09/07/2017). Support Vector Machine (SVM) classifier for dominant tree species classification was used. Classes depicted in graph: birch (yellow), light taiga (bright green), dark taiga (dark green), and grassland/soil (brown). Band selection of variant 4 (B12, B8, B3, NDWI) was used for image classification.

In the classified Sentinel-2 images (variant 4) the distribution and location of the dark taiga appears to be much more realistic than in the Pléiades image. In addition, the Siberian birch also gets a much greater share in comparison. However, both S-2 classifications reveal a different dark taiga pattern, particularly in the north-east of the maps. Since no verification data for those areas exist, any further inferences would be pure speculation. Very small patches of dark taiga in the northwest of compartment 435 are rendered – areas, where most certainly no dark taiga exists. This judgement rests on own on-site observations.

Regarding the analysis of the remaining variant constellations of the S-2 object-based classification the interested reader is referred to the brief portray below and the graphical representations provided in chapter 15.1.1.

Additional findings in Sentinel-2 object-based image classification:

- Variant 1: as for RF some trees south of compartment 435 were misclassified as grass; for SVM this was not the case; however, a patch within the dark taiga was misclassified as light taiga.

- Variant 2: as for RF too many areas were classified as dark taiga; for SVM once again some patches within the dark were misclassified as light aiga.
- Variant 3: as for RF too much light taiga patches are found in the dark taiga; for SVM in general the extent of green grass is inflated.
- Variant 4: see above.

Pixel-based image classification – dominant tree species

The pixel-based analysis comprised the classification of Pléiades and RapidEye imagery with all bands considered. The RapidEye imagery was incorporated in the pixel-based analysis for comparison with another study carried out in the Thunkel area. For the Sentinel-2 assessment the same setup like for the object-based method was exercised. However, a few more appraisals were introduced. The first one concerns the consideration of all 13 spectral bands, and the second one the variation in the number of verification points used (i.e., 130 and 300).

Table 8-17: Pixel-based classification of Pléiades and RapidEye imagery for dominant tree species.

PIXEL-BASED	Producer's Accuracy	User's Accuracy	**Overall Accuracy – Forest Classes**	Overall Accuracy – All Classes	Kappa Value
Pléiades RF; all bands			**81.73**	80.77	0.74
Light taiga	68.75	50.00			
Dark taiga	87.18	91.89			
Birch	74.07	88.89			
Dry grass, soil	90.09	100.00			
Green grass	100.00	62.50			
Pléiades SVM; all bands			**77.88**	77.69	0.70
Light taiga	68.75	36.67			
Dark taiga	94.87	90.24			
Birch	61.11	100.00			
Dry grass, soil	100.00	91.67			
Green grass	90.00	64.29			
RapidEye RF; all bands			**61.32**	63.84	0.52
Light taiga	37.50	23.08			
Dark taiga	92.31	64.29			
Birch	42.59	88.46			
Dry grass, soil	72.72	88.89			
Green grass	100.00	76.92			
RapidEye SVM; all bands			**64.42**	66.15	0.54
Light taiga	43.75	36.84			
Dark taiga	82.05	61.54			
Birch	51.85	82.36			
Dry grass, soil	81.81	90.00			
Green grass	100.00	66.67			

The classification of the Pléiades imagery supports the trend found for the OBIA for the RF classifier to be superior. The direct comparison with the outcomes for the dominant species assignment also illustrates, that the RF applied in the pixel-based mode outperforms the OBIA approach by far (i.e., 81.73% vs 66.22%). This observation also holds to be true for the SVM classifier (77.88% vs 38.79%). Although RapidEye's spatial resolution is inferior to the one of the Pléiades satellite sensor (i.e., 5m vs 2m MS (resampled)), the former features the RedEdge band as an additional response option. However, this does not seem to contribute to the improvement of the tree species assignment. In addition, the proper detection of the 'easy' classes of dry grass and soil apparently constitutes quite a challenge for some reason. In her investigation Zueghart (2017) employed the same RapidEye scene in order to get a distinction between dark and light taiga for the Thunkel surroundings. The achieved overall accuracy with a maximum likelihood classifier applied was 90% with a Kappa Index featuring a high value of 0.8. However, the author found the dark taiga areas to be inadequately represented. The created distribution maps reveal, that not only underrepresentation of the dark taiga constitutes an issue, but also the occurrence of dark taiga chunks within an area dominated by light taiga (e.g., in the northwest of compartment 435). In the graphical representation of the classification analysis further below it can be seen, that the intermingling of dark and light taiga is mainly due to the lack of spectral separability of the two classes. According to Zueghart (2017: 66) the specific illumination conditions (i.e. low sun angle in May in association with the occupation of forests solely on northern slopes) and the selection of the training samples can be considered large contributors to this phenomenon.

When looking at the results of the table below it is obvious, that not only the pick of the appropriate training samples is intrinsically linked with the classification outcomes, but also the number, quality, and distribution of the verification areas. In the first example, where all 13 bands were considered for the Sentinel-2 classification, the choice of employing 300 ground truthing points yielded better results for the overall accuracy in the forest, as well as in all classes appraised when compared to the 130-point variant. In addition, the selection of all 13 spectral bands lead to an overall best performance of the classification, irrespective of the classifier used (e.g., RF or SVM). Nonetheless, such performance is at the expense of computational time. For this reason, various other scenarios were devised for the reduction of the input data. The different variants comprising the different constellations of single band and vegetation indices have been portrayed above already.

Table 8-18: Pixel-based classification of Sentinel-2 imagery for dominant tree species.

PIXEL-BASED	Producer's Accuracy	User's Accuracy	**Overall Accuracy – Forest Classes**	Overall Accuracy – All Classes	Kappa Value
S-2 RF; 13 bands; 300 random points			**88.57**	78.98	0.74
Light taiga	61.53	93.33			
Dark taiga	96.29	86.67			
Birch	73.43	79.66			
Dry grass, soil	87.09	91.52			
Green grass	100.00	42.10			
S-2 RF; 13 bands; 130 points			**83.33**	85.38	0.80
Light taiga	76.47	48.15			
Dark taiga	100.00	97.50			
Birch	71.70	92.68			
Dry grass, soil	100.00	100.00			
Green grass	100.00	90.90			
S-2 SVM; 13 bands; 130 points			**88.68**	88.46	0.84
Light taiga	81.25	59.09			
Dark taiga	97.44	100.00			
Birch	79.63	93.48			
Dry grass, soil	100.00	91.67			
Green grass	100.00	83.33			
S-2 RF var 1			**76.42**	78.46	0.71
Light taiga	62.50	34.48			
Dark taiga	92.31	92.31			
Birch	64.81	92.11			
Dry grass, soil	100.00	100.00			
Green grass	100.00	76.92			
S-2 SVM var 1			**81.55**	80.77	0.74
Light taiga	37.50	40.00			
Dark taiga	100.00	84.78			
Birch	72.22	92.86			
Dry grass, soil	100.00	91.67			
Green grass	100.00	66.67			
S-2 RF var 2			**79.25**	80.76	0.74
Light taiga	81.25	40.63			
Dark taiga	92.31	97.30			
Birch	64.81	94.59			
Dry grass, soil	100.00	100.00			
Green grass	100.00	76.92			
S-2 SVM var 2			**82.86**	82.31	0.76
Light taiga	75.00	46.16			
Dark taiga	94.87	97.37			
Birch	70.37	92.68			
Dry grass, soil	90.90	100.00			
Green grass	100.00	66.67			
S-2 RF var 3			**79.25**	80.77	0.74
Light taiga	81.25	40.63			
Dark taiga	92.31	97.30			
Birch	64.81	94.59			
Dry grass, soil	100.00	100.00			
Green grass	100.00	76.92			
S-2 SVM var 3			**82.69**	82.31	0.82
Light taiga	62.50	43.47			
Dark taiga	94.87	92.50			
Birch	72.22	95.12			
Dry grass, soil	100.00	100.00			

PIXEL-BASED	Producer's Accuracy	User's Accuracy	**Overall Accuracy – Forest Classes**	Overall Accuracy – All Classes	Kappa Value
Green grass	100.00	66.67			
S-2 RF var 4			**81.90**	82.31	0.76
Light taiga	75.00	42.85			
Dark taiga	94.87	97.37			
Birch	68.52	94.87			
Dry grass, soil	100.00	100.00			
Green grass	100.00	71.43			
S-2 SVM var 4			**86.79**	86.92	0.82
Light taiga	68.75	9500			
Dark taiga	97.44	55.00			
Birch	79.63	93.48			
Dry grass, soil	100.00	91.67			
Green grass	100.00	83.33			

From above table various conclusions can be drawn:

1. The consideration of all 13 bands yields the best overall results (i.e., OA of 88.68% for forest classes; Kappa of 0.84).
2. In the object-based approach the RF classifier was the clear winner, whereas in the pixel-based method the SVM has proven to be superior.
3. As far as input data reduction is concerned variant 4 (i.e., Green, Near-Infrared, shortwave-Infrared, NBR index) outperforms all other variants. For the OBIA it was variant 1 for the most suitable option.
4. Variant 4 is a strong competitor for the 'all bands' solution (i.e., OA 86.79% vs 88.68%; Kappa index 0.82 vs 0.84).
5. The classes green grass and dry grass/soil have been identified perfectly.
6. Dark taiga assignments are all superb in all scenarios according to the figures.
7. Light taiga and birch class accuracies range from 37.50 to 81.25%, and from 64.61 to 79.63%, reflecting the challenging spectral signature overlap.

When moving away from the stern figures above, the graphics below offer the opportunity to gain an extended perception and comprehension of the 'intimacies' of a classification at a larger scale.

The classification conducted on the Pléiades images in general shows an overrepresentation of the dark taiga (SVM performs slightly better than RF) and a very low proportion of the birch class. As indicated above dark taiga is also to be found in light taiga territories.

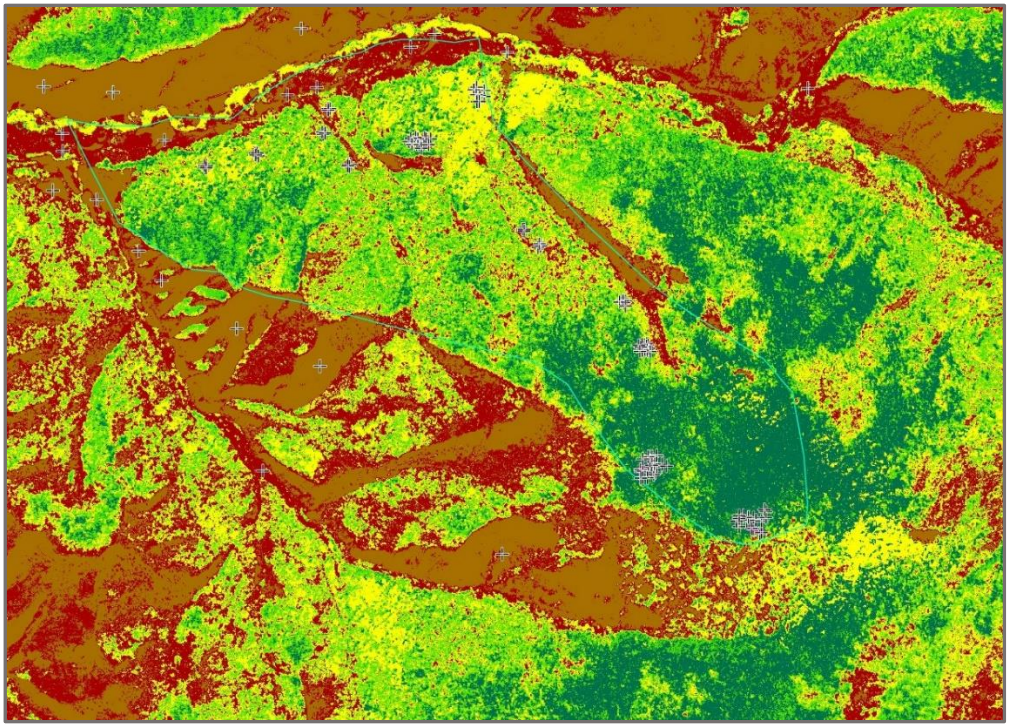

Figure 8.64: Pixel-based classification of Pléiades image (10/05/2015) – dominant tree species. Random Forest classifier was used for all bands. The classification verification points are marked with a cross. Portrayed classes are: birch (yellow), light taiga (bright green), dark taiga (dark green), dry grass/soil (brown), green grass (red).

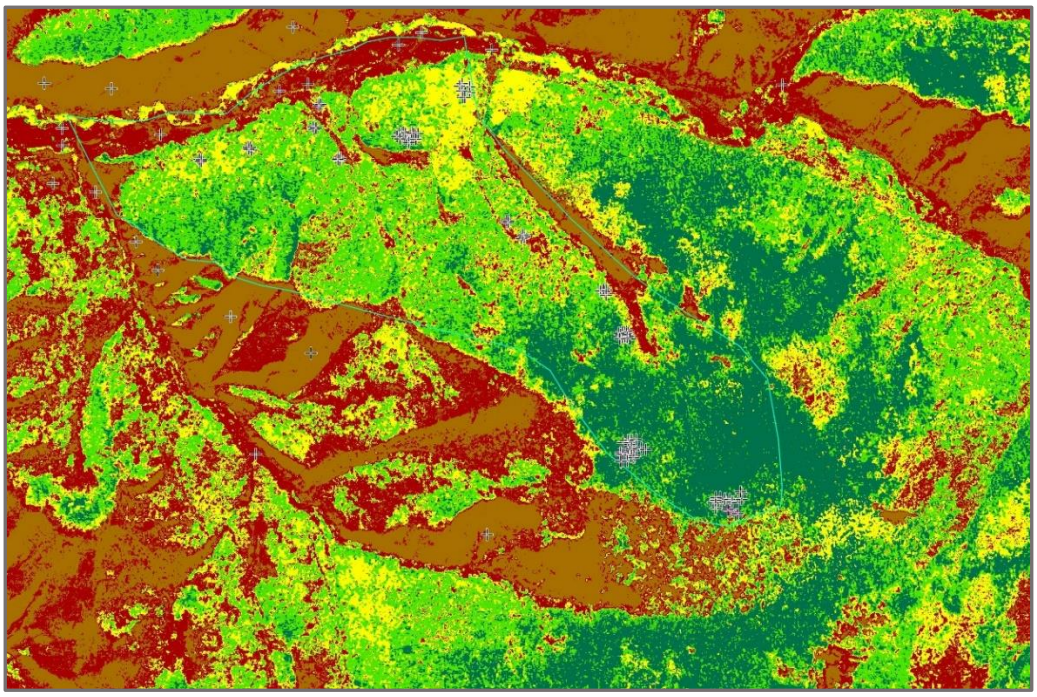

Figure 8.65: Pixel-based classification of Pléiades image (10/05/2015) – dominant tree species. Support Vector Machine classifier was used for all bands. The classification verification points are marked with a cross. Portrayed classes are: birch (yellow), light taiga (bright green), dark taiga (dark green), dry grass/soil (brown), green grass (red).

In the RapidEye classification the SVM approach seems a bit more realistic with the dark taiga not dominating the scenery - the birch also has a bigger share.

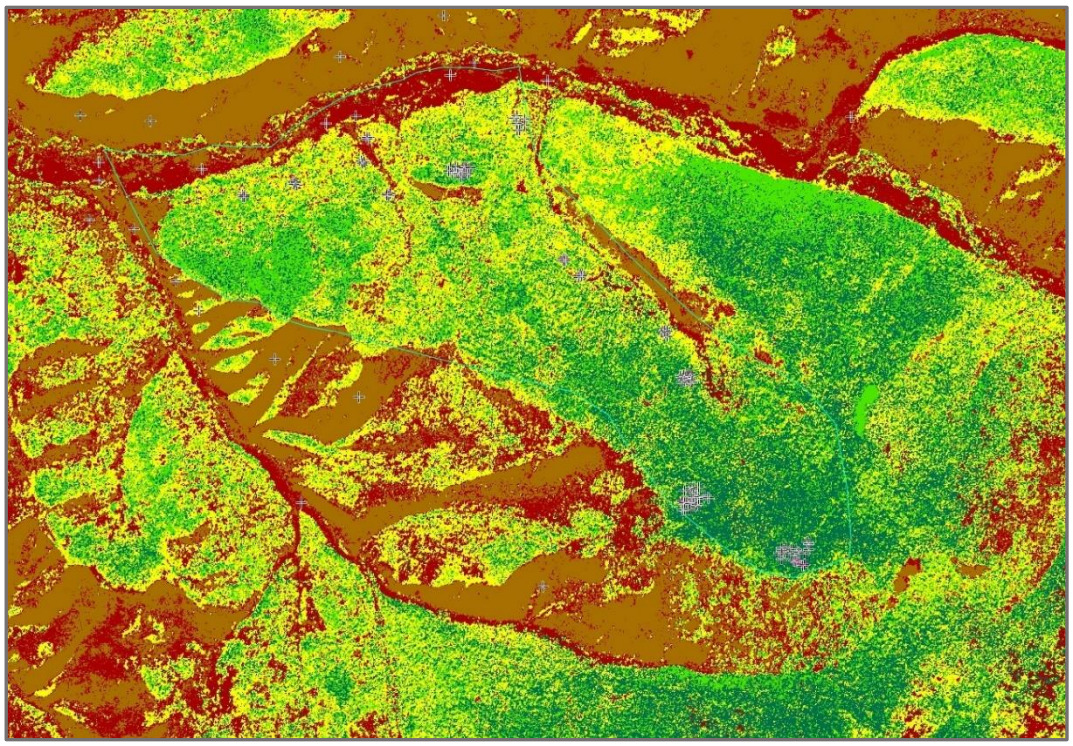

Figure 8.66: Pixel-based classification of RapidEye image (17/09/2015) – dominant tree species. Random Forest classifier was used for all bands. The classification verification points are marked with a cross. Portrayed classes are: birch (yellow), light taiga (bright green), dark taiga (dark green), dry grass/soil (brown), green grass (red).

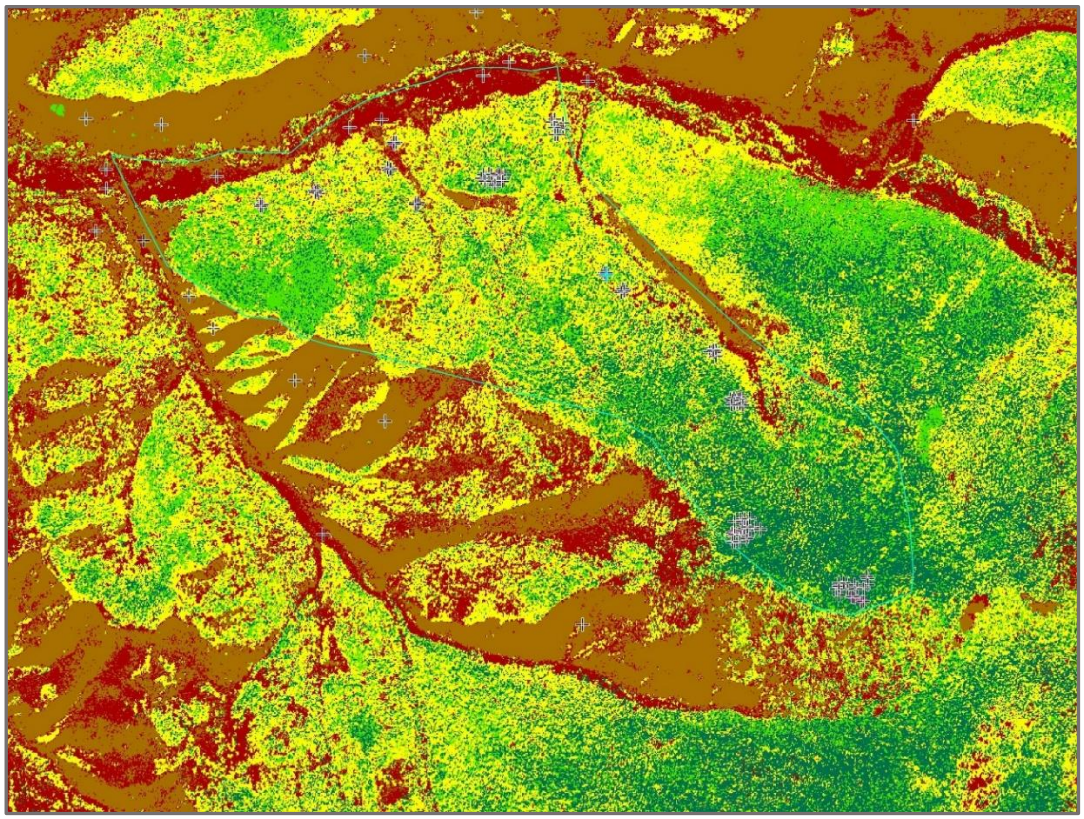

Figure 8.67: Pixel-based classification of RapidEye image (17/09/2015) – dominant tree species. Support Vector Machine classifier was used for all bands. The classification verification points are marked with a cross. Portrayed classes are: birch (yellow), light taiga (bright green), dark taiga (dark green), dry grass/soil (brown), green grass (red).

However, the contribution of the dark taiga in general is out of proportion. In contrast, the Sentinel-2 classification reveals a much better dedication to a realistic distribution of all classes, although displaying a much coarser spatial resolution. When compared to the NDVI winter representation the dark taiga areas exhibit a fairly good match. Nevertheless, some dark taiga patches are found in zones, where it most certainly exceeds its natural range (e.g., northwest of compartment 435). The birch areas reflect a good representation of its habitat and the green grass and dry grass/soil delineations appear to be near to perfect. The difference in performance between RF and SVM evidently is marginal on visual inspection.

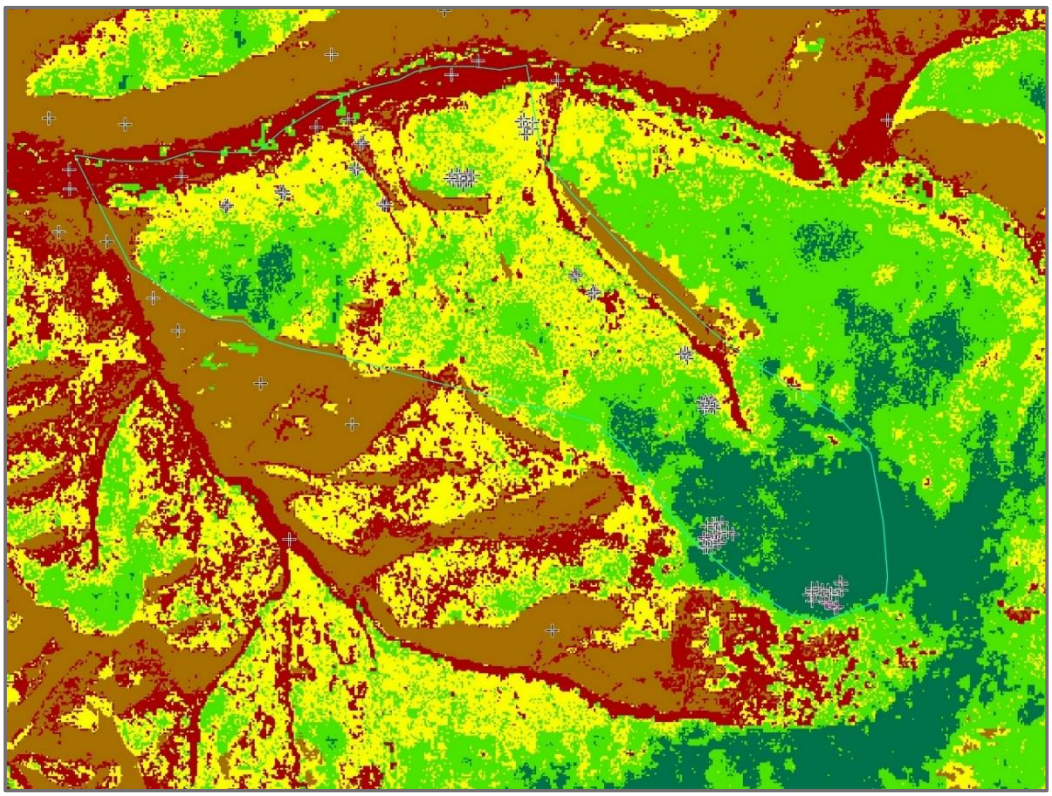

Figure 8.68: Pixel-based classification of Sentinel-2 image (09/07/2017) – dominant tree species. Random Forest classifier was used for bands variant 1 (B8, B11, NDVI, NDWI). The classification verification points are marked with a cross. Portrayed classes are: birch (yellow), light taiga (bright green), dark taiga (dark green), dry grass/soil (brown), green grass (red).

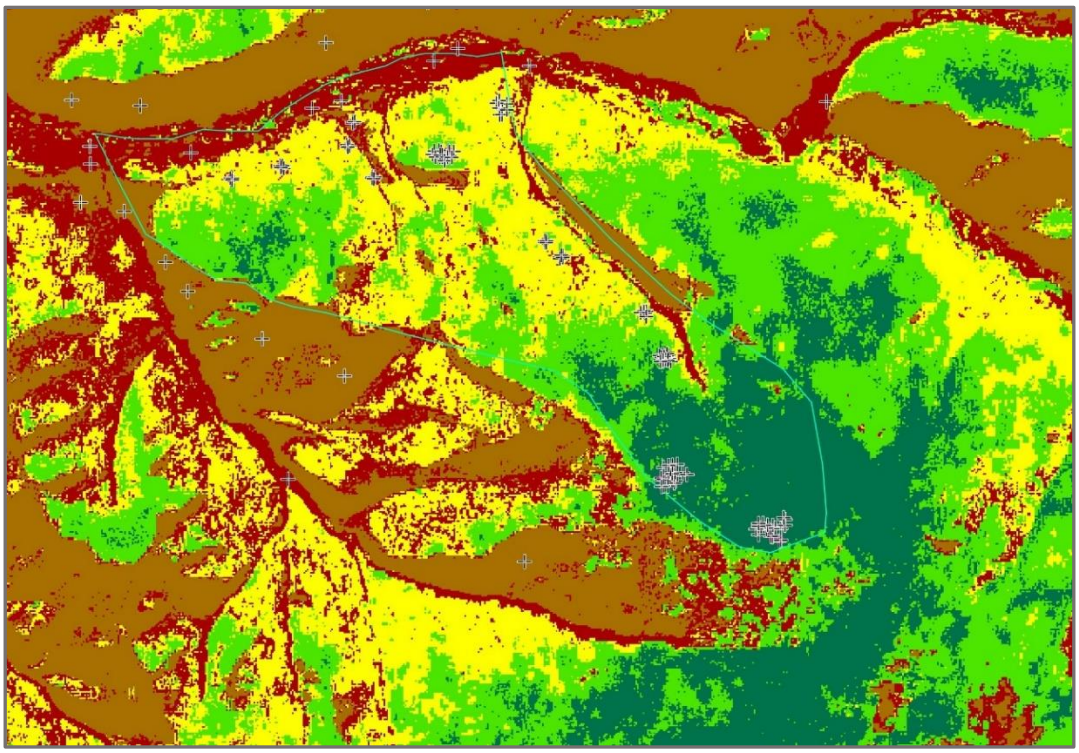

Figure 8.69: Pixel-based classification of Sentinel-2 image (09/07/2017) – dominant tree species. Support Vector Machine classifier was used for bands variant 1 (B8, B11, NDVI, NDWI). The classification verification points are marked with a cross. Portrayed classes are: birch (yellow), light taiga (bright green), dark taiga (dark green), dry grass/soil (brown), green grass (red).

To avoid overload of the thesis the interested reader is referred to the graphical representation in Appendix chapter 15.1.2 for the further classification results on the remaining variants. In denial of the confinements the most relevant observations are shared herewith:

- Variant 1: both SVM and RF yield excellent results in general, however, dark taiga has been classified in areas, where this forest type simply does not occur naturally.
- Variant 2: as for SVM too many areas were classified as territories occupied by birch – this is not commensurate with my personal observations.; the dark taiga areas are slightly better represented by the RF classifier, but the assignation of the green grass zones is out of proportion.
- Variant 3: once again, the RF classifier yields marginally more realistic dark taiga areas compared to SVM.
- Variant 4: this variant excels in all respects. The only difference between SVM and RF classification is that the former displays a bit less dark taiga, than the latter, which is closer to reality.
- All 13 bands used: the outcomes looked extremely promising initially for both SVM and RF, as confirmed by the statistics. There seems to be no misclassification of the dark

taiga, as there is no proof of this forest type to exceed its natural range. However, this remarkable accuracy comes to the expense of the trees being undetected in the riparian areas (see graph below).

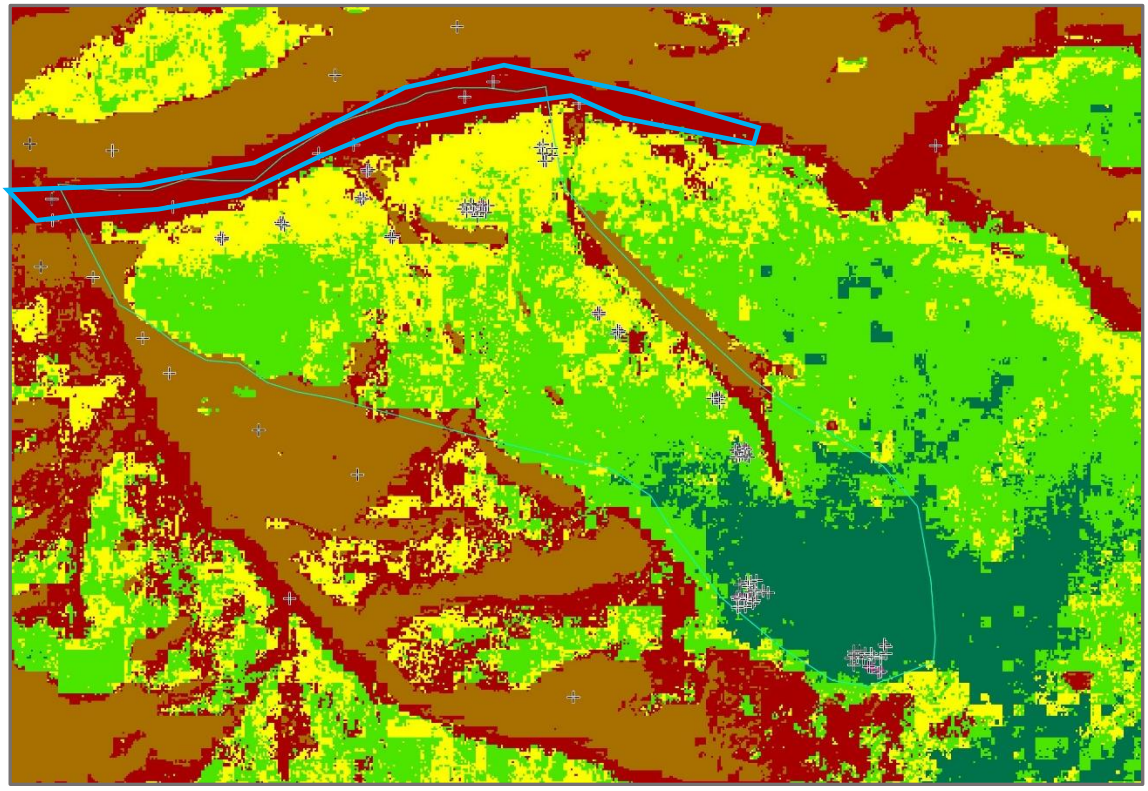

*Figure 8.70: Pixel-based classification of Sentinel-2 image (09/07/2017) – dominant tree species. Support Vector Machine classifier was used for all **13 bands**. The classification verification points are marked with a cross. Portrayed classes are: birch (yellow), light taiga (bright green), dark taiga (dark green), dry grass/soil (brown), green grass (red). The classification reflects the best outcomes for dark taiga detection, especially with no misclassification displayed in the northwest of compartment 435. However, almost all trees are missed in the riparian zone (see polygon in blue).*

The most relevant conclusions of the image classification are as follows:

- There is no 'one-size-fits-all' classifier.
- Both machine learning classifiers (i.e., RF and SVM) generate excellent results, with RF performing slightly better in an OBIA environment, whereas SVM works better for pixel-based analysis.
- The utilisation of all spectral bands yielded the best overall classification results. However, the selection of the most relevant spectral bands (R, NIR, SWIR) in combination with vegetation indices (NDVI, NBR) resulted in similar classification accuracies.

- Image segmentation works best for high-, and medium-resolution imagery. UAV photographs with a resolution of 3 centimetres displayed many over-segmented areas (i.e. split tree crowns), which was detrimental for subsequent classification.
- The dark taiga class is over-represented in all imagery and classification modes.
- Illumination conditions and topography, in conjunction with shadow occurrences within the forest affect classification (e.g. shadow areas in forest misclassified as dark taiga).
- Poor separation of birch and larch (light taiga) class is due to overlap of spectral signatures.
- Dense undergrowth of grass and shrubs, as well as the defoliation of trees have an impact on the class identification and segregation.
- Dark taiga not only occurs in elevations above around 1550m a.s.l., but also populates ecological niches in the riparian areas.

In the following the findings are discussed in relation to the literature published. On closer inspection of the publications on tree species classification, it becomes clear that the following factors are amalgamated, defying any clear cause – effect assignment:

- Image pre-processing (e.g., atmospheric correction)
- Topography
- Illumination conditions / sun angle (shadows)
- Forest understorey
- Image classifier
- Image segmentation parameters
- Temporal, spatial, radiometric resolution
- Tree density and forest structure (vertical, horizontal)
- Tree species
- Selection of spectral bands and indices
- Quality and quantity of training and verification areas
- Tree defoliation / tree damages

With respect to the object-based classification (**OBIA**) the classification results in this study ranged from being high for the high-resolution imagery to being very poor for the UAV images. Over-, and under-segmentation were the main causes for the lack of performance in some images. In addition, the quality of the training samples made an impact on the outcomes. These observations are shared by authors like Aguilar *et al.* (2013), who report that the analysis of GeoEye-1 and WorldView-2 images yielded overall accuracies of between 89% and 83%, when looking at urban environments. According to them the accuracy of the classification is driven by three main factors, namely (i) sensor used, (ii) sets of image objects employed, and (iii) the size and quality of the training samples to feed the classifier. Deng *et al.* (2014) found improvements of up to 34% compared to pixel-based classification of WorldView-2 imagery for the identification of tree tops in the Purple Mountain National Park close to Nanjing, China.

Yan *et al.* (2006) found even a higher gain (36.77%) when classifying land cover from 15m ASTER datasets. In his investigation on tree species determination from multispectral UAV imagery Franklin (2018) reports classification accuracies of 50% to 60% for pixel-based classifiers, and 80% for OBIA. The relatively good results were achieved by using a multispectral instead of a consumer-grade RGB camera. In addition, the flying altitude was 120m above ground generating much smaller objects as compared to my flying missions. As such, the unsatisfactory outcomes of my trials have to be seen in the light of the use of an RGB camera in conjunction with a low flying altitude. Hajek (2004) confirms excellent classification results (i.e. 95%) for tree species discrimination extracted from 4m Ikonos imagery. OBIA was also applied to WorldView-2 images in the study presented by Karlson *et al.* (2014). The overall detection rate for individual tree crowns in a managed forest in Burkina Faso was 85.4%, with lower accuracies in areas featuring high tree density and dense understorey vegetation. Machala and Zejdová (2014) applied OBIA for forest classification of aerial imagery. According to them the overall accuracy of almost 90% deteriorated to a mere 70% by integrating tree height information into the classification process. The authors address high tree density (i.e. low object separation) and poor tree height class definition as major culprits for mediocre outcomes. Kavzoglu and Yildiz (2014) report good OBIA classification accuracies for aerial and Quickbird-2 imagery to discriminate several land use features. An important observation of the authors was, that segmentation parameters have a direct effect on the classification accuracy, with low scale-shape combinations generating the best results. This view is extended by Karakis *et al.* (2006) and Dong *et al.* (2020), who suggest not to neglect sun elevation and topography when selecting segmentation parameters. In an extensive survey Myburgh and van Niekerk (2014) investigated the performance of various classifiers in an OBIA environment in relation to the size of the training set. They deduce that: (i) the performance of all the classifiers (i.e., SVM, Nearest Neighbour, Maximum Likelihood) improved significantly as the size of the training set increased, and (ii) SVM was the superior classifier for all training-set sizes. Although multi-scale segmentation seems to be working very well for very high-resolution imagery, authors like Jing *et al.* (2012) do not fail in stressing, that forests consist of multi-scale branches, complex tree crowns, and tree clusters causing an over-segmentation of the imagery.

In my study both classifiers performed on a high accuracy level (80 to 89%) in the **pixel-based** analysis to yield similar results. By applying OBIA RF generated better outcomes, however. Since only these two classifiers were used, no conclusions can be drawn with respect to other classification approaches. In studies by Adam *et al.* (2014) and Ghosh and Joshi (2014), RF and SVM performed almost equally well, when considering classification of RapidEye and WorldView-2 imagery. In a meta-analysis Khatami *et al.* (2016) found clear indications of SVM, kNN, and RF being clearly superior to other supervised classifiers and other image spectral

information manipulation and feature extraction such as vegetation indices and Principal Component Analysis (PCA). They also constitute, that SVM has achieved the best overall performance in all studies investigated. Pouteau *et al.* (2011) compared the six most popular machine learning algorithms applied to different satellite datasets (Landsat 7, SPOT, airSAR, TerraSAR-X, Quickbird, and WorldView-2) for tropical ecosystem classification. They testify, that SVM outperformed all other tested classifiers in 75% of the situations. In a recently published meta-study Sheykhmousa *et al.* (2020) perused the impressive body of literature concerning the performance of RF and SVM in various remote sensing applications. The authors conclude, that in the majority of the publications the authors found the complexity of the landscape in a study area, as well as limited and usually imbalanced training data making the classification a challenging task. The meta-study also reveals excellent species classification results for both classifiers to be between 82 and 88% accurate. The survey in the database also revealed that medium and high-resolution images are the most used images. In addition, SVM seems to be better geared for smaller training sets, whereas RF performs better as training sets get larger. Apparently, RF is intrinsically suited for multiclass problems and are better interpretable than SVM. Heydari and Mountrakis (2018) examined the effects of the classifier selection, reference sample size, reference class, and scene heterogeneity in per-pixel classification accuracy on 26 Landsat test sites employing five favoured classification algorithms. Obviously, SVM and kNN performed much better, when concentrating on edge pixels bordering adjacent object classes. The authors also state, that, with the exception of Naïve Bayes (NB), all classifiers performed similarly well for the entire image block. Thanh Noi and Kappas (2017) compared SVM, k-NN and RF for classifying Sentinel-2 imagery showing the Red River Delta in Vietnam. An overall high accuracy was obtained for all classifiers (90 to 95%) for designating six various land use classes. Albeit, the SVM delivered better results for smaller sample sizes, thus confirming the observations by other authors. By applying CNN, SVM, and RF to fused hyperspectral and photogrammetric data, Sothe *et al.* (2020) discovered, that all classifiers generated satisfactory results for tree species determination. However, CNN was between 22% and 26% more accurate, when only the hyperspectral bands were employed.

In my investigation I also observed that a higher spatial resolution does not necessarily improve the classification accuracy. For the identification of a single tree and the related species a proper delineation of an object is crucial. However, the outcomes clearly prove that for the correct assignment of tree clusters or dominant species the higher radiometric resolution is a very big bonus. This is also shared by Ghosh *et al.* (2014), who found out, that tree species classification results do not necessarily improve with spatial resolution of the imagery using the same classifier (i.e. RF). RF performed better with 8m resolution images, than with 4m – even the 30m resolution of the hyperspectral data produced sound results. A contradictory

example is provided by Immitzer *et al.* (2016b), who attempted to identify seven different tree species in test sites located in Bavaria, Germany. They employed imagery from WorldView-2, Sentinel-2 and Landsat 8 to perform classifications based on image segmentation and Random Forest (RF). Overall accuracies for the various sensors are 0.74 for WV-2, 0.68 for Sentinel-2, and 0.49 for Landsat 8, thus proving the leverage of high spatial resolution on classification results. However, the mentioned statement needs to be seen in relation to the range of image resolutions available these days. I find it very difficult to compare the classification outcomes of various sensors with inherently different band widths and numbers of spectral bands. At least the literature on hyperspectral data analysis provides a good indication on the superiority of utilising a high number of spectral bands for species discrimination (Alonzo *et al.*, 2014, Dalponte *et al.*, 2014, Fassnacht *et al.*, 2014, Heinzel and Koch, 2012, Nezami *et al.*, 2020, Vauhkonen *et al.*, 2013, Zarco-Tejada *et al.*, 2018).

The outcomes of the classification looking into a specific selection of spectral bands and indices have proven that a careful consideration of this aspect can make a big difference in achievable accuracies. The focus on only two spectral bands yielded a much lower performance of the classification as compared to the involvement of a high number or even all available bands. The spectral separability analysis showed quite impressively that the spectral bands representing the NIR, RedEdge, and SWIR are the most suitable for tree species discrimination in this part of Mongolia. Unfortunately, only the Landsat 8 and the Sentinel-2 sensors used in this study provide SWIR bands. A number of other authors also investigated the suitability of various spectral bands for tree species determination. For instance, Immitzer *et al.* (2019) employed Landsat 8 and Sentinel-2 imagery to find out, that, although the spectral band characteristics of the two sensors show very little difference, the coarser spatial resolution of Landsat seemed to result in the poorer overall discriminatory performance. Best results for species identification were achieved in Landsat 8 and Sentinel-2 in the RedEdge (RE) and Short Wave Infrared (SWIR) bands. The authors also state that the spectral signature of pine and spruce appeared to be similar. Although no discrimination between the dark taiga species was carried out in the presented study, the dark taiga showed lower reflectance values as compared to the light taiga in most of the spectral bands. The findings by Immitzer (2019) indicate that a more detailed look at the spectral separability of the dark taiga species would be sensible. Quite recently, some more authors explored Sentinel-2 images to find the best time period and optimal spectral bands and indices for gaining best results. For example, Mirończuk and Hościło (2017), Ma *et al.* (2019), Wang *et al.* (2018) and Wittke *et al.* (2019) detected the Sentinel-2 bands B5 (RedEdge 1), B7 (RedEdge 3), B8 (NIR), B11 (SWIR 1), as well as the NDVI to best suited for forest classification in late summer imagery in the temporal

and boreal biomes by applying modern machine learning algorithms (i.e. RF and SVM). Adelabu *et al.* (2014) achieved an increase of the overall accuracy of about 20% by integrating the red-edge band of RapidEye images. Immitzer *et al.* (2019) favour Sentinel-2 band B4 (Red) for the identification of conifers in Central European forests, B11 (SWIR 1) for broad-leafed forests, as well as a mix of B4, B5, B11, NDVI and NBR for mixed forests. van Aardt and Wynne (2007) achieved the best results for spectrally separating various pine species by using Red, NIR, SWIR, but also the Green spectral band. To the best of the author's knowledge, only one investigation looked into the detailed discrimination of taiga species in the Thunkel area. In her study Zueghart (2017) RapidEye imagery was the reference for distinguishing between dark and light taiga. The overall accuracy was 90% by exploiting all spectral bands. The author found the bands of Red, RE, and NIR to be the most suited for her task. Interestingly, the introduction of the RE band did not yield better results in any of the band combinations. Her separability assessment also confirms my observation, that a trend of increasing separability can be achieved by including of more bands. In another study on Mongolian forests Klinge *et al.* (2018) employed remote sensing technology to assess the climate effects on vegetation vitality in Mongolia. However, the Landsat imagery was not used for species discrimination, but rather for the derivation of NDVI and the delineation of forest areas.

The consideration of phenology for species discrimination is a particularly daunting task considering the fact that the vegetation period in Mongolia is very short. Thus, the full exploitation of the phenology aspect in the classification process requires the selection of the appropriate imagery in a very specific and narrow time window. This observation is underpinned by the NDVI timeline I carried out in this study, showing that the characteristics of the vegetation can change in a very short period of time. Snowfall can happen very easily at the beginning of September during the start of the senescence period, when larch and birch change colours due to the decreasing chlorophyll content in the foliage. In turn, foliation can start very quickly after the thawing period. In general, since phenology usually varies with species, the specific knowledge on phenology (e.g., leafing period, senescence) can be a sharp tool to determine species discrimination. This species specific fingerprint is a valuable aid in species discrimination and quantification (Lisein *et al.*, 2015). The consideration of seasonal effects such as senescence (leaf discolouration; leaf-on, leaf-off) ,flowering, and knowledge on site quality also contribute largely to the identification accuracies (Getzin *et al.*, 2012). In their meta-study Ma *et al.* (2019) found indications, that a combination different sensors (e.g. optical and radar), as well as the exploitation of multi-temporal imagery sems to yield best results (see also Elatawneh *et al.*, 2013). The improvement in classification accuracy (here: 5-10%) by utilising Sentinel-2 images of various time series instead of focusing on a single image is also confirmed by authors like Grabska *et al.* (2019), Persson *et al.* (2018), Klosterman and Richardson (2017), Wessel *et al.* (2018) and Denisova *et al.* (2019).

Pasquarella *et al.* (2018) used imagery from the Landsat family to map forest type characteristics in New England. They conclude that '…the spectral-temporal features consistently and significantly (…) outperformed all features derived from individual images and multidate combinations'. In contrast, Wittke *et al.* (2019) found only a miniscule improvement of the prediction accuracy, when adding multidate imagery. All the findings above, however, do not reflect the specific conditions prevailing in Mongolia. At least some indication is found in Klinge *et al.* (2020), who constitute, that the phenology of the deciduous larch trees and the ground vegetation created another problem for the NDVI signal. According to them 'Various topo-climatic conditions, e.g., cold air masses cumulating in topographic depressions during spring, cool conditions at higher elevations, droughts in late summer, produce temporally and spatially inhomogeneous patterns of tree vitality and thus NDVI'. Despite the fact, that phenology does not arise concurrently and uniformly, Zueghart (2017: 85) was able to obtain a fairly good spectral separation between dark and light taiga thanks to the acquisition period of the RapidEye satellite image in September. The outcomes of my study, however, suggest that the discrimination of dark and light can be achieved with an accuracy of almost 90% by considering summer imagery. Nevertheless, a more detailed analysis on the species distribution based on exhaustive ground truthing (especially in the dark taiga) including temporal effects would be very conducive to the exploration of the potentials of remote sensing technology related to vegetation cover analysis in Mongolia.

In general, this thesis confirms the observation made by various authors, that evergreen coniferous tree species show different spectral properties in comparison with deciduous broad-leafed trees. The machine learning classifiers applied (i.e., RF and SVM) performed very well. An overall very satisfactory discrimination of the light and dark taiga can be reported. However, due to the spectral overlap of specific tree classes, a sufficiently distinct separability between the two deciduous tree species larch and birch could not be obtained. Despite the fact that topographic correction was carried out on the Sentinel-2 imagery (see also Dong *et al.*, 2020) an additional effect of shading was detected. In the imagery the shaded areas were often misclassified as dark taiga. This observation is very much in line with the findings by Zueghart (2017: 83–84), who surveyed the same test area. For instance, Dong *et al.* (2020) found an improvement of 13% on their Landsat tree classification, when just using shadowless training areas. The shadowing effect can even reach such proportions that a classification turns out not to be meaningful (Teusan, 2018: 41,112). In the GIZ management plan (Gaschick, 2013) and in the study by Wecking (2017) a distinct transition between dark and light taiga is reported for the zone at medium elevations. Even though the classification outcomes of my investigation potentially and allegedly confirm this phenomenon, neither the assessment of the NDVI, nor

my personal observations made on-site carry sufficient evidence to support this assertion. As mentioned before the outcomes of my classification trials suggest that the dark taiga area is over-represented. What I observed in the field, however, was the occurrence of Scots pine in the zone designated by the two authors previously quoted. According to the commonly agreed definition, however, *Pinus sylvatica* is not considered a member of the dark taiga realm. When talking about classification accuracy the structure of the forest and the forest undergrowth also deserve attention, since these factors can greatly have an impact on the outcomes and the interpretation thereof (Knipling, 1970, Ustin and Gamon, 2010). In the dark taiga areas in particular, very heterogenous vertical and horizontal structures were observed in the field, lending the representation in the imagery an impression of clustering with gaps interspersed. Measurements of the canopy cover, the LAI and observations by Gradel and Mühlenberg (2011) support this perception. The fact that many trees were encountered by me in an at least partially defoliated condition, in combination with the observed dense forest undergrowth, give rise to the suspicion, that the spectral response of the trees are subject to an interference with the spectral signature by other forest flora. Klinge *et al.* (2020) also found the forest floor vegetation to be confounding their investigation on the NDVI in the taigas. A proper on-site investigation involving spectroradiometer gauges would most certainly provide useful insights on this issue. There are still numerous other factors modifying the spectral response of forested areas such as soil, crown closure, or tree age. However, as Ustin and Gamon (2010) happened to be urging, that physical remote sensing needs to be combined with ecological theory and seen in a multidisciplinary context to achieve a truly successful classification. Although this may be an understandable and reasonable argument, this undertaking would most certainly be beyond the scope of this thesis.

Rest of page intentionally left blank

8.9. Extraction of timber volume

In the last few decades various new methods have been devised for mapping and prediction of forest inventory attributes such as new regression techniques, artificial neural networks, and random forest decision tree algorithm (Brosofske *et al.*, 2014). Amongst the more recent developments is the so-called k-NN (nearest neighbour) approach, in which the response variable (e.g., timber volume, basal area) is predicted in an unsampled pixel by computing a distance metric (e.g., Euclidian) between the target and reference samples, and subsequently assigning the value of the closest neighbour to the target unit. This technique is described in more detail in chapter 4.6.2. and its methodological implementation in chapter 7.3.5.9. The k-NN method was employed in this study to predict timber volume and basal area for the area of compartment 435, but it can of course be extended to much larger areas as described for national inventories in Scandinavia, and to other parameters such as mean DBH and tree density (see also Kangas and Maltamo, 2009: 179–224, McRoberts *et al.*, 2010, Tomppo, 1991, Tomppo *et al.*, 2010). The k-NN was selected for this investigation due to its fairly simple applicability, the integration of satellite and other ancillary data (e.g., field data), and the efficacy in the prediction of inventory attributes without going through the arduous procedure of exhaustive ground truthing.

The Terrset environment offers the option of carrying out the k-NN regression technique with considerable ease – the workflow is portrayed in chapter 7.3.5.9. The satellite data input comprised the bands of Blue, Green, Red, NIR, SWIR, with the calculated NDVI for reproducing the most effective range of spectral signatures for vegetation discrimination. Other settings were 'Euclidian distance' for distance metrics and 'Minimum' for extraction type (see also k-NN regression manual by Chirici, 2012, for details) Unfortunately, no suitable climate data was available for the Thunkel area for further potential improvement of the regression model. In the table below the results of the calculations are shown for an estimated optimal *k* of 5 (see also graphs below). The timber volumes were extracted from the field data computation for all 15 test plots. For validation purposes five plots were selected randomly to calculate the RMSE.

Table 8-19: Comparison between actual and predicted timber volume using the k-NN regression.

Plot ID / point ID	Timber volume (m^3) from field data	Predicted timber volume (m^3) from k-NN	RMSE volume (m^3)
0 / 1	66.4		
1 / 2	84.7		
2 / 7	86.0		
3 / 5	58.1	83.8	

Plot ID / point ID	Timber volume (m^3) from field data	Predicted timber volume (m^3) from k-NN	RMSE volume (m^3)
4 / 6	78.7		
5 / 15	223.5		
8 / 14	331.8	200.5	
11 / 12	157.3		
12 / 13	153.0	162.3	
22 / 10	80.2		
24 / 11	239.4	151.2	
31 / 8	94.4		
34 / 9	93.6		
60 / 3	188.1	137.0	
64 / 4	165.2		
			75.351

The calculated RMSE value of 75.351 m^3 per hectare reflects a considerable error for the predicted timber volume. The dimension of this RMSE exceeds the total timber volume determined for plots like no.1 and no.4. As such, the predicted volumes have to be considered with a critical view and cannot be applied without a detailed ex-post evaluation. In the presented case three out of five samples show an underestimate of the predicted volume. However, with only five plots as validation points it is fairly speculative trying to infer a clear trend regarding over-, or underestimation.

A graphical representation of the resulting timber volume predictions is shown in Figure 8.71. In this case the timber volume from all 15 test plots was used for predicting the volume for compartment 435. In congruence with the input data resolution the output raster features a resolution of 30 metres for prediction. For contrast, the resulting timber volume raster is portrayed in the figure beneath with only 10 plots used for prediction.

Rest of page intentionally left blank

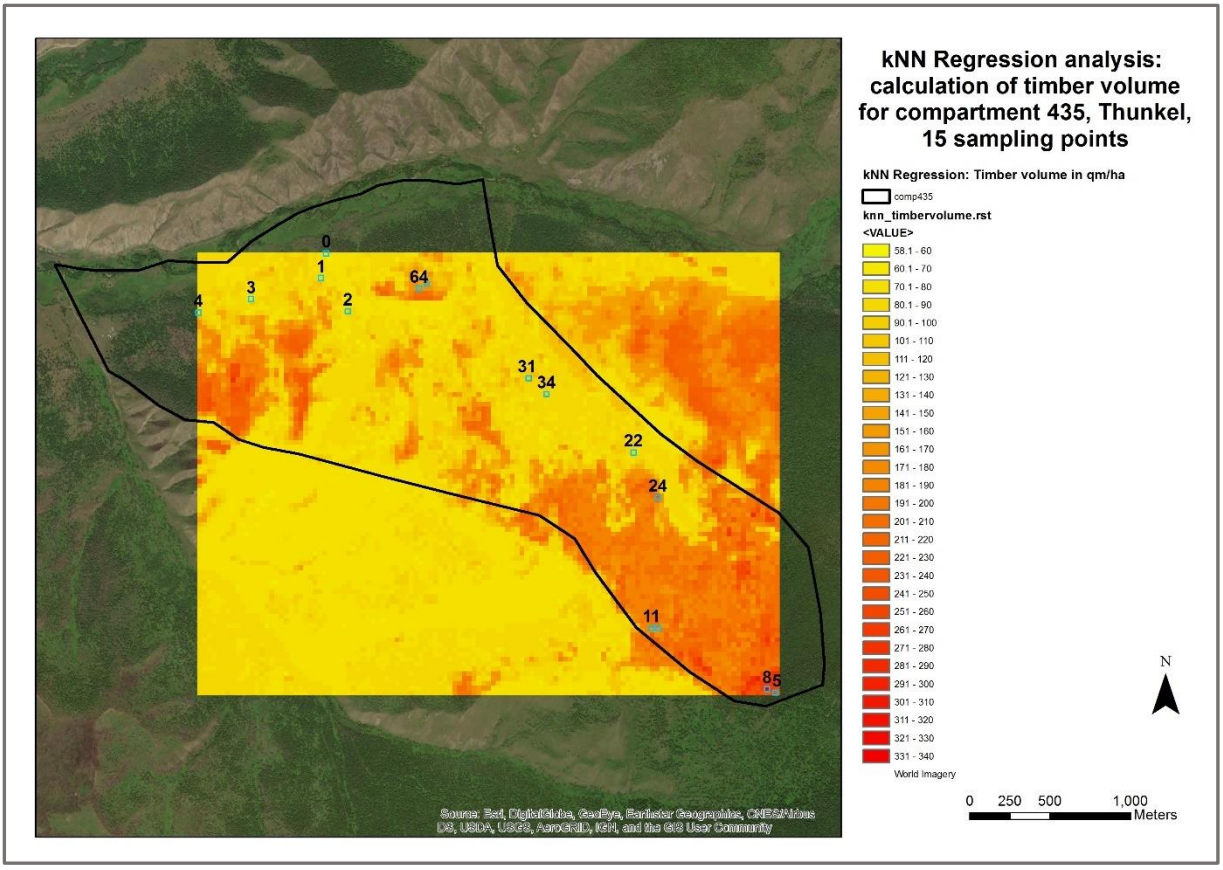

Figure 8.71: k-NN regression prediction for timber volume for compartment 435. The volume calculations from all 15 test plots were used as input.

With the consideration of all test plots the predicted timber volumes seemingly represent the stock volume for compartment 435 quite realistically. The plots reflecting the highest volumes (i.e., plot no. 5, 8, 24, and 60 (in the graph superimposed by the figure 64)) are characterised either by high tree numbers (which translates into high BA), or by a large mean DBH. In the graph there appears to be an aggregation of high volumes in the southeast corner of the compartment and south of plot no.3 (not measured). This observation is supported by the fact, that based on own inspections and surveys, the dark taiga areas are rich in tree numbers and old tree individuals with a high DBH. In comparison, the plots in the lower part of compartment 435 (e.g., no. 0, 1, 2, 3, 4) represent lower volumes due to exploitation and removal of the larch featuring higher tree volumes than birch. In conclusion, the predicted volumes show a reasonable outcome for the entire compartment. With having used only 10 test plot mean volumes as regression computation input, the graph below depicts a different picture.

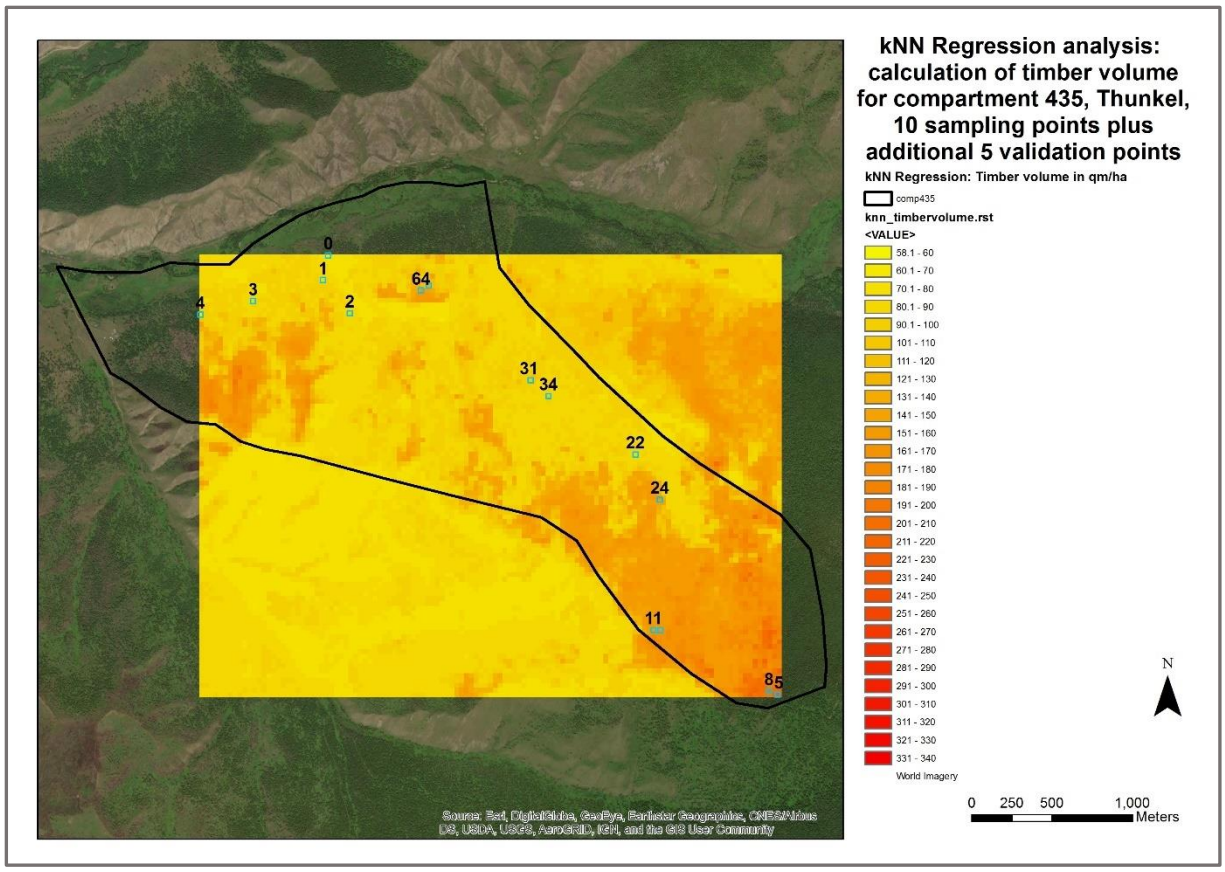

Figure 8.72: k-NN regression prediction for timber volume for compartment 435. The volume calculations from only 10 test plots were used as input – the data of 5 plots were used for validation of the prediction.

Although the trend of featuring higher timber volumes in the dark taiga areas still prevails, in general the variations within the compartment are less pronounced causing a blurring effect with volume hot spots becoming rather indistinct. For both graphical representations the same colour code was created to reflect the timber volume values for a specific class bracket. On closer inspection, the figure reflecting the 10-plot sample variant appears to mirror a lower mean timber volume for most of the areas within and even outside the confines of compartment 435. This phenomenon suggests, that not only the quality and the number of plots used for volume prediction play a decisive role for the outcomes, but also their spatial distribution and the range of their data. Another important determinant is the definition of the correct ***k*** value for imputation (Chirici *et al.*, 2008). Fortunately, the regression procedure in Terrset allows for a computation of the optimal *k* value with a graphical representation of (Pearson's) R and RMSE calculated corresponding to certain *k* values. The graph below shows an optimal k of 5 for both variants (i.e., 15 and 10-plot version). For the higher number of the k-threshold (i.e., 15) there seems to be a trade-off between the calculated R and RMSE values – apparently a low RMSE value is favoured by the underlying algorithm when calculating optimal k. For the threshold value of 10 the lowest RMSE matches very nicely with the peak of the R value. For

explanation, the maximum k-threshold value to be entered is identical with the maximum

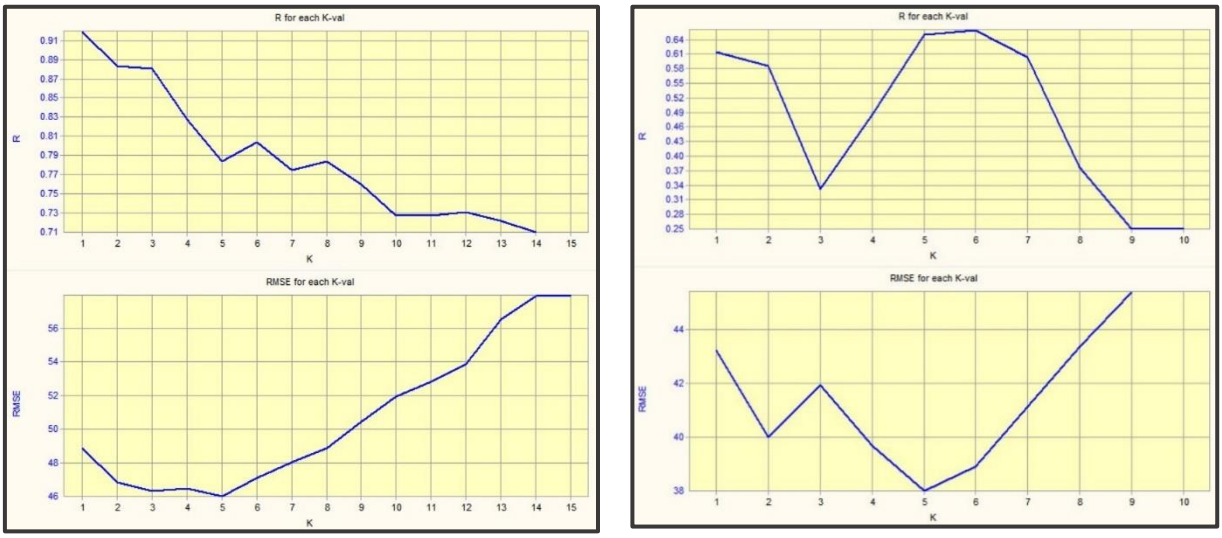

*Figure 8.73: Calculation of optimal **k** value for variant 1 with all 15 test plots considered (left) and variant 2 with only 10 test plots for timber volume prediction. The calculated R (top) and RMSE (bottom) for each **k** are presented.*

number of k neighbours to be considered. The subsequent regression analysis is carried out with the chosen (optimal) k value. Since the k-NN regression technique was applied for both, tree volume, and basal area prediction, a more exhaustive discussion is being dealt with in the subsequent chapter 8.10.

8.10. Extraction of balsa area (BA)

As stretched before, k-NN regression deserved another attempt by extending the prediction of timber volume to basal area (BA). Basal area is another important parameter for describing and analysing forest structure. There is no difference in the determination process from above method, other than that, that instead of timber volume the basal area was used as dependent variable – the predictors were kept identical. The optimal k-values were calculated as being 4 for the 15-plot version and 2 for the 10-plot variant.

In the table below the predicted basal area values are set against the field values as 'real' data. The RMSE of 6.467 m^2 shows an error value, that cannot be ignored as being miniscule. Although there is a clear trend of an over-estimate in comparison with the results for timber volume prediction, the number of five plots for validating the outcomes is too small for making substantiated inferences. In general, the predictions for BA seem closer to the true values as compared to the outcomes for timber volume. Nevertheless, the variation in prediction versus real data for plot no.12 is striking with an over-estimate of about 100%.

Table 8-20: Comparison between actual and predicted basal area (BA) using the k-NN regression.

Plot ID / point ID	Basal area (m^2) from field data	Predicted basal area (m^2) from k-NN	RMSE basal area (BA) in m^2
0 / 1	13.5		
1 / 2	13.3		
2 / 7	15.6		
3 / 5	15.5	19.72	
4 / 6	17.5		
5 / 15	29.4		
8 / 14	28.6	29.3	
11 / 12	28.8		
12 / 13	15.2	28.9	
22 / 10	21.0		
24 / 11	26.8	27.74	
31 / 8	20.5		
34 / 9	19.0		
60 / 3	26.3	24.76	
64 / 4	26.5		
			6.467

Let us now see, whether the graphical representation helps us in gaining more insights. In the following figure (8.74) the picture is very similar to the one generated for the prediction of the timber volume with the dark taiga plots (no. 5, 8, 11) taking the lead. The more sparsely populated areas are displayed in brighter colours, indicating a relatively low basal area – the dark taiga areas are rendered much darker. Since basal area and timber volume are correlated, the similarity between the findings comes as no surprise. Another area with relatively high BA values stands out south of plot no.3 – unfortunately, no ground truth data are available for this sector. There is, however, a slight chance of getting a few useful clues from the tree species classification, which allows to make a few referrals. As opposed to the graphs related to timber volume prediction the ones for the basal area computation look quite congruous with only minor changes regarding an overall impression. However, the dark taiga areas (see also pots no.5 and 12 (concealed, but denoted as 11 because of superimposition) seem somewhat over-estimated in the graph representing the 10-plot variant (Figure 8.75), which also shows in the figures provided in the table.

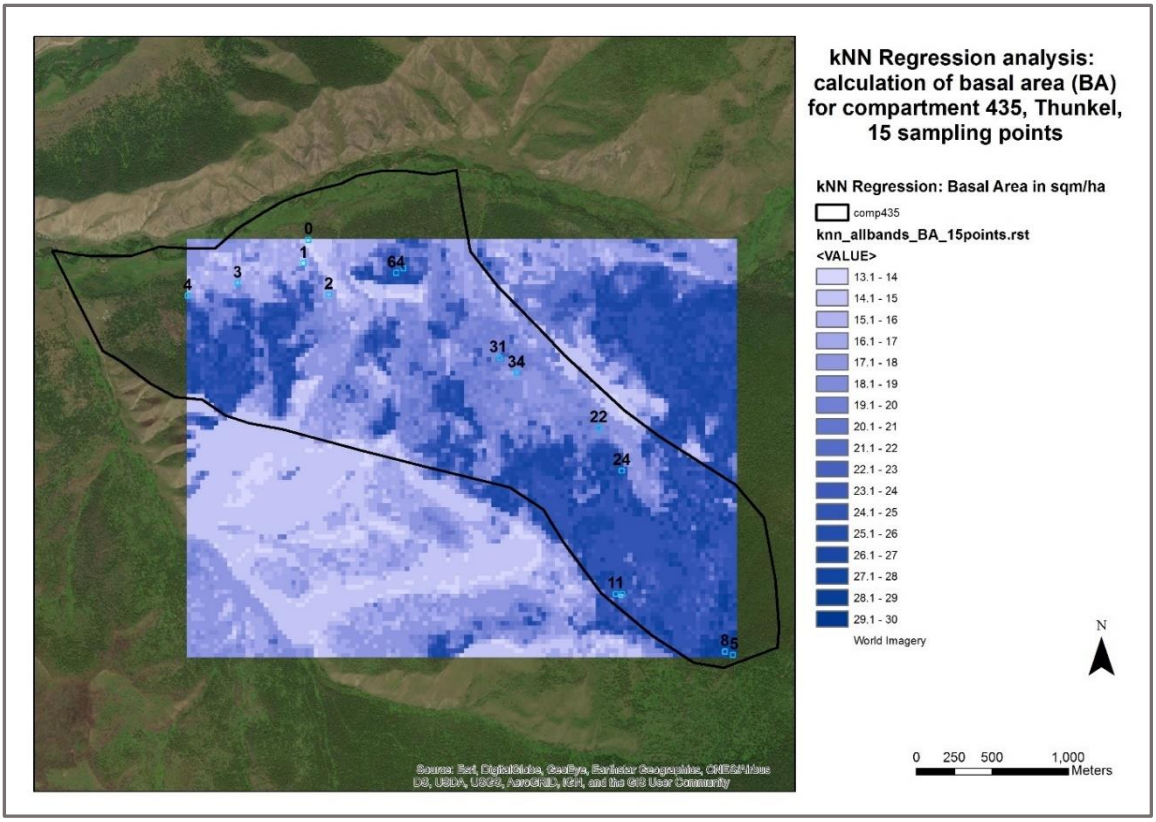

Figure 8.74: k-NN regression prediction for basal area (BA) for compartment 435. The basal area calculations from all 15 test plots were used as input.

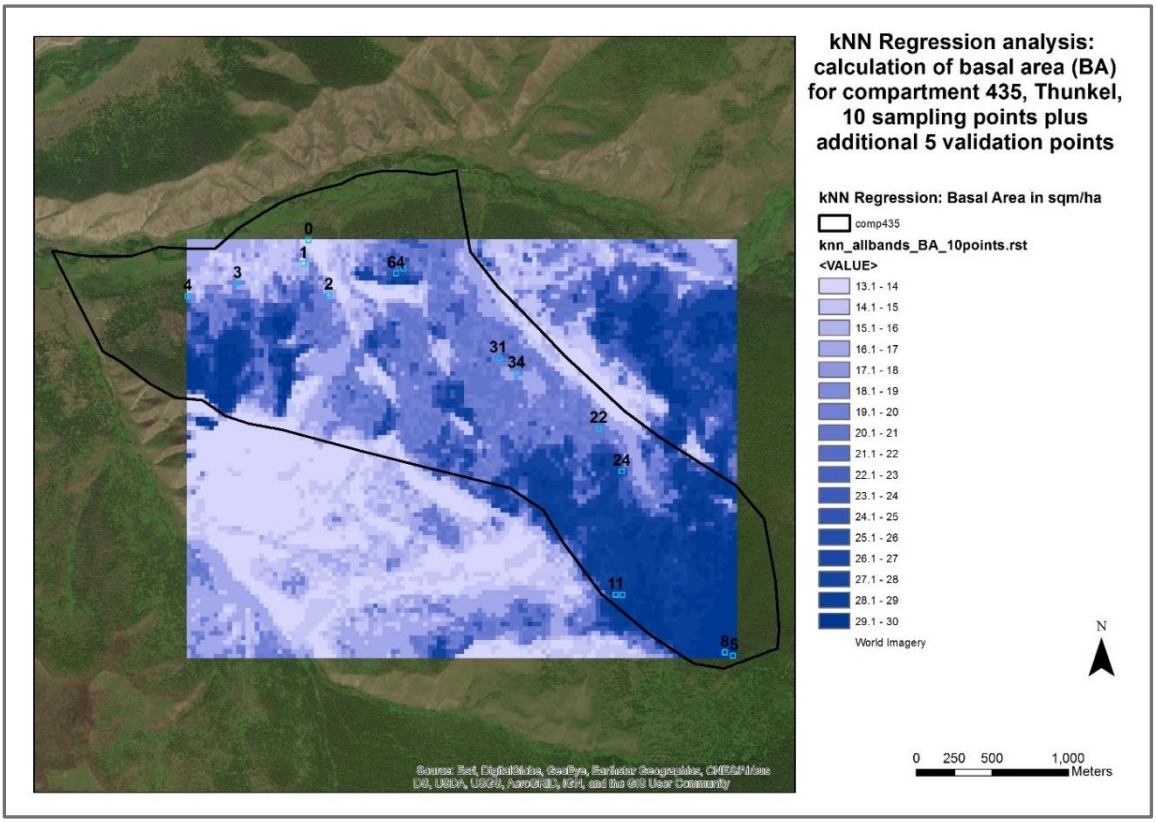

Figure 8.75: k-NN regression prediction for basal area (BA) for compartment 435. The basal area calculations from only 10 test plots were used as input – the data of 5 plots were used for validation of the prediction.

The shape of the graphs for *R* and *RMSE* for finding the optimal *k* value appear to be more logical than the ones related to the prediction of timber volume. The general trend of low RMSE values associated with a high coefficient of correlation seems much more compelling than in the representation in chapter 8.9.

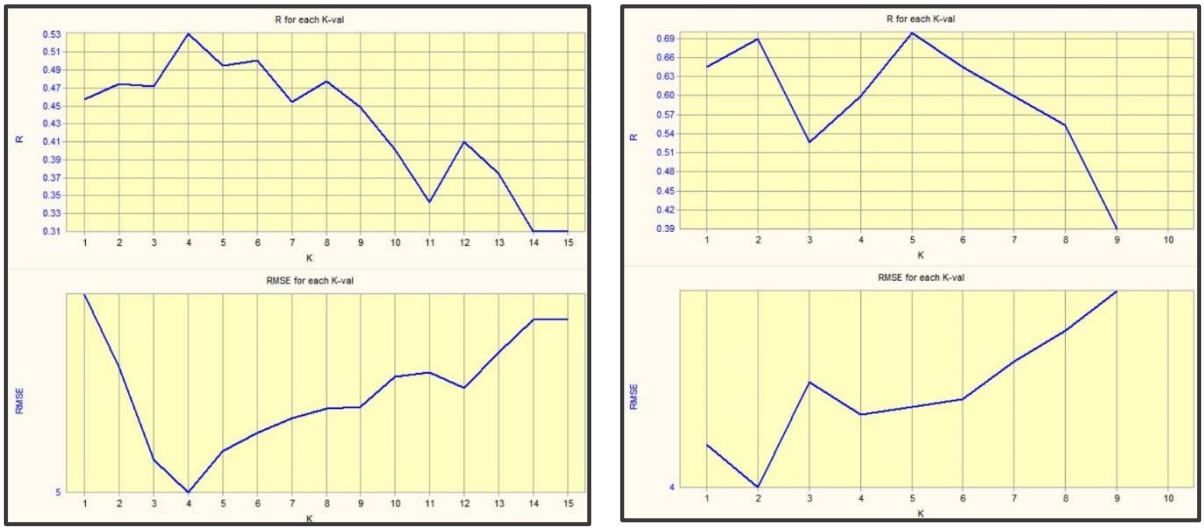

*Figure 8.76: Calculation of optimal **k** value for variant 1 with all 15 test plots considered (left) and variant 2 with only 10 test plots for basal area (BA) prediction. The calculated R (top) and RMSE (bottom) for each **k** are presented.*

The optimal *k* values were computed to be 4 and 2 respictively, but the relatively low R value for the 15 plot variant is quite unsatisfactory. It is quite unfortunate, though, that no information of assistance could be derived from the literature to explain the oddities in curve performance for the timber volume imputation and the low correlation coefficient concerning basal area. With such great number of independent variables a tracking of the relevant issues seems disproportionate.

As far as the discussion on the obained results for the k-NN regression is concerned, only a small proportion of references can be considered conducive. To the author's knowledge, there is only one publication dealing with this specific regression method linked to Mongolian taiga forest attributes. In his work Baasan (2010: 73–75) looked into the prediction of basal area and stem number distribution. He considered a much bigger area (10,375 ha in the southwest of the Khentii mountains) with systematic cluster sampling (in L shape) conducted for gathering field data. Landsat 7 imagery acquired at various dates the ground truthing data and provided the input for the k-NN regression. For the basal area distribution Baasan found the estimate distortions to be lower for single image bands. The accuracy for the various scenarios (i.e. band and k-value combinations) ranged between 26.94 and 76.94%. In contrast to the findings related to basal area the integration of all spectral bands yielded the best results related to the prediction ofstem number. The claculated RMSE for stem number distribution was 28.79%.

The author concludes by stating, that finding the optimal k value is pivotal for gaining useful results. He further remarks, that the k-NN method is a useful tool for conducting forest inventory in easing the burden of arduous field work, but also stresses, that there is still room for improving the performance of the k-NN regression.

When looking at the body of literature on k-NN regression, the technique has proven to be very successful especially when dealing with huge forested areas to be inventoried. Thus, the Nordic countries, such as Finland and Norway, have favoured k-NN to support their National forest Inventories (NFIs) for many years (Kangas *et al.*, 2018, McRoberts *et al.*, 2010, Tomppo, 1991, Tomppo *et al.*, 2009, Tomppo *et al.*, 2010). Various applications of k-NN can be attributed to the successful classification (Overall Accuracy (OA) of 91%) of boreal forests in Finland (Haapanen *et al.*, 2004), the prediction of biomass outperforming RF and SVM (López-Serrano *et al.*, 2016), the imputation of tree-level stem volume and basal area from LIDAR resulting in small RMSE of $5m^2$/ha and $16m^3$/ha (Falkowski *et al.*, 2010), or the determination of forest structure attributes (basal area, tree density) from LiDAR data (Hudak *et al.*, 2008). Notwithstanding, there are examples of second-rate performance of k-NN, like the ones reported by Gjertsen (2007), who found an Overall Accuracy of only 63% for the classification of Norwegian forests derived from Landsat imagery.

In a number of investigations useful suggestions are to be found on how to improve the quality of the k-NN outcomes and how to avoid glitches: Jung *et al.* (2013), and Eskelson *et al.* (2009) for instance point out very clearly, that image registration (positional) errors need to be shunned. Gjertsen (2007) suggests the use of image band ratios (indices) as additional input for ancillary data, whereas Franco-Lopez *et al.* (2001) ask for more research on multi-sensor k-NN approaches. Koukal *et al.* (2007) dedicated an entire study on the possible ramifications of radiometric calibration on the k-NN predictions of forest attributes to ascertain, that image calibration is vital for achieving good k-NN results. McRoberts (2008) found the selection of the optimal feature space crucial for his study on stand density and basal area derived from Landsat imagery, and suggests in another investigation to either use a high amount of sampling plots, or stratify the field data prior to further analysis (McRoberts *et al.*, 2002). Good results on k-NN derived basal area of a forest in the Kyiv region (Ukraine) were yielded in a study conducted by Myroniuk *et al.* (2019). The authors conclude, that the pixel size of the satellite imagery proved to be less important than a high temporal resolution to capture the variation in spectral response. An important observation was made by Maltamo *et al.* (2011), which is rarely object of investigation in conjunction with nearest neighbour strategies. The critical discussion related to the quality and number of training plots is usually taken for granted, but a very limited body of literature has been looking in detail into the matter. The team found

a decreasing accuracy of the results at specific levels, especially when dealing with tree height estimations. The authors strongly advise to select at least 50 plots for inventory purposes, with lower numbers being a more hypothetical calculation.

In the light of the remarks and findings by other authors the outcomes of my own study can be rated as being good for the basal area prediction, but unsatisfactory with regard to the timber volume estimation. Despite the fact, that the most relevant satellite bands were used with an additional NDVI as ancillary data, there seems to be room for improvement. In an extended subsequent study, for instance, the employment of satellite scenes with a higher temporal resolution and a higher variety of bands used as independent input variables would be sensible. In addition, an increase in number of sampling plots and a consideration of more ancillary data concerning climate and topography would most certainly be conducive to the success story of k-NN regression for forest attribute prediction.

8.11. Shannon Index

An impressive body of literature exists on the various facets reflecting the richness in species in Mongolia (e.g. Department of Biology, School of Arts and Sciences, National University of Mongolia, 2017, Gunin *et al.*, 1999, Gradel, 2010a, Mühlenberg *et al.*, 2004, and Dulamsuren *et al.*, 2005c). Despite the relatively low number of tree species found in Mongolian forests, the taiga forests are home to a very diverse spectrum of flora and fauna (Dulamsuren *et al.*, 2005a, Mühlenberg, 2012). A great number of various indices have been devised to reflect the quality and quantity of such diversity. One of them is the distance-independent measure to characterise forest structure at stand level, the so-called Shannon Index (Gadow *et al.*, 2012: 55–56, Gradel, 2010b: 12–13, Magurran, 1988: 34–37). The Shannon Index is straightforward in the calculation process (see also chapter 3.1.4. for formula), and, despite being a secondary theatre of this study, it sufficiently reflects the management practices and the status of the ecosystem itself. Below graph demonstrates the results as calculated from the field data.

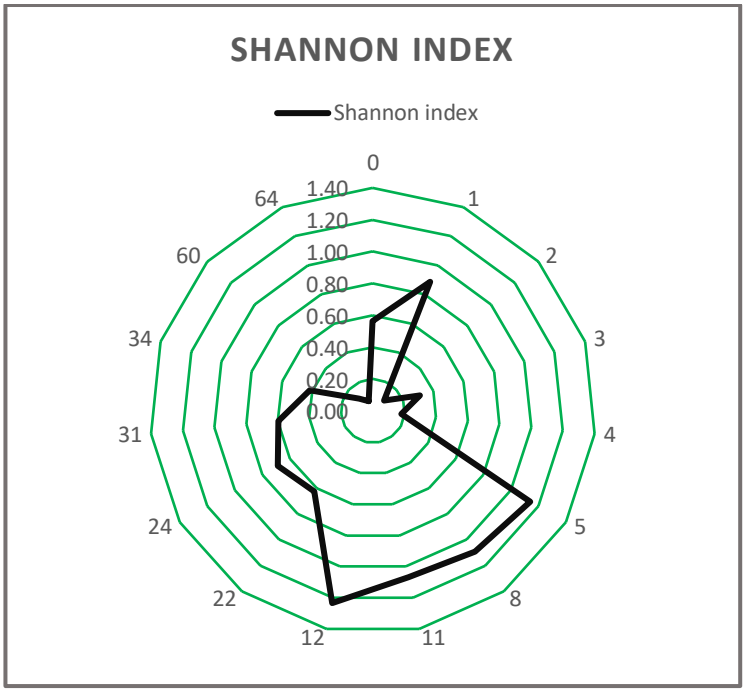

Figure 8.77: Calculated Shannon index for all test plots (0 to 64). The test plots of the dark taiga (5,8,11,12) show the highest values and thus the highest species diversity. Based on a good birch – larch ratio light taiga plot no.1 also ranks high.

The graphical representation illustrates quite strikingly the wide range of diversity found in compartment 435. The dark taiga plots 5, 8, 11, and 12 stand out with an index beyond 1.0, which is accounted for by the fact, that at least three different tree species are present. In addition, the relative proportion of the specific species greatly affects the magnitude of the index value. An excellent example makes the structural situation and composition at plot no.1, which is characterised by featuring only two tree species (birch and larch), but reflecting a 50/50 ratio of the species. A contrasting illustration is plot no. 0 with an index value of close to zero – the tree species ratio here is 1/99 (larch/birch). This specific plot is located in the lower part of compartment 435 showing indications of severe exploitation, with the larch being almost gone. The same is true for other plots with a low number of larch individuals. However, it also has to be taken into account, that the impact of fire incidents on the tree species distribution and composition is not negligible. According to the NFI report (Altrell and Erdenejav, 2016: 63) the Khentii mountain area ranks as number one in the Shannon Index list in contrast to the other forest inventory regions assessed. With an average index value of 1.51, however, it is hard to believe that the dominating feature of the light taiga presents itself in such a diverse manner. Unfortunately, only very limited research has been conducted in Mongolian forests with regard to the Shannon Index to be suited for direct comparison. Luckily, Gradel (2010b: 22,33) presents an index value of 0.96 for a test site at Khonin Nuga in the Selenge Aimag. The test plot reflects a section of a dark taiga area with a ratio of 51.85% for Abies sibirica, 1.48% for Larix sibirica, 7.41% for Picea obovata, and 39.2% for Pinus sibirica. In an

exhaustive study on the diversity of taiga forests in the same region Mühlenberg *et al.* (2012a) acknowledges this specific area as being particularly rich in species with a high nature conservation value. In his investigation Byambasuren (2011: 81–82) also supports the observation of dark taiga forests being characterised by species richness and higher complexity compared to the light taigas. Given the fact, that dark taiga forests support more tree species than the light taiga, the index figure values as provided in the NFI report appear overly optimistic.

Tree species can be detected in virtually all very high-resolution imagery, particularly in UAV imagery (e.g. Getzin *et al.*, 2012, Saarinen *et al.*, 2018). Subsequently, the Shannon index can be calculated with considerable ease. The tree species were determined in the UAV images used in this study by visual inspection. Unfortunately, some of the generated orthophotos from the 3D point cloud turned out to be of minor quality, so the process of getting tree species related to a specific area could not be finalised. However, if tree species plus correct location are identified, then it is feasible to calculate various other forest structural diversity factors such as the one proposed by Gadow *et al.* (2012: 56–58), the so-called 'tree species spatial mingling factor' based on the neighbourhood relationship.

Rest of page intentionally left blank

8.12. Results matrix

Table 8-21: Results matrix with grading of results based on findings and statistical analysis.

Methods	**Forest attributes**											
	Tree height single	Stand height	Tree species	Tree count	Basal area	Timber volume	Crown diameter	LAI	NDVI	dNBR	Slope	Aspect
DEM GIZ	NA	NA	NA	NA	NA	NA	NA	NA	NA	NA	++	++
UAV visual inspection	NA	NA	++	++	NA	NA	++	NA	NA	NA	NA	NA
UAV automatic extraction	++	+	-	o	NA	NA	-	NA	NA	NA	NA	NA
S-2 pixel-based	NA	NA	++	NA	NA	NA	NA	-	+	++	NA	NA
k-NN S-2	NA	NA	NA	NA	+	o	NA	NA	NA	NA	NA	NA
S-2 pixel-based SVM	NA	NA	+++	NA	NA	NA	NA	NA	NA	NA	NA	NA
S-2 pixel-based RF	NA	NA	++	NA	NA	NA	NA	NA	NA	NA	NA	NA
S-2 OBIA	NA	NA	-	NA	NA	NA	NA	NA	NA	NA	NA	NA
S-2 OBIA SVM	NA	NA	-	NA	NA	NA	NA	NA	NA	NA	NA	NA
S-2 OBIA RF	NA	NA	+	NA	NA	NA	NA	NA	NA	NA	NA	NA
Pléiades pixel-based	NA	NA	+	- -	NA	NA	NA	NA	NA	NA	NA	NA
Pléiades pixel-based SVM	NA	NA	+	NA	NA	NA	NA	NA	NA	NA	NA	NA
Pléiades pixel-based RF	NA	NA	+	NA	NA	NA	NA	NA	NA	NA	NA	NA
Pléiades OBIA	NA	NA	+/-	NA	NA	NA	NA	NA	NA	NA	NA	NA
Pléiades OBIA SVM	NA	NA	-	NA	NA	NA	NA	NA	NA	NA	NA	NA
Pléiades OBIA RF	NA	NA	+	NA	NA	NA	NA	NA	NA	NA	NA	NA
RapidEye pixel-based	NA	NA	o	NA	NA	NA	NA	NA	NA	NA	NA	NA
RapidEye pixel-based SVM	NA	NA	o	NA	NA	NA	NA	NA	NA	NA	NA	NA
RapidEye pixel-based RF	NA	NA	o	NA	NA	NA	NA	NA	NA	NA	NA	NA
WV-2 pixel-based	NA	NA	NA	-	NA	NA	NA	NA	++	NA	NA	NA
WV-2 pixel-based SVM	NA	NA	NA	NA	NA	NA	NA	NA	NA	NA	NA	NA
WV-2 pixel-based RF	NA	NA	NA	NA	NA	NA	NA	NA	NA	NA	NA	NA
WV-2 OBIA	NA	NA	++	NA	NA	NA	NA	NA	NA	NA	NA	NA
WV-2 OBIA SVM	NA	NA	++	NA	NA	NA	NA	NA	NA	NA	NA	NA
WV-2 OBIA RF	NA	NA	++	NA	NA	NA	NA	NA	NA	NA	NA	NA

Grading (based on findings): ++ = excellent + = good o = mediocre - = poor - - = very poor

DEM = Digital Elevation Model

UAV = Unmanned Aerial Vehicle

WV-2 = WorldView-2 (winter) image

S-2 = Sentinel-2 image

OBIA = Object Based Image Analysis

SVM = Support Vector Machine

RF = Random Forest

dNBR = difference Normalised Burn Ratio index

Above-mentioned matrix condenses all outcomes of the presented investigation. The grading of the results is based on the findings, however, with no calculated index involved. The matrix is meant to provide a decision tool for practitioners with limited resources at their disposal.

Rest of page intentionally left blank

9. Conclusions and outlook

For many decades, Mongolia's forests have been suffering from degradation due to human and natural causes such as overexploitation and wildfire occurrences. In addition, forest management practices have not proven to be sustainable. All decisions related to forest resources operations hinge on the quality of the information exhausted. Although a National Forest Inventory was conducted in 2016, hardly any reliable and scientifically substantiated information exists related to a regional or even local level. This lack of detailed information warranted a study performed in the Thunkel taiga area in 2017 in cooperation with the GIZ In this context, we hypothesised, that (i) tree species and composition can be identified based on the aerial imagery, (ii) tree height can be extracted from the resulting canopy height model with accuracies commensurate with field survey measurements, and (iii) high-resolution satellite imagery is suitable for the extraction of tree species, the number of trees, and the upscaling of timber volume and basal area based on the spectral properties.

Although exhaustive field work was planned to be carried out for gathering reference data, this endeavour was constrained due to wildfire events. A drone (UAV) was deployed for capturing aerial imagery, and an ample set of satellite imagery (i.e., Sentinel-2, WorldView-2, RapidEye, Pléiades, Landsat 8) was obtained. Field data were subsequently subjected to analysis to be compared with the findings of the extraction of forest attributes from the imagery.

The analysis of the field data revealed huge discrepancies between the data gathered for this study and the GIZ management plan. This can in part be attributed to the fact, that only small plots were surveyed by the GIZ by applying the 6th-tree method. This approach has proven to be very useful in situations where no inventory data exist. The resulting inaccuracies are even amplified if the tree measurements are not carried out properly. In the literature, the training level of the field staff has been mentioned to make a large difference in the quality of the data to be processed. Insinuations found in the National Forest Inventory report suggest that there is still a lot of room for improvement regarding expertise and training of the surveyors. In addition, calculation errors bear the potential to amplify the inaccuracies. In the literature it has also been mentioned that the Mongolian growth and yield tables need to be reconsidered, implying that this circumstance also contributes to the potential error sources. Unfortunately, only a very limited number of accounts on field surveys in Mongolia is available. The National Forest Inventory report is one of the few credible sources. In addition, the investigations by Gradel (2017) and Mühlenberg (2012) are useful references. The lack of extensive scientific

research on the taigas related to forest attributes is profound and warrants further efforts in the future.

One of the most exciting and challenging tasks was to extract *tree height* from the UAV canopy height model (CHM). The outcomes give rise to positive expectations, since at least the manually derived height values have proven to be very close to the reference data. However, the appropriate settings in the photogrammetry software and the proper planning of image overlap (i.e. > 90%) and flying altitude play an important role in the accurate creation of the height model. Image quality (contrast, sharpness) is another determinant in this respect. Even under optimal conditions model blunders and deficiencies can occur – authors having scrutinised all available photogrammetry software packages found it quite deplorable that tree canopies are not represented well in some cases. According to the Metashape software programmer Semyonov (2011), the various algorithms struggle with the complexity of tree surfaces. Apparently, there is still scope for further improvement. Slowly, but surely, manufacturers of consumer-grade UAVs are beginning to look into the furnishing of better camera specifications such as increased image sensor sizes and the provision of changeable lenses with different focal lengths. All these developments will most certainly contribute to the quality of photogrammetric flying missions. Multi-sensor platforms and multi-angle camera systems have been tested successfully and will hopefully become fully operational and available in the near future to help enhance the applicability of UAVs in other fields.

Once the canopy height models are exported as orthophotos and/or elevation models, tree *species*, tree *positions*, and tree *crown diameters* can be determined. In general, the manual extraction of all three attributes works very well, provided that the quality of the models is satisfactory and the image interpreter has been trained well. For the automatic extraction of tree position, crown diameter, and species classification, image segmentation procedures have become kind of gold-standard. However, co-dominant trees, tree clusters, and individual trees featuring large crowns are either not represented well, or are over-represented as multiple trees. As such, the segmentation process has to be executed with great care. Proper tree species identification also depends on the classifier used, but primarily on the spectral separability of the species. Multispectral sensors provide a good remedy in this context. With a correct location and classification of the individual trees, the calculation of the Shannon index and other structural indicators is quite straightforward. As to be expected, the Shannon index reflected higher values for the dark, than for the light taiga, thus indicating a higher diversity.

The automatic determination of tree numbers constitutes another big challenge for high-resolution imagery. Segmentation procedures often result in over-, or under-segmentation,

yielding inaccurate tree numbers. In turn, the complex nature of tree crowns also causes huge problems during template matching activities. For instance, palm trees are easy to extract due to their distinct star-like shape of the crowns and their sufficient spacing within the plantations. With tree and forest structures as complex as the dark taiga, the outcomes of the automatic process were very unsatisfactory, no matter what imagery was used. In contrast, the manual determination of tree numbers by visual inspection worked relatively well, however, at the expense of interpretation time. It also needs to be noted that due to the viewing angle of the air-, or spacebourne platforms and the associated nadir view, usually only trees representing the upper canopy layer are captured.

The *DEM* provided by the GIZ showed excellent characteristics with high accuracies in position and elevation (1-2m). The analysis of the model confirmed the findings by other authors like Dulamsuren (2005, 2008, 2019) that taiga forests primarily populate the northern slopes of the landscape. If combined with the high gradient of the slopes, this can result in large shadows within the forest, impeding the correct classification. A low sun angle can also exacerbate this situation (see also Teusan, 2017, and Zueghart, 2017). In addition, topography plays an important role in the correct representation of the spectral signature of the objects. Luckily, the atmospheric correction tool (which was applied in this study) designed for the Sentinel-2 imagery accounts for this in part by integrating an SRTM elevation model into the compensation algorithm.

The analysis of various vegetation indices provided additional insight into the characteristics of the taiga and the impacts of natural causes thereof. By generating a timeline of the *NDVI*, the effect of drought and the regeneration of the vegetation after a fire event could be proven. It was also quite interesting to see the effects of snowfall and senescence, which were reflected in the NDVI. In addition, the assessment of the NDVI in a WorldView-2 winter image provided some invaluable information on the location and extent of the dark taiga, due to the non-deciduous character of the conifers. The calculation of the dNBR showed in detail the burn severity of the areas afflicted by *wildfires* in 2017. However, the selection of the appropriate dates for the before-, and after-fire satellite scenes is crucial for the correct delineation of the affected areas. If the time lag between the before- and after-images is too long, regrowth of vegetation influences the classification and determination of the burn severity.

The determination of the *tree species* has been one of the most laborious parts of this thesis. By drawing on my experience as a trained forester and the utilisation of interpretation key portrayed in chapter 7.3.4.1., the correct identification of the tree species was carried out with considerable ease, given, that the UAV imagery provided enough detail and contrast. The trial

on the computer-aided classification was quite unsuccessful, due to the lack of spectral separability of the tree classes in the RGB image. This fact once again supports the idea that the human brain can easily outperform the computer algorithms when sophisticated pattern recognition abilities are required. Image segmentation was carried out on the very high-resolution UAV and satellite imagery prior to classification. The selection of the appropriate parameters can largely contribute to the success of the subsequent image classification process, but a large amount of editing is required to eliminate the errors caused by over-, or under-segmentation. In conclusion, the best classification results were obtained by executing OBIA on the WorldView-2 image. When applied to the UAV photographs characterized by a resolution of 3cm and the coarsely resolved Sentinel-2 imagery OBIA either caused a complete failure of the method (UAV) or did not contribute to the improvement of the classification at all (S-2). The selection of the most suitable classifier also affects the outcomes. Interestingly, the Random Forest classifier worked best for the OBIA approach, whereas the Support Vector Machine classifier excelled in the pixel-based version. Contradicting performances of both classifiers are also reported in the literature – apparently, there is no overall winner in the classifier contest. An important observation was that the exploitation of all spectral bands used for the classification process resulted in the best assignment to the tree species. However, with a case-specific selection of spectral bands (e.g., NIR, SWIR) and vegetation indices (e.g., NDVI, NBR) the amount of data to be used can be reduced considerably without sacrificing accuracy. The so-called Principal Component Analysis (PCA) can greatly assist in finding the optimal combinations. Despite determination of the best possible input parameter setting, a few caveats apply. Firstly, one must not be fooled by the accuracies achieved in the confusion matrix during accuracy assessment. A comparison of the outcomes with reality can be quite disillusioning. Secondly, with one exception, all input variants applied to RF and SVM yielded results for the dark taiga delineation that seem somewhat out of proportion. This particularly concerns a forest patch in the northwest of compartment 435 – in almost all classifications, dark taiga classes were created in places where most certainly no dark taiga species occur on the ground. Upon closer inspection of the specific area, a few things appeared to be different from the other school forest zones. The analysis of the DEM revealed that the terrain is relatively steep and rugged, and more exposed to the east, thus inducing a more irregular hill-shade pattern. This is also reflected in the rendering of the forest by exhibiting more shadows. On closer inspection, the calculated MSI showed water content values similar to the dark taiga vegetation, although this area is populated by light taiga species. In conclusion, the effects of topography and the occurrence of shadows appears to influence classification, but these factors are hard to definitively characterize. An investigation solely dealing with these issues is suggested. Another relevant indication is provided by the spectral separability analysis, where some overlap between dark and light taiga signatures is apparent. This characteristic is

even more pronounced in the birch / larch segregation by displaying very similar spectral footprints. As such, seasonal effects like senescence or the beginning of foliation can be valuable ancillary information for the classification process. This investigation also showed that the selection of training and verification samples in terms of quality and quantity can affect the classification. One particularly surprising finding is the fact that dark taiga species (here: *Picea obovata*) also populate riparian areas, even though they only occur in some particular ecological niches. Such instances were initially attributed to classification errors, but closer inspection confirmed the occurrence of dark taiga species in riparian areas, which was also confirmed by other experts. In my opinion, this phenomenon is not pure semantics, but needs to be considered in every tree species classification conducted on Mongolian taiga ecotones. The natural habitat of the dark taiga would appear to be more complex than suggested in the literature.

With respect to the k-nn regression approach for the upscaling of *timber volume* and *basal area*, a few important observations are noteworthy. The determination of basal area was more successful for the test area than the estimation of timber volume. In the literature, many success stories are detailed. However, it is also stressed that the number and quality of the training and verification areas are pivotal for the applicability of the k-nn method. The outcomes of my investigation greatly support this observation. The selection of the raster image used for the regression procedure and the fidelity of the reference data also need to be taken into account. Since the spectral characteristics of the object represented in a satellite image change over time, so do the outcomes of the regression due to the intrinsic properties of the calculation procedure. Although the k-nn approach seems to be working well in the Scandinavian countries, conditions can be fundamentally different in Mongolia. In particular, with the factors outlined above affecting classification accuracy, more research is needed to address those issues related to k-nn.

With regards to the hypotheses framed for this study, the outcomes illustrate quite clearly the potential of employing UAV imagery for tree height extraction as well as for species and crown diameter determination. However, in a few instances, the visual interpretation of the aerial photographs was superior to the computer-aided automatic extraction of forest attributes. Furthermore, recently developed sophisticated classifying approaches such as Support Vector Machines and Random Forest demonstrate excellent suitability for tree species discrimination. Object-based classification approaches appear to be tailored for very high-resolution imagery, however, at medium scale, pixel-based classifiers outperformed the former in this study. The presented results suggest that in almost all instances, the accuracy requirements of forest

inventory on a local scale can be met. However, there is no such thing as a universal 'fits all' application method.

Since the Mongolian forests are under increasing pressure to provide the ecosystem services demanded for, a sustainable forest management cannot do without sound information on the condition of the taigas. Sophisticated remote sensing and GIS technology bear the potential to at least support people in the field and decision makers by providing highly accurate data on a local scale. As such, extended capacity building and training of the forest experts is warranted. The increased deployment of UAVs can also improve the knowledge on forest structure attributes and growth and yield matters. One of the most important prerequisites, however, is the establishment of permanent sampling plots to be used for monitoring and appraisal purposes. This could also help improve and update the existing growth and yield tables. In my view, another aspect deserves attention – it concerns the fundamental lack of knowledge in respect to the specific growing conditions of forests and the impact of a changing climate in Mongolia. For this reason, it is suggested to initiate investigations in the soil – forest growth relationship and the potential expansion of the meteorological network. Remote sensing technology can also play an important role in this respect. All things considered, the increasing number of remote sensing experts that are being trained at certain institutions in Mongolia to expedite the propagation of this expertise provides reason for optimism. Nevertheless, without the implementation of specific aid programmes, certain goals will not be able to be achieved.

10. References

3D Natives. **2019** *TOP 10 der besten Photogrammetrie Software*. https://www.3dnatives.com/de/top-10-der-besten-photogrammetrie-software-190920191/ (accessed on 20 April, 2020).

Aasen, H. and Bolten, A. **2018** Multi-temporal high-resolution imaging spectroscopy with hyperspectral 2D imagers – From theory to application. *Remote Sensing of Environment* 205, 374–389.

Abdi, A.M. **2020** Land cover and land use classification performance of machine learning algorithms in a boreal landscape using Sentinel-2 data. *GIScience & Remote Sensing* 57, 1–20.

Abdollahnejad, A.; Panagiotidis, D. and Surový, P. **2018** Estimation and Extrapolation of Tree Parameters Using Spectral Correlation between UAV and Pléiades Data. *Forests* 9, 1–15.

Abdullah S, S.; Tahar, K.N.; Rashid, M.F.A. and Osoman, M.A. **2019** Capabilities of UAV-Based Watershed Segmentation Method for Estimating Tree Crown: A Case Study of Oil Palm Tree. *IOP Conf. Ser.: Earth Environ. Sci.* 385, 1–8.

Abedi, R. and Bonyad, A.E. **2015** Estimation and Mapping Forest Attributes Using “k Nearest Neighbor” Method on IRS-P6 LISS III Satellite Image Data. *Ecologia Balkanica*.

Ackerman, S.A. and Knox, J. **2012** *Meteorology: Understanding the atmosphere.* 3rd edn. Jones & Bartlett Learning.

Adam, E.; Mutanga, O.; Odindi, J. and Abdel-Rahman, E.M. **2014** Land-use/cover classification in a heterogeneous coastal landscape using RapidEye imagery: evaluating the performance of random forest and support vector machines classifiers. *International Journal of Remote Sensing* 35, 3440–3458.

Adams, H.D.; Macalady, A.K.; Breshears, D.D.; Allen, C.D. and Stephenson, N.L. *et al.* **2010** Climate-Induced Tree Mortality. Earth System Consequences. *Eos Trans. AGU* 91, 153.

Adams, M.A. **2013** Mega-fires, tipping points and ecosystem services. Managing forests and woodlands in an uncertain future. *Forest Ecology and Management* 294, 250–261.

Adão, T.; Hruška, J.; Pádua, L.; Bessa, J. and Peres, E. *et al.* **2017** Hyperspectral Imaging: A Review on UAV-Based Sensors, Data Processing and Applications for Agriculture and Forestry. *Remote Sensing* 9, 1–30.

Adelabu, S.; Mutanga, O. and Adam, E. **2014** Evaluating the impact of red-edge band from Rapideye image for classifying insect defoliation levels. *ISPRS Journal of Photogrammetry and Remote Sensing* 95, 34–41.

Agisoft. **2011** *Agisoft Lens: Manual Version 0.4.0*.

Agisoft. **2015** *Algorithms used in Photoscan: Forum*. https://www.agisoft.com/forum/index.php?topic=89.0 (accessed on 13 April, 2020).

Agisoft. **2018** *Agisoft PhotoScan User Manual: Professional Edition, Version 1.4.* Agisoft.

Aguilar, M.A.; Saldaña, M.M. and Aguilar, F.J. **2013** GeoEye-1 and WorldView-2 pan-sharpened imagery for object-based classification in urban environments. *International Journal of Remote Sensing* 34, 2583–2606.

Ahrens, W. **2001** Analyse der Waldentwicklung in Naturwaldreservaten auf Basis digitaler Orthobilder. Dissertation, Freiburg.

Akar, Ö. **2017** Mapping land use with using Rotation Forest algorithm from UAV images. *European Journal of Remote Sensing* 50, 269–279.

Albertz, J. **1970** Sehen und Wahrnehmen bei der Luftbildinterpretation. *Bildmessung und Luftbildwesen*, 25–34.

Albertz, J. **2009** *Einführung in die Fernerkundung: Grundlagen der Interpretation von Luft- und Satellitenbildern.* 4th edn. WBG (Wiss. Buchges.).

Albertz, J. **2013** *Einführung in die Fernerkundung: Grundlagen der Interpretation von Luft- und Satellitenbildern.* 5th edn. WBG (Wissenschaftliche Buchgesellschaft).

Alidoost, F. and Arefi, H. **2017** Comparison of UAS-based photogrammetry software for 3D point cloud generation: a survey over a historical site. *ISPRS Annals of Photogrammetry, Remote Sensing and Spatial Information Sciences* IV-4/W4, 55–61.

Allen, C.D.; Macalady, A.K.; Chenchouni, H.; Bachelet, D. and McDowell, N. *et al.* **2010** A global overview of drought and heat-induced tree mortality reveals emerging climate change risks for forests. *Forest Ecology and Management* 259, 660–684.

Allen, J.L. and Sorbel, B. **2008** Assessing the differenced Normalized Burn Ratio's ability to map burn severity in the boreal forest and tundra ecosystems of Alaska's national parks. *Int. J. Wildland Fire* 17, 1–13.

Alonzo, M.; Andersen, H.-E.; Morton, D. and Cook, B. **2018** Quantifying Boreal Forest Structure and Composition Using UAV Structure from Motion. *Forests* 9.

Alonzo, M.; Bookhagen, B. and Roberts, D.A. **2014** Urban tree species mapping using hyperspectral and lidar data fusion. *Remote Sensing of Environment* 148, 70–83.

Altrell, D. **2017** Forest inventory, Ulaanbaatar. Personal communication.

Altrell, D. and Erdenejav, E. **2016** *Mongolian Multipurpose National Forest Inventory (NFI) 2014-2016.* Ministry of Environment and Tourism, Mongolia.

Alvarez-Taboada, F.; Paredes, C. and Julián-Pelaz, J. **2017** Mapping of the invasive species hakea sericea using Unmanned Aerial Vehicle (UAV) and WorldView-2 imagery and an object-oriented approach. *Remote Sensing* 9, 913.

Andersen, H.-E.; Reutebuch, S.E. and McGaughey, R.J. **2006** A rigorous assessment of tree height measurements obtained using airborne lidar and conventional field methods. *Canadian Journal of Remote Sensing* 32, 355–366.

Arbeitsgruppe Forstlicher Luftbildinterpreten. **2012** *Das digitale Luftbild.* Universitätsverlag Göttingen.

Ardila, J.P.; Bijker, W.; Tolpekin, V.A. and Stein, A. **2012** Multitemporal change detection of urban trees using localized region-based active contours in VHR images. *Remote Sensing of Environment* 124, 413–426.

Assmann, J.J.; Kerby, J.T.; Cunliffe, A.M. and Myers-Smith, I.H. **2019** Vegetation monitoring using multispectral sensors — best practices and lessons learned from high latitudes. *J. Unmanned Veh. Sys.* 7, 54–75.

Astola, H.; Ahola, H.; Andersson, K.; Häme, T. and Kilpi, J. *et al.* **2010** *Towards operative forest inventory by extraction of tree level information from VHR satellite images.* European Space Agency.

Australian Bureau of Agricultural and Resource Economics and Sciences. **2019** *State of the Forests Report 2018.* Department of Agriculture and Water Resources (ABARES), Australia.

Baasan, B. **2010** Entwicklung eines Inventurmodells als Grundlage einer nachhaltigen Bewirtschaftung am Beispiel eines Waldgebiets im südwestlichen Teil des Khentii-Gebirges der Mongolei. Dissertation. Forstliche Biometrie, Freiburg.

Baldocchi, D.; Kelliher, F.M.; Black, T.A. and Jarvis, P. **2000** Climate and vegetation controls on boreal zone energy exchange. *Global change biology* 6, 69–83.

Baltsavias, E. **1999** Airborne laser scanning: basic relations and formulas. *ISPRS Journal of Photogrammetry and Remote Sensing* 54, 199–214.

Baltsavias, E.; Gruen, A.; Eisenbeiss, H.; Zhang, L. and Waser, L.T. **2008** High-quality image matching and automated generation of 3D tree models. *International Journal of Remote Sensing* 29, 1243–1259.

Banerjee, K.; Panda, S.; Bandyopadhyay, J. and Jain, M.K. **2014** Forest canopy density mapping using advance geospatial technique. *IJISET - International Journal of Innovative Science, Engineering and Technology* Vol 1, 358–361.

Bannari, A.; Morin, D.; Bonn, F. and Huete, A.R. **1995** A review of vegetation indices. *Remote Sensing Reviews* 13, 95–120.

Banu, T.P.; Borlea, G.F. and Banu, C. **2016** The Use of Drones in Forestry. *JESE-B* 5, 557–562.

Barbedo, J.G.A. **2019** A Review on the Use of Unmanned Aerial Vehicles and Imaging Sensors for Monitoring and Assessing Plant Stresses. *Drones* 3, 1–27.

Baret, F. and Guyot, G. **1991** Potentials and Limits of Vegetation LAI and APAR Assessment. *Remote Sensing of Environment*, 161–173.

Bartsch, N.; Lüpke, B. von and Röhrig, E. **2020** *Waldbau auf ökologischer Grundlage.* 8th edn. Verlag Eugen Ulmer.

Batima, P.; Natsagdorj, L.; Gombluudev, P. and Erdenetsegtseg, B. **2005** *Observed climate change in Mongolia.* AIACC, Ulaanbaatar.

Bayer, S. **2018** *Automatisierte Einzelbaumextraktion im Forst*.

Beaudoin, A.; Bernier, P.Y.; Guindon, L.; Villemaire, P. and Guo, X.J. *et al.* **2014** Mapping attributes of Canada's forests at moderate resolution through k NN and MODIS imagery. *Canadian Journal of Forest Research* 44, 521–532.

Beck, M. **2019** UAV regulations. Niedersächsische Landesbehörde für Straßenbau und Verkehr. Persönliche Mitteilung.

Beck, P.S.A.; Goetz, S.J.; Mack, M.C.; Alexander, H.D. and Jin, Y. *et al.* **2011** The impacts and implications of an intensifying fire regime on Alaskan boreal forest composition and albedo. *Global change biology* 17, 2853–2866.

Beebe, G.; Lund, E.W.; Wilcox, C.; Kaage, W. and Ben Jr, L. **2020** *Interagency Standards for Fire and Fire Aviation Operations.* Department of the Interior, USA; USDA Forest Service, Boise, Idaho, USA.

Beguet, B.; Chehata, N.; Boukir, S. and Guyon, D. **2014** Classification of forest structure using very high resolution Pleiades image texture. In *IGARSS 2014*. IGARSS (ed), pp. 2324–2327.

Begum, F.; Bajracharya, R.M.; Sharma, S. and Sitaula, B.K. **2010** Influence of slope aspect on soil physico-chemical and biological properties in the mid hills of central Nepal. *International Journal of Sustainable Development & World Ecology* 17, 438–443.

Belgiu, M. and Drăguţ, L. **2016** Random forest in remote sensing: A review of applications and future directions. *ISPRS Journal of Photogrammetry and Remote Sensing* 114, 24–31.

Belouard, T.; Py, N.; Maillet, G.; Guyon, D. and Pausader, M. *et al.* **2015** PINASTEREO - estimation de la hauteur dominante et de la biomasse forestiere dans le Massif des Landes de Gascogne a partir d'images stereoscopiques Pleiades. *Revue Francaise de Photogrammetrie et de Teledetection*, 133–139.

Belward, A.S. and Skøien, J.O. **2015** Who launched what, when and why; trends in global land-cover observation capacity from civilian earth observation satellites. *ISPRS Journal of Photogrammetry and Remote Sensing* 103, 115–128.

Benomar, L.; DesRochers, A. and Larocque, G.R. **2013** Comparing growth and fine root distribution in monocultures and mixed plantations of hybrid poplar and spruce. *Journal of Forestry Research* 24, 247–254.

Bergeron, Y.; Irulappa Pillai Vijayakumar, D.B.; Ouzennou, H.; Raulier, F. and Leduc, A. *et al.* **2017** Projections of future forest age class structure under the influence of fire and harvesting: implications for forest management in the boreal forest of eastern Canada. *Forestry: An International Journal of Forest Research* 90, 485–495.

Bergseng, E.; Ørka, H.O.; Næsset, E. and Gobakken, T. **2015** Assessing forest inventory information obtained from different inventory approaches and remote sensing data sources. *Annals of Forest Science* 72, 33–45.

Bernhard, O. **2003** *Einführung in die Fernerkundung: Lehrveranstaltung 60-304, Waldinventur II.* Eidg. Forschungsanstalt WSL, Birmensdorf, Schweiz.

Berni, J.; Zarco-Tejada, P.J.; Suarez, L. and Fereres, E. **2009** Thermal and Narrowband Multispectral Remote Sensing for Vegetation Monitoring From an Unmanned Aerial Vehicle. *IEEE Transactions on geoscience and remote sensing* 47, 722–738.

Berterretche, M.; Hudak, A.T.; Cohen, W.B.; Maiersperger, T.K. and Gower, S.T. *et al.* **2005** Comparison of regression and geostatistical methods for mapping Leaf Area Index (LAI) with Landsat ETM+ data over a boreal forest. *Remote Sensing of Environment* 96, 49–61.

Beyerer, J.; Richter, M. and Nagel, M. **2018** *Pattern recognition: Introduction, features, classifiers and principles.* De Gruyter.

Birdal, A.C.; Avdan, U. and Türk, T. **2017** Estimating tree heights with images from an unmanned aerial vehicle. *Geomatics, Natural Hazards and Risk* 8, 1144–1156.

Bishop, C.M. **2009** *Pattern recognition and machine learning.* 8th edn. Springer.

Blaschke, T. **2010** Object based image analysis for remote sensing. *ISPRS Journal of Photogrammetry and Remote Sensing* 65, 2–16.

Boer, M.P.; Macfarlane, C.; Norris, J.; Sadler, R.J. and Wallace, J. *et al.* **2008** Mapping burned areas and burn severity patterns in SW Australian eucalypt forest using remotely-sensed changes in leaf area index. *Remote Sensing of Environment* 112, 4358–4369.

Bögre, L.; Magyar, Z. and López-Juez, E. **2008** New clues to organ size control in plants. *Genome biology* 9, 226.

Bohannon, J. **2008** The Big Thaw Reaches Mongolia's Pristine North. *Science Magazine*, 567–568.

Bohlin, J.; Wallerman, J. and Fransson, J.E.S. **2012** Forest variable estimation using photogrammetric matching of digital aerial images in combination with a high-resolution DEM. *Scandinavian Journal of Forest Research* 27, 692–699.

Böhner, J. and Antonić, O. **2009** Land-Surface Parameters Specific to Topo-Climatology. In *Geomorphometry*: *Concepts, software, applications*. 1st edn. T. Hengl and H.I. Reuter (eds). Elsevier, pp. 195–226.

Boiarskii, B. and Hasegawa, H. **2019** Comparison of NDVI and NDRE Indices to Detect Differences in Vegetation and Chlorophyll Content. *Journal of Mechanics of Continua and Mathematical Sciences* 2019, 20–29.

Bonan, G.B. **2008** Forests and climate change: forcings, feedbacks, and the climate benefits of forests. *Science (New York, N.Y.)* 320, 1444–1449.

Bonan, G.B. and Shugart, H.H. **1989** Environmental Factors and Ecological Processes in Boreal Forests. *Annual Review of Ecology and Systematics* 20, 1–28.

Bosak, K. **2011** *Secrets of UAV photomapping*.

Bowie, R.; Brown, J. and Felix, F. **2015** *Biennial Report, FY 2013-2015: Sagehen Creek Field Station.* University of California, Berkeley.

Braga, J.R.; Peripato, V.; Dalagnol, R.; Ferreira, M.P. and Tarabalka, Y. *et al.* **2020** Tree Crown Delineation Algorithm Based on a Convolutional Neural Network. *Remote Sensing* 12, 1–27.

Breidenbach, J.; Koch, B.; Kändler, G. and Kleusberg, A. **2008** Quantifying the influence of slope, aspect, crown shape and stem density on the estimation of tree height at plot level using lidar and InSAR data. *International Journal of Remote Sensing* 29, 1511–1536.

Breidenbach, J.; Næsset, E.; Lien, V.; Gobakken, T. and Solberg, S. **2010** Prediction of species specific forest inventory attributes using a nonparametric semi-individual tree crown approach based on fused airborne laser scanning and multispectral data. *Remote Sensing of Environment* 114, 911–924.

Breiman, L. **2001** Random forests. *Machine Learning* 45, 5–32.

Brieger, F.; Herzschuh, U.; Pestryakova, L.A.; Bookhagen, B. and Zakharov, E.S. *et al.* **2019** Advances in the Derivation of Northeast Siberian Forest Metrics Using High-Resolution UAV-Based Photogrammetric Point Clouds. *Remote Sensing* 11, 1447.

Broge, N. and Leblanc, E. **2001** Comparing prediction power and stability of broadband and hyperspectral vegetation indices for estimation of green leaf area index and canopy chlorophyll density. *Remote Sensing of Environment* 76, 156–172.

Brosofske, K.D.; Froese, R.E.; Falkowski, M.J. and Banskota, A. **2014** A Review of Methods for Mapping and Prediction of Inventory Attributes for Operational Forest Management. *Forest Science* 60, 733–756.

Brovkina, O.; Cienciala, E.; Surový, P. and Janata, P. **2018** Unmanned aerial vehicles (UAV) for assessment of qualitative classification of Norway spruce in temperate forest stands. *Geo-spatial Information Science* 21, 12–20.

Büchi, R. **2018** *Das große Buch der Drohnen: Grundlagen - Technik - Flugpraxis.* 1st edn. vth.

Buho, H.; Kaneko, M. and Ogaw, K. **2009** Correction of NDVI Calculated from ASTER L1B and ASTER (AST07) Data Based on Ground Measurement. In *Jedlovec (Hg.) Advances in Geoscience and Remote*, pp. 45–56.

Bunting, P. and Lucas, R. **2006** The delineation of tree crowns in Australian mixed species forests using hyperspectral Compact Airborne Spectrographic Imager (CASI) data. *Remote Sensing of Environment* 101, 230–248.

Bussler, H. and Walentowski, H. **2011** *Wälder in der Mongolei.* LWF Freising.

Byambasuren, O. **2011** Fire and stand dynamics in different forest types of the West Khentey Mountains, Mongolia. Dissertation, Göttingen.

Byambasuren, O. **2018** *Mongolia – Tackling REDD+ in Boreal Forest Ecosystems: Development of a National Strategy*.

Calderón, R.; Navas-Cortés, J.A.; Lucena, C. and Zarco-Tejada, P.J. **2013** High-resolution airborne hyperspectral and thermal imagery for early detection of Verticillium wilt of olive using fluorescence, temperature and narrow-band spectral indices. *Remote Sensing of Environment* 139, 231–245.

Campbell, G.S. **2012** *The researcher's complete guide to Leaf Area Index (LAI)*. https://www.metergroup.com/environment/articles/lp80-pain-free-leaf-area-index-lai/ (accessed on 12 November, 2020).

Campbell, G.S. and Norman, J.M. **1998** *An Introduction to Environmental Biophysics.* Springer New York.

Campion, M.; Ranganathan, P. and Faruque, S. **2018** A Review and Future Directions of UAV Swarm Communication Architectures. In *2018 IEEE International Conference on Electro/Information Technology (EIT)*: *3-5 May 2018*. IEEE (ed). IEEE, pp. 903–908.

Canty, M.J. **2014** *Image analysis, classification and change detection in remote sensing: With algorithms for ENVI/IDL and Python.* 3rd edn. CRC Press.

Cao, J.; Leng, W.; Liu, K.; Liu, L. and He, Z. *et al.* **2018** Object-Based Mangrove Species Classification Using Unmanned Aerial Vehicle Hyperspectral Images and Digital Surface Models. *Remote Sensing* 10, 89.

Cao, L.; Liu, H.; Fu, X.; Zhang, Z. and Shen, X. *et al.* **2019** Comparison of UAV LiDAR and Digital Aerial Photogrammetry Point Clouds for Estimating Forest Structural Attributes in Subtropical Planted Forests. *Forests* 10, 145.

Carbonneau, P.E. and Dietrich, J.T. **2017** Cost-effective non-metric photogrammetry from consumer-grade sUAS: implications for direct georeferencing of structure from motion photogrammetry. *Earth Surf. Process. Landforms* 42, 473–486.

Cardil, A.; Otsu, K.; Pla, M.; Silva, C.A. and Brotons, L. **2019** Quantifying pine processionary moth defoliation in a pine-oak mixed forest using unmanned aerial systems and multispectral imagery. *PloS one* 14, 1-19.

Carleer, A. and Wolff, E. **2004** Exploitation of Very High Resolution satellite data for tree species identification. *Photogrammetric Engineering & Remote Sensing* 70, 135–140.

Carr, J.C. and Slyder, J.B. **2018** Individual tree segmentation from a leaf-off photogrammetric point cloud. *International Journal of Remote Sensing* 39, 5195–5210.

Carrivick, J.L.; Quincey, D.J. and Smith, M. **2016** *Structure from motion in the geosciences.* Wiley Blackwell.

Carvajal-Ramírez, F.; Marques da Silva, J.R.; Agüera-Vega, F.; Martínez-Carricondo, P. and Serrano, J. *et al.* **2019** Evaluation of fire severity indices based on pre- and post-fire multispectral imagery sensed from UAV. *Remote Sensing* 11, 993.

Catapano, I.; Gennarelli, G.; Ludeno, G.; Noviello, C. and Esposito, G. *et al.* **2020** Small multicopter-UAV-based radar imaging: performance assessment for a single flight track. *Remote Sensing* 12, 774.

Chao, H.; Gu, Y. and Napolitano, M. **2013** A survey of optical flow techniques for UAV navigation applications. In *International Conference on Unmanned Aircraft Systems (ICUAS), 2013*: *28-31 May 2013, Grand Hyatt Atlanta, Atlanta, Georgia ; conference proceedings*. IEEE, pp. 710–716.

Chapuis, A. **1995** Developments in digital photogrammetry and a description of the flow of data through a digital photogrammetric system. In *Digital Photogrammetry and Remote Sensing '95*. E.A. Fedosov (ed). SPIE, pp. 49–56.

Chason, J.W.; Baldocchi, D.D. and Huston, M.A. **1991** A comparison of direct and indirect methods for estimating forest canopy leaf area. *Agricultural and Forest Meteorology* 57, 107–128.

Chavez, P.S. **1988** An improved dark-object subtraction technique for atmospheric scattering correction of multispectral data. *Remote Sensing of Environment* 24, 459–479.

Chavez, P.S. **1996** Image-Based Atmospheric Corrections - Revisited and Improved. *Photogrammetric Engineering & Remote Sensing* 1996, 1025–1036.

Chemura, A. **2012** Determination of the age of oil palm from crown projection area detected from WorldView-2 multispectral remote sensing data. Master thesis. International Institute for Geo-Information Science and Earth Observation (ITC), Enschede.

Chemura, A.; van Duren, I. and van Leeuwen, L.M. **2015** Determination of the age of oil palm from crown projection area detected from WorldView-2 multispectral remote sensing data. The case of Ejisu-Juaben district, Ghana. *ISPRS Journal of Photogrammetry and Remote Sensing* 100, 118–127.

Chen, G.; Hay, G.J. and St-Onge, B. **2012a** A GEOBIA framework to estimate forest parameters from lidar transects, Quickbird imagery and machine learning: A case study in Quebec, Canada. *International Journal of Applied Earth Observation and Geoinformation* 15, 28–37.

Chen, G.; Wulder, M.A.; White, J.C.; Hilker, T. and Coops, N.C. **2012b** Lidar calibration and validation for geometric-optical modeling with Landsat imagery. *Remote Sensing of Environment* 124, 384–393.

Chen, J.M. and Cihlar, J. **1996** Retrieving leaf area index of boreal conifer forests using Landsat TM images. *Remote Sensing of Environment* 55, 153–162.

Chen, J.M.; Menges, C.H. and Leblanc, S.G. **2005** Global mapping of foliage clumping index using multi-angular satellite data. *Remote Sensing of Environment* 97, 447–457.

Chen, Q.; Baldocchi, D.; Gong, P. and Kelly, M. **2006** Isolating Individual Trees in a Savanna Woodland Using Small Footprint Lidar Data. *Photogrammetric Engineering & Remote Sensing* 72, 923–932.

Chen, S.; McDermid, G.; Castilla, G. and Linke, J. **2017a** Measuring Vegetation Height in Linear Disturbances in the Boreal Forest with UAV Photogrammetry. *Remote Sensing* 9, 1–22.

Chen, X.; Vogelmann, J.E.; Rollins, M.; Ohlen, D. and Key, C.H. *et al.* **2011** Detecting post-fire burn severity and vegetation recovery using multitemporal remote sensing spectral indices and field-collected composite burn index data in a ponderosa pine forest. *International Journal of Remote Sensing* 32, 7905–7927.

Chen, Y.; Hakala, T.; Karjalainen, M.; Feng, Z. and Tang, J. *et al.* **2017b** UAV-Borne Profiling Radar for Forest Research. *Remote Sensing* 9, 1–17.

Chen, Y.; Lin, Z.; Zhao, X.; Wang, G. and Gu, Y. **2014** Deep learning-based classification of hyperspectral data. *IEEE Journal of Selected Topics in Applied Earth Observations and Remote Sensing* 7, 2094–2107.

Chianucci, F. **2016** A note on estimating canopy cover from digital cover and hemispherical photography. *Silva Fennica* 50.

Chirici, G. **2012** K-NN FOREST. A software for the non-parametric prediction and mapping of environmental variables by the k-Nearest Neighbors algorithm. *European Journal of Remote Sensing*, 433–442.

Chirici, G.; Barbati, A.; Corona, P.; Marchetti, M. and Travaglini, D. *et al.* **2008** Non-parametric and parametric methods using satellite images for estimating growing stock volume in alpine and Mediterranean forest ecosystems. *Remote Sensing of Environment* 112, 2686–2700.

Chisholm, R.A.; Cui, J.; Lum, S.K.Y. and Chen, B.M. **2013** UAV LiDAR for below-canopy forest surveys. *Journal of Unmanned Vehicle Systems* 01, 61–68.

Chu, T.; Guo, X. and Takeda, K. **2016** Temporal dependence of burn severity assessment in Siberian larch (Larix sibirica) forest of northern Mongolia using remotely sensed data. *Int. J. Wildland Fire* 25, 685.

Ciesla, W.M. **2000** *Remote sensing in forest health protection.* USDA Forest Service Remote Sensing Applications Center, Salt Lake City.

Cipar, J.; Cooley, T. and Lockwood, R. **2008** Summer to autumn changes in vegetation spectral indices of deciduous trees. In *Remote Sensing and Modeling of Ecosystems for Sustainability V*. W. Gao and H. Wang (eds). SPIE, p. 708306.

Cleve, K.; Chapin, F.S.; Flanagan, P.W.; Viereck, L.A. and Dyrness, C.T. **1986** *Forest Ecosystems in the Alaskan Taiga: A Synthesis of Structure and Function.* Springer New York.

Colomina, I. and Molina, P. **2014** Unmanned aerial systems for photogrammetry and remote sensing: A review. *ISPRS Journal of Photogrammetry and Remote Sensing* 92, 79–97.

Coogan, S.C.; Robinne, F.-N.; Jain, P. and Flannigan, M.D. **2019** Scientists' warning on wildfire — a Canadian perspective. *Canadian Journal of Forest Research* 49, 1015–1023.

Cook, K.L. and Dietze, M. **2019** Short Communication: A simple workflow for robust low-cost UAV-derived change detection without ground control points. *Earth Surf. Dynam.* 7, 1009–1017.

Coops, N.; Delahaye, A. and Pook, E. **1997** Estimation of Eucalypt Forest Leaf Area Index on the South Coast of New South Wales using Landsat MSS Data. *Australian Journal of Botany* 45, 757–769.

Corona, P., Köhl, M. and Marchetti, M. (eds). **2003** *Advances in forest inventory for sustainable forest management and biodiversity monitoring.* Kluwer Academic Publ.

Corsi, A.; Dore, G.; Nagpal, T.; Whitten, T. and Iyer, R. *et al.* **2002** *Mongolia Environment Monitor 2002: Report in Mongolian.* World Bank Group.

Côté, J.-F.; Fournier, R.A. and Egli, R. **2011** An architectural model of trees to estimate forest structural attributes using terrestrial LiDAR. *Environmental Modelling & Software* 26, 761–777.

Cracknell, A.P. and Hayes, L. **2007** *Introduction to remote sensing.* 2nd edn. CRC Press.

Cramer, M., Sabow, F. and Förg, P. (eds). **2016** *Direkte Georeferenzierung in UAS-Anwendungen – Eine Beispielanwendung der Landesvermessung Baden-Württemberg*.

Crisp, N.; Dick, J. and Mullins, M. **2004** *Mongolia Forestry Sector Review.* World Bank, Victoria, B.C.

Culvenor, D.S. **2002** TIDA: an algorithm for the delineation of tree crowns in high spatial resolution remotely sensed imagery. *Computers & Geosciences* 28, 33–44.

Cutler, A.; Cutler, D.R. and Stevens, J.R. **2012** Random Forests. In *Ensemble Machine Learning*: *Methods and Applications*. C. Zhang and Y. Ma (eds). Springer US, pp. 157–175.

Dagvardoj, D.; Batjargal, Z. and Natsagdorj, L. **2014** *MARCC 2014: Mongolia Second Assessment Report on Climate Change*.

Daliman, S.; Abu Bakar, S. A. R. and Busu, I. **2015** *Oil Palm Tree Enumeration Based on Template Matching: World Virtual Conference On Applied Sciences And Engineering Applications*.
https://www.researchgate.net/publication/287608447_Oil_Palm_Tree_Enumeration_Based_on_Template_Matching, Johor Bahru, Malaysia.

Dall'Asta, E.; Thoeni, K.; Santise, M.; Forlani, G. and Giacomini, A. *et al.* **2015** Network design and quality checks in automatic orientation of close-range photogrammetric blocks. *Sensors (Basel, Switzerland)* 15, 7985–8008.

Dalponte, M.; Ørka, H.O.; Ene, L.T.; Gobakken, T. and Næsset, E. **2014** Tree crown delineation and tree species classification in boreal forests using hyperspectral and ALS data. *Remote Sensing of Environment* 140, 306–317.

Dalponte, M.; Ørka, H.O.; Gobakken, T.; Gianelle, D. and Naesset, E. **2013** Tree Species Classification in Boreal Forests With Hyperspectral Data. *IEEE Transactions on geoscience and remote sensing* 51, 2632–2645.

Dandois, J.; Olano, M. and Ellis, E. **2015** Optimal Altitude, Overlap, and Weather Conditions for Computer Vision UAV Estimates of Forest Structure. *Remote Sensing* 7, 13895–13920.

Dandois, J.P. and Ellis, E.C. **2010** Remote sensing of vegetation structure using computer vision. *Remote Sensing* 2, 1157–1176.

Dandois, J.P. and Ellis, E.C. **2013** High spatial resolution three-dimensional mapping of vegetation spectral dynamics using computer vision. *Remote Sensing of Environment* 136, 259–276.

Danilin, I.M. and Tsogt, Z. **2014** Dynamics of structure and biological productivity of post-fire larch forests in the Northern Mongolia. *Contemp. Probl. Ecol.* 7, 158–169.

Danson, F.M.; Hetherington, D.; Morsdorf, F.; Koetz, B. and Allgower, B. **2007** Forest canopy gap fraction from Terrestrial Laser Scanning. *IEEE Geoscience and Remote Sensing Letters* 4, 157–160.

Daponte, P.; Vito, L. de; Glielmo, L.; Iannelli, L. and Liuzza, D. *et al.* **2019** A review on the use of drones for precision agriculture. *IOP Conference Series: Earth and Environmental Science* 275, 1–11.

Dashtseren, A.; Ishikawa, M.; Iijima, Y. and Jambaljav, Y. **2014** Temperature Regimes of the Active Layer and Seasonally Frozen Ground under a Forest-Steppe Mosaic, Mongolia. *Permafrost and Periglacial Processes* 25, 295–306.

Davi, H.; Soudani, K.; Deckx, T.; Dufrene, E. and Le Dantec, V. *et al.* **2006** Estimation of forest leaf area index from SPOT imagery using NDVI distribution over forest stands. *International Journal of Remote Sensing* 27, 885–902.

Dell, M.; Stone, C.; Osborn, J.; Glen, M. and McCoull, C. *et al.* **2019** Detection of necrotic foliage in a young Eucalyptus pellita plantation using unmanned aerial vehicle RGB photography – a demonstration of concept. *Australian Forestry* 82, 79–88.

DellaSala, D.A. and Hanson, C.T. **2015** *The ecological importance of mixed-severity fires: Nature's Phoenix.* Elsevier.

Dempewolf, J.; Nagol, J.; Hein, S.; Thiel, C. and Zimmermann, R. **2017** Measurement of within-season tree height growth in a mixed forest stand using UAV imagery. *Forests* 8, 1–15.

Deng, S.; Katoh, M.; Guan, Q.; Yin, N. and Li, M. **2014** Interpretation of Forest Resources at the Individual Tree Level at Purple Mountain, Nanjing City, China, Using WorldView-2 Imagery by Combining GPS, RS and GIS Technologies. *Remote Sensing* 6, 87–110.

Denisova, A.; Kavelenova, L.; Korchikov, E.; Prokhorova, N. and Terentyeva, D. *et al.* **2019** Tree species classification for clarification of forest inventory data using Sentinel-2 images. In *Seventh International Conference on Remote Sensing and Geoinformation of the Environment (RSCy2019)*: *18-21 March 2019, Paphos, Cyprus*. K. Themistocleous (ed). SPIE, p. 3.

Department of Biology, School of Arts and Sciences, National University of Mongolia (NUM) (ed). **2017** *Biodiversity Research of Mongolia*.

Desale, R.; Chougule, A.; Choudari, M.; Borhade, V. and Teli, S.N. **2019** Unmanned Aerial Vehicle for pesticides spraying. *IJSART* 5, 79–82.

Deutscher Wetter Dienst. **2021** *Klima Atlas Deutschland*. https://www.dwd.de/DE/leistungen/deutscherklimaatlas/deutscherklimaatlas.html?nn=480164 (accessed on 23 February, 2021).

Dezsö, B.; Fekete, I.; Ger, D.; Giachetta, R. and Laszlo, I. **2012** *Object-based image analysis in remote sensing applications using various segmentation techniques.* Faculty of Informatics, Eötvös Lorand University, Budapest.

Ding, W.; Wang, J.; Han, S.; Almagbile, A. and Garratt, M. *et al.* Adding optical flow into the GPS/INS integration for UAV navigation. In *IGNSS Symposium 2009*, pp. 1–14.

Dobrowski, S.Z.; Abatzoglou, J.T.; Greenberg, J.A. and Schladow, S.G. **2009** How much influence does landscape-scale physiography have on air temperature in a mountain environment? *Agricultural and Forest Meteorology* 149, 1751–1758.

Dong, C.; Zhao, G.; Meng, Y.; Li, B. and Peng, B. **2020** The Effect of Topographic Correction on Forest Tree Species Classification Accuracy. *Remote Sensing* 12, 1–21.

Dong, P. and Chen, Q. **2018** *LiDAR remote sensing and applications.* CRC Press, Taylor & Francis Group.

Dore, S.; Kolb, T.E.; Montes-Helu, M.; Eckert, S.E. and Sullivan, B.W. *et al.* **2010** Carbon and water fluxes from ponderosa pine forests disturbed by wildfire and thinning. *Ecological applications : a publication of the Ecological Society of America* 20, 663–683.

Dufrêne, E. and Bréda, N. **1995** Estimation of deciduous forest leaf area index using direct and indirect methods. *Oecologia* 104, 156–162.

Dulamsuren, C. **2004** Floristische Diversität, Vegetation und Standortbedingungen in der Gebirgstaiga des Westkhentej, Nordmongolei. Dissertation, Göttingen.

Dulamsuren, C. and Hauck, M. **2008** Spatial and seasonal variation of climate on steppe slopes of the northern Mongolian mountain taiga. *Grassland Science* 54, 217–230.

Dulamsuren, C.; Hauck, M.; Bader, M.; Oyungerel, S. and Osokhjargal, D. *et al.* **2009** The different strategies of Pinus sylvestris and Larix sibirica to deal with summer drought in a northern Mongolian forest–steppe ecotone suggest a future superiority of pine in a warming climate. *Canadian Journal of Forest Research* 39, 2520–2528.

Dulamsuren, C.; Hauck, M.; Khishigjargal, M.; Leuschner, H.H. and Leuschner, C. **2010a** Diverging climate trends in Mongolian taiga forests influence growth and regeneration of Larix sibirica. *Oecologia* 163, 1091–1102.

Dulamsuren, C.; Hauck, M. and Leuschner, C. **2010b** Recent drought stress leads to growth reductions in Larix sibirica in the western Khentey, Mongolia. *Global change biology*, no-no.

Dulamsuren, C.; Hauck, M.; Leuschner, H.H. and Leuschner, C. **2011** Climate response of tree-ring width in Larix sibirica growing in the drought-stressed forest-steppe ecotone of northern Mongolia. *Annals of Forest Science* 68, 275–282.

Dulamsuren, C.; Hauck, M. and Mühlenberg, M. **2005a** Vegetation at the taiga forest–steppe borderline in the western Khentey Mountains, northern Mongolia. *Annales Botanici Fennici*, 411–426.

Dulamsuren, C.; Khishigjargal, M.; Leuschner, C. and Hauck, M. **2014** Response of tree-ring width to climate warming and selective logging in larch forests of the Mongolian Altai. *Journal of Plant Ecology* 7, 24–38.

Dulamsuren, C.; Klinge, M.; Degener, J.; Khishigjargal, M. and Chenlemuge, T. *et al.* **2016** Carbon pool densities and a first estimate of the total carbon pool in the Mongolian forest-steppe. *Global change biology* 22, 830–844.

Dulamsuren, C.; Solongo, B. and Mühlenberg, M. **2005b** Comments on the Red Data Book of endangered plant species of Mongolia. *Mongolian Journal of Biological Sciences* 3, 1–6.

Dulamsuren, C.; Welk, E.; Jäger, E.J.; Hauck, M. and Mühlenberg, M. **2005c** Range-habitat relationships of vascular plant species at the taiga forest-steppe borderline in the western Khentey Mountains, northern Mongolia. *Flora - Morphology, Distribution, Functional Ecology of Plants* 200, 376–397.

Dunford, R.; Michel, K.; Gagnage, M.; Piégay, H. and Trémelo, M.-L. **2009** Potential and constraints of Unmanned Aerial Vehicle technology for the characterization of Mediterranean riparian forest. *International Journal of Remote Sensing* 30, 4915–4935.

Durisova, L. and Asche, H. **2013** Mapping land cover with commercial and freeware image classification software. An example form Bavaria, Germany. In *Cartography in Central and Eastern Europe*: *Selected papers of the 1st ICA symposium on cartography for Central and Eastern Europe*. 1st edn. G. Gartner and F. Ortag (eds). Springer Berlin.

Eastman, J.R. **2020** *TerrSet2020 Manual: Geospatial Monitoring and Modeling System.* Clark University, Wocester, Massachusettes, USA, Wocester.

Ediriweera, S.; Danaher, T. and Pathirana, S. **2016** The influence of topographic variation on forest structure in two woody plant communities. A remote sensing approach. *Forest Systems* 25, 1–11.

Edson, C. and Wing, M.G. **2011** Airborne Light Detection and Ranging (LiDAR) for individual tree stem location, height, and biomass measurements. *Remote Sensing* 3, 2494–2528.

Edwards, P.N. **1998** *Timber Measurement - A Field Guide.* Forestry Commission, Edinburgh.

Eick, C. and Villaverde, K. **1996** Robust algorithms that locate local extrema of a function of one variable from interval measurement results: A remark. *Reliable Comput* 2, 213–218.

Eisenbeiss, H. **2009** UAV photogrammetry. Dissertation, Zürich.

Elatawneh, A.; Rappl, A.; Rehush, N.; Schneider, T. and Knoke, T. **2013** Forest tree species communities identification using multi phenological stages RapidEye data: case study in the forest of Freising. *From the basics to the service*, 21–38.

Endicott, E. **2012** *History of land use in mongolia: The thirteenth century to the present.* Palgrave Macmillan.

Endicott, M.L. **2018** *100 Best Agisoft PhotoScan Videos*. https://meta-guide.com/videography/100-best-agisoft-photoscan-videos (accessed on 03 May, 2020).

Enebish, B.; Dashkhuu, D.; Renchin, M.; Russell, M. and Singh, P. **2019** Impact of Climate on the NDVI of Northern Mongolia. *Journal of the Indian Society of Remote Sensing* 2, 4–11.

Erasmi, S.; Semmler, M.; Schall, P. and Schlund, M. **2019** Sensitivity of Bistatic TanDEM-X Data to Stand Structural Parameters in Temperate Forests. *Remote Sensing* 11, 1–18.

Erdenebat, E. **2014** Die Entwicklung des Waldbestandes der Zentralmongolei in den letzten 40 Jahren. Einsatz von Fernerkundung und GIS beim Waldmonitoring. Dissertation. Geowissenschaften, Berlin.

Erdenechuluun, T. **2006** *Wood Supply in Mongolia: The Legal and Illegal Economies.* World Bank, Washington, D.C.

Erikson, M. **2004a** Segmentation and classification of individual tree crowns. In high spatial resolution aerial images. Dissertation, Umeå.

Erikson, M. **2004b** Species classification of individually segmented tree crowns in high-resolution aerial images using radiometric and morphologic image measures. *Remote Sensing of Environment* 91, 469–477.

Erikson, M. and Olofsson, K. **2005** Comparison of three individual tree crown detection methods. *Machine Vision and Applications* 16, 258–265.

ESA. **2017** *Burned area mapping with Sentinel-2 using SNAP.* ESA.

ESA. **2020a** *SNAP - Sen2Cor v2.8*. http://step.esa.int/main/third-party-plugins-2/sen2cor/sen2cor_v2-8/ (accessed on 16 November, 2020).

ESA. **2020b** *SNAP toolbox*. https://step.esa.int/main/toolboxes/snap/ (accessed on 03 July, 2020).

Eskandari, S.; Reza Jaafari, M.; Oliva, P.; Ghorbanzadeh, O. and Blaschke, T. **2020** Mapping Land Cover and Tree Canopy Cover in Zagros Forests of Iran: Application of Sentinel-2, Google Earth, and Field Data. *Remote Sensing* 12, 1–31.

Eskelson, B.N.I.; Temesgen, H.; Lemay, V.; Barrett, T.M. and Crookston, N.L. *et al.* **2009** The roles of nearest neighbor methods in imputing missing data in forest inventory and monitoring databases. *Scandinavian Journal of Forest Research* 24, 235–246.

Etzelmüller, B.; Heggem, E.S.F.; Sharkhuu, N.; Frauenfelder, R. and Kääb, A. *et al.* **2006** Mountain permafrost distribution modelling using a multi-criteria approach in the Hövsgöl area, northern Mongolia. *Permafrost and Periglacial Processes* 17, 91–104.

Eugster, W.; Rouse, W.R.; Pielke Sr, R.A.; Mcfadden, J.P. and Baldocchi, D.D. *et al.* **2000** Land-atmosphere energy exchange in Arctic tundra and boreal forest: available data and feedbacks to climate. *Global change biology* 6, 84–115.

European Commission. **2001** *Remote sensing applications for forest health status assessment.* OPOCE.

European Space Agency. **2009** *SAR Land Applications Tutorial.* ESA.

European Union Aviation Safety Ageny. **2018** *Opinion No 01/2018: Introduction of a regulatory framework for the operation of unmanned aircraft systems in the open and sepcific categories.* EASA.

Evans, J.S. and Cushman, S.A. **2009** Gradient modeling of conifer species using random forests. *Landscape Ecology* 24, 673–683.

Fabrika, M.; Scheer, L.; Sedma, R.; Kurth, W. and Schön, M. **2019** Crown architecture and structural development of young Norway spruce trees: a basis for more realistic growth modelling. *BioResources* 14, 908–921.

Falkowski, M.J.; Gessler, P.E.; Morgan, P.; Hudak, A.T. and Smith, A.M. **2005** Characterizing and mapping forest fire fuels using ASTER imagery and gradient modeling. *Forest Ecology and Management* 217, 129–146.

Falkowski, M.J.; Hudak, A.T.; Crookston, N.L.; Gessler, P.E. and Uebler, E.H. *et al.* **2010** Landscape-scale parameterization of a tree-level forest growth model: a k- nearest neighbor imputation approach incorporating LiDAR data. *Canadian Journal of Forest Research* 40, 184–199.

Falkowski, M.J.; Wulder, M.A.; White, J.C. and Gillis, M.D. **2009** Supporting large-area, sample-based forest inventories with very high spatial resolution satellite imagery. *Progress in Physical Geography* 33, 403–423.

Fankhauser, K.; Strigul, N. and Gatziolis, D. **2018** Augmentation of Traditional Forest Inventory and Airborne Laser Scanning with Unmanned Aerial Systems and Photogrammetry for Forest Monitoring. *Remote Sensing* 10, 1562.

FAO. **2007** *Brief on National Forest Inventory (NFI) Mongolia.* Forest Resources Development Service, FAO, Rome.

FAO. **2010** *Mongolia forestry outlook study: Asia-Pacific forestry sector outlook study II.* FAO, Bangkok.

FAO. **2013** *Mongolia - To save forests, Mongolia devolves forestry management to locals.* FAO.

FAO. **2014a** *Global Forest Ressources Assessment - 2015 Country Report - Mongolia.* FAO, Rome.

FAO. **2014b** *Global Forest Ressources Assessment 2015: Country report - Russian Federation.* FAO, Rome.

FAO. **2020a** *Global Forest Resources Assessment 2020: Main report.* FAO, Rome.

FAO. **2020b** *Global Forest Ressources Assessment: Country Report - Mongolia,* Rome.

Farjon, A. **2017** *A handbook of the world's conifers.* Koninklijke Brill NV.

Fassnacht, F.E.; Latifi, H.; Stereńczak, K.; Modzelewska, A. and Lefsky, M. *et al.* **2016** Review of studies on tree species classification from remotely sensed data. *Remote Sensing of Environment* 186, 64–87.

Fassnacht, F.E.; Neumann, C.; Forster, M.; Buddenbaum, H. and Ghosh, A. *et al.* **2014** Comparison of Feature Reduction Algorithms for Classifying Tree Species With Hyperspectral Data on Three Central European Test Sites. *IEEE Journal of Selected Topics in Applied Earth Observations and Remote Sensing* 7, 2547–2561.

Federal Aviation Administration (ed). **2016** *Small unmanned aircraft rule (Part 107).* United States Department of Transportation.

Fernández-Manso, A.; Fernández-Manso, O. and Quintano, C. **2016** SENTINEL-2A red-edge spectral indices suitability for discriminating burn severity. *International Journal of Applied Earth Observation and Geoinformation* 50, 170–175.

Finney, D.J. **1950** Investigations in Random and Systematic Sampling. *The Incorporated Statistician* 1, 15–20.

Flannigan, M.; Cantin, A.S.; Groot, W.J. de; Wotton, M. and Newbery, A. *et al.* **2013** Global wildland fire season severity in the 21st century. *Forest Ecology and Management* 294, 54–61.

Flannigan, M.; Stocks, B.; Turetsky, M. and Wotton, M. **2009** Impacts of climate change on fire activity and fire management in the circumboreal forest. *Global change biology* 15, 549–560.

Foody, G.M. **2002** Status of land cover classification accuracy assessment. *Remote Sensing of Environment* 80, 185–201.

Foody, G.M. **2020** Explaining the unsuitability of the kappa coefficient in the assessment and comparison of the accuracy of thematic maps obtained by image classification. *Remote Sensing of Environment* 239, 111630.

Förstner, W. and Wrobel, B. **2016** *Photogrammetric computer vision: Statistics, geometry, orientation and reconstruction.* Springer.

Franco-Lopez, H.; Ek, A.R. and Bauer, M.E. **2001** Estimation and mapping of forest stand density, volume, and cover type using the k-nearest neighbors method. *Remote Sensing of Environment* 2001, 251–274.

Franklin, J. **1986** Thematic mapper analysis of coniferous forest structure and composition. *International Journal of Remote Sensing* 7, 1287–1301.

Franklin, S.E. **2018** Pixel- and object-based multispectral classification of forest tree species from small unmanned aerial vehicles. *Journal of Unmanned Vehicle Systems* 6, 195–211.

Freitas, S.R.; Mello, M.C. and Cruz, C.B. **2005** Relationships between forest structure and vegetation indices in Atlantic Rainforest. *Forest Ecology and Management* 218, 353–362.

Frey, J.; Kovach, K.; Stemmler, S. and Koch, B. **2018** UAV photogrammetry of forests as a vulnerable process. A sensitivity analysis for a Structure from Motion RGB-image pipeline. *Remote Sensing* 10, 912.

Fromm, M.; Schubert, M.; Castilla, G.; Linke, J. and McDermid, G. **2019** Automated Detection of Conifer Seedlings in Drone Imagery Using Convolutional Neural Networks. *Remote Sensing* 11, 1–15.

Fryer, J.G. and Mitchell, H.L. **1987** Radial distortion and close-range stereophotogrammetry. *Australian journal of geodesy, photogrammetry, and surveying*, 123–138.

Fuchs, H.; Magdon, P.; Kleinn, C. and Flessa, H. **2009** Estimating aboveground carbon in a catchment of the Siberian forest tundra. Combining satellite imagery and field inventory. *Remote Sensing of Environment* 113, 518–531.

Furukawa, Y. and Ponce, J. **2007** Accurate, dense, and robust Multi-View Stereopsis. In *IEEE Computer Society 2007*, pp. 1–8.

Gadow, K.v. **2003** *Waldstruktur und Wachstum: Beilage zur Vorlesung im Wintersemester 2003/2004.* Univ.-Verl. Göttingen.

Gadow, K. von; Zhang, C.Y.; Wehenkel, C.; Pommerening, A. and Corral-Rivas, J. *et al.* **2012** Forest Structure and Diversity. In *Continuous Cover Forestry*. T. Pukkala and K. Gadow (eds). Springer Science+Business Media B.V, pp. 29–83.

Galar, D. and Seneviratne, D. **2020** *Robots, drones, UAVs and UGVs for operation and maintenance.* CRC Press.

Galiatsatos, N.; Donoghue, D.N.; Watt, P.; Bholanath, P. and Pickering, J. *et al.* **2020** An Assessment of Global Forest Change Datasets for National Forest Monitoring and Reporting. *Remote Sensing* 12, 1–10.

Gamon, J.A.; Huemmrich, K.F.; Wong, C.Y.S.; Ensminger, I. and Garrity, S. *et al.* **2016** A remotely sensed pigment index reveals photosynthetic phenology in evergreen conifers. *Proceedings of the National Academy of Sciences of the United States of America* 113, 13087–13092.

Ganz, S.; Käber, Y. and Adler, P. **2019** Measuring Tree Height with Remote Sensing—A Comparison of Photogrammetric and LiDAR Data with Different Field Measurements. *Forests* 10, 694.

Gao, B. **1996** NDWI—A normalized difference water index for remote sensing of vegetation liquid water from space. *Remote Sensing of Environment* 58, 257–266.

Garrigues, S.; Shabanov, N.V.; Swanson, K.; Morisette, J.T. and Baret, F. *et al.* **2008** Intercomparison and sensitivity analysis of Leaf Area Index retrievals from LAI-2000,

AccuPAR, and digital hemispherical photography over croplands. *Agricultural and Forest Meteorology* 148, 1193–1209.

Gaschick, F. **2013** *Forest management plan for compartment 435, Thunkel.* GIZ, Ulaanbaatar.

Gatziolis, D.; Fried, J.S. and Monleon, V.S. **2010** Challenges to estimating tree height via LiDAR in closed-canopy forests: a parable from Western Oregon. *Forest Science*, 139–155.

Gebreslasie, M.T.; Ahmed, F.B. and van Aardt, J.A.N. **2011** Extracting structural attributes from IKONOS imagery for Eucalyptus plantation forests in KwaZulu-Natal, South Africa, using image texture analysis and artificial neural networks. *International Journal of Remote Sensing* 32, 7677–7701.

George, C.; Rowland, C.; Gerard, F. and Balzter, H. **2006** Retrospective mapping of burnt areas in Central Siberia using a modification of the normalised difference water index. *Remote Sensing of Environment* 104, 346–359.

Gerke, M. and Przybilla, H.-J. **2016** Accuracy analysis of photogrammetric UAV image blocks: influence of onboard RTK-GNSS and cross flight patterns. *Photogrammetrie - Fernerkundung - Geoinformation* 2016, 17–30.

Getzin, S.; Nuske, R. and Wiegand, K. **2014** Using Unmanned Aerial Vehicles (UAV) to quantify spatial gap patterns in forests. *Remote Sensing* 6, 6988–7004.

Getzin, S.; Wiegand, K. and Schöning, I. **2012** Assessing biodiversity in forests using very high-resolution images and unmanned aerial vehicles. *Methods in Ecology and Evolution* 3, 397–404.

Ghandi, R. **2018** *Support Vector Machine — Introduction to Machine Learning Algorithms*. https://towardsdatascience.com/support-vector-machine-introduction-to-machine-learning-algorithms-934a444fca47 (accessed on 27 June, 2020).

Ghosh, A.; Fassnacht, F.E.; Joshi, P.K. and Koch, B. **2014** A framework for mapping tree species combining hyperspectral and LiDAR data: Role of selected classifiers and sensor across three spatial scales. *International Journal of Applied Earth Observation and Geoinformation* 26, 49–63.

Ghosh, A. and Joshi, P.K. **2014** A comparison of selected classification algorithms for mapping bamboo patches in lower Gangetic plains using very high resolution WorldView 2 imagery. *International Journal of Applied Earth Observation and Geoinformation* 26, 298–311.

Giannetti, F.; Chirici, G.; Gobakken, T.; Næsset, E. and Travaglini, D. *et al.* **2018** A new approach with DTM-independent metrics for forest growing stock prediction using UAV photogrammetric data. *Remote Sensing of Environment* 213, 195–205.

Gini, R.; Passoni, D.; Pinto, L. and Sona, G. **2014** Use of Unmanned Aerial Systems for multispectral survey and tree classification: a test in a park area of northern Italy. *European Journal of Remote Sensing* 47, 251–269.

Gitelson, A.A. **2004** Wide Dynamic Range Vegetation Index for remote quantification of biophysical characteristics of vegetation. *Journal of Plant Physiology* 161, 165–173.

Gjertsen, A.K. **2007** Accuracy of forest mapping based on Landsat TM data and a kNN-based method. *Remote Sensing of Environment* 110, 420–430.

Glenn, E.P.; Huete, A.R.; Nagler, P.L. and Nelson, S.G. **2008** Relationship Between Remotely-sensed Vegetation Indices, Canopy Attributes and Plant Physiological Processes: What Vegetation Indices Can and Cannot Tell Us About the Landscape. *Sensors (Basel, Switzerland)* 8, 2136–2160.

Gobakken, T.; Bollandsås, O.M. and Næsset, E. **2015** Comparing biophysical forest characteristics estimated from photogrammetric matching of aerial images and airborne laser scanning data. *Scandinavian Journal of Forest Research* 30, 73–86.

Gobakken, T. and Næsset, E. **2004** Estimation of diameter and basal area distributions in coniferous forest by means of airborne laser scanner data. *Scandinavian Journal of Forest Research* 19, 529–542.

Goldammer, J.G. **2013** *Vegetation Fires and Global Change: Challenges for Concerted International Action: A White Paper directed to the United Nations and International Organizations. A publication of the Global Fire Monitoring Center (GFMC).* 1st edn. Kessel, Norbert.

Goldammer, J.G. and Furyaev, V.V. **2010** *Fire in Ecosystems of Boreal Eurasia.* Springer Netherlands.

Goldbergs, G.; Maier, S.; Levick, S. and Edwards, A. **2018** Efficiency of individual tree detection approaches based on light-weight and low-cost UAS imagery in Australian savannas. *Remote Sensing* 10, 1–19.

Goldbergs, G.; Maier, S.W.; Levick, S.R. and Edwards, A. **2019** Limitations of high resolution satellite stereo imagery for estimating canopy height in Australian tropical savannas. *International Journal of Applied Earth Observation and Geoinformation* 75, 83–95.

Goldstein, E.B. and van Hooff, J. **2018** *Cognitive psychology.* 1st edn. Cengage Learning.

Gomes, M.F. and Maillard, P. **2013** Identification of urban tree crown in a tropical environment using WorldView-2 data: Problems and perspectives. In *SPIE Remote Sensing*. U. Michel, D.L. Civco, K. Schulz, M. Ehlers and K.G. Nikolakopoulos (eds). SPIE.

Gomes, M.F. and Maillard, P. **2016** Detection of tree crowns in very high spatial resolution images. In *Environmental Applications of Remote Sensing*. M. Marghany (ed). InTech, pp. 41–71.

Gómez, C.; Wulder, M.A.; Montes, F. and Delgado, J.A. **2011** Forest structural diversity characterization in Mediterranean pines of central Spain with QuickBird-2 imagery and canonical correlation analysis. *Canadian Journal of Remote Sensing* 37, 628–642.

Gómez, C.; Wulder, M.A.; Montes, F. and Delgado, J.A. **2012** Modeling Forest Structural Parameters in the Mediterranean Pines of Central Spain using QuickBird-2 Imagery and Classification and Regression Tree Analysis (CART). *Remote Sensing* 4, 135–159.

Gonzalez, R.C. and Woods, R.E. **2018** *Digital image processing.* Pearson.

Goodbody, T.R.; Coops, N.C.; Hermosilla, T.; Tompalski, P. and Crawford, P. **2018a** Assessing the status of forest regeneration using digital aerial photogrammetry and unmanned aerial systems. *International Journal of Remote Sensing* 39, 5246–5264.

Goodbody, T.R.; Coops, N.C.; Hermosilla, T.; Tompalski, P. and McCartney, G. *et al.* **2018b** Digital aerial photogrammetry for assessing cumulative spruce budworm defoliation and enhancing forest inventories at a landscape-level. *ISPRS Journal of Photogrammetry and Remote Sensing* 142, 1–11.

Goodbody, T.R.; Coops, N.C.; Marshall, P.L.; Tompalski, P. and Crawford, P. **2017a** Unmanned aerial systems for precision forest inventory purposes: a review and case study. *The Forestry Chronicle* 93, 71–81.

Goodbody, T.R.; Tompalski, P.; Coops, N.C.; Hopkinson, C. and Treitz, P. *et al.* **2020** Forest Inventory and Diversity Attribute Modelling Using Structural and Intensity Metrics from Multi-Spectral Airborne Laser Scanning Data. *Remote Sensing* 12, 2109.

Goodbody, T.R.H.; Coops, N.C.; Tompalski, P.; Crawford, P. and Day, K.J.K. **2017b** Updating residual stem volume estimates using ALS- and UAV-acquired stereo-photogrammetric point clouds. *International Journal of Remote Sensing* 38, 2938–2953.

Goodbody, T.R.H.; Coops, N.C. and White, J.C. **2019** Digital aerial photogrammetry for updating area-based forest inventories: a review of opportunities, challenges, and future directions. *Current Forestry Reports* 5, 55–75.

Google. **2020** *Earth Engine*. https://earthengine.google.com/ (accessed on 25 June, 2020).

Goos, G., Hartmanis, J., van Leeuwen, J., Triggs, B., Zisserman, A. and Szeliski, R. (eds). **2000** *Vision Algorithms: Theory and Practice.* Springer Berlin Heidelberg.

Goude, M.; Nilsson, U. and Holmström, E. **2019** Comparing direct and indirect leaf area measurements for Scots pine and Norway spruce plantations in Sweden. *European Journal of Forest Research* 138, 1033–1047.

Gougeon, F.; Cormier, R.; Labrecque, P.; Cole, B. and Pitt, D. *et al.* **2003** Individual tree crown (ITC) delineation on Ikonos and QuickBird imagery: the Cockburn Island study. In *Canadian Symposium on Remote Sensing*, pp. 1–9.

Gougeon, F. and Leckie, D. **2006** The individual tree crown approach applied to Ikonos images of a coniferous plantation area. *Photogrammetric Engineering & Remote Sensing*.

Gougeon, F.A. **1995** A Crown-Following Approach to the Automatic Delineation of Individual Tree Crowns in High Spatial Resolution Aerial Images. *Canadian Journal of Remote Sensing* 21, 274–284.

Gougeon, F.A. and Leckie, D.G. **2003** *Forest information extraction from high spatial resolution images using an individual tree crown approach.* Pacific forestry Center.

Gower, S.T.; Krankina, O.N.; Olson, R.J.; Apps, M. and Linder, S. *et al.* **2001** Net primary production and carbon allocation patterns of boreal forest ecosystems. *Ecological Applications* 11, 1395–1411.

Gower, S.T. and Norman, J.M. **1991** Rapid Estimation of Leaf Area Index in Conifer and Broad-Leaf Plantations. *Ecology* 72, 1896–1900.

Grabherr, G. **1997** *Farbatlas Ökosysteme der Erde: Natürliche, naturnahe und künstliche Land-Ökosysteme aus geobotanischer Sicht.* Ulmer.

Grabska, E.; Hostert, P.; Pflugmacher, D. and Ostapowicz, K. **2019** Forest Stand Species Mapping Using the Sentinel-2 Time Series. *Remote Sensing* 11, 1197.

Gradel, A. **2007** Forest Structure in Fire-disturbed Boreal Ecosystems in Northern Mongolia. Master Thesis. Naturschutz, Göttingen.

Gradel, A. **2010a** *Anthropogenic drivers of biodiversity change in the mountain forest steppe of Mongolia.* Asia Pacific Mountain Network.

Gradel, A. **2010b** *Monitoring and forecasting of forest diversity: Application examples of diversity indicators and indices.* Lambert Academic Publishing.

Gradel, A. **2017** Reaktion von Waldbeständen am Rande der südlichen Taiga auf Klimafaktoren, natürliche und waldbauliche Störungen. Dissertation. Waldbau und Waldökologie der gemäßigten Zonen, Göttingen.

Gradel, A.; Ammer, C.; Ganbaatar, B.; Nadaldorj, O. and Dovdondemberel, B. *et al.* **2017a** On the Effect of Thinning on Tree Growth and Stand Structure of White Birch (Betula platyphylla Sukaczev) and Siberian Larch (Larix sibirica Ledeb.) in Mongolia. *Forests* 8, 105.

Gradel, A.; Ganbaatar, B.; Nadaldorj, O.; Dovdondemberel, B. and Kusbach, A. **2017b** Climate-growth relationships and pointer year analysis of a Siberian larch (Larix sibirica Ledeb.) chronology from the Mongolian mountain forest steppe compared to white birch (Betula platyphylla Sukaczev). *For. Ecosyst.* 4, 1–12.

Gradel, A. and Mühlenberg, M. **2011** Spatial characteristics of near-natural Mongolian forests at the southern edge of the taiga. *Allg. Forst- u. J.-Ztg.* 182, 40–52.

Gradel, A.; Nadaldorj, O.; Altaev, A.A.; Voinkov, A.A. and Bazarradnaa, E. **2015** Spatial distribution of trees on light taiga plots before selective thinning. *Mongolian J Agric Sci* 15, 91.

Gradel, A.; Sukhbaatar, G.; Karthe, D. and Kang, H. **2019** Forest Management In Mongolia – A Review Of Challenges And Lessons Learned With Special Reference To Degradation And Deforestation. *GES* 12, 133–166.

Granwal, L. **2020** *Bushfire damage area in Australia 2020 by state*. https://www.statista.com/statistics/1089996/australia-total-area-burned-by-bushfires-by-state/ (accessed on 13 July, 2020).

Grassi, G. and Giannini, R. **2005** Influence of light and competition on crown and shoot morphological parameters of Norway spruce and silver fir saplings. *Annals of Forest Science* 62, 269–274.

Grayson, B.; Penna, N.T.; Mills, J.P. and Grant, D.S. **2018** GPS precise point positioning for UAV photogrammetry. *The Photogrammetric Record* 33, 427–447.

Green, R.M. **1979** *Sampling design and statistical methods for environmental biologists.* John Wiley & Sons.

Greiwe, A. **2018** UAV flying mission and data analysis. Personal communication.

Grenzdörffer, G.J.; Engel, A. and Teichert, B. **2008** The photogrammetric potential of low-cost UAVs in forestry and agriculture. *The International Archives of Photogrammetry, Remote Sensing and Spatial Information Sciences* 27, 1207–1214.

Grenzdörffer, G.J. and Niemeyer, F. **2011** UAV based BRDF-measurements of agricultural surfaces with Pfiffikus. *ISPRS - International Archives of the Photogrammetry, Remote Sensing and Spatial Information Sciences* XXXVIII-1/C22, 229–234.

Groner, M. and Wartburg, R. von. **2020** *Entscheidungsbaum statistischer Testverfahren*. https://etools.fernuni.ch/entscheidungsbaum/index.html (accessed on 26 January, 2021).

Grossmann, E.; Ohmann, J.; Kagan, J.; May, H. and Gregory, M. **2010** Mapping Ecological Systems with a Random Forest Model. Trafeoffs between Error and Bias. *GAP Analysis Bulletin* 17, 16–22.

Guerra-Hernández, J.; Cosenza, D.N.; Rodriguez, L.C.E.; Silva, M. and Tomé, M. *et al.* **2018** Comparison of ALS- and UAV(SfM)-derived high-density point clouds for individual tree detection in Eucalyptus plantations. *International Journal of Remote Sensing* 39, 5211–5235.

Guerra-Hernández, J.; González-Ferreiro, E.; Monleón, V.; Faias, S. and Tomé, M. *et al.* **2017** Use of Multi-Temporal UAV-Derived Imagery for Estimating Individual Tree Growth in Pinus pinea Stands. *Forests* 8, 1–19.

Guerra-Hernández, J.; González-Ferreiro, E.; Sarmento, A.; Silva, J. and Nunes, A. *et al.* **2016** Using high-resolution UAV imagery to estimate tree variables in Pinus pinea plantation in Portugal. *Forest Systems* 25, 1–6.

Guimarães, N.; Pádua, L.; Marques, P.; Silva, N. and Peres, E. *et al.* **2020** Forestry Remote Sensing from Unmanned Aerial Vehicles: A Review Focusing on the Data, Processing and Potentialities. *Remote Sensing* 12, 1–35.

Gülci, S. **2019** The determination of some stand parameters using SfM-based spatial 3D point cloud in forestry studies: an analysis of data production in pure coniferous young forest stands. *Environmental monitoring and assessment* 191, 495.

Gunin, P.D.; Vostokova, E.A.; Dorofeyuk, N.I.; Tarasov, P.E. and Black, C.C. **1999** *Vegetation Dynamics of Mongolia.* Springer Netherlands.

Guo, Q.; Su, Y.; Hu, T.; Zhao, X. and Wu, F. *et al.* **2017** An integrated UAV-borne lidar system for 3D habitat mapping in three forest ecosystems across China. *International Journal of Remote Sensing* 38, 2954–2972.

Gupta, S.G.; Ghonge, M. and Jawandhiya, P.M. **2013** Review of Unmanned Aircraft System (UAS). *SSRN Journal*, 1–13.

Guski, R. **1996** *Wahrnehmen: Ein Lehrbuch.* Kohlhammer.

Gustafson, E.J.; Shvidenko, A.Z. and Scheller, R.M. **2011** Effectiveness of forest management strategies to mitigate effects of global change in south-central Siberia. *Can. J. For. Res.* 41, 1405–1421.

Gustafson, E.J.; Shvidenko, A.Z.; Sturtevant, B.R. and Scheller, R.M. **2010** Predicting global change effects on forest biomass and composition in south-central Siberia. *Ecological Applications* 20, 700–715.

Haala, N. and Rothermel, M. **2012** Dense Multi-Stereo Matching for High Quality Digital Elevation Models. *Photogrammetrie - Fernerkundung - Geoinformation* 2012, 331–343.

Haapanen, R.; Ek, A.R.; Bauer, M.E. and Finley, A.O. **2004** Delineation of forest/nonforest land use classes using nearest neighbor methods. *Remote Sensing of Environment* 89, 265–271.

Haeseler, S. and Schmitt. **2017** *Dzud in der Mongolei in den Wintern 2015/2016 und 2016/2017: Bericht des Deutschen Wetterdienstes DWD.* DWD.

Hajek, F. **2004** *Object-oriented classification of remote sensing data for the identification of tree species composition.* Department of Forestry Management, Faculty of Forestry and Environment CUA Prague, Prague.

Hansen, M.C.; Potapov, P.V.; Moore, R.; Hancher, M. and Turubanova, S.A. *et al.* **2013** High-resolution global maps of 21st-century forest cover change. *Science (New York, N.Y.)* 342, 850–853.

Hao, Z.; Lin, L.; Post, C.J.; Jiang, Y. and Li, M. *et al.* **2021** Assessing tree height and density of a young forest using a consumer unmanned aerial vehicle (UAV). *New Forests*.

Harden, J.W.; Trumbore, S.E.; Stocks, B.J.; Hirsch, A. and Gower, S.T. *et al.* **2000** The role of fire in the boreal carbon budget. *Global change biology* 6, 174–184.

Harwin, S. and Lucieer, A. **2012** Assessing the Accuracy of Georeferenced Point Clouds Produced via Multi-View Stereopsis from Unmanned Aerial Vehicle (UAV) Imagery. *Remote Sensing* 4, 1573–1599. https://www.mdpi.com/2072-4292/4/6/1573.

Hasel, K. **1985** *Forstgeschichte: E. Grundriss für Studium u. Praxis ; mit 6 Tab.* Parey.

Hastie, T.; Tibshirani, R. and Friedman, J. **2009** *The elements of statistical learning, second edition: Data mining, inference, and prediction.* 2nd edn. Springer.

Hauglin, M.; Astrup, R.; Gobakken, T. and Næsset, E. **2013** Estimating single-tree branch biomass of Norway spruce with terrestrial laser scanning using voxel-based and crown dimension features. *Scandinavian Journal of Forest Research* 28, 456–469.

Hauglin, M.; Gobakken, T.; Astrup, R.; Ene, L. and Næsset, E. **2014** Estimating single-tree crown biomass of Norway Spruce by Airborne Laser Scanning: a comparison of methods with and without the use of Terrestrial Laser Scanning to obtain the ground reference data. *Forests* 5, 384–403.

Heikkilä, T.V.; Grönqvist, R. and Jurvelius, M. **2010** *Wildland Fire Management: Handbook for Trainers.* FAO, Rome.

Heinzel, J. and Koch, B. **2012** Investigating multiple data sources for tree species classification in temperate forest and use for single tree delineation. *International Journal of Applied Earth Observation and Geoinformation* 18, 101–110.

Heipke, C. **2017** *Photogrammetrie und Fernerkundung.* 1st edn. Springer.

Heipke, C. and Rottensteiner, F. **2020** Deep learning for geometric and semantic tasks in photogrammetry and remote sensing. *Geo-spatial Information Science* 23, 10–19.

Heller, R.C.; Doverspike, G.E. and Aldrich, R.C. **1964** *Identification of tree species on large-scale panchromatic and color aerial photographs: Agriculture Handbook.* U.S. Department of Agriculture Forest Service.

Hernández-Clemente, R.; Navarro-Cerrillo, R.M. and Zarco-Tejada, P.J. **2012** Carotenoid content estimation in a heterogeneous conifer forest using narrow-band indices and PROSPECT+DART simulations. *Remote Sensing of Environment* 127, 298–315.

Heydari, S.S. and Mountrakis, G. **2018** Effect of classifier selection, reference sample size, reference class distribution and scene heterogeneity in per-pixel classification accuracy using 26 Landsat sites. *Remote Sensing of Environment* 204, 648–658.

Hilbig, W. **1990** Zur Klassifizierung der Vegetation der Mongolischen Volksrepublik durch B. M. MIRKIN et al. 1982-1986. *Feddes Repert.* 101, 571–576.

Hilbig, W. **1995** *The vegetation of Mongolia.* SPB academic publ.

Hilbig, W. **2006** Die Vegetationszonen der Mongolei und ihre wichtigen Pflanzengesellschaften. *Verhandlungen der Zoologisch-Botanischen Gesellschaft in Österreich*, 119–164.

Hildebrandt, G. **1996** *Fernerkundung und Luftbildmessung: Für Forstwirtschaft, Vegetationskartierung und Landschaftsökologie.* 1st edn. Wichmann.

Hilker, T.; van Leeuwen, M.; Coops, N.C.; Wulder, M.A. and Newnham, G.J. *et al.* **2010** Comparing canopy metrics derived from terrestrial and airborne laser scanning in a Douglas-fir dominated forest stand. *Trees* 24, 819–832.

Hirata, Y. **2008** Estimation of stand attributes in Cryptomeria japonica and Chamaecyparis obtusa stands using QuickBird panchromatic data. *Journal of Forest Research* 13, 147–154.

Hirsch, K.G. and Fuglem, P. **2006** *Canadian Wildland Fire Strategy: Background Syntheses, Analyses, and Perspectives,* Edmonton, Alberta, Canada.

Holopainen, M.; Vastaranta, M. and Hyyppä, J. **2014** Outlook for the next generation's precision forestry in Finland. *Forests* 5, 1682–1694.

Holopainen, M.; Vastaranta, M.; Kankare, V.; Räty, M. and Vaaja, M. *et al.* **2011** Biomass estimation of individual trees using stem and crown diameter TLS measurements. *ISPRS - International Archives of the Photogrammetry, Remote Sensing and Spatial Information Sciences* XXXVIII-5/W12, 91–95.

Holopainen, M.; Vastaranta, M.; Karjalainen, M.; Karila, K. and Kaasalainen, S. *et al.* **2015** FOREST INVENTORY ATTRIBUTE ESTIMATION USING AIRBORNE LASER SCANNING, AERIAL STEREO IMAGERY, RADARGRAMMETRY AND INTERFEROMETRY–FINNISH EXPERIENCES OF THE 3D TECHNIQUES. *ISPRS Ann. Photogramm. Remote Sens. Spatial Inf. Sci.* II-3/W4, 63–69.

Holopainen, M.; Vastaranta, M.; Rasinmäki, J.; Kalliovirta, J. and Mäkinen, A. *et al.* **2010** Uncertainty in timber assortment estimates predicted from forest inventory data. *European Journal of Forest Research* 129, 1131–1142.

Honkavaara, E. and Khoramshahi, E. **2018** Radiometric Correction of Close-Range Spectral Image Blocks Captured Using an Unmanned Aerial Vehicle with a Radiometric Block Adjustment. *Remote Sensing* 10, 1–29.

Honkavaara, E.; Rosnell, T.; Oliveira, R. and Tommaselli, A. **2017** Band registration of tuneable frame format hyperspectral UAV imagers in complex scenes. *ISPRS Journal of Photogrammetry and Remote Sensing* 134, 96–109.

Howard, J.A. **1991** *Remote sensing of forest resources: Theory and applications.* 1st edn. Chapman and Hall.

Huang, H.; Roy, D.; Boschetti, L.; Zhang, H. and Yan, L. *et al.* **2016** Separability analysis of Sentinel-2A Multi-Spectral Instrument (MSI) data for burned area discrimination. *Remote Sensing* 8, 1–18.

Hudak, A.T.; Crookston, N.L.; Evans, J.S.; Falkowski, M.J. and Smith, A.M.S. *et al.* **2006** Regression modeling and mapping of coniferous forest basal area and tree density from discrete-return lidar and multispectral satellite data. *Canadian Journal of Remote Sensing* 32, 126–138.

Hudak, A.T.; Crookston, N.L.; Evans, J.S.; Hall, D.E. and Falkowski, M.J. **2008** Nearest neighbor imputation of species-level, plot-scale forest structure attributes from LiDAR data. *Remote Sensing of Environment* 112, 2232–2245.

Hudak, A.T.; Morgan, P.; Bobbitt, M.J.; Smith, A.M.S. and Lewis, S.A. *et al.* **2007** The Relationship of Multispectral Satellite Imagery to Immediate Fire Effects. *Fire Ecology* 3, 64–90.

Huete, A.R. **2012** Vegetation Indices, Remote Sensing and Forest Monitoring. *Geography Compass* 6, 513–532.

Hugenholtz, C.H.; Whitehead, K.; Brown, O.W.; Barchyn, T.E. and Moorman, B.J. *et al.* **2013** Geomorphological mapping with a small unmanned aircraft system (sUAS): Feature detection and accuracy assessment of a photogrammetrically-derived digital terrain model. *Geomorphology* 194, 16–24.

Hyer, E.J. and Goetz, S.J. **2004** Comparison and sensitivity analysis of instruments and radiometric methods for LAI estimation: assessments from a boreal forest site. *Agricultural and Forest Meteorology* 122, 157–174.

Hyyppä, J.; Hyyppä, H.; Inkinen, M.; Engdahl, M. and Linko, S. *et al.* **2000** Accuracy comparison of various remote sensing data sources in the retrieval of forest stand attributes. *Forest Ecology and Management* 128, 109–120.

Hyyppä, J.; Hyyppä, H.; Leckie, D.; Gougeon, F. and Yu, X. *et al.* **2008** Review of methods of small-footprint airborne laser scanning for extracting forest inventory data in boreal forests. *International Journal of Remote Sensing* 29, 1339–1366.

Hyyppä, J.; Kaartinen, H.; Jaakkola, A.; Holopainen, M. and Vastaranta, M. *et al.* **2018** Forest inventory using laser scanning. In *Topographic laser ranging and scanning*: *Principles and processing*. J. Shan and C.K. Toth (eds). CRC Press, pp. 379–413.

Iglhaut, J.; Cabo, C.; Puliti, S.; Piermattei, L. and O'Connor, J. *et al.* **2019** Structure from Motion Photogrammetry in Forestry: a Review. *Current Forestry Reports* 110.

Iizuka, K.; Yonehara, T.; Itoh, M. and Kosugi, Y. **2018** Estimating Tree Height and Diameter at Breast Height (DBH) from Digital Surface Models and Orthophotos Obtained with an Unmanned Aerial System for a Japanese Cypress (Chamaecyparis obtusa) Forest. *Remote Sensing* 10, 13.

Immitzer, M.; Neuwirth, M.; Böck, S.; Brenner, H. and Vuolo, F. *et al.* **2019** Optimal Input Features for Tree Species Classification in Central Europe Based on Multi-Temporal Sentinel-2 Data. *Remote Sensing* 11, 1–23.

Immitzer, M.; Stepper, C.; Böck, S.; Straub, C. and Atzberger, C. **2016a** Use of WorldView-2 stereo imagery and National Forest Inventory data for wall-to-wall mapping of growing stock. *Forest Ecology and Management* 359, 232–246.

Immitzer, M., Vuolo, F., Einzmann, K., Ng, W.T., Böck, S. and Atzberger, C. (eds). **2016b** *Verwendung von multispektralen Sentinel-2 Daten für die Baumartenklassifikation und Vergleich mit anderen Satellitensensoren*.

Ingram, J.C.; Dawson, T.P. and Whittaker, R.J. **2005** Mapping tropical forest structure in southeastern Madagascar using remote sensing and artificial neural networks. *Remote Sensing of Environment* 94, 491–507.

Innovatek. **2020** *World's first autonomous UAV flight under a forest canopy?* https://foresttech.events/worlds-first-autonomous-uav-flight-under-a-forest-canopy/ (accessed on 26 May, 2020).

Inoue, T.; Nagai, S.; Yamashita, S.; Fadaei, H. and Ishii, R. *et al.* **2014** Unmanned aerial survey of fallen trees in a deciduous broadleaved forest in eastern Japan. *PloS one* 9, 1-7.

Iost Filho, F.H.; Heldens, W.B.; Kong, Z. and Lange, E.S. de. **2020** Drones: Innovative Technology for Use in Precision Pest Management. *Journal of economic entomology* 113, 1–25.

IPCC. **2020** *Climate Change and Land: An IPCC Special Report on climate change, desertification, land degradation, sustainable land management, food security, and greenhouse gas fluxes in terrestrial ecosystems.* IPCC.

ITC. **2020** *Satellite and sensor database*. https://www.itc.nl/research/research-facilities/labs-resources/satellite-sensor-database/ (accessed on 04 July, 2020).

Jaakkola, A.; Hyyppä, J.; Yu, X.; Kukko, A. and Kaartinen, H. *et al.* **2017** Autonomous Collection of Forest Field Reference—The Outlook and a First Step with UAV Laser Scanning. *Remote Sensing* 9, 785.

Jackson, R.D. and Huete, A.R. **1991** Interpreting vegetation indices. *Preventive Veterinary Medicine* 11, 185–200.

Jakubowski, M.K.; Guo, Q. and Kelly, M. **2013** Tradeoffs between lidar pulse density and forest measurement accuracy. *Remote Sensing of Environment* 130, 245–253.

James, M.R. **2017** *SfM-MVS PhotoScan image processing exercise.* Lancaster University, Lancaster.

James, M.R.; Chandler, J.H.; Eltner, A.; Fraser, C. and Miller, P.E. *et al.* **2019** Guidelines on the use of structure-from-motion photogrammetry in geomorphic research. *Earth Surf. Process. Landforms* 44, 2081–2084.

James, M.R. and Robson, S. **2014** Mitigating systematic error in topographic models derived from UAV and ground-based image networks. *Earth Surf. Process. Landforms* 39, 1413–1420.

James, T.M. **2011** Temperature sensitivity and recruitment dynamics of Siberian larch (Larix sibirica) and Siberian spruce (Picea obovata) in northern Mongolia's boreal forest. *Forest Ecology and Management* 262, 629–636.

James R. Frankenberger; Chi-Hua Huang and Kossi Nouwakpo. **2008** Low-altitude digital photogrammetry technique to assess ephemeral gully erosion. In *IEEE International Geoscience & Remote Sensing Symposium, IGARSS 2008, July 8-11, 2008, Boston, Massachusetts, USA, Proceedings*. IEEE, pp. 117–120.

Järnstedt, J.; Pekkarinen, A.; Tuominen, S.; Ginzler, C. and Holopainen, M. *et al.* **2012** Forest variable estimation using a high-resolution digital surface model. *ISPRS Journal of Photogrammetry and Remote Sensing* 74, 78–84.

Jasvilis, G.; Weise, C. and Zenger-Landolt, B. **2016** Finding complex patterns using template matching. In *GEOBIA 2016*: *Solutions and synergies : 14 September 2016 - 16 September 2016, University of Twente, Faculty of Geo-Information and Earth Observation (ITC) : proceedings*. N. Kerle, M. Gerke and S. Lefevre (eds). University of Twente.

Jaud, M.; Passot, S.; Le Bivic, R.; Delacourt, C. and Grandjean, P. *et al.* **2016** Assessing the Accuracy of High Resolution Digital Surface Models Computed by PhotoScan® and MicMac® in Sub-Optimal Survey Conditions. *Remote Sensing* 8, 465.

Jayathunga, S.; Owari, T. and Tsuyuki, S. **2018a** Evaluating the Performance of Photogrammetric Products Using Fixed-Wing UAV Imagery over a Mixed Conifer–Broadleaf Forest: Comparison with Airborne Laser Scanning. *Remote Sensing* 10, 1–24.

Jayathunga, S.; Owari, T. and Tsuyuki, S. **2018b** The use of fixed–wing UAV photogrammetry with LiDAR DTM to estimate merchantable volume and carbon stock in living biomass over a mixed conifer–broadleaf forest. *International Journal of Applied Earth Observation and Geoinformation* 73, 767–777.

Jayathunga, S.; Owari, T. and Tsuyuki, S. **2019** Digital aerial photogrammetry for uneven-aged forest management: assessing the potential to reconstruct canopy structure and estimate living biomass. *Remote Sensing* 11, 338.

Jensen, J. and Mathews, A. **2016** Assessment of image-based point cloud products to generate a bare Earth surface and estimate canopy heights in a woodland ecosystem. *Remote Sensing* 8, 50.

Jensen, J.R. **2016** *Introductory digital image processing: A remote sensing perspective.* 4th edn. Pearson Education.

Jeziorska, J. **2019** UAS for wetland mapping and hydrological modeling. *Remote Sensing* 11, 1–39.

Jia, J.; Wang, Y.; Chen, J.; Guo, R. and Shu, R. *et al.* **2020** Status and application of advanced airborne hyperspectral imaging technology: A review. *Infrared Physics & Technology* 104, 1–16.

Jiang, Z.; Huete, A.; Didan, K. and Miura, T. **2008** Development of a two-band enhanced vegetation index without a blue band. *Remote Sensing of Environment* 112, 3833–3845.

Jiao, L., Shang, R., Liu, F. and Zhang, W. (eds). **2020** *Brain and nature-inspired learning, computation and recognition.* Elsevier.

Jing, L.; Hu, B.; Noland, T. and Li, J. **2012** An individual tree crown delineation method based on multi-scale segmentation of imagery. *ISPRS Journal of Photogrammetry and Remote Sensing* 70, 88–98.

Jolly, W.M.; Cochrane, M.A.; Freeborn, P.H.; Holden, Z.A. and Brown, T.J. *et al.* **2015** Climate-induced variations in global wildfire danger from 1979 to 2013. *Nature communications* 6, 7537.

Jones, H.G. and Vaughan, R.A. **2010** *Remote sensing of vegetation: Principles, techniques, and applications.* 1st edn. Oxford Univ. Press.

Joshi, N.; Mitchard, E.T.A.; Brolly, M.; Schumacher, J. and Fernández-Landa, A. *et al.* **2017** Understanding 'saturation' of radar signals over forests. *Scientific reports* 7, 1–11.

Jung, J.; Kim, S.; Hong, S.; Kim, K. and Kim, E. *et al.* **2013** Effects of national forest inventory plot location error on forest carbon stock estimation using k-nearest neighbor algorithm. *ISPRS Journal of Photogrammetry and Remote Sensing* 81, 82–92.

Juřička, D.; Novotná, J.; Houška, J.; Pařílková, J. and Hladký, J. *et al.* **2020** Large-scale permafrost degradation as a primary factor in Larix sibirica forest dieback in the Khentii massif, northern Mongolia. *Journal of Forestry Research* 31, 197–208.

Jurjević, L.; Gašparović, M.; Milas, A.S. and Balenović, I. **2020** Impact of UAS Image Orientation on Accuracy of Forest Inventory Attributes. *Remote Sensing* 12, 1–19.

Kaartinen, H.; Hyyppä, J.; Yu, X.; Vastaranta, M. and Hyyppä, H. *et al.* **2012** An International Comparison of Individual Tree Detection and Extraction Using Airborne Laser Scanning. *Remote Sensing* 4, 950–974.

Kachamba, D.; Ørka, H.; Gobakken, T.; Eid, T. and Mwase, W. **2016** Biomass Estimation Using 3D Data from Unmanned Aerial Vehicle Imagery in a Tropical Woodland. *Remote Sensing* 8, 968.

Kahn, B. **2016** *Here's the Climate Context For the Fort McMurray Wildfire*. https://www.climatecentral.org/news/climate-context-fort-mcmurray-wildfire-20311 (accessed on 14 July, 2020).

Kameyama, S. and Sugiura, K. **2021** Effects of Differences in Structure from Motion Software on Image Processing of Unmanned Aerial Vehicle Photography and Estimation of Crown Area and Tree Height in Forests. *Remote Sensing* 13, 1–22.

Kangas, A.; Astrup, R.; Breidenbach, J.; Fridman, J. and Gobakken, T. *et al.* **2018** Remote sensing and forest inventories in Nordic countries – roadmap for the future. *Scandinavian Journal of Forest Research* 33, 397–412.

Kangas, A. and Maltamo, M. **2009** *Forest inventory: Methodology and applications.* Springer.

Kangas, A.S. **2010** Value of forest information. *European Journal of Forest Research* 129, 863–874.

Kankare, V.; Räty, M.; Yu, X.; Holopainen, M. and Vastaranta, M. *et al.* **2013** Single tree biomass modelling using airborne laser scanning. *ISPRS Journal of Photogrammetry and Remote Sensing* 85, 66–73.

Kappas, M. **2009** *Klimatologie: Klimaforschung im 21. Jahrhundert - Herausforderung für Natur- und Sozialwissenschaften.* Spektrum Akad. Verl.

Kappas, M.W. and Propastin, P.A. **2012** Review of Available Products of Leaf Area Index and Their Suitability over the Formerly Soviet Central Asia. *Journal of Sensors* 2012, 1–11.

Karakis, S.; Marangoz, A.M. and Buyuksalih, G. **2006** *Analysis of segmentation parameters in eCognition software using high resolution Quickbird MS imagery.* ISPRS, Ankara.

Karila, K.; Vastaranta, M.; Karjalainen, M. and Kaasalainen, S. **2015** Tandem-X interferometry in the prediction of forest inventory attributes in managed boreal forests. *Remote Sensing of Environment* 159, 259–268.

Karlson, M.; Reese, H. and Ostwald, M. **2014** Tree crown mapping in managed woodlands (parklands) of semi-arid West Africa using WorldView-2 imagery and geographic object based image analysis. *Sensors (Basel, Switzerland)* 14, 22643–22669.

Karnieli, A.; Bayasgalan, M.; Bayarjargal, Y.; Agam, N. and Khudulmur, S. *et al.* **2006** Comments on the use of the Vegetation Health Index over Mongolia. *International Journal of Remote Sensing* 27, 2017–2024.

Kasischke, E.S.; Christensen, N.L. and Stocks, B.J. **1995** Fire, Global Warming, and the Carbon Balance of Boreal Forests. *Ecological Applications* 5, 437–451.

Kasser, M. and Egels, Y. **2002** *Digital photogrammetry.* 1st edn. Taylor & Francis.

Kato, A.; Obanawa, H.; Hayakawa, Y.; Watanabe, M. and Yamaguchi, Y. *et al.* **2015** Fusion between UAV-SFM and terrestrial laser scanner for field validation of satellite remote sensing. In *2015 IEEE International Geoscience and Remote Sensing Symposium (IGARSS)*. IEEE, pp. 2642–2645.

Katoh, M. and Gougeon, F.A. **2012** Improving the Precision of Tree Counting by Combining Tree Detection with Crown Delineation and Classification on Homogeneity Guided Smoothed High Resolution (50 cm) Multispectral Airborne Digital Data. *Remote Sensing* 4, 1411–1424.

Kavzoglu, T. and Yildiz, M. **2014** Parameter-Based Performance Analysis of Object-Based Image Analysis Using Aerial and Quikbird-2 Images. *ISPRS Annals of Photogrammetry, Remote Sensing and Spatial Information Sciences* II-7, 31–37.

Kayes, I. and Mallik, A. **2020** Boreal Forests: Distributions, Biodiversity, and Management. In *Life on Land*. W. Leal Filho, A.M. Azul, L. Brandli, P.G. Özuyar and T. Wall (eds). Springer International Publishing; Imprint: Springer, pp. 1–12.

Kayitakire, F.; Hamel, C. and Defourny, P. **2006** Retrieving forest structure variables based on image texture analysis and IKONOS-2 imagery. *Remote Sensing of Environment* 102, 390–401.

Ke, Y. and Quackenbush, L. **2009** *Individual tree crown detection and delineation from high spatial resolution imagery using active contour and hill-climbing methods.* ASPRS, Baltimore.

Ke, Y. and Quackenbush, L.J. **2011a** A comparison of three methods for automatic tree crown detection and delineation from high spatial resolution imagery. *International Journal of Remote Sensing* 32, 3625–3647.

Ke, Y. and Quackenbush, L.J. **2011b** A review of methods for automatic individual tree-crown detection and delineation from passive remote sensing. *International Journal of Remote Sensing* 32, 4725–4747.

Ke, Y.; Quackenbush, L.J. and Im, J. **2010** Synergistic use of QuickBird multispectral imagery and LIDAR data for object-based forest species classification. *Remote Sensing of Environment* 114, 1141–1154.

Keeley, J.E. **2009** Fire intensity, fire severity and burn severity: a brief review and suggested usage. *International Journal of Wildland Fire* 18, 1–12.

Kentsch, S.; Lopez Caceres, M.L.; Serrano, D.; Roure, F. and Diez, Y. **2020** Computer vision and deep learning techniques for the analysis of drone-acquired forest images, a transfer learning study. *Remote Sensing* 12, 1–19.

Keukelaere, L. de; Sterckx, S.; Adriaensen, S.; Knaeps, E. and Reusen, I. *et al.* **2018** Atmospheric correction of Landsat-8/OLI and Sentinel-2/MSI data using iCOR algorithm: validation for coastal and inland waters. *European Journal of Remote Sensing* 51, 525–542.

Key, C.H. **2006** Ecological and Sampling Constraints on Defining Landscape Fire Severity. *Fire Ecology* 2, 34–59.

Khansaritoreh, E.; Dulamsuren, C.; Klinge, M.; Ariunbaatar, T. and Bat-Enerel, B. *et al.* **2017** Higher climate warming sensitivity of Siberian larch in small than large forest islands in the fragmented Mongolian forest steppe. *Global change biology* 23, 3675–3689.

Kharuk, V.I.; Ranson, K.J.; Petrov, I.A.; Dvinskaya, M.L. and Im, S.T. *et al.* **2019** Larch (Larix dahurica Turcz) growth response to climate change in the Siberian permafrost zone. *Regional Environmental Change* 19, 233–243.

Khatami, R.; Mountrakis, G. and Stehman, S.V. **2016** A meta-analysis of remote sensing research on supervised pixel-based land-cover image classification processes. General guidelines for practitioners and future research. *Remote Sensing of Environment* 177, 89–100.

Khuldumur, S. and Erdenetuya, M. **2010** *Remote Sensing Activities in Mongolia*. https://www.geospatialworld.net/article/remote-sensing-activities-in-mongolia/ (accessed on 23 February, 2021).

Kirilenko, A.P. and Sedjo, R.A. **2007** Climate change impacts on forestry. *Proceedings of the National Academy of Sciences of the United States of America* 104, 19697–19702.

Kitahara, F.; Mizoue, N. and Yoshida, S. **2010** Effects of training for inexperienced surveyors on data quality of tree diameter and height measurements. *Silva Fennica* 44.

Klawunn, T. **2018** Camera and image quality of the Typhoon CGO3+. Personal communication.

Kleinn, C. **2014** *Lecture Notes for the Teaching Module Forest Inventory. Department of Forest Inventory and Remote Sensing.* http://wiki.awf.forst.uni-goettingen.de/wiki/index.php/Forest_inventory (accessed on 26 February, 2021).

Kleinn, C. **2017** *Sources of error in remotely sensed data: Lecture:Remote Sensing,* Göttingen.

Klinge, M.; Böhner, J. and Erasmi, S. **2014** Modelling forest lines and forest distribution patterns with remote sensing data in a mountainous region of semi-arid Central Asia. *Biogeosciences Discussions* 11, 14667–14698.

Klinge, M.; Dulamsuren, C.; Erasmi, S.; Karger, D.N. and Hauck, M. **2018** Climate effects on vegetation vitality at the treeline of boreal forests of Mongolia. *Biogeosciences* 15, 1319–1333.

Klinge, M.; Dulamsuren, C.; Schneider, F.; Erasmi, S. and Hauck, M. *et al.* **2020** Modelled potential forest area in the forest-steppe of central Mongolia is about three times of actual forest area. *Biogeosciences Discussions*, 1–37.

Klosterman, S. and Richardson, A.D. **2017** Observing Spring and Fall Phenology in a Deciduous Forest with Aerial Drone Imagery. *Sensors (Basel, Switzerland)* 17, 1–17.

Kniemeyer, O.; Buck-Sorlin, G. and Kurth, W. **2007** Groimp as a Platform for Functional-Structural Modelling of Plants. In *Functional-structural plant modelling in crop production*. J. Vos (ed). Springer, pp. 43–52.

Knipling, E.B. **1970** Physical and physiological basis for the reflectance of visible and near-infrared radiation from vegetation. *Remote Sensing of Environment* 1, 155–159.

Köhl, M.; Magnussen, S. and Marchetti, M. **2010** *Sampling methods, remote sensing and GIS multiresource forest inventory.* Springer.

Komárek, J.; Klouček, T. and Prošek, J. **2018** The potential of Unmanned Aerial Systems: A tool towards precision classification of hard-to-distinguish vegetation types? *International Journal of Applied Earth Observation and Geoinformation* 71, 9–19.

Kopp, B.J.; Minderlein, S. and Menzel, L. **2014** Soil Moisture Dynamics in a Mountainous Headwater Area in the Discontinuous Permafrost Zone of northern Mongolia. *Arctic, Antarctic, and Alpine Research* 46, 459–470.

Korhonen, L.; Hadi; Packalen, P. and Rautiainen, M. **2017** Comparison of Sentinel-2 and Landsat 8 in the estimation of boreal forest canopy cover and leaf area index. *Remote Sensing of Environment* 195, 259–274.

Korhonen, L.; Korhonen, K.; Rautiainen, M. and Stenberg, P. **2006** Estimation of forest canopy cover: a comparison of field measurement techniques. *Silva Fenn.* 40, 577–588.

Korom, A.; Phua, M.-H.; Hirata, Y. and Matsuura, T. **2014** Extracting oil palm crown from WorldView-2 satellite image. *IOP Conference Series: Earth and Environmental Science* 18, 1–7.

Korpela, I.; Ørka, H.; Maltamo, M.; Tokola, T. and Hyyppä, J. **2010** Tree species classification using airborne LiDAR – effects of stand and tree parameters, downsizing of training set, intensity normalization, and sensor type. *Silva Fennica* 44, 319–339.

Koukal, T.; Suppan, F. and Schneider, W. **2007** The impact of relative radiometric calibration on the accuracy of kNN-predictions of forest attributes. *Remote Sensing of Environment* 110, 431–437.

Kraus, K. **2003** *Photogrammetry: Advanced methods and applications.* Dummler.

Krause, S.; Sanders, T.G.; Mund, J.-P. and Greve, K. **2019** UAV-based photogrammetric tree height measurement for intensive forest monitoring. *Remote Sensing* 11, 1–18.

Kravtsova, V.I. **2012** Features of interpretation of Northern forests in ultrahigh resolution satellite images. *Contemporary Problems of Ecology* 5, 612–620.

Kukavskaya, E.A.; Soja, A.J.; Petkov, A.P.; Ponomarev, E.I. and Ivanova, G.A. *et al.* **2013** Fire emissions estimates in Siberia: evaluation of uncertainties in area burned, land cover, and fuel consumption. *Canadian Journal of Forest Research* 43, 493–506.

Kunneke, A. **2019** UAV flying mission and data analysis. Personal communication.

Küstner, G. **2017** Dark taiga; water catchment areas Thunkel, Thunkel. https://www.biozentrum.uni-wuerzburg.de/zoo3/team/kuestner/.

Kuusela, K. **1992** *The boreal forests: An overview*. http://www.fao.org/3/u6850e/u6850e03.htm (accessed on 23 February, 2021).

Kwak, D.-A.; Lee, W.-K.; Lee, J.-H.; Biging, G.S. and Gong, P. **2007** Detection of individual trees and estimation of tree height using LiDAR data. *Journal of Forest Research* 12, 425–434.

Laliberte, A.S.; Herrick, J.E.; Rango, A. and Winters, C. **2010** Acquisition, Orthorectification, and Object-based Classification of Unmanned Aerial Vehicle (UAV) Imagery for Rangeland Monitoring. *Photogrammetric Engineering & Remote Sensing* 76, 661–672.

Laliberte, A.S. and Rango, A. **2011** Image Processing and Classification Procedures for Analysis of Sub-decimeter Imagery Acquired with an Unmanned Aircraft over Arid Rangelands. *GIScience & Remote Sensing* 48, 4–23.

Laliberte, A.S.; Winters, C. and Rango, A. **2011** UAS remote sensing missions for rangeland applications. *Geocarto International* 26, 141–156.

Lamchin, M.; Park, T.; Lee, J.-Y. and Lee, W.-K. **2015** Monitoring of Vegetation Dynamics in the Mongolia Using MODIS NDVIs and their Relationship to Rainfall by Natural Zone. *Journal of the Indian Society of Remote Sensing* 43, 325–337.

Lamonaca, A.; Corona, P. and Barbati, A. **2008** Exploring forest structural complexity by multi-scale segmentation of VHR imagery. *Remote Sensing of Environment* 112, 2839–2849.

Larsen, M.; Eriksson, M.; Descombes, X.; Perrin, G. and Brandtberg, T. *et al.* **2011** Comparison of six individual tree crown detection algorithms evaluated under varying forest conditions. *International Journal of Remote Sensing* 32, 5827–5852.

Latysheva, N. **2016** *Implementing your own k-nearest neighbour algorithm to Python: KDnuggets*. https://www.kdnuggets.com/2016/01/implementing-your-own-knn-using-python.html.

Lausch, A.; Erasmi, S.; King, D.; Magdon, P. and Heurich, M. **2016** Understanding Forest Health with Remote Sensing -Part I—A Review of Spectral Traits, Processes and Remote-Sensing Characteristics. *Remote Sensing* 8, 1029.

Le, C.T. and Eberly, L.E. **2016** *Introductory biostatistics.* John Wiley & Sons Inc.

Le Maire, G.; Marsden, C.; Nouvellon, Y.; Grinand, C. and Hakamada, R. *et al.* **2011** MODIS NDVI time-series allow the monitoring of Eucalyptus plantation biomass. *Remote Sensing of Environment* 115, 2613–2625.

Le Wang; Gong, P. and Biging, G.S. **2004** Individual Tree-Crown Delineation and Treetop Detection in High-Spatial-Resolution Aerial Imagery. *Photogrammetric Engineering & Remote Sensing* 70, 351–357.

Leberl, F.; Irschara, A.; Pock, T.; Meixner, P. and Gruber, M. *et al.* **2010** Point clouds. *Photogrammetric Engineering & Remote Sensing* 76, 1123–1134.

Leberl, F. and Thurgood, J. **2004** The promise of softcopy photogrammetry revisited. *ISPRS - International Archives of the Photogrammetry, Remote Sensing and Spatial Information Sciences*, 1–6.

Leboeuf, A.; Beaudoin, A.; FOURNIER, R.; Guindon, L. and LUTHER, J. *et al.* **2007** A shadow fraction method for mapping biomass of northern boreal black spruce forests using QuickBird imagery. *Remote Sensing of Environment* 110, 488–500.

Leboeuf, A.; Fournier, R.A.; Luther, J.E.; Beaudoin, A. and Guindon, L. **2012** Forest attribute estimation of northeastern Canadian forests using QuickBird imagery and a shadow fraction method. *Forest Ecology and Management* 266, 66–74.

Lebourgeois, V.; Bégué, A.; Labbé, S.; Mallavan, B. and Prévot, L. *et al.* **2008** Can Commercial Digital Cameras Be Used as Multispectral Sensors? A Crop Monitoring Test. *Sensors* 8, 7300–7322.

Leckie, D.G.; Gougeon, F.A.; Tinis, S.; Nelson, T. and Burnett, C.N. *et al.* **2005** Automated tree recognition in old growth conifer stands with high resolution digital imagery. *Remote Sensing of Environment* 94, 311–326.

LeCun, Y.; Bengio, Y. and Hinton, G. **2015** Deep learning. *Nature* 521, 436–444.

Lee, J.; Han, D.; Shin, M.; Im, J. and Lee, J. *et al.* **2020** Different Spectral Domain Transformation for Land Cover Classification Using Convolutional Neural Networks with Multi-Temporal Satellite Imagery. *Remote Sensing* 12, 1097.

Lee, T.S.; Mumford, D.; Romero, R. and Lamme, V.A. **1998** The role of the primary visual cortex in higher level vision. *Vision Research* 38, 2429–2454.

Lefsky, M.A.; Cohen, W.B.; Acker, S.A.; Parker, G.G. and Spies, T.A. *et al.* **1999** Lidar remote sensing of the canopy structure and biophysical properties of Douglas-fir Western Hemlock forests. *Remote Sensing of Environment* 70, 339–361.

Lehmann, J.; Nieberding, F.; Prinz, T. and Knoth, C. **2015** Analysis of Unmanned Aerial System-based CIR Images in forestry—a new perspective to monitor pest infestation levels. *Forests* 6, 594–612.

Lehmkuhl, F.; Hilgers, A.; Fries, S.; Hülle, D. and Schlütz, F. *et al.* **2011** Holocene geomorphological processes and soil development as indicator for environmental change around Karakorum, Upper Orkhon Valley (Central Mongolia). *CATENA* 87, 31–44.

Leiterer, R.; Morsdorf, F.; Schaepman, M.E.; Mücke, W. and Pfeifer, N. *et al.* **2012** *3D Vegetationskartierung: flugzeuggestütztes Laserscanning für ein operationelles Waldstrukturmonitoring: DGPF Workshop 2012.* ETH Zürich, Zürich.

Lentile, L.B.; Holden, Z.A.; Smith, A.M.S.; Falkowski, M.J. and Hudak, A.T. *et al.* **2006** Remote sensing techniques to assess active fire characteristics and post-fire effects. *International Journal of Wildland Fire* 15, 1–27.

Leonhart, R. **2017** *Lehrbuch Statistik: Einstieg und Vertiefung.* 4th edn. Hogrefe Verlag.

level 80. **2015** *Agisoft PhotoScan Tutorial: Aerial Data Processing*. https://www.youtube.com/watch?v=doXm3pThz3s (accessed on 10 April, 2020).

Li, M.; Ma, L.; Blaschke, T.; Cheng, L. and Tiede, D. **2016** A systematic comparison of different object-based classification techniques using high spatial resolution imagery in agricultural environments. *International Journal of Applied Earth Observation and Geoinformation* 49, 87–98.

Li, W.; Fu, H.; Le Yu and Cracknell, A. **2017** Deep learning based oil palm tree detection and counting for high-resolution remote sensing images. *Remote Sensing* 9, 1–13.

Li, Y.; Chen, J.; Ma, Q.; Zhang, H.K. and Liu, J. **2018** Evaluation of Sentinel-2A Surface Reflectance Derived Using Sen2Cor in North America. *IEEE Journal of Selected Topics in Applied Earth Observations and Remote Sensing* 11, 1997–2021.

Li, Z.; Fraser, R.; Jin, J.; Abuelgasim, A.A. and Csiszar, I. *et al.* **2003** Evaluation of algorithms for fire detection and mapping across North America from satellite. *Journal of Geophysical Research: Biogeosciences* 108, 1–22.

Liang, S. and Wang, J. (eds). **2020** *Advanced remote sensing: Terrestrial information extraction and applications.* Academic Press, an imprint of Elsevier.

Liang, X.; Hyyppa, J.; Kukko, A.; Kaartinen, H. and Jaakkola, A. *et al.* **2014** The use of a mobile laser scanning system for mapping large forest plots. *IEEE Geoscience and Remote Sensing Letters* 11, 1504–1508.

Liaw, A. and Wiener, M. **2002** Classification and Regression by random Forest. *R News* December 2002, 18–22.

LI-COR. **1992** *LAI-2000 Plant Canopy Analyzer: Operating Manual,* Lincoln, Nebraska, USA.

Lillesand, T.M.; Kiefer, R.W. and Chipman, J.W. **2015** *Remote sensing and image interpretation.* Wiley.

Lim, K.; Treitz, P.; Wulder, M.; St-Onge, B. and Flood, M. **2003** LiDAR remote sensing of forest structure. *Progress in Physical Geography* 27, 88–106.

Lin, J.; Wang, M.; Ma, M. and Lin, Y. **2018** Aboveground Tree Biomass Estimation of Sparse Subalpine Coniferous Forest with UAV Oblique Photography. *Remote Sensing* 10, 1–19.

Lin, Q.; Huang, H.; Wang, J.; Huang, K. and Liu, Y. **2019** Detection of Pine Shoot Beetle (PSB) Stress on Pine Forests at Individual Tree Level using UAV-Based Hyperspectral Imagery and Lidar. *Remote Sensing* 11, 1–20.

Linder, W. **2016** *Digital Photogrammetry: A Practical Course.* 4th edn.

Lintunen, A. **2013** Crown architecture and its role in species interactions in mixed boreal forests. Dissertationes Forestales. Dissertation. Faculty of Agriculture and Forestry.

Lisein, J.; Michez, A.; Claessens, H. and Lejeune, P. **2015** Discrimination of Deciduous Tree Species from Time Series of Unmanned Aerial System Imagery. *PloS one* 10.

Lisein, J.; Pierrot-Deseilligny, M.; Bonnet, S. and Lejeune, P. **2013** A Photogrammetric workflow for the creation of a forest Canopy Height Model from small Unmanned Aerial System Imagery. *Forests* 4, 922–944.

Listopad, C.M.; Masters, R.E.; Drake, J.; Weishampel, J. and Branquinho, C. **2015** Structural diversity indices based on airborne LiDAR as ecological indicators for managing highly dynamic landscapes. *Ecological Indicators* 57, 268–279.

Liu, D. and Xia, F. **2010** Assessing object-based classification. Advantages and limitations. *Remote Sensing Letters* 1, 187–194.

Liu, J.G. and Mason, P.J. **2009** *Essential image processing and GIS for remote sensing.* 1st edn. Wiley-Blackwell.

Liu, J.-G. and Mason, P.J. **2016** *Image processing and GIS for remote sensing: Techniques and applications / Jian Guo Liu and Philippa J. Mason, Department of Earth Science and Engineering, Imperial College London.* Wiley Blackwell.

Loetsch, F. and Haller, K.E. **1964** *Forest inventory: Volume I.* BLV.

Lohr, S.L. **2010** *Sampling: Design and analysis.* 2nd edn. Brooks/Cole.

López-Serrano, P.M.; López-Sánchez, C.A.; Álvarez-González, J.G. and García-Gutiérrez, J. **2016** A Comparison of Machine Learning Techniques Applied to Landsat-5 TM Spectral Data for Biomass Estimation. *Canadian Journal of Remote Sensing* 42, 690–705.

Lorenz, J. **2020** Statistics support for PhD students - statistical analysis of field data Holger Vogt, Göttingen.

Lowe, D.G. **2004** Distinctive image features from scale-invariant keypoints. *International Journal of Computer Vision* 60, 91–110.

Lu, D. and Weng, Q. **2007** A survey of image classification methods and techniques for improving classification performance. *International Journal of Remote Sensing* 28, 823–870.

Ludeno, G.; Catapano, I.; Renga, A.; Vetrella, A.R. and Fasano, G. *et al.* **2018** Assessment of a micro-UAV system for microwave tomography radar imaging. *Remote Sensing of Environment* 212, 90–102.

Ludovisi, R.; Tauro, F.; Salvati, R.; Khoury, S. and Mugnozza Scarascia, G. *et al.* **2017** UAV-based thermal imaging for high-throughput field phenotyping of black poplar response to drought. *Frontiers in plant science* 8, 1681.

Ludwig, M.; M. Runge, C.; Friess, N.; Koch, T.L. and Richter, S. *et al.* **2020** Quality Assessment of Photogrammetric Methods—A Workflow for Reproducible UAS Orthomosaics. *Remote Sensing* 12, 1–18.

Luhmann, T. and Schumacher, C. (eds). **2019** *Photogrammetrie - Laserscanning - Optische 3D-Messtechnik: Beiträge der Oldenburger 3D-Tage 2019.* Wichmann.

Lutes, D.C.; Keane, R.E.; Caratti, J.F.; Key, C.H. and Benson, N.C. *et al.* **2006** *FIREMON: Fire effects monitoring and inventory system.* USDA Forest Service, Fort Collins, Colorado.

Ma, L.; Liu, Y.; Zhang, X.; Ye, Y. and Yin, G. *et al.* **2019** Deep learning in remote sensing applications: A meta-analysis and review. *ISPRS Journal of Photogrammetry and Remote Sensing* 152, 166–177.

Maas, H.-G.; Bienert, A.; Scheller, S. and Keane, E. **2008** Automatic forest inventory parameter determination from terrestrial laser scanner data. *International Journal of Remote Sensing* 29, 1579–1593.

Machala, M. and Zejdová, L. **2014** Forest Mapping Through Object-based Image Analysis of Multispectral and LiDAR Aerial Data. *European Journal of Remote Sensing* 47, 117–131.

Magnussen, S.; Naesset, E. and Gobakken, T. **2013** Prediction of tree-size distributions and inventory variables from cumulants of canopy height distributions. *Forestry: An International Journal of Forest Research* 86, 583–595.

Magurran, A.E. **1988** *Ecological Diversity and Its Measurement.* Springer Netherlands.

Mahiny, A.S. and Turner, B.J. **2007** A Comparison of Four Common Atmospheric Correction Methods. *Photogrammetric Engineering & Remote Sensing* 73, 361–368.

Main-Knorn, M.; Pflug, B.; Louis, J.; Debaecker, V. and Gascon, F. **2017** Sen2Cor for Sentinel-2. In *Remote Sensing, Security & Defence*. SPIE (ed), p. 3.

Majasalmi, T. and Rautiainen, M. **2016** The potential of Sentinel-2 data for estimating biophysical variables in a boreal forest. A simulation study. *Remote Sensing Letters* 7, 427–436.

Makoto, K.; Nemilostiv, Y.P.; Zyryanova, O.A.; Kajimoto, T. and Matsuura, Y. *et al.* **2007** Regeneration after Forest Fires in mixed Conifer Broad-leaved Forests of the Amur Region in Far Eastern Russia: the Relationship between Species Specific Traits Against Fire and Recent Fire Regimes. *Eurasian Journal Forest Resources* 10, 51–58.

Malhi, Y.; Baldocchi, D.D. and Jarvis, P.G. **2002** The carbon balance of tropical, temperate and boreal forests. *Plant, Cell and Environment* 22, 715–740.

Mallinis, G.; Koutsias, N.; Tsakiri-Strati, M. and Karteris, M. **2008** Object-based classification using Quickbird imagery for delineating forest vegetation polygons in a Mediterranean test site. *ISPRS Journal of Photogrammetry and Remote Sensing* 63, 237–250.

Mallinis, G.; Mitsopoulos, I. and Chrysafi, I. **2018** Evaluating and comparing Sentinel 2A and Landsat-8 Operational Land Imager (OLI) spectral indices for estimating fire severity in a Mediterranean pine ecosystem of Greece. *GIScience & Remote Sensing* 55, 1–18.

Malory, J. **2015** *Creating a 3D Model with DJI Phantom 3 and Agisoft Tutorial*. https://www.youtube.com/watch?v=1iYtjLlm8eI (accessed on 05 April, 2020).

Maltamo, M. (ed). **2014** *Forestry applications of airborne laser scanning: Concepts and case studies.* Springer.

Maltamo, M.; Bollandsas, O.M.; Naesset, E.; Gobakken, T. and Packalen, P. **2011** Different plot selection strategies for field training data in ALS-assisted forest inventory. *Forestry: An International Journal of Forest Research* 84, 23–31.

Maltamo, M.; Eerikäinen, K.; Pitkänen, J.; Hyyppä, J. and Vehmas, M. **2004** Estimation of timber volume and stem density based on scanning laser altimetry and expected tree size distribution functions. *Remote Sensing of Environment* 90, 319–330.

Manfreda, S.; McCabe, M.; Miller, P.; Lucas, R. and Pajuelo Madrigal, V. *et al.* **2018** On the use of Unmanned Aerial Systems for environmental monitoring. *Remote Sensing* 10, 641.

Matasci, G.; Hermosilla, T.; Wulder, M.A.; White, J.C. and Coops, N.C. *et al.* **2018** Large-area mapping of Canadian boreal forest cover, height, biomass and other structural attributes using Landsat composites and lidar plots. *Remote Sensing of Environment* 209, 90–106.

Mather, P.M. **2011** *Computer processing of remotely-sensed images: An introduction.* 4th edn. Wiley.

Mauro, G. **2004** *High resolution satellite imagery for forestry studies: the beechwood of the Prodenone mountains (Italy).* ISPRS.

Maximovich, S.V. **2004** Geography and ecology of cryogenic soils of Mongolia. In *Cryosols*: *Permafrost-Affected Soils*. J.M. Kimble (ed). Springer Berlin Heidelberg, pp. 253–270.

Mayer, R.R. and Scribner, D.A. **2002** Extending the normalized difference vegetation index (NDVI) to short-wave infrared radiation (SWIR) (1- to 2.5-µm). In *Imaging Spectrometry VIII*. S.S. Shen (ed). SPIE, pp. 182–193.

McDonald, A.J.; Gemmell, F.M. and Lewis, P.E. **1998** Investigation of the Utility of Spectral Vegetation Indices for Determining Information on Coniferous Forests. *Remote Sensing of Environment* 66, 250–272.

McFeeters, S.K. **1996** The use of the Normalized Difference Water Index (NDWI) in the delineation of open water features. *International Journal of Remote Sensing* 17, 1425–1432.

McGlone, J.C. (ed). **2004** *Manual of photogrammetry.* 5th edn. American Soc. for Photogrammetry and Remote Sensing.

McRae, D.J.; Conard, S.G.; Baker, S.P.; Samsonov, Y.N. and Ivanova, G.A. **2009** Fire emissions in central Siberia. *The Canadian Smoke Newsletter*, 9–13.

McRoberts, R.E. **2008** Using satellite imagery and the k-nearest neighbors technique as a bridge between strategic and management forest inventories. *Remote Sensing of Environment* 112, 2212–2221.

McRoberts, R.E. **2012** Estimating forest attribute parameters for small areas using nearest neighbors techniques. *Forest Ecology and Management* 272, 3–12.

McRoberts, R.E.; Nelson, M.D. and Wendt, D.G. **2002** Stratified estimation of forest area using satellite imagery, inventory data, and the k-Nearest Neighbors technique. *Remote Sensing of Environment* 82, 457–468.

McRoberts, R.E. and Tomppo, E. **2007** Remote sensing support for national forest inventories. *Remote Sensing of Environment* 110, 412–419.

McRoberts, R.E.; Tomppo, E.O. and Næsset, E. **2010** Advances and emerging issues in national forest inventories. *Scandinavian Journal of Forest Research* 25, 368–381.

Medvedev, A.A.; Telnova, N.O.; Kudikov, A.V. and Alekseenko, N.A. **2020** Use of photogrammetric point clouds for the analysis and mapping of structural variables in sparse northern boreal forests. *Sovremennye problemy distantsionnogo zondirovaniya Zemli iz kosmosa* 17, 150–163.

Méndez-Toribio, M.; Meave, J.A.; Zermeño-Hernández, I.; Ibarra-Manríquez, G. and Woods, K. **2016** Effects of slope aspect and topographic position on environmental variables, disturbance regime and tree community attributes in a seasonal tropical dry forest. *Journal of Vegetation Science* 27, 1094–1103.

Meng, J.; Li, S.; Wang, W.; Liu, Q. and Xie, S. *et al.* **2016** Estimation of Forest Structural Diversity Using the Spectral and Textural Information Derived from SPOT-5 Satellite Images. *Remote Sensing* 8, 1–24.

Meng, Q.; Cieszewski, C.J.; Madden, M. and Borders, B.E. **2007** K Nearest Neighbor Method for Forest Inventory Using Remote Sensing Data. *GIScience & Remote Sensing* 44, 149–165.

Meng, X.; Gao, X.; Li, S. and Lei, J. **2020** Spatial and Temporal Characteristics of Vegetation NDVI Changes and the Driving Forces in Mongolia during 1982–2015. *Remote Sensing* 12, 1–25.

Merino, L.; Caballero, F.; Martínez-de-Dios, J.R.; Maza, I. and Ollero, A. **2012** An Unmanned Aircraft System for Automatic Forest Fire Monitoring and Measurement. *Journal of Intelligent & Robotic Systems* 65, 533–548.

Mestemacher, U. and Doelle, K. **2003** Waldstrukturkartierung im Untersuchungsgebiet Khan Khentii. In *Mongolei, Strictly protected area „Khan Khentii"- Wälder und Waldsteppen borealer Breiten.*: *Postgraduierten – und Nachwuchsförderungsprogramm internationale und interdisziplinäre Urwaldforschung.* Internal report. University of Goettingen (ed), pp. 7–37.

Michez, A.; Piégay, H.; Lisein, J.; Claessens, H. and Lejeune, P. **2016** Classification of riparian forest species and health condition using multi-temporal and hyperspatial imagery from unmanned aerial system. *Environmental monitoring and assessment* 188, 19.

Miehe, G.; Schlütz, F.; Miehe, S.; Opgenoorth, L. and Cermak, J. *et al.* **2007** Mountain forest islands and Holocene environmental changes in Central Asia. A case study from the southern Gobi Altay, Mongolia. *Palaeogeography, Palaeoclimatology, Palaeoecology* 250, 150–166.

Mielcarek, M.; Kamińska, A. and Stereńczak, K. **2020** Digital Aerial Photogrammetry (DAP) and Airborne Laser Scanning (ALS) as Sources of Information about Tree Height: Comparisons of the Accuracy of Remote Sensing Methods for Tree Height Estimation. *Remote Sensing* 12, 1–22.

Mikhail, E.M.; Bethel, J.S. and McGlone, J.C. **2001** *Introduction to modern photogrammetry.* Wiley.

Minařík, R. and Langhammer, J. **2016** Use of a multispectral UAV photogrammetry for detection and tracking of forest disturbance dynamics. *ISPRS - International Archives of the Photogrammetry, Remote Sensing and Spatial Information Sciences* XLI-B8, 711–718.

Ministry of Agriculture, Forestry and Fisheries. **2009** *Report on national forest and water policy of Mongolia.* Ministry of Agriculture, Forestry and Fisheries, Japan, Tokyo.

Ministry of Environment and Green Development of Mongolia. **2014** *MARCC-2014 Mongolia Second Assessment Report on Climate Change-2014,* Ulaanbaatar.

Ministry of Environment and Tourism, Mongolia. **2020** *Database Environment: In Mongolian*. https://eic.mn/ (accessed on 04 August, 2020).

Ministry of Environment, Japan. **2014** *Climate Change in Mongolia.* Ministry of Environment, Japan, Tokyo.

Miranda, A.M.; Ribeir, P. and Megill, W.M. **2018** *Drone-based remote sensing application in the field of forestry: Technical Report.* Rhine-Waal University of Applied Sciences.

Mirończuk, A. and Hościło, A. **2017** Mapping tree cover with Sentinel-2 data using the Support Vector Machine (SVM). *Geoinformation Issues* 9, 27–38.

Misheel, B. **2019** *The changing world of Mongolia's boreal forests*. https://montsame.mn/en/read/181648 (accessed on 21 February, 2020).

Miyoshi, G.T.; Arruda, M.d.S.; Osco, L.P.; Marcato Junior, J. and Gonçalves, D.N. *et al.* **2020** A novel deep learning method to identify single tree species in UAV-based hyperspectral images. *Remote Sensing* 12, 1–18.

Moe, K.; Owari, T.; Furuya, N. and Hiroshima, T. **2020** Comparing Individual Tree Height Information Derived from Field Surveys, LiDAR and UAV-DAP for High-Value Timber Species in Northern Japan. *Forests* 11, 223.

Mohan, M.; Silva, C.; Klauberg, C.; Jat, P. and Catts, G. *et al.* **2017** Individual Tree Detection from Unmanned Aerial Vehicle (UAV) Derived Canopy Height Model in an Open Canopy Mixed Conifer Forest. *Forests* 8, 340.

Moisen, G.G. and Frescino, T.S. **2002** Comparing five modelling techniques for predicting forest characteristics. *Ecological Modelling* 157, 209–225.

Mongolian Ministry of Environment and Tourism. **2016** *Mongolian Multipurpose National Forest Inventory 2014-2016.* Mongolian Ministry of Environment and Tourism, Ulaanbaatar.

Mongolian Ministry of Justice. **2012** *Mongolian Law on Forest*. https://www.legalinfo.mn/law/details/15624.

Mora, B.; Wulder, M.; White, J. and Hobart, G. **2013a** Modeling stand height, volume, and biomass from Very High Spatial Resolution satellite imagery and samples of Airborne LiDAR. *Remote Sensing* 5, 2308–2326.

Mora, B.; Wulder, M.A.; Hobart, G.W.; White, J.C. and Bater, C.W. *et al.* **2013b** Forest inventory stand height estimates from very high spatial resolution satellite imagery calibrated with lidar plots. *International Journal of Remote Sensing* 34, 4406–4424.

Mora, B.; Wulder, M.A. and White, J.C. **2010a** Identifying leading species using tree crown metrics derived from very high spatial resolution imagery in a boreal forest environment. *Canadian Journal of Remote Sensing* 36, 332–344.

Mora, B.; Wulder, M.A. and White, J.C. **2010b** Segment-constrained regression tree estimation of forest stand height from very high spatial resolution panchromatic imagery over a boreal environment. *Remote Sensing of Environment* 114, 2474–2484.

Morales, G.; Kemper, G.; Sevillano, G.; Arteaga, D. and Ortega, I. *et al.* **2018** Automatic Segmentation of Mauritia flexuosa in Unmanned Aerial Vehicle (UAV) Imagery Using Deep Learning. *Forests* 9, 1–14.

Moritz, M.A.; Morais, M.E.; Summerell, L.A.; Carlson, J.M. and Doyle, J. **2005** Wildfires, complexity, and highly optimized tolerance. *Proceedings of the National Academy of Sciences of the United States of America* 102, 17912–17917.

Mosbrucker, A.R.; Major, J.J.; Spicer, K.R. and Pitlick, J. **2017** Camera system considerations for geomorphic applications of SfM photogrammetry. *Earth Surf. Process. Landforms* 42, 969–986.

Mostegel, C.; Rumpler, M.; Fraundorfer, F. and Bischof, H. **2016** UAV-based autonomous image acquisition with multi-view stereo quality assurance by confidence prediction. In *2016 IEEE Conference on Computer*. IEEE Computer Society (ed), pp. 1–10.

Mountrakis, G.; Im, J. and Ogole, C. **2011** Support vector machines in remote sensing: A review. *ISPRS Journal of Photogrammetry and Remote Sensing* 66, 247–259.

Mühlenberg, M. **2012** Long-term research on biodiversity in West Khentey, Northern Mongolia. *Erforschung biologischer Ressourcen der Mongolei* 12, 27–37.

Mühlenberg, M.; Appelfelder, J.; Hoffmann, H.; Ayush, E. and Wilson, K.J. **2012a** Structure of the montane taiga forests of West Khentii, Northern Mongolia. *Journal of Forest Science*, 45–56.

Mühlenberg, M.; Appelfelder, J.; Hoffmann, H.; Ayush, E. and Wilson, K.J. **2012b** Structure of the montane taiga forests of West Khentii, Northern Mongolia. *Journal of Forest Science* 58, 45–56.

Mühlenberg, M.; Batkhishig, T.; Dashzeveg, T.; Drößler, L. and Neusel, B. *et al.* **2006** *MONGOLIA - Lessons from Tree Planting Initiatives.* World Bank, Washington, D.C.

Mühlenberg, M.; Hondong, H.; Dulamsuren, C. and Gadow, K. **2004** Large-scale biodiversity research in the southern Taiga, Northern Mongolia. *Forest, Snow and Landscape Research*, 93–118.

Muhsoni, F.F.; Sambah, A.B.; Mahmudi, M. and Wiadnya, D. **2018** Comparison of different vegetation indices for assessing mangrove density using Sentinel-2 imagery. *International Journal of GEOMATE* 14, 42–51.

Mukhortova, L.; Schepaschenko, D.; Shvidenko, A.; McCallum, I. and Kraxner, F. **2015** Soil contribution to carbon budget of Russian forests. *Agricultural and Forest Meteorology* 200, 97–108.

Münch, D. **1993** Bestandesdynamik von Naturwaldreservaten. Eine Dauerbeobachtung in Luftbildzeitreihen. Dissertation, Freiburg.

Munkhzorig, D. **2009** *Report on National Forest and Water Policy of Mongolia.* Ministry of Environment and Tourism, Mongolia.

Murphy, M.A.; Evans, J.S. and Storfer, A. **2010** Quantifying Bufo boreas connectivity in Yellowstone National Park with landscape genetics. *Ecology* 91, 252–261.

Muukkonen, P. **2006** Forest inventory-based large-scale forest biomass and carbon budget assessment: new enhanced methods and use of remote sensing for verification. *Dissertationes Forestales* 2006.

Myburgh, G. and van Niekerk, A. **2014** Impact of Training Set Size on Object-Based Land Cover Classification. *International Journal of Applied Geospatial Research* 5, 49–67.

Myers, B.J. and Benson, M.L. **1981** Rainforest species on large-scale color photos 1:2000 scale color aerial photographs. *Photogrammetric Engineering & Remote Sensing* 47, 505–513.

Myroniuk, V.V.; Bilous, A.M. and Diachuk, P.P. **2019** Predicting forest stand parameters using the k-NN approach. *Ukrainian Journal of Forest and Wood Science* 10, 51–63.

Næsset, E. **1997** Determination of mean tree height of forest stands using airborne laser scanner data. *ISPRS Journal of Photogrammetry and Remote Sensing* 52, 49–56.

Næsset, E. **2002a** Estimating tree height and tree crown properties using airborne scanning laser in a boreal nature reserve. *Remote Sensing of Environment* 79, 105–115.

Næsset, E. **2002b** Predicting forest stand characteristics with airborne scanning laser using a practical two-stage procedure and field data. *Remote Sensing of Environment* 80, 88–99.

Næsset, E. **2004** Practical large-scale forest stand inventory using a small-footprint airborne scanning laser. *Scandinavian Journal of Forest Research* 19, 164–179.

Næsset, E. **2007** Airborne laser scanning as a method in operational forest inventory: Status of accuracy assessments accomplished in Scandinavia. *Scandinavian Journal of Forest Research* 22, 433–442.

Næsset, E. **2014** Area-Based Inventory in Norway – From Innovation to an Operational Reality. In *Forestry applications of airborne laser scanning*: *Concepts and case studies*. M. Maltamo (ed). Springer, pp. 215–240.

Næsset, E. **2015** Vertical Height Errors in Digital Terrain Models Derived from Airborne Laser Scanner Data in a Boreal-Alpine Ecotone in Norway. *Remote Sensing* 7, 4702–4725.

Næsset, E. **2016** photogammetry, forest inventory. E-mail.

Næsset, E. and Gobakken, T. **2008** Estimation of above- and below-ground biomass across regions of the boreal forest zone using airborne laser. *Remote Sensing of Environment* 112, 3079–3090.

Næsset, E.; Gobakken, T.; Solberg, S.; Gregoire, T.G. and Nelson, R. *et al.* **2011** Model-assisted regional forest biomass estimation using LiDAR and InSAR as auxiliary data: A case study from a boreal forest area. *Remote Sensing of Environment* 115, 3599–3614.

Næsset, E.; Ørka, H.O.; Solberg, S.; Bollandsås, O.M. and Hansen, E.H. *et al.* **2016** Mapping and estimating forest area and aboveground biomass in miombo woodlands in Tanzania using data from airborne laser scanning, TanDEM-X, RapidEye, and global forest maps. A comparison of estimated precision. *Remote Sensing of Environment* 175, 282–300.

Nagel, J. **2001** *Skript Waldmesslehre.* Nordwestdeutsche Forstliche Versuchsanstalt (NW-FVA), Göttingen.

Naidoo, L.; Cho, M.A.; Mathieu, R. and Asner, G. **2012** Classification of savanna tree species, in the Greater Kruger National Park region, by integrating hyperspectral and LiDAR data in a Random Forest data mining environment. *ISPRS Journal of Photogrammetry and Remote Sensing* 69, 167–179.

Nandintsetseg, B. and Shinoda, M. **2011** Seasonal change of soil moisture in Mongolia: its climatology and modelling. *Int. J. Climatol.* 31, 1143–1152.

NASA. **2021** *Fire Information for Resource Management System (FIRMS)*. https://earthdata.nasa.gov/earth-observation-data/near-real-time/firms (accessed on 17 March, 2021).

Näsi, R.; Honkavaara, E.; Blomqvist, M.; Lyytikäinen-Saarenmaa, P. and Hakala, T. *et al.* **2018** Remote sensing of bark beetle damage in urban forests at individual tree level using a novel hyperspectral camera from UAV and aircraft. *Urban Forestry & Urban Greening* 30, 72–83.

National Council for Fire and Emergency Services. **2020** *Wildfire statistics Australia*. https://www.afac.com.au/initiative/nrsc (accessed on 14 July, 2020).

Navarro, G.; Caballero, I.; Silva, G.; Parra, P.-C. and Vázquez, Á. *et al.* **2017** Evaluation of forest fire on Madeira Island using Sentinel-2A MSI imagery. *International Journal of Applied Earth Observation and Geoinformation* 58, 97–106.

Nebiker, S.; Annen, A.; Scherrer, M. and Oesch D. **2008** A light-weight multispectral sensor for Micro UAV - opportunities for very high resolution airborne remote sensing. *The International Archives of Photogrammetry, Remote Sensing and Spatial Information Sciences* 37, 1193–1200.

Nevalainen, O.; Honkavaara, E.; Tuominen, S.; Viljanen, N. and Hakala, T. *et al.* **2017** Individual Tree Detection and Classification with UAV-Based Photogrammetric Point Clouds and Hyperspectral Imaging. *Remote Sensing* 9, 1–34.

Newnham, G.J.; Armston, J.D.; Calders, K.; Disney, M.I. and Lovell, J.L. *et al.* **2015** Terrestrial Laser Scanning for plot-scale forest measurement. *Current Forestry Reports* 1, 239–251.

Nex, F. and Remondino, F. **2014** UAV for 3D mapping applications: a review. *Applied Geomatics* 6, 1–15.

Nezami, S.; Khoramshahi, E.; Nevalainen, O.; Pölönen, I. and Honkavaara, E. **2020** Tree Species Classification of Drone Hyperspectral and RGB Imagery with Deep Learning Convolutional Neural Networks. *Remote Sensing* 12, 1–20.

Ni, W.; Liu, J.; Zhang, Z.; Sun, G. and Yang, A. Evaluation of UAV-based forest inventory system compared with LiDAR data. In *2015 IEEE International Geoscience*, pp. 3874–3877.

Niedersächsische Landesbehörde für Straßenbau und Verkehr. **2019** *Drohnen: Unbemannte Luftfahrtgeräte: Gemeinsames Informationsangebot des Bundesministeriums für Verkehr und der DFS (Deutsche Flugsicherung GmbH)*. https://www.strassenbau.niedersachsen.de/startseite/aufgaben/luftverkehr/drohnen_unbemannte_luftfahrtgerate/drohnen-unbemannte-luftfahrtgeraete-114884.html (accessed on 10 April, 2020).

Niemann, A.-L. **2020** *Wald liegt in der Luft: Droneseed*. https://www.faz.net/aktuell/technik-motor/so-koennen-baeume-mit-drohnen-gepflanzt-werden-16783098.html?GEPC=s5 (accessed on 27 May, 2020).

Niemeyer, I.; Listner, C. and Nussbaum, S. **2012** Object-based image analysis using very high-resolution satellite data. *Journal of Nuclear Materials Management*, 100–109.

Niethammer, U.; James, M.R.; Rothmund, S.; Travelletti, J. and Joswig, M. **2012** UAV-based remote sensing of the Super-Sauze landslide: Evaluation and results. *Engineering Geology* 128, 2–11.

Nilsson, M.; Nordkvist, K.; Jonzén, J.; Lindgren, N. and Axensten, P. *et al.* **2017** A nationwide forest attribute map of Sweden predicted using airborne laser scanning data and field data from the National Forest Inventory. *Remote Sensing of Environment* 194, 447–454.

Noordermeer, L.; Bollandsås, O.M.; Ørka, H.O.; Næsset, E. and Gobakken, T. **2019** Comparing the accuracies of forest attributes predicted from airborne laser scanning and digital aerial photogrammetry in operational forest inventories. *Remote Sensing of Environment* 226, 26–37.

Norzaki, N. and Tahar, K.N. **2019** A comparative study of template matching, ISO cluster segmentation, and tree canopy segmentation for homogeneous tree counting. *International Journal of Remote Sensing* 40, 7477–7499.

Nurminen, K.; Karjalainen, M.; Yu, X.; Hyyppä, J. and Honkavaara, E. **2013** Performance of dense digital surface models based on image matching in the estimation of plot-level forest variables. *ISPRS Journal of Photogrammetry and Remote Sensing* 83, 104–115.

Nussbaum, S.; Tueshaus, J. and Niemeyer, I. **2013** Images objects vs. pixels: A comparison of new methods from both domains. *ESARDA BULLETIN*, 66–74.

NW-FVA. **2020** *NorthWest German Forest Research Institute: ForestSimulator*. https://www.nw-fva.de/index.php?id=194 (accessed on 21 June, 2020).

Olivas, P.C.; Oberbauer, S.F.; Clark, D.B.; Clark, D.A. and Ryan, M.G. *et al.* **2013** Comparison of direct and indirect methods for assessing leaf area index across a tropical rain forest landscape. *Agricultural and Forest Meteorology* 177, 110–116.

Olofsson, P.; Foody, G.M.; Stehman, S.V. and Woodcock, C.E. **2013** Making better use of accuracy data in land change studies. Estimating accuracy and area and quantifying uncertainty using stratified estimation. *Remote Sensing of Environment* 129, 122–131.

Orefice, M.; Di Vito, V. and Torrano, G. **2010** Sense and Avoid: Systems and Methods. In *Encyclopedia of aerospace engineering*. R. Blockley and W. Shyy (eds). Wiley, pp. 1–9.

Ørka, H.O.; Gobakken, T.; Næsset, E.; Ene, L. and Lien, V. **2012** Simultaneously acquired airborne laser scanning and multispectral imagery for individual tree species identification. *Canadian Journal of Remote Sensing* 38, 125–138.

Ōsawa, A. **2010** *Permafrost ecosystems: Siberian larch forests.* Springer.

Osborn, J.; Dell, M.; Stone, C.; Iqbal, I. and Lacey, M. *et al.* **2017** *Photogrammetry for Forest Inventory: Planning Guidelines.* Forest & Wood Products Australia Limited.

Ota, T.; Ogawa, M.; Mizoue, N.; Fukumoto, K. and Yoshida, S. **2017** Forest Structure Estimation from a UAV-Based Photogrammetric Point Cloud in Managed Temperate Coniferous Forests. *Forests* 8, 1–10.

Otero, V.; van de Kerchove, R.; Satyanarayana, B.; Martínez-Espinosa, C. and Fisol, M.A.B. *et al.* **2018** Managing mangrove forests from the sky: Forest inventory using field data and Unmanned Aerial Vehicle (UAV) imagery in the Matang Mangrove Forest Reserve, peninsular Malaysia. *Forest Ecology and Management* 411, 35–45.

Otoda, T.; Doi, T.; Sakamoto, K.; Hirobe, M. and Nachin, B. *et al.* **2013** Frequent fires may alter the future composition of the boreal forest in northern Mongolia. *Journal of Forest Research* 18, 246–255.

Otsu, K.; Pla, M.; Vayreda, J. and Brotons, L. **2018** Calibrating the severity of forest defoliation by pine processionary moth with Landsat and UAV imagery. *Sensors (Basel, Switzerland)* 18, 1–14.

Ozdemir, I. and Karnieli, A. **2011** Predicting forest structural parameters using the image texture derived from WorldView-2 multispectral imagery in a dryland forest, Israel. *International Journal of Applied Earth Observation and Geoinformation* 13, 701–710.

Pachauri, R.K., Mayer, L. and IPCC SYR TSU (eds). **2015** *Climate change 2014: Synthesis report.* Intergovernmental Panel on Climate Change.

Pacifici, F.; Longbotham, N. and Emery, W.J. **2014** The Importance of Physical Quantities for the Analysis of Multitemporal and Multiangular Optical Very High Spatial Resolution Images. *IEEE Trans. Geosci. Remote Sensing* 52, 6241–6256.

Pádua, L.; Guimarães, N.; Adão, T.; Marques, P. and Peres, E. *et al.* **2019** Classification of an Agrosilvopastoral System Using RGB Imagery from an Unmanned Aerial Vehicle. In *Progress in Artificial Intelligence*. P. Moura Oliveira, P. Novais and L.P. Reis (eds). Springer International Publishing, pp. 248–257.

Pádua, L.; Marques, P.; Adáo, T.; Hruška, J. and Peres, E. *et al.* **2018** UAS-based imagery and photogrammetric processing for tree height and crown diameter extraction. In *2018 the International Conference on Geoinformatics and Data Analysis (ICGDA 2018) ;*: *Workshop, 2018 the International Conference on Software and Services Engineering (ICSSE 2018) : April 20-22, 2018, Prague, Czech Republic*. V. Vozenilek (ed). The Association for Computing Machinery, pp. 87–91.

Pádua, L.; Vanko, J.; Hruška, J.; Adão, T. and Sousa, J.J. *et al.* **2017** UAS, sensors, and data processing in agroforestry: a review towards practical applications. *International Journal of Remote Sensing* 38, 2349–2391.

Pajares, G. **2015** Overview and current Status of remote sensing applications based on Unmanned Aerial Vehicles (UAVs). *Photogrammetric Engineering & Remote Sensing* 81, 281–330.

Pałaś, K.W. and Zawadzki, J. **2020** Sentinel-2 Imagery Processing for Tree Logging Observations on the Białowieża Forest World Heritage Site. *Forests* 11, 1–16.

Panagiotidis, D.; Abdollahnejad, A.; Surový, P. and Chiteculo, V. **2017** Determining tree height and crown diameter from high-resolution UAV imagery. *International Journal of Remote Sensing* 38, 2392–2410.

Paris, C. and Bruzzone, L. **2015** A three-dimensional model-based approach to the estimation of the ree top height by fusing low-density LiDAR data and Very High Resolution optical images. *IEEE Trans. Geosci. Remote Sensing* 53, 467–480.

Paris, C.; Kelbe, D.; van Aardt, J. and Bruzzone, L. **2017** A Novel Automatic Method for the Fusion of ALS and TLS LiDAR Data for Robust Assessment of Tree Crown Structure. *IEEE Trans. Geosci. Remote Sensing* 55, 3679–3693.

Park, T.; Cho, J.-K.; Lee, J.-Y.; Lee, W.-K. and Choi, S. *et al.* **2014** Unconstrained approach for isolating individual trees using high-resolution aerial imagery. *International Journal of Remote Sensing* 35, 89–114.

Parks, S.; Dillon, G. and Miller, C. **2014** A New Metric for Quantifying Burn Severity: The Relativized Burn Ratio. *Remote Sensing* 6, 1827–1844.

Parsons, A.; Robichaud, P.R.; Lewis, S.A.; Napper, C. and Clark, J.T. **2010** *Field Guide for Mapping Post-Fire Soil Burn Severity.* USDA Forest Service, Fort Collins, Colorado.

Pasquarella, V.J.; Holden, C.E. and Woodcock, C.E. **2018** Improved mapping of forest type using spectral-temporal Landsat features. *Remote Sensing of Environment* 210, 193–207.

Pausas, J.G. **2015** Bark thickness and fire regime. *Functional Ecology* 29, 315–327.

Pechony, O. and Shindell, D.T. **2010** Driving forces of global wildfires over the past millennium and the forthcoming century. *Proceedings of the National Academy of Sciences of the United States of America* 107, 19167–19170.

Pellegrini, A.F.A.; Anderegg, W.R.L.; Paine, C.E.T.; Hoffmann, W.A. and Kartzinel, T. *et al.* **2017** Convergence of bark investment according to fire and climate structures ecosystem vulnerability to future change. *Ecology letters* 20, 307–316.

Pelz, D.R. **1983** Sixth-tree sampling in forest inventories. *Revista Floresta*, 54–58.

Peña, J.M.; de Castro, Ana, I.; Torres-Sánchez, J.; Andújar, D. and San Martín, C. *et al.* **2018** Estimating tree height and biomass of a poplar plantation with image-based UAV technology. *AIMS Agriculture and Food* 3, 313–323.

Peng, J.; Fan, W.; Wang, L.; Xu, X. and Li, J. *et al.* **2018** Modeling the Directional Clumping Index of Crop and Forest. *Remote Sensing* 10, 1–22.

Persson, A.; Holmgren, J. and Soderman, U. **2002** Detecting and measuring individual trees using an airborne laser scanner. *Photogrammetric engineering and remote sensing* 68, 925–932.

Persson, H. **2016** Estimation of Boreal Forest Attributes from Very High Resolution Pléiades Data. *Remote Sensing* 8, 736.

Persson, H.; Wallerman, J.; Olsson, H. and Fransson, J.E. **2013** Estimating forest biomass and height using optical stereo satellite data and a DTM from laser scanning data. *Canadian Journal of Remote Sensing* 39, 251–262.

Persson, M.; Lindberg, E. and Reese, H. **2018** Tree Species Classification with Multi-Temporal Sentinel-2 Data. *Remote Sensing* 10, 1–17.

Petrie, G. **2013** Commercial operation of leightweight UAVs for aerial imaging and mapping. *Geoinformatics* January/February, 28–39.

Petrie, G. and Walker, A.S. **2007** Airborne digital imaging technology: a new overview. *The Photogrammetric Record* 22, 203–225.

Petrokofsky, G.; Holmgren, P.; Goetz, S. and Joosten, H. **2012** Comparison of methods for measuring and assessing carbon stocks and carbon stock changes in terrestrial carbon pools. How do the accuracy and precision of current methods compare? A systematic review protocol. *Environ Evid*, 1–21.

Pflug, B.; Main-Knorn, M.; Bieniarz, J.; Debaecker, V. and Louis, J. **2015** *Early validation of Sentinel-2 L2A processor and products.* DLR.

Pierce, K.B.; Ohmann, J.L.; Wimberly, M.C.; Gregory, M.J. and Fried, J.S. **2009** Mapping wildland fuels and forest structure for land management: a comparison of nearest neighbor imputation and other methods. *Canadian Journal of Forest Research* 39, 1901–1916.

Piermattei, L.; Karel, W.; Di Wang; Wieser, M. and Mokroš, M. *et al.* **2019** Terrestrial Structure from Motion Photogrammetry for Deriving Forest Inventory Data. *Remote Sensing* 11.

Piermattei, L.; Marty, M.; Karel, W.; Ressl, C. and Hollaus, M. *et al.* **2018** Impact of the Acquisition Geometry of Very High-Resolution Pléiades Imagery on the Accuracy of Canopy Height Models over Forested Alpine Regions. *Remote Sensing* 10, 1–22.

Pocewicz, A.L.; Gessler, P. and Robinson, A.P. **2004** The relationship between effective plant area index and Landsat spectral response across elevation, solar insolation, and spatial scales in a northern Idaho forest. *Canadian Journal of Forest Research* 34, 465–480.

Poley, L.G. and McDermid, J.G. **2020** A systematic review of the factors influencing the estimation of vegetation aboveground biomass using Unmanned Aerial Systems. *Remote Sensing* 12, 1052.

Poli, D.; Anguili, E. and Remondino, F. **2010** *Radiometric and geometric analysis of WorldView-2 stereo scenes.* ISPRS Commission I, WG I/4, Hannover.

Pollet, J. and Omi, P.N. **2002** Effect of thinning and prescribed burning on crown fire severity in ponderosa pine forests. *International Journal of Wildland Fire* 11, 1–10.

Polychronaki, A. and Gitas, I.Z. **2010** The development of an operational procedure for burned-area mapping using object-based classification and ASTER imagery. *International Journal of Remote Sensing* 31, 1113–1120.

Pommerening, A. **2002** Approaches to quantifying forest structures. *Forestry* 75, 305–324.

Pope, G. and Treitz, P. **2013** Leaf Area Index (LAI) Estimation in Boreal Mixedwood Forest of Ontario, Canada Using Light Detection and Ranging (LiDAR) and WorldView-2 Imagery. *Remote Sensing* 5, 5040–5063.

Popescu, S.C. **2007** Estimating biomass of individual pine trees using airborne lidar. *Biomass and Bioenergy* 31, 646–655.

Popescu, S.C.; Wynne, R.H. and Nelson, R.F. **2002** Estimating plot-level tree heights with lidar: local filtering with a canopy-height based variable window size. *Computers and Electronics in Agriculture* 37, 71–95.

Popescu, S.C.; Wynne, R.H. and Nelson, R.F. **2003** Measuring individual tree crown diameter with lidar and assessing its influence on estimating forest volume and biomass. *Canadian Journal of Remote Sensing* 29, 564–577.

Popescu, S.C. and Zhao, K. **2008** A voxel-based lidar method for estimating crown base height for deciduous and pine trees. *Remote Sensing of Environment* 112, 767–781.

Pouliot, D. and King, D. **2005** Approaches for optimal automated individual tree crown detection in regenerating coniferous forests. *Canadian Journal of Remote Sensing* 31, 255–267.

Pouliot, D.; King, D.; Bell, F. and Pitt, D. **2002** Automated tree crown detection and delineation in high-resolution digital camera imagery of coniferous forest regeneration. *Remote Sensing of Environment* 82, 322–334.

Pouteau, R.; Collin, A. and Stoll, B. **2011** A comparison of machine learning algorithms for classification of tropical ecosystems observed by multiple sensors at multiple scales. International Geoscience and Remote Sensing Symposium: Vancouver, Canada. *International Geoscience and Remote Sensing Symposium*, 1–4.

Powell, S.L.; Cohen, W.B.; Healey, S.P.; Kennedy, R.E. and Moisen, G.G. *et al.* **2010** Quantification of live aboveground forest biomass dynamics with Landsat time-series and field inventory data: A comparison of empirical modeling approaches. *Remote Sensing of Environment* 114, 1053–1068.

Prasad, A.M.; Iverson, L.R. and Liaw, A. **2006** Newer Classification and Regression Tree Techniques: Bagging and Random Forests for Ecological Prediction. *Ecosystems* 9, 181–199.

Pretzsch, H. **2010** *Forest Dynamics, Growth and Yield: From measurement to model.* Springer Verlag.

Probst, A.; Gatziolis, D. and Strigul, N. **2018** Intercomparison of photogrammetry software for three-dimensional vegetation modelling. *Royal Society open science* 5, 1–18.

Prodan, M. **2014** *Forstliche Biometrie.* 1961st edn. Kessel.

Przybilla, H.-J.; Lindstaedt, M. and Kersten, T. **2019a** Investigations into the quality of image-based pointclouds from UAV imagery. *ISPRS - International Archives of the Photogrammetry, Remote Sensing and Spatial Information Sciences* XLII-2/W13, 539–545.

Przybilla, H.-J.; Lindstaedt, M. and Kersten, T. **2019b** Untersuchungen zur Qualität bildbasierter Punktwolken aus UAV Bildflügen. In *Photogrammetrie - Laserscanning - Optische 3D-Messtechnik*: *Beiträge der Oldenburger 3D-Tage 2019*. T. Luhmann and C. Schumacher (eds). Wichmann, pp. 236–248.

Puliti, S.; Ørka, H.O.; Gobakken, T. and Næsset, E. **2015** Inventory of small forest areas using an Unmanned Aerial System. *Remote Sensing* 7, 9632–9654.

Puttonen, E.; Suomalainen, J.; Hakala, T.; Räikkönen, E. and Kaartinen, H. *et al.* **2010** Tree species classification from fused active hyperspectral reflectance and LIDAR measurements. *Forest Ecology and Management* 260, 1843–1852.

Rahlf, J.; Breidenbach, J.; Solberg, S. and Astrup, R. **2015** Forest parameter prediction using an image-based point cloud: a comparison of semi-ITC with ABA. *Forests* 6, 4059–4071.

Ramalho de Oliveira, L.F.; Lassiter, H.A.; Wilkinson, B.; Whitley, T. and Ifju, P. *et al.* **2021** Moving to Automated Tree Inventory: Comparison of UAS-Derived Lidar and Photogrammetric Data with Manual Ground Estimates. *Remote Sensing* 13, 72.

Rango, A.; Laliberte, A.; Herrick, J.E. and Havstad, K.M. **2009** Unmanned aerial vehicle-based remote sensing for rangeland assessment, monitoring, and management. *Journal of Applied Remote Sensing* 3, 33542.

Räty, M. and Kangas, A. **2012** Comparison of k-MSN and kriging in local prediction. *Forest Ecology and Management* 263, 47–56.

Raudies, F. **2013** *Optical flow*. http://www.scholarpedia.org/article/Optic_flow (accessed on 06 June, 2020).

Rautiainen, M.; Stenberg, P. and Nilson, T. **2005** Estimating canopy cover in Scots pine stands. *Silva Fenn.* 39, 137–142. https://silvafennica.fi/pdf/article402.pdf.

Rehak, M.; Mabillard, R. and Skaloud, J. **2013** A mirco-UAV with the capability of direct georeferencing. *ISPRS - International Archives of the Photogrammetry, Remote Sensing and Spatial Information Sciences* XL-1/W2, 317–323.

Reich, P.B.; Bakken, P.; Carlson, D.; Frelich, L.E. and Friedman, S.K. *et al.* **2001** Influence of logging, fire, and forest type on biodiversity and productivity in Southern boreal forests. *Ecology* 82, 2731–2748.

Reitberger, J.; Schnörr, C.; Krzystek, P. and Stilla, U. **2009** 3D segmentation of single trees exploiting full waveform LIDAR data. *ISPRS Journal of Photogrammetry and Remote Sensing* 64, 561–574.

Remondino, F.; Spera, M.G.; Nocerino, E.; Menna, F. and Nex, F. **2014** State of the art in high density image matching. *Photogrammetric Record* 29, 144–166.

Rhody, B. **1983** Erfassung mitteleuropäischer Hauptbaumarten im Rahmen von Waldinventuren mit Hilfe kleinformatiger Luftaufnahmen. *Schweizerische Zeitschrift für Forstwesen*, 17–36.

Riemann, R.; Wilson, B.T.; Lister, A. and Parks, S. **2010** An effective assessment protocol for continuous geospatial datasets of forest characteristics using USFS Forest Inventory and Analysis (FIA) data. *Remote Sensing of Environment* 114, 2337–2352.

Roberts, S.D.; Dean, T.J.; Evans, D.L.; McCombs, J.W. and Harrington, R.L. *et al.* **2005** Estimating individual tree leaf area in loblolly pine plantations using LiDAR-derived measurements of height and crown dimensions. *Forest Ecology and Management* 213, 54–70.

Röder, M.; Latifi, H.; Hill, S.; Wild, J. and Svoboda, M. *et al.* **2018** Application of optical unmanned aerial vehicle-based imagery for the inventory of natural regeneration and standing deadwood in post-disturbed spruce forests. *International Journal of Remote Sensing* 39, 5288–5309.

Rogan, J.; Franklin, J. and Roberts, D.A. **2002** A comparison of methods for monitoring multitemporal vegetation change using Thematic Mapper imagery. *Remote Sensing of Environment* 80, 143–156.

Rogan, J.; Franklin, J.; Stow, D.; Miller, J. and Woodcock, C. *et al.* **2008** Mapping land-cover modifications over large areas: A comparison of machine learning algorithms. *Remote Sensing of Environment* 112, 2272–2283.

Roteta, E.; Bastarrika, A.; Padilla, M.; Storm, T. and Chuvieco, E. **2019** Development of a Sentinel-2 burned area algorithm: Generation of a small fire database for sub-Saharan Africa. *Remote Sensing of Environment* 222, 1–17.

Ryu, Y.; Nilson, T.; Kobayashi, H.; Sonnentag, O. and Law, B.E. *et al.* **2010** On the correct estimation of effective leaf area index: Does it reveal information on clumping effects? *Agricultural and Forest Meteorology* 150, 463–472.

Sá, N.C. de; Castro, P.; Carvalho, S.; Marchante, E. and López-Núñez, F.A. *et al.* **2018** Mapping the Flowering of an Invasive Plant Using Unmanned Aerial Vehicles: Is There Potential for Biocontrol Monitoring? *Frontiers in plant science* 9, 293.

Saarinen, N.; Vastaranta, M.; Näsi, R.; Rosnell, T. and Hakala, T. *et al.* **2018** Assessing Biodiversity in Boreal Forests with UAV-Based Photogrammetric Point Clouds and Hyperspectral Imaging. *Remote Sensing* 10, 1–22.

Sabins, F.F. **2020** *Remote Sensing: Principles, interpretation, and applications.* 4th edn. Waveland Press.

Sabloff, P.L. **2011** *Mapping Mongolia: Situating Mongolia in the World from Geologic Time to the Present.* University of Pennsylvania Press.

Said, Y.A.; Petropoulos, G.P. and Srivastava, P.K. **2015** Assessing the influence of atmospheric and topographic correction and inclusion of SWIR bands in burned scars detection from high-resolution EO imagery: a case study using ASTER. *Natural Hazards* 78, 1609–1628.

Salamí, E.; Barrado, C. and Pastor, E. **2014** UAV flight experiments applied to the remote sensing of vegetated areas. *Remote Sensing* 6, 11051–11081.

Sankey, T.; Donager, J.; McVay, J. and Sankey, J.B. **2017** UAV lidar and hyperspectral fusion for forest monitoring in the southwestern USA. *Remote Sensing of Environment* 195, 30–43.

Sanz-Ablanedo, E.; Chandler, J.; Rodríguez-Pérez, J. and Ordóñez, C. **2018** Accuracy of Unmanned Aerial Vehicle (UAV) and SfM Photogrammetry Survey as a Function of the Number and Location of Ground Control Points Used. *Remote Sensing* 10, 1–19.

Sayn-Wittgenstein, L. **1978** *Recognition of tree species on aerial photographs.* Forest Management Institute, Ottawa, Ontario, Ottawa.

Scher, C.L.; Griffoul, E. and Cannon, C.H. **2019** Drone-based photogrammetry for the construction of high-resolution models of individual trees. *Trees* 166, 869.

Scheuber, M. **2010** Potentials and limits of the k-nearest-neighbour method for regionalising sample-based data in forestry. *European Journal of Forest Research* 129, 825–832.

Schmidt-Corsitto, K. **2016** *Sustainable forest management in Mongolia: New development objectives after National Forest Inventory interpretation.* GIZ.

Schmidt-Corsitto, K. **2017** Forest inventory, forest policy, Ulaanbaatar. Personal communication.

Schneider, S. **1974** *Luftbild und Luftbildinterpretation.* De Gruyter.

Schöning, J. and Heidemann, G. **2015** Evaluation of Multi-view 3D Reconstruction Software. In *Computer analysis of images and patterns*: *16th international conference, CAIP 2015, Valletta, Malta, September 2 - 4, 2015; proceedings*. G. Azzopardi and N. Petkov (eds). Springer, pp. 450–461.

Schulze, E.-D.; Wirth, C.; Mollicone, D.; Lüpke, N. von and Ziegler, W. *et al.* **2012** Factors promoting larch dominance in central Siberia: fire versus growth performance and implications for carbon dynamics at the boundary of evergreen and deciduous conifers. *Biogeosciences* 9, 1405–1421.

Schulze, E.-D.; Wirth, C.; Mollicone, D. and Ziegler, W. **2005** Succession after stand replacing disturbances by fire, wind throw, and insects in the dark Taiga of Central Siberia. *Oecologia* 146, 77–88.

Schwanghart, W. **2008** Climate and Landscape Evolution of the Ugii Nuur basin, Mongolia. Dissertation. Geowissenschaften, Berlin.

Scott, C.T. and Gove, J.H. **2002** Forest Inventory. In *Encyclopedia of environmetrics*. A.H.e. Shaarawi (ed). Wiley, pp. 814–820.

Seidel, D. **2011** Terrestrial laser scanning. Applications in forest ecological research. Dissertation. Göttinger Zentrum für Biodiversitätsforschung und Ökologie, Göttingen.

Seidel, D. **2018** A holistic approach to determine tree structural complexity based on laser scanning data and fractal analysis. *Ecology and evolution* 8, 128–134.

Seidel, D.; Annighöfer, P.; Ehbrecht, M.; Magdon, P. and Wöllauer, S. *et al.* **2020** Deriving Stand Structural Complexity from Airborne Laser Scanning Data—What Does It Tell Us about a Forest? *Remote Sensing* 12, 1–15.

Seidel, D.; Annighöfer, P.; Stiers, M.; Zemp, C.D. and Burkardt, K. *et al.* **2019** How a measure of tree structural complexity relates to architectural benefit-to-cost ratio, light availability, and growth of trees. *Ecology and evolution* 9, 7134–7142.

Seidl, R.; Thom, D.; Kautz, M.; Martin-Benito, D. and Peltoniemi, M. *et al.* **2017** Forest disturbances under climate change. *Nature climate change* 7, 395–402.

Seifert, E.; Seifert, S.; Vogt, H.; Drew, D. and van Aardt, J. *et al.* **2019** Influence of drone altitude, image overlap, and optical sensor resolution on multi-view reconstruction of forest Images. *Remote Sensing* 11, 1–19.

Seifert, T. **2019** UAV flying mission and data analysis. Personal communication.

Semyonov, D. **2011** Agisoft Photoscan algorithms. Email.

Shakhatreh, H.; Sawalmeh, A.H.; Al-Fuqaha, A.; Dou, Z. and Almaita, E. *et al.* **2019** Unmanned Aerial Vehicles (UAVs): A Survey on Civil Applications and Key Research Challenges. *IEEE Access* 7, 48572–48634.

Shao, Z. and Zhang, L. **2016** Estimating Forest Aboveground Biomass by Combining Optical and SAR Data: A Case Study in Genhe, Inner Mongolia, China. *Sensors (Basel, Switzerland)* 16.

Sharkhuu, A.; Sharkhuu, N.; Etzelmüller, B.; Heggem, E.S.F. and Nelson, F.E. *et al.* **2007** Permafrost monitoring in the Hovsgol mountain region, Mongolia. *Journal of Geophysical Research: Biogeosciences* 112, 1–12.

Sharma, R.; Ghosh, A. and Joshi, P.K. **2013** Decision tree approach for classification of remotely sensed satellite data using open source support. *Journal of Earth System Science* 122, 1237–1247.

Sheykhmousa, M.; Mahdianpari, M.; Ghanbari, H.; Mohammadimanesh, F. and Ghamisi, P. *et al.* **2020** Support Vector Machine Versus Random Forest for Remote Sensing Image Classification: A Meta-Analysis and Systematic Review. *IEEE Journal of Selected Topics in Applied Earth Observations and Remote Sensing* 13, 6308–6325.

Shin, J.; Seo, W.; Kim, T.; Park, J. and Woo, C. **2019** Using UAV Multispectral Images for Classification of Forest Burn Severity—A Case Study of the 2019 Gangneung Forest Fire. *Forests* 10, 1025.

Shvidenko, A.Z. and Schepaschenko, D.G. **2013** Climate change and wildfires in Russia. *Contemporary Problems of Ecology* 6, 683–692.

Sibona, E.; Vitali, A.; Meloni, F.; Caffo, L. and Dotta, A. *et al.* **2017** Direct Measurement of Tree Height Provides Different Results on the Assessment of LiDAR Accuracy. *Forests* 8, 1–7.

Skowron, M.; Chmielowiec, W.; Glowacka, K.; Krupa, M. and Srebro, A. **2019** Sense and avoid for small unmanned aircraft systems: Research on methods and best practices. *Proceedings of the Institution of Mechanical Engineers, Part G: Journal of Aerospace Engineering* 233, 6044–6062.

Soja, A.J.; Tchebakova, N.M.; French, N.H.; Flannigan, M.D. and Shugart, H.H. *et al.* **2007** Climate-induced boreal forest change. Predictions versus current observations. *Global and Planetary Change* 56, 274–296.

Sokal, R.R. and Rohlf, F.J. **2012** *Biometry: The principles and practice of statistics in biological research.* 4th edn. W.H. Freeman.

Sona, G.; Pinto, L.; Pagliari, D.; Passoni, D. and Gini, R. **2014** Experimental analysis of different software packages for orientation and digital surface modelling from UAV images. *Earth Science Informatics* 7, 97–107.

Sothe, C.; Almeida, C.M. de; Schimalski, M.B.; La Rosa, L.E.C. and Castro, J.D.B. *et al.* **2020** Comparative performance of convolutional neural network, weighted and conventional support vector machine and random forest for classifying tree species using hyperspectral and photogrammetric data. *GIScience & Remote Sensing* 57, 369–394.

Sothe, C.; Dalponte, M.; Almeida, C.M.d.; Schimalski, M.B. and Lima, C.L. *et al.* **2019** Tree Species Classification in a Highly Diverse Subtropical Forest Integrating UAV-Based Photogrammetric Point Cloud and Hyperspectral Data. *Remote Sensing* 11.

Sousa da Silva, V. **2019** Lidar-derived methods for volume estimation and individual tree detection in Eucalyptus spp. plantations. Dissertation, Recife.

Soverel, N.O.; Coops, N.C.; Perrakis, D.D.B.; Daniels, L.D. and Gergel, S.E. **2011** The transferability of a dNBR-derived model to predict burn severity across 10 wildland fires in western Canada. *International Journal of Wildland Fire* 20, 1–14.

Spanner, M.A.; Pierce, L. and Peterson, D.L., Running, S.W. **1990** Remote sensing of temperate coniferous forest leaf area index The influence of canopy closure, understory vegetation and background reflectance. *International Journal of Remote Sensing* 11, 95–111.

Sperlich, M.; Kattenborn, T.; Koch, B. and Kattenborn, G. **2014** Potential of Unmanned Aerial Vehicle Based Photogrammetric Point Clouds for Automatic Single Tree Detection. In *Gemeinsame Tagung 2014 der DGfK, der DGPF, der GfGI und des GiN*. DGfK (ed), pp. 1–6.

Steinmann, K.; Mandallaz, D.; Ginzler, C. and Lanz, A. **2013** Small area estimations of proportion of forest and timber volume combining Lidar data and stereo aerial images with terrestrial data. *Scandinavian Journal of Forest Research* 28, 373–385.

Stephanowitz, J. **2020** *Höchsttemperatur in kältester Stadt der Erde - Sibirien*. https://www.zeit.de/wissen/umwelt/2020-07/sibirien-hitzewelle-temperaturrekord-klimawandel-wmo?utm_referrer=https%3A%2F%2Fwww.startpage.com%2F.

Stereńczak, K.; Mielcarek, M.; Wertz, B.; Bronisz, K. and Zajączkowski, G. *et al.* **2019** Factors influencing the accuracy of ground-based tree-height measurements for major European tree species. *Journal of environmental management* 231, 1284–1292.

Stocks, B.J. **2013** *Evaluating Past, Current and Future Forest Fire Load Trends in Canada.* B.J. Stocks Wildfire Investigations Ltd, Sault Ste. Marie, Ontario, Canada.

Stocks, B.J.; Wotton, B.M.; Flannigan, M.D.; Fosberg, M.A. and Cahoon, D.R. *et al.* **2001** Boreal Forest Fire Regimes And Climate Change. In *Remote Sensing and Climate Modeling: Synergies and Limitations*. M. Beniston and M.M. Verstraete (eds). Springer Netherlands, pp. 233–246.

Stone, H.; D'Ayala, D. and Wilkinson, S. **2017** *The use of emerging technology in post-disaster reconnaissance missions: An EEFIT Report.* Instituion of Structural Engineers, London.

St-Onge, B.; Audet, F.-A. and Bégin, J. **2015** Characterizing the height structure and composition of a boreal forest using an individual tree crown approach applied to photogrammetric point clouds. *Forests* 6, 3899–3922.

St-Onge, B.; Vega, C.; Fournier, R.A. and Hu, Y. **2008** Mapping canopy height using a combination of digital stereo-photogrammetry and lidar. *International Journal of Remote Sensing* 29, 3343–3364.

Strahler, A.H.; Jupp, D.L.; Woodcock, C.E.; Schaaf, C.B. and Yao, T. *et al.* **2008** Retrieval of forest structural parameters using a ground-based lidar instrument (Echidna ®). *Canadian Journal of Remote Sensing* 34, S426-S440.

Straub, C. and Koch, B. **2011** Estimating Single Tree Stem Volume of Pinus sylvestris Using Airborne Laser Scanner and Multispectral Line Scanner Data. *Remote Sensing* 3, 929–944.

Streck, C. and Scholz, S.M. **2006** The role of forests in global climate change: whence we come and where we go. *International Affairs*, 861–879.

Stümer, W. **2004** Combination of field data and remote sensing data with the knn-method (k-nearest neighbors method) for classification and mapping of forests. Dissertation. Environmental Sciences - Forestry, Tharandt.

Stych, P.; Jerabkova, B.; Lastovicka, J.; Riedl, M. and Paluba, D. **2019** A comparison of WorldView-2 and Landsat 8 images for the classification of forests affected by bark beetle outbreaks using a Support Vector Machine and a Neural Network: a case study in the Sumava mountains. *Geosciences* 9, 1–24.

Suárez, J.C.; Ontiveros, C.; Smith, S. and Snape, S. **2005** Use of airborne LiDAR and aerial photography in the estimation of individual tree heights in forestry. *Computers & Geosciences* 31, 253–262.

Sugimoto, A.; Yanagisawa, N.; Naito, D.; Fujita, N. and Maximov, T.C. **2002** Importance of permafrost as a source of water for plants in east Siberian taiga. *Ecological Research* 17, 493–503.

Sulla-Menashe, D.; Friedl, M.A. and Woodcock, C.E. **2016** Sources of bias and variability in long-term Landsat time series over Canadian boreal forests. *Remote Sensing of Environment* 177, 206–219.

Suomalainen, J.; Anders, N.; Iqbal, S.; Roerink, G. and Franke, J. *et al.* **2014** A Lightweight Hyperspectral Mapping System and Photogrammetric Processing Chain for Unmanned Aerial Vehicles. *Remote Sensing* 6, 11013–11030.

Surový, P.; Almeida Ribeiro, N. and Panagiotidis, D. **2018** Estimation of positions and heights from UAV-sensed imagery in tree plantations in agrosilvopastoral systems. *International Journal of Remote Sensing* 39, 4786–4800.

Surový, P. and Kuželka, K. **2019** Acquisition of forest attributes for decision support at the forest enterprise level using remote sensing techniques: a review. *Forests* 10, 273.

Sutherland, N.S. **1968** Outlines of a theory of visual pattern recognition in animals and man. *Proceedings of the Royal Society of London. Series B, Biological sciences* 171, 297–317.

Suzuki, T. **2012** Über die 6-Baum-Stichprobe von Prof. M. Prodan. In *Beiträge zur biometrischen Modellbildung in der Forstwirtschaft.* Verein Wissenschaft und Schrifttum e.V. (ed).

Tahir, A.; Böling, J.; Haghbayan, M.-H.; Toivonen, H.T. and Plosila, J. **2019** Swarms of Unmanned Aerial Vehicles — A Survey. *Journal of Industrial Information Integration* 16, 1–7.

Tang, L. and Shao, G. **2015** Drone remote sensing for forestry research and practices. *Journal of Forestry Research* 26, 791–797.

Tansey, K.; Selmes, N.; Anstee, A.; Tate, N.J. and Denniss, A. **2009** Estimating tree and stand variables in a Corsican pine woodland from terrestrial laser scanner data. *International Journal of Remote Sensing* 30, 5195–5209.

Tautenhahn, S.; Lichstein, J.W.; Jung, M.; Kattge, J. and Bohlman, S.A. *et al.* **2016** Dispersal limitation drives successional pathways in Central Siberian forests under current and intensified fire regimes. *Global change biology* 22, 2178–2197.

Tchebakova, N.M. and Parfenova, E.I. **2012** The 21st century climate change effects on the forests and primary conifers in central Siberia. *Bosque (Valdivia)* 33, 7–8.

Tchernykh, V.; Beck, M. and Janschek, K. **2006** Optical flow navigation for an outdoor UAV using wide angle mono camera and DEM matching. *IFAC Proceedings Volumes* 39, 590–595.

Terrier, A.; Girardin, M.P.; Périé, C.; Legendre, P. and Bergeron, Y. **2013** Potential changes in forest composition could reduce impacts of climate change on boreal wildfires. *Ecological Applications* 23, 21–35.

Tesfaye, A.A. and Awoke, B.G. **2020** Evaluation of the saturation property of vegetation indices derived from sentinel-2 in mixed crop-forest ecosystem. *Spatial Information Research*, 1–13.

Teusan, S. **2018** Analyse der Waldentwicklung in der nördlichen Mongolei seit dem politischen Umbruch im Jahre 1991 unter besonderer Berücksichtigung feuerökologischer Aspekte. Dargestellt am Beispiel der Provinz Selenge und in zwei ausgewählten Untersuchungsgebieten im Zeitraum 1990 - 2015. Dissertation. Geowissenschaften, Berlin.

Thales Alenia Space. **2017** *Sentinel-2 Products Specification Document.* ESA.

Thanh Noi, P. and Kappas, M. **2017** Comparison of Random Forest, k-Nearest Neighbor, and Support Vector Machine Classifiers for Land Cover Classification Using Sentinel-2 Imagery. *Sensors (Basel, Switzerland)* 18.

The Secretariat of the State Great Hural. **2016** *Mongolia Sustainable Development Vision 2030.* The Secretariat of the State Great Hural, Ulaanbaatar.

Theodoridis, S. and Koutroumbas, K. **2009** *Pattern recognition.* 4th edn. Elsevier/Acad. Press.

Thiel, C.; Drezet, P.; Weise, C.; Quegan, S. and Schmullius, C. **2006** Radar remote sensing for the delineation of forest cover maps and the detection of deforestation. *Forestry: An International Journal of Forest Research* 79, 589–597.

Thiel, C. and Schmullius, C. **2017** Comparison of UAV photograph-based and airborne lidar-based point clouds over forest from a forestry application perspective. *International Journal of Remote Sensing* 38, 2411–2426.

Thies, M.; Pfeifer, N.; Winterhalder, D. and Gorte, B.G.H. **2004** Three-dimensional reconstruction of stems for assessment of taper, sweep and lean based on laser scanning of standing trees. *Scandinavian Journal of Forest Research* 19, 571–581.

Thode, H.C. **2002** *Testing for normality.* Dekker.

Thurner, M.; Beer, C.; Santoro, M.; Carvalhais, N. and Wutzler, T. *et al.* **2014** Carbon stock and density of northern boreal and temperate forests. *Global Ecology and Biogeography* 23, 297–310.

Tian, J.; Dai, T.; Li, H.; Liao, C. and Teng, W. *et al.* **2019** A Novel Tree Height Extraction Approach for Individual Trees by Combining TLS and UAV Image-Based Point Cloud Integration. *Forests* 10, 537.

Tiede, D.; Hochleitner, G. and Blaschke, T. A full GIS-based workflow for tree identification and tree crown delineation using laser scanning. In *Proceedings of the ISPRS workshop CMRT 2005*.

Tillack, A.; Clasen, A.; Kleinschmit, B. and Förster, M. **2014** Estimation of the seasonal leaf area index in an alluvial forest using high-resolution satellite-based vegetation indices. *Remote Sensing of Environment* 141, 52–63.

Tmušić, G.; Manfreda, S.; Aasen, H.; James, M.R. and Gonçalves, G. *et al.* **2020** Current Practices in UAS-based Environmental Monitoring. *Remote Sensing* 12, 1–35.

Tompalski, P.; Coops, N.C.; White, J.C. and Wulder, M.A. **2014a** Simulating the impacts of error in species and height upon tree volume derived from airborne laser scanning data. *Forest Ecology and Management* 327, 167–177.

Tompalski, P.; Wężyk, P.; Weidenbach, M.; Kok, R. de and Hawryło, P. **2014b** A comparison of Lidar and image derived canopy height models for individual tree crown segmentation with object based image analysis. *South Eastern European Journal of Earth Observation and Geomtics* 3, 667–670.

Tomppo, E., Gschwantner, T., Lawrence, M. and McRoberts, R.E. (eds). **2010** *National Forest Inventories: Pathways for Common Reporting.* Springer.

Tomppo, E.; Katila, M.; Mäkisara, K. and Peräsaari, J. **2014** *The multi-source National Forest Inventory of Finland – methods and results 2011.* METLA.

Tomppo, E.; Olsson, H.; Ståhl, G.; Nilsson, M. and Hagner, O. *et al.* **2008** Combining national forest inventory field plots and remote sensing data for forest databases. *Remote Sensing of Environment* 112, 1982–1999.

Tomppo, E.O. **1991** Satellite-based National Forest Inventory of Finland. *International Archives of the Photogrammetry, Remote Sensing and Spatial Information Science* 28, 419–424.

Tomppo, E.O.; Gagliano, C.; Natale, F. de; Katila, M. and McRoberts, R.E. **2009** Predicting categorical forest variables using an improved k-Nearest Neighbour estimator and Landsat imagery. *Remote Sensing of Environment* 113, 500–517.

Tong, H.; Maxwell, T.; Zhang, Y. and Dey, V. **2012** A Supervised and Fuzzy-based Approach to Determine Optimal Multi-resolution Image Segmentation Parameters. *Photogrammetric Engineering & Remote Sensing* 78, 1029–1044.

Toro, F.G. and Tsourdos, A. **2018** *UAV or Drones for Remote Sensing Applications.* MDPI - Multidisciplinary Digital Publishing Institute.

Torres-Sánchez, J.; López-Granados, F.; Borra-Serrano, I. and Peña, J.M. **2018** Assessing UAV-collected image overlap influence on computation time and digital surface model accuracy in olive orchards. *Precision Agriculture* 19, 115–133.

Toth, C. and Jóźków, G. **2015** Remote sensing platforms and sensors: A survey. *ISPRS Journal of Photogrammetry and Remote Sensing* 115, 22–36.

Tran, B.; Tanase, M.; Bennett, L. and Aponte, C. **2018** Evaluation of Spectral Indices for Assessing Fire Severity in Australian Temperate Forests. *Remote Sensing* 10, 1–19.

Treter, U. **1996** Exposure as a factor in the mountain forest-steppe landscape of Mongolia. *Geographische Rundschau*, 655–661.

Troycke, A.; Habermann, R.; Wolff, B.; Gärtner, M. and Engels, F. *et al.* **2003** *Bestimmungsschlüssel für die Beschreibung von strukturreichen Waldbeständen im Color-Infrarot-Luftbild: Landesforstpräsidium Freistaat Sachsen.* LFP Sachsen.

Tso, B. and Mather, P.M. **2009** *Classification methods for remotely sensed data.* 2nd edn. CRC Press Taylor & Francis.

Tsogtbaatar, J. **2004a** Deforestation and reforestation needs in Mongolia. *Forest Ecology and Management* 201, 57–63.

Tsogtbaatar, J. **2004b** *Forest Policy Development in Mongolia.* Geoecology Institute, Mongolian Academy Sciences, Mongolia.

Tsogtbaatar, J. **2013** Deforestation and Reforestation of Degraded Forestland in Mongolia. In *The Mongolian ecosystem network*: *Environmental issues under climate and social changes*. N. Yamamura (ed). Springer, pp. 83–98.

Tu, Y.-H.; Phinn, S.; Johansen, K. and Robson, A. **2018** Assessing radiometric correction approaches for multi-spectral UAS imagery for horticultural applications. *Remote Sensing* 10, 1–22.

Tuominen, S.; Balazs, A.; Honkavaara, E.; Pölönen, I. and Saari, H. *et al.* **2017a** Hyperspectral UAV-imagery and photogrammetric canopy height model in estimating forest stand variables. *Silva Fennica* 51, 1–22.

Tuominen, S.; Balazs, A.; Saari, H.; Pölönen, I. and Sarkeala, J. *et al.* **2015** Unmanned aerial system imagery and photogrammetric canopy height data in area-based estimation of forest variables. *Silva Fennica* 49, 1–19.

Tuominen, S.; Näsi, R.; Honkavaara, E.; Balazs, A. and Hakala, T. *et al.* **2018** Assessment of classifiers and remote sensing features of hyperspectral imagery and stereo-photogrammetric point clouds for recognition of tree species in a forest area of high species diversity. *Remote Sensing* 10, 1–28.

Tuominen, S. and Pekkarinen, A. **2005** Performance of different spectral and textural aerial photograph features in multi-source forest inventory. *Remote Sensing of Environment* 94, 256–268.

Tuominen, S.; Pitkänen, T.; Balazs, A. and Kangas, A. **2017b** Improving Finnish Multi-Source National Forest Inventory by 3D aerial imaging. *Silva Fennica* 51, 1–22.

Tymstra, C.; Stocks, B.J.; Cai, X. and Flannigan, M.D. **2020** Wildfire management in Canada: Review, challenges and opportunities. *Progress in Disaster Science* 5, 1–9.

UAV Campus Group. **2018** *UAV Campus Group. Universität Göttingen*. https://uavcampus.wordpress.com/ (accessed on 04 April, 2020).

UAV Campus Group. **2020** UAV Campus Group. Universität Göttingen. https://uavcampus.wordpress.com/. Personal communication.

Undraa, M.; Kawada, K.; Dorjsuren, C. and Kamijo, T. **2015** After Fire Regenerative Successions in Larch (Larix sibirica Ledeb.) Forests of the Central Khangai in Mongolia. *SJFS*.

Unger, J. **2018** SFM; Agisoft, IPI, Hannover. Personal communication.

University of Greifswald. **2010** *FloraGREIF - Virtual Flora of Mongolia*. https://floragreif.uni-greifswald.de/ (accessed on 21 April, 2020).

UN-REDD. **2018** *Mongolia's Forest Reference Level submission to the UNFCCC: UN-REDD Mongolia National Programme,* Ulaanbaatar.

Urbahs, A. and Jonaite, I. **2013** Features of the use of unmanned aerial vehicles for agriculture applications. *Aviation* 17, 170–175.

Ustin, S.L. and Gamon, J.A. **2010** Remote sensing of plant functional types. *The New phytologist* 186, 795–816.

Valérie, T. and Marie-Pierre, J. **2006** Tree species identification on large-scale aerial photographs in a tropical rain forest, French Guiana—application for management and conservation. *Forest Ecology and Management* 225, 51–61.

van Aardt, J.A. **2019** UAV missions and data analysis; UAV sensors, Rochester. https://www.rit.edu/directory/jvacis-jan-van-aardt. Personal communication.

van Aardt, J.A.N. and Wynne, R.H. **2007** Examining pine spectral separability using hyperspectral data from an airborne sensor. An extension of field-based results. *International Journal of Remote Sensing* 28, 431–436.

van Cleve, K. and Yarie, J. **1986** Interaction of Temperature, Moisture, and Soil Chemistry in Controlling Nutrient Cycling and Ecosystem Development in the Taiga of Alaska. In *Forest Ecosystems in the Alaskan Taiga*: *A Synthesis of Structure and Function*. W.D. Billings, F. Golley, O.L. Lange, M.M. Billington, J.P. Byrant, L.A. Viereck and C.T. Dyrness (eds). Springer New York, pp. 160–189.

van Deusen, P.C. **1987** 3-p sampling and design versus model-based estimates. *Canadian Journal of Forest Research* 17, 115–117.

van Herk, M. **1992** A fast algorithm for local minimum and maximum filters on rectangular and octagonal kernels. *Pattern Recognition Letters* 13, 517–521.

van Laar, A. **1991** *Forest biometry.* Univ. of Stellenbosch.

van Laar, A. and Akça, A. **2007** *Forest mensuration.* 2nd edn. Springer.

Vanonckelen, S.; Lhermitte, S. and van Rompaey, A. **2013** The effect of atmospheric and topographic correction methods on land cover classification accuracy. *International Journal of Applied Earth Observation and Geoinformation* 24, 9–21.

Vanonckelen, S.; Lhermitte, S. and van Rompaey, A. **2015** The effect of atmospheric and topographic correction on pixel-based image composites: Improved forest cover detection in mountain environments. *International Journal of Applied Earth Observation and Geoinformation* 35, 320–328.

Vastaranta, M.; Wulder, M.A.; White, J.C.; Pekkarinen, A. and Tuominen, S. *et al.* **2013** Airborne laser scanning and digital stereo imagery measures of forest structure: comparative results and implications to forest mapping and inventory update. *Canadian Journal of Remote Sensing* 39, 382–395.

Vatsavai, R.R. **2013** Object based image classifiaction: state of the art and computational challenges. In *the 2nd ACM SIGSPATIAL International Workshop*. V. Chandola and R.R. Vatsavai (eds), pp. 73–80.

Vauhkonen, J. **2010** Estimating crown base height for Scots pine by means of the 3D geometry of airborne laser scanning data. *International Journal of Remote Sensing* 31, 1213–1226.

Vauhkonen, J.; Ene, L.; Gupta, S.; Heinzel, J. and Holmgren, J. *et al.* **2012** Comparative testing of single-tree detection algorithms under different types of forest. *Forestry: An International Journal of Forest Research* 85, 27–40.

Vauhkonen, J.; Hakala, T.; Suomalainen, J.; Kaasalainen, S. and Nevalainen, O. *et al.* **2013** Classification of spruce and pine trees using active hyperspectral LiDAR. *IEEE Geoscience and Remote Sensing Letters* 10, 1138–1141.

Vega, C. and St-Onge, B. **2008** Height growth reconstruction of a boreal forest canopy over a period of 58 years using a combination of photogrammetric and lidar models. *Remote Sensing of Environment* 112, 1784–1794.

Venzke, J.-F. **2008** *Die Borealis: Die Zukunft der nördlichen Wälder.* WGB (Wiss. Buchges.).

Veraverbeke, S.; Lhermitte, S.; Verstraeten, W.W. and Goossens, R. **2011** Evaluation of pre/post-fire differenced spectral indices for assessing burn severity in a Mediterranean environment with Landsat Thematic Mapper. *International Journal of Remote Sensing* 32, 3521–3537.

Vesper, M. **2005** *Bäume und Sträucher der Mongolei*. http://www.manfred-vesper.de/?show=498&pshow=15 (accessed on 23 February, 2021).

Vogt, H. **2000** An investigation into the feasibility of forest inventory by means of stereo satellite imagery employing digital photogrammetry technology. Master thesis. Forest Science, Stellenbosch.

Vogt, H. **2017** *Aerial and terrestrial photographs of the Thunkel forest compartment 435; own observations*.

Vogt, H. **2020** UAV technology, flying mission, data processing,

Vries, P.G. de. **1986** *Sampling theory for forest inventory: A teach-yourself course.* Springer.

Wackrow, R. and Chandler, J.H. **2008** A convergent image configuration for DEM extraction that minimises the systematic effects caused by an inaccurate lens model. *The Photogrammetric Record* 23, 6–18.

Wallace, L.; Lucieer, A.; Malenovský, Z.; Turner, D. and Vopěnka, P. **2016** Assessment of Forest Structure Using Two UAV Techniques. A Comparison of Airborne Laser Scanning and Structure from Motion (SfM) Point Clouds. *Forests* 7, 62.

Wallace, L.; Lucieer, A.; Watson, C. and Turner, D. **2012** Development of a UAV-LiDAR System with Application to Forest Inventory. *Remote Sensing* 4, 1519–1543.

Wallace, L.; Watson, C. and Lucieer, A. **2014** Detecting pruning of individual stems using Airborne Laser Scanning data captured from an Unmanned Aerial Vehicle. *International Journal of Applied Earth Observation and Geoinformation* 30, 76–85.

Wang, B.; Jia, K.; Liang, S.; Xie, X. and Wei, X. *et al.* **2018** Assessment of Sentinel-2 MSI Spectral Band Reflectances for Estimating Fractional Vegetation Cover. *Remote Sensing* 10, 1–20.

Wang, S.; Ren, W.; Zhang, Y. and Liang, F. **2019a** Random Forest Classifier for Distributed Multi-plant Order Allocation. In *Proceeding of the 24th International Conference on Industrial Engineering and Engineering Management 2018*. G.Q. Huang, C.-F. Chien and R. Dou (eds). Springer, pp. 123–132.

Wang, Y.; Lehtomäki, M.; Liang, X.; Pyörälä, J. and Kukko, A. *et al.* **2019b** Is field-measured tree height as reliable as believed – A comparison study of tree height estimates from field measurement, airborne laser scanning and terrestrial laser scanning in a boreal forest. *ISPRS Journal of Photogrammetry and Remote Sensing* 147, 132–145.

Waser, L.T.; Ginzler, C.; Kuechle, M.; Thee, P. and Baltsavias, E. *et al.* **2007** Extraction of forest parameters in a mire biotope using high-resolution digital surface models and airborne imagery. In *IEEE International Geoscience and Remote Sensing Symposium, 2007*: *IGARSS*

2007 ; 23 - 27 July 2007, Centre de Convencions Internacional de Barcelona. IEEE (ed). IEEE Service Center, pp. 1265–1270.

Watson, C. **2009** *Forest carbon accounting: overview & principles.* London School of Economics and Political Science.

Watts, A.C.; Ambrosia, V.G. and Hinkley, E.A. **2012** Unmanned Aircraft Systems in Remote Sensing and Scientific Research. Classification and Considerations of Use. *Remote Sensing* 4, 1671–1692.

Wecking, A. **2017** Managing forest ecosystems in Mongolia - the crucial role of soil. Master Thesis. Institute of Physical Geography and Landscape Ecology, Hannover.

Wei, G.; Shalei, S.; Bo, Z.; Shuo, S. and Faquan, L. *et al.* **2012** Multi-wavelength canopy LiDAR for remote sensing of vegetation: Design and system performance. *ISPRS Journal of Photogrammetry and Remote Sensing* 69, 1–9.

Weirather, M.; Zeug, G. and Schneider, T. **2018** Automated Delineation Of Wildfire Areas Using Sentinel-2 Satellite Imagery. *giforum* 1, 251–262.

Weiss, M. and Baret, F. **2016** *S2 ToolBox Level 2 products: LAI, FAPAR, FCOVER: Version 1.1.* European Space Agency.

Wessel, M.; Brandmeier, M. and Tiede, D. **2018** Evaluation of Different Machine Learning Algorithms for Scalable Classification of Tree Types and Tree Species Based on Sentinel-2 Data. *Remote Sensing* 10, 1–21.

West, P.W. **2009** *Tree and Forest Measurement.* Springer Berlin Heidelberg.

Westoby, M.J.; Brasington, J.; Glasser, N.F.; Hambrey, M.J. and Reynolds, J.M. **2012** 'Structure-from-Motion' photogrammetry: A low-cost, effective tool for geoscience applications. *Geomorphology* 179, 300–314.

White, J.; Wulder, M.; Vastaranta, M.; Coops, N. and Pitt, D. *et al.* **2013a** The utility of image-based point clouds for forest inventory: a comparison with Airborne Laser Scanning. *Forests* 4, 518–536.

White, J.C.; Coops, N.C.; Wulder, M.A.; Vastaranta, M. and Hilker, T. *et al.* **2016** Remote sensing technologies for enhancing forest inventories: a review. *Canadian Journal of Remote Sensing* 42, 619–641.

White, J.C.; Wulder, M.A.; Varhola, A.; Vastaranta, M. and Coops, N.C. *et al.* **2013b** A best practices guide for generating forest inventory attributes from airborne laser scanning data using an area-based approach. *The Forestry Chronicle* 89, 722–723.

Whitehead, D.; Grace, J.C. and Godfrey, M.J.S. **1990** Architectural distribution of foliage in individual Pinus radiata D. Don crowns and the effects of clumping on radiation interception. *Tree physiology* 7, 135–155.

Whitehead, K. and Hugenholtz, C.H. **2014** Remote sensing of the environment with small unmanned aircraft systems (UASs), part 1: a review of progress and challenges. *Journal of Unmanned Vehicle Systems* 02, 69–85.

Whiteside, T.G.; Boggs, G.S. and Maier, S.W. **2011** Comparing object-based and pixel-based classifications for mapping savannas. *International Journal of Applied Earth Observation and Geoinformation* 13, 884–893.

Wich, S.A. and Koh, L.P. **2018** *Conservation drones: Mapping and monitoring biodiversity.* Oxford University Press.

Wierzbicki, D. **2018** Multi-camera imaging system for UAV photogrammetry. *Sensors (Basel, Switzerland)* 18.

Wilhelm, S.; Hüttich, C.; Korets, M. and Schmullius, C. **2014** Large Area Mapping of Boreal Growing Stock Volume on an Annual and Multi-Temporal Level Using PALSAR L-Band Backscatter Mosaics. *Forests* 5, 1999–2015.

Wilk, M.B. and Gnanadesikan, R. **1968** Probability plotting methods for the analysis for the analysis of data. *Biometrika* 55, 1–17.

Wilson, B.T.; Lister, A.J. and Riemann, R.I. **2012** A nearest-neighbor imputation approach to mapping tree species over large areas using forest inventory plots and moderate resolution raster data. *Forest Ecology and Management* 271, 182–198.

Wittke, S.; Yu, X.; Karjalainen, M.; Hyyppä, J. and Puttonen, E. **2019** Comparison of two-dimensional multitemporal Sentinel-2 data with three-dimensional remote sensing data sources for forest inventory parameter estimation over a boreal forest. *International Journal of Applied Earth Observation and Geoinformation* 76, 167–178.

Wolter, P.T.; Townsend, P.A. and Sturtevant, B.R. **2009** Estimation of forest structural parameters using 5 and 10 meter SPOT-5 satellite data. *Remote Sensing of Environment* 113, 2019–2036.

World Bank. **2021** *Mongolia*. https://www.worldbank.org/en/country/mongolia/overview#1 (accessed on 23 February, 2021).

Wulder, M.A.; Bater, C.W.; Coops, N.C.; Hilker, T. and White, J.C. **2008** The role of LiDAR in sustainable forest management. *The Forestry Chronicle* 84, 807–826.

Wulder, M.A.; LeDrew, E.F.; Franklin, S.E. and Lavigne, M.B. **1998** Aerial Image Texture Information in the Estimation of Northern Deciduous and Mixed Wood Forest Leaf Area Index (LAI). *Remote Sensing of Environment* 64, 64–76.

Wulder, M.A.; Niemann, K.O. and Goodenough, D.G. **2000** Local maximum filtering for the extraction of tree locations and basal area from high spatial resolution imagery. *Remote Sensing of Environment* 73, 103–114.

Wyss, D. **2007** Waldmanagement in der Mongolei - Anwendung von GIS- und Fernerkundungsmethoden im Rahmen der Entwicklungszusammenarbeit. Dissertation. Geowissenschaften, Berlin.

Xie, Y.; Sha, Z. and Yu, M. **2008** Remote sensing imagery in vegetation mapping: a review. *Journal of Plant Ecology* 1, 9–23.

Xie, Y.; Zhao, X.; Li, L. and Wang, H. **2010** Calculating NDVI for Landsat7-ETM data after atmospheric correction using 6S model: A case study in Zhangye city, China. In *Geoinformatics, 2010 18th International Conference on*. IEEE, pp. 1–4.

Xu, Z.; Li, W.; Li, Y.; Shen, X. and Ruan, H. **2020** Estimation of secondary forest parameters by integrating image and point cloud-based metrics acquired from unmanned aerial vehicle. *Journal of Applied Remote Sensing* 14, 1–19.

Xue, J. and Su, B. **2017** Significant Remote Sensing Vegetation Indices: A Review of Developments and Applications. *Journal of Sensors*, 1–17.

Xulu, S.; Gebreslasie, M.T. and Peerbhay, K.Y. **2019** Remote sensing of forest health and vitality: a South African perspective. *Southern Forests: a Journal of Forest Science* 81, 91–102.

Yamamura, N. **2013** *The Mongolian ecosystem network: Environmental issues under climate and social changes.* Springer.

Yan, G.; Hu, R.; Luo, J.; Weiss, M. and Jiang, H. *et al.* **2019** Review of indirect optical measurements of leaf area index: Recent advances, challenges, and perspectives. *Agricultural and Forest Meteorology* 265, 390–411.

Yan, G.; Mas, J.-F.; Maathuis, B.H.P.; Xiangmin, Z. and van Dijk, P.M. **2006** Comparison of pixel-based and object-oriented image classification approaches—a case study in a coal fire area, Wuda, Inner Mongolia, China. *International Journal of Remote Sensing* 27, 4039–4055.

Yang, L.; Mansaray, L.; Huang, J. and Wang, L. **2019** Optimal Segmentation Scale Parameter, Feature Subset and Classification Algorithm for Geographic Object-Based Crop Recognition Using Multisource Satellite Imagery. *Remote Sensing* 11, 1–23.

Yilmaz, V.; Yilmaz, C.S.; Gungor, O. and Taşçi, L. **2017** Determination of Tree Crown Diameters with Segmentation of a UAS-Based Canopy Height Model. *Ipsi bgd transactions on internet research*, 63–67.

Yin, D. and Le Wang. **2019** Individual mangrove tree measurement using UAV-based LiDAR data: Possibilities and challenges. *Remote Sensing of Environment* 223, 34–49.

Ykhanbai, H. **2010** *Mongolia Forestry Outlook Study.* FAO, Bangkok.

Yu, X.; Hyyppä, J.; Holopainen, M. and Vastaranta, M. **2010** Comparison of area-based and individual tree-based methods for predicting plot-level forest attributes. *Remote Sensing* 2, 1481–1495.

Yu, X.; Liang, X.; Hyyppä, J.; Kankare, V. and Vastaranta, M. *et al.* **2013** Stem biomass estimation based on stem reconstruction from terrestrial laser scanning point clouds. *Remote Sensing Letters* 4, 344–353.

Yu, X.; Litkey, P.; Hyyppä, J.; Holopainen, M. and Vastaranta, M. **2014** Assessment of low density full-waveform Airborne Laser Scanning for Individual Tree Detection and tree species classification. *Forests* 5, 1011–1031.

Yu, X. and Zhang, Y. **2015** Sense and avoid technologies with applications to unmanned aircraft systems: Review and prospects. *Progress in Aerospace Sciences* 74, 152–166.

Zainuddin, K.; Jaffri, M.H.; Zainal, M.Z.; Ghazali, N. and Samad, A.M. **2016** Verification test on ability to use low-cost UAV for quantifying tree height. In *2016 IEEE 12th International Colloquium on Signal Processing & Its Applications (CSPA)*. IEEE (ed). IEEE, pp. 317–321.

Zar, J.H. **2010** *Biostatistical analysis.* 5th edn. Prentice Hall.

Zarco-Tejada, P.J.; Diaz-Varela, R.; Angileri, V. and Loudjani, P. **2014** Tree height quantification using very high resolution imagery acquired from an unmanned aerial vehicle (UAV) and automatic 3D photo-reconstruction methods. *European Journal of Agronomy* 55, 89–99.

Zarco-Tejada, P.J.; González-Dugo, V. and Berni, J. **2012** Fluorescence, temperature and narrow-band indices acquired from a UAV platform for water stress detection using a micro-hyperspectral imager and a thermal camera. *Remote Sensing of Environment* 117, 322–337.

Zarco-Tejada, P.J.; Hornero, A.; Hernández-Clemente, R. and Beck, P.S.A. **2018** Understanding the temporal dimension of the red-edge spectral region for forest decline detection using high-resolution hyperspectral and Sentinel-2a imagery. *ISPRS Journal of Photogrammetry and Remote Sensing* 137, 134–148.

Zhang, D.; Liu, J.; Ni, W.; Sun, G. and Zhang, Z. *et al.* **2019** Estimation of Forest Leaf Area Index Using Height and Canopy Cover Information Extracted From Unmanned Aerial Vehicle Stereo Imagery. *IEEE J. Sel. Top. Appl. Earth Observations Remote Sensing* 12, 471–481.

Zhang, Y. **2008** Pan-sharpening for improved information extraction. In *Advances in Photogrammetry, Remote Sensing and Spatial Information Sciences*. E. Baltsavias, Z. Li and J. Chen (eds). CRC Press.

Zhao, F.; Strahler, A.H.; Schaaf, C.L.; Yao, T. and Yang, X. *et al.* **2012** Measuring gap fraction, element clumping index and LAI in Sierra Forest stands using a full-waveform ground-based lidar. *Remote Sensing of Environment* 125, 73–79.

Zhen, Z.; Quackenbush, L. and Zhang, L. **2016** Trends in Automatic Individual Tree Crown Detection and Delineation—Evolution of LiDAR Data. *Remote Sensing* 8, 333.

Zheng, G. and Moskal, L.M. **2009** Retrieving Leaf Area Index (LAI) Using Remote Sensing: Theories, Methods and Sensors. *Sensors (Basel, Switzerland)* 9, 2719–2745.

Zimmerman, T.; Jansen, K. and Miller, J. **2020** Analysis of UAS Flight Altitude and Ground Control Point Parameters on DEM Accuracy along a Complex, Developed Coastline. *Remote Sensing* 12, 1–16.

Zöhrer, F. **1980** *Forstinventur: Ein Leitfaden für Studium und Praxis.* Parey.

Zueghart, G. **2017** A GIS-based Analysis of Spatial Distribution Patterns of Light and Dark Taiga in the Tunkhel Region, Northern Mongolia. Master thesis. Geography; Cartography, GIS and Remote Sensing, Goettingen.

11. Glossary of technical terms and acronyms

Glossary

Above-ground biomass	The entirety of living vegetation above the soil, including stems, stumps, foliage, bark and seeds
Below-ground biomass	Biomass contained within live roots
Biomass	Biological material derived from living, or recently living organisms
Canopy cover	The percentage of the ground covered by a vertical projection of the outermost perimeter of the natural spread of the foliage of plants
Carbon pool	Carbon pools are major components of an ecosystem that can either accumulate or release carbon
Carbon sink	A carbon sink is a carbon pool from which more carbon flows in than out: forests can act as sink through the process of tree growth and resultant biological carbon sequestration
Dead organic matter	The DOM carbon pool contains all non-living woody biomass and can be divided into wood (fallen trees, roots and stumps with diameter over 10cm) and litter (greater than 2mm and less than 10cm diameter) components
Emissions accounting	Emissions accounting assesses the net greenhouse gas emissions to the atmosphere
Forest	There is no universally valid definition per se. The most popular has been coined by the FAO: 'Land spanning more than 0.5 hectares with trees higher than 5 meters and a canopy cover of more than 10 percent, or trees able to reach these thresholds *in situ*. It does not include land that is predominantly under agricultural or urban land use.' (FAO, 2012)
Forest inventory	'Techniques of collecting reliable and satisfactory information on forests[…]'. (Tomppo et al., 2010:1 and Loetsch and Haller, 1964:1)
Greenhouse Gases (GHG)	There are six recognised major greenhouse gases; CO2 (carbon dioxide), CH4 (methane), HFCs (hydrofluorocarbons), PFCs (perfluorocarbons), N20 (nitrous oxide) and SF6 (sulphur hexafluoride). Carbon accounting often refers to the accounting of all major GHGs using a carbon dioxide equivalent (CO2e) that standardises these gases based on their global warming potential
Global Warming Potential (GWP)	Used to enable the comparison of the six common GHG, it is the cumulative radiative forcing effects of a unit mass of gas over a specified time horizon relative to CO2. It is expressed in terms of carbon dioxide equivalents (CO2e). Of relevance to forest carbon accounting: GWPCO2 = 1, GWPCH4 = 21, GWPN2O = 310
Inertial Measurement Unit (IMU)	The IMU is an electronic device that measures and reports a body's specific force, angular rate, and sometimes the orientation of the body, using a combination of accelerometers, gyroscopes, and sometimes magnetometers. (Ahmad, 2013)
Inertial Navigation System (INS)	An INS is navigation device that uses a computer, motion sensors (accelerometers) and rotation sensors (gyroscopes) to continuously calculate by dead reckoning the position, the orientation, and the velocity (direction and speed of movement) of a moving object without the need for external references. (Cook, 2020: 114,255)
Kyoto Protocol	In 1992, the Convention on Climate Change was agreed at the United Nations Conference on Environment and Development and, in 1997, the Kyoto Protocol made this convention operational. Under the Convention Annex I (developed) countries committed to reduce GHG emissions to, on average, 5.2% of 1990 levels before 2012
Remote sensing	'Remote sensing is the science and art of obtaining information about an object, area, or phenomenon through the analysis of data acquired by a device that is not in contact with the object, area, or phenomenon under investigation'. (Lillesand et al., 2015:1)
Soil organic matter	The SOM carbon pool is divided into mineral and organic soil carbon and contains biomass less than 2mm diameter
Unmanned Aerial System (UAS)	An UAS consists of an Unmanned Aircraft (UA), a Control System (CS) -usually a Ground Control System (GCS) - and a communications data link between the UA and the CS. (Eisenbeiß, 2009)

Glossary according to: IPPC and UNEP (see also: Watson, 2009)

Acronyms

2D	2 Dimensional
3D	3 Dimensional
μ	Population mean
ABA	Area Based Approach
AC	Atmospheric Correction
AGB	Above-Ground Biomass
ACRS	Asian Conference on Remote Sensing
ADB	Asian Development Bank
AGL	Above Ground Level
ALOS	Advanced Land Observing Satellite
ALS	Airborne Laser Scanning
ANOVA	Analysis of Variance
Art.	Article
AR	Afforestation/Reforestation
ASCII	American Standard Code for Information Interchange
a.s.l.	Above sea level
ASTER	Advanced Spaceborne Thermal Emission and Reflection Radiometer
AT	Aerial Triangulation
AVHRR	Advanced Very High Resolution Radiometer
BATP	Best Available Terrain Pixel
BGB	Below-Ground Biomass
BIRD	Bispectral Infra-Red Detection
BMZ	Bundesministerium für wirtschaftliche Zusammenarbeit (German Federal Ministry for Economic Cooperation and Development)
BOA	Bottom of the atmosphere
BRDF	Bidirectional Reflectance Distribution Function (MODIS)
CAA	Civil Aviation Authority
CART	Classification And Regression Tree
CASA	Civil Aviation Safety Authority
CBFM	Community Based Forest Management
CBI	Composite Burn Index
CC	Canopy Cover
CCD	Charge-Coupled Device (Sensor)
CD	Cumulative Defoliation
CH_4	Methane
CHM	Canopy Height Model
Cm	Centimeter
CMOS	Complementary Metal-Oxide-Semiconductor
CO_2	carbon dioxide
COP	Conference Of the Parties
CP	Check Points
DAI	Digital Aerial Imagery

DAP	Digital Aerial Photogrammetry
DBH	Diameter Breast Height (1,3m above ground)
DEM	Digital Elevation Model
DGPF	Deutsche Gesellschaft für Photogrammetrie, Fernerkundung und Geoinformation
DHM	Digital Height Model
DI	Disturbance Index
DLR	Deutsches Zentrum für Luft- und Raumfahrt
DN	Digital number
dNBR	differenced Normalized Burn Ratio
DOM	Dead Organic Matter
DSLR	Digital Single-Lens Reflex
DSM	Digital Surface Model
DTM	Digital Terrain Model
EOS	Earth Observation System
EOSDIS	NASA's Earth Observing System Data and Information System
ESA	European Space Agency
ESRI	Environmental Systems Research Institute
ETM	Enhanced Thematic Mapper
ETM+	Enhanced Thematic Mapper Plus
EU	European Union
EVI	Enhanced Vegetation Index
EZ	Entwicklungszusammenarbeit
FAA	Federal Aviation Administration
FAO	Food and Agricultural Organisation
F(A)PAR	Fraction of Absorbed Photosynthetic Active Radiation
FCOVER	Fraction of green vegetation cover
FIR	Far Infra-Red
FIRMS	Fire Information for Resource Management System
FRA	Forest Resource Assessment
FSC	Forest Stewardship Council®
FWRI	Forestry and Wildlife Research Institute
FWS	Fixed tree Window Size
GCP	Ground Control Point
GCS	Ground Control Station
GDOP	Geometric Dilution of Precision
GFMC	Global Fire Monitoring Center
GHGs	GreenHouse Gases
GHz	Gigahertz
GIS	Geographic Information System
GIZ	Gesellschaft für internationale Zusammenarbeit (German Society for International Cooperation)
GLAS	Geoscience Laser Altimeter System
GLCF	Global Land Cover Facility of the University of Maryland, USA
GLCM	Gray Level Co-occurrence Matrix

GLIx	Green Leaf Indices
GNSS	Global Navigation Satellite Systems
GOM	Government of Mongolia
GPS	Global Positioning System
GSD	Ground Sampling Distance
GSM	Global System for Mobile communications; originally from Groupe Spécial Mobile
GTZ	Gesellschaft für technische Zusammenarbeit (now: GIZ)
GUI	Graphical User Interchange
IFMP	Integrated Fire Management
IGBP	International Geosphere Biosphere Program
ICC	Information and Computer Center, National Remote sensing Center of Mongolia
IFOV	Instantaneous Field of View
ICAO	International Civil Aviation Organization
IMU	Inertial Measurement Unit
INS	Inertial Navigation System includes error compensation and a navigation computer
IPCC	Intergovernmental Panel on Climate Change
ISODATA	Iterative Self-Organizing Data Analysis Techniques
ISPRS	International Society for Photogrammetry and Remote Sensing
ITD	Individual Tree Detection
JICA	Japan International Cooperation Agency
KKSPA	Khan Khentii Special Protected Area
L8	Landsat 8
LAI	Leaf Area Index
Laser	Light Amplification by Stimulated Emission of Radiation
Laser-DSM	Digital Surface Model generated out of Laser data
LiDAR	Light Detection And Ranging
LST	Land Surface Temperature
LTS	Landsat Time Series
LULC	Land Use and Land Cover
LULCC	Land Use and Land Cover Change
LVIS	Laser Vegetation Imaging Sensor
m	Meter
mm	Millimeter
MAP21	Mongolian Action Programme for the 21st Century
MAS	Mongolian Academy of Sciences
MAV	Micro Aerial Vehicle
M-class	Micro & Mini UAV systems
MDG	Millenium Development Goals
MEMS	MicroElectroMechanical Systems
MFR	Mongolian Federal Republic
MHz	Megahertz
MicMac	Multi-Images Correspondances, Méthodes Automatiques de Corrélation
MIFA	Mongolian Forest Industries Association

MIT	Ministry of Industry and Trade
MLC	Maximum Likelihood Classification
MMS	Mobile Mapping Systems
MODIS	Moderate Resolution Imaging Spectroradiometer
MNE	Ministry of Natural Resources and Environment, Mongolia
MRAM	Mineral Resources Authority of Mongolia
MSS	Multi-Spectral Scanner
MTU	Mongolian Technical University
NASA	National Aeronautics and Space Administration
NAMHEM	National Hydrometeorological Service
NDVI	Normalized Difference Vegetation Index
NDMI	Normalized Difference Moisture Index
NDVI	Normalized Difference Vegetation Index
NDWI	Normalized Difference Water Index
NFI	National Forest Inventory
NFP	National Forest Policy
NGRDI	Normalized Green Red Difference Index
NGO	Non-Governmental Organisation
NOAA	National Oceanic and Atmospheric Administration
NIR	Near-Infrared
NRAM	Mineral Resources Authority of Mongolia
NRMSE	Normalized Root Mean Square Error
NSOM	National Statistical Office of Mongolia
NTP	Non-Timber Products
NUM	National University of Mongolia
NWFP	Non-Wood Forest Product
OA	Overall Accuracy
OBIA	Object Based Image Analysis
OLI	Operational Land Imager
PA	Producer Accuracy
PCA	Principal Component Analysis
QB	QuickBird
r	Pearson Correlation Coefficient
REDD+	Reducing Emissions from Deforestation and Forest Degradation
RE	Red Edge
RE	RapidEye
RF	Random Forest
RGB	red, green, blue
RMSE	Root Mean Square Error
ROA	Remotely Operated Aircraft
RPA	Remotely Piloted Aircraft
RPV	Remotely Piloted Vehicle
RTK	Real Time Kinematic

RTM	Radiative Transfer Model
S2A	Sentinel-2A
SAVI	Soil-Adjusted Vegetation Index
SfM	Structure from Motion
SIFT	Scale-Invariant Feature Transform
SINDVI	Seasonally Integrated NDVI
SMOS	Soil Moisture and Ocean Salinity (Earth observation satellite)
SNAP	Sentinel Application Platform
SNR	Signal To Noise Ratio
SPA	Strictly Protected Area
SPIE	The international society for optics and photonics
SPOT	Satellite Pour l'Observation de la Terre
SRTM	(Earth) Shuttle Space Radar Topography Mission
SITE	Simulation of Terrestrial Environments
SWIR	Shortwave Infra-Red
SVM	Support Vector Machine
TB	Total Biomass
TBD	To Be Defined
TCB	Tasseled Cap Brightness
TCG	Tasseled Cap Greenness
TCW	Tasseled Cap Wetness
TIN	Triangulated Irregular Network
TIRS	Thermal Infrared Sensor (Landsat)
TM	Thematic Mapper
ToA	Top of Atmosphere
TWI	Topographic Wetness Index
TZ	Technische Zusammenarbeit (technical cooperation)
UA	User Accuracy
UAV	Unmanned Aerial Vehicle
UAV BT	Block Triangulation of image data acquired from an UAV
UAV-DSM	Digital Surface Model which was generated out of image data taken from an UAV
UAS	Unmanned Aircraft System consists of an Unmanned Aircraft (UA), a Control System (CS) a Ground Control System (GCS) and a communications data link between the UA and the CS
UHF	Ultra High Frequency
UNCED	United Nations Conference on Environment and Development
UNDP	United Nations Development Programme
UNEP	United Nations Environmental Programme
UNFCCC	United Nations Framework Convention on Climate Change
USDA	United States Department of Agriculture
USFS	United States Forest Service
USGS	United States Geological Survey
UCT	Coordinated Universal Time
UTM	Universal Transverse Mercator
VCT	Vegetation Change Tracker

VHR	Very High Resolution
VHSR	Very High Spatial Resolution
VIs	Vegetation Indices
VNIR	Visible Near Infrared
VRML	Virtual Reality Modelling Language
VTOL	Vertical take-off and landing
WB	World Bank
WGS84	World Geodetic System 1984
WMO	World Meteorological Organisation
WRS	World-wide Reference System
WV2	WorldView-2 satellite
XML	Extensible Mark-up Language

12. Mongolian terms

Aimag	Province
Bag	Sub-district, smallest administrative unit (municipality)
Dzud	Adverse winter conditions, that make grazing impossible for the cattle.
	1) white dzud: grazing impossible due to snow cover
	2) black dzud: shortage of pasture grass due to dry summer conditions
	3) ice-dzud: grazing hampered due to frozen spring rain
Ger	Traditional bell tent (yurt) of the Mongolian nomads
Gol	River
Khashaa	Fenced confinement of a rectangular plot in a settlement
Nuur	Lake
Ovoo	Traditional, shamanistic conglomeration of stones (wood, Vodka bottles, silken scarfs) in pyramid shape; typical feature along roads and mountain passes as offerings to the deities
Soum	District
Tugrik (Tg)	Mongolian official currency. 1 EUR ± 3050 Tugrik (10/04/2020)
Uul	Mountain

13. List of figures

Figure captions have been curtailed whenever possible

14. List of tables

Table captions have been curtailed whenever possible

15. Appendices

15.1. Tree species classification results – resumption

15.1.1. Object-based classifications of dominant tree species discrimination

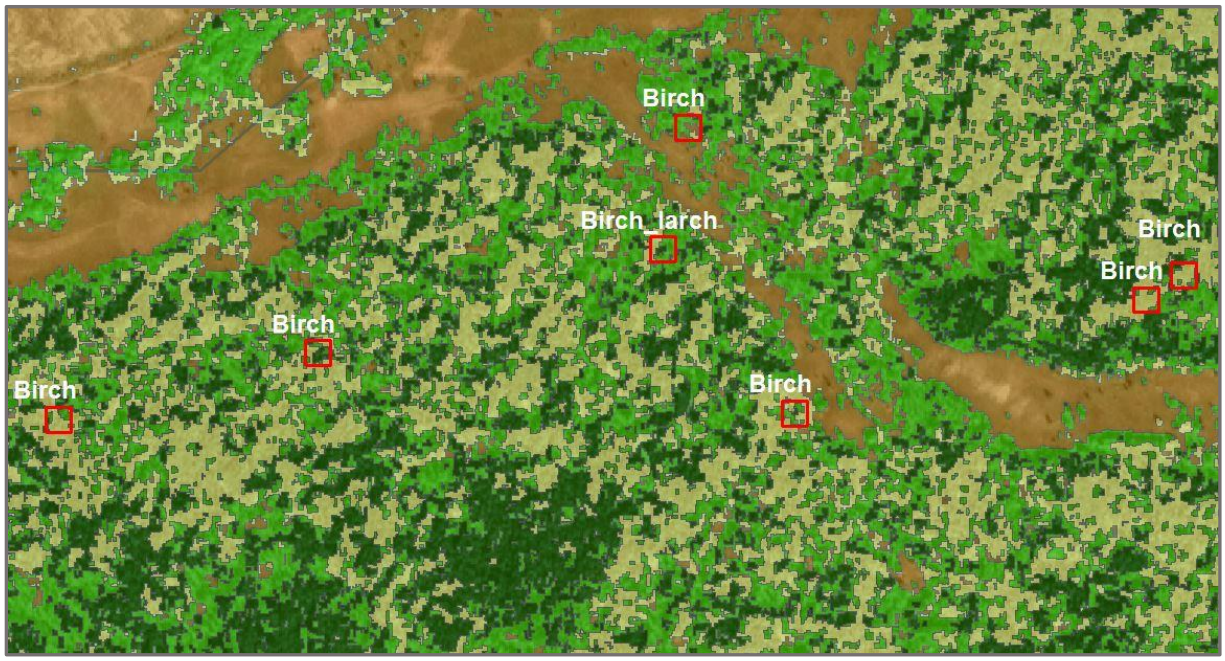

Figure 15.1: Example of misclassification on a Pléiades image (10/05/2015). The red boxes indicate the test plot boundaries, the labels the dominating tree species as found in the field. In some cases, the class birch was misclassified as light or even dark taiga (RF classifier).

Figure 15.2: Example of misclassification on a Pléiades image (10/05/2015). The red boxes indicate the shadow areas misclassified as dark taiga (RF classifier). The classification was superimposed on the Pléiades image.

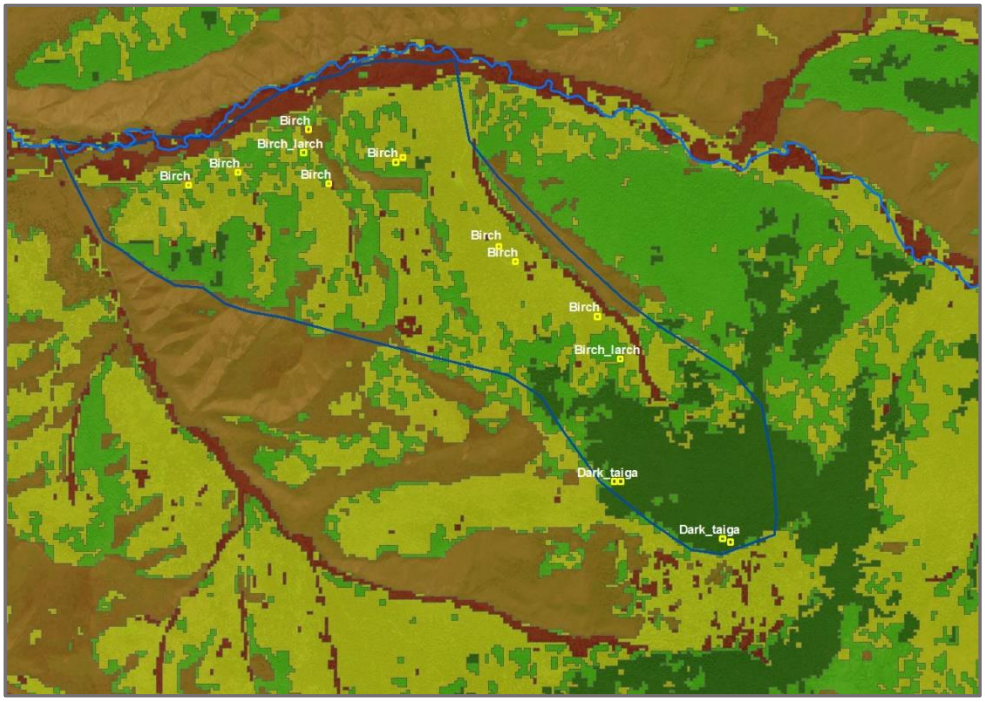

Figure 15.3: Object-based classification of Sentinel-2 image (09/07/2017). Random Forest (RF) classifier for dominant tree species classification was used. Classes depicted in graph: birch (yellow), light taiga (bright green), dark taiga (dark green), and grassland/soil (brown). Band selection of variant 1 (B12, B8, NDVI, NDWI) was used for image classification.

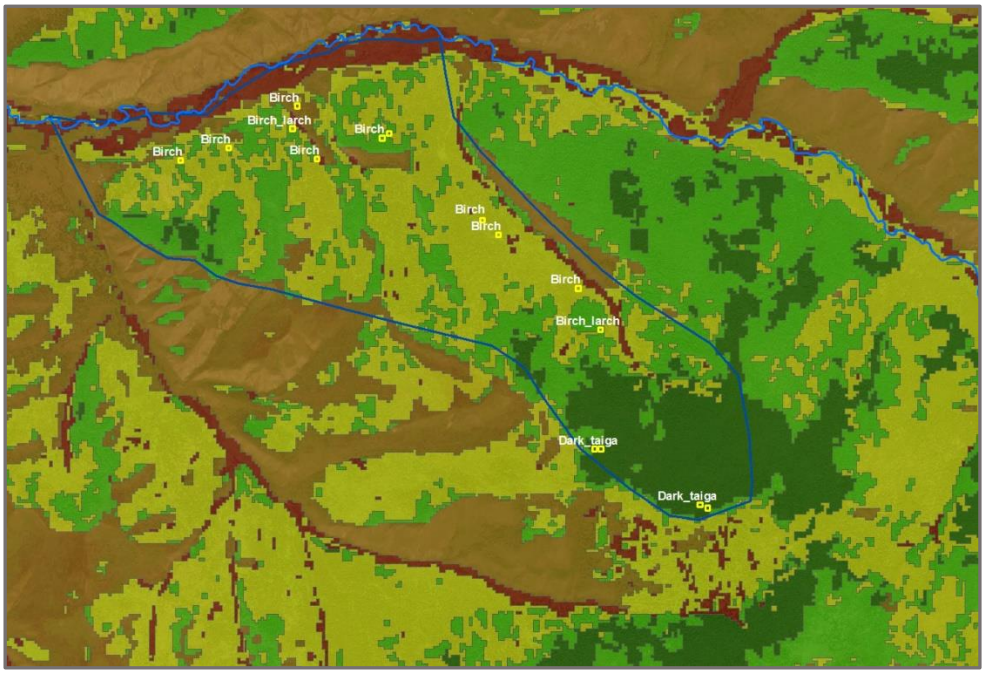

Figure 15.4: Object-based classification of Sentinel-2 image (09/07/2017). Random Forest (RF) classifier for dominant tree species classification was used. Classes depicted in graph: birch (yellow), light taiga (bright green), dark taiga (dark green), and grassland/soil (brown). Band selection of variant 2 (B12, B8) was used for image classification.

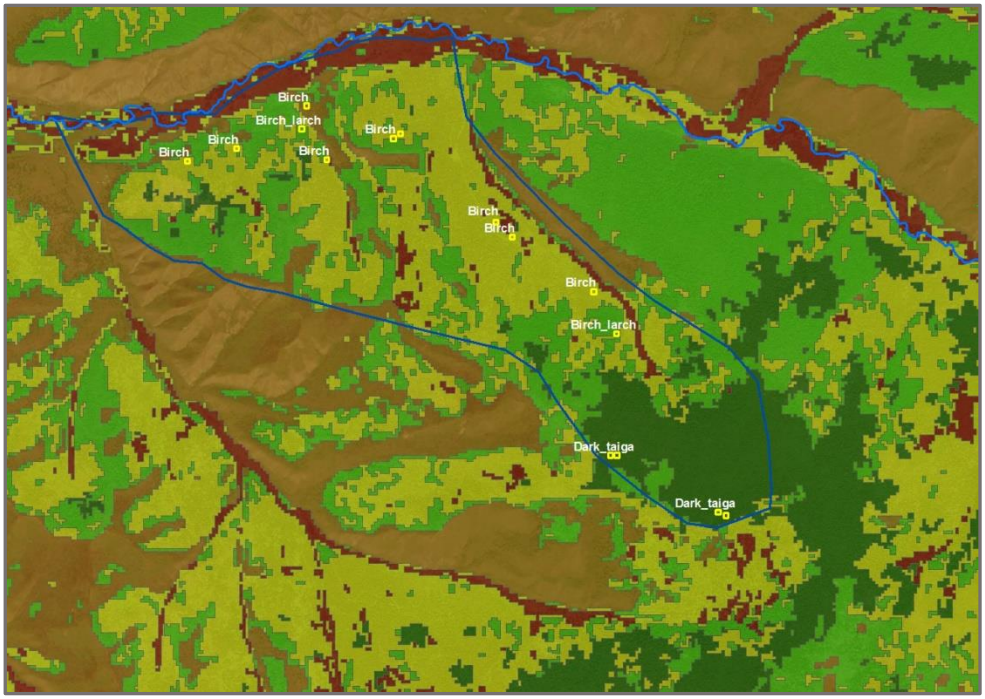

Figure 15.5: Object-based classification of Sentinel-2 image (09/07/2017). Random Forest (RF) classifier for dominant tree species classification was used. Classes depicted in graph: birch (yellow), light taiga (bright green), dark taiga (dark green), and grassland/soil (brown). Band selection of variant 3 (B12, NDVI, NDWI) was used for image classification.

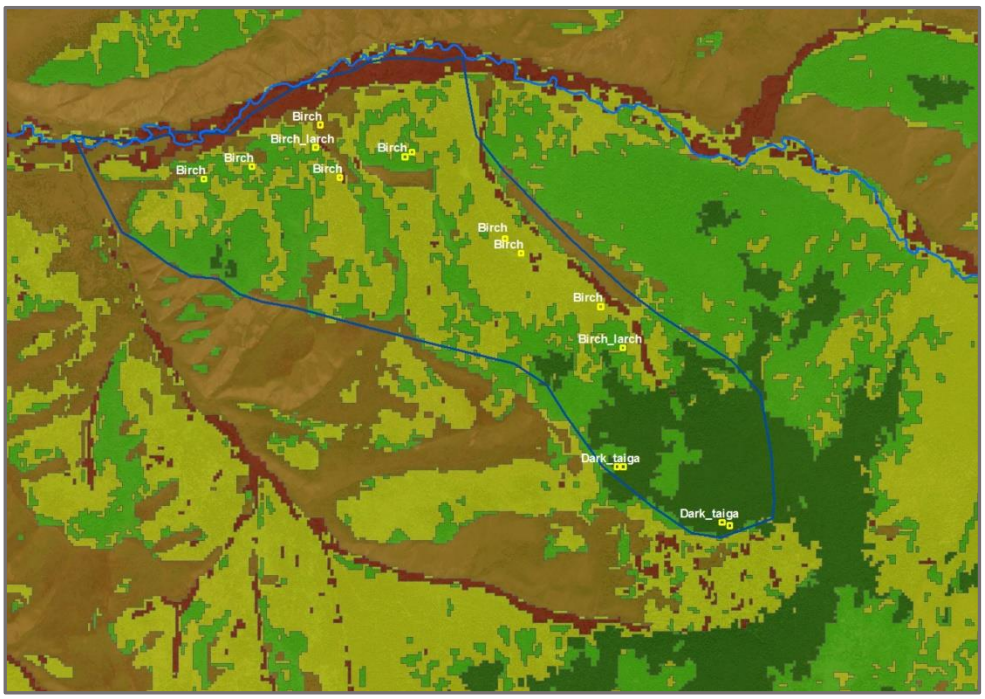

Figure 15.6: Object-based classification of Sentinel-2 image (09/07/2017). Support Vector Machine (SVM) classifier for dominant tree species classification was used. Classes depicted in graph: birch (yellow), light taiga (bright green), dark taiga (dark green), and grassland/soil (brown). Band selection of variant 1 (B12, B8, NDVI, NDWI) was used for image classification.

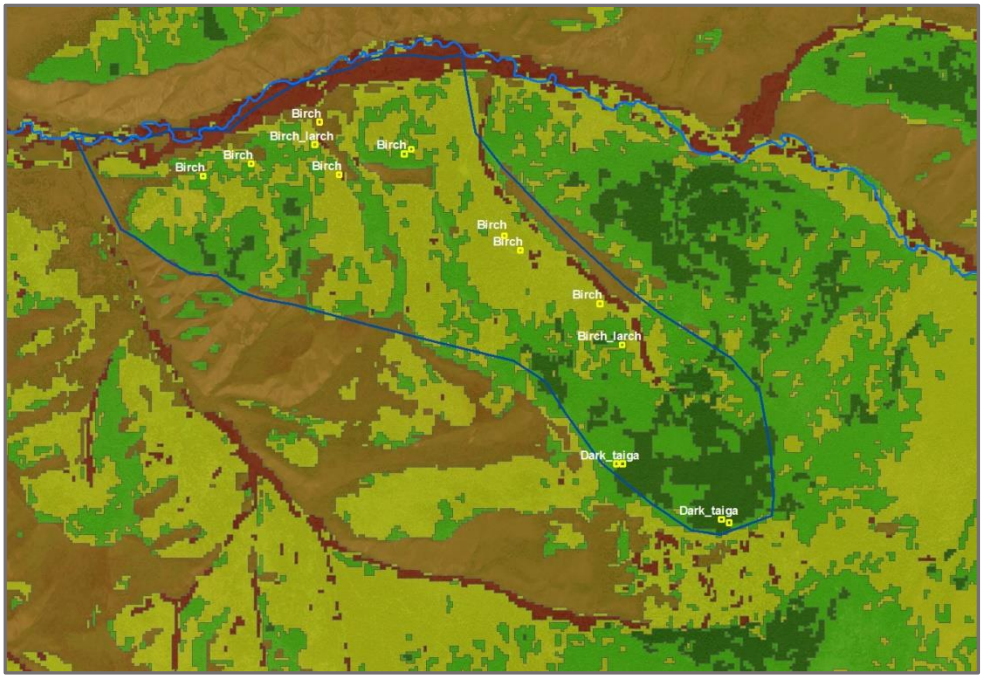

Figure 15.7: Object-based classification of Sentinel-2 image (09/07/2017). Support Vector Machine (SVM) classifier for dominant tree species classification was used. Classes depicted in graph: birch (yellow), light taiga (bright green), dark taiga (dark green), and grassland/soil (brown). Band selection of variant 2 (B12, B8) was used for image classification.

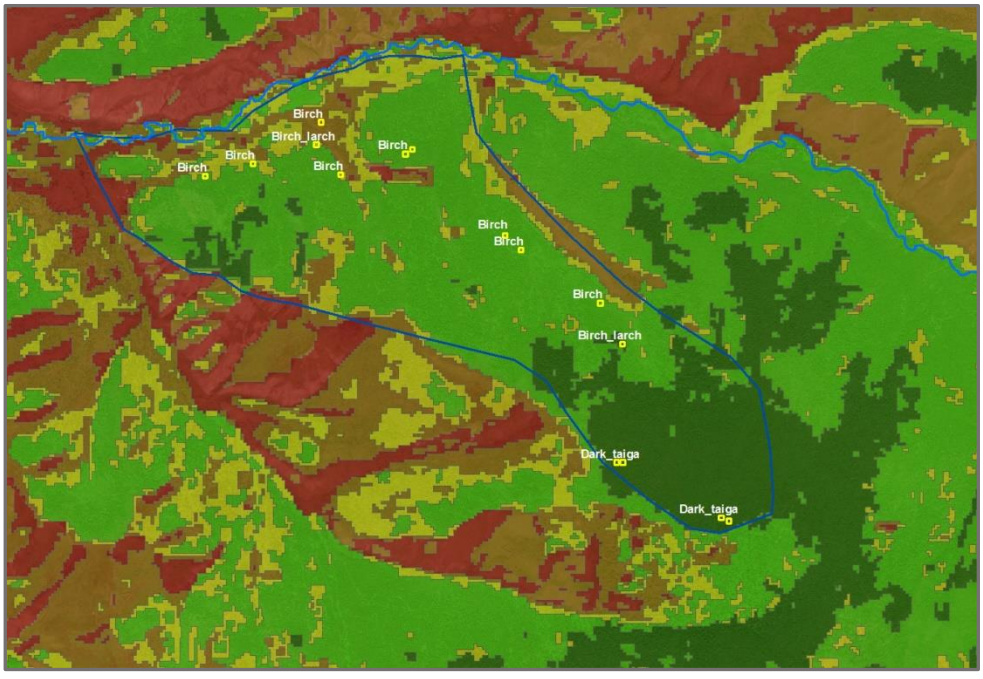

Figure 15.8: Object-based classification of Sentinel-2 image (09/07/2017). Support Vector Machine (SVM) classifier for dominant tree species classification was used. Classes depicted in graph: birch (yellow), light taiga (bright green), dark taiga (dark green), and grassland/soil (brown). Band selection of variant 3 (B12, NDVI, NDWI) was used for image classification.

15.1.2. Pixel-based classifications of dominant tree species discrimination

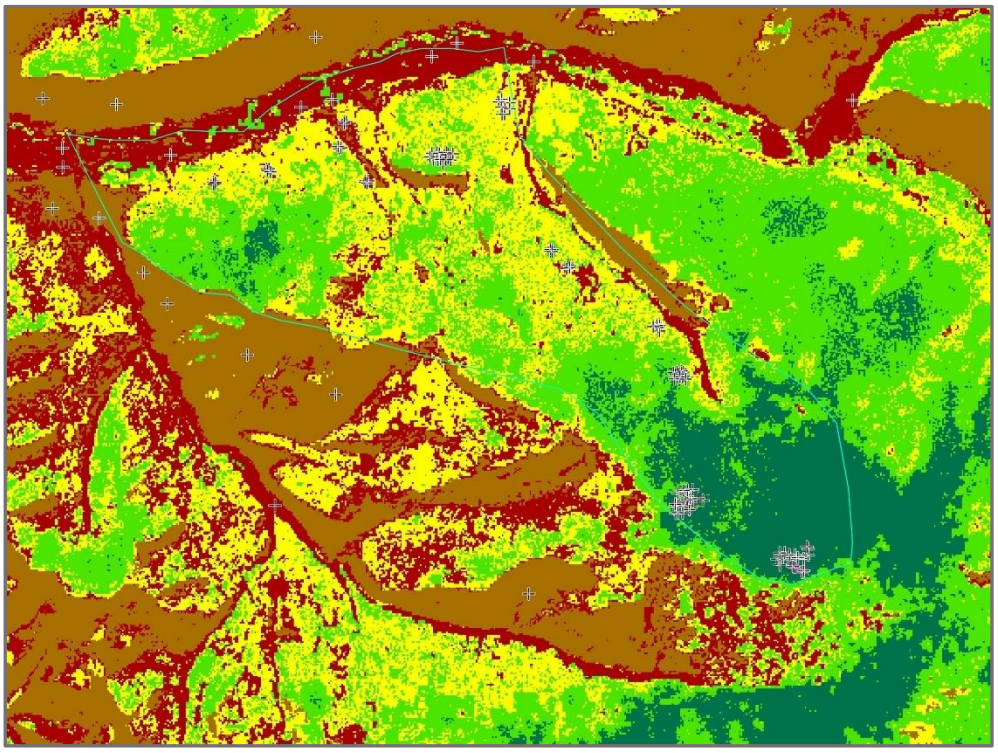

Figure 15.9: Pixel-based classification of Sentinel-2 image (09/07/2017) – dominant tree species. Random Forest classifier was used for bands variant 4 (B3, B8, B11, NDWI). The classification verification points are marked with a cross. Portrayed classes are: birch (yellow), light taiga (bright green), dark taiga (dark green), dry grass/soil (brown), green grass (red).

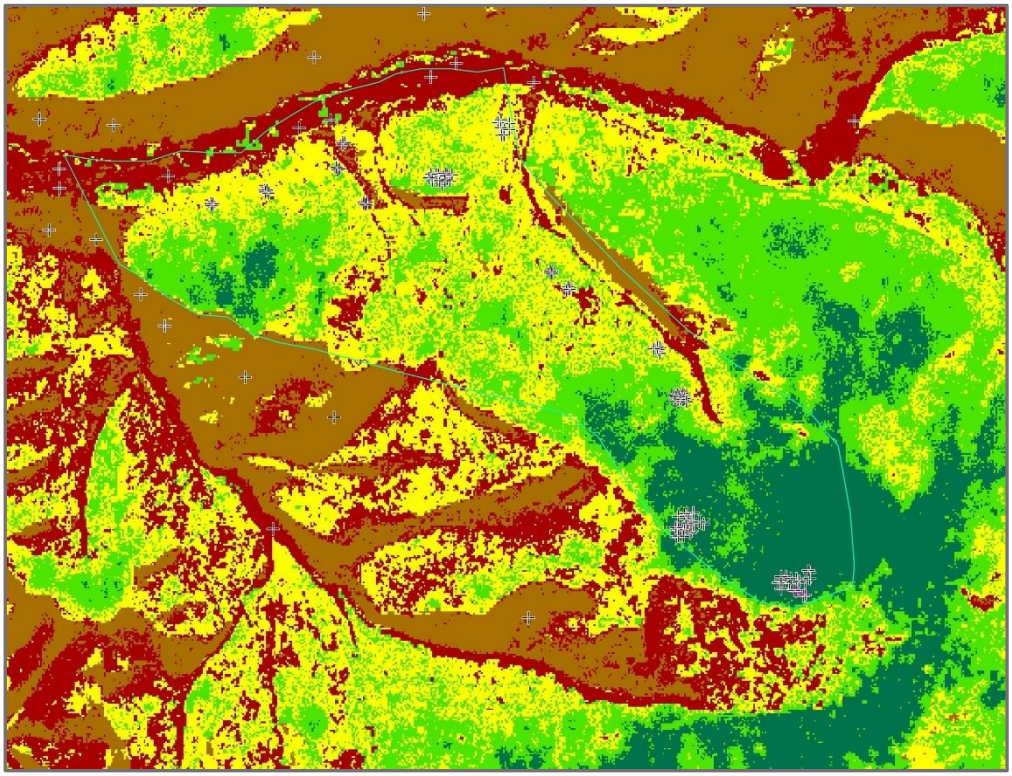

Figure 15.10: Pixel-based classification of Sentinel-2 image (09/07/2017) – dominant tree species. Random Forest classifier was used for bands variant 2 (B8, B11). The classification verification points are marked with a cross. Portrayed classes are: birch (yellow), light taiga (bright green), dark taiga (dark green), dry grass/soil (brown), green grass (red).

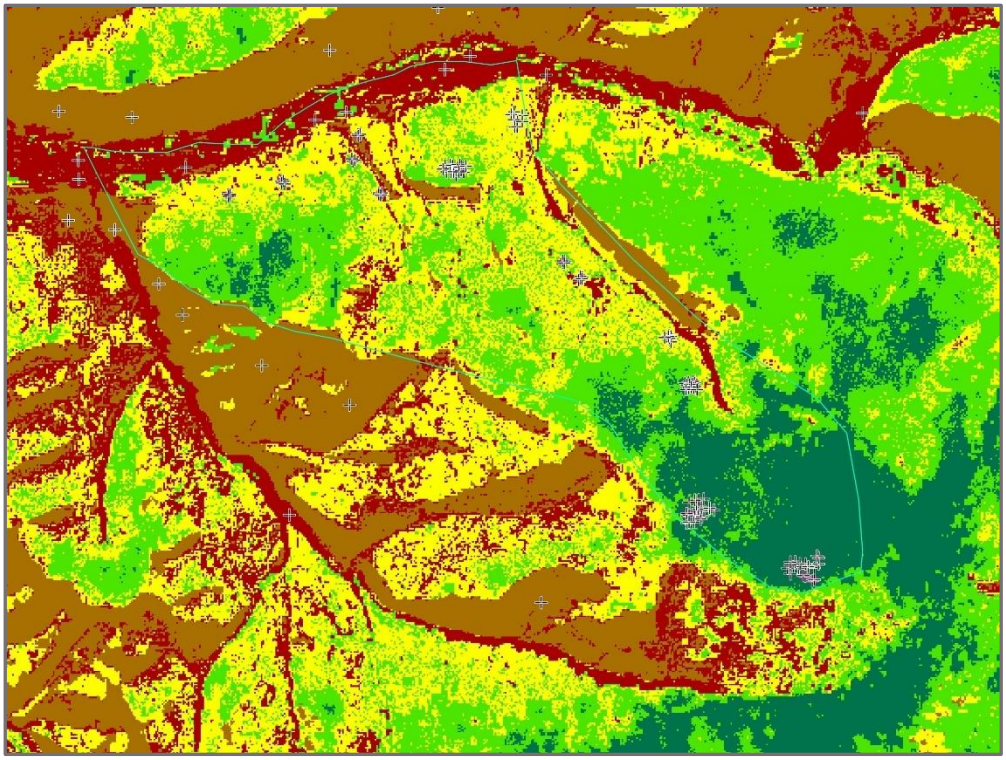

Figure 15.11: Pixel-based classification of Sentinel-2 image (09/07/2017) – dominant tree species. Random Forest classifier was used for bands variant 3 (B11, NDVI, NDWI). The classification verification points are marked with a cross. Portrayed classes are: birch (yellow), light taiga (bright green), dark taiga (dark green), dry grass/soil (brown), green grass (red).

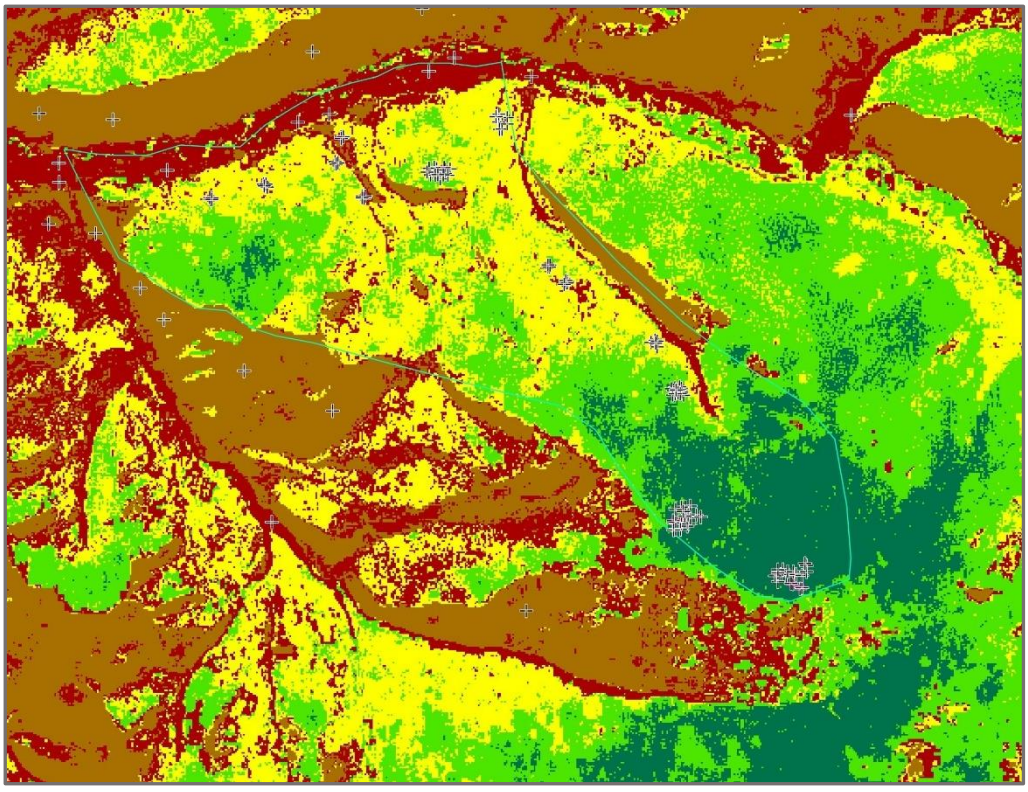

Figure 15.12: Pixel-based classification of Sentinel-2 image (09/07/2017) – dominant tree species. Support Vector Machine classifier was used for bands variant 4 (B3, B8, B11, NDWI). The classification verification points are marked with a cross. Portrayed classes are: birch (yellow), light taiga (bright green), dark taiga (dark green), dry grass/soil (brown), green grass (red).

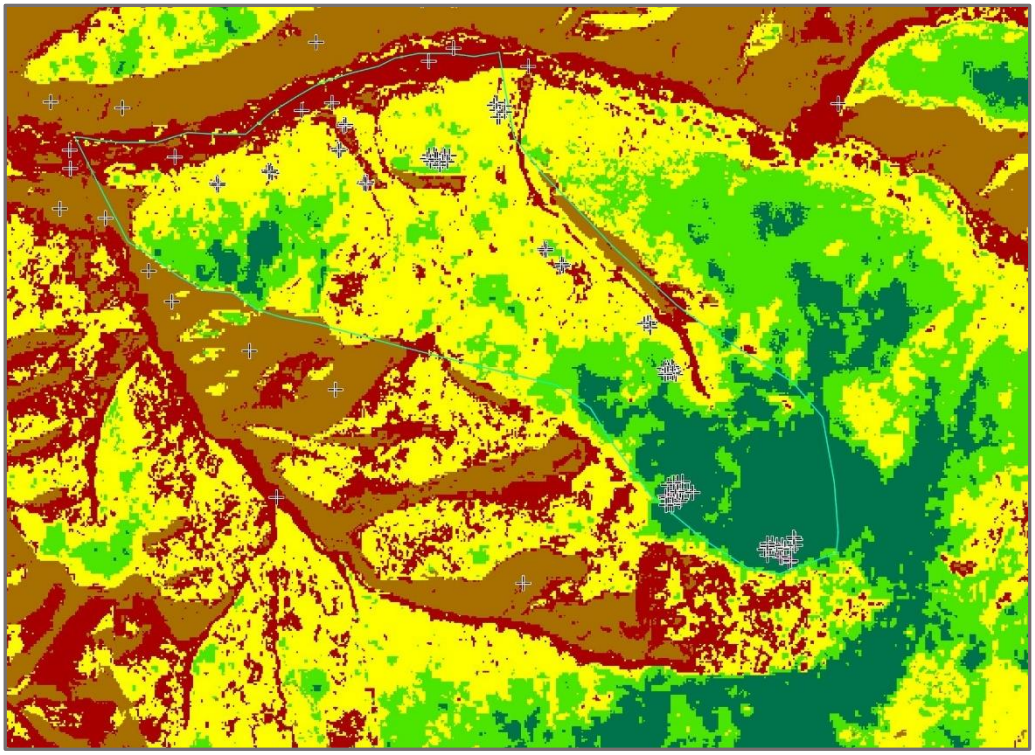

Figure 15.13: Pixel-based classification of Sentinel-2 image (09/07/2017) – dominant tree species. Support Vector Machine classifier was used for bands variant 2 (B8, B11). The classification verification points are marked with a cross. Portrayed classes are: birch (yellow), light taiga (bright green), dark taiga (dark green), dry grass/soil (brown), green grass (red).

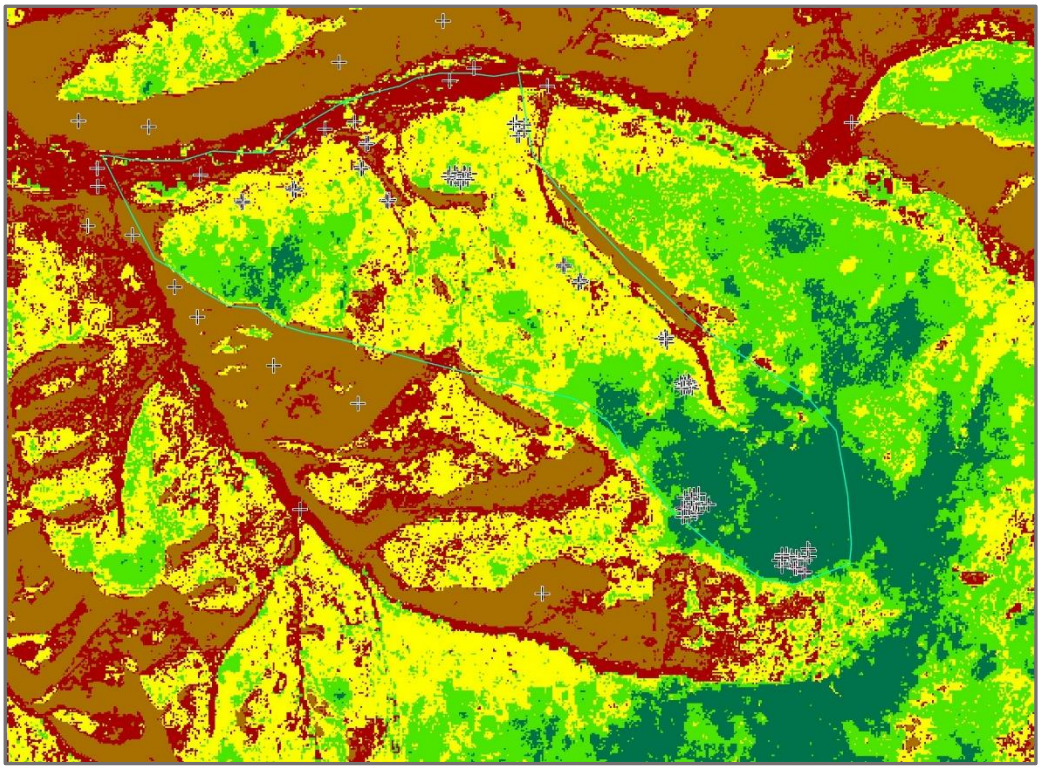

Figure 15.14: Pixel-based classification of Sentinel-2 image (09/07/2017) – dominant tree species. Support Vector Machine classifier was used for bands variant 3 (B11, NDVI, NDWI). The classification verification points are marked with a cross. Portrayed classes are: birch (yellow), light taiga (bright green), dark taiga (dark green), dry grass/soil (brown), green grass (red).

15.2. Photo documentation

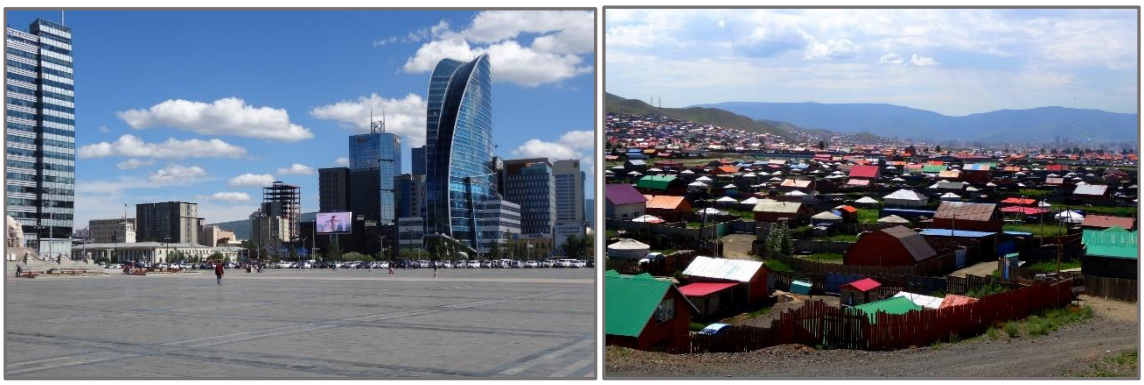

Figure 15.15: Contrasting impressions of the capital Ulaanbaatar. The modern and vibrant city centre (left) and the squatter camps in the north of the city centre, where more than one million people live (right).

Figure 15.17: Devastating fire in compartment 435 (left). Even fire-resistant larch trees were severely affected and charred (right).

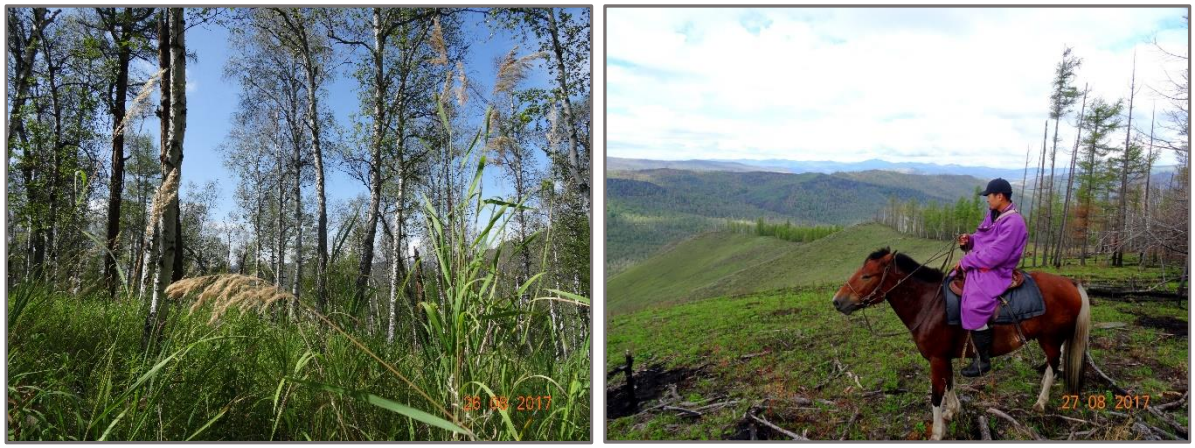

Figure 15.16: Dense carpets of Calamagrostis grass in a birch stand (left). View from a dark taiga vantage point overlooking the rolling hills of the surroundings of the compartment 435 with my assistant Enkhbat on a horse's back (right).

16. Credits

Numerous people encouraged and helped me throughout the course of this assignment.

I first want to thank my supervisor Prof. Dr. Martin Kappas for his unrelenting mentorship. He not only provided the main idea of the topic of this thesis, but also granted sponsorship to get me embarked on this adventurous trip to Mongolia. I am truly grateful for his guidance, knowledge, experience, and patience throughout.

My dear colleagues of the Institute of Cartography, GIS and Remote Sensing also deserve special credit for their extremely fruitful discussions on remote sensing and forestry topics and for making things running more smoothly. In this respect I would like to mention Martina Beck, Dr. Stefan Erasmi (now with J.H. v. Thünen-Institut, Braunschweig), Elbek Erdanaev, Dr. Michael Klinge (now with Department of Physical Geography), Hung Trong Nguyen, Dr. Michael Schlund and Dr. Daniel Wyss. Timo Lehmann and Sören Merkle sustained great technical support.

Dr. Choimaa Dulamsuren (now with Albert-Ludwigs-Universität Freiburg, Chair of Applied Vegetation Ecology) and Oyudari Vova were extremely supportive by aiding me with Mongolian specific issues and in translating Mongolian websites. Great merit has to be extended to Dr. Choimaa Dulamsuren in her selfless efforts to avoid a number of scientists (including myself) of getting apprehended and charged for arson during our stay at Thunkel.

I also wish to thank the staff of the GIZ at Ulaanbaatar, who never got tired of entertaining my numerous requests. In particular I would like express my gratitude to Dr. Klaus Schmidt-Corsitto and Dr. Dan Altrell for sharing their expertise and organising my transport to and stay at the research station camp at Thunkel. The contribution of my assistant Enkhbat was of extreme value in carrying out the field work and in conversing with the local people.

The following people at the Faculty of Forest Sciences and Forest Ecology, Department of Forest Inventory and Remote Sensing, generously and proficiently provided support with regard to forest inventory and remote sensing specific issues, namely: Dres. Lutz Fehrmann, Hans Fuchs, Paul Magdon and Nils Nölke. Their contribution is greatly appreciated.

I am also extremely indebted to Prof. Dr. Thomas Seifert (Albert-Ludwigs-Universität Freiburg, Chair of Forest Growth and Dendroecology) and Anton Kunneke (University of Stellenbosch, Forestry Department, South Africa) for their invaluable talks and input in issues related to UAV mission planning and data analysis. We not only share true South African experiences, but also a long-term friendship and our passion for flying objects.

My thanks also goes to Dr. Jennifer Lorenz at the Centre for Statistics at the Georg-August University of Göttingen, for her guidance in the statistical analysis of this study.

I also would like to express my deepest gratitude to my brother, Helge Vogt, at Edmund Optics Inc., for the immensely rewarding talks on lens systems and sensors.

I gratefully acknowledge the support of Thomas Klawunn, who is a professional photographer. He spared no effort in providing time and equipment to carry out the necessary lens and colour calibration of the UAV camera.

It was great pleasure for me to work with numerous people at Gibs Engineering, Nürnberg, from whom I gained a lot of knowledge in the fields of UAV remote sensing, soldering techniques, and the practical application thereof in the field of civil engineering. This helped a great deal in laying a sound foundation on my current expertise.

Finally, thank you to my family and friends for their great help with their support and encouragement throughout the endeavour of this thesis. I am deeply indebted to my parents, in particular, to the memory of my Dad who greatly appreciated and supported my venture into science.

17. Curriculum Vitae

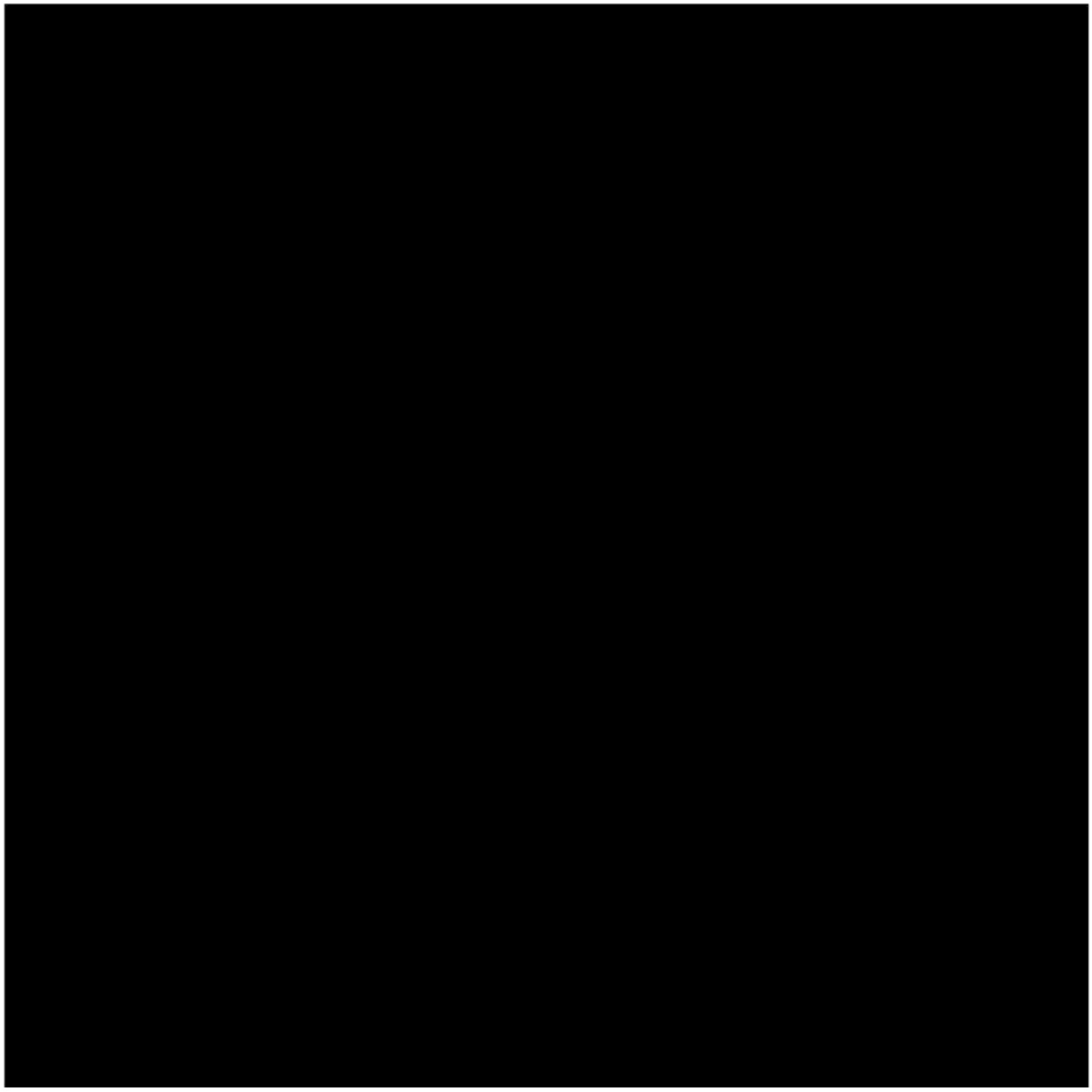

Publication related to thesis:

Seifert, E.; Seifert, S.; Vogt, H.; Drew, D. and van Aardt, J. *et al.* **2019** Influence of drone altitude, image overlap, and optical sensor resolution on multi-view reconstruction of forest images. *Remote Sensing* 11, 1–19.

18. Declaration

Declaration of Authorship

I confirm, that this assignment is my own work and that I have not sought or used any inadmissible help of third parties to produce this work, and that I have clearly referenced all sources used in the work. I have fully referenced and used inverted commas for all text directly or indirectly quoted from a source.

I have clearly indicated the presence of all paraphrased material with appropriate references.

I have acknowledged appropriately any assistance I have received in addition to that provided by my supervisor/adviser.

I have not copied from the work of any other candidate.

I have not used the services of any agency providing specimen, model or ghost-written work in the preparation of this thesis.

This work has not yet been submitted to another examination institution, either partially or full – neither in Germany nor outside Germany – neither in the same nor in a similar way and has not yet been published.

Göttingen, 08.04.2021

_____

(signature) Holger Vogt